Delft University of Technology, Faculty of Aerospace Engineering

Design of a

Primary Mirror Fine Positioning Mechanism

for a Deployable Space Telescope

S.M. Pepper

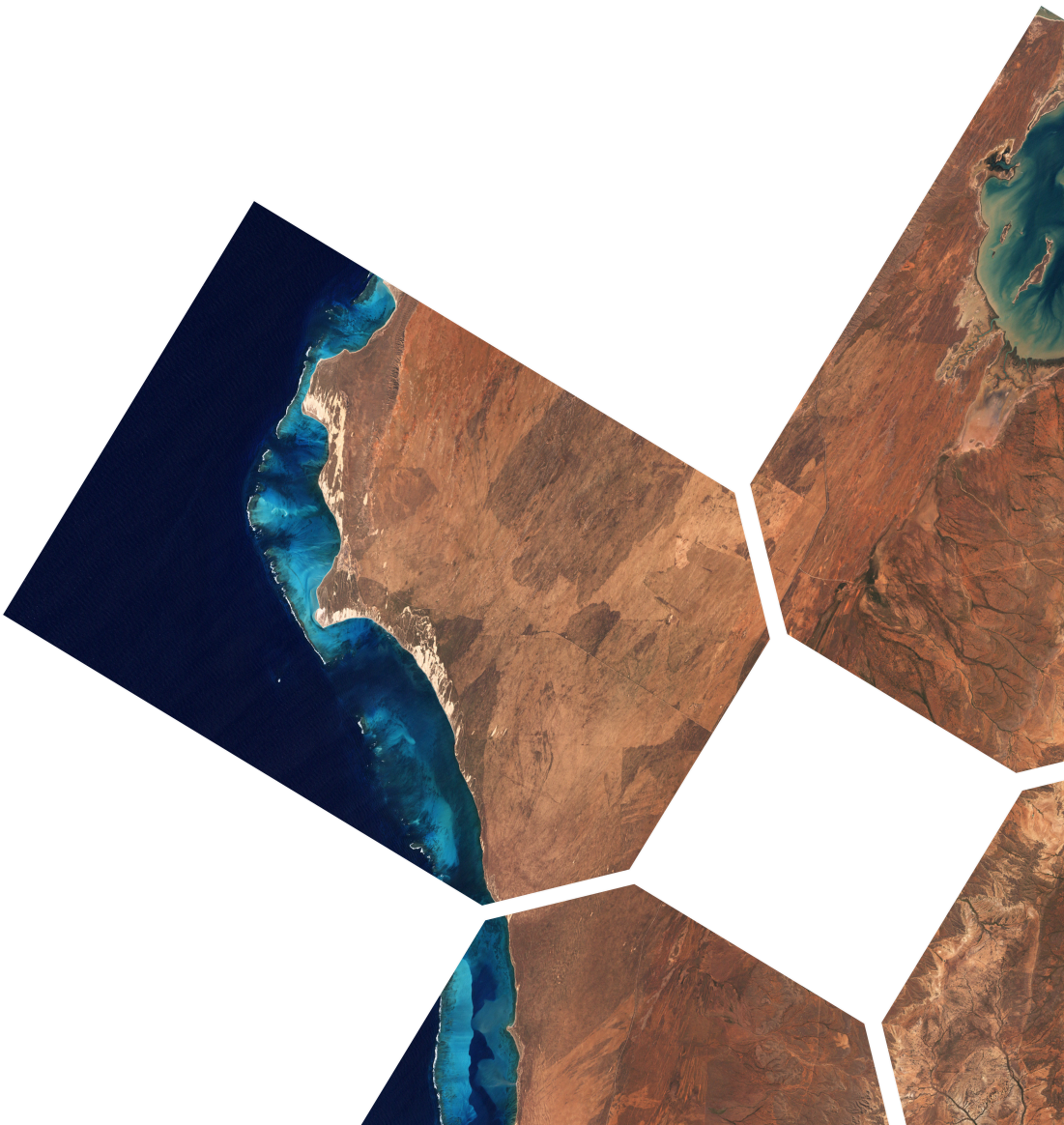

TU Delft

Design of a

Primary Mirror Fine Positioning Mechanism

for a Deployable Space Telescope

by

S.M. Pepper

in partial fulfilment of the requirements for the degree of

Master of Science
in Aerospace Engineering

at the Delft University of Technology,
to be defended publicly on Tuesday November 27, 2018 at 13:00.

Student number:	4616960	
Thesis committee:	A/ Prof. dr. ir. A. Cervone,	TU Delft, Chair
	A/ Prof. dr. ir. J. M. (Hans) Kuiper,	TU Delft, Supervisor
	Dr. ir. B. C. Root,	TU Delft

This thesis is confidential and cannot be made public until November 27, 2019.

Cover image: Ningaloo Reef, along the Western Australian coast. Taken by Landsat 7 [3].

TU Delft

Summary

The TU Delft Deployable Space Telescope (DST) proposes to meet increasing demand for high spatio-temporal resolution Earth observation imagery by reducing the mass, volume and launch cost of space telescopes with the use of segmented deployable optics. A consequence of this approach is the need to approximate a single optical surface with several discrete elements. Their alignment must be maintained in orbit despite deployment errors and perturbations from thermo-elastic drifts and structural vibrations. To that end, a three degree of freedom (DOF) piston/ tip/ tilt fine positioning mechanism has been proposed to actively align the primary mirror segments in orbit.

Two architectures for the Primary Mirror Active Optics (PMAO) mechanism were generated. A trade-off based on first order estimates of their structural, thermal and kinematic performance lead to selection of a final concept. The chosen design uses standard high precision fabrication techniques and high Technology Readiness Level piezoelectric actuators. A preliminary thermo-mechanical design of the mechanism was synthesised and its mechanical performance verified in terms of requirements based on modelling with an efficient, low order finite element model.

The results showed that the mechanism was able to support the mirror through launch without a hold down mechanism; has a piston step size of 10 nm; a range of $\pm 4\ \mu m$ in piston and $\pm 9\ \mu rad$ in tip/ tilt with accuracies of $0.005 \pm 0.780\ \mu m$ (2σ) in position and $0.000 \pm 0.041\ \mu rad$ (2σ) in rotation respectively. A Monte Carlo ray tracing analysis showed that the PMAO was able to successfully align the mirror segments in all considered deployment scenarios. With the addition of continuous wavefront error corrections from the DST Aberration Correction System (ACS), the PMAO and ACS delivered a Strehl ratio greater than 0.8 for all deployment scenarios on the central field within the given tolerance budgets.

This work has shown that it is feasible, at a preliminary level, align a deployable segmented primary mirror in low Earth orbit with a 3DOF mechanism based on existing technology, thus enabling the next generation of very high resolution Earth observation space telescopes.

Keywords: *Deployable Space Telescope, space telescope, Earth observation, fine positioning mechanism, flexures.*

Preface

Though tempting to wax lyrical about journeys and transitions, I'll keep this note short and sweet because the rest of this report is patently not.

I owe a great thanks to Hans Kuiper for giving me the academic freedom to pursue my own ideas and methods within the DST team, and reigning me in when I got lost in the details. Dennis Dolkens provided critical expertise and numerous late nights integrating the PMAO finite element model into the telescope end to end performance model. His deep knowledge of space optics, dedication and openness played no small part in the completion of the final phase of this project.

Werner van de Sande and Jaap Meijaard at the TU Delft Faculty of Mechanical, Maritime and Materials engineering provided invaluable tuition, advice and support throughout the *SPACAR* modelling. I am also grateful to Frank Claeyssen from Cedrat Technologies for a fruitful discussion about fine positioning mechanisms for space optics, which gave me the confidence to pursue the concept that ultimately became the PMAO mechanism.

To the DST team members, I'm grateful to have spent the last year with such an excellent group of motivated and light hearted friends. When I look back at my time at TU Delft I will most fondly remember their attempts to teach an aussie the finer points of living like a Dutchman in the rain. *Het was gezellig.*

Above all else, thank you to my Mum, who taught me to put one foot in front of the other in pursuit of a dream.

S.M. Pepper
Delft, November 2018

Contents

List of Figures

List of Tables

List of Symbols

Upper Case		*Unit*
A	Area	m^2
A_{COM}	Attitude matrix for mirror centre of mass	rad
C	Constraint line	–
C_{ij}	Constraint space	–
D	Mirror diameter	m
D_i	Universal joint inner diameter	m
D_O	Universal joint outer diameter	m
E	Modulus of elasticity	Pa
F_{ij}	Freedom space	–
F_L	Launch load	N
G	Geometric stiffness matrix	N/m
GF	Gauge factor	–
I	Second moment of area	m^4
K	Structural stiffness matrix	N/m
L	Length	m
L_{BP}	Support bipod flexure length	m
$L_{BP,trans}$	Strut transition length	m
$L_{I,II,II,IV}$	Length of actuator in kinematic calculations	m
L_P	In-plane constraint flexure length	m
L_S	Universal joint flexure length	m
L_0	Initial length	m
M	Mass matrix	kg
M	Bending moment	Nm
M_L	Moment from launch load F_L	Nm
$\mathbf{O_{Bi}}$	Local coordinate frame for bipod i	–
$\mathbf{O_M}$	Fixed mechanism coordinate frame	–
$\mathbf{O_{MF}}$	Body fixed moving frame coordinate frame	–
$\mathbf{O_O}$	Telescope optical coordinate frame	–
P_{cr}	Critical (Euler) buckling load	N
$\Delta\mathbf{P}$	Perturbation vector of segment pose	–
Q	Heat	J
$\mathcal{R}$	Rotation matrix	–
R	Freedom line	–
R_B	Bipod mounting radius	m
R_{Bij}	Load on strut j in bipod i	N
R_d	Bounding radius for bipod baselines d_B	m
R_{FF}	Fixed frame cylinder radius	m
R_M	Actuator mounting radius	m
R_{max}	Maximum allowable radius of all parts in usable volume	m
R_P	In-plane constraint attachment radius	m
R_S	Mirror support radius	m
R_0	Initial resistance of strain gauge	Ω
S_Y	Yield strength	Pa
T	Homogeneous transform matrix	–
T	Translation freedom	–

Lower Case		*Unit*
b	Flexure width (breadth)	m
b_{BP}	Support bipod flexure width	m
b_P	In-plane constraint flexure width	m
b_S	Universal joint flexure width	m
c	Distance to neutral axis of a beam section	m
c_p	Specific heat capacity	$J/kg.K$
d_B	Support bipod baseline length (strut spacing)	m
e	Eccentricity of a static load	–
e_P	Parasitic pose error	m, rad
e_{RC}	Remote centre pose error	m, rad
e_T	Total pose error	m, rad
$\mathbf{f_i}$	Buckling load	N
f_n	Natural frequency	Hz
$\mathbf{f_0}$	Reference load	N
g	Acceleration due to Earth gravity	m/s^2
h	Altitude	m
h	Distance from $\mathbf{O_{MF}}$ to mirror centre of mass in Z_M direction	m
h_{FF}	Fixed frame cylinder height	m
k	Stiffness	N/m
k	Thermal conductivity	$W/m.K$
l_0	Initial Z_M distance between mechanism interface planes	m
m	Mass	kg
m_M	Mass of a mirror segment	kg
n	Safety factor	–
p	Distance between radii R_B & R_S in $X_{MF}Y_{MF}$ plane	m
q	Heat flux	W/m^2
q	Distance between mirror COM and backplane	m
$\mathbf{r}$	Position vector	m
$\mathbf{r_F}$	Position of launch load with respect to $\mathbf{O_{MF}}$	m
r_o	Radius of circle for moving frame plate load application	m
s_B	Strut length	m
t	Flexure thickness	m
t_B	Universal joint end interface thickness	m
t_{BP}	Support bipod flexure thickness	m
$t_{BP,base}$	Strut end thickness	m
t_{FF}	Fixed frame plate thickness	m
t_{FFc}	Fixed frame cylinder thickness	m
t_{MF}	Moving frame plate thickness	m
t_P	In-plane constraint flexure thickness	m
t_S	Universal joint flexure thickness	m
$\mathbf{v}$	Eigenmode or linear buckling mode	–
$\Delta_{z,M}$	Translation (piston) of moving frame $\mathbf{O_{MF}}$ along Z_M axis	m

Greek		*Unit*
α	Coefficient of Thermal Expansion	$\mu\epsilon/K$
α	Orientation of actuators at mechanism/ base interface	rad
β	Orientation of actuators at mechanism/ mirror interface	rad
$\delta_{x,y,z}$	Small displacement in x,y or z direction	m
ΔT	Temperature difference	K
ϵ	Strain	m/m
$\theta_{x,M}$	Rotation of moving frame $\mathbf{O_{MF}}$ about X_M axis	rad
$\theta_{y,M}$	Rotation of moving frame $\mathbf{O_{MF}}$ about Y_M axis	rad
λ	Eigenfrequency	$(rad/s)^2$
λ	Wavelength	m
ν	Poisson's ratio	–
ρ	Density	kg/m^3
σ	Standard deviation	–
σ	Stress	Pa
σ_{eq}	Equivalent (von Mises) stress	Pa
τ	Shear stress	Pa
τ_{COM}	Actual (simulated) pose of mirror centre of mass	–
τ^*_{COM}	Ideal pose of mirror centre of mass	–
$\overline{\tau}_{COM}$	Expected pose of mirror centre of mass	–
ψ	In-plane constraint and bipod assembly orientation angle	rad
ω	Frequency	$rad/s, Hz$

Nomenclature

ACS	Aberration Correction System
ADSNL	Airbus Defence & Space Netherlands B.V.
AFTMA	Annular Field Three Mirror Anastigmat
AIT	Assembly, Integration, Testing
AOCS	Attitude & Orbital Control System
APA	Amplified Piezoelectric Actuator
CAD	Computer Aided Design
CDHS	Command & Data Handling System
CFRP	Carbon Fibre Reinforced Plastic
CFSM	Cryogenic Fine Steering Mirror
COM	Centre of Mass
COTS	Commercial Off The Shelf
CTE	Coefficient of Thermal Expansion
DC	Direct Current
DCM	Direction Cosine Matrix
DM	Deformable Mirror
DOF	Degree of Freedom
DST	Deployable Space Telescope
ECSS	European Cooperation for Space Standardisation
E-ELT	European Extremely Large Telescope
EMC	Electromagnetic Compatibility
EO	Earth Observation
ETEP	End To End Performance (model)
EU	European Union
FACT	Freedom And Constraint Topology
FEA	Finite Element Analysis
FEM	Finite Element Modelling
FF	Fixed Frame
FM	Fold Mirror
FORTA	Fast Optical Ray Tracing Algorithm
FR	France
FS	Factor of Safety
GF	Gauge Factor
GSD	Ground Sampling Distance
HDRM	Hold Down & Release Mechanism
HTM	Homogeneous Transform Matrix
IC	Instant Centre
IDEF0	Icam DEFinition for Function Modelling
IPC	In Plane Constraints
ITAR	International Traffic in Arms Regulations
JWST	James Webb Space Telescope
LEO	Low Earth Orbit
LEOP	Launch & Early Operations
M1	Primary Mirror
M2	Secondary Mirror
M2MM	(Euclid) M2 Mirror Mechanism
M3	Tertiary Mirror
MF	Moving Frame
MS	Margin of Safety
MS	Multispectral (detector)
NGO	Non-Governmental Organisation
NLA	Nanometric Linear Actuator
OASPL	Overall Acoustic Sound Pressure Level
OBC	On-Board Computer
OEM	Original Equipment Manufacturer
OPD	Optical Path Difference
PCB	Printed Circuit Board
PCD	Pitch Circle Diameter
PMAO	Primary Mirror Active Optics
PPA	Parallel Pre-stressed (piezoelectric) Actuator
PRBM	Pseudo Rigid Body Model
PV	Peak to Valley
QSL	Quasi-Static Load
RMS	Root Mean Square
RVP	Requirements Verification Plan
SiC	Silicon Carbide
SPL	Sound Pressure Level
SR	Strehl Ratio
STOP	Structural Thermal Optical Performance
TBC	To Be Confirmed
TBD	To Be Determined
TCS	Thermal Control System
TDI	Time Delay & Integration (sensor)
TMT	Thirty Metre Telescope
TRIAD	TRIaxial Attitude Determination
TRL	Technology Readiness Level
VAC	Voltage AC (Alternating Current)
wrt	With respect to

1

Introduction to the Deployable Space Telescope

This chapter provides the context and justification for the broader Deployable Space Telescope project and more specifically, the subject of this thesis: The design of a primary mirror fine positioning mechanism for a Deployable Space Telescope.

Section 1.1 provides a brief analysis of the modern high resolution Earth Observation (EO) market, making the case for a Deployable Space Telescope (DST), formalised in the Mission Need Statement and Mission Goal. It is within this context that the thesis need and research goals were developed, introduced in Section 1.2 along with a description of the expected deliverables. The status of the DST project is summarised in Section 1.3, followed in Section 1.4 by a synopsis of the mission architecture and concept of operations that have been developed to meet the Mission Need. This section also establishes the physical scope of the thesis within the overall architecture. The chapter concludes with a breakdown of the structure of this report in Section 1.5. The bulk of the content in this chapter has been adapted from the Literature Study that preceded this thesis [96].

1.1. The Earth Observation Market & Need for the DST

Remote sensing has become a crucial tool in the evidence-based decision making processes of governments, NGOs, academia, industry and individual users throughout the world. Satellite data is used to address resource management, disaster response, climate change, business analytics, disease outbreaks and to enforce international law [67, 80].

A good first indicator of a satellite imaging platform's performance is ground sampling distance (GSD), the distance between the projection of the centres of two adjacent pixels measured on the ground. A smaller sampling distance generally correlates to a higher resolution image and thus higher fidelity data. It is informative to look at the effect of GSD on spacecraft mass and constellation size, and how this is evolving in the current EO market.

Market data was collected for 19 EO visual spectrum imaging platforms in Low Earth Orbit (LEO), summarised in Figure 1.1. Each bubble represents an individual platform, whether that be a single spacecraft or a constellation. Platforms are categorised by their date of entry into the market. DigitalGlobe (Maxar) and Airbus are the incumbent market leaders, as opposed to "New Space" entrants that largely began operations from 2010 with the increase in popularity of small- and mini-satellites. Future entrants reflect those platforms that have been proposed, but are not yet operational. The data in this category is highly speculative, but it does give valuable insight into future market trends.

Market demand is driving mission architectures towards large numbers of light weight spacecraft to generate high spatio-temporal resolution imagery [25]. Image resolution is fundamentally limited by the diffraction limit, so that larger mirrors are needed to get better resolution[1]. As a result, high resolution imaging platforms are necessarily large, heavy and costly satellites. The global supply of commercially available very high resolution imagery is controlled by the two EO operations market leaders, DigitalGlobe (now Maxar Technologies after a merger with MacDonald, Dettwiler & Associates [55]) and Airbus Defence & Space. No other

[1] More detail is provided in Section 2.4 *Geometric Optics*.

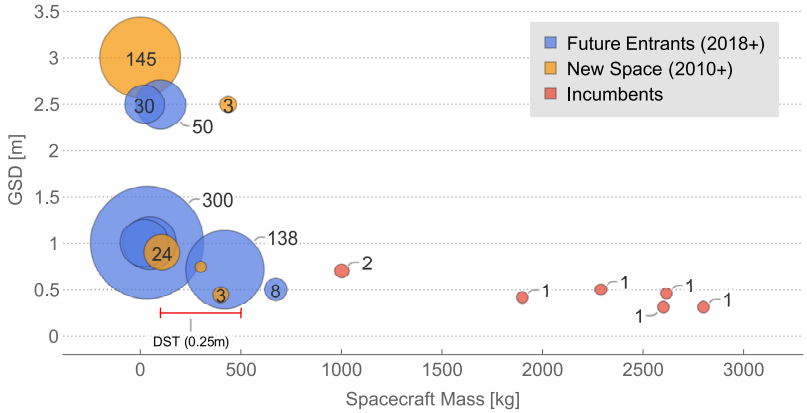

Figure 1.1: Basic performance data for 19 current and future visual spectrum imaging satellite platforms. Bubbles represent individual platforms, rather than companies. Size & labels indicate number of spacecraft in the constellation. Range of possible DST spacecraft mass shown by red bar. See Appendix A for data, sources and further detail. Ground Sampling Distance (GSD) has not been corrected for altitude.

company has been able to afford the expense of sub-0.5 m resolution imagery. The cost of launch alone for WorldView-4, as estimated using the United Launch Alliance RocketBuilder website, was likely on the order of US$127 million[2], with a full development cost of US$850 million including ground station works[3].

Additionally, the realities of orbital dynamics force the use of constellations to re-image the same location on Earth's surface more frequently. To be financially viable, individual spacecraft must be small and light to keep development and launch costs down. To deliver both high spatial and temporal resolution data, a paradigm shift in the way Earth Observation (EO) imaging satellites are designed is needed.

In 2012, Dr.ir. Hans Kuiper identified a possible solution to this need: the Deployable Space Telescope. The DST uses a synthetic aperture telescope [48, 50], which achieves the same or similar aperture diameter as a single mirror but with multiple, smaller (and crucially, lighter) segments. To reduce the launch volume, the spacecraft is delivered to orbit with the segments folded into a compact package, ready to be deployed in space. The DST need statement and mission goal were first formalised by van Marrewijk [116]:

Need Statement
There is a need for a dramatic decrease in launch cost of high-resolution Earth observation telescopes to provide data with a higher temporal resolution and at a lower price than is currently available.

The Mission Goal follows from the need [116]:

Mission Goal
To design and develop a Deployable Space Telescope that is capable of achieving the same GSD as state-of-the-art Earth imaging satellites, but at a fraction of the stowed volume and mass.

1.2. Thesis Need and Research Goals

Building a mechanism that can reliably deploy the segments to a position that will guarantee diffraction limited performance is extremely difficult. Poor alignment is caused by slop in mechanical joints, non-linear microdynamic effects in the mechanism elements, some of which can be very hard to predict and control [74] and small assembly errors. Thermal gradients and on-board structural disturbances will also perturb the alignment after deployment.

Traditionally, optics and the supporting structures used in space instruments rely on heavy, stiff designs to passively meet their position and shape tolerance budgets. This conflicts with the mission goal. Instead, the DST proposes active control of the primary mirror segments [48], using a mechanism that is smaller and lighter than the equivalent traditional, passive structure. Only recently have these mechanisms become

[2]Available from: `https://www.rocketbuilder.com/`, original citation and estimate from [116].
[3]Available from: `https://spacenews.com/geoeye-2-price-tag-rises-ground-system-upgrades-0/`. Accessed: [31 October 2018]. Originally cited by [116].

feasible, thanks to recent advances in light-weight mirror technology [21, 109] and the increasingly mature space-flight heritage of actuators with native nanometre resolution [4].

The DST proposes to use separate subsystems to remove the aberrations caused by misalignment, and deformation of the optical elements. A three degree of freedom (DOF) piston/ tip/ tilt fine positioning mechanism to actively support and align the primary mirror segments in orbit. This mechanism has been dubbed the "Primary Mirror Active Optics" (PMAO). The Aberration Correction System (ACS) uses a Deformable Mirror (DM) to remove the remaining continuous wavefront errors. The ACS was developed by G. van Marrewijk in his MSc thesis [116], where he also derived the useful flow of needs and solutions leading to the PMAO and ACS conceptualisation, shown in Figure 1.2. In that work, he found that it was indeed feasible to correct the continuous wavefront errors using the ACS.

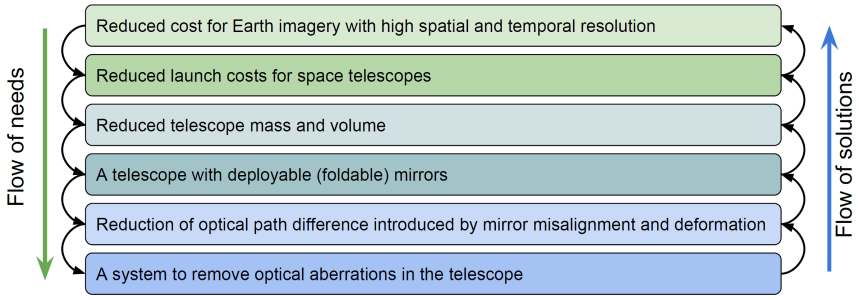

Figure 1.2: The need to remove optical aberrations from the DST imagery, and thus the need for the Primary Mirror Active Optics and Aberration Correction System, follows directly from the mission Need Statement. A bottom up approach, developing solutions to consecutively higher level needs will establish the feasibility of the Deployable Space Telescope. Figure and concept adapted from van Marrewijk's earlier MSc thesis on the ACS [116].

With the feasibility of the ACS confirmed, there remained an open question as to the feasibility of implementing an active optics mechanism on a low-mass/ low-volume Earth observation telescope. To that end, the following thesis goal was formulated:

Thesis Goal
The goal of the thesis will be to generate a preliminary thermo-mechanical design of the primary mirror active optics mechanism to enable diffraction limited performance of the DST, to verify the design through analysis and to assess the feasibility of implementing it in a deployable space telescope. The work shall be done within the time and resource constraints of a normal MSc thesis at TU Delft.

Research Questions

The thesis goal was further distilled into two research questions to guide the academic effort. The objective of the remainder of this report is to answer these questions:

1. What modifications need to be made to the existing PMAO thermo-mechanical design to comply with the requirements, and how can that compliance be verified?
2. Is it technically and economically feasible to implement the verified PMAO thermo-mechanical design in a space telescope?

Thesis Deliverables

The key deliverables of the thesis are listed below. Their purpose was to provide the tools necessary to answer the thesis research questions, as well as facilitate the continuation of research on the PMAO mechanism within the DST team.

1. A preliminary thermo-mechanical design of the PMAO mechanism.
2. Integration of a mechanical model of the PMAO in the End To End Performance (ETEP) model to allow rapid prototyping and analysis of the relationships between the bottom up and top down systems engineering.
3. An assessment of the technical and economic feasibility of implementing the PMAO in the DST.

1.3. Status of the Deployable Space Telescope Project

The TU Delft Deployable Space Telescope project began in 2014 with the MSc thesis project of Dennis Dolkens [48]. It has since remained an active student project, with five MSc students graduating through research on the telescope. The present team structure is shown in Figure 1.3. Currently, two PhD researchers lead the optical and mechanical teams respectively, comprising a further six MSc students. The MSc level research topics generally focus on individual subsystems.

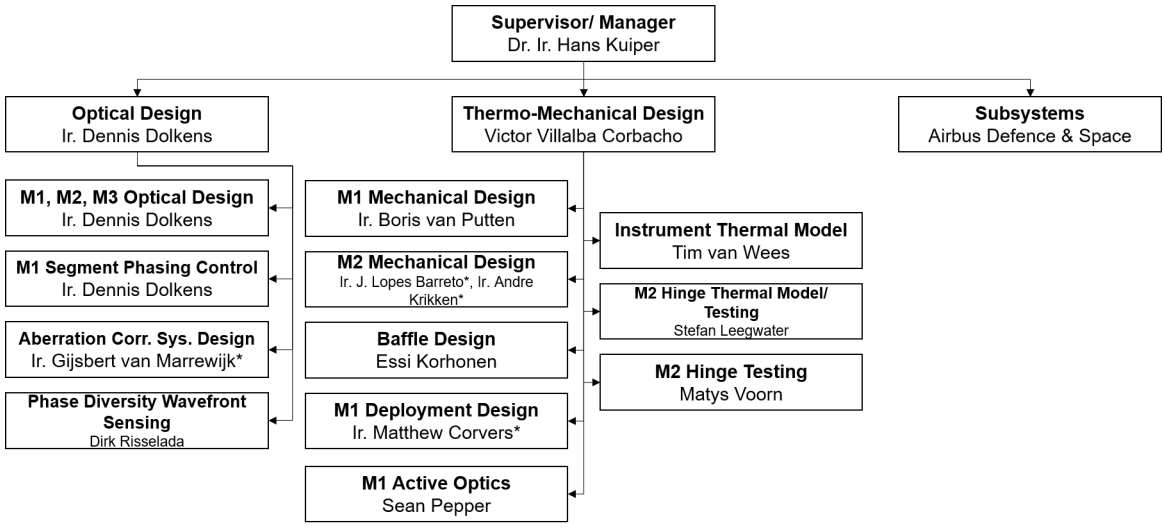

Figure 1.3: The TU Delft DST team structure. Starred names indicate graduated students.

Early work conducted by Dolkens [48] established the optical architecture for the DST. Dolkens also developed FORTA [50], a MATLAB based ray tracing package for segmented optics. It has been wrapped in a Structural, Thermal, Optical Performance (STOP) model of the telescope, capable of simulating the effects of alignment and deformation errors of the optics on the optical performance of the telescope. This model has been dubbed the "End To End Performance" (ETEP) model of the DST and was central to establishing the top down systems budgets [50], introduced later in Chapter 3 *Requirements Generation*, which govern the required performance of the thermo-mechanical subsystems.

The majority of the ensuing research has focussed on establishing a preliminary thermo-mechanical design of each of the major telescope subsystems. Where the optical work used a top down approach to define high level requirements, the mechanical efforts have adopted a bottom up approach to rigorously demonstrate the technical feasibility of implementing the Deployable Space Telescope. The overarching objective of the mechanical work is to prove that each of the opto-mechanical subsystems are able to meet the top down systems budgets, ideally by integrating a valid model of each subsystem into the ETEP model for statistical analysis.

An initial design for the PMAO mechanism was developed by van Putten [117]. That design is referred to as the *original baseline design* throughout this thesis. It is discussed in greater detail in Chapter 5 *Baseline Functional Verification*.

It is emphasised that the DST is a university led project with no commercial funding, though Airbus Defence & Space Netherlands B.V. (ADSNL) have been providing coaching and periodic design reviews. The level of design for each subsystem need not proceed farther than a preliminary design stage. The objective of the project is to establish the *feasibility* of the concept. Throughout this and other DST theses, many design decisions have been made in recognition of this context and limitations.

The current state of the DST concept and architecture are summarised in the next section.

1.4. DST Mission Concept & Architecture

The physical architecture of the DST[4] is shown in Figure 1.4. The instrument housing accommodates the tertiary, deformable and fold mirrors, along with the main detectors. The external envelope of the housing offers mounting points for the M1, M2 and baffle deployment mechanisms. The "piston cam", a sensor suite used to detect misalignment of the primary mirror segments, and the field stop, are permanently mounted to the housing. The spacecraft bus, outside the scope of the current DST project, houses all necessary ancillary functional elements including the payload processor and data storage.

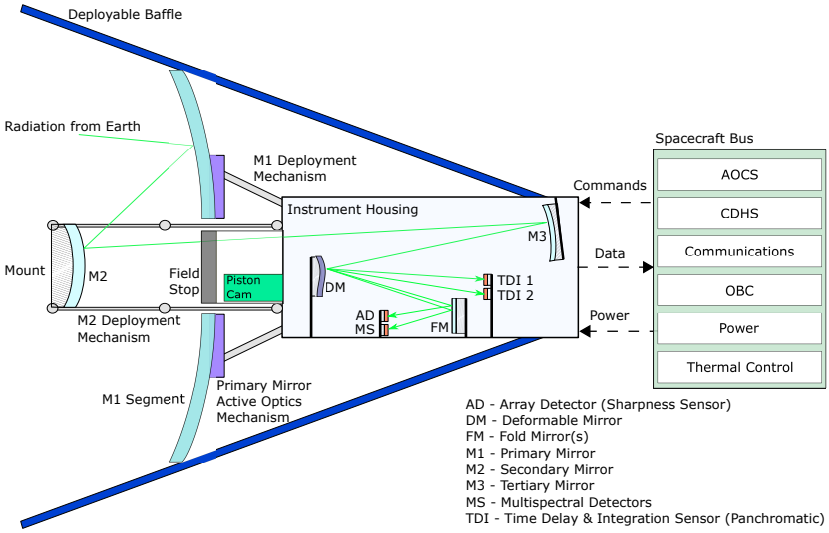

Figure 1.4: Schematic of the Deployable Space Telescope payload physical architecture. The Primary Mirror Active Optics mechanism mates the primary mirror segments to the M1 deployment mechanism.

The DST uses a Korsch annular-field three mirror anastigmat (AFTMA) optical configuration which, thanks to its fully reflective design, does not introduce any chromatic aberrations to the image [50]. Further advantages of the Korsch design include inherent correction of spherical aberration, coma, astigmatism and field curvature, a highly accessible focal plane and a large proportion of usable field [70]. A schematic is shown in Figure 1.5.

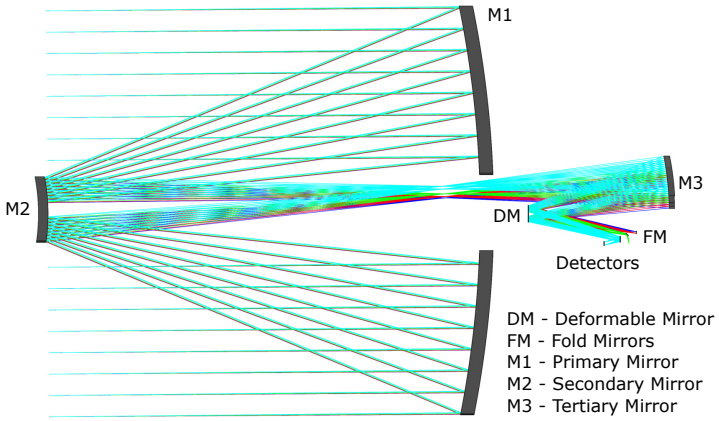

Figure 1.5: DST implementation of the Korsch annular-field three mirror anastigmat. Note that the focal point of M2 lies above the optical axis, giving the off-axis configuration its name. Adapted from [50].

The Cassegrain part (M1 and M2) constitutes most of the focal length of the instrument, thus reducing the amount of magnification needed at the tertiary mirror. This relaxes the misalignment tolerances on the primary and secondary mirrors compared to a full field Korsch design [50, 75]. One of the main disadvantages,

[4]Note that in, this and virtually all other DST project literature, the term Deployable Space Telescope (DST) refers to the telescope itself. The spacecraft bus, which would typically house supporting subsystems such as power supply, propulsion, AOCS and data handling, is not included.

particularly for large fields of view, is that a lot of baffling is required to eliminate straylight [107]. Nevertheless, the same arrangement allows the focal plane to be positioned behind the telescope, so that the baffling does not cast a shadow over the exit pupil or incoming field [75]. Moreover, the larger size and improved accessibility of the focal plane makes it easier to arrange multiple detectors across the focal plane, as is common in space instrumentation [50, 70]. The DST modifies the traditional AFTMA arrangement by replacing one of the fold mirrors with a deformable mirror to correct for continuous wavefront errors via the Aberration Correction System (ACS).

The physical embodiment of this architecture is shown in Figure 1.6. One PMAO mechanism resides beneath each of the four primary mirror segments, not shown in the figure. In the depicted design iteration, which is subject to change, an arrangement of ribbons tension the deployed Cassegrain structure. Though it has little influence on the mechanical realisation of the PMAO mechanism, coupling the M1 and M2 structures does make it much more difficult to meet the top-down budgets by coupling their thermo-mechanical interaction.

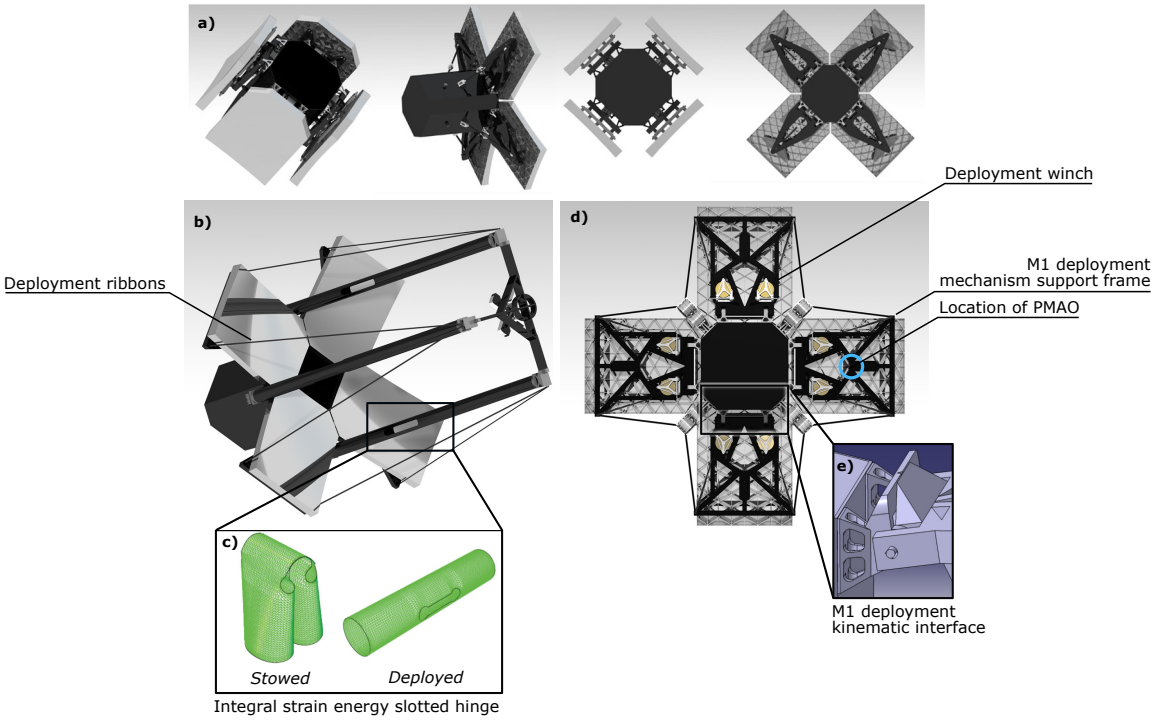

Figure 1.6: a) The stowed and deployed configurations of the primary mirror. Note that the A-frame deployment mechanism support frame and strut have been superseded by the winch and ribbon system depicted in panels b and d. Adapted from [117]. b) The current DST concept in the deployed configuration (baffle and spacecraft bus not shown). The integral strain energy slotted hinges mid way along the M2 booms draw out M2 and pull the M1 segments with them via the deployment ribbons. Adapted from [33]. c) The folded, stowed M2 boom hinges unfold and snap into the deployed configuration similar to a carpenters measuring tape. Adapted from [83], originally cited in [72]. d) Rear view of the deployed M1 assembly. M1 and M2 are coupled via the deployment ribbons. The winches apply tension, which provides the nesting force for the kinematic interface at the root of the deployment mechanism support frame and increases the resonant frequency of the M2 sub-assembly. Adapted from [33].

The concept of operations functional flow block diagram is shown in Figure 1.7. The most relevant blocks to this thesis are F-8, which effect the deployment of the PMAO mechanism, and F-11. The current optical control philosophy assumes that the primary mirror can be deployed directly within the coarse alignment budgets, so block F-10 is considered irrelevant for present design studies. It is retained in the figure in case it is shown in other work that this isn't possible.

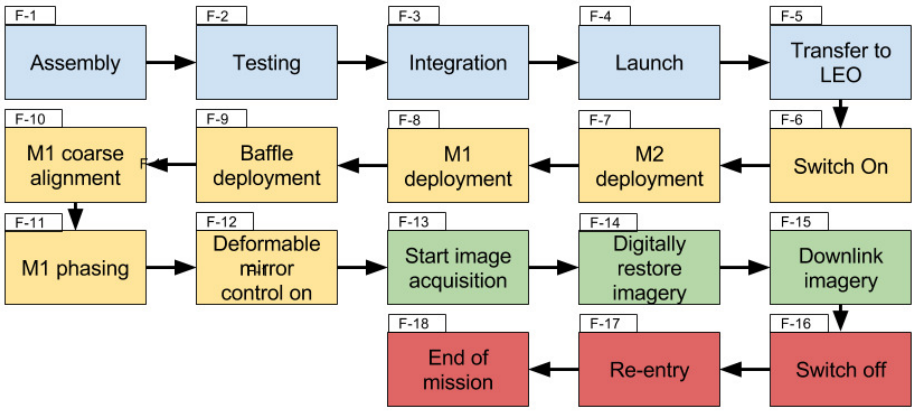

Figure 1.7: Typical DST mission functional flow block diagram. Adapted from [116].

A brief description of the interaction between the prescribed functions in Figure 1.7 relevant to the PMAO and their physical realisations shown in Figure 1.6 is given below.

1. To reduce the mass and volume of the telescope through launch, the primary and secondary mirrors are stowed in a folded configuration. The primary mirror is divided into four segments to allow this. A Hold Down & Release Mechanism (HDRM, not shown in Figure 1.6) secures the M1 deployment mechanism to the DST housing during launch. The PMAO mechanism, mounted between the deployment mechanism and each M1 mirror segment, directly supports the segment during launch.
2. Once in orbit, the deployment mechanism unfolds the stowed mirrors. Strain energy in the M2 boom slotted hinges provides the energy to extend M2, simultaneously bringing the M1 segments with it via the ribbon arrangement. Winches on the rear of the M1 segments control the release.
3. A kinematic interface between the M1 deployment mechanism and DST housing provides a repeatable deployment position of the M1 segments. A nesting force keeps the mirrors in position during operations. In the current iteration, this is provided by the tensioned ribbons.
4. Discontinuous wavefront errors arise due to a difference between the nominal and actual deployed position of the M1 segments. Further sources of error in orbit are small, slow drifts cause by thermoelastic strains and faster structural vibrations caused by excitation sources on board the spacecraft.
5. The PMAO mechanism works in concert with the calibration algorithm to remove discontinuous wavefront errors. Piston cams focused on the adjacent corners of the segments monitor the relative position and orientation of the segments.
6. The aberration correction system removes the remaining continuous wavefront errors to retrieve a diffraction limited image.
7. Steps 5 and 6 are repeated periodically throughout the mission to recalibrate the M1 position due to recurring thermal and structural perturbations.

Thesis Scope

The performance of the PMAO is strongly coupled to the mirror and mirror deployment mechanism designs. Both components were excluded from this thesis to keep the scope of work within the resource constraints of a MSc thesis. With reference to Figure 1.8, the physical limits were drawn at the mirror support/ mirror interface and PMAO mechanism/ deployment mechanism support frame interface.

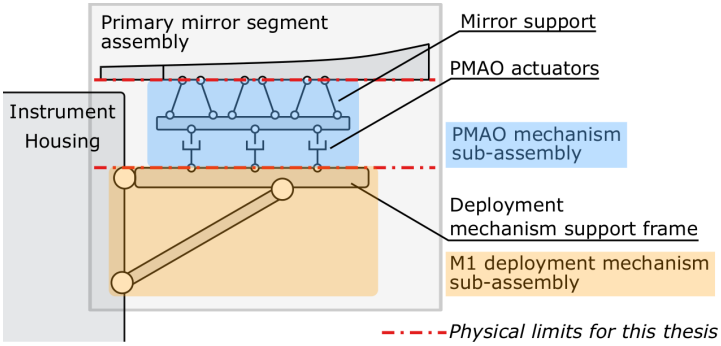

Figure 1.8: Breakdown of the main primary mirror subsystems and components. This thesis is primarily concerned with the PMAO mechanism, demarcated by the dashed red lines.

The existing mirror design is very immature, receiving only cursory attention in the Msc thesis from B. van Putten [117]. The baseline primary mirror design was frozen, to allow exploration of other subsystems. Several flow down requirements are given in Chapter 9 *Verification* to ease integration of future mirror designs with the revised PMAO mechanism design developed in this thesis.

1.5. Introduction to the Report

The Primary Mirror Active Optics mechanism bottom up engineering effort, and subsequently this report, were broadly structured in line with the systems engineering Vee model. The structure of the report is depicted in Figure 1.9.

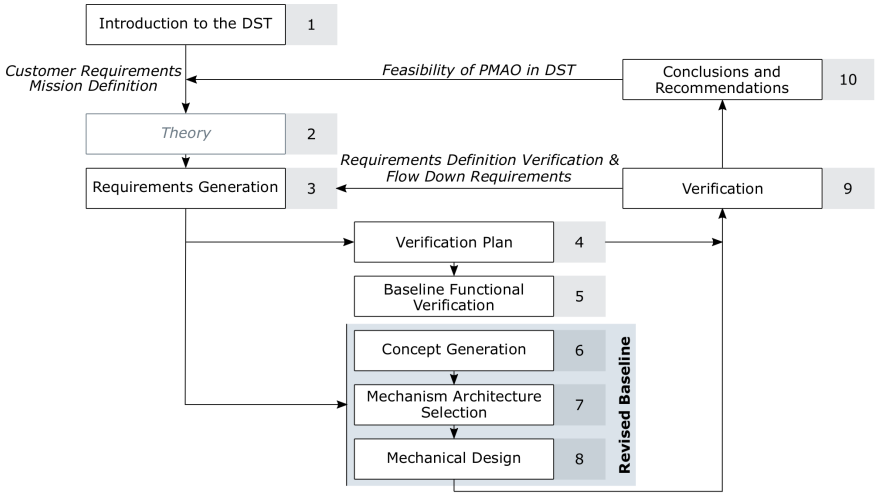

Figure 1.9: Structure of the report. The *Theory* section was not part of the bottom up systems engineering effort.

Chapter 2 *Theory* very briefly covers the most fundamental theory of designing precision mechanisms to provide a basis for the technical discussions that follow. A full treatise on precision mechanisms is beyond the scope of a Masters thesis so in the interest of brevity, the theory is presented "as-is" with no further proof. Many of the concepts follow from good mechanical intuition and several references are provided for further reading.

The technical effort began in earnest with the requirements generation, documented in Chapter 3 *Requirements Generation*. The chapter concludes with a summary of the system requirements used to guide the remainder of the thesis.

The process used to verify the PMAO mechanism was formalised in the verification plan, introduced in Chapter 4 *Verification Plan.* The output of this chapter also lead to the genesis of the *DST Requirements and Verification* guidelines document. This is now a live, team document and will ideally reduce the verification workload for future student theses. The original version, developed by the author of this report, is included in Appendix D.

The verification plan was used twice through the course of the thesis. First, to verify the compliance of the original baseline design with several critical functional requirements. The results are set out in Chapter 5 *Baseline Functional Verification.* It was found that the original baseline mechanism concept needed revision.

A detailed concept generation phase followed. The output of this work package has been divided between two chapters. First, Chapter 6 *Concept Generation* documents a search through the design space, and selection, of concepts at the component level. Chapter 7 *Mechanism Architecture Selection* then documents the synthesis of these elements into two mechanism architectures, and justifies the final selection.

Following the selection of the concept, each of the main components were sized using simple, first principles relations in Chapter 8 *Mechanical Design. SPACAR*[5], a reduced order finite element package for multibody mechanisms, was used to verify the PMAO mechanism design by modelling. The construction of those models, and their verification with similar ANSYS models, are documented in parallel with the mechanical sizing. The final product of the chapter was a verified *SPACAR* model of the integratedPMAO mechanism assembly.

This model was used in the second and final application of the verification plan. Chapter 9 *Verification* documents the verification results, the verification of several requirement definitions generated earlier in Chapter 3 *Requirements Generation* and defines several new flow down requirements for other subsystems.

The report concludes in Chapter 10 *Conclusions and Recommendations* with a summary of the final design, and a discussion of the feasibility of implementing the revised PMAO mechanism baseline design in the Deployable Space Telescope. The thesis research questions are answered and general conclusions drawn with regards to fine positioning mechanisms for space based optics. The chapter closes with a series of recommendations for future work.

The thesis has been written with the objective of meeting both academic requirements and providing a standalone document to ease handover of the design of the PMAO mechanism to future students. To that end, the chapter summaries list major findings, items identified for future work and the most significant assumptions. Considerable supplementary material that may be useful to future students, but is not immediately relevant to the technical arguments made in the body of the report, are included in the appendices.

[5] *SPACAR* is not an acronym

2

Theory

The objective of this chapter is to give the uninitiated reader enough background information on the fundamentals of precision mechanism design to understand the technical decisions made throughout the concept generation and mechanical design chapters. The theory is presented "as-is" with no further proof. Blanding [17], Hale [57] and Hopkins [61, 62] each provide more thorough treatments of the basics presented here. The bulk of the discussion has been adapted from the Literature Study that preceded this thesis [96].

The basic elements of exact constraint design, first introduced by Blanding, are summarised in Section 2.1. Several considerations regarding putting the theory into practice are introduced in Section 2.2. Chapter 6 *Concept Generation* relies heavily on the Freedom And Constraint Topology (FACT) method, introduced in Section 2.3. The chapter concludes in Section 2.4 with the basics of geometric optics as relevant to the PMAO mechanism requirements and performance.

2.1. Elements of Exact Constraint Design

This section details the fundamental elements of exact constraint design. The theory presented here is taken from the foundational text by Blanding [17]. Blanding presents the tenets of exact constraint design as a series of succinct statements. The same approach is used here. This theory applies for small motions only. This is an unfortunately ambiguous definition. As a rule of thumb, "small" motions are those where a rotation about a centre can be locally approximated as a translation over the domain of interest, without exceeding the desired level of accuracy.

Constraints and Degrees of Freedom

All rigid objects in space have six independent degrees of freedom, three each in translation and rotation. In two dimensions, a body has only three degrees of freedom. A constraint is a mechanical connection between a body and a reference object. For every non-redundant constraint added to a body, a degree of freedom (DOF) is lost.

If six non-redundant constraints are imposed upon a body such that no degree of freedom is overconstrained or left underconstrained, then the body is said to be *exactly constrained*. Exact constraint design refers to a deliberate accounting of each of these degrees of freedom during the design process of a machine or mechanism [17]. It is the rigorous application of kinematic principles to machine design in order to produce low cost yet high performance designs [57].

The fundamental constraint element is a link which prohibits translation along its axis but allows rotation about any axis at its ends, for small motions. The axis of the link is called a *constraint line*. Any constraint device can be modelled as one or more constraint lines on a constraint diagram.

This introduces the first and second of Blanding's statements:

B1. **Constraints**
"Points on the object along the constraint line can move only at right angles to the constraint line, not along it" [17, p. 3].

B2. **Functional Equivalence of Constraints Along a Given Line**
"Any constraint along a given constraint line is functionally equivalent to any other constraint along the same constraint line (for small motions)" [17, p. 5].

Overconstraint

Overconstraint occurs when two or more constraints try to remove the same degree of freedom, such as when two links act along the same constraint line, shown in Figure 2.1. This results in a loss of performance (internal stresses, slop, imprecision), higher cost (tight tolerances, advanced assembly techniques), or both.

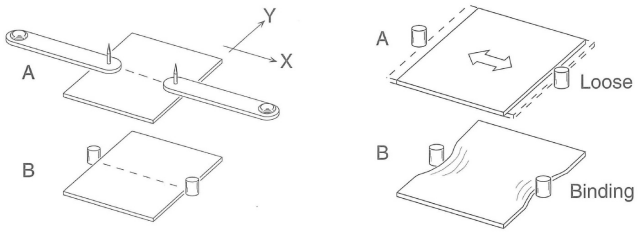

Figure 2.1: Left: Two overconstrained systems, each with two constraint lines lying along the same axis. Right: The consequences of overconstraint are usually poor performance: slop, stress, imprecision; or high cost: tight tolerances, expensive assembly and metrology techniques. Adapted from [17].

Constraint Diagrams

A body's degrees of freedom and constraints can be represented by using *constraint diagrams*. Examples are shown in Figure 2.2 and 2.3. Bold face **R**'s' symbolise a rotational degree of freedom. Boldface **C**'s represent a constraint line. Not demonstrated in the figure is a translational degree of freedom, symbolised by a **T**.

Instant Centres of Rotation

Consider a two dimensional case (three DOFs maximum) where a plate is constrained by two links, shown in Figure 2.2.

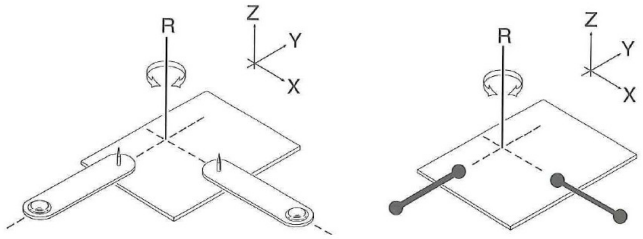

Figure 2.2: Instant centre of rotation. Adapted from [17].

From statement B1, since points along a constraint line can only move at right angles to the constraint line, then the body must rotate about a point along the constraint line. With two constraints imposed upon the object, the only point about which the body is able to rotate is the intersection of the two constraint lines. This point is called the *instant centre of rotation*[1], or simply, the instant centre. Put more generally:

B3. **Equivalence of Intersecting Constraint Pairs I**
*"The axes of a body's rotational degrees of freedom **R**s will each intersect all constraints **C**s applied to the body"* [17, p. 23].

B4. **Equivalence of Intersecting Constraint Pairs II**
"Any pair of constraints whose constraint lines intersect at a given point is functionally equivalent to any other pair in the same plane whose constraint lines intersect at the same point. This is true for small motions and where the angle between the constraints does not approach 0° [17, p. 8].

The instant centre need not necessarily be on the object as illustrated in Figure 2.3. In the limiting case where the angle between the constraint lines tends towards zero, the constraints become parallel and are said to intersect at infinity as in Figure 2.3.

[1] Not to be confused with a *remote* centre of rotation.

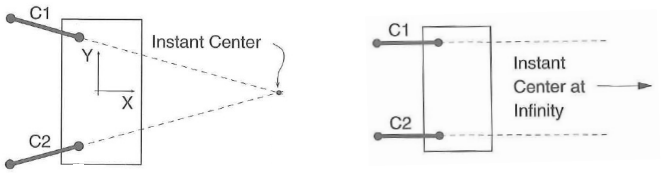

Figure 2.3: Left: Example of instant centre of rotation lying outside of the constrained body. Right: Parallel constraints intersect at infinity, giving an instant centre at infinite distance from the body. Adapted from [17].

Two conclusions can be drawn from this result. First, note that in the right hand frame of Figure 2.3 it would be possible to translate the object up and down a small amount. Yet, the constraints are still considered as intersecting at infinity and must therefore allow a rotation. This gives the next statement:

B5. **Rotations at Infinite Distance**
*"A **T** can be equivalently expressed as an **R** located at infinity"* [17, p. 10].

An extension of this principle to the three dimensional case is shown in Figure 2.4. An object is constrained by five constraints lying in two separate but parallel planes. As for two lines in the 2D case, the two planes in the 3D case intersect at infinity. The resulting translational degree of freedom is shown diagrammatically as an **R** about any tangent line on a circle with infinite radius centred upon the object, and parallel to the two planes.

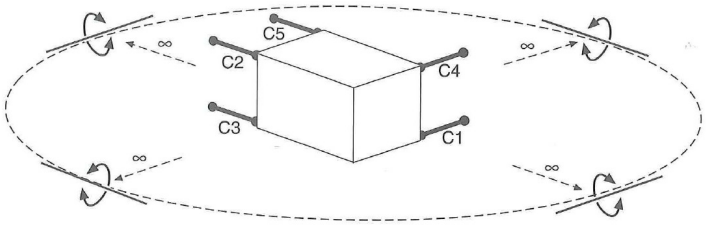

Figure 2.4: Two parallel planes of constraints intersect at infinity to give a single translational degree of freedom. Adapted from [17].

Second, due to the equivalence of intersecting constraint pairs, two pairs of parallel constraints, each also parallel to the other, intersect at infinity and are equivalent:

B6. **Functional Equivalence of Parallel Constraint Pairs**
*"If two lines of an infinite plane of parallel lines represent a pair of **C**s applied to a body, then any two parallel lines from that plane can equivalently represent the two **C**s applied to that body"* [17, p. 11].

In practice, translation **T**'s are normally represented as a rotation **R** at infinity such that all degrees of freedom can be represented as **R**'s and all constraints as **C**'s.

Constraint Pattern Analysis

With the basic basic rules for describing a body's constraints and degrees of freedom in hand, it is possible to use constraint diagrams to *synthesise* a constraint pattern to achieve a desired freedom of motion, or *diagnose* the resulting freedoms from a given constraint pattern. The designer can move from synthesis to diagnosis via the *Rule of Complementary Patterns*, which describes the general relationship between constraints and DOFs in three dimensions:

B7. **Rule of Complementary Patterns**
*"When a pattern of **C**-lines is imposed between two objects, there is a resulting and complementary pattern of **R**-lines that exists between the two objects. Given one or the other of these patterns containing* n *lines without redundancy, the complementary pattern will contain 6-n lines. Furthermore, every line of one pattern will intersect every line of the complementary pattern"* [17, p. 39].

Redundant Constraint Lines

A redundant constraint is one which, if removed from the body, will not lead to a change in the degrees of freedom of the body permitted by the remaining constraints [57, p. 77]. From statement B7, the *Rule of Complementary Patterns* only applies in the absence of redundancy. In order to find the pattern of freedom lines resulting from a given constraint pattern (or vice versa), it is necessary to first identify and remove redundant constraints.

Two further statements, illustrated in Figure 2.5 but given without further justification, can be used to identify redundant lines:

B8. **Intersecting Pairs of R's and C's**
*"An intersecting pair of **C**s or **R**s defines a disk of radial lines any two of which (provided the angle between them is not too small) may be selected to equivalently replace the original pair (for small motions)"* [17, p. 42].

B9. **Parallel R's**
*"If two lines of an infinite plane of parallel lines represent two **R**s of a body, then any two parallel lines from that plane can equivalently represent the two **R**s of that body"* [17, p. 44].

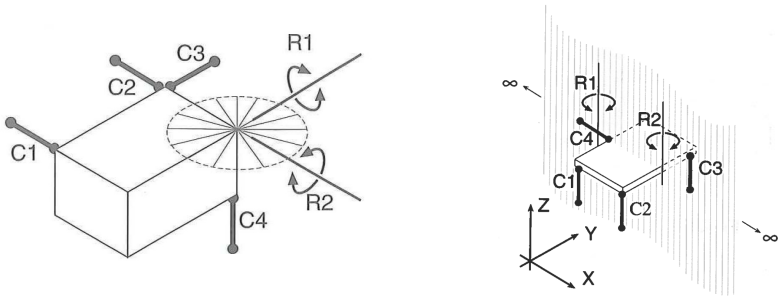

Figure 2.5: Left: Example of Statement B8 - Two **R**s defining a disk of radial lines, any two of which may be selected to equivalently replace them. Right: An example of Statement B9 - Equivalence of two parallel coplanar **R**s to any other two **R**s in the same plane. Adapted from [17].

With these statements in hand, four rules for identifying redundant constraint lines in 3D space can be formulated, listed in Table 2.1.

Table 2.1: Rules for redundant lines in constraint pattern analysis.

1.	Two collinear lines are redundant.
2.	Two coplanar lines intersect each other by definition (parallel lines intersect at infinity). Addition of a third coplanar line is redundant if it intersects the first two lines at the same point.
3.	Three coplanar lines are non-redundant so long as no more than two lines intersect at any one point in the plane (including infinity). Addition of a fourth coplanar line will be redundant, irrespective of its orientation to the first three lines.
4.	Three non-coplanar lines may intersect each other at the same point. Addition of a fourth line intersecting the same point will be redundant, irrespective of its orientation to the first three lines.

Compound Connections

Constraint pattern analysis is normally concerned with understanding the constraint or freedom pattern of a body with respect to a reference body. In some mechanisms, the connection between the two bodies can be mediated by one or more intermediate bodies, as shown in Figure 2.6. Constraints can be imposed through the serial chain of intermediate bodies and/ or directly between the reference and final bodies.

All examples considered so far in this section have been of *direct* connections between two bodies. The resulting constraint pattern of all direct connections between two bodies is found by adding the constraints from each connection.

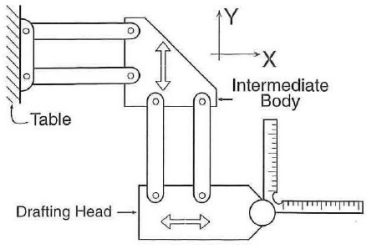

Figure 2.6: Example of cascaded restraints. The vertical translational DOF between the table and intermediate body is added to the horizontal translational DOF between the intermediate body and drafting head. Adapted from [17].

The series connection of two or more rigid bodies is called a *cascade*. The resulting degrees of freedom of the whole assembly are given by the addition of the **R**s permitted by the connection between the reference body and first intermediate body, to those of the second intermediate body and so forth through to the final body in the chain.

Complex arrangements of compound connections can be analysed through an equivalent electrical network analogy. Cascaded connections are modelled as resistances in series and direction connections as resistances in parallel. The problem can then be decomposed into a series of simpler constraint pattern analyses. Treatment of compound connections is summarised in Table 2.2.

Table 2.2: Treatment of compound connections in constraint pattern analysis [17].

	Direct	**Cascade**
Electrical equivalent	Parallel resistance	Series resistance
Add	**C**'s	**R**'s

2.2. Exact Constraint Design in Practice: Compliant Mechanisms

The theory presented so far has only considered ideal constraints: rigid lines with frictionless joints at either end that release all bending moments such that only forces are transferred between bodies, through infinitesimally small point contacts. One of the main tasks of precision mechanism design is how to best make use of, and approximate, exactly constrained arrangements in the physical world.

As stated previously, a constraint line is composed of a rigid link with a joint at either end. Designing the rigid link is straightforward: a beam or pin will suffice. Designing a frictionless joint to connect and interface two or more bodies, however, requires a little extra thought.

A *kinematic* interface derives its name from its mobility: it has a mobility of *exactly* zero. Kinematic interfaces have well defined load paths making analysis and prediction of their performance much easier than for overconstrained interfaces. This can be physically realised by applying six independent, non-redundant forces through infinitesimally small points such that only axial forces and no bending moments are transferred to the part [52, p. 409]. Using small points does however generate very high contact stresses that cause local deformation in the part.

A *semikinematic* interface provides very similar constraint but distributes forces over larger contact areas, including line, annular or larger patch contacts. An example of a semi-kinematic interface is the flexured bipod, which was ultimately selected for the M1 mirror support in Chapter 6 *Concept Generation*. This comes at the expense of the possibility of transferring bending moments to the part. Bending moments can be released by using joints that allow relative motion between two links in a mechanism.

Revolutes and ball joints are common for typical engineering mechanisms though they introduce hysteresis and other micro-dynamic position errors [74]. *Flexures* allow motion through *elastic* deformation of thin, compliant sections without introducing friction or hysteresis. The trade-off for their frictionless performance is a much smaller range of motion compared to contacting, friction-based joints [126, p. 548]. It is the use of flexures and other mechanisms specifically design to be compliant in one or more directions and stiff in others, that gives *compliant mechanisms* their name.

There is a wide range of compliant mechanisms that a designer can choose from. Defining the flexure profile itself (sheet/ blade/ leaf, notch, circular, elliptic, monolithic), and the arrangement of flexures and

their assembly, is a vibrant field of research. For simplicity, the PMAO design utilises the simplest type of flexure: a sheet flexure with rectangular cross-section.

2.2.1. Sheet Flexures

An ideal sheet flexure can be equivalently modelled as three ideal constraint lines in the plane of the sheet. This constraint pattern constrains two in plane translations and one in plane rotation, leaving the three out of plane freedoms unconstrained: translation in z and rotation in θ_x and θ_y per Figure 2.7.

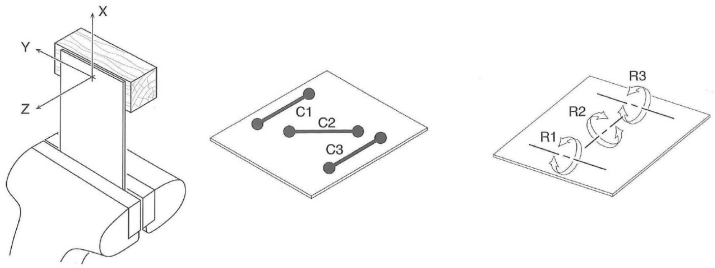

Figure 2.7: Left: An ideal sheet flexure. Centre: Equivalent constraint pattern with three coplanar constraint lines. Note that no more than two constraint intersect at the same point. Right: The complimentary freedom pattern. Adapted from [17].

2.2.2. Example Constraint Pattern Analysis for a System of Sheet Flexures

An example of how to apply the fundamentals of constraint pattern analysis to a simple system of sheet flexures may clarify the theory covered so far.

Consider two sheet flexures directly connecting two bodies: either a crossed flexure, or two parallel flexures as shown in Figure 2.8. Both are examples of a parallel connection in the equivalent electrical network analogy. The system can be analysed using the compound connection rules in Table 2.2.

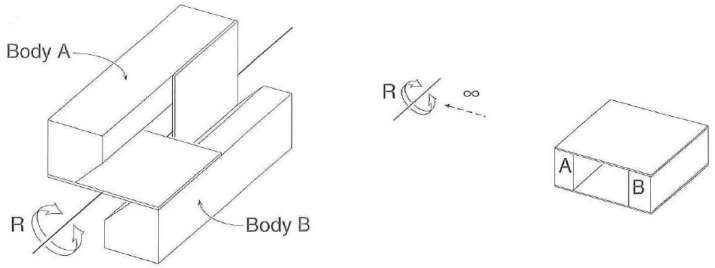

Figure 2.8: Examples of two bodies directly connected with sheet flexures. Left: A cross-hinge. Right: Parallel sheet flexures. Adapted from [17].

Since this is a direct connection, the **C**s of both connections are added to give a total of six **C**s. By applying the redundancy rules in Table 2.1, it can be found that six constraints in two parallel planes results in a single redundant line. Thus for two directly connected ideal sheet flexures, a single degree of freedom **R** results, located at the intersection of the two flexure planes.

The resulting degree of freedom for the cross-hinge is a pure rotation **R** about the axis defined by the intersection of the flexure planes. The parallel flexures in the right hand frame of Figure 2.8 intersect at infinity, resulting in a freedom **R** at infinity, equivalently a translation **T** along the axis perpendicular to the planes of the flexures.

2.2.3. Constraint Redundancy

It was stated earlier that overconstraining a body can lead to undesirable consequences, such as a loss of performance or higher cost. In some cases, and with appropriate forethought, addition of (sometimes many) redundant constraints can actually be beneficial.

Take the two systems in Figure 2.8 as examples. In both instances, it is possible to add an infinite number of extra sheet flexures as direct connections between the two bodies without altering the resulting freedom space so long as [61]:

1. For the cross-hinge, the plane of every new flexure sheet intersects the existing rotation **R** line.
2. For the parallel flexures, every new flexure sheet remains parallel to the existing flexure sheets.

The increased redundancy in either case is often used in machine design to increase stiffness, load bearing capacity and/ or dynamic performance of a mechanism [61]. Redundant constraints are also often added to a mechanism to create symmetry and better balance the stiffness or thermal stability of a system. The main trade-off is that very careful fabrication and assembly is needed to ensure that misalignments do not cause undesired overconstraint. The increased stiffness also naturally reduces the compliance of the flexure system, requiring greater forces to generate a desired motion.

2.2.4. Effectiveness of a Constraint

This section returns to the concept of an instant centre of rotation to explain the effectiveness of a constraint. In the three constraint planar problem, each constraint restricts motion about the instant centre formed by the intersection of the other two constraints. This is demonstrated in Figure 2.9.

In this arrangement, two constraints C1 and C2 produce an instant centre IC at the centre of the segment. An anti-clockwise moment M_{ext} would lead to a small rotation about the IC. Adding a third constraint C3 provides a countering moment M_{C3} through the lever arm acting along the line of length L drawn perpendicular to the third constraint, through the instant centre. The greater the length of the moment arm, the more effective the constraint [57, p. 72]. Equal length constraints fixed to the vertices of an equilateral triangle will have equal moment arms and balanced stiffness, which is often the ideal arrangement.

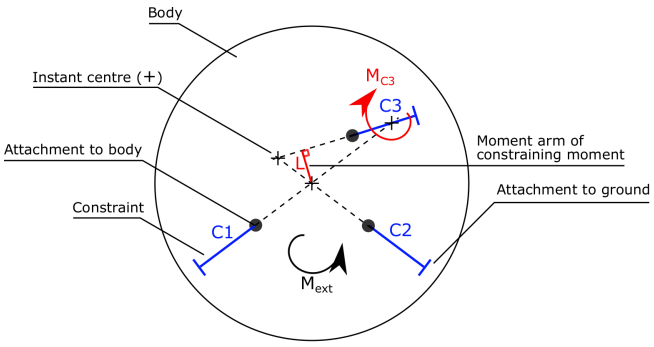

Figure 2.9: Constraining moment of an ideal constraint. An external moment M_{ext} rotates the segment about an instantaneous centre IC at the intersection of constraints C1 and C2. Constraint C3 counters the moment with reaction moment M_{C3} acting over lever arm length L, halting the motion and constraining the segment. Also shown are the instant centre's resulting from the combined action of C2, C3 & C1, C3.

2.2.5. Thermal Centre

As the bulk temperature of a body changes, it expands or contracts according to its coefficient of thermal expansion (CTE). A mechanism can be made insensitive to thermal expansion through careful constraint design.

Consider the case where a feature or location of a part, such as the bore in the left frame of Figure 2.10 needs to remain stationary regardless of thermal expansion. By ensuring that all constraint surfaces lie along lines radial from the target point, expansion or contraction of the part will not result in motion of that point. This is called the *thermal centre*. Not all constraint patterns define a thermal centre.

This principle is very useful in the design of mirror supports, which are often arranged to allow radial growth of the optic without displacing the focal point, as in the right frame of Figure 2.10. Note that the central point will remain stationary even when the support struts themselves expand and contract. However, the body will undergo a "clocking" rotation about the z axis. Mirroring the struts so that each support is opposed by its symmetric opposite will negate this effect, at the expense of a build up of internal stresses in the overconstrained system. Those stresses can be passed on to the optic, deforming the optical surface and ultimately, causing yield or buckling failure in the struts or optic. Clearly, careful design is needed.

An alternative method to reduce the effects of thermal expansion is to *athermalise* the structure by using re-entrant ("switchback") structures or using two materials in series with differing CTE's to tune the net thermal expansion of the structure.

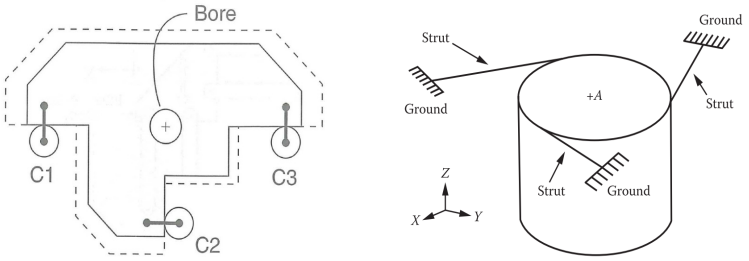

Figure 2.10: Using exact constraint design to define a thermal centre. Left: The point of intersection between the lines drawn along constraint surfaces will be stationary as the body thermally expands and contracts (dotted lines). The position of the bore will therefore be insensitive to thermal expansion. Adapted from [17]. Right: The mirror is free to grow radially while the focus remains aligned with the optical axis A. Adapted from [126].

This concludes the theory regarding exact constraint design. The Freedom And Constraint Topology method was central to the concept synthesis phase documented in Chapter 6 *Concept Generation*. The method is introduced in the next section.

2.3. The Freedom And Constraint Topology (FACT) Method

The Freedom and Constraint Topology (FACT) method was introduced by Hopkins & Culpepper in two foundational papers [61, 62], upon which the following section is based. The FACT method was instrumental to methodically exploring the design space for the PMAO mechanism. It demonstrably facilitates an exhaustive exploration of the available constraint design space, which was the reason it was selected for the synthesis phase of this thesis. This is only a very brief synopsis, with no further justification and several large gaps. The reader is referred to the original papers for a very readable tutorial.

2.3.1. The Principle of Complementary Topologies

Constraint and freedom *sets* are collections of constraint and freedom lines, arranged in several elemental geometries, shown in Figure 2.11. The entities shown in this figure are those most frequently encountered in compliant mechanisms. See the original paper for the complete set of possible constraint sets.

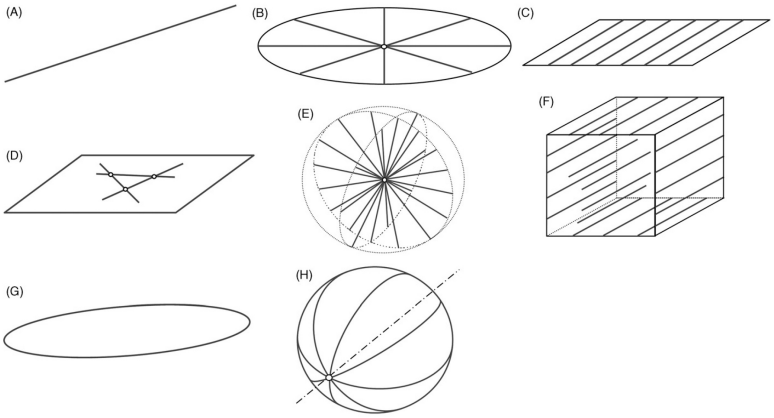

Figure 2.11: Geometric entities used to describe collections of freedom and constraint lines. Only those that are immediately relevant to flexure based design are shown. See the text for a description of each. Adapted from [61].

The descriptions given by Hopkins for each of these entities are repeated below [61]:

A Line: A line of a given orientation.

B Pencil: All co-planar lines that intersect at a common point.

C P-Plane: All co-planar, parallel lines of a given orientation.

D A-Plane: All lines on a given plane.

E Sphere: All lines that intersect at a common point.

F Box: A box of infinite extent that contains all parallel lines of a given orientation.

G Hoop: A circle that has a radius approaching infinity.

H Hoop Surface: All hoops with normal vectors that are orthogonal to a given axis.

A freedom or constraint set is usually insufficient to fully describe the constraint state of a mechanism. Instead, a freedom or constraint *space* is used, which is simply the superposition of two ore more freedom or constraint sets [61].

The central idea of the FACT method is the *Principle of Complementary Topologies*, which extends Blanding's *Rule of Complementary Patterns* from constraint lines to more topologically generic freedom and constraint spaces. Two corollaries also follow:

F1. **Principle of Complementary Topologies**
A freedom space and a constraint space contain complementary freedom and constraint topologies when all lines in the constraint space are complementary to all lines in the freedom space [61].

F2. **Principle of Complementary Topologies: Corollary I**
The freedom and constraint spaces are uniquely mapped to each other [61].

F3. **Principle of Complementary Topologies: Corollary II**
Rotational freedom lines and constraint lines must intersect in order to be complementary [61].

The second corollary has been truncated here to represent the case of rotation freedom lines only. The original also considers screws, which were not necessary for the PMAO concept synthesis. The most important outcome from these statements are that a catalogue of uniquely mapped freedom and constraint spaces, helpfully provided by Hopkins in [61], can be used to synthesise a constraint pattern for a desired freedom space, or the reverse process can be used to find the freedom pattern resulting from an existing arrangement of constraints in a mechanism. These diagnosis and synthesis processes are summarised in Figure 2.12.

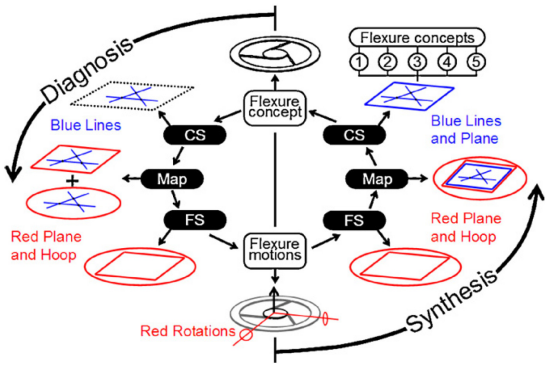

Figure 2.12: Synthesis and diagnosis using the FACT method. Adapted from [61].

It will be shown in Chapter 3 *Requirements Generation* that the PMAO must control the mirror in three degrees of freedom. The complete set of matching freedom and constraint spaces permitting three degrees of freedom is shown in Figure 2.13. The final four sets use geometric entities that were not introduced earlier in Figure 2.11. These provide freedoms that are of no use to the PMAO, but are included to reinforce the notion that this method provides an exhaustive catalogue of all possible constraint patterns that will allow motion in three degrees of freedom.

The terminology used to refer to freedom and constraint spaces in [61] is re-used throughout this thesis. A freedom space is denoted F_{ij} and a constraint space C_{ij}. The case i categorises the number of freedoms allowed by each of the constraint spaces and the type j is simply a sequential ID to catalogue each of the matching spaces in the case family. For example, panel A in Figure 2.13 is formally denoted F_{31} / C_{31}.

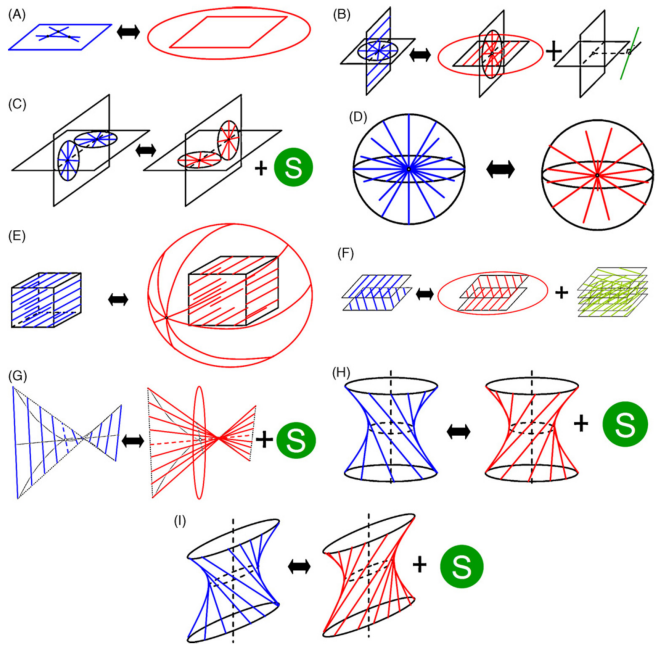

Figure 2.13: All constraint spaces (blue) giving three degrees of freedom in either rotations (red) or screws (green). Adapted from [61].

2.4. Geometric Optics

This section introduces several basic elements of geometric optics relevant to the operation and performance of the PMAO mechanism. The diffraction limit is introduced first, followed by the Strehl ratio which is used to quantify the optical performance of the active optics. The section concludes with the most critical aberrations that effect the PMAO and what causes them.

The Diffraction Limit

The primary task of any optical system is to make an *image* of an *object* or *source*. For many optical performance metrics, it is simplest to look at how the optical system images a point source of light, however for an Earth observation telescope the source is most often a ground scene. For simplicity, the discussion below relates to point sources, though the metrics can be extended to describing imaging performance for scenes as well.

Due to the wave nature of light, light from a point source passing through an optical system is *diffracted* into an *Airy Disk*, shown in Figure 2.14. The Airy Disk describes the best focussed spot of light that can be retrieved from a perfect optical system. Approximately 84% of the incident radiation will be focussed into the central Airy disk with the remaining radiation spread out into surrounding concentric rings.

The *resolution* of a system is a measure of how well it can resolve two closely spaced objects. This is fundamentally limited by diffraction. Thus the best possible resolution is called the *diffraction limit*, defined as the smallest distance between two point sources of light with equal intensity that can still be resolved by the system. The *Rayleigh Criterion* can be used to approximate this theoretical limit for a spacecraft via

$$L \approx 1.22 \frac{\lambda h}{D} \tag{2.1}$$

where the minimum resolvable spacing L on the ground is a function of the wavelength λ of the radiation, the altitude h of the spacecraft and diameter D of a circular primary mirror.

The Strehl Ratio

In practice, imperfections in the shape, position and orientation of the optical elements introduce *aberrations*, which spread the light out from the centre of the Airy disk. The *Strehl ratio* is the ratio of the light in the centre of the Airy disk of the aberrated image to that of the perfect system, shown in Figure 2.14. For a well corrected system, a Strehl ratio of 0.80 indicates that the system has reached the diffraction limit. Thus one of the main DST mission requirements is to design a system capable of imaging ground scenes with a Strehl ratio of at least 0.80.

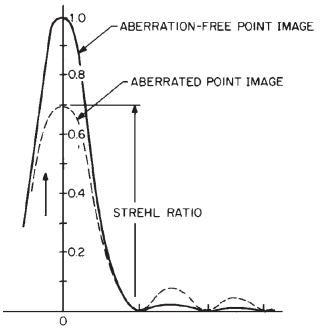

Figure 2.14: The Airy disk and Strehl ratio from a point source of light. Adapted from [107].

Aberrations, Wavefront Errors and Optical Path Difference

Aberrations are the manifestation of *wavefront errors*, deviations between the aberrated and ideal spherical wavefronts emanating from a source, as illustrated in Figure 2.15. As aberrations are introduced, the amount of energy in the central disk decreases, thus decreasing the Strehl Ratio. The combined function of the PMAO and Aberration Correction System (ACS) is to remove these wavefront errors: the PMAO removes discontinuous errors while the deformable mirror in the ACS removes continuous wavefront errors.

The *Optical Path Difference* (OPD) gives a measure of these errors. It is the difference between the distance from a reference point on the optical axis to a point on a reference spherical wave front centred on the reference point, and the distance along the same line from the reference point to the actual wavefront.

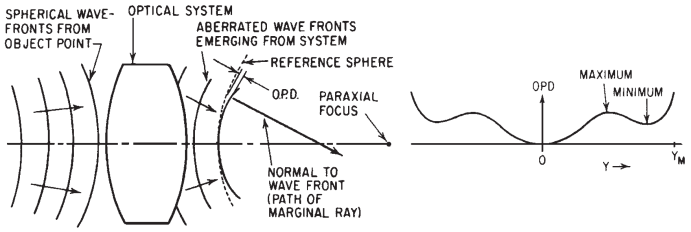

Figure 2.15: Left: Schematic of OPD calculation for a small defocus error. Right: Graphical representation of OPD against zone for third & fifth order spherical aberration. Adapted from [107].

The OPD of the DST optics is calculated via *ray tracing* using the MATLAB FORTA package, which can then be converted to the overall Strehl ratio to verify the mission requirements.

Two of the main aberrations to be corrected by the PMAO are decentre and defocus, caused by translations of the primary mirror segments, depicted in Figure 2.16. A *decentre* occurs when the mechanical axis of an optical element is translated a small amount normal to the optical axis. A *defocus* occurs when the focal point of an optical element is translated along the optical axis away from the image plane. Defocus is corrected with compensating *piston* translations of the M1 segment along the Z_M axis, while decentre can be somewhat corrected by *tip* and *tilt* rotations of the segment about the X_M and Y_M axes.

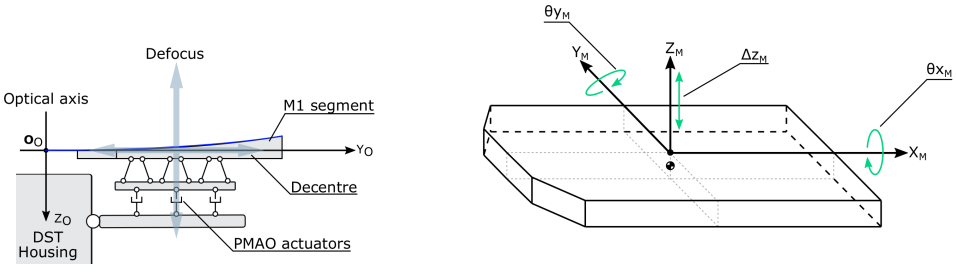

Figure 2.16: Decentre and defocus caused by translations of the M1 segments can be correct with piston, tip and tilt motions driven by the PMAO.

This concludes the basic theory underlying much of the technical work in this report. The next chapter begins the front-end systems engineering efforts, with the requirements generation.

3

Requirements Generation

The need analysis and general concept for the DST were introduced in Chapter 1 *Introduction to the Deployable Space Telescope*. The mission goal was synthesised into two top level mission objectives, listed in Table 3.1.

Table 3.1: DST mission objectives.

ID	Description
MIS-OBJ-01	The Ground Sample Distance of the DST shall be no larger than the state of the art in commercial visual spectrum Earth Observation imaging platforms. As of 2017 this was DigitalGlobe's WorldView-4 satellite with a Ground Sample Distance of 0.31 m in the panchromatic band.
MIS-OBJ-02	The lifetime cost of the DST shall be less than the state of the art in commercial visual spectrum Earth Observation imaging platforms. As of 2017 this was DigitalGlobe's WorldView-4 satellite with an estimated cost of USD$850 million including ground network upgrades.

The requirements generation process was conducted within the context of these two mission objectives. The stakeholder analysis and mission requirements were defined at the mission level, while the functional analysis was conducted at the subsystem level of the primary mirror active optics in line with the research goals of this thesis.

The interaction between the DST instrument and various stakeholders was investigated in a stakeholder analysis, summarised in Section 3.1. The Customer and TU Delft were identified as the critical stakeholders. The key outcome of this section was a series of customer requirements which have been adopted by the DST team as mission requirements. A functional analysis was then carried out in Section 3.2 to extract the functional requirements of the PMAO. These were translated into system requirements in Section 3.3.

DST Requirements and Verification Document

The *DST Requirements and Verification* document is attached in Appendix D. This is a team level document that was the synthesis and culmination of the work carried out in this chapter and Chapter 4 *Verification Plan*. Prior to this work, requirements, requirement ID's, safety factors and other verification inputs were inconsistent and often duplicated across the several student projects already completed for the DST. The document includes the complete list of requirements for the DST as of its writing early on in this thesis. It has since been used by other team members in their work on other subsystems.

Several new requirements were added to the M1 subsystems to propagate the PMAO requirements. Nearly 100 requirements involving the PMAO directly, or in conjunction with other M1 subsystems, were subsequently generated. Designing to so many requirements was far beyond the level of detail expected of a preliminary design. Instead, several critical requirements were identified and taken as the main requirements for this thesis. These are highlighted in Section 3.3.

3.1. Stakeholder Analysis

The requirements generation process began with a stakeholder analysis. The system boundary diagram in Figure 3.1 identifies the numerous stakeholders of a possible DST mission. It is important to note at the outset that the DST project is a *conceptual* study. For the purposes of this requirements generation process, critical stakeholders are those who have an immediate impact on the DST design at the current, conceptual, level. These stakeholders are indicated by the shaded boxes in Figure 3.1.

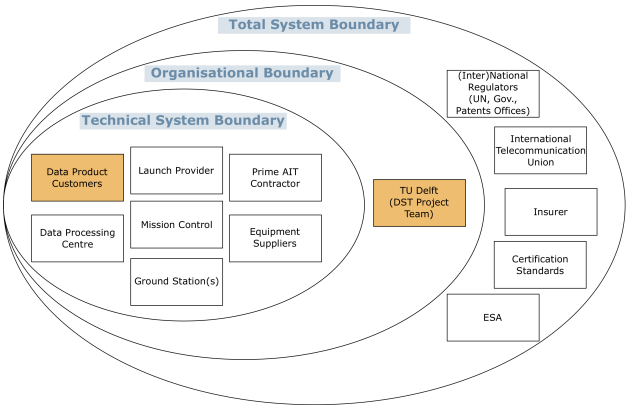

Figure 3.1: DST mission system boundary diagram. The technical system boundary delineates those stakeholders that actively interact with the DST mission; the organisational boundary defines system managers and developers; and the total system boundary encompasses all other stakeholders.

The customer is identified as the first and most critical stakeholder for the DST since the mission need and goal statements are predicated on the basis of the customers' desire to have access to low cost, high spatio-temporal resolution EO imagery. Since the DST has no commercial customer, the "customer" is included as a place holder. For backwards compatibility with prior work, the customer stakeholder requirements are considered synonymous with the existing mission requirements, which were formalised in technical language in [48]. All mission requirements are summarised in Table 3.2 with traceability back to the mission objectives.

The inclusion of TU Delft in Figure 3.1 denotes both the DST project team as well as any academic, commercial or licensing concerns that may be derived from university administrators. The academic nature of the DST project leads to several constraints for the concept development phase of the project thus the TU Delft is also identified as a critical stakeholder. The stakeholder requirements have been derived on the understanding that the DST project may be a future space mission, rather than as an avenue for students to work towards the award of degrees. This means that academic requirements for the DST team projects are not included. However, there is a desire to foster collaboration within European industry and to control procurement & knowledge flows throughout the project. Both needs are traceable to a desire to keep development costs low. This is greatly simplified by avoiding ITAR controlled technologies and designing for a European launcher. These requirements are new to the project, they have not been previously formalised.

The remaining stakeholders are not considered critical for the purposes of this requirements generation process. Airbus Defence & Space NL are included in the "Prime AIT Contractor" stakeholder category as this is the perspective from which they have been providing advice to the DST team. However, they are not driving any requirements for the DST. Although prior work has identified launch cost as a major contributor to the overall cost of providing EO imagery to customers [48, 116], the launch provider is not considered a critical stakeholder as it is the *customer* that drives the need for a low cost product.

3.2. Functional Analysis

With the mission requirements defined, the system requirements for the PMAO could be derived. The usage of the PMAO subsystem within the context of the greater DST payload operation was presented in the functional flow block diagram in Figure 1.7 on page 7. From discussions with DST team members, the DST project manager and experts at ADSNL, it has been widely accepted that the major design challenges lie in designing systems that can fulfil the functions required of functional blocks F-7 to F-14. The main PMAO functionality arises in functional blocks F-8 "M1 Deployment", F-10 "M1 coarse alignment", F-11 "M1 phasing" and F-13 "Start image acquisition". The PMAO must meet the top down budgets through deployment, phasing and image acquisition.

Table 3.2: DST mission requirements with traceability back to the mission objectives. WorldView-4 cost from [116].

Mission Objective	Mission Requirement	Description
MIS-OBJ-01	MIS-REQ-01	The Ground Sampling Distance of the instrument shall be equal to 25 cm in the panchromatic band from an orbital altitude of 500 km.
MIS-OBJ-01	MIS-REQ-02	The swath width of the instrument shall be wider than 1 km (threshold) / 5 km (goal).
MIS-OBJ-01	MIS-REQ-03	The system shall have one panchromatic channel with wavelength range 450 - 650 nm and GSD of 25 cm at 500 km.
MIS-OBJ-01	MIS-REQ-04	The system shall have one blue multispectral band with wavelength range 450 - 510 nm and GSD of 100 cm at 500 km.
MIS-OBJ-01	MIS-REQ-04	The system shall have four multispectral bands with the wavelength ranges and GSD indicated (at 500 km): Blue (450 - 510 nm) - 100 cm Green (518 - 586 nm) - 100 cm Yellow (590 - 630 nm) - 100 cm Red (632 - 692 nm) - 100 cm
MIS-OBJ-01	MIS-REQ-05	The Signal-to-Noise Ratio (SNR) of the instrument shall be higher than 100 for a reflectance of 0.30 and a sun Zenith angle of 60°
MIS-OBJ-01	MIS-REQ-06	The nominal Modulation Transfer Function (MTF) at both the Nyquist frequency and half the Nyquist frequency shall be higher than 5% (threshold) / 15% (goal).
MIS-OBJ-01	MIS-REQ-07	After calibration, the residual Strehl ratio of the system shall be higher than 0.80.
MIS-OBJ-01	MIS-REQ-08	The mass of the instrument shall be lower than 100 kg (threshold) / 50 kg (goal).
MIS-OBJ-01	MIS-REQ-09	In the stowed configuration, the volume of the instrument shall not exceed 1.5 m^3 (threshold) / 0.75 m^3 (goal).
MIS-OBJ-01	MIS-REQ-10	The DST shall not use any ITAR controlled components or technology.
MIS-OBJ-02	MIS-REQ-11	The DST shall be designed for compatibility with the TBD launcher.
MIS-OBJ-02	MIS-REQ-12	The DST shall comply with national (NL) and international regulations during AIT activities, launch, operations and end of life.

A context diagram was used to identify the scope of the system and its interactions with stakeholders, other systems and subsystems in Subsection 3.2.1. Icam DEFinition for Function Modelling (IDEF0) functional flow diagrams were used to formalise the interaction between the PMAO and related systems during a typical use case in orbit in Subsection 3.2.2. The top-down systems budgets, which guide the relationship between the optical and thermo-mechanical domains, are introduced in Subsection 3.2.3. An N2 chart was employed to understand critical interfaces between functions, presented in Subsection 3.2.4. It was found that there was a critical interface between the mechanical design of the PMAO and the optical/ electrical/ control elements of the telescope. In practice, this interaction is embodied by the calibration procedure which was accordingly explored in detail in Subsection 3.2.5. The functional analysis also revealed that the original baseline mechanical design included a coordinate frame rotation that had not been included in the ETEP modelling. This is discussed in Subsection 3.2.6.

3.2.1. PMAO Context Diagram

The context diagram in Figure 3.2 illustrates the context within which the PMAO must operate through the relevant functional blocks described by Figure 1.7. Major inputs, outputs, environments, stakeholders and subsystems are included. The context diagram helped to identify functions, interfaces, inputs and outputs that may be outside of the more obvious use cases.

The main input is light from the Earth ground scene. The primary output is the stacked and phased image from the primary mirror which continues on through the DST optics. Although there are numerous instances of precision mirror fine positioning mechanisms on Earth and in space (for example, [82, 93, 108, 120]), the combination of the environment it must operate in, the mass it must move and the tolerances on its performance are unique. No deployable optics have yet operated in low Earth orbit.

The PMAO must survive the launch environment and survive and operate in the space environment.

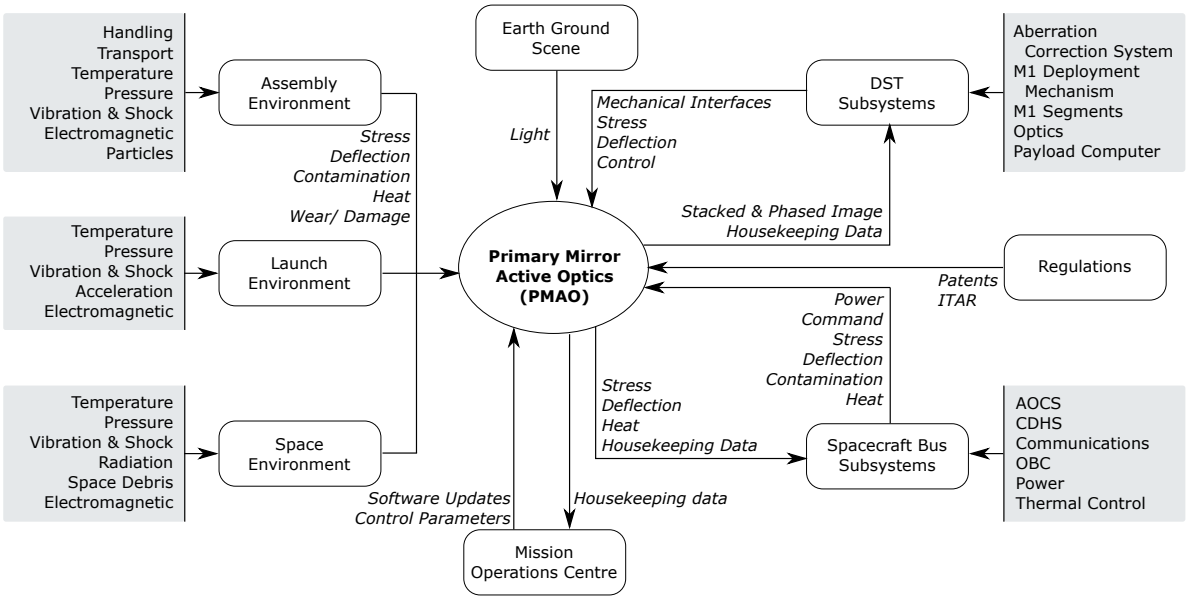

Figure 3.2: Context diagram of Primary Mirror Active Optics (PMAO).

Stresses, deflections, heat, contamination are all environmental inputs. The PMAO will be part of command and control loops at various levels: within the telescope itself, within the larger spacecraft and through direct control from mission operations. Data on the subsystems' status is transmitted to controllers with commands transmitted back. The spacecraft bus itself is also a major contributor to the PMAO performance. Vibration and shocks from onboard mechanisms, power delivery and thermal control are input to the PMAO while stresses, deflection, heat and data are transmitted back to the bus. Regulations restrict certain aspects of design, procurement and operation. The context diagram gives a good picture of how the PMAO will interact with the DST and stakeholders.

3.2.2. Functional Modelling

Since the PMAO must fulfil certain functions at different stages of operation, it is useful to look at the combined functionality of the wider image correction system. The functional architecture of the calibration subsystem was formalised over a series of interviews with the optical design team [49]. The results are illustrated by the contextual level IDEF0 functional architecture in Figure 3.3. The IDEF0 (Icam DEFinition for Function Modelling) diagram compactly summarises the flow, inputs, outputs, controls and mechanisms of a family of related functions.

Some of the major concepts of Figures 3.3 and 3.4 and justification for their inclusion are listed below. The top down systems budgets are central to the bottom up engineering effort. They are discussed in detail in Section 3.2.3.

Active Calibration Functions

The major function of the PMAO will be to phase and stack the primary mirror segments, indicated as functional block F-11 "M1 phasing" in Figure 1.7. Thus there are two main functional blocks within the active calibration subsystem: FCAL-02 “Phase & Stack M1 Segments” and FCAL-03 “Correct Continuous Wavefront Errors”. The first block refers to manipulation of the M1 segments relative to each other, known as “phasing”. This block corrects for errors described by the first three Zernike polynomials. These are often referred to as phasing errors and manifest as discontinuities in the wavefront. The FCAL-03 block refers to manipulation of the deformable mirror to remove continuous wavefront errors. These blocks currently act in series, though it is possible that they could work in parallel. This is a topic for future discussion once a model of the PMAO performance is integrated into the End-to-End Performance (ETEP) model of the telescope.

The required functionality is considered in greater detail in Figure 3.4, which drills down on block FCAL-02 of Figure 3.3. A critical sub-function of block FCAL-02 is that the PMAO must permit independent manipulation of each M1 mirror segment *individually* in three degrees of freedom: Piston, Tip and Tilt. These are defined within the individual segment coordinate frames.

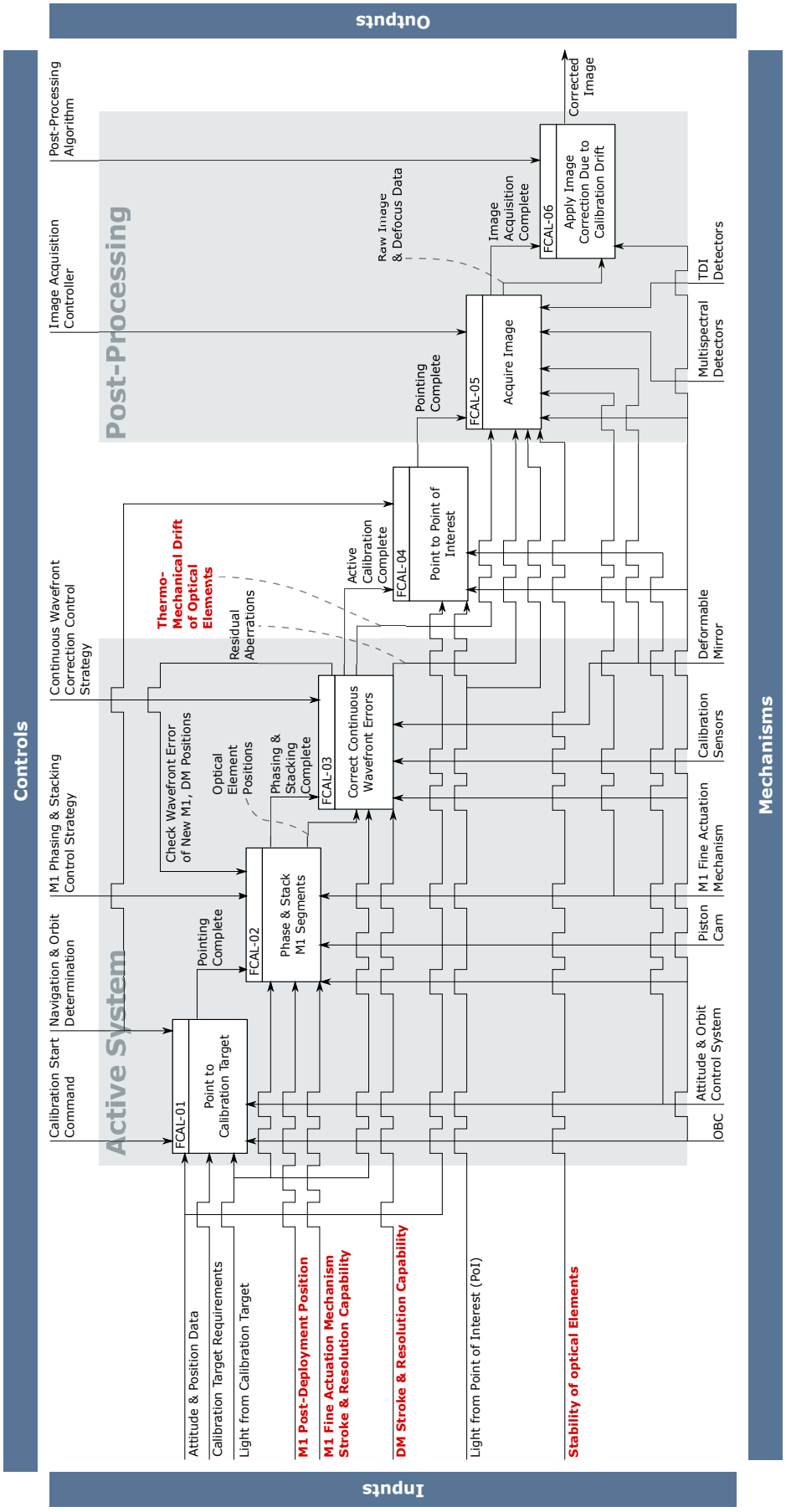

Figure 3.3: Contextual level IDEF0 functional architecture of DST image correction subsystem. Elements referring to top down system budgets are in bold red text.

Calibration Scene

The calibration scene is the image that is used by the telescope for the active calibration subsystem. The AOCS system will need to point the telescope at this scene as the spacecraft traverses its orbit. References to "extended scene" in this report and other project literature refers to the use of an image for calibration instead of a point source (ie. a star or light source carried on board) as is the case for most traditional EO imaging missions.

Sensors

So far, only optical sensing methods, using the telescope itself rather than direct measurement of optical element positions, have been considered. Optical methods provide a direct link between the data out of the calibration sensors and the image quality. If position sensors (such as capacitive edge sensors) are used instead, then additional physical processes are introduced between the sensed property and the performance of the optical system (that is, the image quality, which is optimised by the calibration system). In practical terms this would mean that the position sensors would also need to be calibrated in orbit before they could be used to calibrate the optical elements. It would be strongly preferable to avoid this extra layer of complexity, if possible. The current design uses sharpness and phase diversity methods, though Shack-Hartmann sensing will be considered if the thermo-mechanical design shows poor drift and stability performance.

Actuators (PMAO Actuation and Deformable Mirror)

Figure 3.3 shows that the actuation mechanism cannot be adequately designed by considering the top down budgets alone. The calibration algorithm dictates the full range of motion of the mechanism and how often it will be utilised, leading to fatigue and thermal control requirements.

3.2.3. Top-Down Systems Budgets

A number of interactions between functional blocks in Figures 3.3 and 3.4 are highlighted with bold red text. These interactions must meet specifications defined by the *Top Down Systems Budgets*. These budgets, often referred to as the "Top Down Budgets" or "Top Down Tolerance Budgets" in DST literature, are a series of allowable tolerances on the location, orientation and shape of the optical elements in the optical coordinate frame. They are critical functional requirements dictated by the optical design and guide all bottom up engineering efforts.

The latest budgets, summarised in Table 3.3, were defined by Dolkens in late 2017. Note that the primary mirror budgets are the most strict. A working value of $< 10\ nm$ has been adopted by the team for the PMAO resolution budget [49]. The definitions in the emphasis boxes and following discussion have been adapted from the literature study for this thesis [96].

Table 3.3: Top down systems engineering budgets [51]. Each budget must be met with a standard deviation of 2σ, which is dictated by the top-down modelling. *Note*: These budgets are defined in the telescope reference frame. To apply them in this thesis, they must be converted to the fixed PMAO mechanism coordinate frame $\mathbf{O_M}$ frame, by rotating the frame such that the X and Y axes are switched. See for example the axes in Figure 3.10.

	Position			Orientation			Radius	Shape Error
Element	**X** [μm]	**Y** [μm]	**Z** [μm]	**X** [μrad]	**Y** [μrad]	**Z** [μrad]	[%]	[nm]
				Deployment/ Coarse Alignment Budget				
M1	2	2	2	2	4	50	1×10^{-3}	50
M2	15	15	10	100	100	100	1×10^{-2}	25
M3	4	4	4	10	10	50	1×10^{-3}	10
				In-Orbit Drift Budget				
M1	2×10^{-2}	2×10^{-2}	2×10^{-2}	1×10^{-2}	2×10^{-2}	5	1×10^{-4}	5
M2	4	4	2	6	6	12	1×10^{-4}	5
M3	1×10^{-1}	1×10^{-1}	1×10^{-1}	1	1	5	1×10^{-4}	5
				Stability Budget				
M1	5×10^{-3}	5×10^{-3}	5×10^{-3}	2.5×10^{-3}	1×10^{-2}	5×10^{-1}	n/a	n/a
M2	1	1	5×10^{-1}	1.5	1.5	3	n/a	n/a
M3	2.5×10^{-2}	2.5×10^{-2}	2.5×10^{-2}	2.5×10^{-1}	2.5×10^{-1}	1.25	n/a	n/a

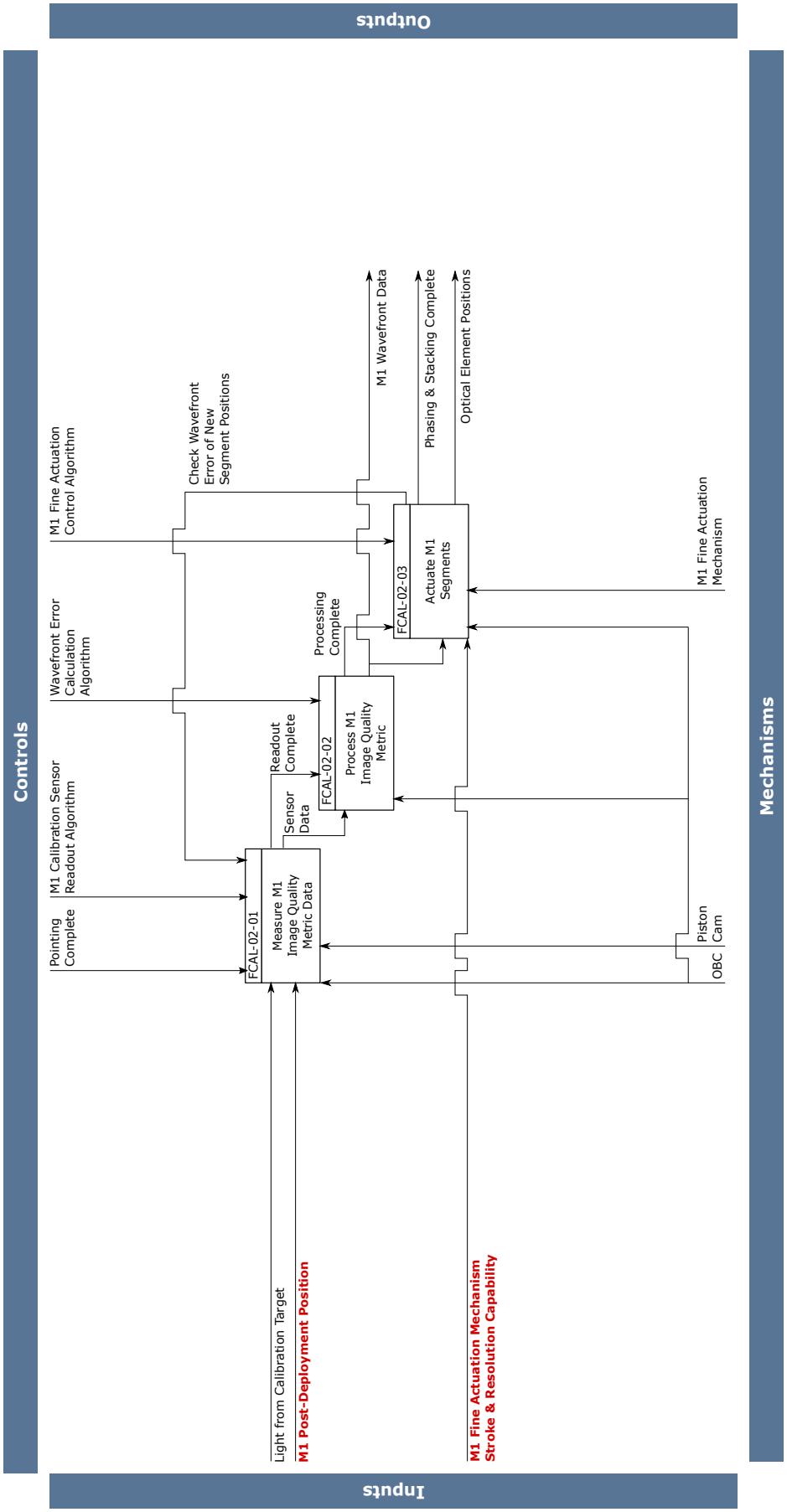

Figure 3.4: IDEF0 functional architecture of DST image correction functional block FCAL-02 "M1 Phasing & Stacking" . Elements referring to top down system budgets are in bold red text.

Deployment Budget
The maximum allowable deviation of the position of the optical surface from the desired datum after deployment and prior to coarse (or fine) calibration. This only applies to the deployable elements: M1 and M2.

Coarse Alignment
The maximum allowable deviation of the position of the optical surface from the desired datum after coarse alignment. This only applies to the active optics elements: M1 and M3.

Active Optics Resolution Budget
The maximum allowable increment between two successive actuated positions of the active optics. Currently only applies to the PMAO actuators.

In-Orbit Drift Budget
The maximum allowable spatial deviation of an optical surface that can occur between completion of the last active calibration procedure and the end of the next image acquisition, provided that the deviation can be considered (pseudo-)static over the period of image acquisition.

Stability Budget
The maximum allowable spatial deviation of an optical surface during image acquisition. Note that this only applies during image acquisition.

Deployment and Coarse Alignment

Figure 3.5 illustrates the deployment, coarse alignment and actuation resolution budgets. The in-orbit drift and stability budget concepts are shown in Figure 3.6. The drift and stability budgets differ from the others in that they must be held only over certain periods of time, though the spatial definitions of “piston” and “tilt” in Figure 3.5 still hold.

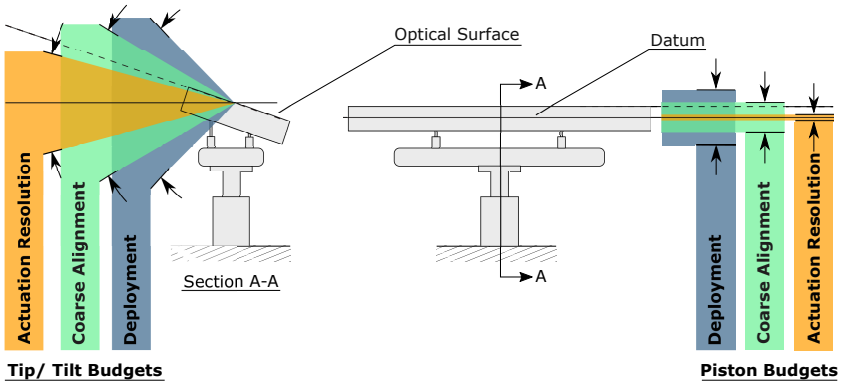

Figure 3.5: Illustration of deployment, coarse alignment and calibration resolution budgets as applicable to an M1 mirror segment. If the segment were to deploy to the position shown, the DST would not need a coarse alignment system. Adapted from [96].

The team has assumed that the deployment mechanism will be able to meet the coarse calibration budget directly, precluding the need for a coarse calibration system. Therefore the deployment budget is considered the same as the coarse alignment budget. If the deployable elements are not able to meet this goal, a coarse actuation mechanism and separate deployment budget will be implemented. An extra sensing system will also be needed as the range of the current optical sensing methods is not big enough to determine the position of the optical surface beyond the coarse alignment budget. This analysis is a topic for future work.

In Orbit Drift and Stability

The purpose of the in-orbit drift budget is to ensure that the optical system delivers an image of sufficient quality that it may be corrected using post-processing. The literature study for this thesis found no quantitative definition in any of the existing project literature of what may be considered a "pseudo-static" periodic displacement. A first attempt was made in that publication and is repeated here [96].

As a minimum, optical modelling has shown that diffraction limited image quality is maintained for displacements no greater than that stipulated by the stability budget. Applying this over the period of image

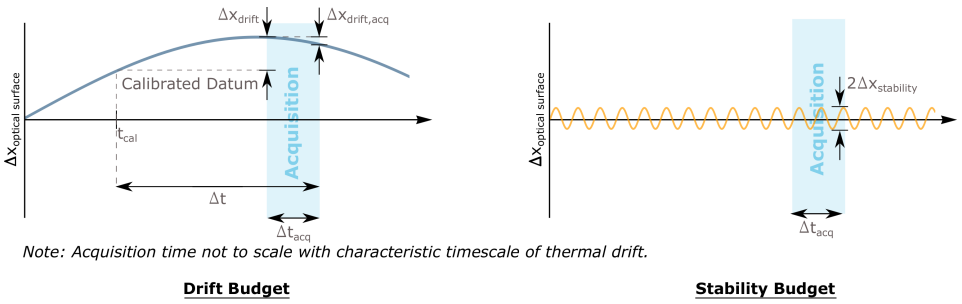

Figure 3.6: Illustration of drift and stability budgets. The time between the last active calibration t_{cal} and completion of an image acquisition is Δt. The calibration establishes a datum from which the maximum allowable displacement Δx_{drift} between t_{cal} and any time during image acquision Δt_{acq} is defined. A periodic motion can be considered pseudo-static if the maximum displacement $\Delta x_{drift,acq}$ is no greater than the stability budget $\Delta x_{stability}$ over the acquisition time. Adapted from [96].

acquisition, currently on the order of one second [51] though an exact number is yet to be defined, gives a threshold for the maximum allowable rate of change of displacement over time.

With reference to the quantities in Figure 3.6 then, a periodic displacement can be considered pseudo-static if, at no point during image acquisition, the instantaneous rate of change of the displacement $\frac{\delta x}{\delta t}$ is no greater than $\frac{\Delta x_{stability}}{\Delta t_{acq}}$.

3.2.4. N2 Chart: System Interfaces

From the context diagram and IDEF0 diagrams, system interfaces can be explicitly identified and documented using an N2 chart. The N2 chart shown in Figure 3.7 helps to visually identify strongly interacting systems and functions. The chart uses the common convention with functions listed across the diagonal, outputs horizontal to the functions and inputs vertical. Its purpose is to optimise and focus tight control of the interfaces between functional blocks. The blocks are not listed sequentially as in the IDEF0 diagrams. Instead, they have been organised so that functions with significant interaction are grouped together into logical modules. Since the subsystem is being considered at an abstract level, interfaces are specified in broad categories of mechanical, thermal, optical, environmental and electrical.

It is logical to separate interface control between the thermo-mechanical and sensing and control functions, indicated by the two shaded boxes in Figure 3.7. Unsurprisingly, the work packages assigned to members of the DST team have been divided into either thermo-mechanical design or optical & control design. The heavy reliance of the mechanical elements on the thermo-mechanical aspects of the environment and mission phases are immediately visible in the top left block of the N2 chart.

Note also the long interaction between synthesis of the actuator commands and actuation of the segments. Care must be taken in defining what these signals must look like, when and how they are transmitted and what information they must contain. This interaction is currently mediated by the M1 calibration algorithm. The results in Section 9.4 *Operations Functionality Verification Activities* will demonstrate the high sensitivity of the PMAO mechanical requirements to decisions made within the calibration algorithm.

The primary interface between the two modules is via the optical performance of the mechanical elements. It helps then to specify the interface between them in terms of optical performance. This has already been done from a top-down perspective: The top-down systems budgets define the allowable motion in the mechanical elements such that diffraction limited imagery is possible. From a bottom-up perspective, it will also be useful to assess the performance of the mechanical elements in terms of optical metrics such as spot size, RMS OPD and/ or Strehl ratio. The literature study for this thesis found that a similar approach was used for the development of the JWST, see for example reference [63]. Integration of the model of the PMAO mechanism performance in the ETEP model, a key deliverable of this thesis, will enable this in future work.

The N2 chart highlighted the need to pay special attention to the interface at the mechanical/ optical boundary. In practice, this interface is mediated by the calibration procedure, which is explored in more detail in the Section 3.2.5. Although the procedure had been set out in other DST publications [50], it had not been translated into mechanical requirements of the PMAO before this thesis.

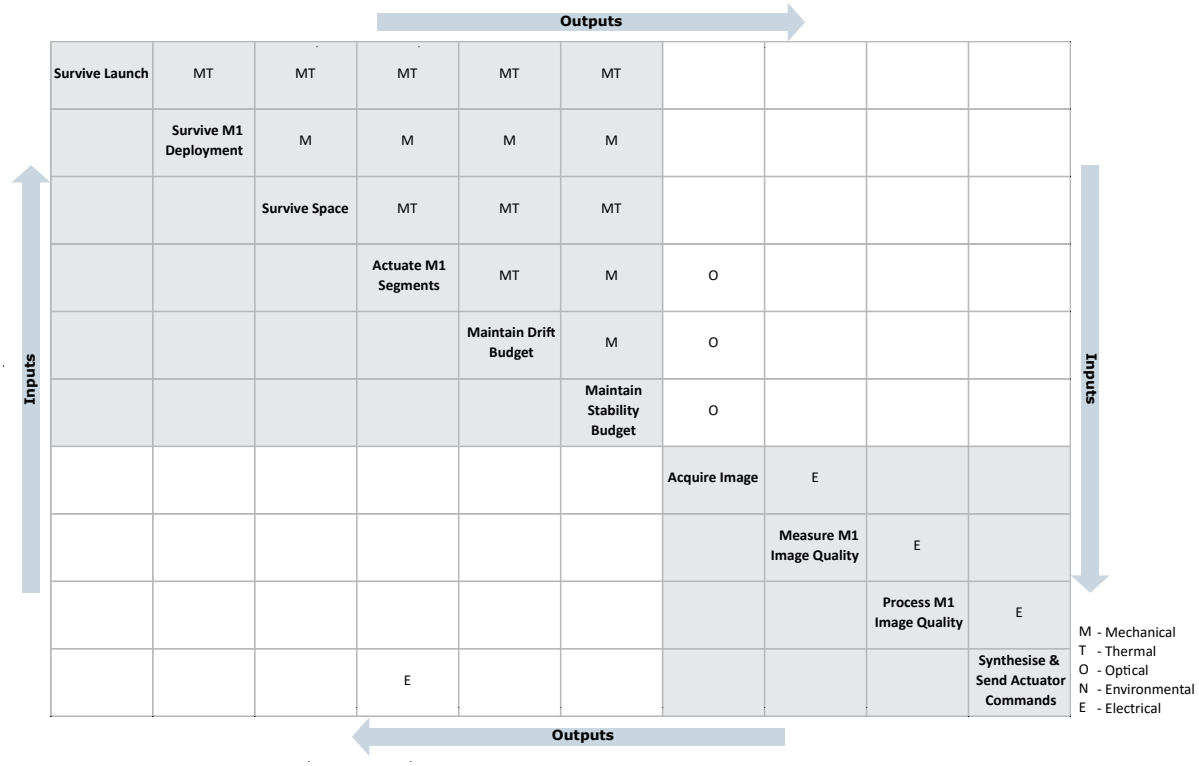

Figure 3.7: N2 chart of PMAO subsystem only, showing mechanical, thermal, optical, environmental and electrical interfaces. Functions are listed across the diagonal, outputs are horizontal from and inputs are vertical to, each function.

3.2.5. Primary Mirror Calibration Procedure

The calibration procedure & required range of motion in each DOF at the segment level is illustrated in Figure 3.8. First, the tilt error is corrected through a Nelder Mead Simplex optimisation algorithm which seeks to minimise the total error in $\theta_{y,M}$, followed by a similar procedure for the tip error. Correcting the tip and tilt orientation of the segments is called *co-alignment*. A piston scan stage then determines the positions of each of the segments relative to one another. This scan procedure dictates the maximum required piston range of motion of the mechanism and is outlined in more detail below. Aligning the segments in the piston direction is called *co-phasing*. New tip and tilt orientation values are then calculated.

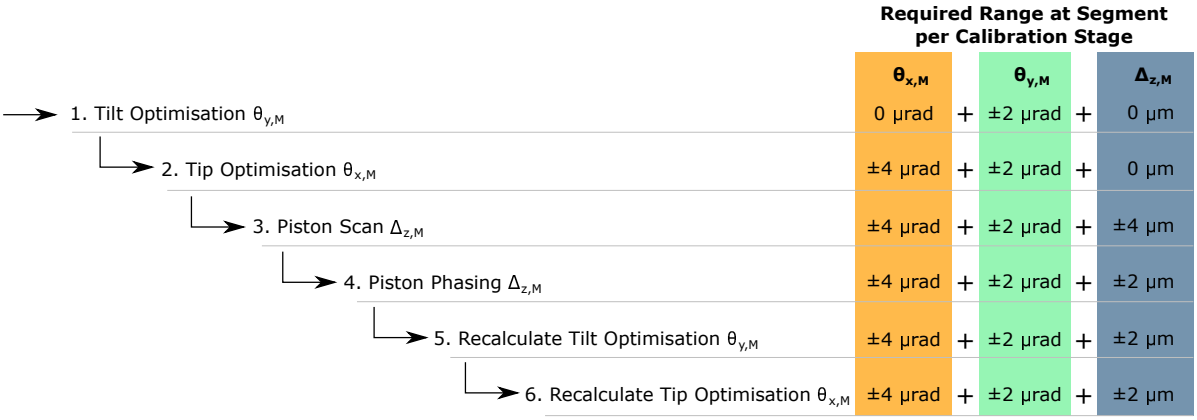

Figure 3.8: Segment calibration procedure and required mechanism range of motion in each DOF at the segment level for the serial scan procedure. The largest combined range of motion requirement is during the piston scan stage. Note that the coordinates given in the figure are in the fixed PMAO mechanism coordinate system $\mathbf{O_M}$, *not* in the telescope optical coordinate system as in other DST project literature.

The mechanism must be capable of delivering the *combined* range of motion in each degree of freedom simultaneously. The ranges are governed by the deployment/ coarse alignment budgets in Table 3.3, and

whether a serial or dual simultaneous scan procedure is used. The largest combined range of motion requirement is during the piston scan stage. Both piston scan procedures are outlined below and illustrated schematically in Figure 3.9.

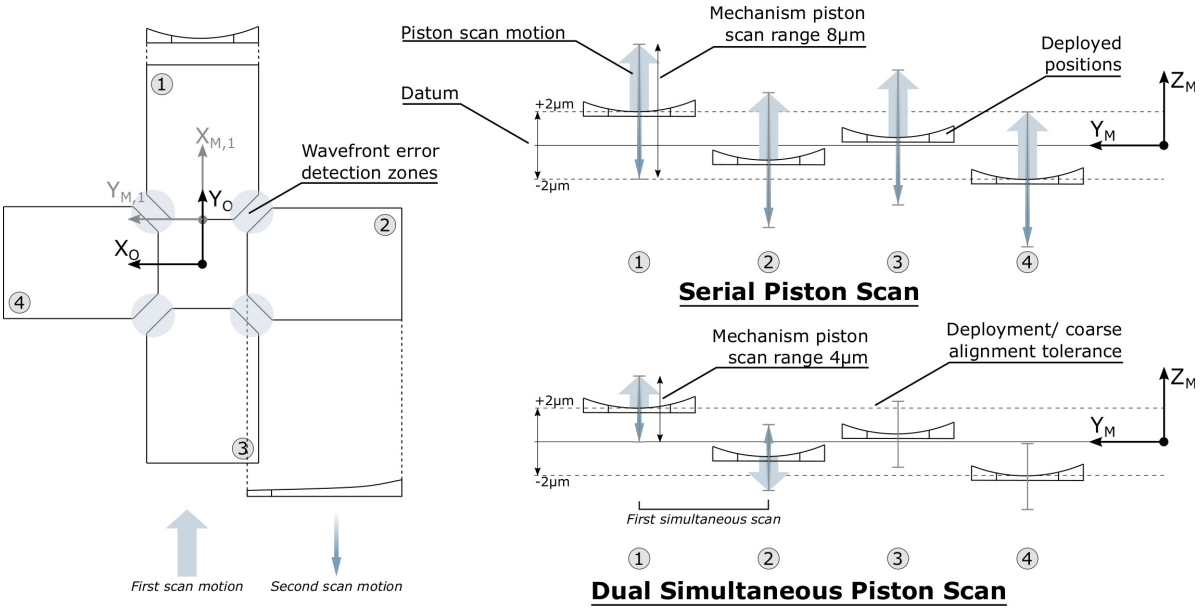

Figure 3.9: Segment phasing schemes. The dual simultaneous scan scheme requires half the piston stroke of the serial scheme but requires each mechanism to scan through its range twice. Only a single scan is illustrated for the simultaneous scheme. In operation, segments 1 and 2 would first scan, then 2 and 3, 3 and 4 then finally 4 and 1. The horizontal dashed lines indicate the nominal deployment/ coarse calibration tolerance budget. The datum is the nominal deployed position.

Serial Piston Scan Procedure

In the serial scan, each segment is scanned through its full range whilst the remaining segments are held stationary. The serial scan method has a segment range of motion equal to twice the full range of the deployment tolerance budget. This is best understood by examining Figure 3.9. The deployment/ coarse alignment tolerance is indicated by the two horizontal dashed lines. In this example, all four segments deployed within the tolerance but there are considerable misalignments. Note that segments 1 and 4 were deployed to the maximum and minimum of the deployment tolerance respectively.

The scanning procedure begins with segment 1. Since there is no knowledge of which side of the datum the adjacent segments deployed to, and to guarantee that segment 1 will align with segment 2 at some point, it must scan through the full deployment tolerance range. Since segment 1 deployed at the deployment tolerance maxima, it must be capable of scanning all the way through to the deployment tolerance minima, a range of -4μm for the piston DOF. Similarly, if the segment had deployed to the deployment tolerance minima as is shown for segment 4, it would have to scan through a range of +4μm in the opposite direction to guarantee that it would capture the adjacent segments. Thus the mechanism must be capable of moving the segment through a bidirectional range of motion twice that of the full range of the deployment tolerance budget.

Throughout the segment scan, the wavefront error is measured in the two detection zones of the actuated segment to find the relative locations of the two adjacent segments. All four segments scan through the Z_M axis one after the other until the relative positions of the segments are known.

Dual Simultaneous Piston Scan Procedure

Instead of scanning a single segment at a time, the dual simultaneous scan method actuates two adjacent segments at once in opposite directions, again illustrated schematically in 3.9. Since both segments operate at once, the simultaneous method requires only half of the segment range of motion in each DOF compared to the serial scan method. The trade-off is that each segment must execute the scan operation twice.

The current calibration scheme utilises the serial piston scan method so there will be no further discussion of the simultaneous scan method. Furthermore, designing for the serial scan method provides greater design flexibility for future iterations of the DST. The top down system budgets listed in Table 3.3 are given to within

two standard deviations. As the DST design matures, these values may need to be adjusted to 3 standard deviations, possibly leading to an increased range of motion requirement. Additionally, future work may show that it is not possible to achieve the larger range of motion needed for the serial method. Using the simultaneous method with half the required range of motion could be a valid backup solution in either case.

3.2.6. Coordinate Frame Rotation

In the initial design of the M1 segment, the rear plane of the mirror and upper plane of the M1 deployment mechanism support frame were parallel to the $X_O Y_O$ plane as in Figure 3.10*a*. This meant that the PMAO mechanism coordinate frame $X_M Y_M$ was also parallel to the optical $X_O Y_O$ plane. This was the ideal geometric arrangement as the system requirements, which are modelled & reported in the optical frame, could be directly translated into the mechanism frame.

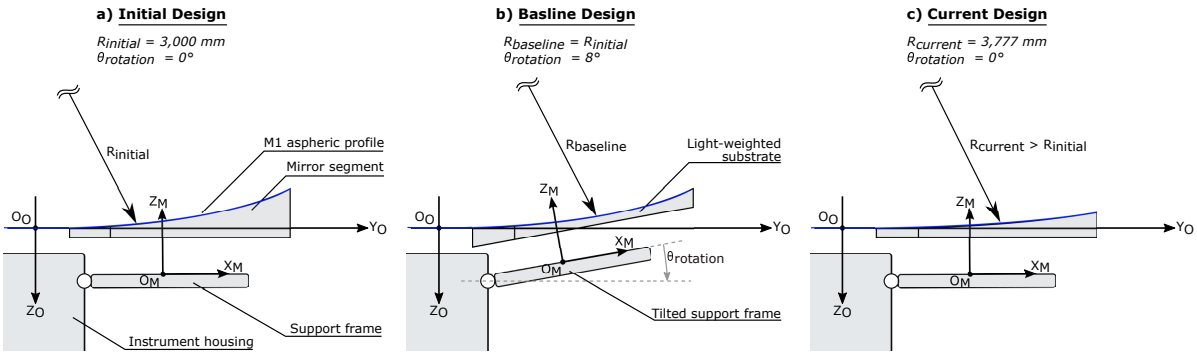

Figure 3.10: History of mechanism coordinate frame rotations. The PMAO design in this thesis uses configuration c) "Current Design".

However, this led to a thick & heavy mirror substrate that occupied a large volume when stowed. To reduce mass, the rear plane of the substrate was given an 8° rotation as indicated in Figure 3.10*b*. The nominal position of the deployment mechanism support frame in the deployed position was also rotated 8° such that the interface plane of the support frame and back of the mirror continued to be parallel. This resulted in an 8° rotation between the optical and mechanism coordinate frames about the X_O axis. No consideration of the effect of this decision on the requirements flow down or opto-mechanical performance of the active optics was given at the time. Indeed, the end to end performance modelling continued to model the state in Figure 3.10*a* despite the updated mechanical design in 3.10*b*, and had gone unnoticed until the detailed requirements flow down was conducted for this thesis.

Dolkens conducted a brief analysis of the 8° offset [49]. It was concluded that the 8° rotation could be accommodated by the system and still meet requirement MIS-REQ-07, a minimum Strehl ratio of 0.80. The results are shown in Figure 3.11.

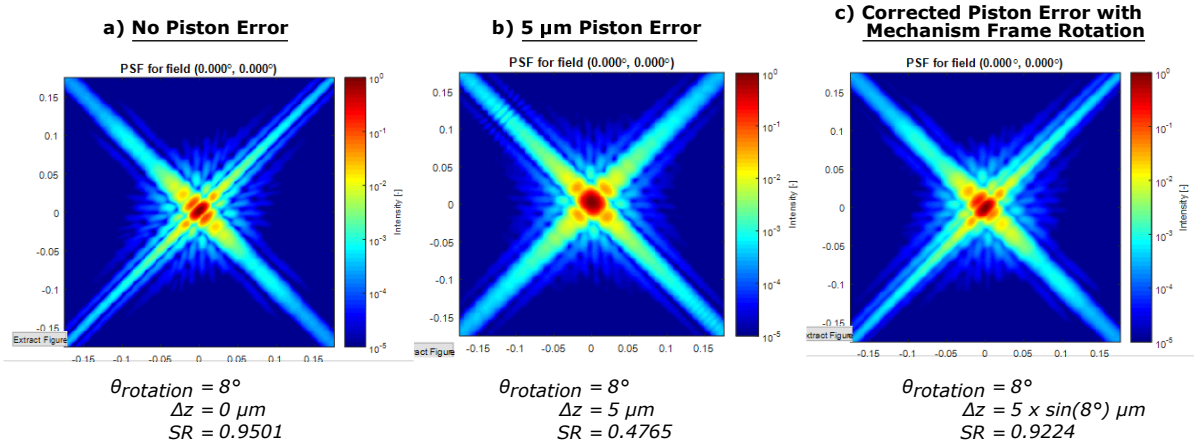

Figure 3.11: Point spread functions of M1 5 μm piston error and correction in presence of 8° PMAO mechanism coordinate frame rotation. MIS-REQ-07 states that the Strehl ratio must be greater than 0.8. Note that after the piston correction this requirement is met, even with the coordinate frame rotation. Figures courtesy of Dennis Dolkens.

The radius of curvature of the M1 optical surface has since also been increased from 3,000 mm to 3,777 mm. The larger radius will not require such a large rotation of the mirror backplane to fit within the stowed envelope. The 8° value is therefore considered a worst-case state. Additionally, forming & polishing off-axis mirrors is much easier if the mirror backplane is parallel to the transverse plane in the mirror's optical frame. For these reasons, it was assumed that the backplane of the mirror could once again be made parallel to the $X_M Y_M$ & deployment mechanism support frame planes. The validity of this assumption will need to be confirmed when the mirror is designed in a future thesis. The requirement for a flat backplane parallel to the deployment mechanism frame has been specified in Section 9.6 *Flow Down Requirements*.

For completeness, it should be mentioned that the PMAO mirror support could, in principle, be modified to accommodate the rotation while still allowing actuation parallel to the optical frame axes. This was not considered in the PMAO design as the mirror angle & design are still subject to change. The simplest, ideal design in Figure 3.10*c* was adopted instead. The analysis summarised in Figure 3.11 demonstrates that this design can still meet the optical requirements even with a rotation of up to 8° if needed.

3.3. System Requirements Analysis

The system requirements analysis translated the functional requirements from Section 3.2 into a set of measurable system requirements. The output of this section was the requirements that the PMAO preliminary design must meet to fulfil the mission requirements. The control and electrical requirements were outside the scope of this thesis; the relevant areas were the upper left thermo-mechanical block of Figure 3.7.

Requirements discovery trees were used to decompose the high level functional requirements into sub-functions until they were at a level that could be described by specific system and functional requirements. The trees are included in Appendix B and introduced briefly in Section 3.3.1. The requirements were then detailed and collated into the full list included in Appendix D.

A number of requirements that were identified as being critical to establishing the feasibility of the PMAO were extracted and used to guide the design of the PMAO in this thesis. These requirements are discussed within the broad themes of system level requirements, operations functionality, launch survival and operations survival in Sections 3.3.2 to 3.3.5. These requirements are listed in several tables at the end of the chapter on pages 40 and 41.

To facilitate continuity from this project to future projects on the PMAO, further discussion and information regarding a number of requirements included in the full list but excluded from the requirements targeted in this thesis is provided in Appendix D. The note below aims to provide some clarity on the terminology used throughout the remainder of the report to describe the different configurations and states of the telescope.

A Note on Configurations and HDRM

A broad categorisation of the PMAO mechanism requirements can be divided into those which must be fulfilled in different instrument configurations: deployed, stowed, or requirements applicable to both states. For simplicity, throughout this thesis whenever the spacecraft is in the stowed configuration it will be assumed that any HDRM (Hold Down and Release Mechanism), if present, is engaged. Conversely, whenever the spacecraft is in the deployed state the HDRM will be disengaged. It was assumed that no HDRM will be used between the mirror and PMAO. This means that the structural interface between the mirror and PMAO mechanism will not change between the stowed launch and stowed/ deployed operational configurations. It was assumed that there *would* be an HDRM between the M1 deployment mechanism and the instrument housing.

Additionally, throughout the requirements development, a distinction has been made between the deployed configuration and *nominal* deployed configuration. The nominal deployed configuration is the ideal position of the primary mirror segment upon deployment. It is the position that would occur in the absence of any manufacturing, assembly, deployment, thermal drift and/ or stability errors. Lack of the world "nominal" in a requirement description implies that the requirement applies for all segment positions whilst in the deployed state.

3.3.1. Requirements Discovery Trees

Requirements discovery trees are a simple method of systematically exploring what a system must do. They were used to decompose the high level functional requirements into sub-functions until they were at a level that could be described by specific system requirements. Separate trees were developed for the functional requirements (capabilities), characteristics (system objectives, non-functional requirements) and constraints.

They are reported in Appendix B. Survival requirements were treated as functional requirements whereas compatibility requirements were treated as constraints since survival is generally performance based whereas compatibility constrains interfaces, volumes, standards and so on.

The context diagram in Figure 3.2 informed all trees while the IDEF0 and N2 charts from Section 3.2 primarily informed the functional requirements tree. Check lists [54, p. 619], [114] were also employed to check that all aspects of the mission and system were considered. Although the requirements discovery trees are extensive, only requirements relevant to the short to medium term objectives of the wider DST project were developed to maintain a realistic scope. Many requirements are still To Be Determined (TBD) because of immaturity in the payload and spacecraft bus definitions. It was beyond the scope of this thesis to rectify these design immaturities.

3.3.2. System Level Requirements

The system level requirements for the PMAO are given in Table 3.5 on page 40. They focus on the high level characteristics and programmatic requirements of the PMAO.

Requirement M1-MEC-13 formalises the need for the primary mirror to be deployable. PMAO-SYS-03 restricts the use of all parts to non-ITAR controlled components in a flow down from mission requirement MIS-REQ-10. In line with the goal to develop a feasible PMAO design, the PMAO manufacture, fabrication and assembly should not require new or low TRL technology, equipment or processes. This is captured in PMAO-SYS-06. Although there is an overall mission cost target for the DST defined in mission objective MIS-OBJ-02, no top-down analysis has been conducted to define sub-assembly level cost requirements. A placeholder requirement is included in the full list but is not included in the thesis requirements.

The mass requirement was also included in the system level requirements list. Review of space mechanism literature found that the original mass requirement for the M1 subsystems was optimistic. A revision was necessary, as discussed below.

Revision of PMAO Mass Requirement

The 6 kg mass of the baseline mirror design [117] was used to generate the mass requirement for the M1 segment, PMAO-SYS-01 (see the full requirements list in Appendix D), and thereby the PMAO mechanism mass requirement. This is relatively heavy by modern standards at an areal density of 21.5 kg/m^2 so this value was taken as a conservative first estimate.

The original mass requirement for the PMAO was 4 kg for each segment deployment mechanism and PMAO mechanism *combined*. The literature study for this thesis found that this was very optimistic. Take for example the GAIA and Euclid secondary mirror mechanisms which provided five and three DOF control for mirrors of mass 1.9 kg and 3.1 kg respectively. The mechanisms themselves had masses of 5.0 kg and 3.0 kg respectively[8]. The Euclid mechanism completed development in 2017, reflective of a more modern design compared to that of GAIA which was developed circa 2011 [32]. No data was found for the mass of other space telescope mirror fine steering mechanisms.

Therefore, the mass requirement for the PMAO mechanism was separated from the deployment mechanism mass requirement and revised by scaling the M1 segment mass by the Euclid 3DOF mechanism to mirror mass ratio. Requirement PMAO-SYS-02 now states a PMAO mechanism mass of no more than 6.2 kg per segment assembly.

3.3.3. Operations Functionality

The top level functional requirement for the PMAO is to remove discontinuous wavefront errors from the full field of view during operations and AIT. This flows down to the PMAO mechanism which must enable controlled manipulation of the primary mirror segments in three degrees of freedom, and to the PMAO support which must provide a load path without over constraining the mirror. The kinematics of the mechanism dictate the flow down to the mechanism and individual actuators, so TBD values were assigned until a concept was selected. The operations functionality requirements are listed in Table 3.8 on page 41.

Further discussion for specific requirements is given below, starting with the top down tolerance budgets which define the range of allowable mirror deployment positions, and motions during image acquisition.

Top Down Tolerance Budgets

Flowing down the top-down system budget requirements to the PMAO was complicated by the lack of design maturity in all of the M1 subsystems. There were two options to define the top-down tolerance budgets for the PMAO.

First, their definition could be left at the M1 level per Table 3.3 so that no analysis would be necessary to decompose them to the deployment and PMAO mechanism levels. However, the top down requirements would then only be verifiable by modelling or testing both subsystems together. The preliminary M1 deployment mechanism design, system thermal modelling and definition of sources of on-board excitations would have to be relatively mature to allow this. Each of these elements were ongoing topics of research in parallel with this thesis, so it was reasonable to assume that this might occur. An analysis tool capable of modelling the whole M1 subsystem would also be needed, but was not yet available to the team.

Secondly, the requirements could have been flown down to the PMAO level, via either extrapolation of budgets from similar systems or statistical modelling akin to that already used to define the top down budgets at the telescope level (see for example [73]). The former option was not possible since there are very few systems comparable to the DST and its application, much less publications providing detailed tolerance breakdowns. The latter option would have required models of the deployment and PMAO subsystems to be integrated into the ETEP model to provide a basis for the statistical analysis. An objective of this thesis was to produce such a model for the PMAO however at the conclusion of the thesis, an equivalent model for the deployment mechanism remains a topic for future work.

Thus, the top down tolerance budget requirements were left at the M1 level, reflected in requirements M1-MEC-01, -04 and -07, listed in Table 3.8. This exposed the project to the risk that they would be unverifiable should the other subsystems not reach a useful level of maturity, or the necessary analysis tools not become available by the time verification started. These risks were fully acknowledged.

Mirror Radius of Curvature and Shape Error Tolerance Budgets

Mirror radius of curvature and shape error requirements were excluded as they are integrally linked to verification of the mirror design, which is outside the scope of the thesis. The PMAO design does, however, need to be aware of these requirements, so they are included in Appendix D.

Image Quality

In reality, the PMAO must operate in both flight and terrestrial Assembly, Integration and Testing (AIT) operations. This is reflected in the description of requirement PMAO-OPT-01. To keep this thesis work within reasonable bounds, it was assumed that the flight mechanical, thermal and electromagnetic environments will be more onerous than those during AIT and thus that if it could be shown that PMAO-OPT-01 could be met in the space environment then it could be met for terrestrial AIT.

Thermal Centre

For a mirror, it is desirable for the focal point to remain stationary under thermo-elastic strains to minimise decentre errors. This can be achieved by aligning the thermal centre with the focal point. Additionally, the mirror should be allowed to expand symmetrically about the thermal centre (and thus, focal point). Any stresses generated within the mirror due to the expansion should also be as symmetrical as possible to create symmetrical distortions of the optical surface, and to minimise astigmatism and/ or higher order optical aberration errors.

Since the M1 segments are off-axis mirrors, the focal point is far outside the footprint of the mirror support, so the above guideline could not be met. After discussion with the optics team, it was decided to set the thermal centre to the mirror centroid in requirement M1-MEC-35 as a first estimate [49].

Revision of Clearance Requirement

Requirement M1-MEC-08, derived in earlier work [117], stipulated that the M1 deployment and PMAO subsystems shall not position the back of the mirror more than 100 mm away from the instrument housing wall. This is not physically possible since the mirror segment would conflict with the space reserved for the stowed M2 booms. The actual minimum acceptable clearance is 120 mm, reflected in the removal of requirement M1-MEC-08 and inclusion of requirement M1-MEC-17.

Mechanism and Actuator Level Requirements

Requirements PMAO-MEC-23 and PMAO-MEC-29 to -31 define the range of motion and step size requirements at the mechanism level. These were defined through interviews with the optics team [49]. Note that there is no step size requirement in tip and tilt: there is freedom for these performance characteristics to flow on from the piston step size requirement PMAO-MEC-23. The actuator level requirements flow down directly from the mechanism requirements. Their definition was one of the outcomes of this thesis.

DST Compatibility

The PMAO must be compatible with the rest of the telescope. At the current level of design maturity, the main compatibility requirements relate to location and configuration of the components, including allowing the primary and secondary mirrors to deploy, being correctly located in the optical path and defining a usable volume. Future compatibility requirements will undoubtedly involve contamination, electrical interfaces & protocols, data rate, EMC and computational aspects.

3.3.4. Launch Survival

The launch survival requirements are given in Table 3.6 on page 40. Survival is defined as no degradation of the functional capabilities of the system as a result of being exposed to a given environment. It was clear that the DST design was too immature to allow detailed launch survival analysis. Instead, a survey of launch requirements across common European launchers was carried out to justify definition of a set of simple, conservative launch survival requirements. The data collected as part of this analysis is collated in Appendix D.

The survey found that the requirements recommended by subject matter experts at Airbus Defence & Space NL (ADSNL) in earlier DST studies [117] were well justified. Similar values have also been used in other space based fine pointing mechanisms. For example, 20g quasi static loads and minimum natural frequencies of 100 Hz were used in the preliminary design of the GAIA M2M mechanism [115] as well as on the IRIS spectrometer [121].

Therefore, the launch survival requirements stipulated by ADSNL were retained. Namely, that the design must survive 30g quasi-static loads which encompass the worst-case simultaneous loading by the actual quasi-static loads and various sources of vibration, as well as have a minimum natural frequency of 100 Hz. To account for worst-case loading and to verify survival against shear, the quasi-static loads were to be applied simultaneously along two axes in the launch vehicle coordinate system at once. Loads imposed by the thermal environment and any further qualification or safety factors were assumed to be included in this value already as well.

Finally, it was decided that the PMAO mechanism should not need power to function during launch so that the PMAO will not dissipate any heat or generate an electric field whilst in the payload fairing, easing launcher compatibility requirements. All of the launch survival requirements apply in the stowed configuration only.

3.3.5. Operations Survival

The operations survival requirements are given in Table 3.7 on page 40. Operations survival is defined as survival in the space flight environment. Assembly, Integration & Testing (AIT) operations were excluded from consideration to maintain a reasonable project scope. The PMAO assembly must survive the operational environment in the stowed configuration during Launch & Early Operations (LEOP), as well as in the deployed configuration during the main operational phase and end of life.

Requirements PMAO-MEC-41 and -42 stipulate that the PMAO must survive operations and deployment. External loads during flight operations can come from thrusting, thermal shocks, pyrotechnic shocks, ADCS pointing, debris impacts, atmospheric drag, radiation pressure and gravity. Internal loads can come from actuation of the PMAO itself and overconstrained thermo-elastic strains.

Since the structural interface between the mirror and PMAO mechanism does not change between launch and operations, it was assumed that if the mechanism could withstand the *launch* loads in the stowed configuration then it should be able to withstand external *operational* loads in both the stowed and deployed configurations. This simplifies the requirements for operational survival: inertial load requirements need only be defined and verified for launch.

LEOP Thermal Calculation

Perhaps the largest difference between the stowed and deployed configurations is the absence of the baffle and the thermal protection it offers prior to deployment in the LEOP mission phase. Stresses from differential thermo-elastic strains, caused either by overconstraint or interfaces between materials with different coefficients of thermal expansion (CTE), can cause structural failures over large temperature swings.

A simple thermal model using the equivalent network method was developed to make a rough prediction of the worst-case steady state hot and cold temperatures experienced by the M1 systems while in orbit, prior to baffle deployment. The calculation, including a discussion of methodology, assumptions and results is included in Appendix C *Stowed Operations Thermal Model*. The results are summarised in Table 3.4.

Table 3.4: Summary of steady state LEOP hot and cold case temperatures for primary mirror segments from the simple nodal equivalent network thermal model. See Appendix C *Stowed Operations Thermal Model* for more detail. Thermal uncertainty margins taken from Appendix D *DST Verification Document and Requirements List.*

Case	**Calculated**	**Design**	**Acceptance**	**Qualification**
Hot [K]	384	399	404	409
Cold [K]	188	173	168	163

It was found that the M1 system could experience temperatures from 188 K to 384 K, which was captured in requirement PMAO-MEC-52. Entries including several thermal uncertainty margins, used at different verification levels, have also been included in Table 3.4 for completeness. These margins are used to provide conservatism in the preliminary design stage and are formally introduced in Chapter 4 *Verification Plan*.

3.4. Verification of Requirement Definitions

Verification of requirement definitions refers to checking that the values and performance encoded in the requirements will lead to a system that provides the *expected* performance, thus meeting stakeholder expectations. This was initially conducted by inspection through interviews and discussions with senior DST team stakeholders. The definitions of several kinematic requirements were later verified as part of the telescope ETEP modelling, discussed in further detail in Chapter 9 *Verification*. The requirements should ultimately be validated with testing of the integrated system.

3.5. Chapter Summary

The boundary diagram helped identify critical stakeholders which led to the high level mission requirements. The IDEF0 diagrams fed into the N2 chart which showed that development of the PMAO should be divided into two logical blocks, first the thermo-mechanical elements and secondly the sensing and control. The N2 chart demonstrated that the interface between these blocks will be critical and established that the performance of the thermo-mechanical elements should, ultimately, be measured in tops of optical metrics.

IDEF0 diagrams were used to generate the requirements discovery trees which were decomposed until each function could be built up from individual requirements. A list of system requirements for the PMAO mechanism at the conceptual design level were developed as a result of each of these systems engineering tools. Critical requirements were extracted as focal points for the remainder of the thesis.

Table 3.5: PMAO system level and programmatic requirements used in this thesis.

ID	Description	Parent
System		
M1-MEC-13	The primary mirror shall consist of four deployable segments.	MIS-REQ-07
PMAO-SYS-02	The combined mass of all four PMAO mechanisms shall be no more than 24.8 kg.	M1-MEC-11
PMAO-SYS-03	The PMAO shall not use any components, technology or processes controlled by ITAR.	MIS-REQ-10
PMAO-SYS-06	The PMAO manufacture, fabrication and assembly shall not require development of new technology, equipment or processes.	MIS-OBJ-02

Table 3.6: PMAO launch survival requirements used in this thesis.

ID	Description	Parent
Structural		
PMAO-MEC-03	The PMAO support shall support the primary mirror segment during launch without overconstraint in the stowed configuration. Support is defined as providing a load path to the instrument housing.	PMAO-OPT-01
Mechanical		
PMAO-MEC-40	The PMAO shall be able to survive launch in the stowed configuration. Survival is defined as no impairment to the nominal functional capabilities of the system resulting from exposure to a given set of environmental conditions.	PMAO-OPT-01
PMAO-MEC-40-01	The PMAO shall survive a quasi-static load of 30g applied simultaneously to the x- and y- axes in the launcher coordinate frame in the stowed configuration during launch.	PMAO-MEC-40
PMAO-MEC-40-02	The PMAO shall survive a quasi-static load of 30g applied simultaneously to the x- and z- axes in the launcher coordinate frame in the stowed configuration during launch.	PMAO-MEC-40
PMAO-MEC-40-03	The PMAO shall survive a quasi-static load of 30g applied simultaneously to the y- and z- axes in the launcher coordinate frame in the stowed configuration during launch.	PMAO-MEC-40
PMAO-MEC-40-04	The PMAO first-mode natural frequency shall be greater than 100 Hz in the stowed configuration during launch.	PMAO-MEC-40
Electrical		
PMAO-ELE-01	The PMAO shall not require power during launch.	MIS-REQ-11

Table 3.7: PMAO operations survival requirements used in this thesis.

ID	Description	Parent
Mechanical		
PMAO-MEC-04	The PMAO support shall support the primary mirror segment during operations without overconstraint in the stowed and deployed configurations. Support is defined as providing a load path to the instrument housing.	PMAO-OPT-01
PMAO-MEC-41	The PMAO shall be able to survive the operational environment in the stowed and deployed configurations. Survival is defined as no impairment to the nominal functional capabilities of the system resulting from exposure to a given set of environmental conditions.	PMAO-OPT-01
PMAO-MEC-41-01	The PMAO shall survive steady state temperatures between 188 and 384 K (calculated temperatures) in the stowed configuration during LEOP.	PMAO-MEC-41
PMAO-MEC-42	The PMAO shall be able to survive deployment. Survival is defined as no impairment to the nominal functional capabilities of the system resulting from exposure to a given set of environmental conditions.	PMAO-MEC-41

Table 3.8: PMAO operations functionality requirements used in this thesis. Note that "primary mirror calibration system" refers to the PMAO.

ID	Description	Parent
Top Down Budgets		
M1-MEC-01	The deployment mechanism and primary mirror calibration system shall meet the deployment tolerance budget with a confidence level of $> 2\sigma$.	MIS-REQ-07
M1-MEC-04	The deployment mechanism and primary mirror calibration system shall meet the in-orbit drift budget with a confidence level of $> 2\sigma$.	MIS-REQ-07
M1-MEC-07	The deployment mechanism and primary mirror calibration system shall meet the stability budget with a confidence level of $> 2\sigma$.	MIS-REQ-07
DST Compatibility		
M1-MEC-14	The distance from the primary mirror plane to the secondary mirror plane along the optical axis shall be 1600 mm ± TBD μm in the nominal deployed configuration.	MIS-REQ-01
M1-MEC-17	The deployment mechanism shall position the mirror segments parallel to the telescope bus with a clearance of less than or equal to 120 mm in the stowed configuration.	MIS-REQ-09
PMAO-MEC-35	The thermal centre of each primary mirror segment shall be at the position of the segment centroid in the XY plane of the telescope optical coordinate frame.	PMAO-OPT-01
PMAO-MEC-50	The PMAO shall not impede deployment of the primary or secondary mirror.	MIS-REQ-01
PMAO-MEC-50-01	The PMAO shall not protrude laterally beyond the periphery of the primary mirror segment in the stowed or deployed configurations.	PMAO-MEC-50
Environment		
M1-MEC-15	The deployment mechanism and primary mirror calibration system shall operate at a nominal temperature of 298 K ±1 K during operations in the deployed configuration.	MIS-REQ-07
Optical		
PMAO-OPT-01	The PMAO shall remove discontinuous wavefront errors from the full field of view during imaging operations and AIT.	MIS-REQ-07
PMAO-MEC-01	The PMAO mechanism shall enable individual control of each primary mirror segment independently in translation parallel to the z-axis, rotation about the x-axis and rotation about the y-axis of the PMAO mechanism body fixed frame during AIT and operations.	PMAO-OPT-01
Mechanical: Mechanism		
PMAO-MEC-23	Each primary mirror segment shall have a maximum step size of 10 nm in the z-axis direction of the PMAO mechanism body fixed frame throughout the entire segment workspace.	PMAO-MEC-01
PMAO-MEC-29	Each primary mirror segment shall have a bidirectional rotational range of motion about the x-axis of the PMAO mechanism body fixed frame equal to the primary mirror deployment accuracy budget about the x-axis.	PMAO-MEC-01
PMAO-MEC-30	Each primary mirror segment shall have a bidirectional rotational range of motion about the y-axis of the PMAO mechanism body fixed frame equal to the primary mirror deployment accuracy budget about the y-axis.	PMAO-MEC-01
PMAO-MEC-31	Each primary mirror segment shall have a bidirectional range of motion in the z-axis direction of the PMAO mechanism body fixed frame equal to twice the primary mirror deployment accuracy budget in the z axis.	PMAO-MEC-01
Mechanical: Actuators		
PMAO-MEC-32	Each actuator of the PMAO mechanism shall have a total range of motion of TBD.	PMAO-MEC-01
PMAO-MEC-33	Each actuator of the PMAO mechanism shall have a maximum step size of TBD.	PMAO-MEC-01

4

Verification Plan

This chapter sets out the verification plan for the PMAO preliminary thermo-mechanical design. The work conducted in this chapter is synthesised into two documents: the *DST Requirements and Verification* guidelines document in Appendix D and the *PMAO Requirements Verification Plan* in Appendix E. The objective of the verification plan was to check that the preliminary design meets the design specifications as flowed down from the mission requirements and top down tolerance budgets within the resource constraints of the thesis.

The *DST Requirements and Verification* guidelines document includes definition and justification of verification methods, factors of safety and verification criteria. In the interest of brevity, this information is not repeated in this chapter and the reader is referred to the Appendices. The guidelines document has helped the team work towards a standardised verification method using clear documentation that is open to internal and external review. It is a "live" document and has undergone minor revisions since its introduction to the team. The version included in the Appendices is the original revision produced for this thesis by the author, with discussion input from A. Krikken and H. Kuiper.

The *Requirements Verification Plan* formalises the application of the guidelines document to the PMAO mechanism preliminary thermo-mechanical design. It lists a series of verification activities which, at their conclusion, will objectively demonstrate compliance of the design with the requirements listed in Tables 3.5 to 3.8.

Section 4.1 introduces the verification objective, constraints and strategy. Section 4.2 defines certain concepts relevant to the PMAO verification not included in the guidelines document. Most verification activities listed in the plan are self explanatory however several activities warrant further explanation, which are included in Section 4.3.

4.1. Verification Philosophy

The verification philosophy governs the type, number and sequencing of verification activities to be carried out. The verification philosophy itself was a function of programmatic and resource constraints, the type of product, the development status and the desired level of development. The verification objective, constraints and strategy are set out in Subsections 4.1.1 to 4.1.3 respectively.

4.1.1. Verification Objective

The objective of the verification plan was to provide a structured approach to generating quantitative proof that the design complies with the requirements to the level expected by the thesis goal. The goal of the thesis was to develop a preliminary thermo-mechanical design for the PMAO mechanism, to verify that design within the capabilities of an MSc thesis and to assess the verified design's technical and economic feasibility. Put plainly, the end product shall be a conceptual design delivered "on paper" to no more than a preliminary level of design completion.

4.1.2. Constraints

Three major constraints limited the scope of the PMAO verification process: level of definition of the DST hardware; availability of verification tools; and time. Each is discussed below.

Design Definition

The top down engineering, governed by the optical requirements, is relatively mature. The bottom up engineering of the mechanical subsystems and characterisation of the thermal environment are ongoing, while the spacecraft bus is still entirely undefined. Useful verification is very difficult if the test conditions are not representative of anticipated flight conditions, which is why many requirements in the full list in Appendix D were not included in Tables 3.5 to 3.8. Indeed, some of the requirements included in these tables in the early stages of the thesis were expected to be verifiable near its conclusion, however this turned out not to be the case. In particular, the feasibility of the deployment mechanism was still being established at the time of writing. Further exploration of this constraint was provided in Chapter 3 *Requirements Generation* and will be referred to again in Chapter 9 *Verification*.

Verification Tools

Rigorous verification of the top down tolerance budgets requires analysis or testing of the integrated systems. Testing a device like the PMAO was beyond the resources available to the thesis so verification relied upon analysis and in particular, the finite element method.

ANSYS Mechanical Workbench v.19[1] was originally selected for consistency with previous and ongoing DST work. When the verification plan was put together, it was known that the ANSYS *Academic Teaching Mechanical and CFD* license available to TU Delft students would not be sufficient to verify compliance with the top down budgets at the integrated mechanism level. A commercial license would be necessary, and a plan was put in place to secure a copy through industry partners.

Ultimately, the commercial license never eventuated. *SPACAR*[2], a low order finite element package written in MATLAB and freely available to TU Delft students, was used instead. *SPACAR* is introduced in Section 8.1 *The SPACAR Finite Element Package*, along with further justification for its selection.

Schedule

The schedule of the design work was limited to that of a standard MSc thesis. Conceptual design and modelling is a highly iterative process. Given the high interdependence of the PMAO on the M1 deployment mechanism and characterisation of the thermal environment during operations, the short schedule exposed the project to the risk that some requirements may not be verifiable due to delays in work by others. This was a natural and accepted consequence of working in a student team on a complex system.

4.1.3. Verification Strategy

Due to the above constraints, verification activities were limited to analysis and review/ inspection methods. Analysis was used when the requirement to be verified was too complex for simple inspection or review and there was sufficient data to permit a meaningful analysis.

Exclusions

To keep the work effort manageable, on-mission contingency events were not considered. These are undesired events that the spacecraft should survive. An example would be a PMAO mechanism actuator inadvertently driving to its full range of motion when the remainder of the kinematic mechanism is not also driving to a compatible position, forcing the mirror segment out of the achievable workspace.

Additionally, fatigue effects from repeated and sustained loads are ignored in this thesis since very little information is available for the DST regarding duty cycle of the PMAO, calibration times, image acquisition time, LEOP duration and so on. The model of the PMAO developed in this thesis can be used to find this information in future work.

Assumed Test Philosophy

The factors of safety listed in Appendix D are based on the assumption that the DST would undergo proto-flight qualification if it were to be built. The objective of verifying to qualification levels is to demonstrate that the design has sufficient margin to accommodate variation between multiple instances of the design [103, p. 398]. This gives the advantage that only one of each identical instance of a flight article must be tested, however it does carry a high factor of safety and thus decreased mass efficiency. In general, this option is useful for a fleet if the first flight article can accommodate the time for test in its schedule [103, p. 371], which is a possible application of the DST.

[1] https://www.ansys.com/

[2] https://www.utwente.nl/en/et/ms3/research-chairs/WAoud_niets_uit_wissen_aub/software/spacar/2015/intro/

Verification Level

The weakness of relying on graphical, mathematical or statistical models without testing is the inability to verify the models. Factors of safety and thermal uncertainty margins were used in the modelling to account for this, with the expectation that they would be reduced in line with correlation between model and test results should they ever be conducted. The factors of safety depend on the desired verification level.

In line with the assumed test philosophy, verification of survival based requirements was conducted to qualification conditions to demonstrate that the concept could not only survive flight, but also testing.

To simplify verification for preliminary design, qualification conditions were captured by using slightly higher factors of safety as listed in the guidelines document. Additionally, the 30g launch loads were assumed to already include qualification loads. The qualification level temperature ranges were used for thermal survival calculations.

4.2. Verification Definitions

The following criteria, methods and assembly levels, summarised in Subsections 4.2.1 to 4.2.3, are referred to throughout the verification plan.

4.2.1. Verification Criteria

The verification criteria for strength requirements are a margin of safety (MS) against yield and/ or buckling greater than or equal to 0. Definition of the margin of safety is given in Appendix D. For non-trivial stress states in members, the "equivalent stress" or von Mises stress was used for comparison with the yield strength of a material.

Yield failure is defined as a permanent detrimental deformation of a part. The yield strength of a material is commonly defined as the stress at which the material has permanently (plastically) deforms by 0.2% [103, p. 367]. This may be too much deformation for the PMAO to continue functioning however it is used throughout the thesis for simplicity. Coupon testing is typically required to determine allowable loads for the candidate material such that no deformation occurs at the design limit load. This is beyond the scope of the thesis so it was assumed that the factors of safety applied sufficient conservatism to ensure yield does not occur.

The verification criteria for most of the functional requirements were the quantities defined in the requirements themselves. Thus for mechanical functional requirements, the limit loads were equal to the calculated loads (no safety factor applied). Per the verification guidelines document, the design temperature range for thermal functional requirements was taken to be the calculated temperature range plus the design thermal uncertainty margin of $\pm 15\ K$. The survival range was the calculated value $\pm 25\ K$.

4.2.2. Verification Methods

The following definitions taken from [76] were used to select the verification activities.

Table 4.1: Summary of verification methods used in the Verification Plan. Definitions adapted from [76].

Method	Description
Analysis	Mathematical or computational techniques. Can be deterministic or stochastic.
Inspection/ Review	Inspection of the product itself (inspection) or inspection of design documentation (review of design).
Test	Physically testing a test model of the design in representative conditions.
Similarity	Checking if the item is similar in design, process and quality control to another that has already been verified to the same or more stringent requirements.
Demonstration	Demonstration of the requirement through operation of the item.

4.2.3. Assembly Levels

The requirements apply variously to different levels of the PMAO mechanism assembly and its integration into the spacecraft. Table 4.2 defines how those levels were broken down within the verification plan. Some of these assembly levels can be further broken down into sub-levels per Table 4.3.

Table 4.2: Assembly levels for verification activities.

Level	Description
Spacecraft	Telescope integrated to spacecraft bus.
Telescope	Whole DST, assembled to instrument housing but not to spacecraft.
M1 Segment Assembly	Includes fully assembled PMAO mechanism assembly with deployment mechanism.
M1 + PMAO Assembly	Includes fully assembled M1 segment, PMAO mechanism with actuators & PMAO support. No deployment mechanism.
PMAO Assembly	PMAO mechanism assembly only, no mirror segment or deployment mechanism.
Actuator	Primary mover used to actuate the PMAO mechanism.

Table 4.3: Assembly sub-levels for verification activities.

Sub-Level	Description
Per item	Four independent verification activities are conducted, one for each segment assembly.
Sum of all items	A single verification activity, covering all four instances at once.
Representative	Representative of all instances. A single verification activity on a single representative item or design. This assumes that the representative item can be instantiated as required with sufficient repeatability to warrant a single verification activity.

4.3. Verification Requirements Plan

The Verification Plan sets out the verification activities necessary to demonstrate compliance of the preliminary PMAO mechanism thermo-mechanical design with the requirements generated in Chapter 3 *Requirements Generation.* Most verification activities are self explanatory however a few warrant further explanation, given below.

M1-MEC-01, M1-MEC-04, M1-MEC-07: Top Down Tolerance Budgets

It was already mentioned that verification of requirements M1-MEC-01, M1-MEC-04 and M1-MEC-07 would require inputs from others, as well as an extended FEA license. In the absence of this license, an estimate of the PMAO's contribution to the thermal drift budget would be made by hand. It was likely that estimating the contribution to the deployment and stability budgets would not be possible without a mature M1 deployment mechanism design.

PMAO-MEC-35: Maintenance of a Thermal Centre During Imaging

The ideal method to verify that the PMAO and support maintain a thermal centre at the mirror segment centroid, is to conduct a finite element simulation at the full M1 segment assembly level in the presence of operational thermal loads. This was not possible so an estimate of the thermal centre drift was to be made by inspection of the kinematics of the mirror support.

PMAO-MEC-03: Supporting the Mirror During Launch

To support the mirror through launch, the mechanism must provide a load path from the mirror through to the DST housing; the support must survive launch; and it must not overconstrain the mirror. Two verification activities, VA-05-02 and VA-05-03, check compliance with this latter requirement.

First, the kinematic design was inspected to make sure it is exactly constrained. Second, the equivalent lateral stiffness of the support (ie. in the direction of radial expansion of the mirror) was checked to be less than 1000 times the opposing stiffness of the mirror. This was to make sure that small displacements of the support do not result in deformation of the optical surface. A crude estimate of the mirror stiffness can be made from finite element simulations. It was assumed in all launch survival strength checks that the actuators are unpowered.

PMAO-MEC-04: Supporting the Mirror During Operations

Activity VA-08-01 assumes that since the load path from the mirror to the PMAO doesn't change with the configuration, then if the PMAO survives and can adequately support mirror through launch (ie. requirement PMAO-MEC-03, -40 are verified), then the PMAO can withstand the inertial loads experienced during operations. Verification activity VA-08-02 makes additional checks for thermo-elastic induced loads.

PMAO-MEC-41 & PMAO-MEC-41-01: Survival of Operations

Verification of requirement PMAO-MEC-41 (survival of operations) via activity VA-09-01 followed the same assumption logic as above for PMAO-MEC-04. Additionally, only components that were overconstrained were to be verified to survive the worst case thermo-elastic stresses in verification activity VA-10. Components that are not overconstrained are free to expand without build-up of internal stress. Yield failure under actuation loads was also checked.

PMAO-MEC-42: Survive Deployment

Verification that the PMAO can survive deployment was difficult given that the deployment concept is still being studied. A basic level of verification was sought by comparing the deployment method and likely deployment loads to the launch loads. If the expected deployment loads were less than the launch loads and that requirement PMAO-MEC-40 was verified, then it was assumed that the PMAO could survive deployment.

4.4. Chapter Summary

With the documents provided in Appendices D and E, this chapter set out the verification plan for the preliminary PMAO thermo-mechanical design. Overall, the verification philosophy was conservative, commensurate with such an early phase of design and exposure to the risk of absence of detailed data and verification tools. This conservatism can be decreased as the design develops by:

- Correlating models with test data to reduce uncertainty factors.
- Improving the fidelity of subsystem design and mission definition.
- Ensuring access to detailed, verified analysis tools.

The verification plan was used twice throughout the PMAO development. In the first instance, the original baseline design was verified for compliance with several critical functional requirements in a bid to answer the first research question of the thesis. The results of this process are documented in the next chapter. It will be shown that the original baseline did not comply with those basic requirements, necessitating a design revision. The verification plan was then applied again, this time to the revised PMAO design. The results of that second process are documented in Chapter 9 *Verification*.

Major assumptions from the verification plan development are summarised in Table 4.4.

Table 4.4: Major assumptions for the verification plan.

ID	Description
ASM-VER-01	External loads during operations including pointing, thrusting, deployment of other parts are less than the launch loads.
ASM-VER-02	Manufacturing loads are not larger than the launch loads.
ASM-VER-03	The yield strength can be used as the yield failure criterion for compliant parts rather than the elastic limit.
ASM-VER-04	Actuators must survive launch and operations in an unpowered state.
ASM-VER-05	Deployment loads will be less than or equal to the 30g launch loads.

5

Baseline Functional Verification

The original baseline design of the primary mirror active optics was developed by van Putten in a single project that also covered conceptual design of the M1 deployment mechanism and mirror segment [117]. The original baseline was divided into two main components: a whiffle tree mirror support and the actuation mechanism. Both components received initial sizing, and structural and thermal analyses.

The objective of the PMAO baseline design verification was to conduct a limited set of verification activities to verify the basic functionality of the baseline prior to more detailed design and verification efforts.

The original PMAO support and mechanism designs are introduced in Section 5.1, along with a summary of requirements to which these designs had not yet been verified. Two major activities were identified. First, verification activity VA-05-02 checked if the support adequately constrained the mirror, documented in Section 5.2. Second, verification activity VA-21 checked if the mechanism was able to provide sufficient, independent 3DOF control of the mirror, documented in Section 5.3.

5.1. Primary Mirror Active Optics Baseline Design

This section begins by introducing the baseline mirror support in Section 5.1.1. The basic functionality of an ideal mirror support is described and outstanding verification activities needed to prove this functionality highlighted. Similarly, the baseline actuation mechanism is introduced in Section 5.1.2 and outstanding requirements highlighted. Section 5.1.3 provides a summary of the outstanding requirements, their associated verification activities and the rationale for the remainder of the baseline verification exercise.

5.1.1. PMAO Baseline Mirror Support

Ideal Mirror Support Functions

An ideal mirror support isolates the mirror from external stresses, and prevents build up of internal stresses caused by thermo-elastic effects by exactly constraining the mirrors' six rigid body degrees of freedom. Since no mechanical system is perfect in reality, an appropriately designed exact constraint ensures, to within some allowable tolerance, that where stresses *are* imparted to the mirror, that they are exerted repeatably and can thus be characterised and calibrated out. A common method used to achieve this condition is a semi-kinematic mount known as a whiffle tree.

Additionally, the arrangement of constraints should be such that a chosen thermal centre of the mirror does not move (again, to within some tolerance) as it undergoes thermo-elastic strains. This is normally most easily achieved by using a symmetric arrangement of constraints. Additionally, the stiffness of the support should be equal in all directions within the plane of the mirror so that stresses imparted to the mirror as it contracts/ expands are symmetrically distributed.

In practice, there are exceptions to these guidelines but they are taken here as a rule for the purposes of the preliminary design.

Baseline PMAO Support Design

The baseline PMAO support consists of a two level whiffle tree, shown in Figure 5.1. The first level utilised the transmission flexure to release the lateral translation degree of freedom of the mirror. Three whiffle plates, bonded to the top of each transmission flexure, form the foundation of the second level of the whiffle tree,

which consists of three sets of three individual whiffle flexures. Together, the whiffle flexures were intended to release a second translational degree of freedom, orthogonal to that of the transmission flexures. Note the difference in terminology between the I-shaped *whiffle* flexures and the monolithic A-frame shaped *transmission* flexures, shown in Figure 5.2.

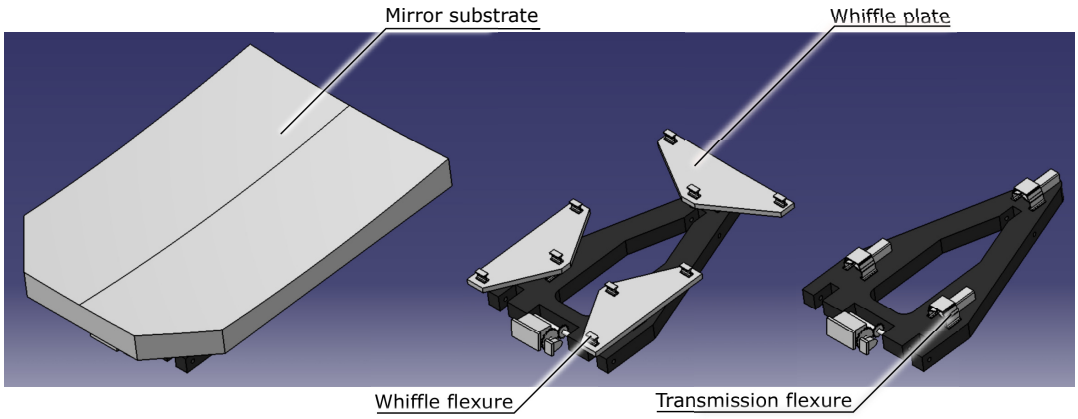

Figure 5.1: Left: Primary mirror segment. Centre and right: PMAO support baseline design with transmission flexures in the first level (right) and whiffle plates with whiffle flexures in the second level (centre). Adapted from [96].

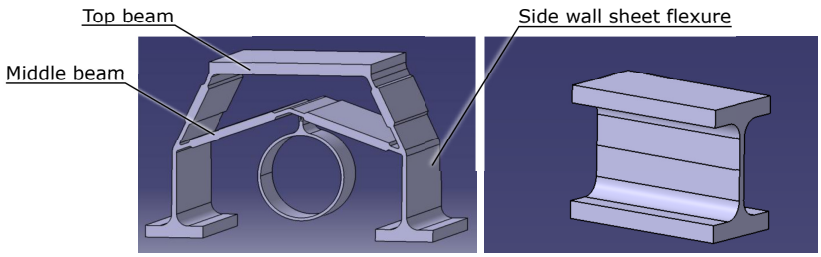

Figure 5.2: Transmission flexure (left) and whiffle flexure (right) from the PMAO baseline design. The transmission flexure design is based on the James Webb Space Telescope (JWST) design [120]. The flexures are not shown to scale. Adapted from [117].

The ability of the baseline whiffletree to provide an exactly constrained support condition, per requirements PMAO-MEC-03 and PMAO-MEC-04, had not been verified. Additionally, a transient thermal simulation using finite element analysis had shown that the mirror support induced an undesired tilt rotation of the optical surface, which was suggestive of a lack of an exactly constrained mirror [117]. There was a need to verify requirement PMAO-MEC-35: that a thermal centre was present and in the correct location.

5.1.2. Baseline PMAO Mechanism

Three DOF control of the mirror segment was provided by three stepper motors. The steppers were coupled to transmission flexures adapted from a similar implementation used in the James Webb Space Telescope (JWST)[1] that converted the rotary motion into a vertical translation, which then drove the whiffle plates. The motors were coupled to the flexure with an eccentric bearing housed in the central ring shown in the left hand frame of Figure 5.2. Then, by designing the side walls of the A-frame as flexures, the macroscopic motion of the middle flexure was able to push the walls in and out, generating a reduced vertical motion of the top beam on the nanometre scale [120]. The advantage of the transmission was that it removed the actuator from the primary structural load path.

Note that the transmission flexures are the same elements that were used in the first level of the whiffle tree. This part had two functions:

1. To act as a transmission for the stepper motors.
2. To provide lateral compliance for the whiffle support.

[1] `https://www.jwst.nasa.gov/`.

In the JWST implementation, the transmission flexure is used as a frictionless reducer *only*: separate devices are used to support the primary mirror segments. It had not been verified that stresses imparted to the PMAO baseline transmission flexure from the small strains needed to allow the lateral compliance required of its role in the whiffle tree, would not alter its ability to provide repeatable reduction of the stepper motion. Therefore it was concluded that requirement PMAO-MEC-01, independent control of each DOF, had not been verified.

Moreover, the stepper motor specified in the baseline is not space rated, which is a vital part of meeting requirements PMAO-MEC-40 and PMAO-MEC-41 (launch and operations survival), although this would be easily rectified by specifying a space rated component. Additionally, it was found that the JWST transmission flexure will remain under US and global patents until 2022 [105, 111], though flexure based motion transmissions are now ubiquitous in precision mechanisms (for example see [30, 69]). It is possible that this may violate requirement PMAO-SYS-03 (no ITAR restricted components).

Therefore, the baseline mechanism was found to either not comply with or not have been shown to comply with requirements PMAO-MEC-01, PMAO-MEC-40, -41 and PMAO-SYS-03.

5.1.3. Summary of Outstanding Verification Activities

In summary, the baseline design was found to be either non-compliant or not yet verified for seven of the key PMAO requirements. These are summarised in Table 5.1 along with their associated verification activities, defined in the Verification Plan.

Table 5.1: Summary of outstanding verification activities for PMAO baseline design. VA = Verification Activity, per Appendix E.

Requirement ID	Description	Compliance	Verification Activity	Comment
PMAO-SYS-03	No ITAR components	Unconfirmed	VA-03	Transmission flexure
PMAO-MEC-01	Independent 3DOF control	Unconfirmed	VA-21	Transmission flexure
PMAO-MEC-03	Support mirror (launch)	Unconfirmed	VA-05-02	Overconstraint?
PMAO-MEC-04	Support mirror (operations)	Unconfirmed	VA-08-01	Overconstraint?
PMAO-MEC-35	Thermal centre location	Unconfirmed	VA-17	Tilt in transient thermal[117]
PMAO-MEC-40	Survive launch	Non-compliant	VA-06-01	Terrestrial stepper
PMAO-MEC-41	Survive operations	Non-compliant	VA-09-01	Terrestrial stepper

It was established in Section 5.1.2 that a space rated stepper motor could be specified to replace the model in the original baseline with relative ease. Similarly for the design of an alternative transmission.

Verification activity VA-05-02 checks that the mirror support does not overconstrain the mirror. Verification activity VA-08-01 assumes that if PMAO-MEC-03 is verified (in part by VA-05-02), then requirement PMAO-MEC-04 is also verified. Therefore, in order to answer the first research question for the thesis, the baseline design was to be verified via activities VA-05-02, VA-17 and VA-21 prior to further detailed design. The results of each of these activities are discussed in the following sections.

Activities VA-05-02 and VA-21 are documented in the following sections. It will be shown in VA-05-02 that the mirror was not exactly constrained and that it did not define a thermal centre, therefore activity VA-17 was not required.

5.2. Baseline PMAO Support Constraint Analysis

Verification Activities: VA-05-02 [fail]

The objective of verification activity VA-05-02 was to check that the mirror support did not overconstrain the mirror. This was achieved by inspecting the support kinematics using the methods introduced in Chapter 2 *Theory*.

Equivalent Electrical Network Representation

The baseline PMAO support can be represented as a combination of direct and cascaded constraints in the equivalent electrical network diagram in Figure 5.3. Each ideal constraint line was modelled as a "resistor" in the network diagram. All motions are assumed to be small with respect to the characteristic dimensions of the system.

When discussing compound connections, the word "parallel" can be used to describe two or more lines or planes that are geometrically parallel to each other, as well as to describe parallel connections in the equiv-

alent electrical network sense. For the purposes of this constraint analysis, "parallel" is used only to describe geometrically parallel features. The terminology "direct" is used to describe multiple connections between the same two bodies.

The constraint analysis assumed that the transmission flexure could be modelled as two parallel clamped flexures with a single translational degree of freedom in the direction of its long axis normal to the two flexure planes. Since this analysis was concerned with checking the ability of the flexure arrangement to fulfil its function as the mirror support, the actuator was assumed to be stationary. Thus the piston degree of freedom of the transmission flexure was constrained and the top and middle beams assumed to behave as a rigid body. Then only the two side wall sheet flexures contributed to the constraint pattern of the support arrangement.

Thus each transmission flexure was modelled as two parallel sheet flexures, directly connecting the deployment mechanism support frame with a single whiffle plate. Three whiffle flexures directly connect each whiffle plate to the mirror substrate, and are each modelled as a single sheet flexure. Each sheet flexure was modelled as a collection of three non-redundant coplanar direct constraints.

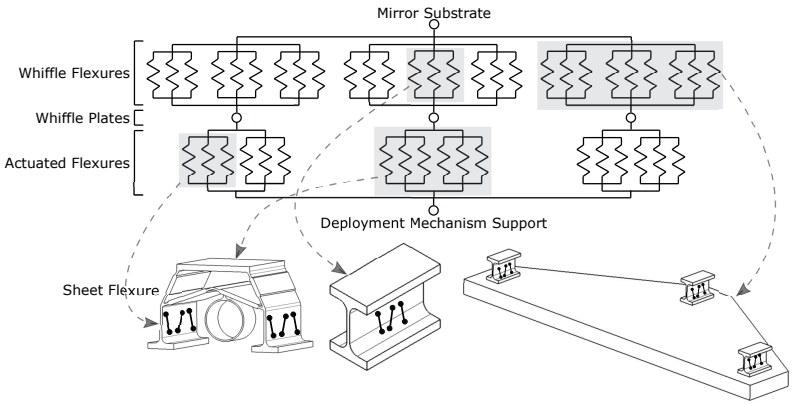

Figure 5.3: Equivalent electrical network of constraints in the baseline PMAO support.

The analysis proceeded by employing the compound connection rules in Table 2.2, working from the inner most level of the network to the outer most.

Adding the constraints of two or more parallel sheet flexures directly connecting two bodies results in a single **R** at infinity, equivalent to a translation perpendicular to the planes of the flexures (see the right hand frame of Figure 2.8). Thus the freedom pattern for the transmission flexures is each a single **R** at infinity. Similarly, the combined freedom pattern for three whiffle flexures between a whiffle plate and the mirror substrate is also a single **R** at infinity orthogonal to that of the transmission flexures, providing a translation perpendicular to the translation allowed by the transmission flexures.

The mirror is connected to the deployment mechanism support by three cascaded connections, mediated by the whiffle plates. Therefore the freedoms **R** are added to give two orthogonal translational degrees of freedom at the centre of the connection of each whiffle plate to the mirror substrate. The resulting freedom pattern is shown in Figure 5.4*a*.

The reduced freedom pattern has six degrees of freedom. Intuitively, there must be some degree of redundancy in these freedoms. It is easier to identify redundant lines by modifying the freedom diagram such that all **R**s are in the same plane. In three dimensions, a translation **T** is equivalent to a **R** line tangent to any point on a circle whose plane is perpendicular to the translation. Thus each of the **R**s in Figure 5.4*a* can be shifted to tangent lines on the same circles with infinite radius without any loss of definition of the freedom space as shown in Figure 5.4*b*.

There are now six **R**s in the same plane, each allowing an in-plane translation of the mirror. A rigid body has only two in-plane translational degrees of freedom, so there were four redundant constraints. The overall freedom pattern for the baseline PMAO support was two rotations **R** located at infinity, equivalent to two in-plane translations **T**. Requirement PMAO-MEC-03 requires that all six rigid body degrees of freedom be restrained. The baseline support restrains only four. This lack of constraint partly explains the twist about the longitudinal axis of the mirror segment in the transient thermal analysis of the baseline design [117].

Local Overconstraint

Inspection of the arrangement of the whiffle tiers reveals that although the mirror can expand along its long axis, it cannot expand along its short axis within the lengths between the outer whiffle flexures of each whiffle

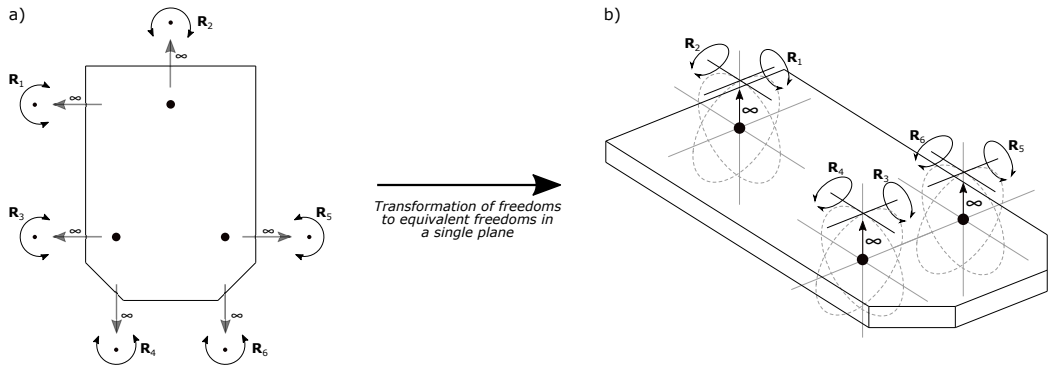

Figure 5.4: Freedom patterns for the baseline PMAO support. a) Equivalent freedom pattern after reduction from compound network. b) Equivalent freedom pattern with all **R**s in the same plane. The **R** lines are tangents to circles of infinite radius, shown by the grey dashed lines. For small motions, a rotation about an axis an infinite distance away is equivalent to a translation at the segment.

plate. This is illustrated schematically in Figure 5.5. This is a function of the orthogonal, cascaded arrangement of flexures. Unless the support, mirror and support base are all made of the same material and have the same bulk temperature, the mirror substrate will be stressed due to coefficient of thermal expansion (CTE) mismatch, leading to deformation of the optical surface.

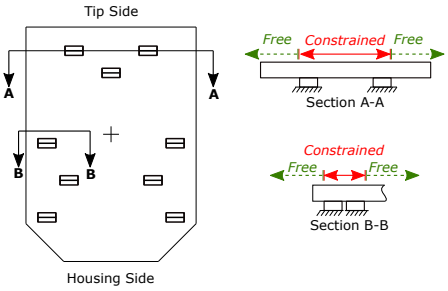

Figure 5.5: Constrained thermal expansion of mirror segment in baseline PMAO support design.

Finally, there is an asymmetric distribution of stiffnesses between the two whiffle tiers as well as between the inner and outer portions of the mirror segment in the length direction either side of the centroid. Six whiffle flexures are located on the "inner" side of the centroid whilst only three are located at the tip side of the centroid. This will cause an asymmetric stress response in the mirror substrate, ultimately manifested as astigmatism in the optical performance.

Thermal Centre

Since the mirror is underconstrained, there is no thermal centre [17]. This can also be confirmed by inspection: To have a thermal centre, all constraint surfaces in a mechanism must be oriented radially from the thermal centre, whereas the baseline PMAO support has multiple constraint surfaces orthogonal to each other.

5.3. Baseline PMAO Mechanism DOF Control Analysis

Verification Activities: VA-21 [fail]

The objective of verification activity VA-21 was to demonstrate that the PMAO mechanism was able to supply independent 3DOF control of the mirror segment. This was achieved, in this instance, with finite element analysis of the transmission flexure to check the input/ output performance of the transmission in the presence of the nominal operational thermal environment. The results were compared to a similar verification study conducted when the transmission was originally designed [117].

The premise of the relationship between the stiffness of a flexure and its displacement is established in Subsection 5.3.1. The verification model setup is described in Subsection 5.3.2. The results are given in Subsection 5.3.3 followed by a discussion in Subsection 5.3.4.

5.3.1. Change in Stiffness of a Flexure with Deflection

It has been shown in the literature that the stiffness in the supporting direction of parallel leaf spring guiding compliant mechanisms decreases as the mechanism translates in its compliant direction [23]. This is shown schematically in Figure 5.6. The plot on the right of Figure 5.6 shows results from FEA simulations for various ratios of flexure length, width and thickness, plotting the stiffness in the z direction as a function of displacement in the y direction. The stiffness is normalised with respect to the undeformed mechanism support stiffness. The displacement u is scaled by the leaf spring thickness t. It is evident that support stiffness decreased dramatically for all simulated flexure geometries.

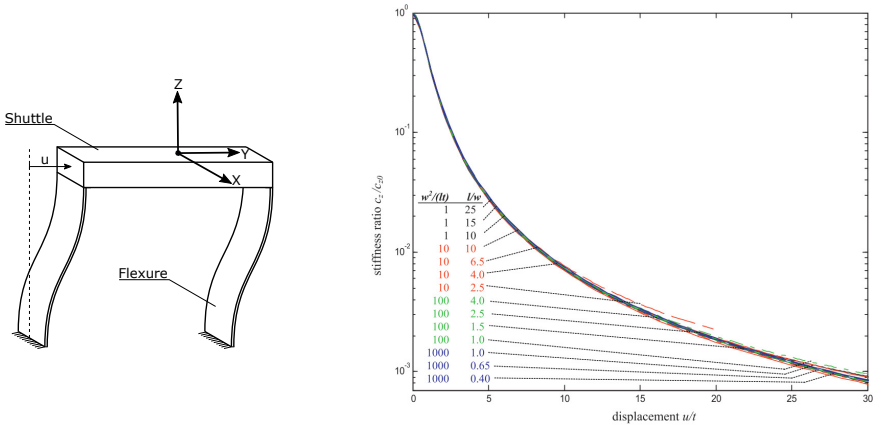

Figure 5.6: A displacement u of a parallel guiding compliant mechanism in its compliant (y) direction leads to a dramatic decrease in the stiffness of the mechanism in its supporting (z) direction. The plot shows the normalised supporting stiffness in the z direction as a function of displacement in the y direction, from [23].

The lower portion of the PMAO baseline transmission flexure approximates this type of compliant mechanism. For the purposes of this analysis, the mirror was assumed to be sufficiently stiff so that it could be considered rigid relative to the transverse compliance of the transmission flexure, similar to the y direction in Figure 5.6. A scenario could be foreseen where the mirror thermo-elastically deforms, driving a horizontal motion of the top beam of the transmission flexure along its long axis. It was expected that this would alter the internal stress state and thus the stiffness in the vertical, supporting direction. The transmission flexure is more complex than the simple parallel guiding mechanism shown in Figure 5.6, so results from the literature [23] could not be immediately extrapolated. A simple finite element model was used instead, described below.

5.3.2. Finite Element Model Setup

A brief finite element analysis study was conducted to understand the effects of the dual usage. It was expected that lateral displacement of the top beam would modify the input/ output relationship of the transmission. The influence would be considered strong if the change in output was larger than the maximum expected step size of 10.72 nm due to expansion of the mirror within the nominal operation temperature range of ± 1 K. Note that this was a forgiving temperature condition since the verification guidelines document stipulates a design range of ± 15 K.

A static structural analysis was conducted in ANSYS. The transmission flexure was modelled as Ti-6Al-4V at 22°C per the material properties used in the original verification to ensure like-for-like comparison of data [117]. Those properties are repeated in Table 5.2.

Note that the initial verification of the transmission range with a solid 10 mm plate of Titanium alloy integral to the upper beam of the flexure to simulate the effect of the whiffle plate [117]. This was not repeated in the present analysis as it artificially increased the stiffness of the upper beam (the baseline design actually used an adhesive bond between the upper beam and CFRP whiffle plate).

Thermo-Elastic Expansion of Mirror

The maximum anticipated lateral displacement of the top beam was calculated assuming thermal expansion of the mirror substrate from the rest state through a 1 K bulk temperature increase. The transmission flexures nominally relieve thermal expansion across the width of the mirror segment. Since the baseline mirror

Table 5.2: Material properties for Ti-6Al-4V used in transmission flexure verification. From [117]. These are marginally different from the material properties given in Appendix K, which were used in the remainder of this thesis.

Property	**Value**
Density	4430 kg/m^3
Tensile Yield Strength	880 MPa
Compressive Yield Strength	970 MPa
Young's Modulus	113.8 MPa
Poisson's Ratio	0.24
CTE	8.6 $\mu\epsilon/K$

support arrangement blocks the flexure at the tip end of the mirror from "seeing" the thermal expansion of the mirror, only the two transmission flexures at the housing end were considered. See Figure 5.5 on page 53.

The centres of the housing end flexure are 95 mm from the centreline of the segment. Assuming a Silicon Carbide mirror with CTE given in Appendix K *Material Properties* and a 1 K temperature rise the transmission flexures would need to accommodate a lateral displacement of approximately 209 nm. The maximum vertical displacement of the middle beam was calculated in earlier work to be 0.1 mm in either direction [117]. This value was re-used here for consistency.

The finite element simulation was conducted with the same vertical displacements of the middle beam either side of the rest position as the original verification study. One series of simulations investigated the resulting vertical displacement of the top beam with no lateral displacement (ie. no mirror expansion), and a second series of simulations investigated the effects of a 209 nm transverse displacement (ie. akin to the y direction shown in Figure 5.6, as applied to the transmission flexure). Only the vertical translation DOF of the middle beam was constrained in the analysis.

The mean vertical displacement of all nodes on the upper surface of the top beam was used for the results given in Table 5.3. The initial verification [117] gave no indication of whether the results refer to the dummy whiffle plate or transmission flexure displacement, nor whether they are the averaged displacement or from a chosen node.

5.3.3. Results

A summary of the results from the FEA study are given in Table 5.3 and plotted in Figure 5.7. An extract of the FEA results is given in Appendix F. An indicative comparison of the results for a 0.1 mm vertical displacement of the middle beam, with a 0 nm and 209 nm lateral displacement of the top beam, is shown in Figure F.1.

Table 5.3: Transmission flexure FEA verification results. Analysis results with dummy whiffle plate from [117], for comparison. $\Delta\mathbf{z_T}$ is the piston displacement of the top beam (output of the transmission). $\Delta\mathbf{z_M}$ is the piston displacement of the middle beam (input of the transmission).

$\Delta\mathbf{z_M}$ [μm]	$\Delta\mathbf{z_T}$ **With Whiffle** [μm]	$\Delta\mathbf{z_T}$ **No Whiffle Plate** [μm]	
Δ_y	0	0	0.209
100	17.09	19.189	17.451
87	14.80	16.694	15.183
50	8.54	9.594	8.726
0	0.00	0.000	0.000
-50	-8.52	-9.594	-8.726
-87	-14.74	-16.694	-15.182
-100	-17.01	-19.189	-17.451

The von-Mises stress throughout the structure was checked in each simulation to make sure that the structure stayed within the linear-elastic region. The highest stress state was with 0.1 mm vertical displacement of the middle beam and 209 nm displacement of the top beam in the -y direction, giving an equivalent stress of 111.2 MPa, well below the yield strength of Ti-6Al-4V.

Comparison of the results with no transverse displacement with and without the 10 mm "dummy" whiffle plate, shows that the addition of the plate reduced the output range of the transmission.

5.3.4. Discussion

Linear fits to the data both with and without the transverse displacement, shown in Figure 5.7, were excellent, with R^2 values of 1.0. This was expected since the flexures were not stressed beyond their linear elastic region.

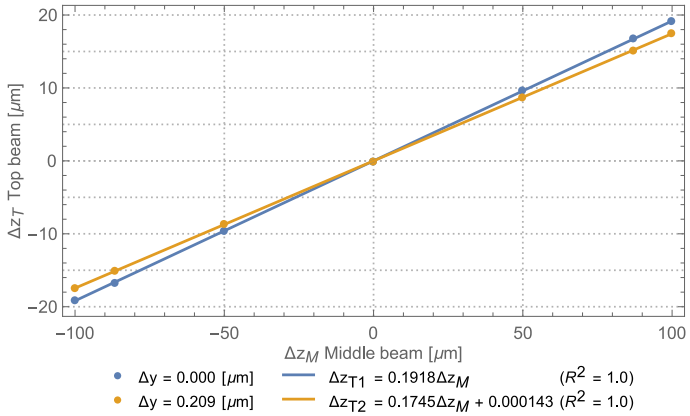

Figure 5.7: Results from finite element analysis of transmission flexure performance with and without thermal expansion induced displacement of top beam.

The average difference between the output of the top beam with and without the transverse displacement was 9.05%. Consider a scenario where the mechanism was commanded to deliver the maximum required piston displacement of 4 μm after the mirror had expanded due to a 1 K bulk temperature change. Relationship ΔZ_{T1} shown in Figure 5.7 can be used to find that the necessary mid-beam displacement would be 20.85 μm. Relationship ΔZ_{T2} then gives an actual expected displacement of 3.64 μm at the top beam, a difference of nearly 34 maximum size steps at 10.72 nm. This would change as a function of the temperature distribution of the mirror, a result which strongly diminishes the expected repeatability of the baseline design. The original baseline mechanism did not comply with requirement PMAO-MEC-01.

With a maximum piston displacement of ≈19 μm, the FEA results suggest that the nominal transmission has a total piston range nearly five times that required by the top down system budgets. Forseeably, it could correct the displacement error in conjunction with a method to sense the output motion, though knowledge of the temperature distribution of the segment would be needed for accurate control. Both a temperature map of the segment and/ or edge sensors would themselves need to be calibrated once in obit.

Capacitive edge sensors could, and indeed have been considered, as additional inputs to control the segments. However, at the time of writing there was a strong desire from the optics and control team to develop a fine actuation mechanism concept that did not rely on such sensors [49] that would largely serve to only add more cost, complexity and risk.

5.4. Chapter Summary

The constraint pattern analysis in Section 5.2 demonstrated that the baseline PMAO support constrained only four of the mirrors' six rigid body DOFs. The whiffletree also locally *overconstrained* the mirror, exposing the optical surface to deformations from build up of internal stresses. The original baseline support did not meet requirements PMAO-MEC-03 or PMAO-MEC-04 and the absence of a thermal centre meant that PMAO-MEC-35 was also not met.

The support additionally relied upon the transmission flexure to release a degree of freedom. A brief finite element analysis simulation demonstrated that this dual use strongly reduced the transmissions' ability to reliably perform its core function: provide a repeatable piston output. It was shown that requirement PMAO-MEC-01 was not met.

It was concluded that the mirror support needed to be redesigned. It was also desirable to use a transmission and actuator that could be confidently used free of ITAR complications. A methodical concept generation process was initiated in an effort to explore alternative actuation and support options. This is documented in the next chapter.

6

Concept Generation

Chapter 5 demonstrated that the original baseline design for the PMAO mechanism did not meet the basic kinematic requirements. A rigorous concept generation and synthesis exercise was undertaken to revise the design, detailed in this chapter and the next. An overview of the main synthesis tasks is given in Figure 6.1.

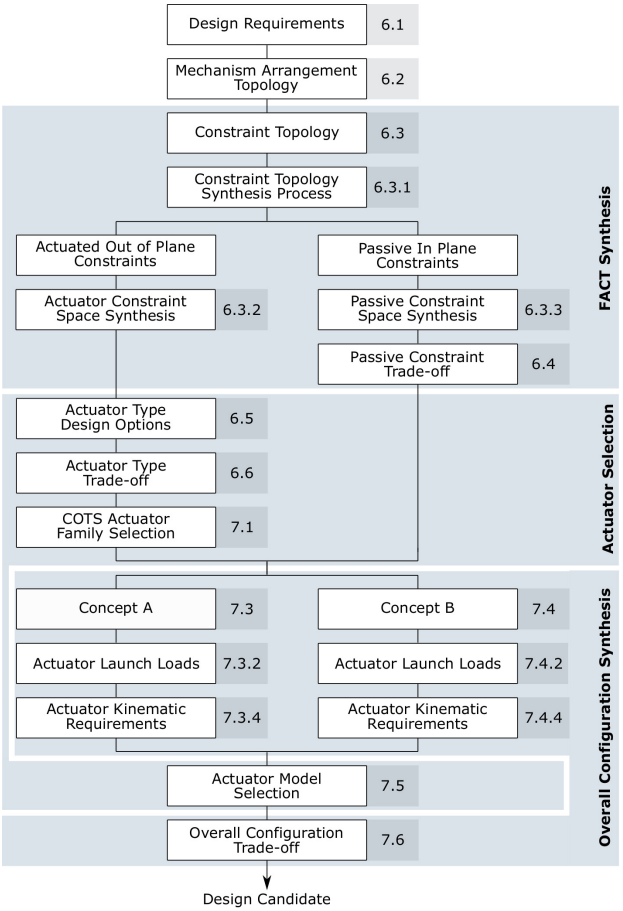

Figure 6.1: Major tasks within the PMAO concept generation & synthesis process as documented in Chapters 6 & 7. Several subsections have been omitted for clarity.

This chapter details the concept generation process. The design requirements are set out in Section 6.1. The mechanism arrangement selection is documented in Section 6.2 followed by definition and trade-off of the constraint topology Sections 6.3 and 6.4. The actuator type is selected in Section 6.5.

6.1. Design Requirements

This section summarises the design requirements for the PMAO mechanism, summarised in Table 6.1. Several clarifying notes for the requirements set out in Table 6.1 are also given in the following subsections.

Table 6.1: Summary of design requirements for concept generation.

Domain	Description	Comment
Kinematic Performance		
DOFs	3DOF - piston $\Delta_{z,M}$, tip $\theta_{y,M}$, tilt $\theta_{x,M}$	
Segment Range	$\pm 4\mu m\ \Delta_{z,M}$	PMAO-MEC-29, scan procedure
	$\pm 4\mu rad\ \theta_{x,M}$	PMAO-MEC-30
	$\pm 2\mu rad\ \theta_{y,M}$	PMAO-MEC-31
Resolution	$10nm\ \Delta_{z,M}$	M1-MEC-01, PMAO-MEC-23
Thermal stability	Per top down budgets, Table 3.3	M1-MEC-04. With deployment mechanism
Structural stability	Per top down budgets, Table 3.3	M1-MEC-07. With deployment mechanism
Stiffness	First natural freq. $> 100Hz$	PMAO-MEC-40-04, -05
Mass	$< 6.2kg$	PMAO-SYS-02, per segment. Excludes electronics.
Volume	120 x 450 x 620 mm	PMAO-MEC-50. With deployment mechanism. Excludes electronics.
Interfaces	M1 depl. mechanism support frame.	PMAO-MEC-50
	Mirror.	Mirror design TBC
Environmental		
Survival temp.	188 - 384 K (calculated), Table 3.4	DST-WP1-CALC-001 (rev. L), App. C
Operational temp.	$298 \pm 1K$	M1-MEC-15, deployed with baffle
Load	2× orthogonal, combined $30g$ QSL	PMAO-MEC-40-01 to -03, launch
Atmosphere	Operate Earth ambient 50% relative humidity for testing. Space LEO for operations.	PMAO-SYS-06, PMAO-MEC-43
TRL	≥ 6 for components	MIS-OBJ-02
Other	HDRM	PMAO-ELE-01
	Regulations: ITAR free only	Undefined, assume not needed
	Power off hold	PMAO-SYS-03 If possible (soft requirement)

Volume

The stowed height of the combined deployment and active optics mechanisms must be no more than 120 mm from the instrument housing to the backplane of the mirror. This keeps the stowed configuration within the minimal possible volume which is dictated by the segment size, whilst still providing space for the stowed M2 booms.

The mechanism must not extend beyond the periphery of each segment in the stowed configuration so that it does not conflict with the stowed booms, as well as in the deployed configuration to minimise stray light reflections during imaging. The usable volume in the stowed state is a trapezoidal prism of dimensions 120 x 450 x 620 mm, to be shared with the M1 deployment mechanism. See Figure 8.14 on page 127 for an indicative sketch, which was used to size part of the selected mechanism architecture.

Cost

The DST project does not have the funds to support development and space qualification of fundamentally new technology. The primary objective of the project is to demonstrate the feasibility of very high resolution Earth observation imagery at an affordable price. Therefore the minimum acceptable TRL is set to 6[1], a *Model demonstrating the critical functions of the element in a relevant environment* for components.

[1] `http://sci.esa.int/sci-ft/50124-technology-readiness-level/` [Accessed: 21 march 2018].

Interfaces

The physical interfaces of the PMAO mechanism with the mirror and deployment mechanism were indicated schematically in Figure 1.8 on page 8. They demarcate the scope of the thesis. The deployment mechanism support frame is nominally a planar surface. The only equipment currently residing on the upper surfaces is the PMAO. The underside, shown in Figure 6.2 houses the winches for the ribbons that control & tension the M1 & M2 deployment mechanisms. The frame geometry shown in Figure 6.2 is indicative only and can be modified to suit the PMAO. The material is Carbon Fibre Reinforced Polymer (CFRP), likely with a non-isotropic coefficient of thermal expansion (CTE). The mirror support must mate to the back of the mirror to keep the optical surface free from obstruction.

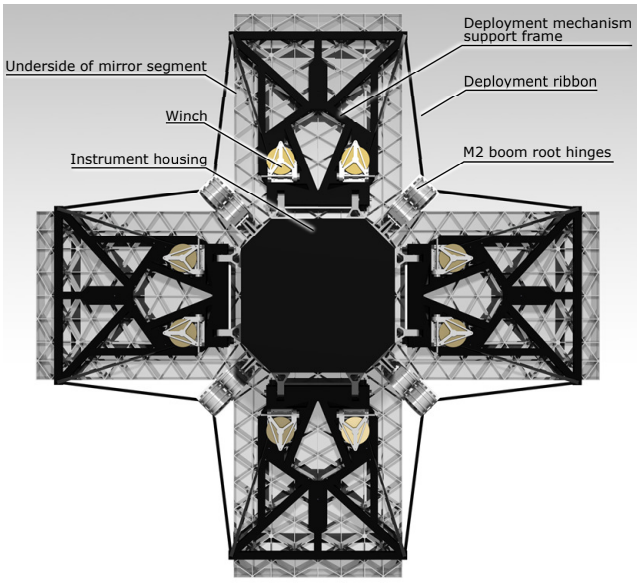

Figure 6.2: Underside of the DST primary mirror, showing the deployment mechanism support frame, winches, ribbons and M2 deployment boom root hinges. Render courtesy of André Krikken.

Other Requirements

A locking or caging mechanism utilising a Hold Down & Release Mechanism (HDRM) is often used to protect optical systems through launch [125]. There are also examples of fine steering mechanisms without an HDRM, such as in the GAIA & Euclid space telescopes [8, 115]. There is no fundamental need for an HDRM to secure each primary mirror segment during launch for the DST.

Discussions with a precision mechanism subject matter expert found that the combined 30g quasi-static launch loads would be difficult to meet without an HDRM [58], whereas a supplier of space rated precision opto-mechanical mechanisms suggested that it is strongly preferable to design the mechanism so that it can support the mirror *without* an HDRM through launch [31]. In the latter case, the penalty to system reliability due to an extra mechanism with moving parts, power, volume, expense & integration complexity was considered to outweigh the advantages of using smaller, lighter compliant elements that do not have to support the relatively massive mirror, which was the main concern in the former case.

Since there are examples of space optics with and without hold down mechanisms, and with conflicting advice from two subject matter experts, it was decided to pursue the simplest design option first. That is, to design the PMAO to support the mirror through launch *without* an HDRM. Ultimately, the verification resulted in Chapter 9 *Verification* showed that this was a feasible approach.

6.2. Mechanism Arrangement Options

This section discusses the mechanism arrangement options, set out in Figure 6.3. The mechanism arrangement refers to the topological layout of the links, joints and bodies in the mechanism. When discussing mechanisms, the mirror segment is often referred to as the end effector and the deployment frame as the base.

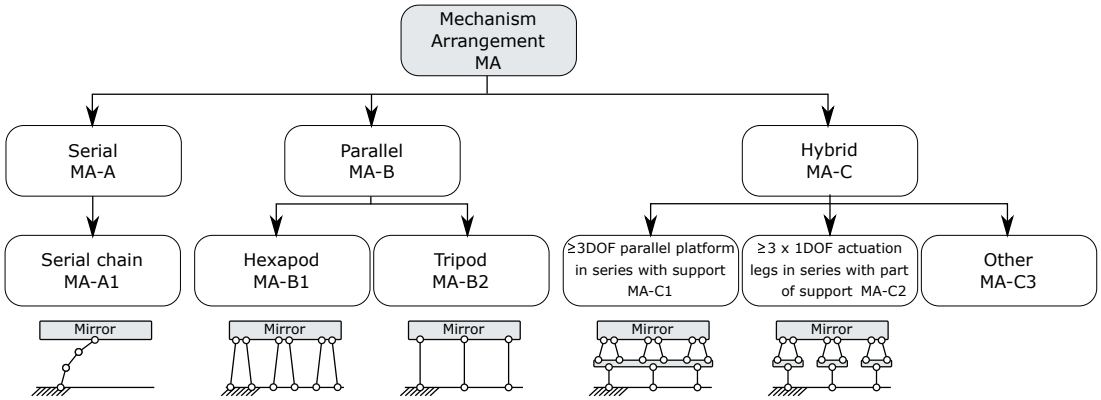

Figure 6.3: Design option tree for Mechanism Arrangement options.

The mechanism arrangement is the highest level design choice that can be made for the PMAO. The required out of plane degrees of freedom of the end effector dictate the use of a spatial mechanism, thus planar mechanisms were not considered. Only options that provided a minimum of three controlled DOFs were considered. For completeness, options with more than three controlled DOFs were considered as this meets the performance requirements, but were quickly eliminated as this would lead to unnecessary mass, volume, cost & power. Each arrangement concept is investigated briefly in the following subsections, culminating in a final selection.

6.2.1. Serial

A serial mechanism is comprised of two or more linkages joined together consecutively, illustrated by design option *MA-A1* in Figure 6.3. The position of the end effector is controlled through actuation of one or more joints or links, allowing great flexibility in the choice of DOFs. Perhaps the most ubiquitous controlled serial mechanism is the industrial robot, which has found widespread use in car assembly lines.

Serial mechanisms are more susceptible to stacking of position errors through the linkage than parallel mechanisms [61] which must be controlled with more rigorous (and thus expensive) assembly jigs, fixtures, metrology and sensing. In the DST, these errors could be compensated with the PMAO and Aberration Correction System (ACS) though this would diminish their ability to correct errors caused by other perturbations.

The range of motion of serial chains is usually larger than that of parallel mechanisms [119], though it is difficult to maintain a symmetric arrangement, and thus thermal stability, of the serial chain. The literature study for this thesis found that no purely serial mechanisms were in use for either terrestrial or space based fine pointing mechanisms, further discouraging this design option.

In light of the shortcomings of serial mechanisms, they were not considered for the PMAO.

6.2.2. Parallel

A parallel mechanism is made of direct connections between the mechanism base and end effector only. A very common type of parallel mechanism is the hexapod as shown in design option *MA-B1* in Figure 6.3. Hexapods are also known as *Stewart platforms* [110], commonly used in flight simulators. An example is shown in Figure 6.4.

In contrast to serial mechanisms, parallel mechanisms are generally stronger, stiffer and have better dynamic behaviour [61, 119]. In some configurations, they also offer a limited degree of failure tolerance thanks to coupling between individual actuators and the output degrees of freedom. This was the case for the hexapods used in the James Webb Space Telescope primary mirror segment fine position mechanisms which could continue to meet requirements even after two actuator failures [79]. As mentioned in the serial mechanism section, a downside of parallel mechanisms typically have a small range of motion compared to serial mechanisms [119].

A hexapod was also considered for 6 DOF control of the secondary mirror in the HYPATIA/ STOIC active optics concept for application to future European UV, optical and Infra-Red space telescopes [38]. The authors noted that although a 3 DOF tripod could have been used to provide the necessary decentre correction for that application, the ability to fully control the mirror's position with the hexapod led to smaller RMS wavefront errors. However, optical analyses for the DST have already shown that 6DOF control is not

necessary with the current optical design.

Figure 6.4: A commercial off the shelf (COTS) hexapod, providing 6 DOF control for laboratory use. [92].

Hale provides a table of all possible orthogonal constraints that generate zero to six independent rotational and/ or translational degrees of freedom [57, p. 74], reproduced from Blanding [17] and shown again in Figure 6.5. It can be used as a starting point for exact constraint design.

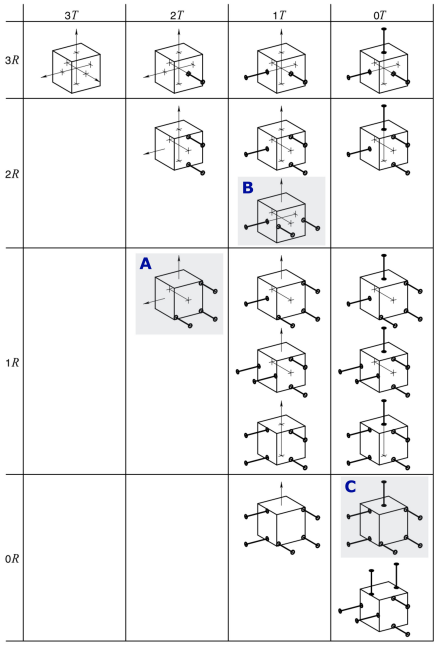

Figure 6.5: Table of all possible parallel orthogonal constraint sets giving combinations of rotational and translational degrees of freedom. The combination of the 1R/ 2T set (A) with the 2R/ 1T set (B) constrain in and out of plane motions respectively. When combined in parallel they give full 6DOF constraint (C). Adapted from [57] and in turn from [17].

Note that each of these constraint patterns is purely parallel and that the combination of the 1R/ 2T set *A*, a tripod of parallel actuators as shown in design option *MA-B2*, with the 2R/ 1T set *B* constrains out- and in-plane motions respectively, and when added in parallel give full 6DOF constraint (C). This demonstrates that a purely parallel mechanism *can* meet the basic kinematic requirements. Indeed, this is demonstrably the only purely parallel combination of constraints that can be used to deliver the required exactly constrained kinematic performance. Freedom and Constraint Topology synthesis can be used to further refine the concept. The interface of the tripod option will also be smaller than that of the hexapod since it needs half the number of actuators.

It was concluded that a parallel mechanism may offer the necessary dynamic, strength and symmetry performance for the PMAO. With the very small stroke requirements, the diminished range of motion compared to a serial arrangement is not considered an issue. The hexapod option was ruled out based on the complexity of including six actuators. The tripod concept with three actuated constraints and three passive constraints was considered feasible.

6.2.3. Hybrid

A hybrid mechanism uses a combination of serial and parallel connections between the mechanism base and end effector. They combine several of the advantages and disadvantages of purely serial and parallel mechanisms but offer a much larger design space to meet the design requirements. The original DST baseline design from [117] was an example of hybrid design option *MA-C2*.

An example of option *MA-C2* with flight heritage is the 3 DOF tip/ tilt/ piston tripod style parallel mechanism shown in Figure 6.6 used on the 0.95 m, 87 kg primary mirror for the Kepler space telescope [71]. Three vertical, linear actuator assemblies provide the actuated out of plane degrees of freedom while parallel sheet flexures constrain in-plane motions. Three bipod supports stacked on top of each of the vertical actuators connect the mechanism to the mirror.

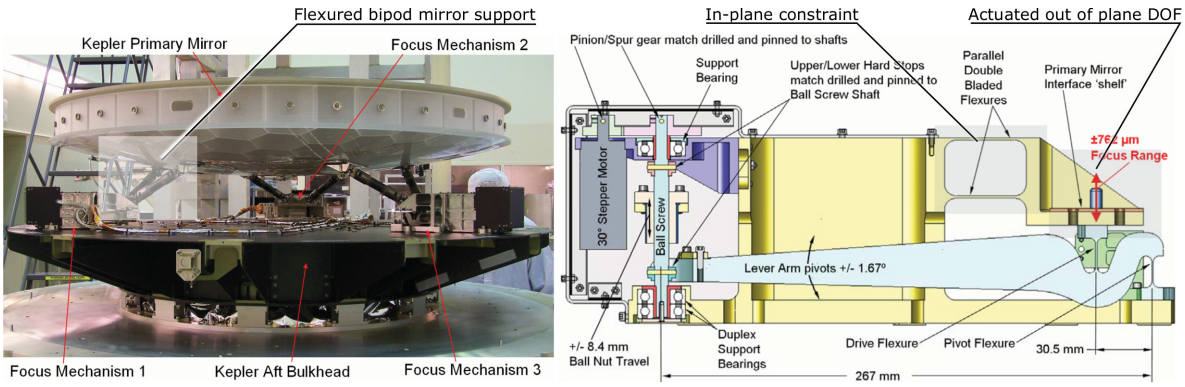

Figure 6.6: Kepler space telescope primary mirror focus mechanism. Left: Primary mirror mounted via flexured hexapod to three actuator mechanisms, each providing single DOF vertical actuation of a bipod. Right: Section view of one of the actuator mechanisms. Note stepper motor coupled to ball screw via reduction gearing, lever arm and drive, pivot and parallel flexures. Bipod mates to the interface shelf. Adapted from [71].

Hybrid mechanisms were also used for the Thirty Metre Telescope (TMT) and European Extremely Large Telescope (E-ELT) primary mirror segment support designs, shown in Figure 6.7, and are good examples of design option *MA-C1* [90, 93]. This allowed separation of the 3DOF actuation mechanism and mirror support sub-assemblies to isolate the mirror from the actuation forces and differential thermo-elastic deformations of the mirror & support cell. This was an important trait that can be used to simplify component design by separating challenging functional requirements out across multiple parts.

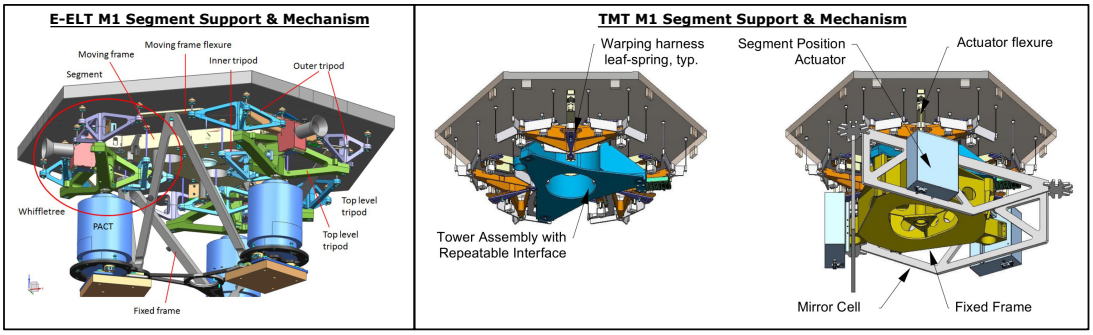

Figure 6.7: Left: Support and actuation assembly for the European Extremely Large Telescope [93]. Centre & right: Similarly for the Thirty Metre Telescope primary mirror segments [90].

A hybrid concept is attractive for the extra design freedom and mirror isolation it permits. However, this is at the cost of the disadvantages of a serial mechanism: reduced load capability and stiffness, as well as stacking of errors at each joint. The hybrid options MA-C1 and MA-C2 were considered feasible.

6.2.4. Mechanism Arrangement Selection

While parallel mechanisms generally offer the best stiffness, strength and dynamic performance, the ability of a hybrid arrangement to isolate the mirror from thermal and actuation loads that would otherwise distort it make hybrids the most favourable option. Hybrid arrangements also lends itself well to modularisation of

the mirror, mirror support and actuation mechanism. An arrangement using the layout in design option *MA-C1* was chosen. Like the E-ELT & TMT primary mirror segment mechanisms, a parallel actuation mechanism is attached serially to a parallel mirror support assembly. The arrangement is shown schematically in Figure 6.8.

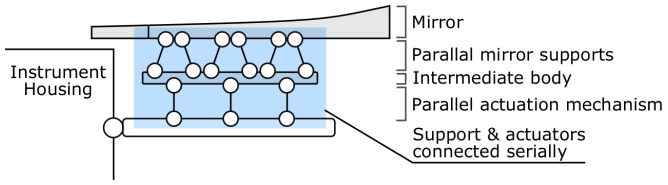

Figure 6.8: Elements and layout of hybrid arrangement design option *MA-C1*.

Sections 6.3 to 6.5 step through the selection of constraints and actuators for the actuation mechanism. The mirror support assembly is described in Chapter 7 *Mechanism Architecture Selection*.

6.3. Constraint Topology Design Options

This section details the selection and arrangement of ideal constraints to provide the desired degrees of freedom of the mechanism. Constraint topology design options were synthesised using the Freedom & Constraint Topology (FACT) method [61, 62] introduced in Section 2.3. The following assumptions were made to simplify the design synthesis:

- Compliant mechanisms were considered exclusively. Sliding contact joints (bearings, ball joints, guideways) are ignored due to friction effects such as hysteresis & other microdynamic effects.
- Work on phasing algorithms has already begun [50] and assumes that tip, tilt and piston motion can each be controlled independently. To ease integration of the PMAO design with existing work, mechanisms with coupled translation and rotation freedoms were not considered.
- For the purposes of the constraint synthesis, the mirror was assumed to be a rigid body.
- The intermediate body is sufficiently rigid so that actuation deformations are not passed on to the mirror and support.

The constraint synthesis process is described in Subsection 6.3.1. The actuator constraint space is selected in Subsection 6.3.2 followed by the passive constraint space selection in Subsection 6.3.3. Several design options for redundancy of the support constraint space were found. Selection was conducted using a graphical trade-off documented in Section 6.4.

6.3.1. Constraint Topology Synthesis Process

The FACT method guarantees an exhaustive exploration of the design space of flexure based mechanisms. It gives the designer confidence that all topologies have been considered and allows rapid negation of those that give incorrect freedoms, would have poor symmetry and/ or are difficult to fabricate or assemble [61, 62].

The synthesis objective was to actively control tip, tilt and piston motions of the mirror whilst providing passive constraint of the remaining rigid body freedoms. The mechanism should be symmetrical to aid thermal stability and be low profile to minimise both the volume occupied in the stowed state and the mechanical advantage of the massive mirror during launch. It should be simple, robust and meet the dynamic performance requirements.

The synthesis process was conducted as follows, adapted from the process devised in [61]:

1. **Define the system geometry**:
   The end effector to be manipulated, available volume and interfaces for the mechanism.
2. **Identify the freedom space containing the freedoms that should be *actuated***:
   Identify the corresponding complimentary constraint space. This constraint space constitutes the set of fixed constraints for the passive support of the mechanism. Here, it is called the *support constraint space*.
3. **Identify the freedom space that should be left *unconstrained* by the actuators**:
   The complementary constraint space is the constraints to be controlled by the actuators. Here, it is called the *actuator constraint space*.

4. **Identify available sub-constraint spaces for each of the support and actuator constraint spaces**:
   Sub-constraint spaces ensure that the constraints in each space are independent. This is not relevant to the 3DOF constraint space and is skipped. Constraint spaces with more than one constraint set benefit more from the use of sub-constraint spaces.
5. **Select sub-constraint spaces**:
   To satisfy geometry, symmetry and performance requirements for support and actuator constraint spaces.
6. **Select non-redundant constraints for each constraint space**:
   For exact constraint design.
7. **Select redundant constraints**:
   To improve symmetry, stiffness, load bearing & dynamic performance.

6.3.2. Actuator Constraint Space Synthesis

The usable volume and interfaces were defined in the summary of design requirements in Table 6.1. There are no strict requirements on where the constraints must attach to the deployment mechanism support frame. The constraints should all mate to the intermediate body. All parts must reside behind and within the periphery of the mirror to keep the optical surface free and minimise stray light reflections.

Recall from Chapter 2 *Theory* that Hopkins found all possible constraint sets giving three degrees of freedom using flexure based mechanisms [61], repeated in Figure 2.13 on page 20. The actuator constraint space must constrain the actuated freedoms: two out of plane rotations (tip, tilt) and one out of plane translation (piston). Physically, the constraints will be the actuators themselves. Changing the dimension of the constraint by actuating it then alters the pose of the platform. Inspection of Figure 2.13 shows that the only constraint set satisfying these conditions is set (E), a box of every parallel constraint line parallel to a chosen direction [61]. To avoid redundancy, the only choice is to have no more than two coplanar constraints.

Selection of non-redundant constraints for each of the constraint spaces must also take into account the possibility of incurring redundancy once the actuator and support constraint spaces are combined in parallel. The constraint redundancy rules in Table 2.1 can be applied to the combined constraint space to check that this does not happen. It will be shown in Subsection 6.3.3 that the support constraints use constraint space (A) in Figure 2.13. Examining the rules in Table 2.1 confirms that so long as the constraints selected for each of the two individual constraint spaces are not internally redundant, the combined constraint space will also not be redundant.

It was mentioned in Chapter 2 *Theory* that symmetry aids thermal stability and balance of stiffness. The preferred configuration is then three parallel constraint lines positioned at the vertices of an equilateral triangle, giving three lines of symmetry. The result is shown in Figure 6.9.

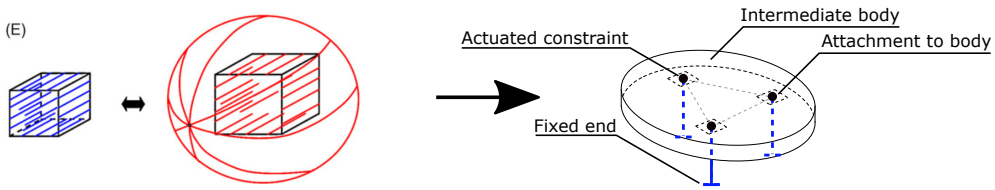

Figure 6.9: Non-redundant actuator constraint set. Three actuated parallel constraint lines, shown by thick blue dashed lines, arranged on the vertices of an equilateral triangle, attached to the intermediate body. FACT constraint set diagram adapted from [61].

Selection of redundancy in the actuator constraint space is dependent upon the choice of actuator, so is left to the synthesis of the mechanism architecture in Chapter 7 *Mechanism Architecture Selection*.

6.3.3. Passive Constraint Space Synthesis

The support constraint space must constrain the non-actuated freedoms. Inspection of Figure 2.13 reveals that only option (A) meets this condition. The passive support must therefore supply three co-planar constraints, no more than two of which intersect at the same point on the plane, including at infinity. Four options are illustrated in Figure 6.10.

Symmetry can help select the ideal arrangement. The three coplanar constraint lines should intersect to form an equilateral triangle [57, p. 72] for balanced stiffness. Their lengths should be equal with the fixed ends also forming the vertices of an equilateral triangle [126, p. 516].

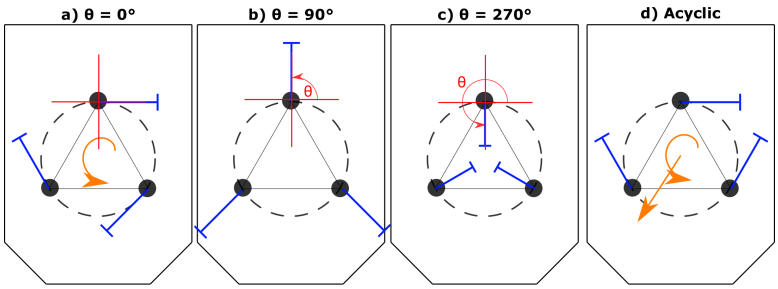

Figure 6.10: Multiple arrangements of three ideal constraints attached to the segment at the vertices of an equilateral triangle. The arrangement in a) was selected. Orange arrows indicate direction of in-plane thermal drift due to expansion of the constraints. The in plane constraints (solid blue lines with cross-bars) are attached to the intermediate body (dashed circle). The mirror segment is shown for illustrative purposes.

Recall from Section 2.2 that the greater the length of the moment arm of a constraint, the more effective it is at maintaining the position of a body. For three constraints attached to a body equidistant from a central point, the moment arm is maximised when the constraints are oriented tangent to the circle that circumscribes the attachment points. This is illustrated in Figure 6.10*a* in the $\theta = 0°$ case. This arrangement also defines a thermal centre and allows radial growth of the body or base without building up internal stresses.

Note that it is not possible to arrange three in-plane constraints such that they are all independent *and* would not cause a rotation and/ or translation of the body as they undergo thermal expansion. For example, consider the limiting cases in Figures 6.10*b* & *c* with the constraints arranged radially. Thermal expansion of the constraints will not cause a twist about the Z axis but they have zero length moment arms, so would make for mechanically poor constraints. Moreover, since the three constraints intersect at the same point, there are actually only two non-redundant constraints, resulting in a 4DOF structure for small motions.

A further example is the acyclic case in Figure 6.10*d*. The moment arms are all roughly equal, but the stiffnesses are not balanced and there is no thermal centre.

Therefore, it was concluded that the arrangement shown in Figure 6.10*a* was the ideal passive constraint configuration despite the thermal drift rotation. A first approximation of the magnitude of the rotation θ in radians due to thermal expansion of the tangential flexures made from a material with CTE α and heated by temperature differential ΔT is given by [124, p. 381]

$$\theta = \sqrt{3}\alpha\Delta T \tag{6.1}$$

Constraints made of Ti-6Al-4V with CTE of 10 $\mu\epsilon/K$ expanding over the design operational temperature differential of ± 1 K, produce a drift of approximately ± 17.3 μrad. This is more than three times larger than the allowable thermal drift budget of 5 μrad. Either athermalisation of the tangential constraints and/ or appropriate addition of redundant constraints would be needed. This is investigated in the next subsection.

Addition of Redundant Constraints

There is considerable design freedom within the selected tangent constraint arrangement. Six initial design options were considered, illustrated in Figure 6.11. This section summarises the merits of each before narrowing the field down to three candidates for a final graphical trade-off, documented in Subsection 6.4. It must also be noted that the thermal performance could also be improved by athermalising the constraints, but it is simpler to first try to meet the requirements without addition of other complex parts.

PS-A: Strut/ Wire Constraints

The canonical physical embodiment of an ideal constraint is a wire, or wire flexure. These are strong in tension but comparatively much weaker in compression and bending. Struts, similar to the design shown in Figure 6.12, can be used to improve the buckling strength of the constraint. The increased thickness along the centre of the flexure improves the out of plane stiffness and dual orthogonal flexures at each end act as universal joints, preserving the single constraint line of the link.

Each of the *PS-A* design options could be equivalently designed with struts or wire flexures, depending on the need for buckling strength. The finer choice of whether to use a wire or strut depends on the launch loads, so is left to Chapter 8 *Mechanical Design*.

The three strut option *PS-A1* was included as the baseline. Since it does not mitigate the thermal clocking issue, it is excluded from the trade-off.

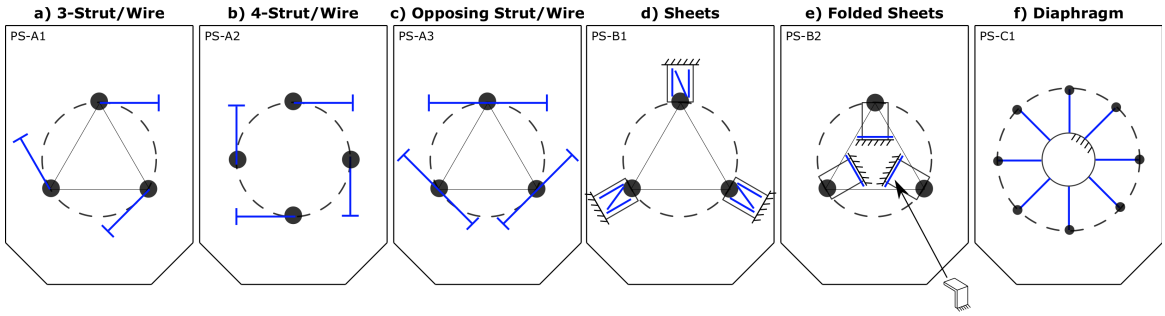

Figure 6.11: Three families of selected design options for passive constraints with redundancy. Passive support constraints (thick blue lines) grounded to the deployment mechanism support frame (cross-hatching or small blue cross-bars) and intermediate body (dashed circle). Segment geometry shown for illustrative purposes. Design option ID's shown in the top left corner of each concept.

The four strut option *PS-A2* was included as an example of the infinite number of $3+N$ redundant constraint options. It makes the system stiffer but still suffers from thermo-elastic rotation. This constraint pattern and its variations are commonly seen in the spider that holds the secondary mirror in Cassegrain telescopes. Since it is preferable to control the thermal clocking with the passive constraints, option *PS-A2* was not retained.

The opposing strut option *PS-A3* uses mirrored constraints to oppose the thermo-elastic deformation of the constraints and to ensure that one constraint in each pair is always in tension (under axial loads) to avoid buckling of the other constraint. The trade-off is a build-up of internal stress in the constraints that will ultimately cause them to yield or buckle. This can be compensated for with careful design. For mechanisms that can be constructed monolithically, thermo-elastic stresses can be avoided as the parts grow & contract together. Design option *PS-A3* was selected for trade-off.

Figure 6.12: Example of a rigid strut used to replace an ideal wire flexure. Note dual orthogonal flexures at either end. These are the flexure equivalent of a ball joint. This strut is used with the actuators on the E-ELT. Adapted from [126].

PS-B: Sheet Flexures

The *PS-B* family of sheet flexure design options replaces the idealised wire flexures with sheet flexures. Option *PS-B1* illustrates a version with three radial sheet flexures.

The centreline of each of the sheets intersects at the centre of the mirror to remove the clocking motion. Since sheet flexures can be modelled as three coplanar constraints, those constraints do not all intersect at the same point. Thus, unlike concepts 6.10*b* and *c*, the constraint redundancy doesn't result in a fourth freedom. However, the radial orientation does reduce the effective moment arm of the constraints. A benefit of this option is the small, simple design. Athermalisation or compensating flexures are still necessary to avoid internal stresses and buckling if the coefficients of thermal expansion of the flexures and base material differ.

Design option *PS-B2* consists of three folded sheet flexures. An example from the European Extremely Large Telescope is given in Figure 6.13. Only one of several ways to arrange these flexures is given in Figure 6.11*e*. It has similar costs and benefits to the sheet option and so is considered a subset of the sheet flexure option for the purposes of the trade-off.

PS-C: Diaphragm

The literature study for this thesis found the diaphragm to be the most commonly implemented method of providing radial support for terrestrial segmented mirrors [96], finding use on the Keck and the future E-ELT and TMT primary mirrors [14, 93, 113]. The James Webb Space Telescope is the only known segmented space telescope and uses a hexapod with whiffle tree to support the primary mirror segments.

The diaphragm adds significant constraint redundancy and therefore stiffness, as well as symmetry. The diaphragm requires a mushroom type support which can be large. Examples are shown in Figure 6.14. A

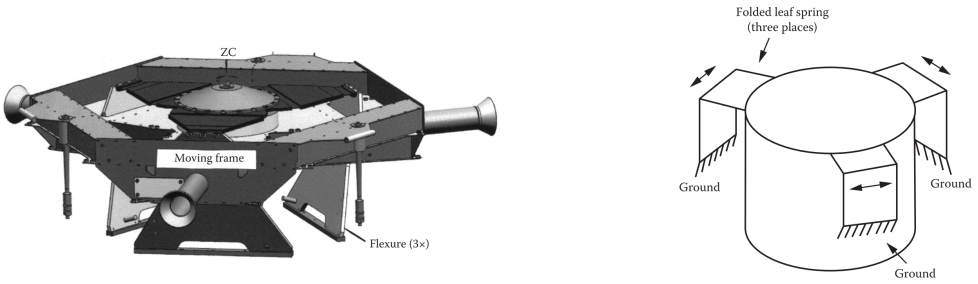

Figure 6.13: Example of the folded sheet flexure support for the E-ELT primary mirror segment moving frame support. Three triangular folded flexures mounted to the central hub of the moving frame constrain its motion. A simpler representation of the folded sheet flexure concept is shown in the right graphic. Adapted from [126].

flexured interface between the diaphragm support ring and mirror accounts for CTE mismatch between the support and mirror materials.

The diaphragm option was included in the trade-off as the "tried and true" option for segmented optics. This concludes the FACT constraint synthesis exercise. The final selection of the passive constraint set is conducted in the next section.

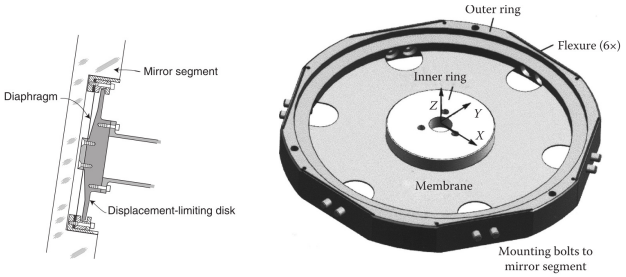

Figure 6.14: Examples of a diaphragm support. Left: Support for the segments of the Keck telescope primary mirror, adapted from [14]. Right: Detail view of the diaphragm in the same type of support used on the E-ELT primary mirror segments. Note the six outer flexures, which are used to compensate for differential thermal expansion between the mirror substrate and outer membrane support ring. Adapted from [126].

6.4. Passive Constraint Redundancy Trade-off

A candidate for detailed design was chosen using a qualitative trade-off. Quantitative methods were not favourable since it would have taken considerable design effort to assess each candidate fully. The validity of a trade based on analogous systems would have been questionable since the assumptions and conditions of performance are not always communicated clearly or uniformly across different publications.

Since the DST is an ongoing project, it is important to communicate design decisions clearly and succinctly. The graphical method was used for all trade-offs in this thesis as it is fast, transparent for both the designer and future users and clearly identifies unacceptable performances.

Subsection 6.4.1 outlines the trade-off criteria and scoring method. The latter was also used for all subsequent trade-offs. The trade-off is then conducted, and justified, in Subsection 6.4.2.

6.4.1. Trade-off Criteria & Scoring

The four mission requirements listed in Table 6.2 were identified as the critical stakeholder requirements by their direct correlation to the mission objective. They were translated into the trade-off criteria listed in Table 6.3. The design candidates were assessed relative to each other rather than against absolute performance metrics using coarse scoring over these criteria.

Note that in all trade-offs, cost could not be directly quantified without a costed bottom-up design or by analogy from similar systems. The latter option was very difficult as publicly available mechanism budget data is virtually never broken down into this level of detail. In the absence of this data, cost was assumed to correlate with the complexity of each design candidate throughout the system life cycle. The label "cost" was

Table 6.2: Stakeholder requirements for all concept trade-offs.

ID	Description
MIS-OBJ-02	The lifetime cost of the DST shall be less than the state of the art in commercial visual spectrum Earth Observation imaging platforms. As of 2017 this is DigitalGlobe's WorldView-4 satellite with an estimated cost of USD$850 million including ground network upgrades.
MIS-REQ-08	The mass of the instrument shall be lower than 100 kg (threshold) / 50 kg (goal).
MIS-REQ-09	In the stowed configuration, the volume of the instrument shall not exceed 1.5 m^3 (threshold)/ 0.75 m^3 (goal).
MIS-REQ-07	After calibration, the residual Strehl ratio of the system shall be higher than 0.80.

retained to indicate that this was the higher objective in using this criteria.

Table 6.3: Passive support constraint redundancy option trade-off criteria.

Criteria	Weight	Considerations
Mass	1/6	Flow down of MIS-REQ-08. Mass of mechanism parts as well as impact mechanism has on mass of other parts (for increased stiffness or surface area for interfaces).
Volume	1/6	Flow down of MIS-REQ-09. Space occupied by parts. Considers interface requirements - size, number of interfaces and accommodations that must be made in other parts.
Cost	2/6	Flow down of MIS-OBJ-02. Includes cost driven by complexity. Difficulty of analysis and ability to predict accurate performance. Design flexibility - how easily can it accommodate changes in design of interfacing parts. Number of parts. Constructibility of parts (minimum dimensions, need for non-standard methods). Difficulty of assembly, integration and testing.
Performance	2/6	Flow down of MIS-REQ-07. Thermal stability. Relative effectiveness of constraint moment.
Sum	1	

Mass is arguably a flow down of cost due to launch costs, however these criteria were separated since mass also affects the dynamic behaviour of the mechanism. Additionally, the mass of the mechanism is small compared to the expected overall mass of the spacecraft and will make only a small contribution to launch cost. The cost of the mechanism itself is expected to be more strongly linked to development and programmatic costs, and thus complexity, rather than material and launch cost.

Volume and performance as criteria follow logically from the stakeholder requirements. Volume is separated from mass since the stowed volume of the instrument is linked to the goal of decreasing launch costs. For the in-plane passive support, the constraints can occupy a large plan-form envelope. For example, the options in Figure 6.11*c,d,f*.

More weight is given to the cost and performance criteria in a 2:1 ratio to mass and volume. The overarching objective of the mission is to reduce cost, which is assumed to be more tightly linked to design complexity than mass or volume of the mechanism itself, for the reasons given above. Good performance is equally critical, from a qualitative perspective.

A simple, qualitative scoring system was used, as defined in Table 6.4.

Table 6.4: Concept trade-off scoring categories.

Category	Description
++	Excellent performance. Possible over-fulfilment of requirement.
+	Good performance. Fulfils requirement.
0	Minor deficiencies in performance but could be corrected within scope of resource constraints.
-	Several deficiencies. Would require dedicated effort to correct, likely at the expense of other systems.
- -	Unacceptable performance. No foreseeable way to correct deficiencies within scope of project.

6.4.2. Trade-off Justification

The results of the trade-off are given in Figure 6.15. The diaphragm option was the least feasible while the opposing strut/ wire and sheet options received similar scores. The opposing strut/ wire option was considered less complex than the sheet options, driving cost down. *PS-A3* also had the best performance thanks to its symmetry and absence of parasitic motions. Overall, it is clear from Figure 6.15 that option *PS-A3* with opposing strut/ wire flexures was the favourable choice with higher scores in the two most heavily weighted criteria. It was selected for integration into the overall concept. Justification for each of the scores is given below.

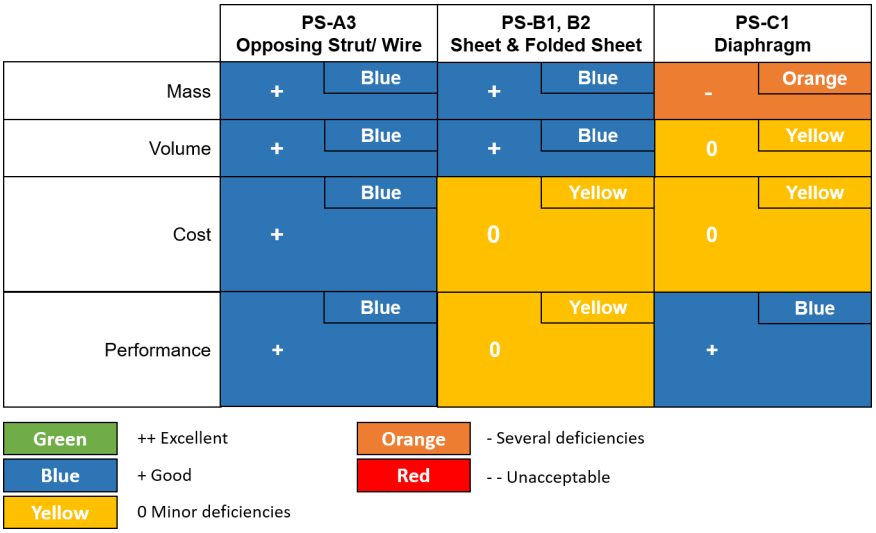

Figure 6.15: Graphical trade-off for passive constraint redundancy options. Row height is indicative of relative weight of trade-off criteria.

PS-A3: Opposing Struts or Wires

This option has good mass performance (+) since the constraints nominally have very small cross-sections, are low profile and they can be machined as a single part with their mating parts (ie. monolithically), removing the need for additional interfaces. They also leave the centre of the mirror free for the possibility of an HDRM. This gives it a good volume performance (+).

The presence of overconstraint complicates assembly. Precise jigs, metrology and fabrication techniques would be needed unless the constraints and structure can be made monolithically, which is possible and indeed common, with standard wire-EDM (Electro Discharge Machining). This reduces the number of discrete parts as well. Due to this simplicity, this option also has good cost performance (+).

This option has good performance (+). The tangential orientation of the constraints gives the best possible mechanical advantage. Thermo-elastic clocking is mitigated & constraint buckling prevented during launch by the opposing constraint. The symmetry maintains a well defined thermal centre and the geometry can be easily modified to change the stiffness.

PS-B1,B2: Sheet and Folded Sheet

The sheet option has a small cross section and therefore good mass performance (+). The interfaces could be bonded onto, or integral to, the mating parts. The flexure can be shorter than the opposing strut/ wire option since only a single sheet needs to be accommodated, rather than the four sheets needed if a strut is used. If the flexures are external to the circle of interfaces to the intermediate body as depicted in Figure 6.11*d*, then a larger support base will likely be needed though. If arranged internally, there may not be room in the centre to house a hold down mechanism if needed in the future. Overall, this design option has good volume performance (+).

Option *PS-B1,B2* has minor deficiencies in cost performance (**0**). Like option *PS-A3*, application of sheet flexures is well understood and documented and readily fabricated with wire EDM techniques. However, there is less design freedom since the constraints must be oriented radially to the centre of the segment. A further deficiency is that the flexures would need to be fabricated separate to the intermediate body or base, leading to a more complex assembly procedure.

The two sheet options have minor functional deficiencies (**0**). They have a much shorter lever arm over which the restraining moment can be applied compared to the strut/ wire option. Although this option removes the thermal clocking, radial thermal expansion of the intermediate body can lead to parasitic piston shifts of the body with folded sheets, illustrated in Figure 6.16.

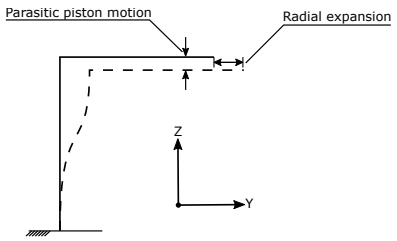

Figure 6.16: Parasitic motion of a folded sheet flexure undergoing radial displacement.

PS-C1: Diaphragm

The diaphragm option has several mass deficiencies (-). Both the support pillar & outer diaphragm support ring require large & more numerous interface components than the other design options, as illustrated in the example of Figure 6.14. The diaphragm option is better suited to ground based mirrors where mass is less of a problem. The large central post can be hollow to accommodate a hold down mechanism but it still dominates the central area of the segment and must be high enough to accommodate the membrane, clamping assembly and travel stops. It is therefore not a low profile option. Overall, the diaphragm option has minor volume deficiencies (**0**).

The diaphragm option has minor cost deficiencies (**0**). The diaphragm itself is simple, though the mating interfaces require multiple components and assembly jigs. This is in contrast to the simple monolithic design of option *PS-A3*. It may also require an extra flexure based interface with the intermediate body to account for CTE mismatch between materials. Otherwise, the diaphragm option has good performance (**+**). It is symmetric, does not generate thermal expansion induced clocking and provides balanced radial support without addition of parasitic motions. CTE mismatch will still impart stresses to the mating components as mentioned above. It is a valuable support method but is heavy and not well suited to space applications.

6.5. Actuator Design Options

The PMAO mechanism design strongly depends on the type of actuator that drives it, from the mechanical load rating and the interface requirements, to the arrangement, sensing and thermal considerations. Likewise, selecting a specific actuator model requires knowledge of likely loads, stroke and resolution requirements, each of which depend on the mechanism design.

An iterative approach was therefore needed to develop a cohesive design and to select an appropriate actuator. First, a specific *type* of actuator was selected, which is documented in this section. Two overall architectures based on this actuator were then synthesised, allowing reasonable estimates of the actuator strength and kinematic requirements. These requirements were then used to select a specific actuator. These latter operations are documented in Chapter 7 *Mechanism Architecture Selection*.

Thus, the objective of this section was to select systematically reduce the field of design options to a list of feasible candidates. Subsection 6.6 documents the trade-off based on analogous performance data sourced from commercial and academic literature, from which a single actuator type was selected.

6.5.1. Actuator Type Down Selection

The design option tree in Figure 6.17 shows the many different families of actuators that can be used in modern space mechanisms. In line with the actuator constraint set selected in Section 6.3, and to simplify the investigation, only linear output actuators were considered, where available. Additionally, only high TRL COTS actuators, preferably with space flight heritage, were considered since the DST project does not have the resources to qualify fundamentally new actuator technology.

This subsection documents the down selection of this broad field to no more than three feasible candidates for trade-off. Each of the actuator types are analysed.

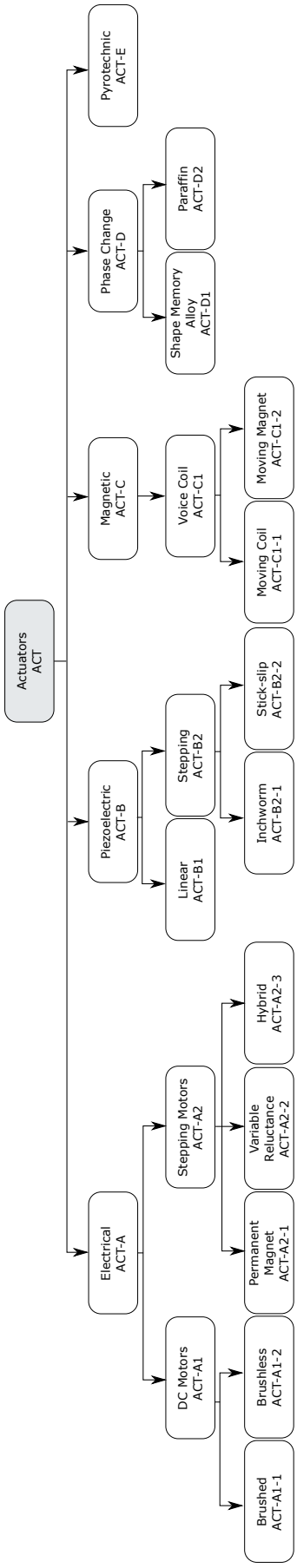

Figure 6.17: Actuator type design option tree.

ACT-A1: Electrical - DC Motors

DC motors are ubiquitous throughout terrestrial and space servomotor devices, available in either brushed or brushless variants. They offer good efficiency, low cost and simple driving electronics. Brushless DC motors avoid the lifetime limiting wear of brushed motors, which are not commonly used in space applications [103, p. 686]. They also have fixed coils and rotating magnets which can ease control of heat dissipation during operation compared to brushed DC motors, which have rotating coils [34], [103, p. 690]. Both types of motor are best suited to continuous or servo-style operation applications. Since the PMAO mechanism will undergo a lot of move and hold duties, they were not considered a feasible option.

ACT-A2: Electrical - Stepping Motors

A stepper motor is a brushless DC motor with two to five phases. Motors with more phases tend to have less vibration at each step but are more expensive. There are three types of stepper motor: permanent magnet, variable reluctance and hybrids [103]:

- Permanent magnet steppers are able to hold their position without power provided external torques do not exceed the unpowered holding torque (detent torque) of the motor. Gearing can help increase the effective detent torque and can be used to prevent back driving.
- Variable reluctance steppers do not have a detent torque but can hold a position when powered.
- Hybrids combine the operation of permanent and variable reluctance steppers and are normally used for very fine steps, on the order of 200 steps/ rev or 1.8° per step. The output torque of hybrid steppers is more variable than for the other two types.

Stepper motors have been the actuator of choice for fine actuation space mechanisms for many years (see for example [8, 71, 104, 115, 120]. A summary of the advantages and disadvantages of stepper motors is given in Table 6.5. They were included included in the trade-off as the feasible "tried and true" method of actuating space mechanisms.

Table 6.5: Advantages and disadvantages of stepper motors. Compiled from [4, 60, 120].

Advantages	**Disadvantages**
Significant space heritage and COTS availability.	Requires lubricant.
Simple, standard power and control.	Can have backlash, hysteresis, non-linear effects.
Detent torque can provide power-off hold.	Comparatively large, heavy. Lower power density.
Range of motion only limited by external mechanism.	Require extra parts (gearing, reducers) for nano level steps and transmission.
Can use open loop control.	Hard to accurately calculate torque in long transmissions due to uncertain efficiencies.

ACT-B1: Piezoelectric - Linear

Piezoelectric actuators are the most mature "smart" material technology used in space actuators [4], with growing flight heritage, finding use on SOHO, LISA, LISA Pathfinder, Rosetta, Curiosity, Gaia, Solar Orbiter and others [4, 11, 22, 60, 77, 78]. Notably, many of these opto-mechanical systems operate without actuator supplied power-off hold. The Cedrat Technologies APA model is shown in use for the ATLID instrument in Figure 6.18*b*.

These actuators make use of the inverse piezoelectric effect: the production of a mechanical force upon application of a voltage, typically on the order of 100 VAC, across stacks of piezo ceramic wafers. Resolutions down to the sub-nanometre level are possible [28] though their range is typically no more than a few tens of microns.

One of the major disadvantages of piezo actuators is the need for continuous power to hold a position. The driving frequency dictates the speed and acceleration of the actuator with higher frequencies causing greater self-heating of the ceramic. Thermal management of the stack is crucial in vacuum and can limit the duty cycle of the actuator at high loads and/ or bandwidths. The DST PMAO will likely be driven in "quasi-static" mode at no more than 10 Hz so total heat dissipation is expected to be no more than a few Watts at most and certainly less than inductive coil actuators [31].

The major advantages and disadvantages of piezoelectric actuators are summarised in Table 6.6. Linear piezoelectric actuators are attractive as they provide the necessary range and resolution without the need for

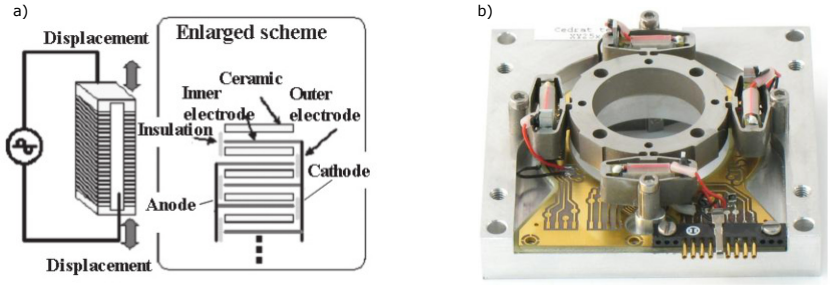

Figure 6.18: Left: Operating concept of a piezoelectric stack, adapted from [127]. Right: Four Cedrat Technologies APA amplified piezoelectric actuators in a beam steering mechanism for the ATLID (ATmospheric LIDar) instrument on the ESA-JAXA EarthCARE spacecraft. Note use of elliptical frame for mechanical amplification of stroke. Adapted from [22].

a transmission and can be designed to survive launch without use of an HDRM [31]. They were included in the trade-off.

Table 6.6: Advantages and disadvantages of piezoelectric actuators. Compiled from [4, 12, 127]

Advantages	**Disadvantages**
High power density.	Normally no power-off hold.
High reliability, no sliding parts.	Non-traditional power bus requirements.
No lubrication.	Performance sensitive to temperature of ceramic.
Compact, light (not considering electronics).	Large non-linearities without closed-loop control.
Low power losses in quasistatic operation.	Low stroke.
Space heritage.	Sensitivity to humidity (complicates ground testing).
Magnetic cleanliness.	Less standardisation than other actuators.
High force production.	Piezo ceramic is brittle, must be isolated from torsion and bending.
Stiff, even when not powered.	
Very high resolution, accuracy & repeatability with closed-loop control.	

ACT-B2: Piezoelectric - Stepping

Two types of stepping piezoelectric actuators were considered: inchworm and stick-slip. No COTS stick-slip style actuators with space environment qualification or heritage were found in an extensive survey so were not considered further.

Inchworm style actuators can have different configurations but all operate on the principle of the alternating expansion and contraction of at least two sets of piezoelectric stacks in contact with a driven runner. Figure 6.19 illustrates the working principle.

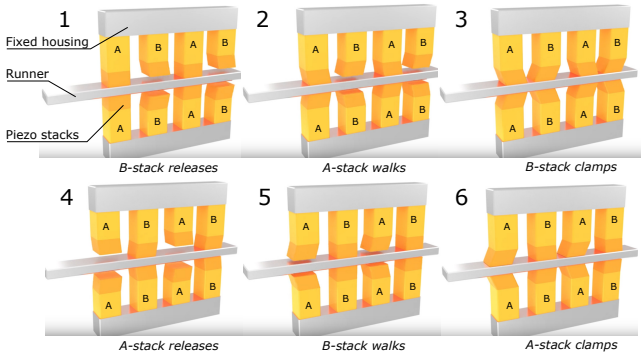

Figure 6.19: Example of the walking drive inchworm style piezoelectric actuator in "nano-step" mode. The parallelogram shaped piezoelectric elements expand and contract alternately along an axis oblique to the central runner. Adapted from [97].

An adaptation of a COTS Physik Instrumente NEXLINE walking drive style inchworm actuator was used on the LISA Pathfinder spacecraft as part of the test mass Grabbing, Positioning and Release Mechanism

(GRPM) [20, 85, 91]. A model from PiezoMotor Uppsala AB will also be used on the evolved LISA spacecraft for the In-Field Pointing Mechanism [123].

Although stepping piezo actuators offer power-off hold, the available clamping force is not very high. They are also not as stiff as linear piezo actuators when clamped due to their reliance on friction. An HDRM would be needed with piezo steppers holding large masses through launch [31] though the power-off hold would still be useful during operations. Otherwise, stepping piezoelectric actuators have much the same advantages and disadvantages as regular piezoelectric actuators per Table 6.6. They were included in the list of feasible concepts.

ACT-C1: Magnetic - Voice Coil

Also called moving coil actuators, voice coils have found application on several space missions in both rotary and linear output forms [15]. A controlled current is passed through a coil of wire attached to the part to be displaced. The coils' associated magnetic field opposes that of a magnet fixed to the stationary frame of the actuator, displacing the coil. Voice coils can be built with redundant coils and/ or stators as shown in Figure 6.20. No space heritage for moving magnet actuators could be found, so they were eliminated from the list of options due to low TRL.

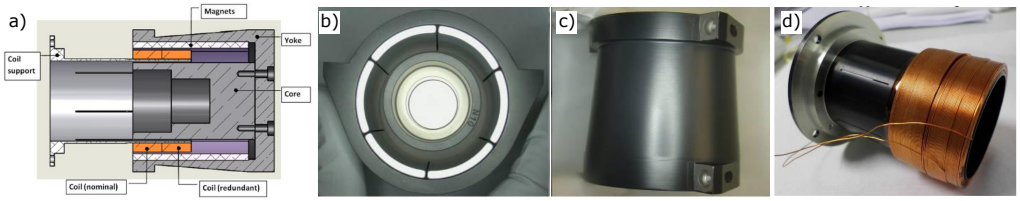

Figure 6.20: a) Profile view of a voice coil. b,c) Voice coil stator assembly. d) Voice coil coil assembly. Note second, redundant coil. Adapted from [15].

Commercially available voice coils for space applications have strokes between 1 - 30 mm and can generate forces between 1 - 200 N in packages weighing less than 250 g[2]. They typically demonstrate constant force and can be adapted to use flexures for high precision applications. Voice coils are more robust to temperature excursions than piezoelectric actuators as they are not limited by the Curie temperature of the piezo ceramic but are essentially small heaters when in use. A summary of the advantages and disadvantages of voice coils is given in Table 6.7.

Table 6.7: Advantages and disadvantages of voice coils. Compiled from [15, 82]

Advantages	**Disadvantages**
Larger stroke than piezo actuators.	No inherent stiffness.
Constant force output, can be large.	No power-off hold.
No cogging, low hysteresis give very linear motion.	Require sensor for position knowledge.
High bandwidth.	Continuous power draw and heat dissipation.
Light, relatively compact.	Less space heritage than other actuators.
No lubrication or contacting parts, high reliability.	Moving coil is hard to cool.
High resolution.	

Voice coils were not considered a feasible candidate as they require power for both stiffness and stability. Thermal control is also difficult as the dissipating element, the coils, are mobile during operation.

ACT-D1: Phase Change - Shape Memory Alloy

Shape memory alloy actuators (SMA) operate by heating an alloy beyond their transition temperature, typically about 343 K. At this point the alloy changes its geometry to a pre-defined shape, thus they are typically only used in binary position applications such as hold down & release mechanisms or valves. Shape memory alloy actuators were not considered feasible for the PMAO mechanism since fine position control is required. Additionally, the nominal operating temperature of the DST is 298 K. Heating several devices to 343 K behind the primary mirror would unnecessarily complicate the thermal design.

[2]See `http://www.cedrat-technologies.com/fileadmin/user_upload/CTEC/Technologies/Actuators/Magnetic_actuators_motors/Voice_coils/Voice_Coils_Actuators.pdf`. Accessed: [22 February 2018].

ACT-D2: Phase Change - Paraffin

Paraffin based phase change actuators rely upon the change in volume of paraffin stored in a reservoir as it is heated up and beyond its phase change temperature. These actuators offer a high load bearing capability due to the low compressibility of paraffin [94] but only binary actuation. They are not well suited to fine motion control applications so were not considered feasible candidates.

ACT-E: Pyrotechnic

Pyrotechnic actuators are single use devices, generate very high shock loads, are hazardous and can release particulates and material detrimental to the performance of optical surfaces [59]. They have been included in the design option tree in Figure 6.17 for completeness but were not considered feasible candidates.

6.6. Actuator Type Trade-off

Brushless DC stepper motors and linear and inchworm piezoelectric actuators were selected as feasible design options. A graphical trade-off was conducted using indicative performance values taken from space rated COTS components per mission objective MIS-OBJ-02. Preference was given to European suppliers in line with mission requirement MIS-REQ-10. Each of the selected indicative models are shown in Figure 6.21. The performance characteristics of each actuator are summarised in Table 6.8. The mass, volume, range, resolution and load/ torque characteristics are all exclusive of any transmission components.

Figure 6.21: Indicative models for feasible actuator types. a) Cedrat Technologies (FR) APA120ML amplified piezoelectric actuator. b) PI (DE) Nexline N-111.2A1 walking/ stepping piezoelectric actuator. c) Phytron (DE) phySPACE two phase hybrid stepper motor. Adapted from [28, 97, 98].

The linear piezoelectric actuator are from the Cedrat Technologies APA120ML. The APA family has already seen use in space [28]. The APA50S was used in the MIDAS XYZ scanning mechanism on the Rosetta spacecraft [77]; the APA35XS will be used as part of double tilt translator for the PHARAO atomic clock to be sent to the ISS in 2018 [78]; and the APA60S will be used in the ATLID Beam Steering Mechanism for ESA's EarthCARE satellite also due for launch in 2018 [22]. Data for the APA120ML is given, rather than these other actuators as it is more comparable in size to the Phytron stepper motor and PI NEXLINE walking mode piezo actuator. For comparison, the masses of the APA35XS and APA60S actuators are 2.0 g and 8.5 g respectively. Data for the APA in Table 6.8 is also indicative of some of Cedrat's PPA non-amplified linear piezo actuators.

A customised Physik Instrumente (PI) Nexline walking mode/ stepping piezoelectric actuator was used on the LISA Pathfinder Grabbing, Positioning and Release Mechanism (GPRM) [85, 91]. A prototype from the same family has also undergone thermal vacuum testing in the literature [27]. Since this was a customised actuator, indicative performance values are given for a COTS Nexline N-111.2A1 with integral linear encoder instead.

Finally, a Phytron phySPACE 32-2 two phase hybrid stepper motor was used to supply indicative performance data for the stepper motor option. The phySPACE family of stepper motors are COTS space rated products [98]. The 32-2 is selected for its comparable dimensions with the piezoelectric actuators. Several smaller and larger stepper motors are available in the space qualified phySPACE family.

6.6.1. Trade-off Criteria & Scoring

The actuator type was selected based on a graphical trade-off method using the selection criteria in Table 6.9. This table also explicitly traces the criteria back to the relevant stakeholder requirements in Table 6.2.

As was the case for the passive support constraint trade-off, cost could not be directly quantified without a bottom-up design or by analogy from similar systems. Suppliers were unwilling to provide cost data without

Table 6.8: Summary of indicative performance characteristics for feasible actuator candidates. N/A indicates property is Not Applicable to the actuator. Hyphen (-) indicates data not available. Compiled from [28, 97, 98].

	ACT-B1 Linear Piezo [28]	**ACT-B2-1 Stepper Piezo [97]**	**ACT-A2 Stepper Motor [98]**
Manufacturer	Cedrat Technologies	Physik Instrumente	Phytron
Country	France	Germany	Germany
Model	APA120ML	Nexline N-111.2A1	phySPACE 32-2
Motion type	Linear	Linear	Rotary
Power-off hold	No	Yes	Yes
TRL (assumed)	7	7	7
Mass	0.160 kg	0.325 kg	0.211 kg
Volume	45 x 78.9 x 22.5 mm	62 x 28 x 46 mm	47 x 47 x 60 mm
Range	130 μm	$\pm$ 5 mm	Continuous
Resolution	1.3 nm	5 nm closed loop	1.8°
Accuracy	-	-	3 - 5 % of step
Speed	Variable	0.4 mm/s	400 rpm continuous
Driving force/ torque	700 N	50 N	28 mNm
Unpowered holding force/ torque	N/A	70 N	2 mNm
First eigenfrequency	1750 Hz	-	-
Transmission requirements	Nil	Nil	Yes
Power requirements	-20 to 150 V	$\pm$ 250 V	48 V
Lubrication required	No	No	Wet or dry
Displacement sensing required	Yes	Yes	Recommended
Thermal control required?	For high duty cycles	For high duty cycles	Possibly

Table 6.9: Actuator trade-off criteria. Tribology is the study of interacting surfaces.

Criteria	**Weight**	**Considerations**
Total mass	2/11	Flow down of MIS-REQ-08. Mass of actuator and auxiliary components (transmission, driving electronics).
Volume	2/11	Flow down of MIS-REQ-09. Includes auxiliary components. Considers interface requirements - size, accommodations that must be made in other parts.
Range & resolution	2/11	Flow down of MIS-REQ-07. Ability to meet actuation needs.
Cost	2/11	Flow down of MIS-OBJ-02. Complexity, need for additional or non-standard power, sensing, transmission or thermal control elements. Difficulty of assembly, integration and testing including tribological complexity.
Driving force/ torque	1/11	Flow down of MIS-REQ-07. Greater driving force/ torque advantageous as stiffer flexures can be used to improve the dynamic performance of the mechanism.
Holding force/ torque	1/11	Unpowered only. Flow down of MIS-REQ-07. May minimise required duty cycle of mechanism, ease thermal control requirements. Reliability of PMAO improved if mirror is stable in case of power failure. Inherent stiffness.
Risk	1/11	Flow down of MIS-OBJ-02. Low risk components require less project resources for testing & qualification. Improves reliability of system. Also includes consideration of auxiliary components.
Sum	1	

the likelihood of a sale, so again cost was assumed to correlate with various aspects of programmatic and technical complexity.

The functional performance of each actuator was broken down into range & resolution, driving force/ torque and holding force/ torque to provide better discrimination between the relative strengths of each design option. Total mass of the actuators and driving electronics was a critical trade-off criteria. A lighter actuator eases support requirements as well as overall mass. Similarly for volume.

Technical and programmatic risk were considered together. Although each actuator type has space flight heritage, the exact model that may be used in the DST conceptual design may not. This introduces programmatic risk as additional final qualification could be necessary. Furthermore, even though the actuator may

have a high TRL, auxiliary components such as a custom transmission may have low TRL. This was considered in the trade-off.

Mass, volume, range & resolution and cost were considered primary trade-off criteria each with twice the weighting of the secondary criteria: volume, risk, and driving & holding force/ torque.

6.6.2. Trade-off Justification

The trade-off results are summarised in Figure 6.22. Scores were applied using the definitions in Table 6.4.

The DC stepper motor option was at a strong disadvantaged due to the need for an additional transmission. The two piezoelectric actuators could only be separated on the secondary criteria. The linear piezoelectric actuator was selected since power-off hold is only a soft requirement. It is also conceivable that these actuators can hold the mirror through launch without an HDRM which is very unlikely with the piezo stepper as it relies on friction between the piezo stacks and runner.

The lower programmatic risk & much greater availability of performance data for the linear piezo actuators was also a strong advantage. The linear type was ultimately selected.

Comments regarding the performance of each actuator across the seven criteria are given below.

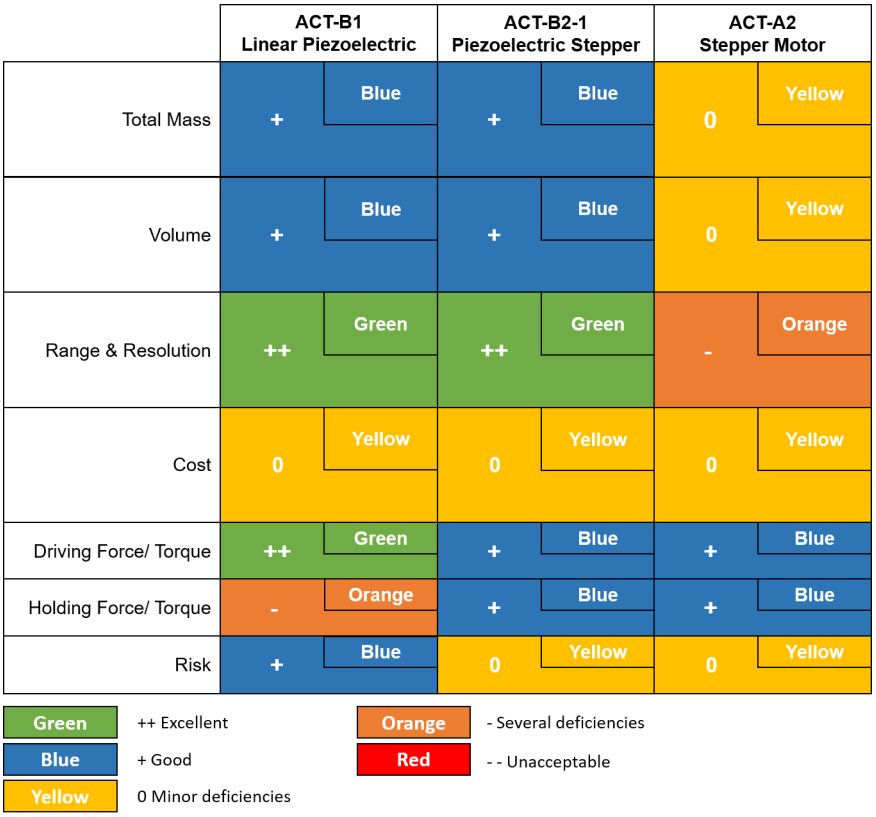

Figure 6.22: Graphical trade-off table for actuator type selection. Row height indicates relative weighting of the trade-off criteria.

Total Mass

Mass and volume specifications for the space rated power electronics for each actuator are not publicly advertised. A rough estimate was inferred from terrestrial OEM products. For example, three Cedrat linear amplified piezoelectric actuators can be driven by the LA75A-3 linear amplifier with mass 1 kg and four amplifiers can be supplied by a single LC75A AC/ DC converter with mass 0.68 kg [28]. The approximate mass of driving electronics per actuator unit is then 0.39 kg, not including cable harness. It is assumed a similar per unit mass would be required for the PI Nexline stepping actuator.

Similarly, the Phytron MCC-2 programmable controller is a compact industrial stand alone unit providing power, CPU and motor indexer for two stepper motors. The total mass is 0.75 kg for a mass of 0.375 kg per actuator [99]. Given this first estimate, there is no clear discrimination between the mass performance of either driving electronics package.

The Amplified Piezoelectric Actuator (APA) type typically has lower mass than the other two actuator types thanks to its simple construction. The piezo stepper is roughly twice the mass due to the encapsulating housing. A transmission is not mandatory for either piezoelectric actuator type. A gearbox and motion translation transmission certainly will be mandatory for the DC stepper. Assuming that the stepper motor gearbox and transmission are of similar mass to the motor itself, the combined motor plus transmission assembly could weigh up to twice that of a piezo based solution.

The linear amplified and stepper piezoelectric actuators were each given a score of (**+**) as both meet the initial, albeit rough, mass requirement. The stepper motor was given a score of (**0**) because of the added mass of the transmission.

Volume

The power electronics typically consist of several PCBs arranged in a compact fashion. No engineering drawings or specifications were available, so the volume of these parts were neglected in the trade-off.

The length & width dimensions of the usable volume are less constrained than the height. The two piezoelectric actuators have similar total volumes, albeit in different form factors. The APA is wider and planar, while the piezo stepper is more box like. Other linear piezos are typically columnar. Either of the piezo actuators can be accommodated in the available volume. The stepper motor occupies approximately 65% more volume than the piezo options *without* addition of a transmission. It is likely that there would be enough space to accommodate the extra components, though it would be congested.

The piezoelectric actuators were both given a score of (**+**) and the stepper motor (**0**).

Range & Resolution

The piezo stepper couples a large range of motion with very good resolution in closed loop operation which could be utilised in a lever type transmission to increase its drive and holding force capabilities. The piezo stepper was given a score of (**++**).

The linear piezo actuator had a much smaller range but better resolution. Both parameters still easily met the requirements. As discussed in the following driving force section, the APA has a natively high driving force so may not need the large range of the piezo stepper for amplification. The linear amplified piezoelectric actuator was given a score of (**++**).

A review of the relevant space mechanism literature has shown that all stepper motors require a reducing transmission of some kind to meet nano-scale resolutions [8, 71, 115, 120]. Thus the stepper motor was given a score of (**-**) for not meeting the required motion resolution without dedication of additional resources to transmission development.

Cost

Closed loop operation is necessary for each of the actuator types. Piezoelectric actuators suffer from significant hysteresis and the stepper motor suffers from backlash.

Stepper motors and their electronics have broad space flight heritage. Fabrication, product assurance, AIT tasks and facilities are well standardised and widely available. Thanks to their adoption in a growing number of precision space mechanisms, similar standardisation and facilities are increasingly available for piezoelectric actuators [4, 31].

It is difficult to assess flow-on requirements and additional complexity for the thermal control system without knowing actuation loads and duty cycle. Qualitatively, the piezo stepper will dissipate comparatively little heat since it can hold a position without power. The linear amplified piezo must be continuously powered though in the quasi-static mode, can be expected to dissipate no more than tens of milliwatts, typically much less than the inductive losses in a DC stepper motor [31]. The piezo ceramic temperature must be controlled to avoid excursions above its Curie temperature.

If considered in isolation, the power supply requirements for the stepper motor are preferable to those of the piezoelectric actuators as the voltage is lower, product assurance and AIT methods are very well characterised and there is greater standardisation across buses, adapters and protocols. However, other work on the DST aberration correction system has shown that a deformable mirror driven by piezoelectric actuators should be included in the instrument [116]. This means there will already be a high voltage power supply requirement for the spacecraft bus.

The APA linear piezoelectric actuator was given a cost score of (**0**) as extra sensing and thermal control mechanisms may be required to compensate for minor deficiencies in the system. The piezoelectric stepper was also given a cost score of (**0**) mostly for the higher programmatic risk compared to the APA type actuator.

The piezo stepper option has much less space flight heritage as a purely COTS component than the APA and DC stepper motor options. Finally, the stepper motor was given a cost score of (**0**). The comparatively low cost of using a true COTS space qualified actuator was offset by the need to develop a transmission mechanism.

Driving force/ torque

This trade-off is based on the qualitative assumption that greater available driving forces are better as they enable stiffer flexures and thus better dynamic performance.

The APA actuator has a very high available driving load even without a transmission to amplify the force. Smaller actuators from the same family are available if less force is necessary. It received a score of (**++**).

The piezo and DC stepper motors also produce a reasonable driving force and torque. Assuming a 100:1 reduction ratio similar to that used on the Kepler M2 mechanism stepper motor [71] and lever arm of 23.5 mm equal to the radius of the phySpace 32-2 housing [98] gives an output driving force of approximately 119 N for the stepper motor. The piezo stepper has a driving force of 50 N. Both actuator options are assumed to meet the requirements and given a scored of (**+**). These assumptions were later verified in the driving forces found in the *SPACAR* modelling, reported in Subsection 9.4.5.

Holding force/ torque

The linear amplified piezoelectric actuator has no power off hold capability. It is conceivable that a brake or clamp like mechanism could be designed to rectify this deficiency, which would require a dedicated effort to develop. This option was given a score of (**-**).

Both the piezoelectric and DC stepper motors offer power-off hold. Although this was considered a soft requirement, it adds flexibility to the technical feasibility of the PMAO mechanism. The piezo stepper offers 50 N hold force. With the same reduction and lever arm assumptions discussed above, the DC stepper motor could hold between 8 and 9 N on detent torque alone. Neither capability would be enough to hold the mirror during launch but they could be adapted through a transmission to increase this capability. Both options were given a score of (**+**).

Risk

APA linear piezoelectric actuator received the best score for risk (**+**). Several different linear amplified piezoelectric actuators from European suppliers have flown on past missions and are scheduled for use on future missions. From a programmatic point of view, continuity of development and AIT facilities can therefore be relied upon. It is also not strictly necessary to design and qualify a transmission stage.

Given the use of a custom Nexline on LISA Pathfinder [20], it was assumed that the actuator TRL is at least 7 *A model demonstrating the element performance for the operational environment has been built*[3]. However, the manufacturer was unwilling to provide documentation declaring the true TRL, or specifications of the space rated Nexline family. A prototype from the same actuator family has undergone thermal vacuum testing in the literature, improving confidence in its applicability to space applications [27]. It would be better if a true COTS model, rather than a customised version, had space flight heritage, therefore the piezo stepper is given a score of (**0**) for risk.

The DC stepper motor is a true COTS space qualified component. On its own it has the lowest technical and programmatic risk of all three actuator types. However, the need for a custom transmission reduced the risk score to (**0**), similar to the piezo stepper. Review of the literature has shown that development of such mechanisms can be complicated, largely due to the tribological requirements [32, 71, 120].

6.7. Chapter Summary

This chapter documented a methodical exploration of the PMAO mechanism design space. A hybrid arrangement was selected and the actuator and passive constraint constraint spaces selected. A final configuration for the passive constraints, including redundancy to improve the thermal performance, was selected via graphical trade-off. The linear piezoelectric family of actuators was also selected by graphical trade-off, largely thanks to their excellent native resolution capabilities and burgeoning space heritage.

With the actuator type selected, the concept generation exercise continued on to synthesis of two mechanism architectures and final selection of an actuator model. These activities are covered in the next chapter.

Major assumptions from this chapter are aggregated with those of Chapter 7 *Mechanism Architecture Selection* at the conclusion of the concept generation & selection process. See Table 7.4 on page 99.

[3] `http://sci.esa.int/sci-ft/50124-technology-readiness-level/` [Accessed: 21 march 2018].

7

Mechanism Architecture Selection

This chapter details the final actuator model choice and trade-off between two architectures to deliver the revised PMAO mechanism design. Section 7.1 details the selection of a family of COTS actuators based on the results of the trade-off in Section 6.6. Derivation of the top down system budgets assumed that the M1 segments could be rotated about a point on the optical surface of the mirror. This is very hard to achieve in practice within the usable volume and interface constraints. Section 7.2 establishes that a more reasonable arrangement uses a remote centre of rotation below the mirror instead. Sections 7.3 and 7.4 describe two architectures for the PMAO mechanism. Each sets out that concept's operating principles and delves into sizing calculations for the launch loads and kinematic performance requirements for the actuators. A discussion of the actuator model selection is given in Section 7.5, which facilitated the final architecture trade-off in Section 7.6. The chapter concludes with a summary of the main findings and assumptions in Section 7.7.

7.1. Actuator Family Selection

The actuator type trade-off in Section 6.6 led to selection of a linear amplified piezoelectric actuator. Suppliers were contacted to find a specific model that had space flight heritage and could meet the system requirements. The Parallel Pre-stressed Actuators (PPA) XL family of actuators from Cedrat Technologies (FR) were selected for initial analysis in the concept trade-off. This product offers a standardised interface across the actuator family for interchangeability as the PMAO design matures. The core technology of the actuators can also be readily modified to suit individual applications whilst still using the same manufacturing, assembly, integration and testing procedures that led to success in prior space missions. Figure 7.1 shows a COTS Cedrat PPA40XL actuator. The form factor is indicative of all PPA XL actuators.

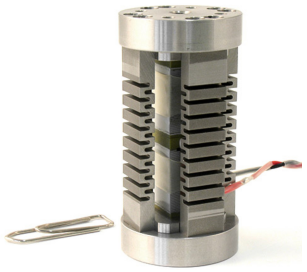

Figure 7.1: Cedrat Technologies PPA40XL piezoelectric actuator [29]. A paper clip is shown for scale.

The PPA actuator uses an external metallic elastic frame to pre-stress the piezo ceramic. Since they are solid state they are very stiff and have very good dynamic performance. When holding a static position they consume on the order of tens of milliwatts [31]. These actuators are not covered by ITAR restrictions, are available off the shelf with ECSS compliant strain gauge sensors for closed loop control and can be modified to provide different strokes. For example, the PPA40XL is approximately 60 mm high and offers 42.90 μm stroke. It is possible to make a 20 mm high actuator with ≈10 μm stroke using the same technology [31].

These actuators can only withstand axial loads and must be mounted with flexures at either end to isolate

them from bending and transverse loads. Two architectures using the PPA XL family were synthesised. Cedrat was consulted to verify that the actuator mechanical interface, loading and sensing specifications were met.

7.2. Remote Centre of Rotation

The passive constraint set selected in Section 6.4 defines the plane in which the tip and tilt axes are located. Since the constraint flexures cannot occupy the same space as the mirror, the rotations must necessarily be about a point *remote* from the optical surface of the mirror. This is contrary to the definition of the top down systems budgets, which were derived assuming rotations about a point on the optical surface of the mirror.

No space borne, precision, opto-mechanical mechanism with an axis of rotation defined in the plane of the optical surface was found during the thesis literature study [96]. Cedrat Technologies, subject matter experts in space qualified precision mechanisms, also noted the severe difficulty of implementing this [31].

After discussion with the optical team, it was decided that the PMAO mechanism would not need to provide pure rotations at the optical surface, provided that the parasitic translations at the surface were less than the deployment/ coarse alignment system budgets in Table 3.3. The residual decentring caused by the parasitic translations in the co-alignment calibration step would then be compensated in a later optimisation stage of the M1 calibration procedure.

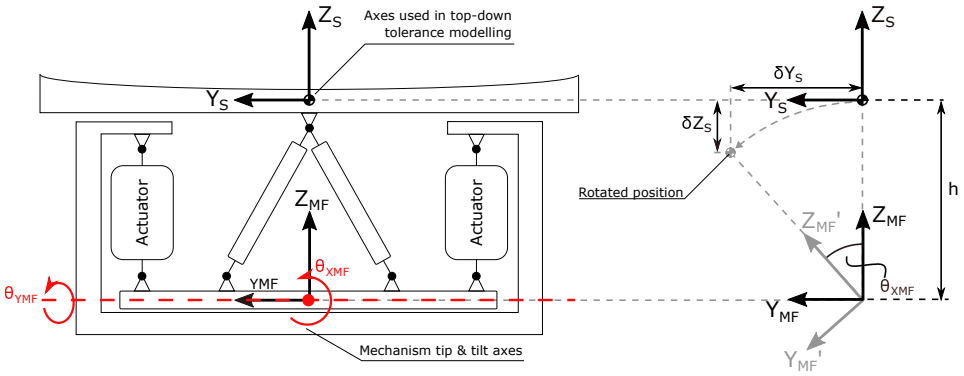

Figure 7.2: Geometry for calculation of parasitic decentre and defocus caused by remote centre of rotation during a worst-case $\theta_{X_{MF}}$ rotation.

Indicative geometry of both architectures is illustrated schematically in Figure 7.2. Concept B is depicted in the figure since it gives the worst-case offset h. The results apply equally to concept A. Both concepts are explained in more detail in the next sections. For now, it is sufficient to know simply that the tip and tilt axes are far from the mirror. The worst-case decentring occurs for the largest tip or tilt rotation at the greatest allowable distance between between the rotation axes and the optical surface of the mirror. The maximum distance between the constraint plane and optical surface is ≈150 mm. The largest rotation is ±4 μrad about the mechanism X_{MF} axis, causing a parasitic decentre δY_S and defocus δZ_S. From the geometry, the parasitic motions are then

$$\delta Y_S = h sin(\theta_{X_{MF}}) \tag{7.1}$$
$$= 0.15m \times sin(4.0 \times 10^{-6} \mu rad) \tag{7.2}$$
$$= 0.6 \mu m \tag{7.3}$$
$$\delta Z_S = h\left(1 - cos(\theta_{X_{MF}})\right) \tag{7.4}$$
$$= 0.15m \times \left(1 - cos(4.0 \times 10^{-6} \mu rad)\right) \tag{7.5}$$
$$= 1.2 \times 10^{-6} \mu m \approx 0 \mu m \tag{7.6}$$

Per Table 3.3 the deployment & coarse alignment tolerances in the Y_S and Z_S directions are both 2 μm. Therefore the effect of a worst-case decentre and defocus caused by the shift in tip & tilt rotation axes is acceptable. This result also suggested that the segment range requirements could be applied in the mechanism coordinate frame without significant loss of accuracy in order to simplify the flow down of the kinematic requirements from the segment level to the actuators. The workspace verification activity in Chapter 9 *Verification* was used to verify this assumption.

7.3. Concept A: 3x NLA Actuator Assemblies

Concept A uses six PPA actuators in three Nanometric Linear Actuator (NLA) sub-assemblies offered as a tested, but custom, product from Cedrat. The main driver behind this design was the very good thermal stability of the NLA actuator assemblies, demonstrated by thermal vacuum testing [101]. The concept is shown schematically in Figure 7.3.

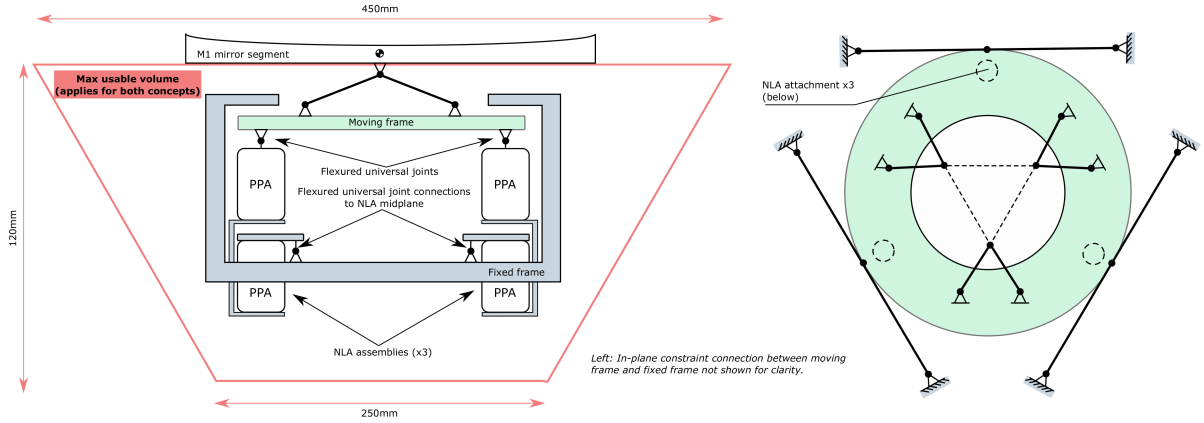

Figure 7.3: Mechanism architecture concept A with three NLA actuator assemblies. Six PPA10XL actuators are used, two each in three Nanometric Linear Actuator (NLA) assemblies. Left: Profile view of the concept with in-plane constraints not shown for clarity. The usable volume, indicated by the trapezoidal outline, also applies for concept B. Right: Top view of the moving frame assembly showing in-plane constraints.

Each of the basic building blocks of the concept are described in more detail in Subsection 7.3.1. The launch loads on the actuators are estimated in Subsection 7.3.2. The linearised inverse kinematic equations are derived in Subsection 7.3.3 and are then used to find the flow down actuator stroke requirements in Subsection 7.3.4. The section concludes with a summary of the concept in Subsection 7.3.5.

7.3.1. Description of Mechanism Elements

This subsection describes each of the major elements in concept A starting with the fixed and moving frames, to the in-plane constraints, universal joints and mirror support bipods. The final two subsections introduce the Nanometric Linear Actuators and the displacement sensing approach that gives them their very good thermal stability.

Fixed Frame

The fixed frame provides the foundation for the mechanism and the primary interface to the deployment mechanism support frame. All parts in the 3DOF mechanism are nominally the same material so that they expand and contract at the same rate, avoiding stresses from CTE mismatch and thermal drift.

Encapsulating the mechanism in a single housing rather than attaching the actuators directly to the deployment mechanism as in the original baseline design (see Figure 5.1) has both systems and programmatic benefits. It simplifies the mechanical interface between the PMAO and the deployment mechanism so that, within the framework of the DST project, it can be developed & tested independently of the deployment mechanism.

Moving Frame

The moving frame is the intermediate body referenced in the arrangement selection of Section 6.2. It provides an interface between the parallel, out of plane, actuators, the passive in-plane support constraints and the mirror support. As anticipated in the hybrid topology trade-off, the moving frame adds complexity and weight but it plays the vital role of isolating the mirror and mirror support from the bending loads induced by the actuators.

In-plane Constraints

In-plane constraint is provided by three pairs of tangentially oriented wires or struts per the trade-off in Subsection 6.4.2. The moving frame and in-plane constraints can be manufactured monolithically to simplify assembly and provide a continuous heat conduction path.

The in-plane constraint methodology is the same for both concepts A and B. The monolithic wire flexure option was pursued first as it was nominally simpler, lighter and easier to assemble than the strut option.

Universal Joints

The PPA XL actuators in both their standard and NLA formats can only withstand axial loads. Flexured universal joints are included at either end of the actuators in both concepts A and B to make sure no transverse loads or moments are transmittedl. These loads are instead reacted by the in-plane constraints.

Examples of compact flexured universal joints are given in Figure 7.4. These joints constrain only translation in the axial direction. They can have a cylindrical form factor per Figure 7.4 or a square form-factor. The latter is stronger but heavier due to the increased amount of material in the central annular section.

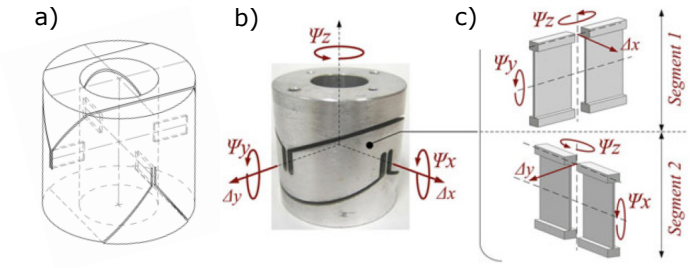

Figure 7.4: An example of a five DOF flexured universal joint a) in schematic form; b) as fabricated, showing rotational degrees of freedom; and c) schematic representations of the degrees of freedom of each of the pairs of orthogonal blade flexures. Adapted from [57, p. 194], [89, p. 2259].

Mirror Support

Rigorous definition of the number and distribution of support points relies upon knowledge of the stiffness of the mirror, however its design remains the subject of a future MSc thesis. It was decided in consultation with the optical team to progress the PMAO design by assuming that the support would only need to define the location and maintain the structural integrity of the mirror in the optical assembly when on Earth and through launch [49]. It was also assumed that a separate metrology mount would be used to maintain the correct optical surface figure for terrestrial AIT activities. This permitted separate, modular development of the mirror and mechanism designs, in line with the stepped development timelines of each of the DST subsystems. Appropriate flow down requirements for the mirror design are given in Section 9.6 *Flow Down Requirements*.

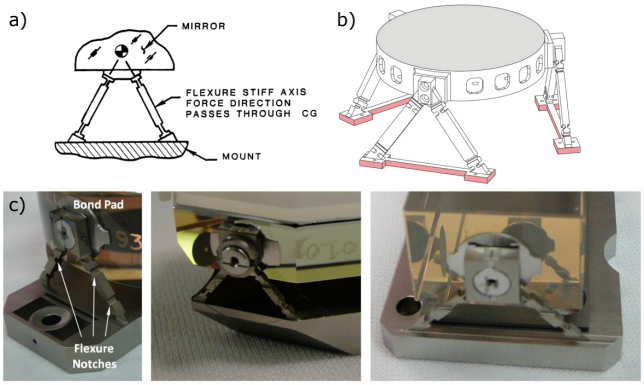

Figure 7.5: Examples of flexured bipods used as mirror mounts. a) The bipods are normally angled so that their lines of constraint intersect at the centre of mass of the mirror. b) A schematic representation of three bipods supporting a mirror at its edge. c) Real world embodiment of flexured bipods, used on various mirrors on NASA's IRIS spectrometer. Adapted from [38, 118, 121].

Three flexured bipods were chosen for the mirror support element. Examples are shown in Figure 7.5. Flexured bipods were used in almost all space optics mechanisms investigated in the literature study [96]. The tangential mounting and radial compliance defines a thermal centre that remains stationary under varying thermal loads which, if it coincides with the focal point of the mirror, avoids decentration aberrations.

To avoid overconstraint, each strut has an integral orthogonal flexure cut into the ends to allow out of plane bending, twist along the axis and small out of plane translations. This arrangement was shown earlier for the strut in Figure 6.12 on 66. This gives each strut a very high axial to bending stiffness ratio.

The struts constrain only a single degree of freedom. With six struts, the combined assembly exactly constrains the six rigid body degrees of freedom of the mirror. Kinematically, this achieves the same constraint condition as the *0R/ 0T* purely parallel constraint arrangements introduced in Figure 6.5 from Hale on page 61. If they are bonded to their mating parts, this constraint is achieved without introducing any friction or hysteresis to the assembly.

A further advantage of the flexured bipod is that the instantaneous centre of rotation of a pair can be controlled by changing the included angle of the two struts such that it intersects the neutral plane passing through the mirror's centre of mass as in Figure 7.5*a*. This minimises the shear forces and bending moments exerted on the mirror, which are liable to cause astigmatism and other aberrations [125, p. 82].

The Nanometric Linear Actuator

The Nanometric Linear Actuator (NLA) utilises two PPA actuators in series. The main advantages of the assembly over a PPA actuator on its own are very good thermal stability and a centred stroke [31, 101]. Testing in vacuum at $298 \pm 1K$ demonstrated a stability of $\pm 5\ nm$ over two weeks [101]. The trade-off is that two PPA actuators are required for a single linear output, requiring twice the driving electronics, mass and volume compared to a regular actuator.

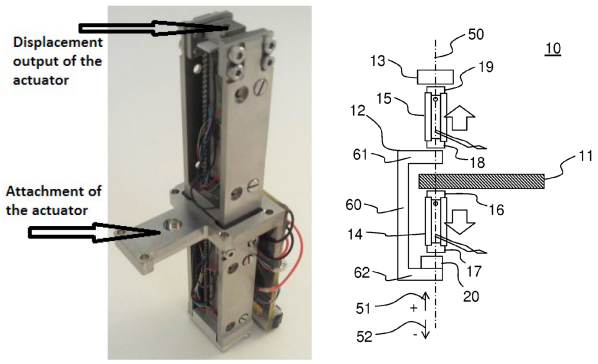

Figure 7.6: The Cedrat Nanometric Linear Actuator. Actuators (14) and (15) are driven to expand/ contract or contract/ expand respectively, providing a linear displacement between the fixed based (11) and mobile interface (13). Adapted from [39, 101].

With reference to the patent extract in Figure 7.6, the central base (11) and output interface (13) must be mated to the mechanism assembly via universal joints to isolate the actuators from shear and moments. The NLA operates through simultaneous opposing motion of the two actuators. That is, as the upper actuator (15) expands, the lower actuator (14) contracts to provide an upwards output at (13) and vice versa for downwards output. The full stroke of the assembly is twice the stroke of the two constituent actuators.

Piezoelectric ceramics exhibit strongly non-linear displacement with very poor repeatability as they expand and contract. This non-linearity, or hysteresis, must be compensated with closed-loop position control to ensure good repeatability. The proposed displacement sensing and control method is described in the next section.

Displacement Sensing

Typical linear piezoelectric actuator displacement sensor choices include non-contact capacitive and eddy current sensors, as well as strain gauges. Capacitive and eddy current sensors have well established high performance at the expense of cost, volume and complexity for multi-axis motion detection. Strain gauges on the other hand are relatively cheap, small and light weight but suffer from thermal sensitivity and creep effects. They are also bonded directly to the piezo ceramic rather than the output, so only provide an implicit measurement of the actual displacement of an actuator. Importantly, strain gauges are a standard option for the PPA actuators from Cedrat. They were selected for closed-loop control of the actuators in both concepts A and B using the same method as Porchez to enable the very high stability of the NLA actuators [101].

A strain gauge is a pattern of resistive material, the resistance of which is proportional to its length. When bonded onto the ceramic stack of the piezoelectric actuator, the length of the strain gauge increases or de-

creases as the stack expands or contracts in response to the driving voltage. The gauge factor GF relates the change in resistance ΔR of the strain gauge with unstrained resistance R_0 to the strain, $\epsilon = \Delta L/L_0$ via

$$GF = \frac{\Delta R/R_0}{\Delta L/L_0} \tag{7.7}$$

If a constant current is passed through the strain gauge, then the change in resistance can be detected by measuring the change in voltage across the gauge over time and in turn, calibrated and mapped to a change in length of the underlying structure. This information can be used in a closed loop control algorithm to correct for the displacement hysteresis commonly experienced in piezoelectric ceramics.

However, the length of both the stack and the strain gauge can also change due to thermal expansion. There is no way to know if the reported strain is caused by the piezoelectric effect or thermal expansion without also measuring the temperature of the stack. One of the main reasons for stacking two PPA actuators in series in the NLA assembly is to render the strain gauge sensing circuit insensitive to changes in the bulk temperature of the actuators & gauges. This is achieved by using a full Wheatstone bridge circuit.

Two high stability strain gauges are bonded onto the ceramic stacks in each of the actuators. Each pair of gauges form half of a full Wheatstone bridge, illustrated in Figure 7.7.

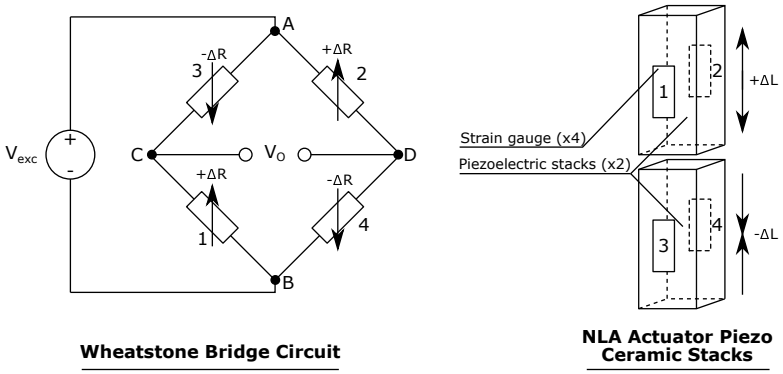

Figure 7.7: Full Wheatstone bridge circuit and Cedrat NLA.

The two PPA actuators in each of the NLA pairs operate in a push/ pull configuration. Thus as one stack increases in length by a small amount $+\Delta L$ the other decreases by an amount $-\Delta L$ leading to changes in the resistance ΔR in each of the gauges proportional to its gauge factor.

In practice, the strain ϵ of each strain gauge has two components: the mechanical strain ϵ_{mech} caused by the driven expansion of the ceramic stack and the thermal strain ϵ_{therm} from the thermal expansion or contraction of the strain gauge caused by a bulk temperature change from the calibrated temperature. Assuming no temperature gradient across across the actuators in each pair, the total strain measured by each strain gauge for a given push/ pull displacement of each stack is

$$\epsilon_{1,2} = +\epsilon_{mech} + \epsilon_{therm} \tag{7.8}$$
$$\epsilon_{3,4} = -\epsilon_{mech} + \epsilon_{therm} \tag{7.9}$$

The mechanical strains are equal but in opposite directions, whereas the thermal strains are all equal and in the same direction. Assuming that the unstrained resistances R_0 and gauge factors GF of each strain gauge are equal[1], the change in the resistance of each gauge ΔR_i is

$$\Delta R_{1,2} = R_0 GF\,(+\epsilon_{mech} + \epsilon_{therm}) \tag{7.10}$$
$$\Delta R_{3,4} = R_0 GF\,(-\epsilon_{mech} + \epsilon_{therm}) \tag{7.11}$$

such that the resulting resistance of each gauge is

[1] In reality, the gauge factors of each strain gauge differ slightly but so long as the factor is known it can be calibrated for without affecting the validity of this discussion.

$$R_{1,2} = R_0 + \Delta R_{1,2} \tag{7.12}$$
$$R_{3,4} = R_0 + \Delta R_{3,4} \tag{7.13}$$

The measured output voltage V_O is the difference between that at nodes C and D in Figure 7.7:

$$V_C = \frac{R_1}{R_1 + R_3} V_{exc} \tag{7.14}$$
$$= \frac{1 + GF(\epsilon_{mech} + \epsilon_{therm})}{2 + 2GF\epsilon_{therm}} \tag{7.15}$$

and similarly for the voltage at V_D:

$$V_D = \frac{R_4}{R_2 + R_4} V_{exc} \tag{7.16}$$
$$= \frac{1 + GF(-\epsilon_{mech} + \epsilon_{therm})}{2 + 2GF\epsilon_{therm}} \tag{7.17}$$

The measured output voltage V_O is then

$$V_O = V_C - V_D \tag{7.18}$$
$$= \frac{GF\epsilon_{mech}}{1 + GF\epsilon_{therm}} V_{exc} \tag{7.19}$$

An approximate estimate for the thermal strain can be found via

$$\epsilon_{therm} = \frac{\Delta L}{L_0} = \alpha \Delta T \tag{7.20}$$

Per Table 6.1, the maximum design bulk temperature deviation ΔT during operation is 1 K. The coefficient of thermal expansion α of the ceramic multilayer material that makes up the piezo stack is on the order of $10^{-6}/K$ [10]. Therefore the thermal strain is also on the order of $10^{-6} m/m$. Gauge factors are typically on the order of 10^0 [95], such that the $GF\epsilon_{therm}$ term of equation 7.18 is on the order of 10^{-6}.

Referring to equation 7.18, it can be seen that $1 >> 10^{-6}$ giving the final result

$$V_O = GF\epsilon_{mech} V_{exc} \tag{7.21}$$

Thus with two strain gauges in a half Wheatstone bridge configuration on each of the actuators in a push/ pull pair and provided there is negligible temperature gradient across those actuators, the output voltage is insensitive to bulk temperature changes.

This is the driving principle behind the use of two actuators in a push/ pull pair in the NLA assembly and why the NLA's have been included in one of the PMAO concepts. Push/ pull pairs have also been used in the design of the tip/ tilt Cryogenic Fine Steering Mirror (CFSM) for ESA's EChO mission [13] which forms the basis of concept B.

7.3.2. Launch Loads on the Actuators

This section estimates the maximum load that will be imposed upon each actuator during launch. The idealised geometry of the concept A architecture for sizing calculations is shown in Figure 7.8. An example load case with a single $30g$ launch load F_L applied in the $+X_{MF}$ direction is shown for illustration purposes. The three NLA actuators are positioned at locations I through III. The in-plane constraints, which react the transverse loads, are not shown for clarity. The compliant universal joints at either end of the actuators ensure that only loads acting along the axis of each actuator are transmitted to and from the actuator. The subscript MF indicates a vector in the coordinate frame O_{MF} fixed to the centre of the moving frame.

The load requirements in Table 6.1 stated that the mechanism must survive combined $30g$ loads in two orthogonal directions, giving 12 possible load cases. The total compressive or tensile load experienced by each actuator during launch can be found by summing the contributions from each of the two individual

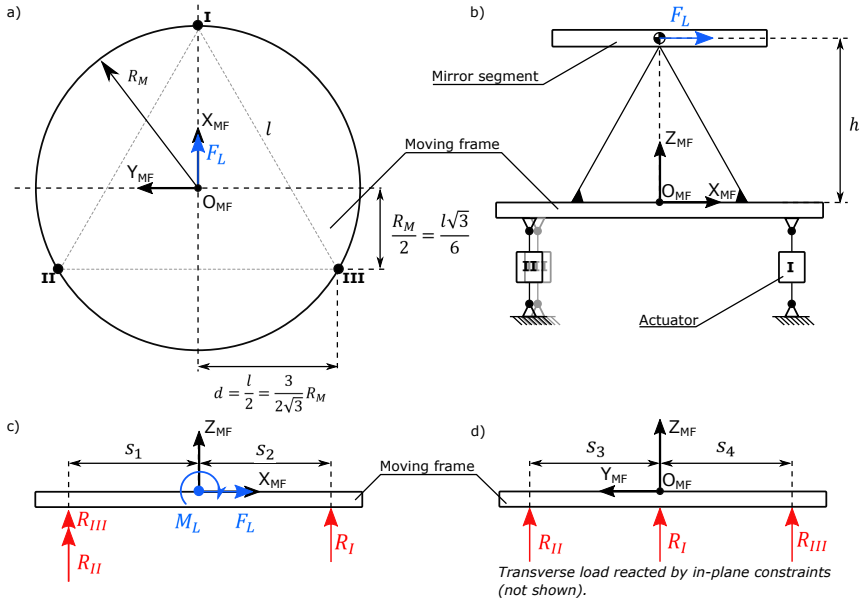

Figure 7.8: Geometry of the idealised mechanism in concept A with an example launch load of $F_L = 30g \times m_{mirror}$ applied in the $+X_{MF}$ direction during launch. a) Geometry of actuator layout in plan view. Actuators are positioned at the vertices of an equilateral triangle of side length l, circumscribed by a circle with radius R_M. b) Geometry of actuator layout in profile. c), d) Equivalent free body diagrams in different planes of the moving frame with moment $M_L = F_L \times h$ imposed by launch load F_L. The moment is reacted by the actuators.

external loads per load case. Recall from Chapter 4 *Verification Plan* that the $30g$ launch loads were assumed to already include a safety factor. Throughout all discussions of launch loads in this document, "in-plane" loads refer to those in the XY plane. An out of plane load refers to a load in the Z direction.

The maximum axial load that can be withstood by a PPA actuator without damage is roughly one third of the rated blocked force[2].

The launch loads F_L were applied at the centre of mass of the mirror segment. It was assumed that the mass of the mirror segment was much greater than that of the bipods, moving frame, universal joints and actuators such that their contribution to the launch loads experienced by the actuators could be neglected for these sizing calculations. It was also assumed that the actuators and mirror are assembled with perfect symmetry such that any actuator sitting on the axis of an imposed moment M_L on the moving frame contributes a negligible reaction force. An example is actuator I in Figure 7.8, which would not react a launch load in the Y_M direction.

The launch load calculations are included in Appendix G *Actuator Strength and Stroke Requirement Calculations*. The largest loads experienced by the actuators due to combined in-plane launch loads were

$$F_{max,in-plane} = \pm\left(\frac{1+\sqrt{3}}{3}\frac{M_L}{R_M}\right) \tag{7.22}$$

Where a positive load indicates compression in the actuator. These loads occur in actuator II for the $-X_{MF}, +Y_{MF}$ and $+X_{MF}, -Y_{MF}$ load cases and in actuator III in the $-X_{MF}, -Y_{MF}$ and $+X_{MF}, +Y_{MF}$ load cases. The largest loads experienced by an actuator in the eight load cases that included an out of plane load was

$$F_{max,out-plane} = \pm\left(\frac{1}{3}F_L + \frac{2}{3}\frac{M_L}{R_M}\right) \tag{7.23}$$

Where loads $F_L = 30g m_M$ are from m_M the estimated mass of a single M1 mirror segment, the corresponding moment $M_L = F_L h$. Tension in the actuator is indicated by a negative sign.

For a given mirror mass, the launch loads on the actuators depend on the ratio h/R_M. For the actuator loads, it is beneficial to have the radius R_M as large as possible and the height h between the centre of mass of the mirror and the moving frame as small as possible. This intuitively makes sense because the height increases the mechanical advantage of the launch load, and radius R_M increases the mechanical advantage

[2]See `http://cedrat-technologies.com/fileadmin/user_upload/CTEC/Mechatronic_products/User_s_manual/Inst_Man_Actuator_v6.1.pdf` [Accessed: 16 June 2018].

of the reacting load imposed by the actuators. However, R_M also drives the size of the moving frame and thereby the whole mechanism. It should be as small as is practical to keep mass down.

Equating equations 7.22 and 7.23 shows that the critical load case transitions when $h/R_M = 1.366$, with the greatest load case on an actuator given by

$$For \frac{h}{R_M} < 1.366, |F_{max,in-plane}| < |F_{max,out-plane}| \tag{7.24}$$

$$For \frac{h}{R_M} > 1.366, |F_{max,in-plane}| > |F_{max,out-plane}| \tag{7.25}$$

Inspection of the original baseline design suggested that the ratio h/R_M would likely be in the range $0.77 \leq h/R_M \leq 1.50$ for most design scenarios and therefore the out of plane launch loads would dominate. To provide future design margin, the largest value for h was taken at roughly 150 mm and an initial estimate of $R_M = 125$ mm was assumed, giving $h/R_M = 1.2$. A more explicit argument supporting these assumptions is given in Appendix G.

Taking this ratio, and assuming a mirror mass of 6 kg per the original baseline design, equation 7.23 gives a maximum load of ≈2,000 N to be withstood by a NLA actuator during launch.

7.3.3. Inverse Position Kinematics

This section derives the inverse position kinematics for concept A. The segment level kinematic requirements and mechanism geometry determine the flow down actuator stroke and step size requirements. The segment range of motion depends on both the deployment/ coarse alignment tolerance budget and the M1 deployment calibration procedure, which was analysed in Section 3.2.5. Ranges of ± 4 μm $\theta_{x,M}$, ± 2 μrad $\theta_{y,M}$ and ± 4 μrad $\Delta_{z,M}$ were derived at the segment level.

Figure 7.9 illustrates a simple model of the concept A system. Note that the passive support constraints do not contribute to the kinematic derivation so are omitted for clarity. Recall from Section 6.3 *Passive Constraint Space Synthesis* that they were selected precisely because they do not constrain the three DOFs controlled by the actuators.

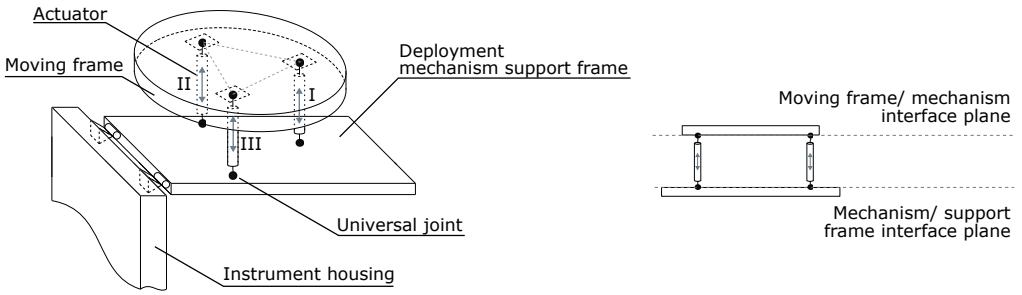

Figure 7.9: Schematic of the 3DOF mechanism for concept A. Changing the length of the actuators adjusts the pose of the moving frame and thus the mirror segment with respect to the base in $\theta_{x,M}$, $\theta_{y,M}$ and $\Delta_{z,M}$ degrees of freedom.

The interface planes are depicted in Figure 7.9. The mechanism base is assumed fixed. The mechanism/ base interface plane is assumed parallel to the moving frame/ mechanism interface plane in the initial position and coplanar with the upper surface of the M1 deployment mechanism support frame. The moving frame/ mechanism interface plane is taken to be the plane of ideal pivot points of the upper universal joints.

For simplicity, the derivation uses a rigid body model which assumes all bodies are rigid and that the universal joints can be modelled as perfect 3DOF ball joints. In reality the pivot point of the flexures in the universal joint will shift giving rise to small *parasitic* translations as well as rotations. These are ignored for the purposes of the flow down requirements but are included in the finite element verification modelling.

Coordinate Frames

Figure 7.10 sets out the geometry and coordinate frames used in the mechanism kinematics. The fixed mechanism coordinate frame $\{\mathbf{O_M}, X_M, Y_M, Z_M\}$ is centred on the projection of the mirror segment centroid onto the mechanism/ support frame interface plane in plan view with axes directions shown in the figure. The body fixed moving frame coordinate frame $\{\mathbf{O_{MF}}, X_{MF}, Y_{MF}, Z_{MF}\}$ is centred on the projection of the segment centroid onto the moving frame/ mechanism interface plane with axes directions as shown in Figure 7.10. The axes of both frames are aligned in the nominal deployed configuration.

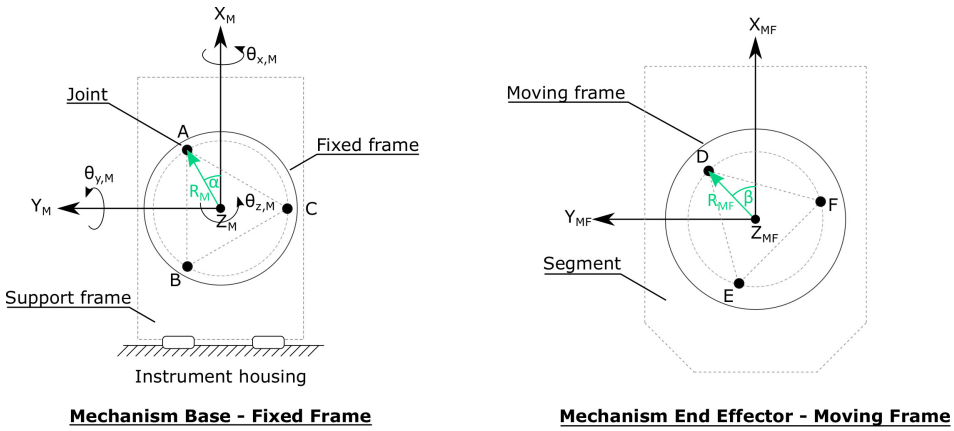

Figure 7.10: Coordinate frame definition for the 3DOF mechanism for concept A. The joints are positioned at the vertices of an equilateral triangle centred on the projection of the centroid of the M1 segment to the fixed and moving frame interface planes. The orientation of the triangles are given by α and β on the fixed and moving frames respectively. Joint attachments are on circles of radius R_M and R_{MF} respectively. Segment and deployment support frame outline shown to illustrate orientation of the coordinate frames.

Linearised Inverse Position Kinematic Equations

The inverse position kinematic equations describe the relationship between the actuator lengths L_i and the pose **P** of the moving frame, and thus mirror segment. The analytical solutions were simplified by linearising using the small angle approximation. This made the interaction between the mechanism geometry and segment pose far more transparent.

Actuator I links joints A, D, actuator II links joints B, E and actuator III links joints C, F. Frame $\mathbf{O_{MF}}$ has pose $\mathbf{P} = \{\Delta_{z,M}, \theta_{x,M}, \theta_{y,M}\}^T$ with respect to mechanism frame $\mathbf{O_M}$ for translation $\Delta_{z,M}$ in the Z_M direction and rotations $\{\theta_{x,M}, \theta_{y,M}\}$ about the $\{X_M, Y_M\}$ axes respectively.

The full derivation of the inverse kinematic equations is provided in Appendix G. The result is the set of linearised equations 7.26 to 7.28 describing the small changes in the length of each actuator ΔL_i necessary to achieve small changes in pose:

$$\Delta L_I = -R_M \theta_{y,M} + \Delta_{z,M} \tag{7.26}$$

$$\Delta L_{II} = \frac{R_M}{2}\left(\sqrt{3}\theta_{x,M} + \theta_{y,M}\right) + \Delta_{z,M} \tag{7.27}$$

$$\Delta L_{III} = -\frac{R_M}{2}\left(\sqrt{3}\theta_{x,M} - \theta_{y,M}\right) + \Delta_{z,M} \tag{7.28}$$

Note that it was assumed that the orientation angles $\alpha = \beta = 0°$. The position and orientation of the mirror segment with respect to the moving frame can be found with a coordinate transform, assuming that the mirror is rigidly connected to the moving frame.

7.3.4. Actuator Kinematic Requirements Flow Down

This section documents the flow down of the segment level kinematic requirements the individual actuators. Both the stroke and step size were investigated.

Actuator Stroke Requirement

For the very small motions used in the PMAO mechanism, the linearised equations show that, in the ideal scenario, there is no coupling between mechanism DOFs in the calculation of each actuator output. Thus, for any given actuator, the stroke required to achieve a commanded displacement in one of the DOFs is linearly independent of the stroke required to achieve commanded displacement in the other DOFs. The largest required actuator stroke will then occur when the moving frame is at the maximum range of each of the three degrees of freedom. Subsection 3.2.5 *Primary Mirror Calibration Procedure* found that the worst-case combination of required ranges was in the piston scan stage of the calibration procedure.

The piston displacement has no dependence on the actuator mounting radius R_M, however both tip and tilt do. As R_M increases, so does the required actuator stroke for a given tip or tilt rotation. The mounting

angle only effects the distribution of actuator output for a given tip or tilt command. The worst-case actuator stroke will be for the largest possible R_M given the usable volume of the mechanism.

Since the mechanism cannot protrude beyond the periphery of the segment, and with reference to the geometry set out in Figure 7.8, $R_M = l\sqrt{3}/3$. For length l set to 450 mm for the shortest side of the segment, the largest possible mounting radius is 259.8 mm. Allowing for a 10 mm buffer radius around each of the mounting points to fit the width of the actuator and mounting to the base gives a maximum useful mounting radius R_M of 239.8 mm.

Substituting these values into equations 7.26 to 7.28 for each of the eight maximal poses gives the results summarised in Table 7.1. The largest required actuator output is ±4.959 μm, found for the actuator at position B in Figure 7.8.

Table 7.1: Worst-case required actuator displacements ΔL_i for calibration piston scan, calculated via linearised inverse kinematic equations for concept A. $R_M = 239.8mm$, $\alpha = 0°$. Maximum actuator displacements are underlined.

$\boldsymbol{\theta_{x,M}}$ [μrad]	$\boldsymbol{\theta_{y,M}}$ [μrad]	$\boldsymbol{\Delta_{z,M}}$ [μm]	$\boldsymbol{\Delta L_I}$ [μm]	$\boldsymbol{\Delta L_{II}}$ [μm]	$\boldsymbol{\Delta L_{III}}$ [μm]
-4.000	-2.000	-4.000	-3.520	<u>-4.959</u>	-4.480
-4.000	-2.000	4.000	4.480	3.041	3.520
-4.000	2.000	4.000	3.520	3.041	4.480
-4.000	2.000	-4.000	-4.480	<u>-4.959</u>	-3.520
4.000	2.000	4.000	3.520	4.959	4.480
4.000	2.000	-4.000	-4.480	3.041	-3.520
4.000	-2.000	4.000	4.480	<u>4.959</u>	3.520
4.000	-2.000	-4.000	-3.520	-3.041	-4.480

Thus the three NLA actuator assemblies must deliver a stroke of no less than 9.918 μm to meet the kinematic performance requirements for concept A. Since the stroke of the two PPA actuators are added to the total output of each NLA assembly, each PPA need only supply 4.959 μm stroke each.

Actuator Step Size Requirement

The Cedrat PPA XL family of actuators are all capable of sub-nanometre level resolution with closed-loop displacement control per their datasheets. The linearised equations show that the piston displacement maps directly to the actuator stroke, so no further analysis is required to verify that these actuators can meet the 10 nm piston step requirement,

7.3.5. Summary of Concept A

In conclusion, the main driver behind concept A is the very good thermal stability, lack of overconstraint in the actuation constraint set and smaller mechanical advantage of the launch loads. The required actuator stroke was also usefully small. It does however require six actuators & supporting electronics so is more expensive.

7.4. Concept B: 4x PPA Actuators

Concept B is illustrated in Figure 7.11 with four PPA actuators in parallel. Concept B is modelled on the Cryogenic Fine Steering Mechanism (CFSM) developed for ESA's EChO space mission [13], which was a candidate for the Cosmic Vision Programme with a launch in 2024. In concept B, the push/ pull actuator pairs from the NLA concept were retained, however where the pairs were stacked in series in concept A, they are mounted in parallel in concept B. The immediate advantage of concept B was that it does not depend on the custom NLA assemblies, and it uses two less actuators than concept A. The downside is that it adds the requirement for a small thermal gradient in each actuator pair.

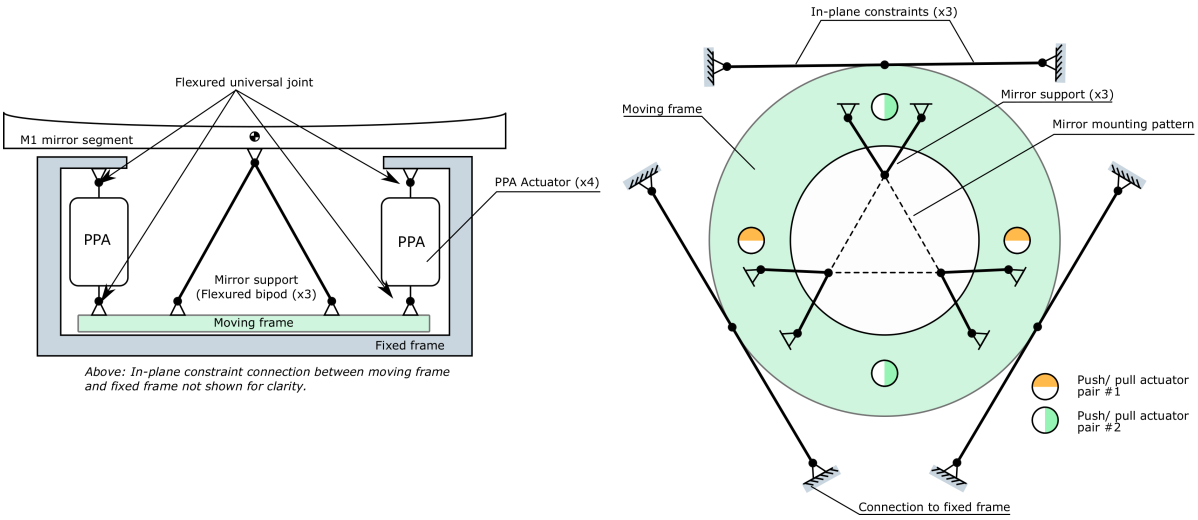

Figure 7.11: Concept B mechanism architecture with four PPA actuators. Left: Profile view of the concept with in-plane constraints not shown for clarity. Right: Top view of the moving frame assembly showing in-plane constraints.

Each of the basic building blocks of the concept are described in more detail in Subsection 7.4.1. The launch loads on the actuators are estimated in Subsection 7.4.2. The linearised inverse kinematic equations are derived in Subsection 7.4.3 and are then used to find the flow down actuator stroke requirements in Subsection 7.4.4. The section concludes with a summary of the concept in Subsection 7.4.5.

7.4.1. Description of Mechanism Elements

The design principles behind the fixed frame, in-plane constraints and mirror support are the same as those in concept A and require no further discussion here. Descriptions of the moving frame, actuators and displacement sensing are given below.

Moving Frame

The moving frame is attached to the bottom of the actuators in a "re-entrant" design to save space. It can also be designed to provide some degree of passive athermalisation. Thermo-elastic growth of the mirror support & fixed frame can be compensated by that of the actuators and universal joints. The functionality of the moving frame is otherwise the same as that as in concept A.

Actuators

The actuation concept is illustrated in Figure 7.12. Each pair of actuators drives one of the rotations. All of the actuators expand or contract together to provide the piston motion. The tops of the actuators are attached to the fixed frame.

The actuator constraint space identified in Section 6.3 specified a need for three actuated constraints. Since there are four parallel actuators in concept B, it is an overconstrained system. The moving frame must be stiff enough that internal stresses from small displacement errors between the actuators in each pair aren't passed on to the mirror.

Avoiding the NLAs foregoes the mass penalties of concept A whilst retaining the thermal stability offered by two push/ pull pairs. Three actuators could be used in the future if ongoing thermal modelling shows that the in orbit drift budget can be met without a full Wheatstone bridge sensing circuit. Complexity is instead

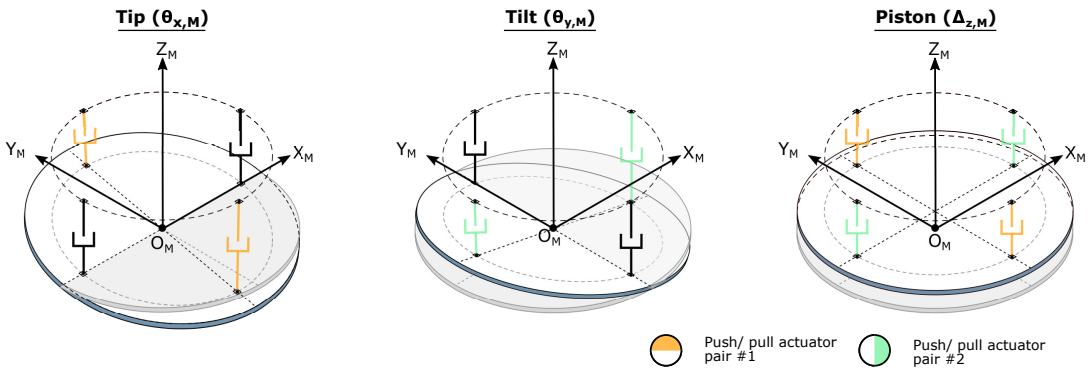

Figure 7.12: Push/ pull concept with four actuators for Concept B. Each opposing pair drives one of the rotations. All actuators expand or contract together to provide the piston motion.

passed on to the mechanical design and AIT activities since the overconstraint must be carefully controlled to avoid build up of internal stresses between the fixed and moving frames.

Displacement Sensing

Again, two strain gauges on each actuator in each pair form a full Wheatstone bridge to null the effect of thermal drift on the actuator displacement sensing. Note that this configuration still relies on a negligible temperature gradient across the two piezo stacks in each push/ pull pair. Maintaining a "negligible" temperature gradient between two actuators at opposite sides of the mechanism may be more onerous for the thermal control system than maintaining the same condition across two actuators next to each other as in concept A.

7.4.2. Launch Loads on the Actuators

The launch loads were calculated using a similar method and the same assumptions as documented for Concept A. The idealised geometry is shown in Figure 7.13 for an example load case with a single 30g launch load applied in the $+X_{MF}$ direction. Again, the in-plane constraints are not shown for clarity. The actuators are mated to the fixed and moving frames with flexural universal joints such that they see only axial loads.

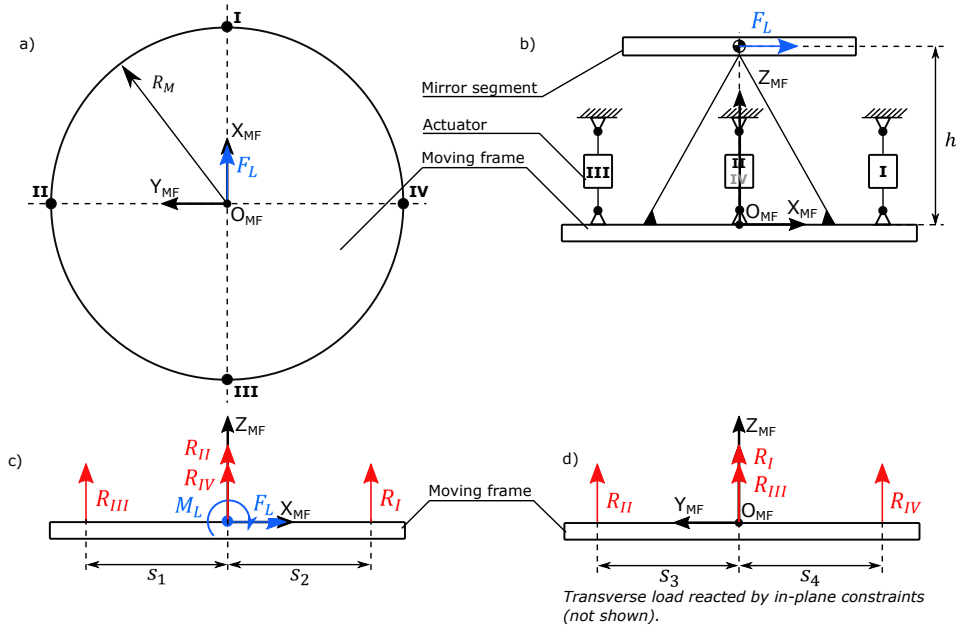

Figure 7.13: Geometry of the idealised mechanism with an example launch load of $F_L = 30g \times m_{mirror}$ applied in the $+X_{MF}$ direction during launch. a) Geometry of actuator layout in plan view. Actuators are positioned at the vertices of an equilateral triangle of side length l, circumscribed by a circle with radius R_M. b) Geometry of actuator layout in profile. c) Equivalent free body diagrams in different planes of the moving frame with moment $M_L = F_L \times h$ imposed by launch load F_L. The moment is reacted by the actuators.

The full derivation of the loads is included in Appendix G. It was found that the critical load case occurs when an out of plane load is applied simultaneously with an in plane load per

$$F_{max,out-plane} = \pm\left(\frac{F_L}{4} + \frac{1}{2}\frac{M_L}{R_M}\right) \tag{7.29}$$

Once again assuming a mirror mass of 6 kg, mounting radius R_M of 125 mm and thus $h/R_M = 1.2$, equation 7.29 gives a launch load of 1,501 N, 500 N less than in concept A.

7.4.3. Inverse Position Kinematics

This section derives the inverse position kinematics for concept B. The mechanism planes used to define the kinematic equations are sketched in Figure 7.14. The actuators are mated to the inside of the fixed frame while the moving frame is suspended from their other ends. The entire assembly is fixed to the deployment mechanism support frame, which acts as the base.

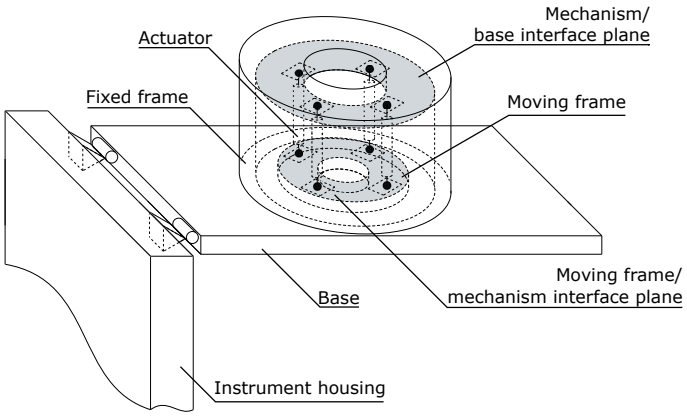

Figure 7.14: Schematic of the 3DOF mechanism for concept B. The fully encapsulating fixed frame is indicative only. In plane constraints between moving and fixed frames not shown for clarity.

The derivation process was much the same as that of concept A with the exception that an extra actuator was included. Again, the full process is documented in Appendix G. Assuming mechanism orientation angles $\alpha = \beta = 0°$, the resulting linearised inverse kinematic relations are given by equations 7.30 to 7.33:

$$\Delta L_I = -R_M\theta_{y,M} + \Delta_{z,M} \tag{7.30}$$
$$\Delta L_{II} = R_M\theta_{x,M} + \Delta_{z,M} \tag{7.31}$$
$$\Delta L_{III} = R_M\theta_{y,M} + \Delta_{z,M} \tag{7.32}$$
$$\Delta L_{IV} = -R_M\theta_{x,M} + \Delta_{z,M} \tag{7.33}$$

7.4.4. Actuator Kinematic Requirements Flow Down

This section documents the flow down of the segment level kinematic requirements the individual actuators. Both the stroke and step size were investigated.

Actuator Stroke Requirement

Following the same arguments as in Section 7.3.4, the greatest range of motion will occur at the worst-case combination tilt, tip and piston displacements. Similarly, the mounting radius R_M was once again set to 239.8 mm. Substituting these values into equations 7.30 to 7.33 gave the predicted stroke requirements over the entire segment workspace, summarised in Table 7.2.

The largest range of motion was needed by those actuators providing the $\theta_{x,M}$ motion since the segment level range in that DOF was $\pm 4\ \mu rad$, compared to the $\pm 2\ \mu rad$ requirement for $\theta_{y,M}$ motion. The PPA actuators must be able to deliver a stroke of no less than 9.918 μm to meet the kinematic performance requirements for concept B. This was twice the stroke required for concept A. Since the length of this style of piezoelectric actuator is roughly linearly proportional to its stroke, concept B requires a PPA actuator that is approximately twice the length of the PPA actuator required in concept A. However, since the two shorter PPA actuators are

Table 7.2: Worst-case required actuator range of motion for calibration piston scan calculated with the linearised inverse kinematic equations for concept B. $R_M = 239.8mm$, $\alpha = 0°$. Maximum actuator displacements are underlined.

$\theta_{x,M}$ $[\mu rad]$	$\theta_{y,M}$ $[\mu rad]$	$\Delta_{z,M}$ $[\mu m]$	ΔL_I $[\mu m]$	ΔL_{II} $[\mu m]$	ΔL_{III} $[\mu m]$	ΔL_{IV} $[\mu m]$
-4.000	-2.000	-4.000	-3.520	-4.959	-4.480	-3.041
-4.000	-2.000	4.000	4.480	3.041	3.520	4.959
-4.000	2.000	4.000	3.520	3.041	4.480	4.959
-4.000	2.000	-4.000	-4.480	-4.959	-3.520	-3.041
4.000	2.000	4.000	3.520	4.959	4.480	3.041
4.000	2.000	-4.000	-4.480	-3.041	-3.520	-4.959
4.000	-2.000	4.000	4.480	4.959	3.520	3.041
4.000	-2.000	-4.000	-3.520	-3.041	-4.480	-4.959

stacked on top of each other in concept A, the total height of the NLA is roughly the same as that of the single PPA actuator needed for concept B. There is no significant difference between the heights of the two actuator concepts.

Actuator Step Size Requirement

The only step size requirement is in piston, with a maximum allowable step size of 10 nm. As for concept A, the segment piston motion maps directly to the actuator step size per equations 7.30 to 7.33 for a pure piston motion. Therefore the actuators need only supply a 10 nm step. Since the Cedrat PPA XL is capable of sub-nanometre resolution, this requirement is met.

7.4.5. Summary of Concept B

In conclusion, concept B reduced the load on each actuator by 500 N through addition of a fourth actuator. This overconstrained the system, complicating assembly, though a well designed moving frame would isolate the mirror from untoward stresses. The stroke requirement per actuator was double that of concept A but this doesn't translate to a larger actuator stack since two actuators are required in series in the NLA concept. Perhaps the greatest advantage was that the mechanism could be tested with analogous actuators, whereas the NLA sub-assemblies are proprietary Cedrat technology.

7.5. Actuator Model Selection

With the flow down requirements for the actuators in both concepts specified, a specific model could be selected to complete the synthesis of both architectures.

The smallest COTS Cedrat PPA XL actuator, the PPA40XL, has a maximum blocked force capability of 6,653 N [28]. Assuming that the maximum external load that can be applied to the actuator is roughly one third of this at 2,218 N gives a design margin of roughly 11% for concept A and 48% for concept B during launch using the 30g launch loads, assumed inclusive of safety factor. The load calculations did not consider the weight of the mirror support, moving frame, flexures or self-weight of the actuators so the extra margin provides a useful design buffer.

The PPA L family of actuators, the next size down in standard models available from Cedrat, have a blocked force capability of approximately 985 N. This is less than the imposed launch loads of ≈ 2 kN and 1.5 kN respectively. Therefore the PPA XL family was needed for both concept A and B.

The PPA40XL offers a 42.90 μm stroke in a 60 mm high package. After discussion with Cedrat, it was found that a PPA10XL with 10 μm stroke in a 20 mm high package could be easily manufactured using identical technology and processes used for the PPA40XL [31]. Cedrat also confirmed that the specifications for such an actuator could be approximated by those of the PPA40XL for preliminary design purposes. Although this is not a pure COTS component, the PPA10XL meets the stroke and load requirements of both concepts A and B in a package a third the size of the PPA40XL with no significant extra development requirements. All actuators in the PPA XL family are capable of providing sub-nanometre steps with closed-loop control via strain gauges.

The PPA10XL was ultimately selected for the following reasons:

- **Standardisation**
  The PPA10XL is a custom part, though it is derived from an existing COTS part, the PPA40XL. The

PPA10XL is a shortened variant as the DST 3DOF mechanism does not require the full stroke of the PPA40XL and the reduction in height makes it easier to fit into the usable volume.

- **Design Flexibility**
  The PPA10XL has been selected based on conservative QSL launch loads of $30g$. Cedrat supplies PPA actuators in less robust (and thus lighter) form factors that provide the same stroke and resolution. The PPA10XL could be interchanged for larger or smaller models if required in future design iterations.
- **Heritage**
  The PPA family of actuators with strain gauge sensing have flown on the PICARD/ SODISM telescope [86], ESA ROSETTA/ MIDAS scan mechanism of the SPICE spectrometer [60]. While the PPA10XL is a new model, the technology (the piezo ceramic stack, strain gauge sensing and design and AIT qualification processes) has well established space heritage.
- **Kinematic performance**
  The PPA10XL has approximately 10 μm stroke and resolution better than 1 nm, although reproducibility must be tested [29, 31].
- **Thermal performance**
  The actuators dissipate very little heat when holding a static position, typically tens of milliWatts and conservatively no more than 0.2 W each [31]. The PICARD/ SODISM mechanism consumed 2 W maximum during active operation [86] to drive three PPA40M actuators.
- **Dynamic performance**
  The PPA actuators have very high stiffness and can be used in the mechanism to hold the mirror during launch without the need for a separate hold down and release mechanism and still be able to meet the 100 Hz minimum natural frequency requirement [31]. This simplifies the overall design of the M1 subsystem and improves reliability by using fewer separate mechanisms.

7.6. Architecture Trade-off

This section details the trade-off to select the final concept to start preliminary design. The graphical trade-off method was used for the same reasons given in the prior trade-offs. The trade-off criteria are introduced in Subsection 7.6.1, followed by the trade-off results and justification in Subsection 7.6.2.

7.6.1. Trade-off Criteria

As with the prior trade-offs, the stakeholder requirements identified in Table 6.2 were used to define the trade-off criteria and weights, given in Table 7.3. All criteria were equally weighted.

Table 7.3: Overall concept trade-off criteria.

Criteria	Weight	Considerations
Mass	1/5	Flow down of MIS-REQ-08. Mass of mechanism parts as well as impact mechanism has on mass of other parts.
Stowed volume	1/5	Flow down of MIS-REQ-09. Space occupied by parts. Considers interface requirements: size, number and accommodations that must be made in other parts.
Performance	1/5	Flow down of MIS-REQ-07. Static performance: loads imparted on sensitive components (actuators), kinematic performance (range, resolution etc), thermal stability.
Cost	1/5	Flow down of MIS-OBJ-02. Also indicated by complexity. Design flexibility: how easily can it accommodate changes in design of interfacing parts. Number of parts. Constructibility of parts. Difficulty of assembly, integration and testing.
Programmatics & Risk	1/5	Flow down of MIS-OBJ-02. Low risk components require less resources for testing & qualification. Can the concept be broken down into smaller but relevant elements for further design & testing using resources available to MSc students?
Sum	1	

Again, complexity was used as a cost indicator. Programmatics & risk were included as there was a strong desire within the team to begin testing of prototypical hardware to demonstrate the feasibility of the DST mechanisms. To aid this, a 3DOF mechanism with high TRL and short lead time parts would be highly desirable. The scoring system defined in Table 6.4 was used once again.

7.6.2. Trade-off Justification

Concept B was scored at or above the same level as concept A in all trade-off criteria. Since all criteria also have the same weighting, concept B was selected for further design work. The trade-off results are given in Figure 7.15. Justification for each of the scores are set out below.

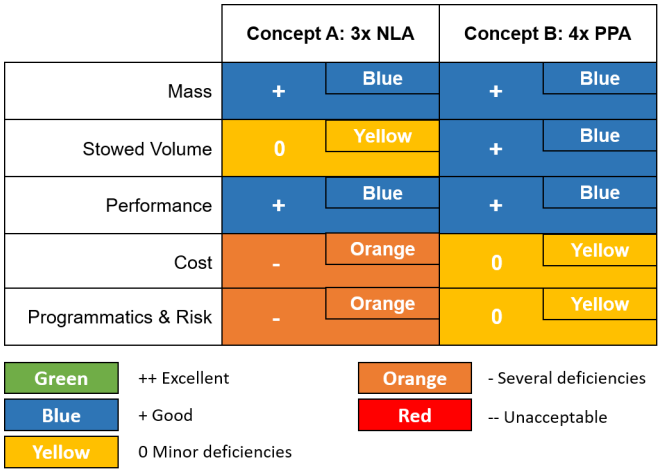

Figure 7.15: Graphical trade-off for final 3DOF mechanism concept selection. Row heights indicate relative weighting of trade-off criteria.

Mass

Scores for both concepts were based on the ≈6 kg mechanism mass requirement. The fixed and moving frames were expected to dominate the mechanism mass budget for both concepts and were expected to have similar forms and masses. The total mass of the actuators in either concept did not make a large contribution to the mass budget. A single Cedrat PPA40XL weighs 254 g and is 60 mm high. Assuming a 20 mm high PPA10XL is roughly one third the mass of a PPAXL gives a total actuator mass of 85 g. For concept A with six actuators this gave roughly 500 g for total actuator mass alone or about 8% of the total mass budget. The mass contribution from the concept B actuators was even less. The remaining elements are very similar across both concepts so there was no strong discriminator. Both received a score of good (+).

Stowed Volume

The usable volume in the stowed configuration is trapezoidal, shown in Figure 7.3. As the occupied height increases, the available length and width of the mechanism decreases. The load calculations showed that it is preferable to have a low, wide mechanism to reduce the launch loads on the actuators.

It was mentioned in Subsection 7.4.4 that the total height of the actuator stacks in both concepts was expected to be similar. With its re-entrant design, concept B gives more design flexibility as the height of the components do not stack whereas concept A could become congested quite quickly. There is no reason to differentiate the volume needed by either concept in the length & width dimensions at this stage.

Concept A has minor deficiencies (**0**) due to the stacking of components whilst concept B is considered to have good (+) performance since it is easier to fit all elements within the limited height.

Performance

Performance was assessed based on the actuator launch loads and stroke requirements. The PPA10XL was selected for both concepts and can handle axial loads up to 2.2kN. Concept A required that the actuators withstand loads of up to 2,000 N during launch and that each actuator be able to provide slightly less than 5 μm stroke. Concept B generated loads up to 1,500 N on the actuators and a stroke requirement of a little less than 10 μm. The larger margin of safety in Concept B was attractive since the sizing calculations only took the mass of the mirror into account though both concepts were workable. The additional stroke capability in concept A was not necessarily an advantage as the calibration algorithm uses the telescope itself to measure phasing errors. This technique is unable to detect - and thus control - displacements beyond the deployment tolerance budget.

The NLA actuator assemblies used in concept A have been shown to exhibit excellent thermal stability whereas there is no testing data for the thermal stability of the configuration in concept B. However, the

push/ pull configuration in concept B operates on the same principle as concept A, so good thermal stability should also be possible.

There were no stand-out differences between the anticipated performance of the two concepts upon which to separate them. Both concepts scored with good (**+**) performance.

Cost

An immediate discrepancy between the two concepts was the cost of the actuators. The supplier was unwilling to provide a hard cost estimate though they did confirm that if optimising for cost, that concept B would be best [31].

From an instrument systems perspective, both concepts require a very small temperature gradient to be maintained across the actuator pairs. This will likely require active thermal control, to be defined in future MSc theses. The complexity of implementing such a system for concept B is greater than that for concept A because of the larger distance over which the gradient must be maintained.

Most of the components in both concepts rely upon precision CNC and wire EDM machining, as well as precision assembly techniques - particularly for the overconstrained elements. Both concepts are expected to have similar manufacturing costs and complications.

Cost is most relevant in the short term for breadboarding which will be largely limited to equipment already available at TU Delft. The working principle of concept B could be demonstrated by testing with an analogous, non-space rated (and thus cheaper) piezoelectric actuators. Testing and demonstration of concept A necessarily requires the NLA assemblies from Cedrat which are custom products and are invariably more expensive.

Concept B has minor deficiencies (**0**) with respect to cost as, over the short to mid term, breadboarding could be possible, but difficult with the available resources. Concept A has several deficiencies (**-**) as testing would require a dedicated effort or extended support from the supplier.

Programmatics & Risk

There is a strong desire in the team to begin testing the design concepts to demonstrate their feasibility. The necessary test infrastructure, including a vibration isolation tables, interferometers and climate control, are nominally available at Airbus Defence & Space NL who are supporting the project. The mechanism hardware however, must be supplied by the project.

As alluded to in the previous discussion of cost, concept B, or elements thereof, could forseeably be tested with an analogous actuator whereas the NLA assemblies in concept A cannot. Structural & engineering models of the fixed and moving frames, in-plane constraints, and mirror supports can be fabricated at one of several TU Delft workshops which have prior experience manufacturing precision mechanisms for other research purposes. Therefore in terms of short to medium term DST programme objectives concept B has, qualitatively, lower schedule and resource risk. Unless the supplier is willing to donate or loan the NLA actuators, selection of concept A would likely require significant diversion of resources from other DST activities to test.

In terms of technical risk, flight models of the PPA actuators have demonstrated adequate operation in space and thus have high TRL whereas the NLA has only undergone thermal vacuum testing on Earth. All components in both concepts are ITAR free so do not present a regulatory risk.

Concept A had several deficiencies (**-**) with respect to programmatics & risk. Concept B on the other hand only had minor deficiencies (**0**) as the DST programme could still be progressed with this concept, albeit with an analogous actuator.

7.7. Concept Synthesis Summary

A methodical concept generation and synthesis process led to definition and selection of a mechanism that represents a considerable evolution from the original baseline design.

A hybrid arrangement was chosen to isolate the mirror and support from the actuation loads. Four Cedrat PPA10XL linear piezoelectric actuators were selected to operate in two push/ pull pairs to provide subnanometre level resolution motion. Displacement of the actuators is monitored with strain gauges bonded directly onto the piezo ceramic stacks in a circuit configuration that renders the assembly immune to bulk temperature changes. However, this requires very small thermal gradients across the actuator pair, which represents the greatest technical risk in the mechanism. Ongoing and future thermal modelling will determine if this is viable.

The actuators do not need a transmission and an HDRM is not required to support the mirror through launch, simplifying its design. All parts are ITAR free.

Major assumptions made throughout the concept synthesis work detailed in both Chapters 6 and 7 are listed in Table 7.4. The next chapter details the preliminary mechanical design and development of the mechanism finite element model.

Table 7.4: Major assumptions for concept generation work.

ID	Description
ASM-CON-01	The M1 segments were assumed to be rigid bodies. Future work will need to verify effects of gravity off-load on mirror surface figure with the flexured bipod support.
ASM-CON-02	A metrology mount will be available for terrestrial AIT unless the mirror segments are design to be sufficiently stiff so that gravity sag is not a problem. The flight mirror support was not designed to maintain the surface figure tolerances in Earth gravity.
ASM-CON-03	The M1 deployment tolerance budgets, which were defined in the segment coordinate frame, were assumed to apply in the mechanism coordinate frame without transformation or loss of accuracy.
ASM-CON-04	The 8° rotation of the mirror backplane in the original baseline design was ignored. It was assumed that the backplane can once again be made parallel to the deployment mechanism support frame plane.
ASM-CON-05	A high voltage power bus will be available since the deformable mirror will also be driven by piezoelectric actuators.

8

Mechanical Design

The objective of the bottom up mechanical design was to develop a preliminary design that could be verified by modelling against the system requirements, and thereon used to assess the feasibility of implementing a fine pointing mechanism for the DST. This chapter steps through the design process for the architecture selected in Chapter 7 *Mechanism Architecture Selection*.

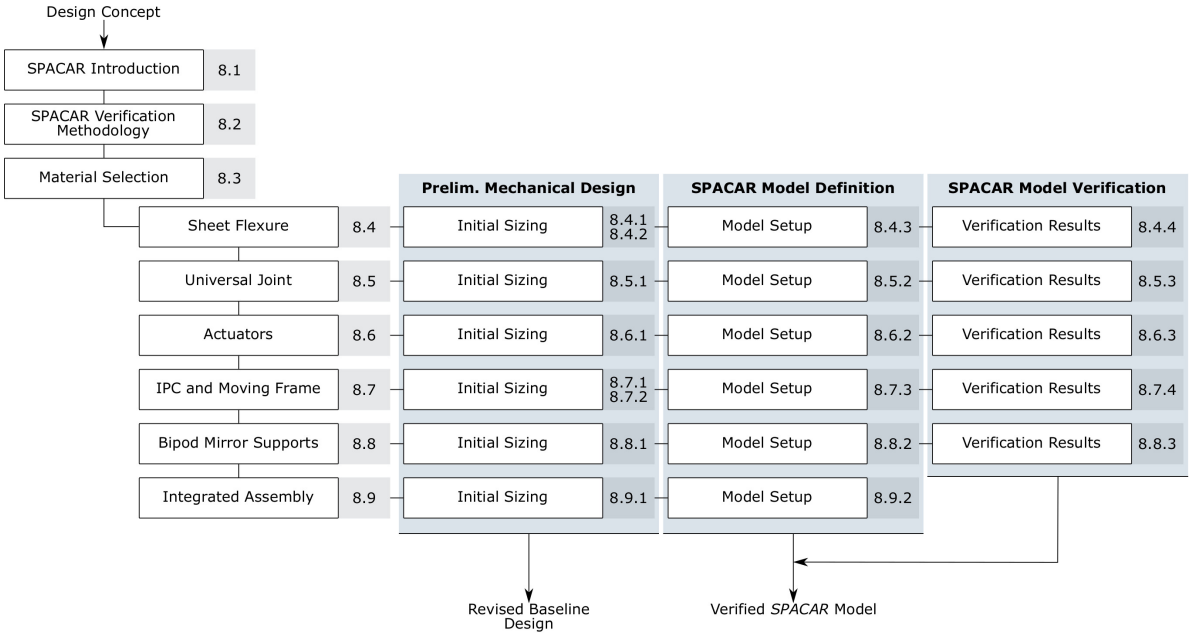

Figure 8.1: Major tasks in the mechanical design chapter. IPC = In Plane Constraint.

The main tasks of the chapter are set out in Figure 8.1. Each of the main components were sized in turn. To provide some context for the component level work, the reader is encouraged to turn to the final product in Figure 8.30 on page 146, and examine the general layout of the mechanism.

The bulk of the mechanical verification analysis presented in Chapter 9 *Verification* was conducted using *SPACAR*, a low order multi-body finite element modelling package written in MATLAB. ANSYS was used to verify the *SPACAR* models, however because of the ANSYS license limits, this could only take place at the component level. Therefore, the *SPACAR* and ANSYS finite element model development, and verification of the *SPACAR* models with the ANSYS results, were executed in parallel with the component level mechanical sizing. This is reflected in the presentation of those results throughout this chapter. The verified *SPACAR* models of each component were then combined into a single assembly level model, extrapolating the verified performance of the component models to the assembly model. The major weakness of this approach was that the interactions between components predicted by the *SPACAR* assembly model have not been verified. This is a topic for future work, either through acquisition of a commercial FEA license or ideally, testing.

8.1. The *SPACAR* Finite Element Package

SPACAR is a MATLAB compatible software package for kinematic and dynamic analysis of flexible multibody systems [66, 87]. It provides an avenue to calculate the rigid & flexible body kinematics, stresses, natural frequencies & mode shapes, linear buckling, state space input/ output matrices and dynamic behaviour of a mechanism [2].

SPACAR was selected for the mechanical verification activities first and foremost because it is developed at TU Delft and the University of Twente, so licenses able to model the full PMAO mechanism were freely available. Secondly, computation times were much shorter than those of meshed finite element packages like ANSYS, so it became feasible to include the finite element simulations "in the loop" with the telescope ETEP model for Monte Carlo statistical analyses.

The major trade-off with this method is that the pre-defined elements only exhibit a limited set of behaviours that are strongly dependent upon the user defined setup. Therefore, ANSYS was used to verify the *SPACAR* models.

A survey of the technical literature was conducted to understand what level of accuracy could be expected from *SPACAR*. The results of that survey are given below. A more detailed introduction to the *SPACAR* modelling methodology in Subsection 8.1.1, followed by how it was implemented for the PMAO mechanism in Subsection 8.1.2. A description of ANSYS and the analyses used in the model verification exercises is given in Section 8.2.

Expected Accuracy of the *SPACAR* Models

SPACAR has found use in several other compliant mechanism prototyping, optimisation and modelling studies [1, 19, 65, 88]. Studies using *SPACAR* to model the dynamics of relatively simple mechanisms found that while the trends and overall behaviour were predicted well, the numerical differences were typically on the order of 10% compared to verification with ANSYS and experimental results [56, 87, 88]. The accuracy of the *SPACAR* calculations have also been shown to degrade as the order of the eigenmode or buckling mode increases [56].

Additionally, the performance of precision mechanisms can be strongly influenced by imperfections in the test materials and set up [56] which can be difficult to capture in analytical models. This does apply to all modelling approaches though and not just *SPACAR*. A sensitivity analysis to assembly tolerances can help to understand these effects before committing to testing.

It was concluded that *SPACAR* models are best suited to understanding trends rather than precise results, which was acceptable for the purposes of this feasibility study. It was expected that the *SPACAR* models should be able to predict the first eigenfrequency and critical buckling load to within approximately 10% of the value calculated by the ANSYS verification model. Ultimately, the worst-case error in the prediction of both values were 6% and 11.2% respectively. The degradation in accuracy for higher buckling and eigenmodes was also present. Both outcomes were thus in reasonable agreement with the limitations of *SPACAR* reported in the literature. However, the accuracy of the maximum equivalent stress in launch was much worse, with a maximum error of 29%, caused by *SPACAR*'s inability to predict stress concentrations with the same fidelity as ANSYS.

8.1.1. Modelling Methodology

SPACAR models are defined with keyword based text files. They can be defined in 2D or 3D, built up with one or more elements from a pre-defined library connected via translational and/ or rotational nodes. These coordinates define the position and orientation of each of the elements with respect to a fixed global coordinate frame.

SPACAR has a series of standard elements such as planar beams, spatial beams, hinges and trusses with which a mechanical system can be realised. Each type of element has a fixed number of independent deformation modes which describe the shape of the element and the position of the nodes of that element relative to each other. The position & orientation nodes and the deformation modes can be "fixed" or "released" by the user, allowing fine grained control of the model. It is this mechanism that reduces the computation so much compared to meshed methods: the order of the model - the number of degrees of freedom - is greatly reduced through this selectivity.

The most frequently used, pre-defined, element through all of the PMAO *SPACAR* models is the "spatial beam", a simple beam with closed cross-section, shown in Figure 8.2. In addition to the normal six degrees of freedom in rigid body motion, the spatial beam also has six independent deformation modes, $\mathbf{e_i}$: an elongation deformation along, and a torsional deformation about, the longitudinal axis of the beam; and four

bending deformations, two in each of the planes with normal vectors perpendicular to the longitudinal axis. Including the deformation modes in the model allows the user to model the elastic behaviour of flexible elements in a compliant mechanism.

Mass and inertia can be assigned by the user to elements as a distributed property or lumped at nodes. Stiffness properties of elastic elements must also be specified. Additionally, external loads, internal stress-states and inertial acceleration of the whole model all provide avenues for a variety of mechanisms and load cases. Further description of how to set up and use *SPACAR* can be found in the user manual [1]. An example *SPACAR* setup file for a sheet flexure model is given in Appendix I.

In all of the PMAO models, only the flexures were modelled as elastic elements. This was verified by confirming that the equivalent stress in all elements remained below the yield strength of the material. All other elements were modelled as rigid beams, as it was assumed that their stiffnesses were several orders of magnitude greater than the flexures. The ANSYS verification confirmed the validity of this assumption.

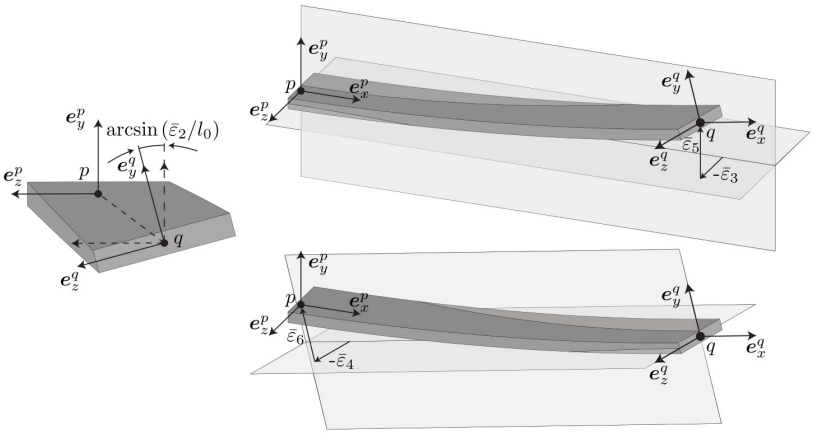

Figure 8.2: Spatial beam element as modelled in *SPACAR* with deformation modes $\mathbf{e_i}$. The location of each beam is defined with location nodes p and q. Adapted from [19].

8.1.2. Implementation

A suite of handler functions were written to automate definition of each of the *SPACAR* models and test cases, batch process each of the *SPACAR* runs and automate post processing of the load, stress, modal and displacement data. A flow chart describing the operation of this suite is given in Figure 8.3.

`runManager` can be operated as a standalone function for prototyping or called from an external function, such as `pmaoFORTA`, to interface with the DST end to end performance (ETEP) model. As its name suggests, it manages all user inputs, calls `datBuilder` to write the *SPACAR* setup file for the tests requested by the user, calls *SPACAR* to execute the simulation then passes the data to `postProcessing` to extract loads, stresses, deformations, modal and buckling results. *SPAvisual* is part of the *SPACAR* package and provides a visualisation of the model. A very useful package, *spascripting* developed by S. Boers[1], was used to synthesise the *SPACAR* input *.dat files in `datBuilder`.

Assumptions universal to all of the *SPACAR* modelling are set out in Table 8.18 on page 148 at the end of this chapter. The methods used to calculate the equivalent stress, eigenmodes, frequencies and buckling modes are given in the following subsections. Figures mapping out the element and nodal setup for each of the *SPACAR* models are given in Appendix I.

[1]Contact: `s.e.boer@utwente.nl`.

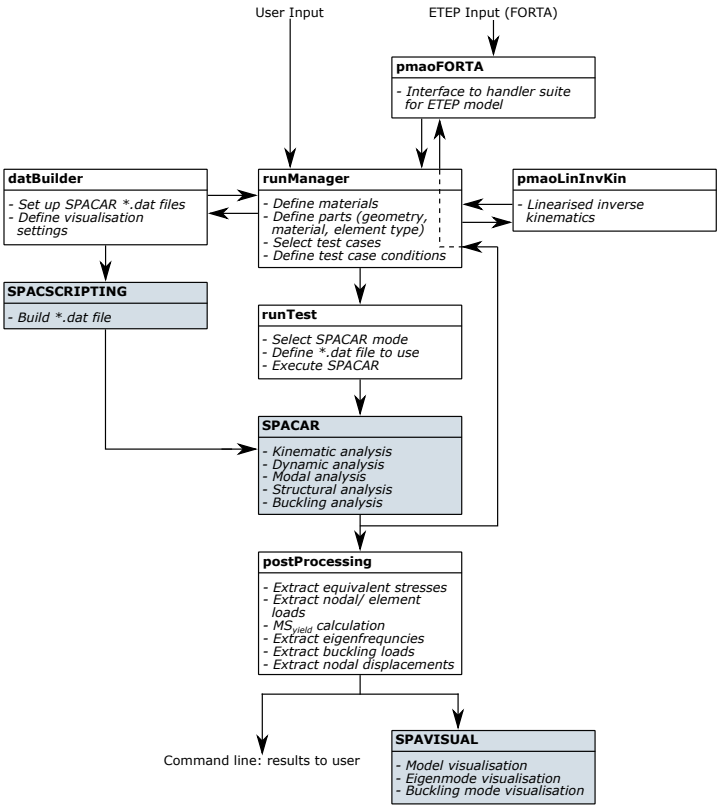

Figure 8.3: Flow diagram of *SPACAR* handling functions. *spascripting*, *SPACAR* and *SPAvisual* were developed by others.

Equivalent Stress

SPACAR reports a series of cross-sectional stress resultants for every element in a model. For the elements used in the PMAO *SPACAR* models, which were all spatial rigid beams, these can be translated into normal and shear stresses, and there-on to an equivalent stress using von Mises theory via [19]

$$\sigma_{eq} = \sqrt{\sigma_x^2 + 3\tau_{xy}^2 + 3\tau_{xz}^2} \tag{8.1}$$

where the subscripts are given in the local coordinate frame of the beam element. A more detailed description of the process is available in [19]. *SPACAR* provides an internal function to execute this calculation. The accuracy of the stress calculation can suffer under the following conditions [18]:

- In the vicinity of supports or concentrated loads.
- Thick walled circular hollow cross-sections. Stresses are calculated using thin-walled assumptions.
- For cross-sections where the shape would undergo gross deformation. *SPACAR* assumes that the cross-section does not change shape.

Eigenmodes, Eigenvalues & Buckling Modes

SPACAR calculates the mass **M**, structural stiffness **K** and geometric stiffness **G** matrices based on linearisation of the system behaviour for each load or time step [18]. Vibration modes and eigenfrequencies can be found for an undamped system by solving the generalised eigenvalue problem,

$$\mathbf{Kv} = \lambda \mathbf{Mv} \tag{8.2}$$

where **v** is an eigenmode with eigenvalue λ for eigenfrequency ω in rad/s per $\lambda = \omega^2$.

The linear buckling analysis is valid for static equilibrium or steady state motion conditions [1]. Using this analysis for the highly dynamic launch environment is acceptable for now since the launch loads are conservatively estimated using quasi-static values.

The critical buckling load parameters λ_i can be found from the solution to a second eigenvalue problem,

$$\mathbf{Kv} = -\lambda \mathbf{Gv} \tag{8.3}$$

The critical loading parameters relate buckling loads $\mathbf{f_i}$ to reference input loads $\mathbf{f_0}$ via

$$\mathbf{f_i} = \lambda_i \mathbf{f_0} \tag{8.4}$$

To obtain the system matrices and extract the buckling results, the user must specify a reference load, nominally 1 N, at a location of interest and in a specific direction. The buckling loads are simply then the critical buckling loads for external loads applied at that location and in that direction.

Note that this is a linear analysis based on the standard assumptions of Euler buckling. It does not accurately simulate non-linear buckling phenomena. Since any amount of buckling & local yielding is detrimental to the PMAO performance, the conservatism of Euler buckling was considered acceptable for prototyping.

8.2. *SPACAR* Model Verification Methods

The accuracy of *SPACAR* depends on the fidelity of the model and validity of its assumptions. That is, the number of elements and DOFs the user assigns to each physical member, and their material properties. ANSYS, which can have orders of magnitude more elements in each member and thus greater fidelity and accuracy, was used to verify the accuracy of the *SPACAR* component models. This verification is not final: there were still many assumptions in the ANSYS modelling. Only testing could truly verify the *SPACAR* models.

The following analyses were carried out to verify the static and dynamic results generated by *SPACAR*:

- Modal analysis for eigenmodes & eigenfrequencies.
- Linear buckling analysis for critical buckling loads and mode shapes.
- Static structural analysis for maximum equivalent stress under launch loads.
- Static structural analysis for maximum equivalent stress under maximum nominal displacement during operations.

The setup and assumptions for each analysis method are described in Subsections 8.2.1 to 8.2.4 respectively. In general, automatic meshing was used with an adaptive sizing function based on a minimum element size. All simulations used linear elastic models, which remain valid so long as no components were stressed beyond the linear elastic region. This was acceptable since any degree of yield was considered a failure for the PMAO.

Unless noted otherwise, the same method was applied for each component model with the only major change being the component geometry and locations of fixity or force application, which are generally self explanatory. Some component models required extra analyses. These are noted in the component model descriptions in Sections 8.4 to 8.8. An initial note on the ANSYS license limitations is given below.

License and Limitations

ANSYS Mechanical Workbench v19.0 with *Academic Teaching Mechanical and CFD* license was used for the *SPACAR* model verification. This license is available to TU Delft students as standard, and has a 256,000 mesh node limit. This was insufficient to gain mesh independence for the integrated assembly model, and was only just sufficient for the component analyses. The main challenge was that the smallest dimensions of the flexures, which dictated the nominal mesh element size, were up to four orders of magnitude smaller than the largest dimension of the greater part. Filling out a larger part with very small elements inevitably lead to very large mesh node counts. Exploiting symmetry and varying the density of the mesh throughout a part did improve the efficiency of the analysis, but not enough that the integrated model could be verified.

8.2.1. Modal Analysis

The modal analysis was conducted with the parts in the nominal unloaded, non-displaced resting state in static equilibrium conditions. The modal verification was the primary method used to verify the choice of which deformation modes to include in the *SPACAR* models. No pre-stress was applied to the model for the modal analysis.

The first three eigenfrequencies and eigenmodes were extracted from the ANSYS model to check the *SPACAR* models' ability to predict the *qualitative* performance of each PMAO component. The same logic was applied for the linear buckling verification described below.

8.2.2. Linear Buckling Analysis

The buckling modes and critical buckling loads were calculated using the eigenvalue buckling analysis toolset, which uses the classical Euler solution. This is the same solution used in the linear calculations in *SPACAR*. It is an optimistic solution since imperfections in the material, and fabrication/ assembly alignment tolerances not included in the model decreases the buckling performance of almost all structures.

Similar to the modal analysis, the linear buckling analysis was conducted in the non-displaced resting state in static equilibrium conditions with no pre-stress. As in the *SPACAR* analysis, the ANSYS buckling analysis calculates the critical buckling loads in a reference direction defined by a reference load set by the user. Each of the PMAO components were primarily susceptible to buckling along their slender axes, so critical buckling loads were calculated in both *SPACAR* and ANSYS those single directions only.

One end of the part was fixed in all degrees of freedom with a 1 N reference load applied at the other end of the part, along the slender axis. The same load and end conditions were also applied in the *SPACAR* buckling analysis.

8.2.3. Maximum Equivalent Stress: Launch

SPACAR uses the von Mises stress to calculate the equivalent stress in a beam, so the same output was generated in ANSYS. The objective of this analysis was to compare the location and magnitude of the maximum equivalent stress in each part. However, the use of rectangular section flexures without corner fillets gave rise to large stress concentrations at the roots of each flexure in the ANSYS models. It was found that the finite elements in the *SPACAR* models were incapable of predicting the presence of these stress concentrations with the same fidelity, so the maximum stress through the centreline of a part in ANSYS, away from sharp corners, was often used instead. More detail is provided on a per part basis throughout the rest of this chapter.

It was assumed that this would still give a reasonable indication of whether a part could be expected to survive the launch loads, since the stress concentrations would certainly be designed out during detailed design. The maximum stress through the body of the flexure would then be more indicative of the stress state in launch.

8.2.4. Maximum Equivalent Stress: Displacement

The largest loads experienced by the mechanism throughout its lifetime will be in either testing, or launch. However, the *SPACAR* models were also used to confirm that the components will not yield during nominal operations.

The maximum equivalent stress was found for each part after a nominal displacement had been applied. As for the launch stresses, the von Mises stress was used to find the maximum equivalent stress away from stress concentrations.

The first step in the sizing and modelling operations was selecting the material. This process is documented in the next section.

8.3. Material Selection

The preliminary PMAO mechanism design uses a single material to simplify the thermal design. Material cost is expected to be a small percentage of total system cost so the focus of this selection was on attaining high performance instead.

The PMAO material selection process uses much of the method and justifying arguments first presented by Smith & Chetwynd for precision mechanisms [106]. General requirements were translated into desired material behaviours characterised by quantifiable property groups, typically a ratio of material properties such as density, yield strength or thermal conductivity. The property groups for each material were then collated into a property profile which is a graphical representation of the performance of the material across each of the desired behaviours. Candidate materials could then be readily compared over a broad range of criteria with a single tool. Flexures require a strong, elastic material with homogeneous and isotropic properties, so only metals were considered.

Important property groups are discussed in Subsection 8.3.1, separated into mechanical and thermal domains. Candidate materials and their property profiles are constructed in Subsection 8.3.2 based on data tabulated in Appendix K *Material Properties*. The comparison and selection are documented in Subsection 8.3.3.

8.3.1. Material Property Groups

This section translates the general PMAO requirements into desirable material behaviours and derives the appropriate property groups. The main use cases for the PMAO mechanism will be:

1. In the stowed configuration during launch.
2. In the stowed configuration with no baffle during LEOP (Launch and Early Operations).
3. In the deployed configuration with the baffle also deployed during nominal operations.

The flexures must provide highly repeatable behaviour whilst also restraining the comparatively massive mirror segment through the rigours of launch. The whole assembly should undergo very little shape change in the presence of dynamic thermal loads and reach equilibrium with its surroundings as quickly as possible. A high thermal stability is necessary to meet the thermal drift budget. Appropriate material selection is central to achieving all of these requirements.

The following property groups were derived using simple physical models to estimate how the material influences the behaviour of more complex structures.

Mechanical Properties

Material Response to Static Loads

The PMAO will undergo severe mechanical loads during launch and similarly severe thermal excursions during LEOP. During both phases, it will be sufficient for the mechanism simply to survive these conditions: the stress in all components shall not exceed the yield strength[2] S_Y.

An appropriate property group given the need to minimise weight is strength to weight ratio S_Y/ρ with ρ the material density. This maximises the load capacity of small structural members.

Very high repeatability is a critical behaviour of the flexures, requiring that they not undergo any amount of local yielding. The maximum strain of a flexure is governed by the Young's Modulus E and yield strength of the material,

$$\epsilon = \frac{S_Y}{E} \tag{8.5}$$

Maximising this ratio S_Y/E will therefore provide a larger allowable deflection without a loss of mechanical repeatability. Yield strength is taken instead of ultimate strength since the flexural components must remain in the linear elastic region at all times.

Material Response to Dynamic Loads

It is desirable to have high resonant frequencies both to meet the launch requirements and to maximise the bandwidth of the mechanism. The fundamental frequency of a simple mass-spring system is given by

$$f_n = \frac{1}{2\pi}\sqrt{\frac{k}{m}} \tag{8.6}$$

where f_n is expressed in Hz, k is the stiffness of the spring and m the mass supported at its end. Considering a beam of length L, cross-sectional area A, tensile stiffness EA/L and mass ρAL, gives a fundamental frequency of

$$f_n = \frac{1}{2\pi}\sqrt{\frac{E}{L^2\rho}} \tag{8.7}$$

So for all other parameters held constant, the resonant frequency of a beam is maximised by increasing the ratio $(E/\rho)^{1/2}$. Increasing the ratio E/ρ also minimises self-weight deflection of a beam [106], which is desirable for elastic mechanisms calibrated on the ground but operated in the microgravity environment of low Earth orbit.

[2] Recall from Subsection 4.2.1 that it has been assumed that the yield strength of a material can be used to approximate the elastic limit throughout this thesis.

Thermal Properties

It is expected that the largest thermal transients and gradients will occur as the spacecraft transits the terminator, moving from the coldest to hottest conditions. This is also when the actuators are expected to be most active, dissipating heat behind the mirror as they work to compensate for the ensuing thermal drift. Once the position of the primary mirror has been calibrated, the actuators must hold their position, dissipating a small but steady quantity of heat.

The operational thermal environment can therefore be characterised by longer periods of equilibrium with stable internal heat dissipation, punctuated by short intervals of abrupt change, in external radiative heat input and varying internal dissipation from the actuators.

Material Response to a Temperature Gradient

Each of the actuators will have different displacement profiles and thus differing self-heating profiles. Since they are overconstrained, the ensuing thermal expansion will cause an increase in internal stress governed by

$$\sigma = E\alpha\Delta T \tag{8.8}$$

where α is the coefficient of thermal expansion of the material and ΔT the difference in temperature between the warmer actuators and cooler bulk of the fixed & moving frames. This relationship holds so long as the material is homogeneous, isotropic and does not exceed its elastic limit. Similar behaviour may occur if one actuator stack is inadvertently powered while the others are left stationary and cold. Internal stress can cause stress stiffening of flexures, degrading the repeatability of their force/ displacement behaviour.

Minimising αE is clearly desirable to keep the induced stresses low. This same principle is applicable to any other clamped, constrained components that may undergo differential heating, including the in-plane constraints.

As a general comment, where the coefficient of thermal expansion α appears in a property group, the quantity αE should be used for clamped members, rather than just α, since it is usually desirable to keep internal stresses low. Free members are not overconstrained so don't have this problem. In that case, the objective is normally to minimise dimension growth by minimising α alone.

Material Response to Steady Heat Sources

The operation of the actuator push/ pull pairs relies upon a negligible thermal gradient across the ceramic stacks. It is also desirable to conduct the internally dissipated heat away from the actuators to prevent them from exceeding their Curie temperatures. Once the mirror is calibrated, the structure will also have to exhibit very high thermal stability in the presence of steady state heat from the actuators during image acquisition. The very thin in-plane constraints are also one of the primary conduction paths between the moving and fixed frames.

For each of these reasons, materials with a high thermal conductivity and/ or a high volume specific heat are desirable. This means that fluctuations in heat flux lead to comparatively smaller temperature changes for a given volume of material.

To find an appropriate property group, consider a source generating a heat flux $q\ W/m^2$ through a beam of constant cross-section A and length L. From Fourier's law for heat conduction, this will cause a temperature gradient ΔT across the beam [106],

$$\Delta T = \frac{qL}{k} \tag{8.9}$$

To ensure good dimensional stability, the strain in the beam resulting from the average temperature increase $\Delta T/2$ over the beam should be minimised. Thus from

$$\epsilon = \frac{qL}{2}\frac{\alpha}{k} \tag{8.10}$$

the ratio α/k should be kept as low as possible for free members and $\alpha E/k$ for clamped members.

Material Response to Unsteady Heat Sources

The mission concept of operations anticipates a settling period upon exiting each transition through the terminator so that the components can fall back within the thermal drift tolerance budget. It is desirable for this to happen as fast as possible to maximise imaging time. Materials with high diffusivity are advantageous in this case.

The one dimensional heat equation [106] gives

$$\frac{\partial T}{\partial t} = \frac{k}{c_p \rho} \frac{\partial^2 T}{\partial x^2} \tag{8.11}$$

with x the position along the conductive path and t the time. c_p is the specific heat capacity of the material at constant pressure and is considered negligibly different from the value at constant volume in solids for the purposes of this analysis. Thus the diffusivity $k/c_p\rho$ can be increased by using with materials with better thermal conductivity or lower density and specific heat capacity.

The calibration procedure puts the actuators through a period of very dynamic use and equivalently, unsteady heat dissipation, after deployment and possibly after every transition through the terminator. Assuming all of the heat is absorbed by the structure, the change in temperature is given by

$$Q_{in} = Q_{out} \tag{8.12}$$

$$Q_{actuator} = mc_p \Delta T \tag{8.13}$$

$$= AL\rho c_p \Delta T \tag{8.14}$$

The quantity ρc_p is called the volume specific heat and should be maximised to reduce the rise in temperature of structure for a given heat input. The resulting strain ϵ from that temperature rise is

$$\epsilon = \alpha \Delta T = \frac{\alpha Q}{AL\rho c_p} \tag{8.15}$$

Ideally, a free, thermally stable structure such as the mirror supports should have a small $\alpha/\rho c_p$ to be dimensionally robust in the presence of transient heat sources. Clamped structures should have low $\alpha E/\rho c_p$.

Table 8.1 summarises the results of the property group derivations.

Table 8.1: Summary of property groups used in material selection.

Property Group	Behaviour	Desired Trend
$\frac{S_Y}{\rho}$	Increases strength to weight ratio.	High
$\frac{S_Y}{E}$	Increases flexure repeatability.	High
$\frac{E}{\rho}$	Increases fundamental frequency. Decreases self-weight deflection.	High
$\frac{k}{c_p\rho}$	Increases thermal diffusivity.	High
$\frac{\alpha}{\rho c_p}$	Decreases dimensional stability in presence of unsteady heat sources for free members.	Low
$\frac{\alpha E}{\rho c_p}$	Increases thermal stresses in presence of unsteady heat sources for clamped members.	Low
α	Decreases dimensional stability in presence of temperature gradient for free members.	Low
αE	Increases thermal stresses in presence of temperature gradient for clamped members.	Low
$\frac{\alpha}{k}$	Decreases dimension stability in presence of steady state heat sources for free members.	Low
$\frac{\alpha E}{k}$	Increases thermal stresses in presence of steady state heat sources for clamped members.	Low

8.3.2. Material Profiles

Material profiles were created by ordering each of the materials' quantified property groups side-by-side in a line plot. A logarithmic scale helps comparison of order of magnitude differences in performance. Normalisation to a "standard", but fictitious, material allows property groups with widely different magnitudes to be compared next to each other on that same scale.

The "standard" material has properties that would normally be considered "good" for the application under review. This is somewhat subjective but avoids the danger of a user considering a certain material to be the "standard" option before conducting a proper comparison of the available options [106]. Properties for the fictional standard material are given in Table 8.2, taken from [106] for use in precision mechanism applications.

Table 8.2: Fictitious standard material used to normalise property groups for material comparison. Taken from [106].

Property	**Value**
Young's modulus	200 GPa
Maximum strength	300 MPa
Density	4000 kg/m^3
Coef. thermal expansion	7×10^{-6} K^{-1}
Thermal conductivity	150 $W/m-K$
Specific heat capacity	750 J/kgK

Each of the candidate materials are introduced below. Their property profiles are shown in Figure 8.4. All material data is collated and referenced in Appendix K *Material Properties*. All data was collected at room temperature since the nominal design temperature is 298 K. Only a qualitative understanding of changes in material behaviour for large temperature excursions were used when considering performance during LEOP.

Aluminium

One of the most common Aluminium alloys used in structural applications is 6061-T6. It has medium strength, good dimensional stability and machinability, and excellent weldability [126]. It is comparatively cheap and easy to source. It has a high thermal expansion coefficient. 7075-T6 is another common high strength alloy though is prone to stress corrosion cracking. It also has good machinability but poor weldability. Pure Aluminium is very weak and not considered.

Steel

Steel is rarely used in optical applications due to its high mass [126] though where it is used in spacecraft, most of it is stainless due to its corrosion resistance and ability to maintain its strength at high temperatures [103]. Steel normally has good machinability and weldability but non-stainless variants require a coating to protect it from corrosion. Stainless steels are more ductile than low carbon steels and the 300 series are non-magnetic and hard to machine due to work hardening [126]. The common 304 stainless alloy is included.

Beryllium

Beryllium is light weight, has high stiffness, high thermal conductivity and has very good properties at cryogenic temperatures [126]. The segmented mirror blanks and support structure of the JWST primary mirror are made of Beryllium [79]. The main advantages of Beryllium are its very high specific stiffness, low CTE and high thermal conductivity, thus it finds a lot of use in alignment applications in space [103]. It is more expensive than many other metals and is toxic in powder form, complicating fabrication. Welding is difficult and the coefficient of thermal expansion can differ strongly, depending on the orientation of the microstructure in its pure form [126]. Beryllium Copper is a popular alloy in aerospace applications and has high strength, high fatigue strength and similarly good cryogenic performance [115].

Invar

Invar 36 and Super Invar are two varieties of very low expansion Iron-Nickel alloys. The main advantage of Invar 36 is its very low coefficient of thermal expansion, though this is only over a limited range and it is very heavy compared to lighter metal alloys [126]. The minimum steady state temperature expected during LEOP is 188 K. Super Invar changes phase at temperatures below 223 K, so is not suitable for use in the primary mirror subsystems and not considered in this comparison. It has a similar CTE to Silicon Carbide, the material of choice for the mirror substrate, reducing the likelihood of stresses from differential thermo-elastic expansion.

Magnesium

Magnesium is very light compared to most other metals, has a high heat capacity and medium strength but poor resistance to corrosion and a high coefficient of thermal expansion [103, 126]. Its influence on galvanic corrosion of other metals cannot be ignored, particularly for stainless steels, Titanium, Copper and Aluminium alloys [126].

Titanium

Titanium alloys are very popular in aerospace structures due to their high strength to weight ratio and good retention of its properties up to 973 K [103]. It has good corrosion resistance, is non-magnetic and has a CTE compatible with many glasses used in optics. Ti-6Al-4V is a common alloy that has reasonable workability though it rapidly degrades cutting elements during machining. Welding is possible though difficult, whereas brazing is a more common method of joining [126].

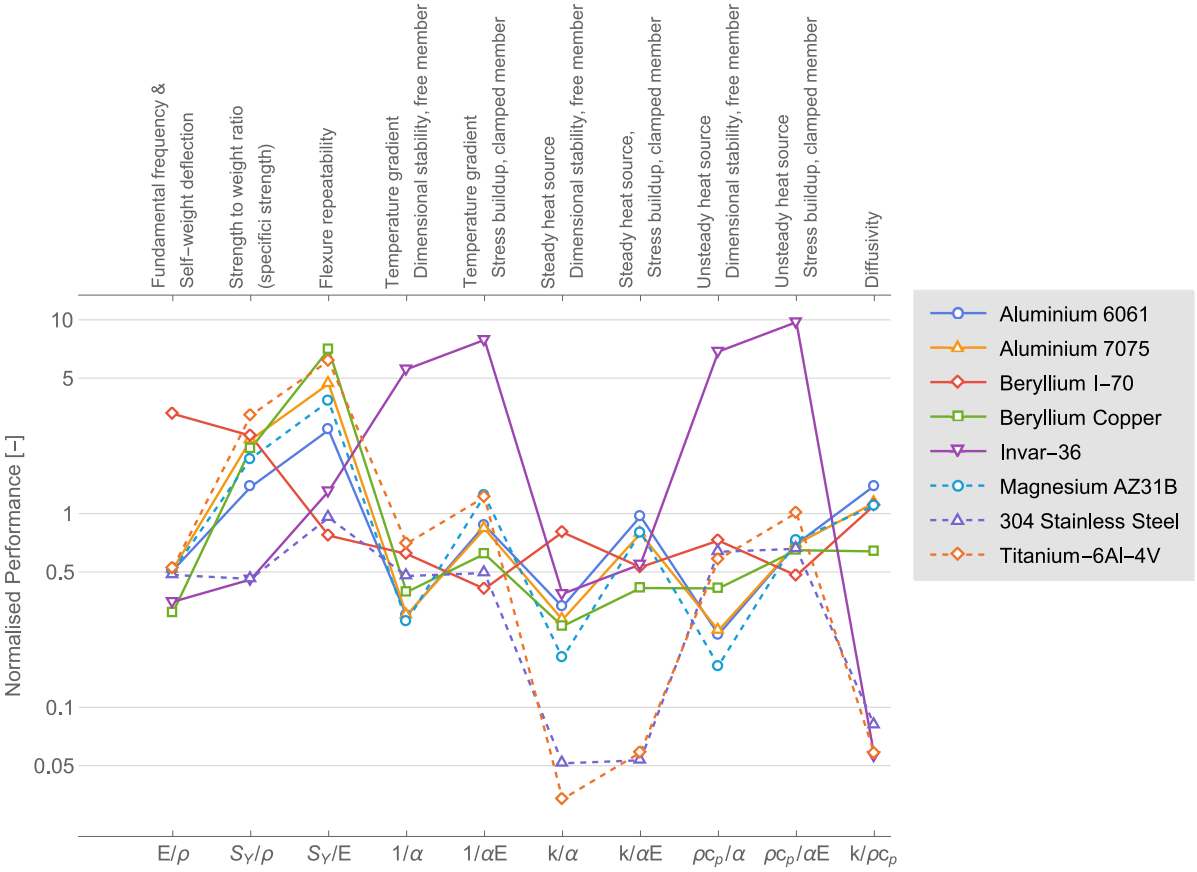

Figure 8.4: Candidate PMAO material property profiles. Note that scores in each property group are linked to provide a visual cue for comparison only, the line has no physical meaning. Successive quantities in each profile are independent. Values are normalised to performance of a fictitious standard material defined in Table 8.2.

8.3.3. Material Selection

Beryllium Copper has the best strength to elasticity ratio, but middling performance over the remaining criteria so was not a strong candidate. Similarly, while Magnesium offers outstanding specific elasticity and strength to weight, it also exhibits mediocre performance in the remaining criteria. 304 Stainless Steel has consistently poor performance. This was expected, its inclusion was mainly to provide a commonly used reference material to gauge the performance of the other, more exotic, metals. Neither stainless Steel nor Magnesium were good candidates.

Despite its excellent performance wherever low CTE was important, Invar-36 is usually considered a poor choice for flexures due to its very low mechanical repeatability and poor deflection under self weight [121]. It was not considered for the flexures. Beryllium I-70 performs very well where dimensional stability around heat sources is important. Its poor strength to elasticity ratio and requirement for special safety precautions

makes it less attractive. Aluminium 7075 outperforms the 6061 alloy across all but three mechanical property groups. It is light and easily workable but was let down by its high CTE.

The Titanium alloy had the best overall performance except where thermal conductivity was concerned. Its mechanical performance is very good - important for flexure repeatability and surviving launch. It also performs very well where dimensional stability is required. Its ability to retain these properties to high temperatures is advantageous for the LEOP use case. Ti-6Al-4V was selected for the preliminary PMAO design, with Beryllium I-70 and Aluminium 7075 as secondary options if further light-weighting or better transient thermal performance is needed. Invar-36 remains a possible choice for the support bipods if the thermal stability needs improving thanks to its closely matched CTE to that of Silicon Carbide.

The Ti-6Al-4V material properties listed in Appendix K were used in the *SPACAR* and ANSYS models.

8.4. Sheet Flexure

The sheet flexure is the fundamental compliant element used throughout the PMAO mechanism. The purpose of this section is to set out the basic design equations and modelling assumptions for sheet flexures, and to verify those design methods and assumptions for re-use throughout the rest of the PMAO. Only slight modifications were necessary to use the same equations and assumptions for the in-plane *wire* flexures.

The design equations are presented in Subsection 8.4.1. As an example, they are applied to the universal joint hinge flexures in Subsection 8.4.2. A description of the *SPACAR* model for the universal joint flexures is given in Subsection 8.4.3, followed by the ANSYS model verification results in Subsection 8.4.4. The section concludes with a summary in Subsection 8.4.5.

8.4.1. Flexure Sizing Relations

Different flexure profiles offer a range of advantages and disadvantages including ease of accurate analysis, ease of manufacture, reduction of stress concentrations and better definition of the rotation axis which leads to smaller parasitic errors. Circular notch flexures, for example, offer a much smaller drift of the rotational axis of the flexure compared to rectangular section sheet flexures [106, p. 118], which is useful if parasitic errors must be controlled.

For simplicity, all PMAO flexures were modelled either as rectangular sheet flexures or square-section wire flexures[3]. The rectangular cross-section lends itself to simple analysis, though the abrupt change of cross-section can lead to high stress concentrations [126, p. 569], which will be seen in the ANSYS verification model results.

The flexures have both stiffness and strength design criteria that can be used to guide the necessary sizing relations:

Strength Criteria

1. To withstand the stresses from deflections during operations without yielding or buckling.
2. To withstand the launch loads without yielding or buckling.

Stiffness Criteria

3. To adequately decouple the desired freedoms from desired constraints.
4. To have a fundamental frequency greater than 100 Hz.

Stresses from Transverse Loads

Sheet flexures are compliant under transverse loads and stiff under axial loads. Thus the strength criteria during operations generally focus on bending stresses due to actuation loads and the strength criteria generally focus on axial stresses due to launch loads.

All of the sizing relations for the sheet and wire flexures are based on Euler-Bernoulli beam theory of a cantilevered beam per Figure 8.5.

The second moments of area are given by

$$I_{XX} = \frac{1}{12} b t^3 \tag{8.16}$$

$$I_{YY} = \frac{1}{12} t b^3 \tag{8.17}$$

[3] References [81], [106] and [126] are good resources to guide selection of new flexure profiles in future iterations of the PMAO.

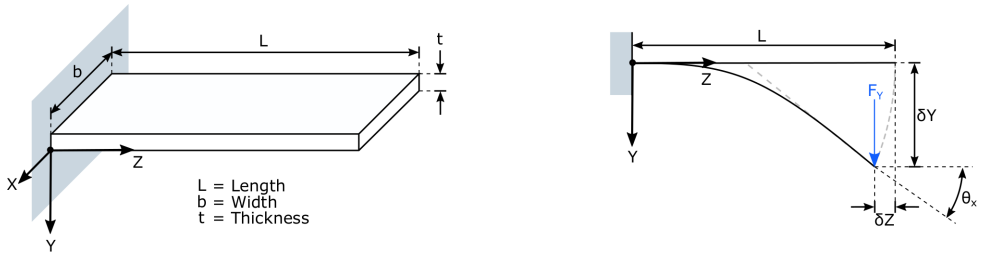

Figure 8.5: Left: Sheet flexure modelled as a cantilevered beam. Right: Bending of cantilevered beam under transverse load F_Y.

Sheet and wire flexures are used in the PMAO mechanism to variously allow translations and/ or rotations about an ideal pivot point. The right hand frame of Figure 8.5 illustrates the resulting geometry for the case with transverse load F_Y. The displacement at the tip of the beam δ_Y is given by [128, p. 189]

$$\delta_Y = \frac{F_Y L^3}{3EI_{XX}} \tag{8.18}$$

Note the small motion δ_Z that occurs due to conservation of length of the beam. In this context, it is called a *parasitic* displacement because it is a small, unwanted motion in a direction that would nominally be a constraint for the sheet flexure, but is unavoidable given the physical realities of the material. It is calculated in *SPACAR*, but ignored in these sizing calculations as it is not one of the main design criteria.

For these sizing purposes, the rotation θ_X of the beam due to the transverse displacement is modelled as the angular deflection at the tip:

$$\theta_X = \frac{F_Y L^2}{2EI_{XX}} \tag{8.19}$$

There is a parasitic shift of the pivot point as the beam deflects which, given the small deflections used in the PMAO, were assumed negligible for sizing purposes. The maximum stress in the beam due to bending is

$$\sigma_{max} = \frac{Mc}{I_{XX}} \tag{8.20}$$

with M the applied bending moment and c the distance from the neutral axis to the point of load application. For small motions $M = F_Y L$. Additionally with $c = t/2$, equation 8.20 can be substituted into equation 8.18 to find the maximum bending stress as a function of transverse displacement δ_Y

$$\sigma_{max} = \frac{3Et\delta_Y}{2L^2} \tag{8.21}$$

Equation 8.21 can similarly be expressed in terms of the rotation θ_X by substituting equation 8.19 into equation 8.20 to give

$$\sigma_{max} = \frac{Et\theta_x}{L} \tag{8.22}$$

To remain in the linear elastic region and prevent yield, the maximum allowable stress is the yield strength S_Y, reduced by a suitable safety factor $n \geq 1$, giving the maximum allowable bending stress,

$$\sigma_{max} \leq \frac{S_Y}{n} \tag{8.23}$$

Either equation 8.21 or 8.22 can be substituted into equation 8.23 to give a limiting design equation for yield strength. Note that transverse shear stress has been ignored. This is acceptable for rectangular beams so long as the length to thickness ratio is greater than 10 [26, p. 98] as is typically the case for sheet and wire flexures.

The transverse displacement δ_Y can also be given in terms of the rotation θ_X of the end of the flexure via [128, p. 18p]

$$\delta_Y = -\frac{2}{3} L\theta_X \tag{8.24}$$

Equation 8.24 is used as a convenient input in ANSYS and *SPACAR* to find the maximum equivalent stress under the nominal maximum deflection.

Stresses from Axial Loads

The stress from an axial load F is calculated via

$$\sigma = \frac{F}{A} \tag{8.25}$$

Equation 8.25 can then be compared to equation 8.23 to check for yield.

Buckling

A simple if optimistic check against buckling can be made. Assuming that the flexure can be modelled as an Eulerian column[4] with fixed-free end conditions, the critical unit load is

$$P_{cr} = \frac{\pi^2 E I_{min}}{4L^2} \tag{8.26}$$

where $I_{min} = bt^3/12$ is the smallest second moment of area of the flexures' cross-section. The flexure will not buckle so long as the cross-sectional area is large enough that the critical unit load is not exceeded. Similarly for a beam with fixed/ fixed end conditions

$$P_{cr} = \frac{4\pi^2 E I_{min}}{L^2} \tag{8.27}$$

Fundamental Frequency

It is useful to have an estimate of the fundamental frequency of a flexure to compare against results from both the *SPACAR* and ANSYS analyses. This can be found by solving the Euler-Lagrange equation for a fixed/ free cantilevered beam. In the absence of external loads, the beam undergoes free vibration. Assuming that the beam has constant rectangular cross-section & material properties along its length, the Euler-Lagrange equation takes the form

$$EI\frac{\partial^4 w(x,t)}{\partial x^4} + \rho A\frac{\partial^2 w(x,t)}{\partial t^2} = 0 \tag{8.28}$$

For transverse displacement $w(x,t)$ of the beam along its length $0 \leq x \leq L$ over time t. For a stationary, unforced beam, the initial conditions are

$$w(x,0) = 0 \qquad \frac{\partial w(x,0)}{\partial t} = 0 \tag{8.29}$$

The boundary conditions with one end clamped and the other free are

$$w(0,t) = 0 \qquad \frac{\partial w(0,t)}{\partial x} = 0 \tag{8.30}$$

$$EI\frac{\partial^2 w(L,t)}{\partial x^2} = 0 \qquad EI\frac{\partial^3 w(L,t)}{\partial x^3} = 0 \tag{8.31}$$

where the last two equations give the bending moment and shear force at the free end of the beam respectively. The general solution gives the modes w_n with natural frequencies ω_n in the form

$$w_n(x,t) = A_4\left(\sin\left(x\beta_n\right)\right) + A_3\left(\cos\left(x\beta_n\right)\right) + A_2\left(\sinh\left(x\beta_n\right)\right) + A_1\left(\cosh\left(x\beta_n\right)\right) \tag{8.32}$$

where the A_i are constants whose values can be found from the specific geometry of the problem and the natural frequencies are given in rad/s by

$$\omega_n = (\beta_n L)^2\sqrt{\frac{EI}{\rho AL^4}} \tag{8.33}$$

If only the fundamental frequencies are of interest, the problem can be reduced to solving the equation

[4] This is not strictly valid. Euler's formula is derived assuming that the length of the column is large relative to the thickness and width of the column, which is not true for dimension b in this case. Nevertheless it provides a quick and simple sanity check of the finite element results.

$$cosh(\beta_n L)cos(\beta_n L) + 1 = 0 \tag{8.34}$$

Note that the Euler-Lagrange equation was solved over the x dimension only. This is sufficient to provide the fundamental mode and frequency of a cantilevered beam undergoing free vibration but is incapable of predicting higher order modes. This is acceptable for the current analyses since its purpose is only to provide a sanity check of the computational methods.

8.4.2. Application: Universal Joint Sheet Flexures

The universal joint was first shown in Figure 7.4 on page 84. A simple implementation is used in the preliminary PMAO design, shown in Figure 8.8 on page 119.

Each of the universal joints are identical, as are the four flexures arranged in two pairs in each joint. Since the flexures are compliant for out of plane motions, the assembly was designed so that the universal joints only undergo axial loads. Each flexure takes half of the axial launch load placed on the joint. It was assumed that the peak stress in the joints will occur in the region of smallest cross-sectional area (ignoring the effects of stress concentrations). That is, the flexures.

Launch Loads

To start, the minimum cross-sectional area needed to withstand the launch loads was found. The width was dictated by the dimensions of the actuators. The centre aperture of the joint must provide clearance for an M5 bolt for one of the actuator/ universal joint interfaces. Assuming hexagonal socket head machine screws are used, the minimum inner diameter must be 10 mm to provide clearance for the 9.8 mm diameter socket head. Since the outer diameter of the actuator is 30 mm, the maximum allowable universal joint flexure width b was then 10 mm.

It was assumed throughout the mechanical design that the minimum feature size for all parts should be no less than 0.5 mm to enable standard high precision machining methods. This dictated the minimum flexure thickness t.

A rule of thumb in flexure design is for the width b to satisfy the condition $L \leq b \leq 2L$ to maintain reasonable stiffness against in-plane shear loads [126, p. 572], whilst still minimising torsional stiffness [57, p. 191]. For the Euler-Bernoulli beam theory to hold, the ratio $L/t > 10$ must be satisfied, as should the ratio $b/t > 10$ so that the flexure is stiff against rotation about the local y axis [102], as defined in Figure 8.5. Assuming a width of 10 mm and length 6 mm satisfies each of these conditions.

The launch load per flexure was derived from equation 7.29 assuming a mirror mass of 6 kg and worst-case ratio h/R_M of 1.2 per the concept B launch load sizing in Section 7.4. Also recall from Section 3.3 *System Requirements Analysis* that the 30g launch loads already include a safety factor and need no further amplification. The resulting launch load per flexure, neglecting self mass of all components except the mirror, was 750 N.

Substituting the assumed flexure geometry into equation 8.26 to find the critical buckling load and comparing to the launch load, as well as substituting the launch load into equations 8.25 and 8.23, revealed that the dominant strength criteria was buckling. The minimum thickness to stay below the critical load was approximately 0.48 mm, confirming that the assumed flexure geometry was acceptable.

The maximum equivalent stress was equal to the normal stress on the flexures' end section, 150.1 MPa per equation 8.25. The critical buckling load was 821 N, larger than the anticipated launch load.

Displacement Loads

Neglecting the influence of parasitic motions and assuming mounting angle $\alpha = 0°$, The linearised inverse kinematic equations 7.30 to 7.33 showed that the rotations $\theta_{x,M}$ and $\theta_{y,M}$ are independent, and that a piston displacement $\Delta_{z,M}$ has no effect on the rotation of the joints. The geometry of the PMAO mechanism is also such that the tip or tilt rotations of the moving frame will always be greater than the rotation needed in the universal joints necessary to accommodate that tip or tilt.

Therefore as a first approximation, the largest rotation of a universal joint will occur when the moving frame rotates about the X_{MF} axis with a magnitude of 4 μrad. Checking that the flexure is able to make this full rotation without yielding therefore provides a conservative check for allowable deflection.

Combining equations 8.22 and 8.23 with the flexure geometry above gives a maximum allowable rotation of 0.11 rad, several orders of magnitude larger than the required rotation. For the 6 mm long flexure and tip rotation of 4 μrad, equation 8.24 gives a transverse displacement of 16 nm.

The von Mises equivalent stress in the beam due to this stress was calculated with

$$\sigma_{eq} = \sqrt{\sigma_x^2 - \sigma_x\sigma_y + \sigma_y^2 + 3\tau_{xy}^2} \tag{8.35}$$

The maximum stress occurs on the top of the beam along the centreline. The shear stress here is zero as is the normal stress in the transverse x direction such that $\tau_{xy} = 0, \sigma_x = 0$. Therefore the equivalent stress simplifies to $\sigma_{eq} = \sigma_y$, the maximum bending stress given by equation 8.20 and related to the transverse displacement by equation 8.21, giving a maximum expected stress of 0.038 MPa.

Fundamental Frequency

The solution to the transcendental equation 8.34 must be found numerically. The `Reduce` function in *Mathematica*[5] was used to determine the quantity $\beta_1 L = 1.8751$. For the sizing geometry derived above, this gives a fundamental frequency of 11.47 kHz. As expected for such a small part, this is considerably higher than the 100 Hz necessary to survive launch.

Design parameters for the flexure are summarised in Table 8.3.

Table 8.3: Design parameters for the universal joint sheet flexures.

Parameter	**Value**
Geometry	
Length L	6 mm
Width b	10 mm
Thickness t	0.5 mm
Material	Ti-6Al-4V
Test Conditions	
Applied launch load F_L	750 N
Nominal rotation θ_X	4 μrad
Nominal transverse displacement δ_Y	16 nm

8.4.3. *SPACAR* Model Definition

This subsection sets out the methodology and assumptions used to model the sheet flexures. The assumptions verified for the simple sheet flexure model discussed in this section were applied in all of the subsequent *SPACAR* modelling, unless specifically noted otherwise.

Selection of Deformation Modes

The flexures were modelled using rectangular cross-section spatial beams. Elongation along the longitudinal axis of the sheet was assumed negligible and thus suppressed, as were the bending deformation modes in the plane of the sheet. Out of plane bending was enabled per the normal freedoms of a sheet flexure.

Torsion-elongation coupling, a shortening of a beam due to twisting, as well as correction factors for shear effects on stiffness, were assumed negligible over the very small deformations used in the mechanism.

Constraint Warping and Flexure Discretisation

Short, wide flexures are susceptible to *constraint warping* which is a torsional stiffening of the flexure in close proximity to a clamped end, reducing the effective length of the flexure [87, 88]. An approximation of this effect was included in the model by suppressing the torsion deformation mode at the fixed ends over the length $b\sqrt{(1+\nu)/24}$ with b the width of the flexure and ν Poisson's ratio of the flexure material.

It is common practice in *SPACAR* modelling to divide a flexure into a discrete number of beam elements of equal length to increase the degrees of freedom, and thus fidelity, of the model. A small discretisation error will result as it is generally not possible for the sum of one or more of those elements to equal to constraint warping length. A brief study, summarised in Appendix H, was conducted to determine the necessity of including constraint warping and to find the minimum number of beam elements needed to retrieve useful results.

It was concluded that three beam elements should be used for the fixed/ free model of the flexure used in this section, and six elements in the fixed/ fixed flexures used in the rest of the *SPACAR* modelling. It was also confirmed that constraint warping *did* need to be included at both fixed ends. Constraint warping was not considered at all for the in plane constraint wire flexures, sized in Section 8.7, due to their very high aspect ratio.

[5] `https://www.wolfram.com/mathematica/`

8.4.4. Results & Discussion

The ANSYS sheet flexure modelling used the method described in Section 8.2 *SPACAR Model Verification Methods*. A minimum mesh element size of 0.3 mm was found to give mesh-converged results, listed in Table 8.4. Theoretical estimates are also provided as a sanity check. A comparison of the first three eigenmodes and longitudinal buckling modes are given in Figures 8.6 and 8.7 respectively.

Table 8.4: Results of sheet flexure modelling in *SPACAR* and verification with ANSYS. The error is the difference between the *SPACAR* and ANSYS results.

Item	Theory	*SPACAR*	ANSYS	Error
Eigenfrequencies				
ω_1	11470 Hz	11.46 kHz	11.99 kHz	4.44%
ω_2	-	18.76 kHz	19.86 kHz	5.53%
ω_3	-	45.30 kHz	41.63 kHz	8.82%
Critical Buckling Loads				
f_1	821 N	821 N	892 N	7.92%
f_2	-	7445 N	2683 N	178%
f_3	-	21500 N	7737 N	178%
Maximum Launch Stress				
σ_{eq}	150.1 MPa	150.1 MPa	153.9 MPa	2.46%
Max. Displacement Stress				
σ_{eq}	0.038 MPa	0.038 MPa	0.040 MPa	4.57%

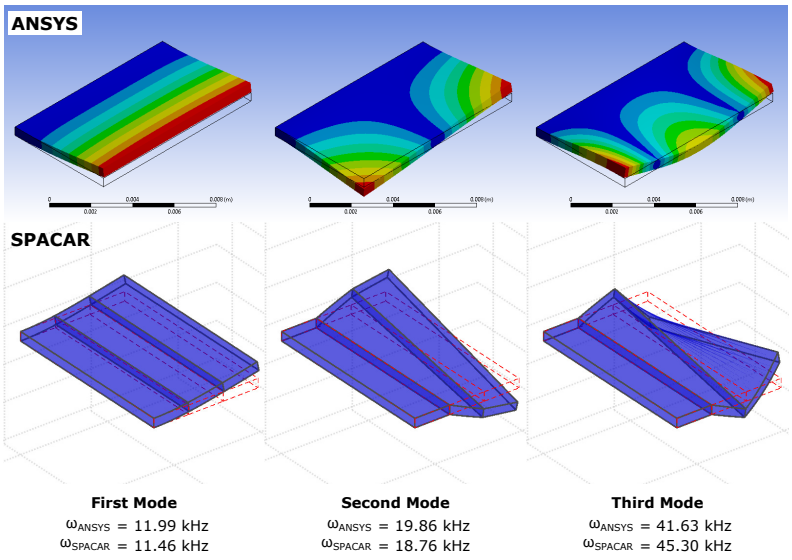

Figure 8.6: Comparison of first three eigenmodes from ANSYS and *SPACAR* simulations of a sheet flexure. Note that *SPACAR* incorrectly predicts the third mode shape. Undeformed geometry depicted by dashed red line. Colouring in the ANSYS results indicates scaled deflection. $L = 6\ mm$, $b = 10\ mm$, $t = 0.5\ mm$.

The launch and displacement stresses reported in the ANSYS results were taken from the centreline from the fixed to free ends, as ANSYS calculated artificially high stresses at the outer vertices of the fixed end. This was a result of using a fixed support condition which is a poor approximation of a real world support. Additionally, fixing the end face constrains the Poisson effect in two directions, leading to higher stresses. The remaining discrepancy between the theoretical and ANSYS values in the displacement load case exists because beam theory is only able to give an approximate answer for three dimensional beams.

The *SPACAR* model very closely replicated the theoretical results for the simple sheet model, with no more than an 8% error compared to the ANSYS values for the quantities of interest. The higher order buckling mode predictions were very poor. Both results were in line with expectations from *SPACAR* results in the literature.

The results showed that the flexure was able to survive the launch and displacement stresses. As expected, the launch loads were the dominant design case.

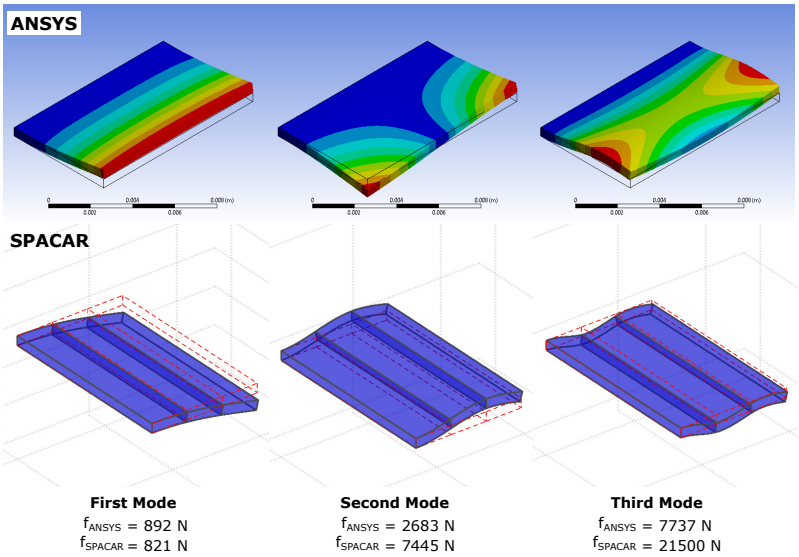

Figure 8.7: Comparison of first three buckling modes from ANSYS and *SPACAR* linear buckling analysis simulations of a sheet flexure. Note that *SPACAR* incorrectly predicts the second and third mode shapes. Colouring in the ANSYS results indicates scaled deflection. L = 6 mm, b = 10 mm, t = 0.5 mm.

8.4.5. Summary: Sheet Flexure

In summary, the universal joint sheet flexure was shown to survive the launch loads in both buckling and yield, as well as the operational displacement loads in yield. The *SPACAR* model was verified with good agreement with the results from ANSYS. The accuracy of the *SPACAR* model diminished for the higher order eigenmodes and buckling modes for the low order results as expected, though these are not critical outputs for prototyping the PMAO.

8.5. Universal Joint

This section describes the remaining thermo-mechanical sizing work for the universal joints. The body and interfaces are sized in Subsection 8.5.1. The *SPACAR* model definition is summarised in Subsection 8.5.2. The *SPACAR* and ANSYS verification results are compared in Subsection 8.5.3, followed by a brief conclusion of the universal joint modelling in Subsection 8.5.4.

8.5.1. Initial Sizing

The universal joints were designed so that they could be fabricated monolithically using wire EDM to reduce manufacturing time, cost and assembly errors, increase reliability and improve repeatability compared to multi-part components. Both mechanical and thermal effects were taken into account with the universal joint sizing. They are discussed below.

Mechanical: Interfaces and Body Geometry

A solid model of the joint is shown in Figure 8.8. A circular cross-section was selected for ease of integration with the standard 30 mm diameter circular mechanical interface on the PPA actuators. This is a bolted connection, via four M3 bolts and/ or a single centred M5 bolt. A rule of thumb for designing bolted joints is to have at least 1.5 diameters of thread engagement depth to avoid thread tear-out [24]. To accommodate M3 bolts, the universal joint must have a thickness of at least 4.5 mm at each end. Further detailed design of the interface is a topic for future work. Repeatability of the bolted connections between the joints and actuators would certainly need to be considered.

The two pairs of flexures are connected by an annulus of material at the joint mid-plane. It was assumed that an uninterrupted depth of material equal to the length of each flexure should be maintained at either end of the flexures so that this annulus could be modelled as a rigid body. The length of the joint was dictated by the length of the flexures and the required thickness for thread engagement. The resulting geometry is summarised in Table 8.5 at the end of this sizing exercise. The flexure geometry is taken from Table 8.3. Note that the full 1501 N launch load was applied to the joint.

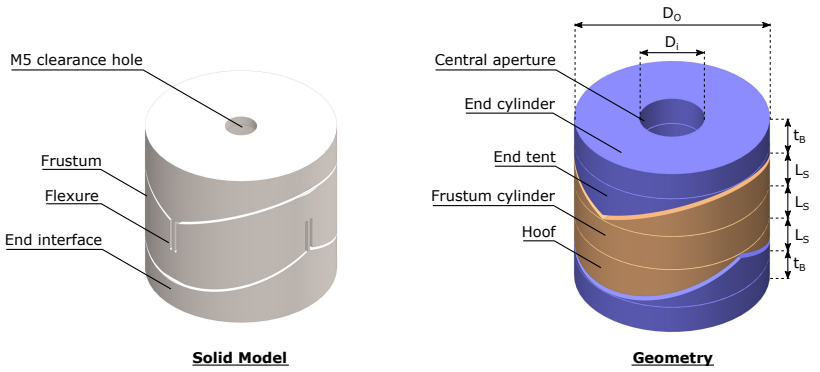

Figure 8.8: Geometric idealisation and parametrisation of universal joint for *SPACAR* analysis. Outer diameter D_O, inner diameter of aperture D_i, height of frustum, frustum hoofs and end tents equal to flexure length L_S, end interface cylinder heights t_B.

Thermal Considerations

It is useful to gain an initial understanding of the thermal characteristics of the joints so that flow-down requirements can be passed on to the thermal control subsystems. Note that thermal uncertainty margins should be applied to the temperatures as necessary, per the *DST Requirements and Verification* guidelines document.

Bulk Temperature Change

The baffle and thermal control system should control the thermal environment around the optics well enough during operations that the components in the PMAO mechanism stay in thermal equilibrium. If that is the case, then stresses from differential bulk temperature changes will be low or almost non-existent. This may not be the case during LEOP when the baffle is stowed, so an estimate of the maximum allowable bulk temperature difference the joint and its surroundings was made.

It was shown in Section 8.3 *Material Selection* that the stress in a clamped structural member due to a change in its bulk temperature ΔT with respect to the surrounding structure is given by

$$\sigma_{bulk} = E\alpha\Delta T \tag{8.36}$$

Temperature gradients from steady state heat sources must also be considered.

Steady State Heat Source

In the absence of additional thermal control equipment, the universal joints act as the sole conductive path from the actuators to the fixed and moving frames. Since the actuators and joints are overconstrained, the worst-case steady state thermal load on a universal joint will be if its mating actuator is powered with the dissipated heat travelling solely via conduction, while the remaining actuators stay cold.

The internal stress from the constrained expansion caused by a steady state heat source through a member can be found via

$$\sigma_{q,ss} = \frac{qL_0E\alpha}{2kA} \tag{8.37}$$

where k is the thermal conductivity of the material, L_0 the initial length and A is the cross-sectional area of the member. This is not a likely scenario during nominal operations, however it is a possible failure mode.

In both the bulk temperature change and steady state heat source cases, the components are put under a compressive load with the flexures liable to buckling first due to their slender cross-section. Thus the thermal stresses will lead to a buckling failure when

$$\sigma_{bulk}A = P_{cr} \quad \text{or} \quad \sigma_{q,ss}A = P_{cr} \tag{8.38}$$

where P_{cr} is the critical Euler buckling load for a beam with fixed/ fixed end conditions given by equation 8.27.

For the universal joint dimensions given in Table 8.5, a temperature difference of 2285 K between the bulk temperature of the flexure with respect to the surrounding structure will lead to buckling failure. Additionally,

the flexures should be able to withstand steady state heat flows of up to 27.4 W. The PPA10XL actuators are expected to dissipate on the order of tens of milliWatts [31].

Neither the bulk temperature change nor steady state heat flow are a problem, even with the qualification thermal uncertainty margins. Transient heat flows from other sources require better definition of the thermo-mechanical environment and are not treated here. They are a topic for future work.

Table 8.5: Design parameters for model of universal joint. SS = steady state.

Parameter	**Value**
Body Geometry	
Length L_B	27 mm
Outer Diameter D_O	30 mm
Inner Diameter D_i	10 mm
Interface thickness (x2) t_B	4.5 mm
Flexure Geometry	
Length L_S	6 mm
Width b_S	10 mm
Thickness t_S	0.5 mm
Material	Ti-6Al-4V
Test Conditions	
Applied launch load F_L	1501 N
Thermal Requirements	
Allowable bulk temp. change ΔT	2285 K
Allowable SS heat flow q_{SS}	27.4 W

8.5.2. *SPACAR* Model Definition

Stresses are transmitted from one pair of flexures to the other via the central frustum cylinder. *SPACAR* is only able to model simple geometric elements, so some simplification of the universal joint geometry was necessary. The interface bolt pattern was ignored, with a constant 10 mm diameter aperture modelled through the whole joint, shown in the right hand frame of Figure 8.8.

The ends and frustum were all assumed to be orders of magnitude stiffer than the flexures, so were modelled as rigid bodies for simplicity. The ends and central frustum were modelled using lumped masses and inertias extracted from the CAD model, listed in Table 8.6. Using the lumped inertia method solves the difficulty of modelling non-standard beam cross-sections in *SPACAR*, however it also means that stresses cannot be calculated in the element. This is no great loss since the critically stressed elements will be the flexures due to their much smaller cross-section. The flexures were modelled per the description in Subsection 8.4.3.

Table 8.6: Mass and inertia properties for universal joint lumped mass modelling in *SPACAR*. Extracted from CAD model of joint with geometry listed in Table 8.5. Coordinates are in the *SPACAR* model global coordinate frame, shown in Figure I.1.

Body	**Mass**	$\mathbf{I_{xx}}$	$\mathbf{I_{xy}}$	$\mathbf{I_{xz}}$	$\mathbf{I_{yy}}$	$\mathbf{I_{yz}}$	$\mathbf{I_{zz}}$
	$[\times 10^{-3} kg]$			$[\times 10^{-9} m/kg^2]$			
Lower end	21.9	1626	0	0	1272	0	2620
Frustum	27.0	2112	0	0	2111	0	3616
Upper end	21.9	1626	0	0	1272	0	2620

The element and nodal setup of the *SPACAR* model is shown schematically in Figure I.1 in Appendix I *SPACAR Model Maps*.

8.5.3. Results and Discussion

This subsection presents the results and discussion for the universal joint *SPACAR* model verification. It starts with a short discussion of the difficulties in generating the ANSYS model, followed by the static, buckling and modal results.

ANSYS Mesh Convergence

Generating a valid mesh within the ANSYS license limits was non-trivial. A mesh convergence study was conducted to ensure that the ANSYS results were as independent of the mesh size as possible, within the license

node limit. The study is documented in Appendix H *Mechanical Design - Supplementary Material*. Ultimately, a quarter model of the joint using spheres of influence over the flexures with 0.3 mm minimum element sizes was used for the modal results. The quarter model gave grossly inaccurate results in the buckling analysis, so an analysis also with spheres of influence over the flexures though with 1 mm element sizes was used to find the critical buckling loads.

The convergence study showed that there was less than a 4% error in the first three eigenfrequency predictions between the 1 mm full and 0.3 mm quarter models which was much less than the expected error between the *SPACAR* and ANSYS models. Therefore it was assumed that the 1 mm full model buckling results would be sufficiently accurate for the *SPACAR* verification.

The results are compared against the *SPACAR* output in Table 8.7. The equivalent stress in the flexures due to deformation during nominal operations was not checked again as the flexure dimensions had not changed from their analysis at the part level in Section 8.4.

Table 8.7: Results of universal joint modelling in *SPACAR* and verification with ANSYS.

Item	***SPACAR***	**ANSYS**	**Error**
Eigenfrequencies			
ω_1	137 Hz	139 Hz	1.0%
ω_2	168 Hz	180 Hz	6.8%
ω_3	706 Hz	693 Hz	1.9%
Critical Buckling Loads			
f_1	318 N	337 N	5.7%
f_2	318 N	339 N	6.1%
f_3	7302 N	7478 N	2.4%
Maximum Launch Stress			
σ_{eq}	150 MPa	205 MPa	27%

Static Analysis Results

The largest stress calculated in *SPACAR* under application of the 1501 N launch load was 150 MPa, simultaneously in each of the four flexures. This was the expected result given the symmetry of the model. ANSYS, however, gave considerably different values.

The left hand frame of Figure 8.9 highlights the presence of a stress concentration at the root of a sheet flexure. It was assumed that since addition of fillets greatly reduces the stress concentration in rectangular flexures [57, 89], a more representative launch stress would be along the centreline of the flexure, shown in the right hand frame of Figure 8.9. Here, the maximum stress was 205 MPa, though still not completely removed from the influence of the stress concentration. This resulted in a large 27% error in the *SPACAR* value. It was concluded that this result would have to be accepted for the preliminary design as *SPACAR* is unable to model fine details such as corner fillets. The static stress analysis results in the integrated assembly verification should therefore be treated as indicative only.

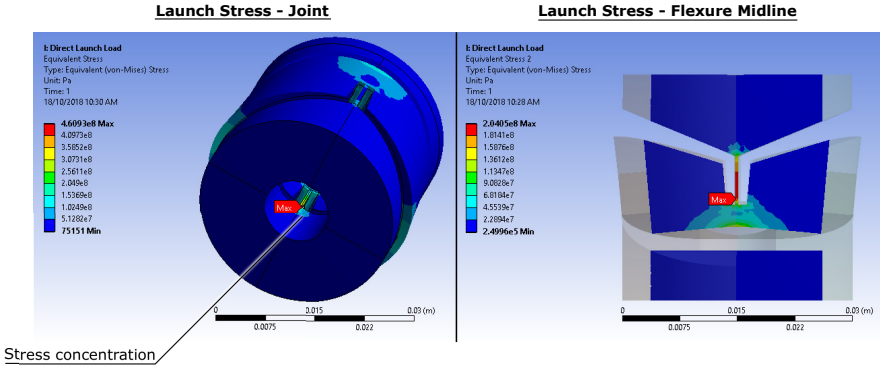

Figure 8.9: Von Mises stress calculation from ANSYS model of universal joint with 1501 N launch load. The left frame shows the full joint highlighting a stress concentration at the root of a flexure, the right frame shows a section through the flexure. Note that different scales are used in each frame.

Buckling Results

The first three buckling modes from both analyses are shown in Figure 8.10. Both models predict a very small or negligible difference in the first two critical buckling loads, which was expected from the symmetry of the joint. Importantly, both analyses predicted that the universal joint would buckle under axial compressive loads less than the expected quasi-static launch load. It will be shown in Chapter 9 *Verification* that the stability of the joints is significantly enhanced by the four actuator stacks acting in parallel at the assembly level, so this was not a concern.

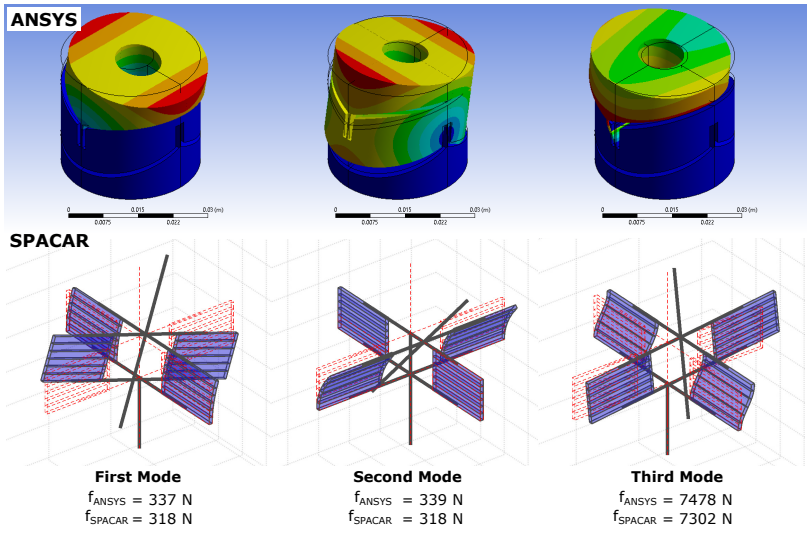

Figure 8.10: Linear buckling analysis results from ANSYS and *SPACAR* for universal joint. Colours in ANSYS results are an indication of displacement, the quantities are unscaled and meaningless. Black lines and dashed red lines in ANSYS & *SPACAR* results respectively indicate non-deformed (non-buckled) state of joint. No beams are visible since the mass properties of the bulk bodies are modelled with lumped mass properties.

Modal Results

Figure 8.11 depicts the first three eigenmodes and frequencies for the universal joint. There was good agreement in the mode shapes between both models which were in line with the expected compliant degrees of freedom of the joint. The *SPACAR* model had excellent accuracy when predicting the fundamental frequency and was only slightly pessimistic for the second eigenfrequency.

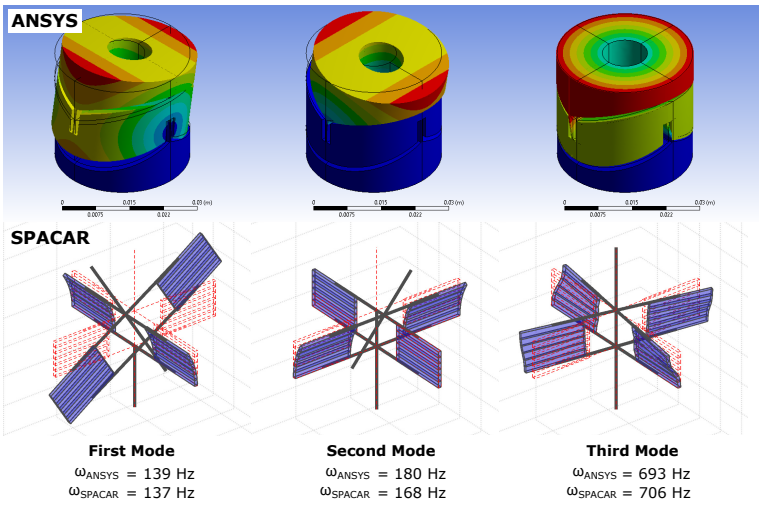

Figure 8.11: Modal analysis results from ANSYS and *SPACAR* for universal joint. Colours in ANSYS results are an indication of displacement, the quantities are unscaled and meaningless. Black lines and dashed red lines in ANSYS & *SPACAR* results respectively indicate resting state of joint. No beams are visible since the mass properties of the bulk bodies are modelled with lumped mass properties.

8.5.4. Summary: Universal Joint

In summary, *SPACAR* was shown to be able to estimate the buckling and dynamic properties of the universal joint with acceptable accuracy. The launch stress prediction was poor, caused by stress concentrations in the ANSYS model which were poorly captured in the *SPACAR* analysis. Regardless, buckling, rather than yield, was found to be the critical failure mode, which was predicted with good accuracy. Conservatism in the input 30g loads and the knowledge that these concentrations would be designed out with the inclusion of fillets (or other flexure profiles) allowed this error to be accepted for the preliminary design.

8.6. Actuators

The PMAO mechanism uses four Cedrat Technologies PPA10XL piezoelectric linear actuators, lightly modified versions of the commercial-off-the-shelf (COTS) Cedrat PPA40XL actuator.

Since no datasheet for the PPA10XL was available, its specifications were scaled from those of the PPA40XL upon recommendation from the supplier [29, 31][6]. The datasheet supplies limited, but critical, information regarding the actuator's performance. The *SPACAR* model is therefore also very simple. The presence of a datasheet with confirmed performance data enabled verification of the *SPACAR* model by comparison with the datasheet, rather than with an ANSYS simulation.

To that end, two *SPACAR* models were developed. The first model simulated the PPA40XL for verification of the *SPACAR* model against the PPA40XL datasheet. The second model utilised the methodology and assumptions verified in the PPA40XL model to create a scaled model for the PPA10XL, to be used later in the integrated PMAO model.

A discussion of the assumptions used to scale the PPA40XL specifications down to the proposed PPA10XL are given in Section 8.6.1. The *SPACAR* modelling methodology and assumptions are detailed in Section 8.6.2, with the results and discussion for both models summarised in Section 8.6.3.

8.6.1. Cedrat PPA10XL Sizing

Table 8.8 summarises the properties necessary to simulate the PPA40XL and PPA10XL actuator models. All of the smaller PPA XL actuators share the same 30 mm diameter form factor. The supplier provided a 20 mm length estimate for the 10 μm PPA 10XL, which was also used to scale the estimated mass of 0.085 kg [31].

Table 8.8: Design parameters for PPA actuator model in *SPACAR*. PPA40XL values from Cedrat [28, 29]. The allowable external load is one third of the blocked force capability.

Parameter	**PPA40XL**	**PPA10XL**
Geometry		
Length L	60 mm	20 mm
Diameter D	30 mm	30 mm
Dynamic Properties		
Mass m	0.254 kg	0.085 kg
Axial stiffness k	155×10^6 N/m	155×10^6 N/m
Test Conditions		
Blocked force capability	6653 N	6653 N
Allowable external load	2218 N	2218 N

Inspection of the extended Cedrat catalogue [28] shows that the axial stiffness of the PPA actuator family increases as the overall length decreases. In terms of dynamic requirements, a stiffer actuator is better as it will have a greater fundamental frequency and bandwidth. In the absence of a verified stiffness for the PPA10XL, the 155×10^6 N/m axial stiffness of the PPA40XL was conservatively used instead. The blocked force and allowable external load were also taken from the PPA40XL specifications. Recall from Subsection 7.3.2 *Launch Loads on the Actuators* that the allowable external load is approximately one third of the actuators' blocked force capability.

Finally, the actuator was modelled assuming that the output stroke was independent of the driven load. This is not true for an unmodified piezoelectric ceramic stack wherein the output displacement decreases as the driven load increases (ie. when driving a spring). It was assumed that since the ceramic stack in the PPA actuator is pre-loaded by a very stiff external spring (the external metallic frame, see Figure 6.22), that

[6]The fixed-free fundamental frequency of the PPA40XL is given in the full Cedrat catalogue [28].

this effect could be considered negligible. It will also be shown in Subsection 9.4.5 *Workspace Definition Verification & Actuator Performance* that the driven loads are on the order of tens of milli-Newtons, far below the maximum capability of the actuators.

8.6.2. *SPACAR* Model Definition

Given the lack of information available to fully characterise the static and dynamic properties of the actuator, the *SPACAR* model could only be expected to provide a first order estimate of its performance. To that end, the PPA actuator was idealised as a one dimensional spring, modelled in *SPACAR* as a single spatial beam with circular cross-section.

Since the axial stiffness was the only known stiffness of the actuator, only the elongation deformation mode was released. The mass was assumed to be homogeneously distributed along the cylinder length. Figure 8.12 shows this simple model with a small elongation from its nominal position.

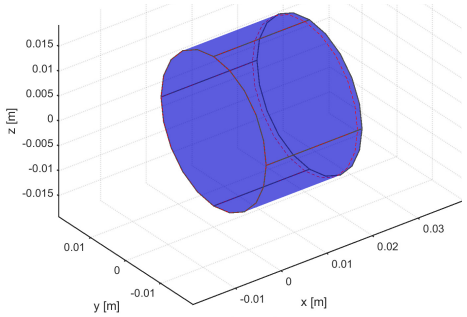

Figure 8.12: Structural model of the PPA10XL actuator in *SPACAR*. A single spatial beam element with cylindrical cross-section was used. The elongation was controlled as a user input. The figure shows elongation of the actuator. The undeformed geometry is depicted by dashed red line. $L = 20\ mm$, $D = 30\ mm$.

To model the first order dynamic behaviour of the actuator, *SPACAR* required specification of the Young's modulus and density. An average density was calculated from the mass and geometry in Table 8.8. An approximation of the stiffness k of a beam with uniform cross-section can be found using beam theory via

$$k = \frac{EA}{L} \tag{8.39}$$

The "equivalent" Young's modulus E for a beam with cylindrical cross-section was then calculated from the parameters in Table 8.8. Since bending and torsion deformations were not considered in the actuator model, the shear modulus G was set to zero and shear effects were not considered. Similarly, since torsion was ignored there was no need to consider the effects of constraint warping.

8.6.3. Results & Discussion

The results are summarised in Table 8.9. As a short, squat column, the actuator was not expected to be susceptible to buckling, so that analysis was not conducted. The only failure checks made for the actuators in the integrated model were that the blocked force (ie. driving force) capability of the actuator was not exceeded by the force needed to drive the mechanism, and that the external load on the actuators did not exceed one third of this capability.

Table 8.9: Results of the actuator modelling in *SPACAR* and verification by comparison with Cedrat PPA40XL datasheet [28, 29].

	***SPACAR* PPA40XL**	**Cedrat PPA40XL**	**Error**	***SPACAR* PPA10XL**
First Eigenfrequency ω_1	$6.81\ kHz$	$6.80\ kHz$	0.15%	$11.79\ kHz$
Mass	$0.254\ kg$	$0.254\ kg$	0.00%	$0.085\ kg$
Longitudinal Stiffness	$155\times10^6\ N/m$	$155\times10^6\ N/m$	0.00%	$155\times10^6\ N/m$

PPA40XL Verification Model

The modal analysis reported a fundamental frequency of $6.81\ kHz$, corresponding very well to the blocked-free (ie. fixed-free) resonant frequency of $6.80\ kHz$ reported in the Cedrat catalogue [28]. Since *SPACAR* also

uses beam theory to model deformations, a check of the stiffness of the beam in its single elongation DOF yielded the trivial and expected result of $155\times10^6\ N/m$, identical to that used to back-calculate the equivalent Young's modulus. It was concluded that the simple beam model with a single elongation deformation mode was able to reliably reproduce the expected first order behaviour of the actuator.

PPA10XL Model

With the scaled down length and mass for the PPA10XL, *SPACAR* reported a resonant frequency of 11.79 kHz. The fundamental frequency, in Hertz, of a cantilevered beam is given by

$$f_n = \frac{1}{2\pi}\sqrt{\frac{k}{m}} \tag{8.40}$$

It is no surprise then, that since the same stiffness k was used, and the mass m scaled by a third compared to the PPA40XL model, that the estimated resonant frequency of the PPA10XL model was approximately a factor $\sqrt{3}$ greater than the PPA40XL value.

Note that since the actuator is modelled as a unidirectional spring, that its first eigenmode is a longitudinal oscillation. If it were modelled as a three dimensional beam, the first mode would be in bending as depicted in the first mode of Figure 8.6. This may, or may not, accurately reflect the true first mode of the PPA10XL and will need to be confirmed in future work via input from the supplier, or from detailed modelling and/ or testing of the PPA10XL.

8.7. In-plane Constraints and Moving Frame

The moving frame assembly consists of a central annular or circular plate and three pairs of in-plane constraint flexures.

The moving frame plate provides an interface for the mirror support bipods, actuator stacks and in-plane constraints. It should isolate the mirror from the bulk of the actuation loads, with the bipods providing further isolation from differential strains between the moving frame and mirror.

The in-plane constraints are the physical embodiment of the passive constraint set, allowing the tip, tilt and & piston freedoms of the moving frame plate. The entire moving frame was designed so that it could be fabricated monolithically with high precision milling and wire electro-discharge machining (EDM). The plane of the constraints defines the moving frame coordinate frame $\mathbf{O_{MF}}$ about which the entire mechanism is manipulated.

The moving frame plate and in-plane constraints are sized in Subsections 8.7.1 and 8.7.2 respectively. Initial estimates of thermal survival flow down requirements are also made. The *SPACAR* models are defined in Subsection 8.7.3. Results and discussion are given in Subsection 8.7.4. The section concludes with a short summary in Subsection 8.7.5.

8.7.1. Initial Sizing: Moving Frame Plate

The main mechanical functions of the moving frame plate include:

1. Provide an interface to mount the actuator stacks, support bipods and in-plane constraints.
2. Isolate the support bipods & mirror from the actuation loads.
3. Survive launch: transfer in-plane loads to in-plane constraints and out of plane loads to actuator stacks.

Each of these functions influence the geometry of the plate. For a mass efficient design that can be assembled and reassembled repeatably, the plate will likely have quite a complex geometry. This work was left to future detailed design. The design philosophy adopted here was to provide an initial crude estimate of the major dimensions based on the launch loads and the basic functional requirements listed above. These are discussed in more detail below. Thermal considerations for the plate are dependent upon, and discussed after, sizing of the in-plane constraints in Subsection 8.7.2.

Interfaces: Layout Geometry

The in-plane constraint flexures are positioned on the vertices of the equilateral triangle circumscribed by the periphery of the plate, ideally providing ample room to house the actuators and supports. A sketch of the moving frame plate geometry, mirror support, in-plane support flexures and out of plane support actuator interfaces is shown in Figure 8.13. Although an annulus could have been modelled, a plate was used instead to give a larger mass and thus more conservative estimate of the dynamic performance.

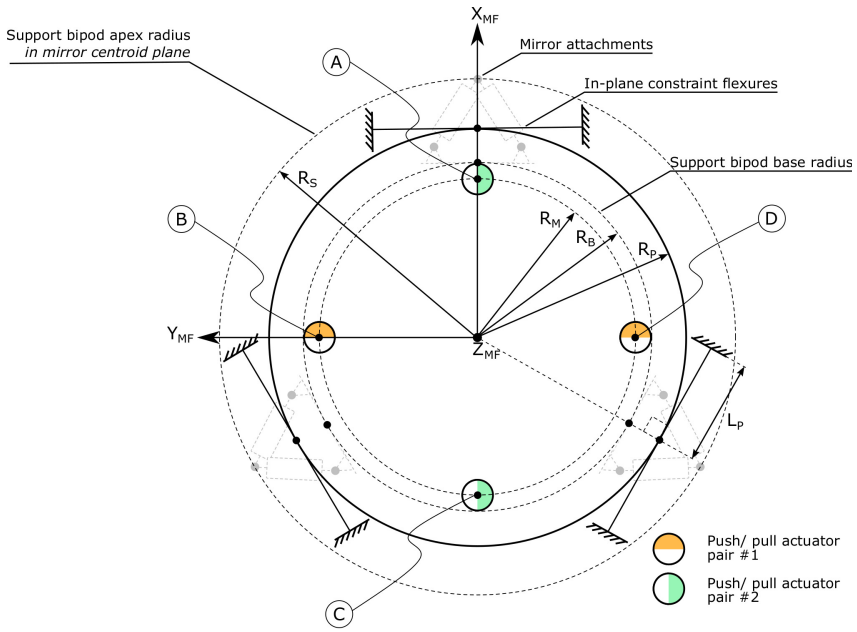

Figure 8.13: Moving frame geometry. The in-plane constraint flexures are oriented tangentially at radius R_P, the actuators are mounted at radius R_M and bipods at base radius R_B in the plane where they interface with the moving frame. The apex of the support bipods must be on radius R_S in the plane of the mirror centroid. The four actuator/ universal joint stacks are identified by circled letters.

Interfaces: Mirror Support Radius

Note that the radius R_B upon which the bipods interface with the moving plate does not necessarily coincide with the radius of their apices R_S. The support bipods could therefore be vertical or canted at an angle with respect to the vertical, possibly conflicting with the actuator stacks. An estimate of the mirror support radius R_S was needed.

Finding the optimum support radius with the non-standard geometry of the M1 segments depended upon a relatively detailed analysis of the mirror design, which was excluded from the scope of this thesis. An initial estimate was taken from the case of a circular mirror with uniform thickness and no occlusions. Yoder & Vukobratovich show that for such a mirror with radius R, the peak to valley surface deflection can be minimised in the presence of gravity by equally spacing the support/ mirror attachments at a radius of $0.645R$ [125, p159]. This is not so much of a problem in space, but it provides a helpful first estimate for R_S.

The mirror segments are rectangular with side lengths 620×450 mm. Taking the inscribed circle with diameter 450 mm, the Yoder & Vukobratovich relation gives a nominal support radius R_S of 145 mm. At this radius, the bipod apices will likely lie outside of the moving frame radius as shown in Figure 8.14.

Interfaces: Usable Volume

Figure 8.14 shows the range of allowable heights of the moving frame origin $\mathbf{O_{MF}}$ within the usable volume based on the universal joint and actuator geometry sized in the previous sections. Two 15 mm buffers at the DST housing wall and the M1 backplane reserve space for interfaces to the mirror and DST housing. Volume reserved for the stowed M2 booms is also shown, along with the position of the current M1 deployment mechanism support frame. The location of this frame is shown for reference and was not considered a critical input to the usable volume since the PMAO fixed frame can be recessed into the deployment support frame.

The black actuator stacks and moving frame indicate the case with the actuators hard up against the upper buffer zone, giving the smallest allowable height h. The greyed design shows the opposite case with the largest allowable height of the moving frame.

The maximum allowable radius R_{max} of the moving frame as a function of the distance h from the mirror centre of mass is given by

$$R_{max}(h)[m] = 0.125 + 0.12 + q - h - 0.015 \tag{8.41}$$

This relationship is dependent upon the desired buffer zone depth and DST housing geometry. The maximum allowable radii for the various moving frame appendages for the maximum and minimum allowable

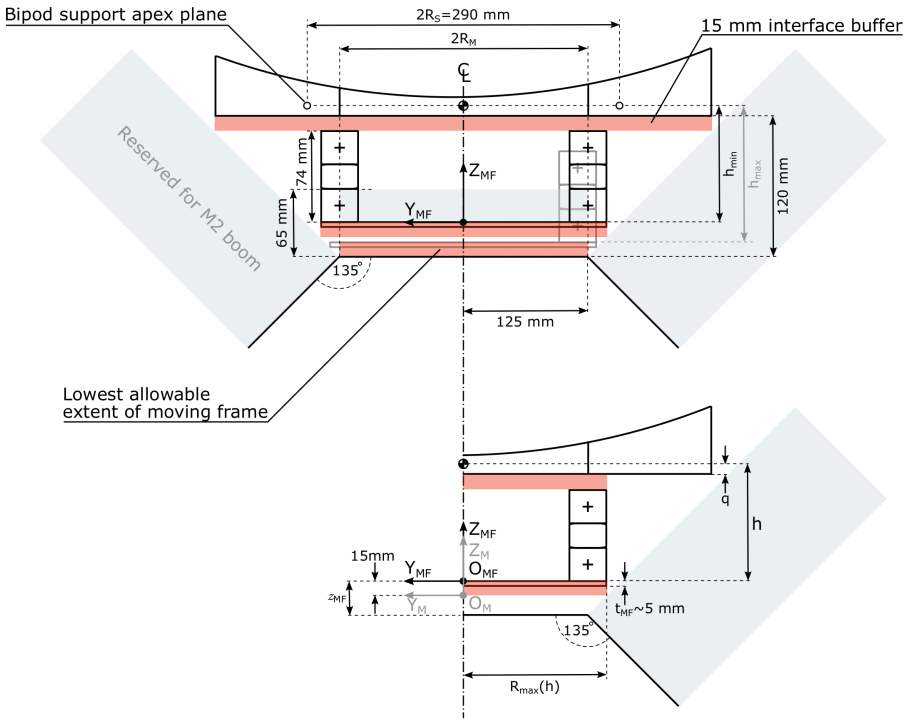

Figure 8.14: Usable volume for the moving frame in the stowed configuration. Light blue rectangles indicate volume occupied by deployment mechanism support frame and stowed M2 booms. Thin red shaded regions are buffer zones to provide space for interfaces and thickness of the moving frame & fixed frame. Minimum and maximum values for h along with the absolute maximum allowable radius R_{max} for all parts at those heights, are given in Table 8.10. The actuator stacks, in their current design, are 74 mm high. The fixed mechanism coordinate frame $\mathbf{O_M}$ shown in the lower figure, resides at the lowest extremity of the reserved volume for the PMAO, 15 mm below the moving frame origin $\mathbf{O_{MF}}$. The distance between the mirror COM and the backplane q is governed by the mirror design.

height h are summarised in Table 8.10. The bipod mounting radius R_B is sized in the next section so has not been included.

Table 8.10: Summary of maximum allowable moving frame appendage radii. See Figures 8.13 and 8.14 for definition of parameters. $R_{P,max}$ assumed equal to R_{max}, $R_{M,max}$ calculated assuming 30 mm diameter universal joint interface, R_S was fixed as discussed in the text. q was taken from the M1 mirror segment design at the time of writing.

	h [mm]	**z_{MF}** [mm]	**q** [mm]	**R_{max}** [mm]	**$R_{P,max}$** [mm]	**$R_{M,max}$** [mm]	**R_S** [mm]
h_{min}	118	31	28.8	141	141	126	145
h_{max}	134	15	28.8	125	125	110	145

Stiffness: Isolation of Mirror from Actuation Loads

The primary stiffness criteria for the plate is that it should not deform excessively under the influence of the actuation loads during operations. Since it is overconstrained by the four actuator stacks, it must also provide a repeatable assembly method so that the effects of small, undesired deformations caused by the overconstrained condition can be reliably calibrated out. For the purposes of preliminary design, it was assumed that this is technically possible and not considered further.

Standard solutions for the deflection of circular plates are well publicised for uniform, axisymmetric boundary conditions and loads, but calculation of the stress distribution for concentrated, eccentric non-uniform loads with non equi-spaced supports is non-trivial. The standard solution method is to use superposition and numerical or iterative approaches [128, p. 439] which were beyond the scope of this preliminary sizing exercise.

To simplify the design and analysis, the plate was assumed to be rigid in the *SPACAR* and ANSYS analyses. The verification results in Subsection 9.4.5 *Workspace Definition Verification and Actuator Performance* will show that the actuation loads should be no more than several tens of milli-Newtons, so this is not considered

a difficult design task. The plate thickness was roughly sized to survive the launch loads and provide a mass estimate. This is discussed in the next subsection.

Strength: Launch Survival

A minimum plate thickness was estimated using a very crude but conservative model of the plate during launch. The moving frame was modelled as a circular plate with uniform cross-section, simply supported around its edge as shown in Figure 8.15. Out of plane and in plane launch loads were applied simultaneously resulting in force F_L and moment M_L.

Roarke [128] gives analytical equations to approximate the maximum bending stresses in a plate for each of these load cases, to be added via superposition to find the resulting stress. The peak stress occurs in the centre of the plate, where the loads are applied.

The support condition was not a good reflection of the supports in reality, as the continuous support distributes the stresses more evenly. However, it is expected that the peak stresses would still be in the centre of the plate. Again, it is reiterated that this is a crude model used as a sanity check for the plate thickness necessary to survive launch.

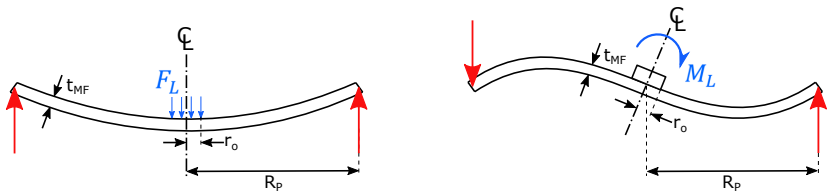

Figure 8.15: Load cases for crude sizing of moving frame plate thickness, a circular plate with radius R_P and uniform thickness t_{MF} simply supported about its circumference. Load and moment applied over a small central area of radius r_o. Adapted from [128].

It was assumed that the loads were applied to the plate over a pad fixed to the centre of the plate with radius $r_o = 5\ mm$, indicative of the foot of a small support bipod, for example. Decreasing this radius increases the stress concentration and makes for a more conservative estimate. The load $F_{L,O}$ and moment $M_L = F_{L,I}\,h$ are taken from $30g$ acceleration of the 6 kg mirror as in Chapter 7 *Mechanism Architecture Selection*, where the subscripts *I,O* indicate an in or out of plane load.

The approximate maximum bending stresses in the plate are given by [128, p. 491, 493]:

$$\sigma_{O,max} = \frac{3}{2}\frac{F_{L,O}}{\pi t_{MF}^2}\left((1+\nu)\ln\frac{R_P}{r_o}+1\right) \tag{8.42}$$

$$\sigma_{I,max} = 9.478\frac{F_{L,I}\,h}{R_P\,t_{MF}^2} \tag{8.43}$$

The maximum bending stress from the out of plane load $\sigma_{O,max}$ occur at the centre of the plate, whereas the maximum stress from the in plane load $\sigma_{I,max}$ occur at the edge of the pad. Since the plate has quite a large diameter, the tensile and compressive stresses from in-plane launch loads were considered negligible compared to the bending stress generated in the plate by the out of plane load[7]. A rough, conservative estimate for the required thickness t_{MF} to prevent yield failure was found by summing the two bending stresses.

The resulting total stress is inversely proportional to the plate radius. The worst-case loading condition occurs for the largest allowable height h of 134 mm and smallest likely diameter 125 mm. A 5.00 mm plate thickness results in a combined bending stress of 896 MPa, giving a 0.18 margin of safety against yield failure. In reality, the launch loads are distributed around the plate, which is a more favourable loading condition.

The moving frame plate radius R_P was set to 125 mm so that some design flexibility was retained to size the bipods. The resulting mass of the plate was 1.08 kg.

With the plate radius sized, the in-plane constraint flexures were designed per the process in the next subsection.

[7] For example, recall that eight flexures with only 0.5 mm by 10 mm rectangular cross-sections were able to withstand the out of plane launch loads.

8.7.2. Initial Sizing: In-plane Constraint Flexures

Wire flexures or struts were selected in Section 6.4 *Passive Constraint Redundancy Trade-off* for the in-plane constraints. This subsection documents the sizing of the wire flexures, which were found to be adequate.

The subsection begins with a brief introduction to the phenomenon of stress stiffening which can degrade the performance of parallel flexure arrangements like the in-plane constraints. The design philosophy is then set out, followed by calculation of the launch loads, the mechanical dimensions and thermal considerations for both the in-plane constraints and moving frame.

Stress Stiffening

Large displacements of single beam compliant elements can cause stress stiffening, which is an increase in the stiffness of the member as a result of an increase in its stress state [68]. An example is shown in Figure 8.16*b*. The use of single beams mirrored about the driving direction is similar to the mirror symmetry of the in-plane constraints.

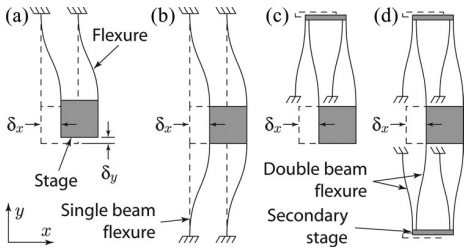

Figure 8.16: Examples of single and double beam flexure guiding arrangements. a) Two single beams; b) Four single beams in symmetric pairs; c) Double parallelogram flexure guide and d) Two double parallelogram flexure guides in symmetric pairs. Note the parasitic motion δ_y in arrangement a). Arrangements a) and b) are susceptible to stress stiffening for large displacements whereas arrangements c) and d) allow large displacements at the cost of decreased out of plane stiffness. Adapted from [68].

Stress stiffening can limit the intended range of motion of the element and increase the required driving force. If the stiffening is too great, alternative arrangements such as those shown in Figure 8.16*c* and *d* can be used. However, additional beams in series diminish the out of plane stiffness, degrading the decoupling between constrained and free DOFs as well as the resonances [68] which is strongly undesirable for the PMAO.

Since the piston motions are on the order of 10^{-6} m and the flexure dimensions are on the order of 10^{-3} to 10^{-2} mm, it was assumed that stress stiffening of the flexures would be negligible [68].

Design Philosophy

When sizing the universal joint sheet flexures, it was found that the launch loads strongly dominated the design criteria. Since the dimensions, range of motion and imposed loads of the in-plane constraints were all of similar orders of magnitude to those of the universal joint flexures, it was assumed that the launch loads would also dominate their design.

Thus the design philosophy was to size to survive launch, accept the resulting stiffness of the flexures and check that the actuators were able to displace them at the integrated mechanism level further on in the design process. Initial thermal flow-on requirements for survival of the flexures were also calculated. The actuation loads calculated in Subsection 9.4.5 *Workspace Definition Verification & Actuator Performance* later verified this method.

Strength: Launch Survival

The worst-case load condition for the in-plane constraints occurs when both the X_{MF} and Y_{MF} in-plane launch loads are applied simultaneously. The resulting free body diagram is depicted in Figure 8.17.

The wire flexures were approximated by a slender prismatic strut with square cross-section of side length b_P and length L_P. Ideal wire flexures are only able to transmit axial loads, so they were modelled as rigid links with pinned connections at either end. The overdetermined system was simplified to a statically determinate system by assuming that the constraint in each pair that was placed under tension in each load case, would take the full launch load.

Assuming quasi-static equilibrium, the loads reacted by the flexures in the directions indicated in Figure 8.17 were then

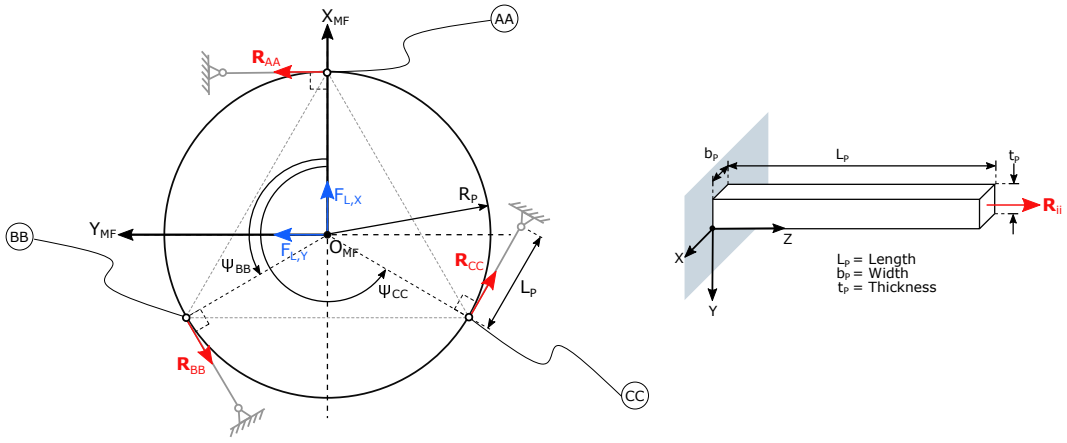

Figure 8.17: Force body diagram (FBD) of the launch loads imposed on the in-plane constraints via the moving frame. A single indicative load case is shown. The flexure attachments to the moving frame are identified by the circled letters. The greyed flexures are not included in the FBD but shown for illustrative purposes.

$$\mathbf{R_{AA}} = -\frac{2}{3}\mathbf{F_{L,y}} \tag{8.44}$$

$$\mathbf{R_{BB}} = \frac{1}{3}\left(\sqrt{3}\mathbf{F_{L,x}} + \mathbf{F_{L,y}}\right) \tag{8.45}$$

$$\mathbf{R_{CC}} = \frac{1}{3}\left(-\sqrt{3}\mathbf{F_{L,x}} + \mathbf{F_{L,y}}\right) \tag{8.46}$$

The greatest load is seen variously by flexures *BB* and *CC* depending on the orientation of the orthogonal launch loads $\mathbf{F_{L,x}}$ and $\mathbf{F_{L,y}}$. Since the constraints take only axial loads, the stress state is given by equation 8.25. Using the design criteria in equation 8.23 to prevent yield failure, the minimum required width b_P of the square cross-section wire flexures was found with

$$b_P = \sqrt{\frac{|\mathbf{R_{ii,max}}|}{S_Y}} \tag{8.47}$$

where $\mathbf{R_{ii,max}}$ is the largest force to be reacted by one of the constraints over each combination of orthogonal in-plane launch loads, given by equations 8.44 to 8.46. Taking the yield strength of Ti-6Al-4V from Appendix K *Material Properties*, the minimum flexure width was found to be $b_P = 1.24\ mm$.

Ultimately, this method was not conservative enough. Initial results from the *SPACAR* modelling, documented in Subsection 8.7.3, indicated that the wires would buckle under the launch loads. A satisfactory design was quickly found with a few rounds of trial and error using the *SPACAR* model, highlighting its value in rapid prototyping new designs. More detail is given in Subsection 8.7.3.

Stiffness: DOF Decoupling

The stiffness criteria for the in-plane constraints was to have a much higher axial stiffness than out of plane bending stiffness, to decouple those degrees of freedom. Twist of the wires is a much smaller motion compared to bending so compliance in that freedom was neglected.

To sufficiently decouple the degrees of freedom of a rigid body, the ratio of the stiffness in the desired constraint direction to that of the desired DOF should be at least on the order 10^3. For mechanisms requiring performance at the nanometre level, the decoupling should be on the order of 10^4 to 10^5 [126, p. 566]. The axial and bending stiffnesses of a constant cross-section beam are

$$k_{axial} = \frac{EA}{L} \qquad k_{bending} = \frac{12EI}{L^3} \tag{8.48}$$

Taking the ratio of stiffness equations 8.48 shows that the length of the beam should be no less than ≈ 30 times the width and ideally greater than ≈ 300 times the width to adequately decouple the axial and transverse degrees of freedom.

For a square section with side length 1.24 mm, the flexure must have a length of at least ≈40 mm to provide the minimum desired separation. A length of 120 to 400 mm would be ideal, but impractical given the volume constraints. This is a good example of the challenging need to design a structure strong enough to withstand launch yet fit in a small package and still provide high accuracy at nanometre length scales.

It was decided to continue with the 40 mm long flexures to make sure that the volume requirements were met, thus accepting that the DOFs may not be sufficiently decoupled.

Thermal Considerations: In-Plane Constraints

The in-plane constraints are one of two structural heat conduction paths from the mirror through the mechanism to the fixed frame. Since heat will be flowing from one end of the flexure to the other, there will be a temperature gradient across its length. The flexures were overconstrained by design so this gradient will give rise to internal stresses and eventually buckling or yield.

The same thermal design checks using equations 8.37, 8.38 and 8.27 for the universal joint flexures in Section 8.5 were repeated again for the in-plane constraints. The results are given in Table 8.11 at the conclusion of this moving frame and wire flexure sizing exercise.

Thermal Considerations: Moving Frame Plate

A change in the bulk temperature of the plate drives a thermo-elastic strain about the thermal centre defined by the in-plane constraints. This strain can be accommodated by deflection of the constraints so long as they remain in their elastic region. Thus there is a maximum allowable change in temperature ΔT of the plate with respect to the surrounding structure that must not be exceeded. The mechanism is immune to this failure mode if all components are at the same bulk temperature and made of the same material.

The stress in a beam as a function of a transverse displacement δ_Y at its tip was given by equation 8.21. The radial strain of a point on a circle due to a change in temperature ΔT is given by $\Delta R = R_0 \alpha \Delta T$. Equating the two equations and taking the yield strength as the failure criterion gives the maximum allowable temperature change of the plate:

$$\Delta T = \frac{2}{3} \frac{S_Y L^2}{E R_0 t \alpha} \tag{8.49}$$

where R_0 is the initial radius, L is the length of the beam and t is the dimension of the beam in the direction of the radial growth. This equation was applied for both the in-plane constraints and universal joint flexures. The results are listed in Table 8.11.

No flow down requirement for the maximum allowable steady state heat flow through the plate is given since the plate has a very large thermal capacity compared to the universal joint and in-plane constraint flexures. They are expected to fail before the plate.

8.7.3. *SPACAR* Model Definition

The *SPACAR* model was defined using the geometry in Table 8.11. The moving frame plate was modelled as a rigid beam per the assumption that this condition could be achieved in detailed design. Each wire flexure was modelled similarly to the sheet flexures of the universal joint with the exception that constraint warping was not considered due to the high aspect ratio of the wires. The longitudinal axes of the wire flexures were modelled in the plane of the plate. The layout and geometry is shown in Figure I.2 in Appendix I.

Initial results suggested that the wire flexure design developed from the hand calculations in Section 8.7.2 was inadequate, with a critical buckling load of 1667 N. Considering only the mirror mass, the compressive load on a wire flexure for launch accelerations along its axis will be at least $30 g m_M$ = 1766 N. Assuming that the wires could be sized without considering buckling was evidently incorrect. The purpose of the hand calculations was only to provide initial sizings, and as a sanity check on the modelling results. *SPACAR* was used to find a revised design.

Trial and error with the *SPACAR* model allowed a very quick fix: increasing the thickness of the flexures to 1.4 mm gave a critical buckling load of 2124 N. The length of the flexures was increased to 45 mm to ensure the minimum decoupling of the axial and transverse stiffnesses, and the thermal flow down calculations were repeated.

The critical failure mode for the moving frame plate thermal expansion was found to be yield of the universal joint flexures at a temperature increase of 402 K. The critical failure mode for the wire flexures due to a temperature difference was buckling at 318 K. Similarly for a steady state heat flow of 0.2 W.

Table 8.11: Summary of moving frame & in-plane constraint design parameters. No out of plane launch loads are applied since the moving frame plate is assumed to be rigid and the in-plane constraints do not experience out of plane loads.

Parameter	**Wire Constraints**	**Moving Frame**
Plate Geometry		
In-plane Constraint Radius R_P	-	125.0 mm
Actuator Mounting Radius R_M	-	110.0 mm
Thickness t_{MF}	-	5.0 mm
Constraint Geometry		
Length L_P	45.0 mm	-
Width b_P	1.4 mm	-
Thickness t_P	1.4 mm	-
Material	Ti-6Al-4V	
Test Conditions		
Applied launch load F_L	$30gm_M$ in X_{MF} and Y_{MF} directions	
Maximum displacement δ_Z	$4\mu m$	
Thermal Requirements		
Allowable bulk temp. increase ΔT	318 K	402 K (for uni joint)
Allowable SS heat flow q_{SS}	0.2 W	N/A

The thermal calculation in Appendix C estimated the worst-case steady state temperature of the M1 subsystem during LEOP. The largest departure from the assumed assembly temperature of 298 K is 135 K to the cold case, including the 25K qualification thermal uncertainty margin per Table 3.4. In the worst-case scenario where one end of a flexure is at the steady state cold case temperature and the other at the hot case temperature, the difference would be 246 K, again including the qualification uncertainty margin.

Additionally, the actuators are not expected to dissipate more than tens of milliWatts during steady state quasi-static operation [31]. Conservatively assuming a power dissipation of 200 mW per actuator and assuming that all heat is transferred through the in-plane constraints to the fixed frame, this equates to a steady state heat flow of 0.134 W per wire flexure.

It was therefore concluded that the moving frame and wire flexures should survive LEOP.

8.7.4. Results and Discussion

The presence of a rigid body in the ANSYS model complicated the verification analysis. This is described in more detail below. The *SPACAR* model verification results are discussed thereafter.

ANSYS Model Definition

The ideal beam geometry used in *SPACAR* was modified so that the wire flexures were connected to the plate using fillets as illustrated in Figure 8.18. Small sectors of the plate were removed in the region of the flexures so as not to excessively reduce their effective length. The good agreement between the ANSYS and *SPACAR* predictions of at least the first eigenfrequency demonstrate that this condition was achieved.

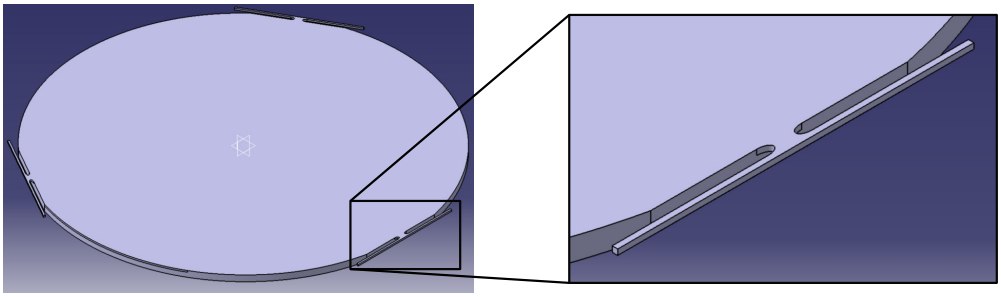

Figure 8.18: Model of moving frame and wire flexures for ANSYS verification analysis. The neck is approximately 5 mm long at the thinnest point.

For the modal analysis, the plate behaviour was set to rigid to reflect the settings in *SPACAR*. Therefore, only the wire flexures were meshed. Approximately 13,000 nodes at an element size of 1 mm were sufficient to find a mesh-converged solution.

ANSYS is not capable of linear eigenvalue buckling analysis for systems including rigid bodies. Additionally, forces cannot be applied to rigid bodies in ANSYS. An alternative method could have been to model the beam as a flexible body with a Young's Modulus four or more orders of magnitude greater than the Titanium flexures, however this gave erratic results with sporadic errors. Therefore the buckling results could not be verified. As with the *SPACAR* model of the integrated assembly, the quality of the in-plane constraint buckling results had to be extrapolated from the verification results of the other models.

For the direct launch load the plate was suppressed and a remote force applied at the moving frame coordinate system origin. The force was equivalent to the load from simultaneous 30g accelerations of the mirror in the X_{MF} and Y_{MF} directions. The equivalent stress was extracted along the midline of the flexure to avoid the stress concentrations near the connection of the flexure to the plate. The peak stress in the direct launch load was found in flexure *BB* in ANSYS, as it was in *SPACAR*. Large deflection mode was turned on.

For the nominal operations deformation case, a remote in-plane displacement was applied instead of a remote force. Equivalent stress in the flexures during the maximum nominal piston displacement of 4 μm was found.

The results from the *SPACAR* analyses and ANSYS model verification are summarised in Table 8.12.

Table 8.12: Results of the moving frame & in-plane constraint modelling in *SPACAR* and verification with ANSYS. The buckling loads are for buckling in the plane of the moving frame. Negative values indicate opposite direction to positive values.

Item	***SPACAR***	**ANSYS**	**Error**
Eigenfrequencies			
ω_1	26.1 Hz	27.7 Hz	6%
ω_2	474 Hz	40.3 Hz	1076%
ω_3	474 Hz	40.4 Hz	1075%
Critical Buckling Loads			
f_1	-2124 N	-	-
f_2	2124 N	-	-
f_3	2159 N	-	-
Maximum Launch Stress			
σ_{eq}	426 MPa	487 MPa	13%
Max. Displacement Stress			
σ_{eq}	0.95 MPa	1.07 MPa	11%

Buckling Results

Results for the *SPACAR* linear buckling analysis are shown in Figure 8.19. The first in-plane buckling modes occur when the in-plane load is parallel to the axis of a wire flexure with a critical load of 2124 N. The second mode equates to the same buckling motion with a load in the opposite direction. The flexures were predicted to survive launch, though this couldn't be verified in ANSYS, as mentioned earlier.

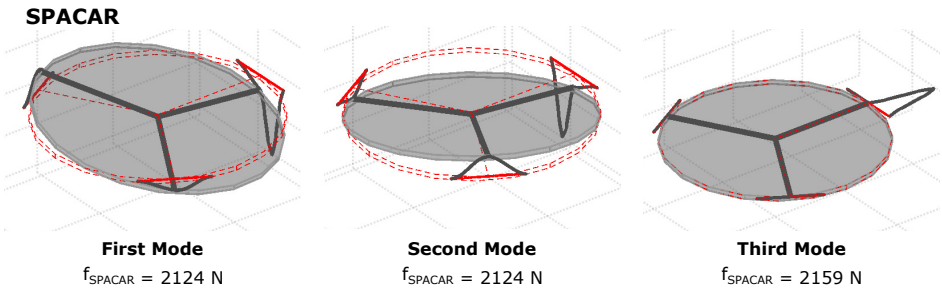

Figure 8.19: *SPACAR* eigen buckling analysis results for moving frame and in-plane constraints for in-plane loads. Displacement exaggerated for illustration purposes, the scale is non-dimensional. Buckling analysis for systems including rigid bodies is unavailable in ANSYS.

Modal Results

A comparison of the modal results is illustrated in Figure 8.20. As expected, the first three modes in both analyses equate to the piston, tip and tilt DOFs. Similarly, the eigenfrequencies of the tip and tilt modes were very closely matched in both analyses, a result of the symmetry of those modes.

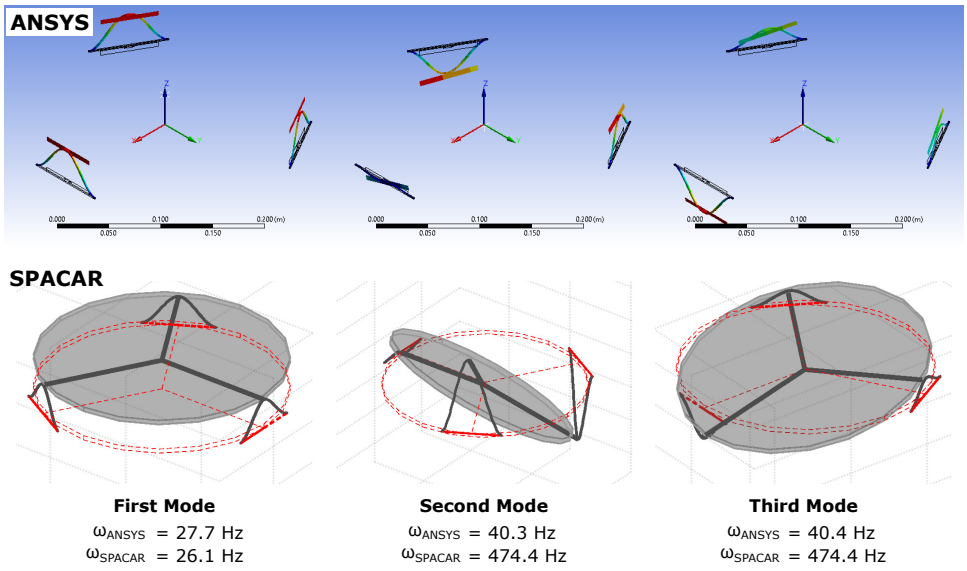

Figure 8.20: *SPACAR* and ANSYS modal analysis results for moving frame and in-plane constraints. Displacement exaggerated for illustration purposes, colouring is non-dimensional. Rigid bodies are unavailable in ANSYS for visualisation of modal results so the plate is not shown in the top row of results.

The first eigenfrequency is very low in the piston direction, far below the requisite 100 Hz. This is rectified later in the integrated model with the addition of the actuator stacks which are very stiff in this direction.

ANSYS predicted much lower eigenfrequencies for the second and third modes than that of *SPACAR*. The difference between the two analyses could not be explained. Modelling the wires in *SPACAR* with more elements, including constraint warping and permitting all deformation modes did not change the results. The largest difference between the two models is the presence of the elliptical fillets in ANSYS. It is not clear that they should cause more than an order of magnitude decrease in the second and third eigenfrequencies compared to *SPACAR*, as they decrease the effective length of the wires and would therefore be expected to increase these frequencies.

Regardless, the most important result is prediction of the fundamental frequency, which *SPACAR* did well with an error of 6%.

Static Analysis Results

Displacement during nominal operation was clearly not a limiting factor for strength. Each of the wire flexures experiences the peak launch stress depending on the direction of the in-plane launch loads. *SPACAR* predicts both the launch and displacement stresses to the correct order of magnitude, however the error was larger than desired, once again due to stress concentrations in the ANSYS modelling.

8.7.5. Summary: In Plane Constraints & Moving Frame

In summary, *SPACAR* does a moderately good job of predicting the launch and deformation stresses. The first three eigenmodes were the same as those found in ANSYS and the first eigenfrequency was predicted with good accuracy, though higher frequencies were incorrect. The buckling loads could not be directly verified due to the limitations of the analysis package and assumption that the plate should be modelled rigidly.

8.8. Bipod Mirror Supports

This section documents the design of the bipod mirror support and verification of the *SPACAR* model. The mirror support consists of three bipods each made from two flexured struts. The orthogonal sheet flexures at either end of the struts ensure that they constrain only a single degree of freedom. An appropriately arranged assembly of three bipods exactly constrains the mirror with respect to the moving frame, and defines a thermal centre at the centroid of the mirror segment.

The launch loads and sizing calculations are detailed in Subsection 8.8.1. The *SPACAR* model is defined in Subsection 8.8.2. The verification results are discussed in Subsection 8.8.3 followed by a short summary to the section in Subsection 8.8.4.

8.8.1. Initial Sizing

Unlike the other compliant elements, the mirror support is a static structure not actively deformed during operations, so the design criteria are slightly different to those in previous sizing exercises. The following thermo-mechanical functions must be fulfilled:

1. Provide an interface between the mirror substrate and moving frame.
2. Survive launch.
3. Survive LEOP.
4. Maintain the M1 optical figure error budgets in the presence of thermal fluctuations during imaging.

The resulting design space has several interlinking criteria and variables. It is desirable to keep the struts as short as possible to minimise the occupied volume and how much their length changes from thermo-elastic strains, yet, long, widely spaced struts provide the smallest launch loads on the struts. The geometry of the flexures too, must strike a balance between sufficient strength to resist failure yet not be so stiff that the optical surface is distorted due to thermal strains.

To that end, the stiffness requirement was defined first with a crude estimate of the transverse stiffness of the mirror and a simple stiffness model of the interaction between the segment and bipod. The bipod geometry was then sized, which dictated the loads on the struts. The flexure geometry was then be found as a function of both the mirror/ bipod stiffness requirement and launch loads. Finally, the worst-case differential thermo-elastic strain between the mirror and moving frame was estimated, to be included in the finite element modelling. The bipod struts are not overconstrained so further thermal survival flow-down requirements were not necessary.

Each of these sizing operations are documented in the following subsections.

Stiffness: Mirror to Bipod Compliance Ratio

The objective of this design criteria was to provide some confidence that the bipod supports were much more compliant than the mirror in certain directions. Ideally, the mirror should be a much stiffer spring than its support so that stresses drive strains in the support structure rather than in the mirror substrate, and by association, the optical surface [125, p. 321].

Finite element analysis is typically the tool of choice to characterise the effect of external stresses on irregularly shaped optical geometries like the M1 segment. This was beyond the resources and scope of the thesis. Moreover, the mirror design is very likely to change over the medium term. A simple order of magnitude estimate of the mirror and bipod stiffnesses was considered sufficient to establish the feasibility of the design.

It was assumed that the transverse bipod stiffness should be three orders of magnitude less than that of the mirror in line with the DOF decoupling design rule used for the wire flexures on page 130. A coarse finite element model of the mirror segment, limited by the available mesh node count, was used to find a crude estimate of the mirror stiffness. This analysis and the derivation of a simple stiffness model for the mirror/ support interaction, are introduced in the subsections below.

Estimate of Mirror Stiffness

Figure 8.21 illustrates the ANSYS model setup and results. The material data is given in Appendix K *Material Properties*. The analysis was conducted at 298 K, the nominal operating temperature.

Symmetry was used to make the most of the license limitations. One end face of the mirror was given a fixed boundary condition while a force of 1 N was applied to the opposing free end. The average deformation

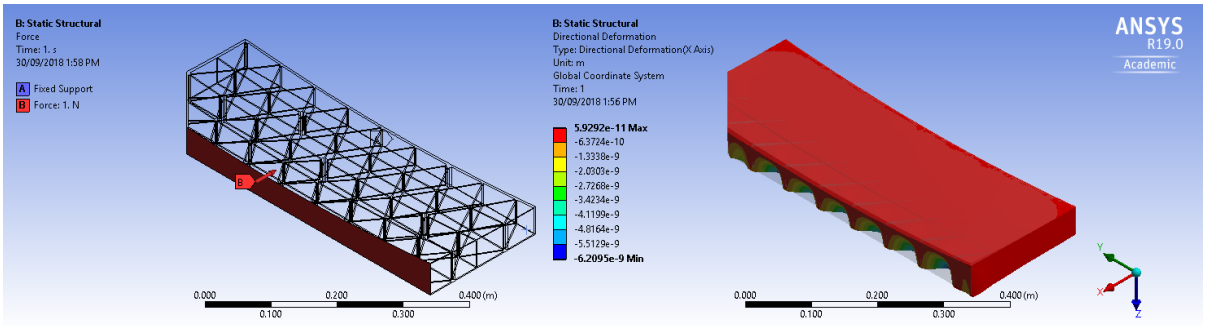

Figure 8.21: Example output of finite element analysis used to derive crude M1 mirror segment stiffness for bipod sizing. Fixed end condition and 1 N load were applied to opposing faces of the half-segment model (left). The average displacement of the whole body in the direction of force application was extracted to calculate the bulk stiffness (right).

over the whole body was extracted, rather than from the end face at which the load was applied, as the thin outer membrane deformed much more than the remainder of the structure, exaggerating the bulk result. See the right hand frame of Figure 8.21, for example.

The spring constant of the mirror in that direction was then found from $F = k\delta x$. The simulation was conducted across the two in-plane dimensions of the mirror, giving the results listed in Table 8.13. The smaller value was used in the sizing calculations as a conservative estimate. This method was crude but gave a fast, order of magnitude estimate to predict the maximum allowable bipod stiffness.

Table 8.13: Results from FEA modelling of mirror to extract approximate bulk stiffness of the M1 mirror segment. Directions are given in the moving frame coordinate system $\mathbf{O_{MF}}$.

Direction	**Force** $[N]$	**Ave. Displacement** $[m]$	**Ave. Stiffness** $[N/m]$
Longitudinal: X_{MF}	1.00	1.03×10^{-9}	7.97×10^{8}
Transverse: Y_{MF}	1.00	2.00×10^{-10}	4.99×10^{9}
Average			2.98×10^{9}

Stiffness Model

Radial growth of the mirror from its centroid is resisted by the transverse stiffness of the bipods. This interaction is idealised in Figure 8.22.

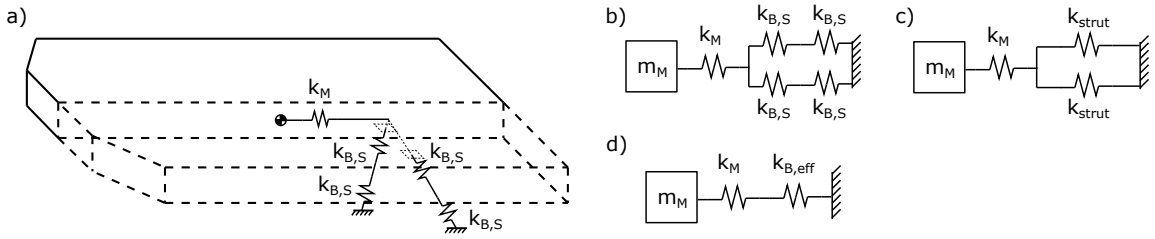

Figure 8.22: Simple stiffness model of M1 mirror segment and flexured bipod. a) Model of in-plane radial stiffness k_M between the mirror and bipod. Each bipod has two flexures contributing to the transverse compliance with stiffnesses $k_{B,S}$; b) Equivalent stiffness model; c) Stiffness model with equivalent stiffness of each strut k_{strut}; and d) Reduced equivalent stiffness model with the effective in-plane stiffness of the bipod $k_{B,eff}$.

For this *rough* approximation it was assumed that since the motions are small, rotation of the flexures and thus rotation of the line of action of the transverse stiffness of the flexures was negligible. That is, that the stiffness of the mirror and of each of the bipod flexures stays along parallel axes. This simplifies the equations by not having to transform the stiffness matrices of each flexure into a single coordinate frame.

All four flexures in each strut have the same geometry. Two of the four flexures are compliant in the direction of interest with stiffnesses $k_{B,S}$ and are included in the stiffness model. The other two flexures are assumed to be rigid in this direction so are excluded. The mirror segment has stiffness k_M in the radial

direction, given by the smaller value in Table 8.13. The flexure stiffnesses combine in series, then parallel, to give the effective transverse stiffness of the bipod $k_{B,eff}$,

$$k_{strut} = k_{B,S}/2 \tag{8.50}$$
$$k_{B,eff} = 2k_{strut} = k_{B,S} \tag{8.51}$$

To ensure that the bipod does not produce excessive deformation of the optical surface due to differential thermo-elastic deformations, it was assumed that the condition $k_M/k_{B,eff} \geq 10^3$ must hold. Thus the effective stiffness of each strut must be 2000 times less than that of the mirror.

The flexure geometry was sized to meet both this and the launch strength criteria. That process is documented at the end of the next subsection.

Strength: Launch Survival

As with all previous strength calculations, it was assumed that the launch loads are dominated by the mirror mass. Figure 8.23 illustrates the assembly geometry, external loads and reaction loads on the mirror from the struts during launch.

Assembly Geometry Parametrisation

The three bipods Bi (i=A,B,C) are each made of two struts B_{ij} (j=1,2). A local coordinate frame $\mathbf{O_{Bi}}$ was set up at the midpoint of the baseline of each bipod, on a circle with radius R_B centred at moving frame origin $\mathbf{O_{MF}}$ in the $X_{MF}Y_{MF}$ plane, on the upper face of the moving frame plate. The upper and lower coordinates of each strut are labelled B_{ijU} and B_{ijL} respectively. Each strut has length s_B between the upper and lower attachment points, with the lower points spaced a distance d_B apart along the bipod local x axis. A bounding circle of radius R_d circumscribing the base spacing lengths d_B of each bipod was used to check that the assembly remained within the maximum allowable radius R_{MAX} calculated in equation 8.41. The bipods were spaced evenly about the circle R_B with angles ψ_{ii}, identical to those also used in the in-plane constraint sizing in Figure 8.17.

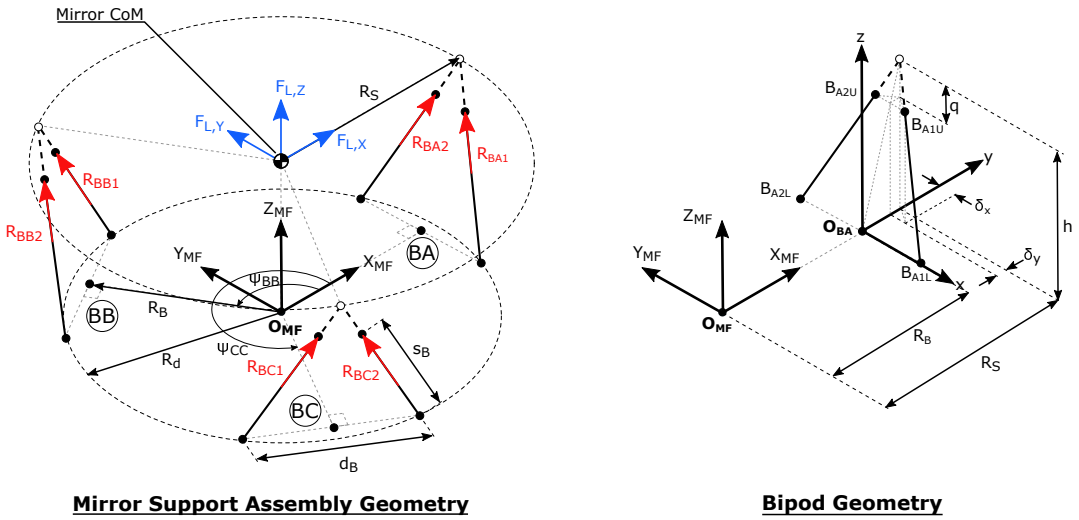

Figure 8.23: Geometry of the mirror support assembly with launch loads. Note that the strut lengths s_B terminate at the backplane of the mirror (not shown), a short distance q below the plane of the centre of mass of the mirror. The constraint lines of the struts intersect in the plane of the centre of mass at a height h from the origin of the moving frame $\mathbf{O_{MF}}$. A local coordinate system $\mathbf{O_{Bi}}$ was used at the base of each bipod in the load derivation, indicated in the right hand figure.

Note that the struts in each bipod terminate a short distance q from their intersection points in the plane of the mirror centre of mass, indicating their physical termination at the mirror backplane (not shown). The extension of the constraint lines of the struts intersect in the plane of the mirror COM, so that the resulting instant centre doesn't impose bending loads on the mirror.

Launch Loads

The launch loads were derived assuming quasi-static equilibrium between the mirror and bipod struts. Fully parametric analytical solutions for the $\mathbf{R_{BAi}}$ are derived in Appendix H *Mechanical Design - Supplementary Material*. The relations are large, so have not been included in this report for brevity. A short program that can be used to derive them in *Mathematica* is also provided in Appendix H.

Other than the launch loads $\mathbf{F_L}$, the strut loads are a function of only three tunable geometric design parameters: the bipod mounting radius R_B, strut spacing length d_B and height h between the centre of mass of the mirror and point $\mathbf{O_{MF}}$. The mirror support radius R_S is also important, but was assumed fixed in this work. The selection of these parameters is described in the next subsection.

Assembly Geometry Selection

An interactive parametric tool was developed in *Mathematica* to visualise the mirror/ support bipod system. An example of the user interface is illustrated in Figure 8.24. The visualisation is drawn to scale and can be interrogated in 3D. This was invaluable for rapid discovery of conflicts between parts without having to build a CAD model.

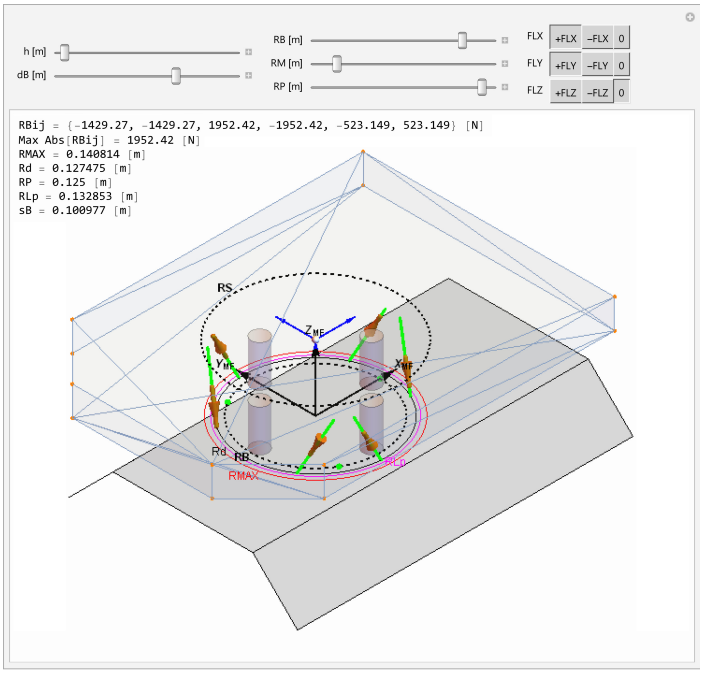

Figure 8.24: Example output of *Mathematica* interactive parametrised bipod geometry and load tool. Configuration shown is the geometry ultimately selected in this sizing exercise.

The six bipod struts are shown in green with the directions of the reaction loads imposed on the mirror overlain as orange arrows. The launch loads are shown in blue at the mirror COM and can be toggled in either direction along orthogonal axes as desired. Four cylinders demarcate the actuator stack positions. Bipod constraint lines intersect at support circle R_S. Bounding circles R_d for the bipod baselines and R_{Lp} for the in-plane constraints must remain within allowable radius R_{MAX}.

The following parametric relations were also used to ensure that the bipods did not conflict with each other nor exceed the usable volume:

$$q + 0.015 + 6L_s + 4t_B + 0.02 \leq h[m] \leq 0.12 + q - 0.015 \tag{8.52}$$

$$0.001 \leq d_B[m] \leq min\left[\frac{6}{\sqrt{3}}R_B, 2\sqrt{R_{MAX}^2 - R_B^2}\right] \tag{8.53}$$

$$\frac{\sqrt{3}}{6}d_B \leq R_B[m] \leq \sqrt{R_{MAX}^2 - d_B^2/4} \tag{8.54}$$

$$h/1.2 \leq R_M[m] \leq R_{MAX} - 0.015 \tag{8.55}$$

where L_s and t_b are the familiar parameters from the universal joint parametric model. The constraints on d_B and R_B are derived from the geometry of equilateral triangles and their inscribed/ circumscribed circles. The various constants in the equation for h are derived from the buffer zones and anticipated thicknesses of components described in Subsection 8.7.1 *Initial Sizing: Moving Frame Plate*. The lower limit for R_M ensures that the ratio $h/R_M = 1.2$ was not exceeded. The upper limit provides a buffer between R_{MAX} and the actuator stacks.

The largest loads in the struts were in the in-plane launch load cases $\{\pm F_{L,X}, \pm F_{L,Y}\}$ in either bipod BB or BC depending on the specific load case. Bipod BB in load case $\{+F_{L,X}, +F_{L,Y}\}$ was taken as the sizing example. The tool confirmed the following expected behaviours irrespective of direction and combination of launch loads:

- Decreasing h reduces the reaction loads.
- Increasing R_B reduces the reaction loads.
- Increasing d_B reduces the reaction loads.

In general, it was found that a wide, low profile arrangement would decrease loads. There was a trade to be made between a large and heavy but low-load arrangement or a small, light arrangement with large launch loads. Larger loads have a flow on to thicker, stiffer flexures that must then be longer to provide sufficient decoupling between the axial and bending stiffnesses.

From the constraint equations 8.52 to 8.55 it is evident that selection of d_B and R_B are interlinked, and that there is an optimum between the two. Sizing the PMAO using parametric optimisation methods would be ideal, however developing such a tool was ultimately beyond the scope of this thesis. Instead, the interactive tool was used to hand pick geometry that led to no conflicts and reasonable launch loads. The area inside the actuator stacks was reserved for the fixed frame and the area outside the stacks was reserved for the bipods and in-plane constraints.

Reasons for selecting a small height h included: reduce the mechanical advantage of the mirror mass; reduce the length of the struts; and to increase the maximum usable area in the $X_{MF}Y_{MF}$ plane. The minimum allowable h for the current design was defined in Table 8.10. A value of 118 mm was selected.

The universal joints were sized, and the actuators selected, based on a ratio h/R_M of 1.2. The actuator mounting radius R_M was reduced to 100 mm to increase the usable area outside of the actuator stacks, giving an h/R_M ratio of 1.7, providing a small design margin for both the universal joint flexures and actuators, which was necessary given that no parts had yet been sized to withstand self-mass through launch.

A bipod radius R_B of 115 mm and spacing d_B of 110 mm resulted in a maximum launch load of ±1952 N along the axis of a strut. This also provided a minimum 15 mm buffer between the actuators and struts to accommodate vibration during launch, though confirmation that this is sufficient spacing is a topic for future work. The system with these parameters selected is shown in Figure 8.24. A summary of the geometry is given in Table 8.14 at the conclusion of this subsection.

Flexure Geometry Selection

The parametrisation of the bipod strut and strut flexures is shown in Figure 8.25. There was a narrow design space for a flexure geometry that could meet the launch strength requirements, the operational (mirror) stiffness requirement and the LEOP survival thermal strength requirement, discussed in the next subsection. Additionally, the combined length of the flexures, base and transitions was not to exceed the total strut length s_B, defined by the assembly geometry.

The solution to find the critical buckling load of a beam with variable cross-section is non-trivial for more than two or three different sections. The bipod strut has nine sections. Trial and error using the ANSYS verification model was used to determine a flexure geometry that could survive launch and still meet the stiffness requirement. Both yield and buckling failure during launch were used as strength criteria. The stiffness criteria was set so that the transverse stiffness of the strut was 2000 times less than the radial stiffness of the mirror, as calculated in the previous subsection. The transverse stiffness of the strut was found by fixing the foot of the strut, applying a 1 N transverse load to the top and extracting the average displacement of the top of the strut in the direction in which the load was applied.

A length of 6 mm, width of 17 mm and thickness of 2 mm were found to be acceptable, giving a critical buckling load of 2021 N and transverse stiffness of 7.22×10^4 N/m per strut. A small transition $L_{BP,trans}$, initially set to 5 mm, was included between each flexure and at the end of the struts. The interface between the strut and mirror/ moving frame was not crucial to establishing the feasibility of the PMAO so its design was left to future work.

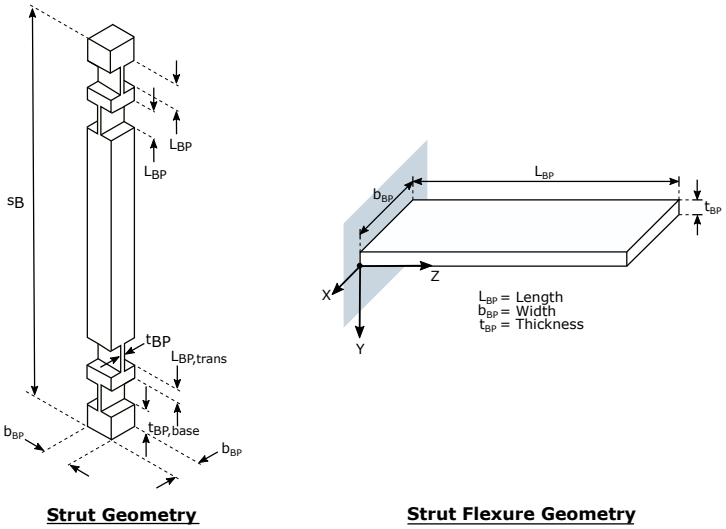

Figure 8.25: Geometry of mirror support bipod strut and strut flexures. All flexures have identical geometry. A minimum transition length $L_{BP,trans}$ is maintained between the flexures to transfer the stresses. The thickness of the ends $t_{BP,base}$ was set to the transition length.

Strength: LEOP Survival

The final design criteria for the bipods was that they withstand the worst-case thermo-elastic strains between the mirror and PMAO mechanism without plastically yielding. Even micro-yielding will unpredictably alter the stiffness of the struts to the detriment of the repeatability of the PMAO.

SPACAR is unable to model thermal phenomena so an estimate of the maximum differential strain was made by hand, documented below. The displacement was then applied to the strut in both the *SPACAR* and ANSYS verification analyses.

Load Case Definition

A case with the moving frame at the coldest temperature and mirror at the hottest temperature was considered, sketched in Figure 8.26. This could forseeably occur in LEOP prior to baffle deployment for an M1 segment fully illuminated by the Sun, shortly after the spacecraft exits the terminator. The worst-case condition would occur if the mirror heats up very quickly to the higher steady state temperature while the moving frame, shielded by the mirror, remains at the steady state cold temperature.

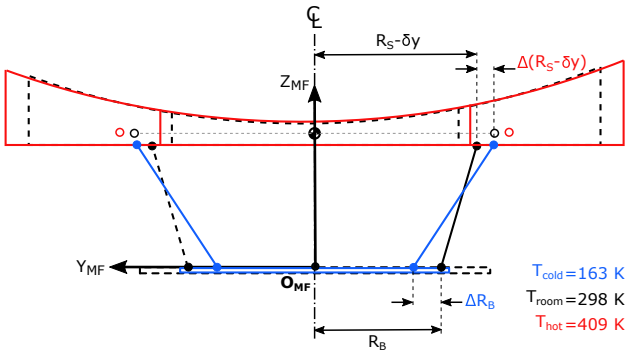

Figure 8.26: Sketch of thermo-elastic strain geometry during LEOP, used for mirror support bipod sizing. Dashed black parts are initial state at room temperature. Solid red parts are in hot displaced state. Solid blue parts are in cold displaced state.

The minimum and maximum estimated steady state temperatures for the M1 subsystem during LEOP with qualification level thermal uncertainty margins were 163 K and 409 K respectively, per Table 3.4. Thermal centres are defined on the moving frame from the in-plane constraints, and in the mirror COM plane by the support bipods. Assuming that they are well aligned, the resulting thermo-elastic strain in both the mirror and moving frame extends radially from the Z_{MF} axis. Room temperature was taken as 298 K, the assumed assembly and operation temperature of the DST.

For simplicity, the bipod was assumed to absorb the entirety of this strain through transverse bending of the flexures, since they should be orders of magnitude more compliant in this direction than both the moving frame and mirror. This is conservative since the struts are not orthogonal to the moving frame/ mirror planes, so the radial strain would be reduced by the sine of the dihedral angle between the plane of the bipod and the horizontal.

Displacement Calculation

With reference to the geometry in Figure 8.26, the change in the radial distance between the centroid of the mirror and the point between the upper attachments of the two struts to the backplane of the mirror is

$$\Delta R_{Sp} = \alpha_{SiC}\left(R_S - \delta y\right)\left(T_{hot} - T_{room}\right) \tag{8.56}$$

The change in radial length between the centre of the moving frame and bipod base radius R_B is

$$\Delta R_B = \alpha_{Ti} R_B \left(T_{cold} - T_{room}\right) \tag{8.57}$$

The combined thermo-elastic strain in the radial direction from the centre of the system through the centre of the bipod is

$$\Delta_{R,tot} = \Delta R_{Sp} - \Delta R_B \tag{8.58}$$

Assuming that the struts are at the steady state cold temperature, their length is reduced by

$$\Delta L_{BP} = \alpha_{Ti} L_{BP} \left(T_{cold} - T_{room}\right) \tag{8.59}$$

The primary mirror material selection is based on the GAIA M1 design, which uses BOOSTEC Silicon Carbide. The CTE varies from 0.9 and 3.0 $\mu\epsilon/K$ between the minimum and maximum LEOP temperatures [21]. The CTE for Titanium is given in Appendix K *Material Properties* and was assumed to apply at the cold temperature. A total differential thermo-elastic strain $\Delta_{R,tot}$ of 0.201 mm was calculated. The resulting stress in the strut was checked in both the *SPACAR* and ANSYS analyses, summarised in Subsection 8.8.3.

Sizing Summary

The bipods were thus sized according to both strength and stiffness criteria. An estimate of the worst-case differential thermo-elastic strain between the mirror and moving frame was also made. The results are summarised in Table 8.14. The next subsection sets out the *SPACAR* and ANSYS verification results.

Table 8.14: Design parameters for mirror support bipods.

Parameter	**Value**
Bipod Geometry	
Actuator radius (updated) R_M	100 mm
Moving frame height h	118 mm
Bipod mounting radius R_B	115 mm
Strut spacing d_B	110 mm
Strut transition length $L_{BP,trans}$	5 mm
Strut end interface thickness $t_{BP,base}$	5 mm
Strut Length s_B	101 mm
Strut Flexure Geometry	
Length L_{BP}	6 mm
Width b_{BP}	17 mm
Thickness t_{BP}	2 mm
Material	Ti-6Al-4V
Test Conditions	
Applied launch load F_L	±1952 N
Thermo-elastic strain $\Delta_{R,tot}$	0.201 mm

8.8.2. *SPACAR* Model Definition

The bipod struts were modelled individually rather than in a bipod pair to avoid the unnecessary complexity of modelling the mirror interface. A sketch of the *SPACAR* model, showing the definition of each node and element, is given in Figure I.3 in Appendix I *SPACAR Model Maps*. The flexures were all modelled per the sheet flexures in Subsection 8.4.3.

The end and transition sections were assumed to have comparatively negligible deformation so were modelled as rigid beams, though mass and inertial effects were included. The transverse displacement predicted by the LEOP survival thermal expansion calculation was applied at the top of the strut.

8.8.3. Results and Discussion

The results of the *SPACAR* and ANSYS verification modelling for the bipod struts are summarised in Table 8.15. The first three buckling modes and eigenmodes are shown in Figures 8.27 and 8.28 respectively. The coarse geometry of the bipod struts simplified the ANSYS mesh generation. The automatic method was used, guided by a minimum element size setting of 1 mm.

Table 8.15: Results of the mirror support bipod strut modelling in *SPACAR* and verification with ANSYS. ANSYS values are taken as truth values for the error estimates.

Item	*SPACAR*	ANSYS	Error
Eigenfrequencies			
ω_1	147 Hz	139 Hz	5.74%
ω_2	180 Hz	168 Hz	6.93%
ω_3	1966 Hz	1678 Hz	17.1%
Critical Buckling Loads			
f_1	2248 N	2021 N	11.2%
f_2	2652 N	2370 N	11.9%
f_3	16180 N	14795 N	9.36%
Maximum Launch Stress			
σ_{eq}	57.4 MPa	80.6 MPa	28.7%
Max. Displacement Stress (LEOP)			
σ_{eq}	48.2 MPa	45.1 MPa	6.85%
Transverse Stiffness (Strut)			
k_{strut}	31973 N/m	29312 N/m	9.08%

Static Analysis Results

As in the previous verification analyses, the maximum equivalent launch stress in the *SPACAR* model was much lower than the value predicted by ANSYS. The predicted stress from the LEOP transverse displacement case was considerably more accurate as the stresses were low enough that stress concentrations weren't a large factor. The 5 mm thickness given to the transitions between flexures was sufficient with equivalent stresses an order of magnitude lower through these sections than that in the flexures.

The *SPACAR* transverse stiffness estimate was approximately 9% higher than that from ANSYS. Given the need to keep this stiffness low, the conservative estimate was acceptable for preliminary design.

Modal & Buckling Results

The *SPACAR* model correctly predicted the first three eigenmode and buckling mode shapes, and did a good job of predicting the fundamental frequency, with an error less than 10%. Its prediction of the critical buckling mode was optimistic with a value 11.2% higher than that of the ANSYS model.

8.8.4. Summary: Bipod Mirror Supports

Trial and error was used to size the flexures so that they would not buckle in launch, yet still meet the stiffness requirement. An optimisation algorithm using the *SPACAR* buckling analysis, constrained by appropriate flexure dimension ratios would be a more efficient method for repeated prototyping in the future. As a minimum, the sizing conducted here provided a reasonable mass estimate and initial geometry to quantify the kinematic performance.

The results from the *SPACAR* model of the bipod strut were generally quite good, with the ANSYS verification showing that the modal, buckling and displacement stress analyses worked quite well. As was the

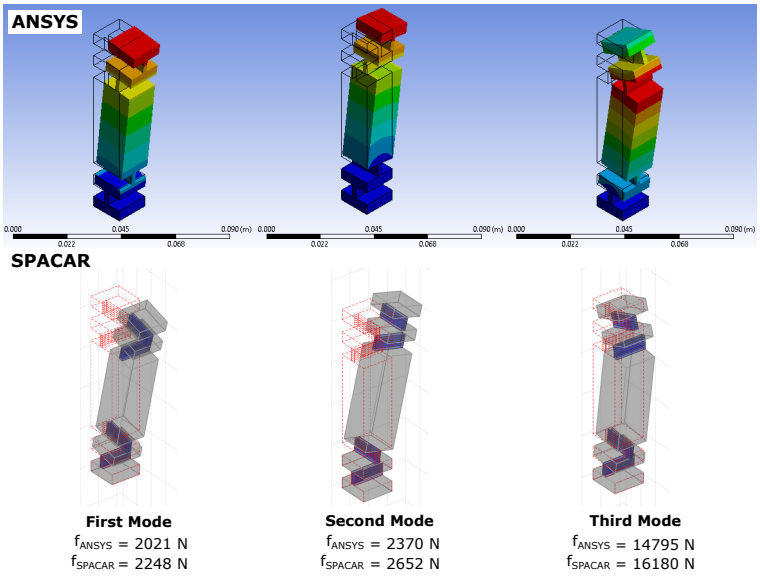

Figure 8.27: *SPACAR* eigen buckling analysis results for bipod strut.

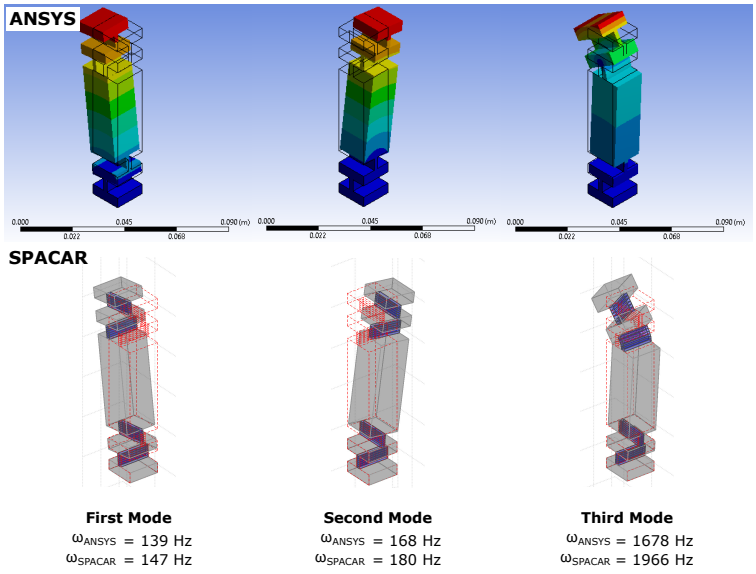

Figure 8.28: *SPACAR* modal analysis results for bipod strut.

case for all of the other component modelling, *SPACAR* did a poor job of predicting the maximum launch stress due to the presence of stress concentrations. Overall, the model was deemed sufficient for the PMAO prototyping.

8.9. Integrated Assembly

This section finalises the preliminary thermo-mechanical design of the PMAO mechanism. The last major component to be sized was the fixed frame. One of the major assumptions made in this chapter was that design of the fixed and moving frames did not pose large technical risks. They would therefore not need to undergo detailed design and verification to prove the feasibility of their inclusion in the PMAO mechanism.

Accordingly, the objective of the fixed frame sizing was simply to find a preliminary mass estimate. Although the sizing was based on strength calculations, it is important not to read too much into them. Their objective was to derive a rough approximation of magnitude of what might be expected in a more thorough design, *only*. They were *not* intended to represent a design that could reasonably expect to meet all of the requirements. The resources of a Masters thesis are finite, the bulk of the technical effort was focussed else-

where.

Subsection 8.9.1 describes the simple method used to generate a preliminary mass estimate for the fixed frame. Subsection 8.9.2 summarises the parameters of the final design, details the integrated assembly *SPACAR* model setup, and the analyses that fed into the verification activities discussed in Chapter 9 *Verification*.

8.9.1. Initial Sizing

It was assumed that the fixed frame would consist of a lower plate and a central cylindrical support. The plate would serve as the interface to the M1 deployment support frame, and mate directly to the PMAO mechanism in-plane constraint wire flexures. A central cylinder with a radius on the order of the actuator mounting radius would then provide the foundation for the structure used to mount the four actuators. A sketch of the sizing geometry is given in Figure 8.29. Each of these components are sized in the following subsections.

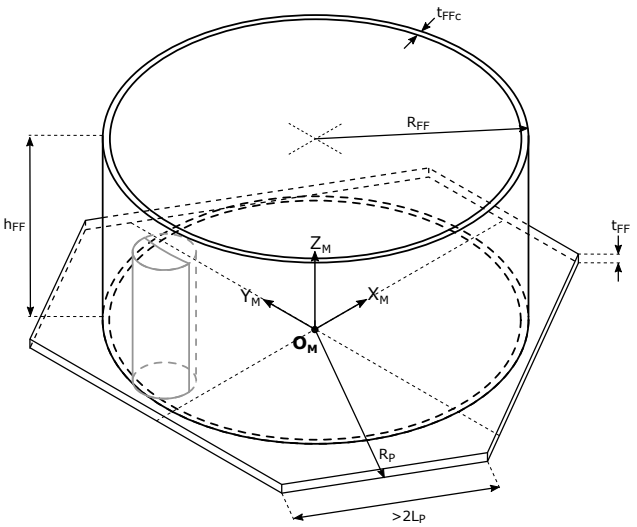

Figure 8.29: Geometry for PMAO fixed frame sizing. An actuator stack (grey) is shown to illustrate relationship with actuators and moving frame. The mechanism fixed frame coordinate origin $\mathbf{O_M}$ is shown at the bottom of the fixed frame base plate.

Fixed Plate

The fixed plate was modelled as an equilateral triangle with truncated corners 100 mm long to accommodate the $2L_P = 90$ mm long in plane constraints. Design of the mounting interfaces was not carried out. The plate was given a thickness t_{FF} of 5 mm per the moving frame sizing, which sees similar loads, leading to a mass of 0.994 kg if made from Ti-6Al-4V.

Central Cylinder

The central cylinder was sized based on two load cases. First, a combined $+F_{L,X}$, $+F_{L,Z}$ combined in and out of plane load and second, a combined $+F_{L,X}$, $+F_{L,Y}$ in plane load. As in all other sizing exercises, the launch loads F_L were assumed to be dominated by the mirror with a 6 kg mass.

The height of the cylinder h_{FF} was assumed to extend to the extremities of the buffer zones at the top and bottom of the PMAO mechanism in Figure 8.14. For the current design, this gives a height $h_{FF} = h - q + 15mm$ of 104 mm.

Shigley's Mechanical Engineering Design gives simple equations for different types of columns in compression [26]. With a radius on the order of $R_M = 100$ mm, the fixed frame cylinder is very short and squat, so can be classified as a short column where Euler buckling does not apply. For the combined in and out of plane load case, the maximum compressive stress can be found with [26, p. 188]

$$\sigma_c = \frac{P}{A}\left(1 + \frac{ec}{k^2}\right) \tag{8.60}$$

where P is the applied load, A is the cross-sectional area $\pi(r_o^2 - r_i^2)$, e is the eccentricity of the load with respect to the column centroid here equal to the outer radius of the column R_{FF}, c is the distance of the outer most fibre of the column section from the centroid, also equal to R_{FF} and k is the radius of gyration

$k = (I/A)^{1/2}$. I is the second moment of area for a cylinder $I = \pi(r_o^4 - r_i^4)$. Equation 8.60 applies for columns with slenderness ratios l/k less than [26, p. 189]

$$\left(\frac{l}{k}\right)_1 = 0.282\left(\frac{AE}{P}\right)^{1/2} \tag{8.61}$$

A cylinder thickness t_{FFc} of 3 mm was selected as the minimum needed to be robust against handling during assembly and transport, as well as provided a minimum thickness for joining to other components.

For a cylinder made of Ti-6Al-4V with height 104 mm, and outer radius R_{FF} equal to the actuator mounting radius R_M = 100 mm, the limiting slenderness ratio $(l/k)_1$ is 98, whilst the actual slenderness ratio l/k is 1.5. Thus equation 8.60 applies.

Assuming that the total applied load would be on the order of four times the launch load on each actuator given by equation 7.29, equation 8.60 gives an estimated maximum compressive yield stress of 9.8 MPa, far below the Ti-6Al-4V yield strength of 1060 MPa.

A simple estimate of the bending stress in the cylinder from the combined $F_{L,X}$ and $F_{L,Y}$ loads can be found with

$$\sigma_{bend} = \frac{Mc}{I} = \frac{h_{FF}\sqrt{F_X^2 + F_Y^2}R_{FF}}{I_{cyl}} \tag{8.62}$$

giving a pure bending stress of 2.9 MPa. Thus the fixed frame cylinder geometry derived here should survive the admittedly strongly simplified load cases given here with a mass of 0.851 kg.

A fixed frame that has undergone detailed design will of course be far more complex than the geometry considered here. The geometry shown in Figure 8.29 would conflict with the bipods and moving frame. It also doesn't include any secondary structure to interface with any other components. These extra appendages are accounted for with an allowance in Subsection 9.1.2 *Mass Budget*.

8.9.2. *SPACAR* Model Definition

The state of the PMAO mechanism geometry at the conclusion of the mechanical design process is summarised in Table 8.16. The verification results for this revised design are presented in Chapter 9 *Verification*, which made use of the *SPACAR* model described in this section.

Table 8.16: Design parameters for the final PMAO design.

Parameter	Value	Parameter	Value
Assembly		Moving Frame Plate	
Actuator mounting radius R_M	100.0 mm	Radius	R_P
In-plane constraint radius R_P	125.0 mm	Thickness t_{MF}	5.0 mm
Bipod mounting radius R_B	115 mm	Mirror Support Bipods	
Mirror support radius R_S	145 mm	Strut spacing d_B	110 mm
Moving frame height h	118 mm	Strut transition length $L_{BP,trans}$	5 mm
Universal Joint Body		Strut end thickness $t_{BP,base}$	5 mm
Outer diameter D_O	30 mm	Strut length s_B	101 mm
Inner diameter D_i	10 mm	Mirror Support Bipod Flexures	
End Interface thickness t_B	4.5 mm	Length L_{BP}	6 mm
Universal Joint Flexure		Width b_{BP}	17 mm
Length L_S	6 mm	Thickness t_{BP}	2 mm
Width b_S	10 mm	Fixed Frame	
Thickness t_S	0.5 mm	Base plate thickness t_{FF}	5 mm
In-Plane Constraints		Cylinder outer diameter R_{FF}	R_M
Length L_P	45 mm	Cylinder thickness t_{FFc}	3 mm
Width b_P	1.4 mm	Cylinder height h_{FF}	104 mm
Thickness t_P	1.4 mm		

The integrated *SPACAR* model is the sum of each of the component models described throughout this chapter. The same assumptions and idealisations used in the verified component models were therefore re-used at the integrated level. Similarly any trust, or lack thereof, built up from the component model verification results was extrapolated to the integrated model.

The fixed frame was not included in the integrated model as it was assumed that it could be designed so that it was stiff enough that it would not degrade the performance of the mechanism. Therefore, the top universal joint interfaces and in-plane constraint interfaces were simply modelled with fixed end conditions. This is indicated by the small, bright green circles in Figure 8.30. The moving frame plate was still modelled as a rigid body.

An example of the *SPACAR* visualisation output for the integrated model is given in Figure 8.30. The *SPACAR* global coordinate frame was aligned to the mechanism fixed frame $\mathbf{O_M}$, shown in Figure 8.14. Beams with deformable elements are blue, rigid beams with mass are grey, "dummy" massless beams used to connect the massive elements are shown as dark grey lines. Note that the in-plane constraint wire flexures look like grey lines, however upon closer inspection they are indeed blue flexible elements.

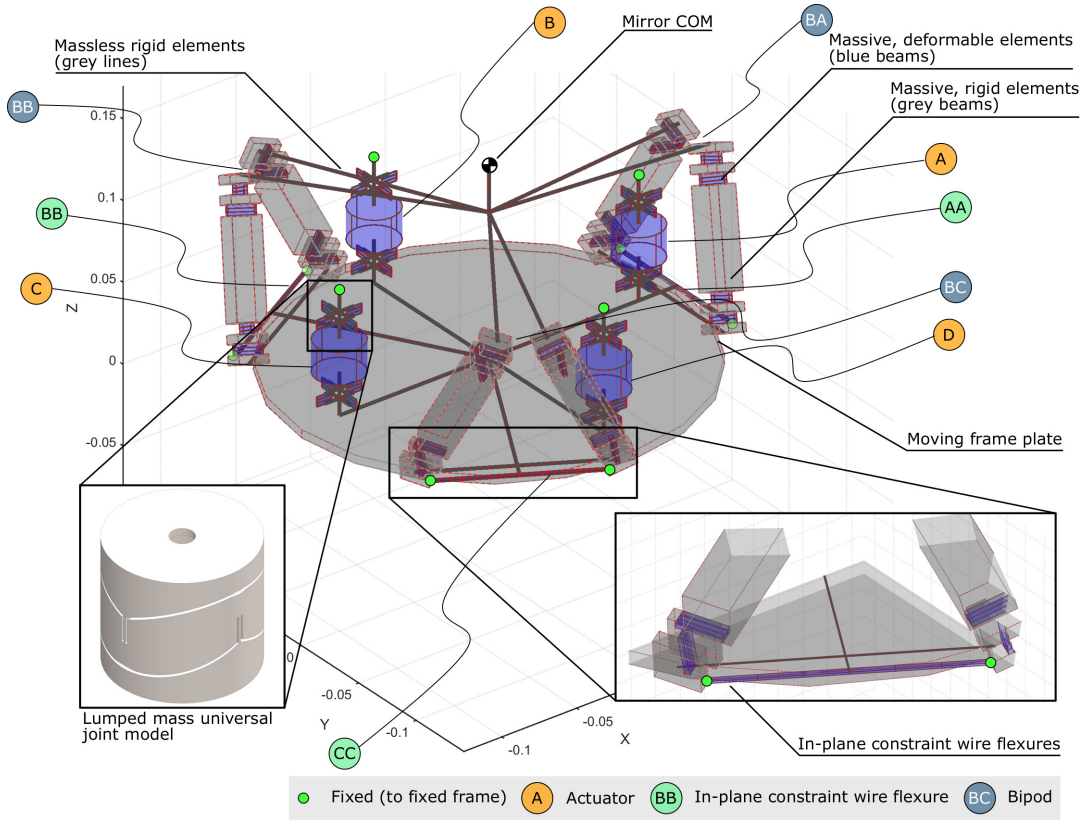

Figure 8.30: *SPACAR* model of the PMAO integrated assembly. Inset images show the physical embodiment of the lumped mass model of the universal joints, and a close up view of an In Plane Constraint (IPC) wire flexure.

The massless rigid beams at the top of the model connect the mirror support bipods to the centre of mass of the mirror, which is modelled using a lumped mass and inertia in a similar fashion to the universal joint body components. The mass and inertia properties were taken from a CATIA model of the current mirror design, repeated in Table 8.17. The mirror was assumed to be rigid for all *SPACAR* analyses.

Table 8.17: Mass and inertia properties for M1 mirror segment lumped mass modelling in *SPACAR*. Extracted from CAD model. Coordinates are in the *SPACAR* global coordinate frame $\mathbf{O_M}$, shown in Figure 8.14.

Mass $[kg]$	$\mathbf{I_{xx}}$	$\mathbf{I_{xy}}$	$\mathbf{I_{xz}}$	$\mathbf{I_{yy}}$ $[m/kg^2]$	$\mathbf{I_{yz}}$	$\mathbf{I_{zz}}$
6.0	0.185	0	0.026	0.101	0	0.276

ETEP Model Integration

The main objective of integrating the *SPACAR* model with the end to end performance model, was to more accurately model the relationship between a desired segment pose commanded by the calibration algorithm, and the actual, final, pose achieved by the mechanism.

It is possible to use *SPACAR* as a MATLAB *Simulink* block to calculate the full non-linear inverse kinematic relations necessary to achieve a certain trajectory, however this requires at least two *SPACAR* executions for every commanded pose. It also requires definition of a trajectory from one point to another. Delving into the details of manipulator control and trajectory planning were beyond the scope of this thesis and perhaps more importantly, the ETEP model is incapable of making use of trajectory data anyway. The optical performance is only concerned with start and end points.

Instead, the `pmaoFORTA` handler function was written to parse the commanded piston, tip & tilt of the segment from the M1 calibration algorithm, calculate the required actuator strokes using the linearised inverse kinematics via `pmaoLinInvKin`, execute the *SPACAR* run and return the achieved positions of the moving frame origin $\mathbf{O_{MF}}$ and centre of mass of the segment. The actuator strokes were discretised to the nearest 10 nm to simulate the actuator step size. See Figure 8.3 at the start of this chapter for the PMAO program suite.

The execution time for each *SPACAR* run in the ETEP implementation ranged between 90 seconds to five minutes depending on the computer hardware and displacement distance. Larger displacements generally took more iterations for the internal solver to converge. These times were deemed acceptable for the ETEP Monte Carlo analysis.

This simpler integration of the *SPACAR* model into the ETEP model was sufficient for the purposes of this thesis, but it is strongly recommended that the non-linear *Simulink* model be implemented in future work. This allows integration of actuator, sensing and control models of the electromechanical systems to provide a rich simulation of the bottom up performance of the active optics.

Buckling Analysis

In all of the component level buckling analyses, one end of each component was fixed while the other was free - the least stable column end condition. The stability of each of the components improved at the assembly level as this condition changed to fixed/ fixed. A new buckling analysis of the integrated assembly was required.

Checking the new critical buckling loads on a per component basis in the integrated assembly would have required an entire buckling analysis for every part, with individual reference loads applied to the ends of each. The PMAO mechanism is strongly dominated by the mass of the mirror through launch, so a more efficient way to gain a reasonable first estimate of the assembly's buckling strength was to treat it as a single part.

Accordingly, buckling failure was checked by applying a 1 N reference load to the mirror centre of mass node in each of the X_M, Y_M or Z_M directions and executing a *SPACAR* buckling analysis to find the critical buckling load in that direction. The assembly was considered to survive if the resulting critical load was greater than the force applied by the mirror mass in that direction during launch, nominally 6 $kg \times 30\ g = \pm 1765\ N$.

8.10. Summary

This chapter detailed the preliminary thermo-mechanical design of the PMAO mechanism. A bottom up approach was used where each of the major components were sized using simple calculations from first principles to meet the critical strength and stiffness requirements. These calculations adequately predicted the necessary geometry for the most part, but in isolated instances were severely inaccurate. The designs were then revised using the *SPACAR* and ANSYS verification models.

It was found that combining flexures with the high aspect ratios necessary to decouple their freedom and constraint DOFs could be a considerable challenge for mechanisms that must also survive large loads and fit into a small volume. The launch loads strongly dominated the design criteria, leading to a wide, relatively low profile assembly to reduce the mechanical advantage of the mirror. The result is somewhat heavy but nevertheless, represents a practical revised baseline.

Several trends were evident in the ANSYS verification modelling. *SPACAR* was able to predict the first eigenfrequencies and critical buckling loads to within 12% of the values predicted by ANSYS. This level of accuracy was in agreement with *SPACAR* models documented in the academic literature. The first buckling and eigenmode shape predictions were also good, however the accuracy degraded quickly for higher orders.

Additionally, the maximum equivalent stress calculations in the *SPACAR* models were sufficiently accurate for small deflections, but routinely under-predicted the maximum stress reported by ANSYS in the launch load cases, by up to 29%. The ANSYS results were dominated by stress concentrations at the roots of the flexures, which *SPACAR* did a poor job of predicting. This was not considered a great cause for concern as such stress concentrations would be designed out in detailed design with fillets or curved flexure profiles.

The *SPACAR* results were therefore assumed to be indicative of reasonable launch stresses for the purposes of this feasibility study.

There is significant scope for improvement. Detailed design of all components is needed, from interfaces and the fixed and moving frames, through to refined flexure profiles and removal of stress concentrations. Other failure criteria such as fatigue also need to be considered, as well as the effects of assembly errors.

Major assumptions used in the mechanical design are summarised in Table 8.18. Verification of the revised design is detailed in the next chapter.

Table 8.18: Major assumptions for mechanical design. Assumptions with ID's "ASM-MEC-XX" refer to the mechanical sizing. Assumptions with ID's "ASM-SPA-XX" refer to the *SPACAR* modelling.

ID	Description
ASM-MEC-01	Assume moving frame plate can be modelled as a rigid body. A corollary is that designing the moving frame to be sufficiently rigid to meet operational requirements does not present a high technical risk.
ASM-MEC-02	Assume fixed frame can be modelled as a rigid body. See also corollary for ASM-MEC-01.
ASM-MEC-03	Assume mirror can be modelled as a rigid body in all analyses. Bipod struts are designed to be >1000× more compliant than the mirror to facilitate this assumption.
ASM-MEC-04	Assume that the PPA40XL specifications provide a conservative estimate of proposed PPA10XL actuator performance.
ASM-MEC-05	Assume that the blocked force capability and output stroke of the actuators are not affected by the driven load, which is very small.
ASM-MEC-06	Assume that connection of bipod struts to mirror and moving frame can be modelled as a pinned connection. This is enabled by a strong decoupling between the bending and axial stiffnesses of the struts, which is not necessarily achieved with the final design. Refinement is a topic for future work.
ASM-MEC-07	Assume minimum allowable feature size is 0.5 mm to enable standard precision machining techniques.
ASM-SPA-01	Damping properties of the material are ignored as they are very difficult to characterise accurately.
ASM-SPA-02	The fixed frame and deployment support frames are assumed to be completely rigid. They are excluded from the model for simplicity. Both components should be included in detailed design modelling as they can strongly impact the resonant frequency in the combined system.
ASM-SPA-03	Only compliant elements (flexures) need to be modelled with deformation modes included, due to their much greater compliance than larger, stiffer members.
ASM-SPA-04	Yield failure need only be checked in flexures due to their much smaller cross-section than larger members.
ASM-SPA-05	Assume verification of the component *SPACAR* models can be extrapolated to the assembly level *SPACAR* model.

9

Verification

This chapter documents the results of the application of the verification plan generated in Chapter 4 *Verification Plan* to the revised PMAO baseline design formulated in Chapter 8 *Mechanical Design*.

The chapter structure is shown in Figure 9.1. The verification activities were decomposed into four major themes: systems level, launch survival, operations survival and operations functionality, each discussed in turn through Sections 9.1 to 9.4. In the interest of brevity, self-explanatory verification activities are not discussed in detail. The results of the verification phase are summarised in a series of convenient tables in Section 9.5. Section 9.6 details a number of flow down requirements to other components or subsystems that follow from the verified PMAO design. The chapter concludes with tables summarising the outcome of each verification activity in Section 9.7.

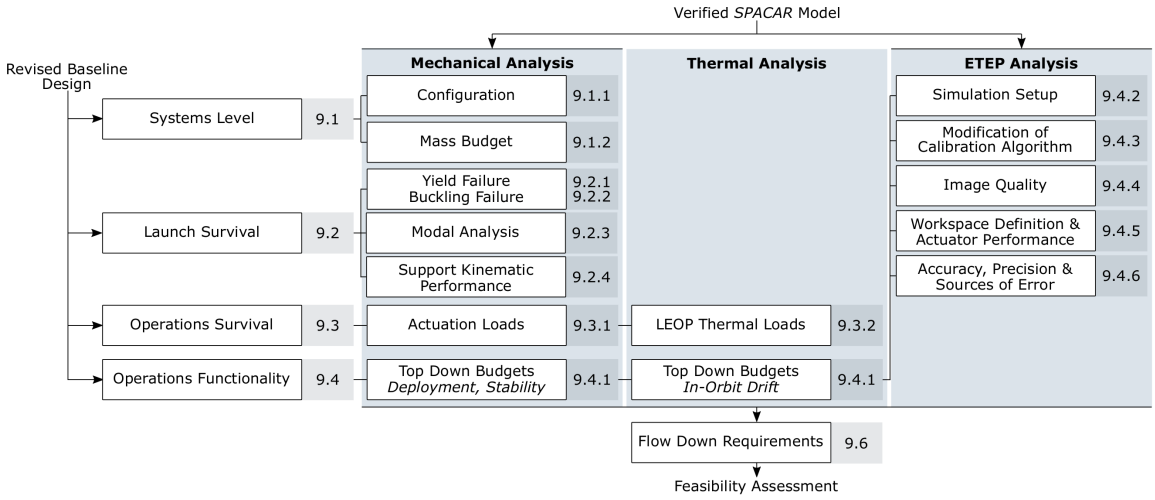

Figure 9.1: Major tasks in the verification chapter.

9.1. System Level Verification Activities

The system level requirements largely cover compatibility and programmatic characteristic requirements. These are verified in Subsection 9.1.1. An itemised mass budget for the PMAO is formulated in Subsection 9.1.2.

9.1.1. Configuration, Manufacturing and Regulations

Verification Activities: VA-01 [pass], VA-03 [pass], VA-04 [pass], VA-15 [pass], VA-16 [pass], VA-18 [pass]

Inspection of the mechanical drawings and parametric visualisation tool in Figure 8.24, as well as the ETEP modelling, confirm that the primary mirror is in the correct location, that the PMAO respects the 120 mm clearance between the back of the mirror and DST housing, that it does not protrude beyond the periphery of

the mirror and that deployment of M1 and M2 will not be obstructed. The minimum dimension throughout all of the major components is 0.5 mm to permit standard high precision fabrication methods.

The actuator is not controlled by ITAR regulations and does not require any new fabrication or testing methods. It is considered a low risk item.

9.1.2. Mass Budget

Verification Activities: VA-02 [pass]

Table 9.1 gives a bill of materials for the preliminary design of the PMAO. A rough allowance of 10% of the primary structure mass was made for secondary structures (brackets, ribs etc) and interfaces (kinematic joints, bolts, adhesive). An additional margin of 20% was applied to reflect the uncertainty in the preliminary design. The total mass with secondary structure allowance and uncertainty margin was 5.854 kg per segment, approximately 0.35 kg below the mass budget in requirement PMAO-SYS-02. An estimate of the power electronics mass is provided, but does not contribute to the instrument mass requirement.

Table 9.1: Mass budget for the primary mirror active optics mechanism. Power supply electronics are a separate line item as this does not contribute to the instrument mass budget.

Item	**Mass/ Unit** [kg]	**No. Units** [$-$]	**Total Mass** [kg]	**Comment**
Universal joints	0.071	8	0.566	Ti-6Al-4V, CAD estimate
Actuators	0.085	4	0.340	Scaled from PPA40XL
Moving frame, in-plane constraints	1.075	1	1.075	Ti-6Al-4V, CAD estimate
Support bipods	0.102	6	0.609	Ti-6Al-4V, CAD estimate
Fixed frame	1.845	1	1.845	Ti-6Al-4V, sizing estimate
Secondary structure, interfaces	-	-	0.443	10% of primary mass (est.)
		Total	4.878	Primary + secondary structure
		20% Margin	0.976	DST Team standard margin
		Total with margin, per segment	5.854	
		Total with margin, four segments	**23.42**	PMAO-SYS-02: 24.8 kg
Power supply electronics	0.390	4	1.560	Per segment, Subsection 6.6

The total mass would be expected to decrease with detailed design since solid sections have been used in the structural components. More structurally efficient sections such as I-beams or channels could be used instead for the moving and fixed frames.

9.2. Launch Survival Verification Activities

The *SPACAR* model was used to perform the yield, buckling and modal analyses. To reduce the burden of analysis, yield and buckling were checked in the compliant members only, comprising some 62 individual flexures. This was automated using the batch processing scripts previously depicted in Figure 8.3. All launch survival analyses included the 6 kg mirror mass. The strength of the mechanism against yield and buckling failure are examined in Subsections 9.2.1 and 9.2.2 respectively. The modal analysis results are discussed in Subsection 9.2.3.

9.2.1. Static Analysis: Yield Failure

Verification Activities: VA-06-[01-03]-01 [pass]

Twelve separate launch load cases were examined, one for each combination of two simultaneous positive and/ or negative x, y and z inertial launch accelerations. Per the verification plan, the limit load for the beams was the yield strength of the material, and for the actuators, one third of their rated maximum blocked force output, approximately 2218 N.

The minimum margin of safety against yield found for each part across all load cases is reported in Table 9.2. Note that the loads and stresses are for the most highly loaded flexures within each part. For example, the margin of safety listed for the lower universal joint in actuator stack A *Uni joint - AL*, is the smallest margin of safety for any part (ie. any flexure) within the *Uni joint - AL* component. Therefore the listed stress is the stress through the limiting flexure, not through the whole universal joint. The part locations were described

in Figure 8.30.

The most critical component in the yield tests were the actuators, with a margin of safety of 0.33 against their rated axial load. This is a comfortable margin, especially given the conservative 30g launch loads and heavy 6 kg mirror mass.

It was shown in the *SPACAR* model verification that there were errors of up to 29% in the maximum predicted stress compared to ANSYS. Thus the results in Table 9.2 are indicative at best. From a purely qualitative perspective, the margin of safety is large enough for all parts that there is still confidence that the PMAO would survive launch if designed without stress concentrations.

The results also confirmed several findings from the initial sizing calculations:

- The dominant load case for the universal joints was any combination of an out of plane load $F_{L,Z}$ and an in-plane load ($F_{L,X}$ or $F_{L,Y}$).
- The dominant load case for the in plane constraint wire flexures was any combination of in plane loads $F_{L,X}$ and $F_{L,Y}$.
- The dominant load case for the bipod struts was a combination of the $F_{L,X}$ and $F_{L,Y}$ load cases on bipods BB and BC.

9.2.2. Static Analysis: Buckling Failure

Verification Activities: VA-06-[01-03]-02 [pass]

The method used to check for failure in buckling at the assembly level was described in Subsection 8.9.2. The critical buckling loads in the X_M, Y_M and Z_M directions for an external load applied at the position of the mirror centre of mass are shown in Figure 9.2. Higher order buckling modes are not shown as the model verification work in Chapter 8 *Mechanical Design* found that the moving frame and in plane constraint *SPACAR* models were unable to accurately predict these.

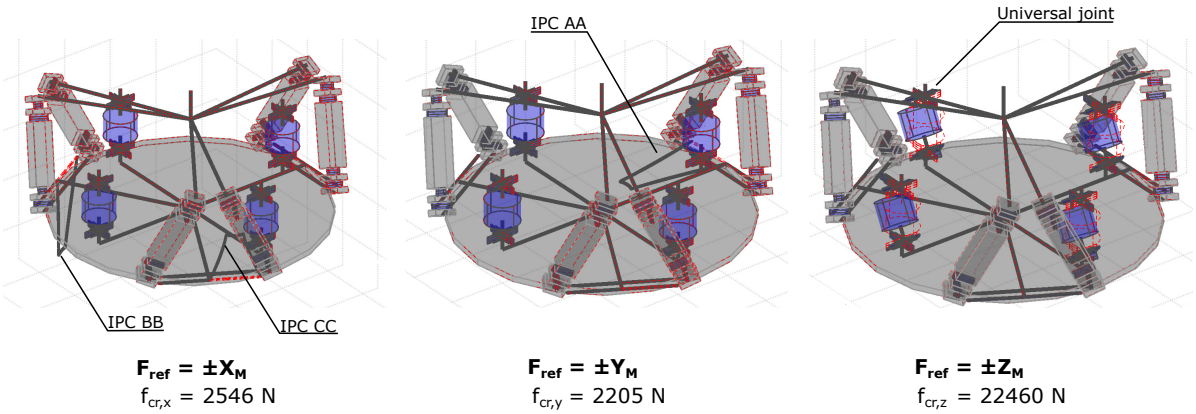

Figure 9.2: First critical buckling load for PMAO mechanism assembly in X_M, Y_M, Z_M directions. In-plane constraint (IPC) wire flexure AA buckles first with a 2205 N load applied in the Y_M direction, followed by simultaneous buckling of IPC wire flexures BB and CC under a 2546 N load in the X_M direction. The universal joints buckle before the bipod struts for loads in the Z_M direction, with a very high critical buckling load of 22.46 kN.

The margins of safety against buckling for the assembly are summarised in Table 9.3. The components most susceptible to buckling were the very slender in-plane constraint wire flexures, though they were still predicted to survive with a margin of safety of 0.25. They are weakest when the external load is applied parallel to their slender axis.

Interestingly, in Section 8.5, the universal joints were predicted to buckle under the launch loads when analysed on their own. In contrast, their buckling strength at the assembly level increased significantly, with a critical buckling load of more than 22 kN. This surprising result was attributed to the change in the end conditions of the joint flexures once integrated into the assembly. The universal joint component models were analysed with fixed/ free boundary conditions, whereas they are fixed/ fixed in the integrated model. Still, the increase in strength is very large and worth further verification with ANSYS if a commercial license becomes available.

Similarly, the bipod strut buckling analysis in Subsection 8.8.3 suggested that the strut flexures would need to be quite thick to avoid buckling, however their stability also greatly improved at the assembly level.

Table 9.2: Margins of safety against yield in launch. "Uni joint - **A[L/U]**" refers to actuator **A**, **L**ower joint/ **U**pper joint. MSy = Margin of Safety (yield). LC = Load Case. IPC = In Plane Constraint wire flexure.

			Compression			Tension		
Part	**Limit Load or Stress**	**MSy**	**Stress/ Load**	**LC**	**MSy**	**Stress/ Load**	**LC**	**Critical Failure Mode**
IPC - AA	1060 MPa	1.34	453 MPa	-FLx, -Fly & -FLx, +FLy	1.25	471 MPa	+FLx, -Fly & +FLx, +Fly	Tension
IPC - BB	1060 MPa	0.82	583 MPa	+FLx, +FLy	0.83	580 MPa	-FLx, -FLy	Compression
IPC - CC	1060 MPa	0.82	583 MPa	+FLx, -FLy	0.83	580 MPa	-FLx, +FLy	Compression
Uni joint - AL	1060 MPa	2.65	290 MPa	-FLx, +FLz	5.32	168 MPa	+FLx, -FLz	Compression
Uni joint - AU	1060 MPa	3.15	256 MPa	-FLx, +FLz	2.94	269 MPa	+FLx, -FLz	Tension
Uni joint - BL	1060 MPa	2.65	290 MPa	-FLy, +FLz	3.41	240 MPa	+FLy, -FLz	Compression
Uni joint - BU	1060 MPa	3.15	256 MPa	-FLy, +FLz	2.93	270 MPa	+FLy, -FLz	Tension
Uni joint - CL	1060 MPa	2.65	290 MPa	+FLx, +FLz	3.41	241 MPa	-FLx, -FLz	Compression
Uni joint - CU	1060 MPa	3.15	256 MPa	+FLx, +FLz	2.93	270 MPa	-FLx, -FLz	Tension
Uni joint - DL	1060 MPa	2.65	290 MPa	+FLy, +FLz	3.41	240 MPa	-FLy, -FLz	Compression
Uni joint - DU	1060 MPa	3.15	256 MPa	+FLy, +FLz	2.93	270 MPa	-FLy, -FLz	Tension
Bipod strut - BA1	1060 MPa	17.16	58 MPa	-FLy, -FLz	17.16	58 MPa	+FLy, +FLz	Tension
Bipod strut - BA2	1060 MPa	17.16	58 MPa	+FLy, -FLz	17.16	58 MPa	-FLy, +FLz	Tension
Bipod strut - BB1	1060 MPa	14.78	67 MPa	+FLx, +FLy	14.76	67 MPa	-FLx, -FLy	Tension
Bipod strut - BB2	1060 MPa	14.83	67 MPa	-FLx, +FLz	14.81	67 MPa	+FLx, +FLy	Tension
Bipod strut - BC1	1060 MPa	14.83	67 MPa	-FLx, +FLy	14.81	67 MPa	+FLx, -FLy	Tension
Bipod strut - BC2	1060 MPa	14.78	67 MPa	+FLx, -FLy	14.77	67 MPa	-FLx, +FLy	Tension
Actuator A	2218 N	0.33	-1674 N	-FLx, +FLz	0.33	1674 N	-FLx, -FLy	Tension or Compression
Actuator B	2218 N	0.33	-1674 N	-FLy, +FLz	0.33	1674 N	+FLy, -FLz	Tension or Compression
Actuator C	2218 N	0.33	-1674 N	+FLx, +FLz	0.33	1674 N	-FLx, -FLz	Tension or Compression
Actuator D	2218 N	0.33	-1674 N	+FLy, +FLz	0.33	1674 N	-FLy, -FLz	Tension or Compression

Table 9.3: Margin of safety against linear buckling MS_{buckle} for the PMAO mechanism assembly. Reference and applied loads applied to the mirror COM. The load applied by the mirror mass $\mathbf{F_{applied}}$ and the critical buckling load $\mathbf{f_{cr}}$ are also given. IPC = In Plane Constraint.

Reference Direction	$\mathbf{f_{cr}}$ $[N]$	$\mathbf{F_{applied}}$ $[N]$	$\mathbf{MS_{buckle}}$ $[-]$	**Critical Component**
X_M	2546	1765	0.44	IPC wire BB & CC
Y_M	2205	1765	0.25	IPC wire AA
Z_M	22460	1765	11.72	Universal joints

Their margins of safety against yield at the component level, given in Table 9.2, were also very large. There is scope here to optimise their design to reduce mass and improve the bending compliance of the flexures. This will further improve their axial and transverse decoupling, to impose even smaller stresses on the mirror.

Overall, the high margins of safety in both yield and buckling failure criteria demonstrate that the PMAO design is conservative, especially considering the large 30g quasi-static loads and generous 6 kg mirror mass. Nevertheless, it should survive launch.

9.2.3. Modal Analysis

Verification Activities: VA-06-04 [pass]

The first three eigenmodes for the PMAO mechanism assembly are shown in Figure 9.3. The results show that the fundamental frequency was predicted to be almost a factor of two greater than the required 100 Hz, much more than the 15% margin considered acceptable at the preliminary design stage [122, p. 671]. It was concluded that the design was compliant with the dynamic launch survival requirement. With light-weighting of the moving mass of the PMAO, this margin could be improved further.

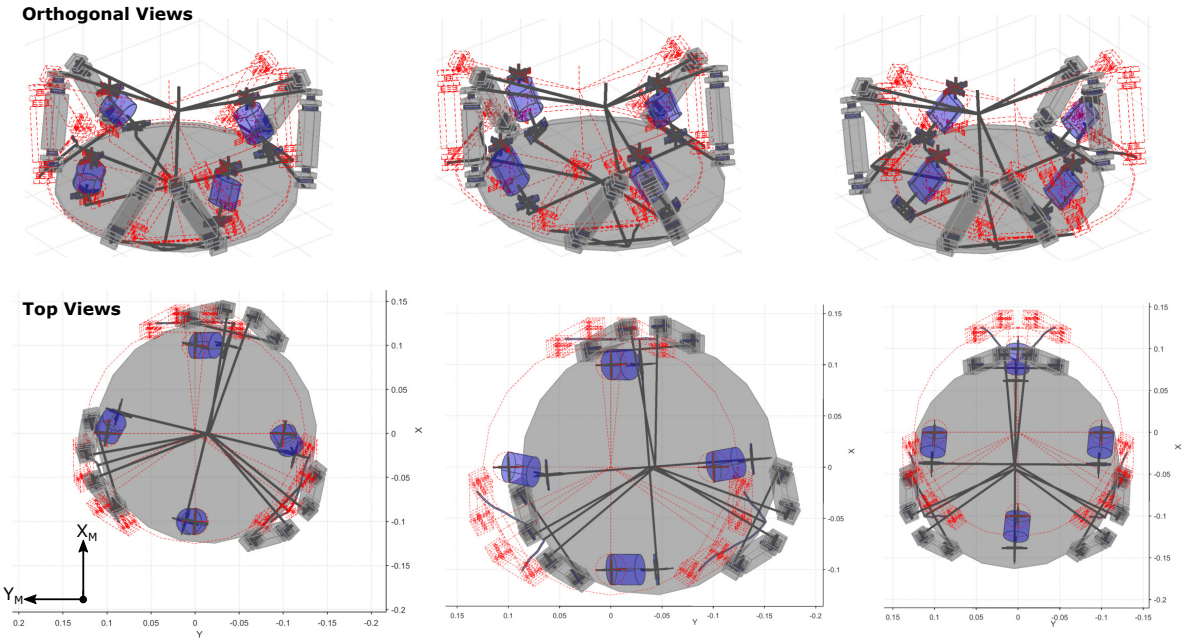

Figure 9.3: First three eigenmodes and eigenfrequencies for the PMAO mechanism assembly.

The first three eigenmodes were dominated by the in-plane freedoms ostensibly constrained by the IPC wire flexures. The first mode was a translation in the Y_M direction coupled with a small Z_M rotation, the second was a more pronounced translation in the Y_M direction and weaker Z_M rotation, and the third mode was a dominant translation in the X_M direction. Unsurprisingly, all three modes were caused by the much lower bending stiffness of the wire flexures compared to the universal joint and bipod strut sub-assemblies.

There was very little separation in these first three eigenfrequencies, a consequence of the symmetry of the in-plane constraint sub-assembly. Recall that the ANSYS verification of the in plane constraint *SPACAR*

model showed that the *SPACAR* analysis made very poor predictions of the second and third eigenfrequencies. These modes are suppressed by the presence of the universal joints at the assembly level, though the results presented here should still be treated as qualitative predictions at best.

Although verification of the top down stability budget was not possible without a coupled loads analysis including the M1 deployment mechanism, these modal results do give a qualitative prediction of the optical effects of exciting the PMAO at its natural frequency. For example, on its own, excitation of the PMAO mechanism will primarily cause a decentre with a small rotation about the z axis of the mirror segment.

9.2.4. Support Kinematic Performance

Verification Activities: VA-05-[01-03] [partial], VA-07 [pass], VA-08-01 [partial]

Requirement PMAO-MEC-03 states the the PMAO must support the mirror through launch. Verification of this requirement was broken down into three activities: A check that the support could survive the launch loads with the mirror; a check that the mirror was not overconstrained and a check that the lateral stiffness of the mirror support was at least 1000 times more compliant than the mirror.

The stress and buckling analysis results in Subsections 9.2.1 and 9.2.2 demonstrated that the PMAO can support the mirror through launch. It was also shown in Subsection 8.8.1 that the radial stiffness of the mirror was at least 7.96×10^8 N/m and that the transverse bending stiffness of one strut was 7.22×10^4 N/m. The combined transverse stiffness of the two struts in each bipod was then 1.44×10^5 N/m, more than 5000 times less stiff than the mirror.

For the bipods to not overconstrain the mirror, the bending stiffness of each *strut* should be at least 1000 times less than that of its axial stiffness. This ensures that each strut constrains only a single rigid body DOF of the mirror. Applying a 1 N reference load to the end of one of the bipod struts along its longitudinal axis in ANSYS yielded an average displacement of 14.2 nm of that end face, giving an effective axial stiffness of 70.3×10^6 N/m. The axial to bending stiffness ratio of the strut was thus 974, marginally less than the benchmark decoupling.

It was concluded that compliance with requirement PMAO-MEC-03 was partial. The requirement that the strut have a decoupling factor of 1000 between axial and bending DOFs is a rule of thumb that is violated by less than 3%. The bending stiffness of the strut can be reduced relatively easily by increasing the flexure lengths, reducing their thickness and/ or width or by changing their profile. The buckling and yield strength analyses showed that the struts, at the assembly level, have considerable margins of safety, so there is some flexibility to weaken them and improve the DOF decoupling.

Moreover, the effect of the less than ideal decoupling on distortions of the optical surface of the mirror also very strongly depends on the mirror design itself, which is a topic for future work.

9.3. Operations Survival Verification Activities

Verification Activities: VA-09-01 [pass], VA-08-01 [partial]

The verification plan assumed that the launch loads will be much larger than any other inertial loads experienced by the mechanism during AIT, LEOP and imaging operations. It was also noted that the configuration of the PMAO does not change between launch and operations, with the exception that the actuators are powered. Thus to simplify the verification, the ability of the PMAO to survive inertial loads in operations was assumed to logically follow from its ability to survive the launch loads. Since requirement PMAO-MEC-40 was verified by activities VA-06-01 to -05 above, it was assumed that the design also passed activity VA-09-01.

Similarly, the The verification plan assumed that if the PMAO mechanism could support the mirror through launch then it could also do so during operations. The partial compliance with the launch requirement therefore flows down to the operations support requirement, PMAO-MEC-04, through activity VA-08-01.

The results of a yield failure analysis under the internal loads generated during actuation of the mechanism are document in Subsection 9.3.1. A similar check for thermal loads during the thermally dynamic LEOP mission phase is made in Subsection 9.3.2. A brief note regarding the inability to verify the design against deployment loads is given in Subsection 9.3.3.

9.3.1. Static Analysis: Actuation Loads

Verification Activities: VA-09-03 [pass]

The objective of verification activity VA-09-03 was to check that the mechanism won't fail due to internal loads from the actuators during nominal operations. It was assumed that the maximum stresses would occur when the end effector is displaced to the eight corners of the workspace, illustrated conceptually in Figure

9.4. The margins of safety were calculated using the same process as for the launch loads although a safety factor for yield of 1.25 was used per the *DST Requirements and Verification* guidelines document in Appendix D. Standard Earth gravity was also applied to simulate the maximum actuation loads during terrestrial AIT.

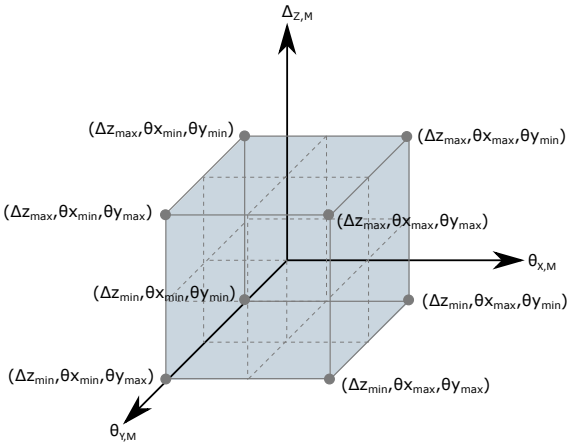

Figure 9.4: Conceptual representation of the workspace of the mechanism end effector. The origin of the moving frame $\mathbf{O_{MF}}$ is manipulated in the region bounded by the minimum and maximum required ranges of motion in tip, tilt and piston.

The results of the load analysis are given in Table 9.4. Only the quasi-static loads required to *hold* the mirror in the listed poses were calculated. These will be less than the loads required to deform the compliant elements *and* accelerate the moving mass. This would be a useful application of the *SPACAR* model, in conjunction with trajectory planning, in future work.

The results show that the location of maximum stress moves around the mechanism as a function of the pose. It is not expected to exceed more than ≈2.1 MPa. As a sanity check, the maximum bending stress in an IPC wire flexure can be estimated with the simple model shown in Figure 9.5. Consider for example a 4 μm pure piston motion of the moving frame, driven by a downwards force via the moving frame in the middle of the wire.

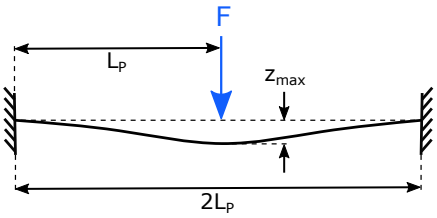

Figure 9.5: Simple model of a piston deflection z_{max} of an IPC wire flexure. Each end is fixed to the fixed frame and a transverse load F is applied to the wire by the moving frame.

Since the length to thickness ratio is large, the bending stresses at the outer fibres of the beam will be larger than the shear stresses along the neutral axis [26, p. 97]. The relationship between the transverse deflection at the centre of the beam and applied load is

$$z_{max} = -\frac{(2L_P)^3 F}{192EI} \tag{9.1}$$

The maximum bending moment is at the centre of the beam, given by $M_{max} = F(2L_P)/8$. The resulting stress is $\sigma = Mc/I$ with c the maximum distance from the centre of the beam to the outer fibre, here equal to $t_P/2$ and I the second moment of area of the cross-section. Combining these equations, the maximum stress due to a transverse displacement is

$$\sigma = \frac{12Et_P z_{max}}{L_P^2} \tag{9.2}$$

This gives a bending stress of 0.95 MPa for the wire flexures under a 4 μm pure piston displacement. The stress can be expected to be a little higher with the addition of tip and tilt displacements, as shown by the

Table 9.4: Margins of safety against yield for nominal displacements in operations. Safety factor of 1.25 applied. "Uni joint - **A[L/U]**" refers to actuator **A**, **L**ower joint/ **U**pper joint. MSy = Margin of Safety (yield). $\theta_{X,M}, \theta_{Y,M}, \Delta_{Z,M}$ give pose of $\mathbf{O_{MF}}$ for each MSy. IPC = In Plane Constraint wire flexure.

		Compression					Tension					
Part	**Limit Load/ Stress**	**MSy**	**Stress/ Load**	$\theta_{\mathbf{X,M}}$	$\theta_{\mathbf{Y,M}}$	$\Delta_{\mathbf{Z,M}}$	**MSy**	**Stress/ Load**	$\theta_{\mathbf{X,M}}$	$\theta_{\mathbf{Y,M}}$	$\Delta_{\mathbf{Z,M}}$	**Critical Failure Mode**
				$[\mu rad]$	$[\mu rad]$	$[\mu m]$			$[\mu rad]$	$[\mu rad]$	$[\mu m]$	
IPC - AA	1060 MPa	722	1.17 MPa	-2	4	-4	722	1.17 MPa	2	4	-4	Tension
IPC - BB	1060 MPa	726	1.17 MPa	-2	-4	-4	737	1.15 MPa	-2	-4	-4	Compression
IPC - CC	1060 MPa	-	-	-	-	-	726	1.17 MPa	2	-4	-4	Tension
Uni joint - AL	1060 MPa	434	1.95 MPa	-2	-4	4	434	1.95 MPa	2	-4	4	Tension or Compression
Uni joint - AU	1060 MPa	-	-	-	-	-	403	2.10 MPa	-2	-4	4	Tension
Uni joint - BL	1060 MPa	429	1.97 MPa	-2	-4	4	429	1.97 MPa	2	-4	4	Tension or Compression
Uni joint - BU	1060 MPa	401	2.11 MPa	2	4	4	401	2.11 MPa	2	-4	4	Tension or Compression
Uni joint - CL	1060 MPa	434	1.95 MPa	2	4	4	432	1.96 MPa	-2	4	4	Tension
Uni joint - CU	1060 MPa	402	2.10 MPa	-2	4	4	402	2.10 MPa	-2	-4	4	Tension or Compression
Uni joint - DL	1060 MPa	439	1.93 MPa	-2	-4	4	429	1.97 MPa	-2	-4	4	Tension
Uni joint - DU	1060 MPa	401	2.11 MPa	-2	-4	4	401	2.11 MPa	-2	4	4	Tension or Compression
Bipod - BA1	1060 MPa	2161	0.39 MPa	2	-4	-4	2060	0.41 MPa	-2	-4	-4	Tension
Bipod - BA2	1060 MPa	2059	0.41 MPa	-2	-4	-4	2059	0.41 MPa	-2	4	-4	Tension or Compression
Bipod - BB1	1060 MPa	-	-	-	-	-	2056	0.41 MPa	-2	-4	-4	Tension
Bipod - BB2	1060 MPa	2155	0.39 MPa	2	-4	-4	2053	0.41 MPa	-2	-4	-4	Tension
Bipod - BC1	1060 MPa	2161	0.39 MPa	2	4	-4	2054	0.41 MPa	-2	-4	-4	Tension
Bipod - BC2	1060 MPa	2057	0.41 MPa	-2	-4	-4	2057	0.41 MPa	-2	4	-4	Tension or Compression

Table 9.5: Summary of critical thermal load strength calculations during LEOP. SS = Steady State. IPC = In Plane Constraint. MF = Moving Frame.

Part	**Thermal Source**	**Failure Mode**	**Allowable Load**	**Design Load**	**Status**	**Comment**
Universal joint	SS bulk temperature change	Buckling	$\Delta T = 2285\ K$	135 K to SS cold temp	OK	§8.5.1, eqn 8.36 & 8.27, App. C.
Universal joint	SS heat source	Buckling	27.4 W	0.05 W (estimate)	OK	Per joint flexure. §8.5.1, eqn 8.37 & 8.27
IPC wire flexures	SS bulk temperature change	Buckling	$\Delta T = 318\ K$	135 K to SS cold temp	OK	§8.7.2, eqn 8.38 & 8.27
IPC wire flexures	SS heat source	Buckling	0.2 W	0.134 W (estimate)	OK	Per wire flexure. §8.7.2, eqn 8.37 & 8.27
MF plate	SS bulk temperature change	Yield (of uni joint)	$\Delta T = 442\ K$	135 K to SS cold temp	OK	§8.7 eqn 8.49

results for the wire flexures in Table 9.4. Evidently the actuation loads will be very small compared to the launch loads.

There are three instances in Table 9.4 where there are no compression loads listed. This is because the analysis was conducted with a gravity vector pointing in the negative Z_M direction. For all poses, the actuation loads were much smaller than the reaction forces in the members due to the self weight of the mirror and mechanism, so some members did not leave the compressive state. A similar analysis could be conducted with a gravity vector in the X_M or Y_M directions to simulate AIT with the mechanism on its side.

It was concluded that the mechanism was more than capable of surviving the internal stresses generated by the mechanism during nominal operations both on the ground and in orbit.

This analysis was conducted for the nominal mechanism range of motion before the larger $\pm 9\ \mu rad$ tip/tilt and $\pm 4\ \mu m$ piston workspace had been confirmed. The very high margins of safety shown in Table 9.4, coupled with the knowledge that the displacements of the flexures are dominated by the piston range, which doesn't change, provide confidence that the mechanism will not fail during actuation for the larger range of motion capability.

9.3.2. LEOP Thermal Loads

Verification Activities: VA-08-02 [pass], VA-09-02 [partial], VA-10 [partial]

Analysis of the LEOP thermal loads was divided into three portions. First, stresses on the support bipods for the worst-case differential thermo-elastic expansion between the mirror and support was checked. This analysis wasn't necessary for the same parts since they were all assumed to be made of the same material. Thus the second portion of analysis focussed on stresses arising from temperature gradients across the individual components. The actuator temperature ratings were also checked.

Mirror/ Support Differential Thermo-Elastic Strain

Activity VA-08-02 checks that the mirror supports do not plastically deform under the worst-case differential thermo-elastic strain between the mirror and support. A strain of 0.201 mm between the mirror and support during LEOP was calculated in the bipod sizing process, Subsection 8.8.1. An equivalent stress of 45.1 MPa with a margin of safety against yield of 22.5 was found in the support struts for this load case during the ANSYS verification modelling. Thus the support should survive the worst-case LEOP thermal loads.

Component Steady State Thermo-Elastic Stresses

The objective of VA-10 was to make sure that no parts plastically deform due to large operational thermal loads. It was assumed that the largest thermal loads would occur in LEOP without the protection of the baffle, and that if the mechanism could be shown to survive the thermal loads of that phase, then it could survive the thermal loads of all other phases. Thus activity VA-09-02 follows logically from VA-10. It was assumed in Chapter 4 *Verification Plan* that the stresses induced by thermal launch loads were captured by the 30g quasi static loads.

Calculations for VA-10 were already performed at the initial sizing stage for each component and were refreshed with the revised PMAO baseline geometry in Table 8.16. The results are summarised in Table 9.5, along with references to the governing equations. The largest predicted departure from the nominal 298 K assembly temperature is to the LEOP steady state cold qualification temperature, a difference of 135 K per Table 3.4. None of the parts were predicted to fail. No strength checks were made for those components able to expand and contract freely (ie. the bipod struts) since their fixture conditions do not drive a build up of internal stresses from thermal strains.

Actuator Temperature Limits

Critically, the Cedrat PPA XL family of actuators are rated for ambient temperatures of only 288 to 298 K during powered operations [29]. The datasheet does not supply a maximum non-operational temperature range however, an environmental temperature limit of 373 K was specified for the SPICE instrument on ROSETTA, which also used Cedrat PPA actuators [60]. Adopting this same limit, which gives a 50 K buffer from the 423 K Curie temperature of the piezoelectric ceramic, shows that the thermal conditions around the actuators must be controlled. This is a key flow down requirement for the thermal control system, formalised in Section 9.6 *Flow Down Requirements*.

The calculations referenced in Table 9.5 are admittedly very rough and should certainly be verified with more detailed coupled thermo-mechanical finite element analysis. This will be possible at the conclusion of the initial thermal modelling for the DST, which was still ongoing at the time of writing. Requirement PMAO-MEC-41-01 can only be considered to be partially verified until the thermal control system design matures.

9.3.3. Deployment Loads

Verification Activities: VA-11 [TBD]

Requirement PMAO-MEC-42 "Survive deployment" could not be verified as the loads generated by the deployment mechanism have not yet been quantified. While deployment would nominally be smooth, there is a known "snapping" phenomena once the M2 booms reach their final position. It is likely that this shock will be less than any to be experienced by the mechanism during launch, which were already accounted for in the 30g launch loads. However, this cannot be guaranteed until further analysis is made available. Therefore, verification of this requirement remains to be determined.

9.4. Operations Functionality Verification Activities

This section sets out the verification status of the PMAO with respect to the functional requirements during on-orbit operations. A large proportion of the functional requirements are contingent upon the outcomes of other ongoing thermal and mechanical design efforts, and remain unverified. Further discussion regarding this is left to Section 10.3 *Future Work*.

The top down system budgets are addressed first in Subsection 9.4.1. The remaining operations functional requirements were verified at the telescope level using the newly developed PMAO *SPACAR* simulation and its integration with the ETEP model. Subsection 9.4.2 introduces the simulation methodology. Initial results found that the M1 calibration procedure was requesting unexpectedly large actuator strokes. A modification to the error function used by the optimisation algorithm lead to a more efficient use of the available actuator stroke. These findings are presented in Subsection 9.4.3.

The remaining functional verification activities were conducted using the ETEP model with the new calibration algorithm. The ability of the mechanism to facilitate diffraction limited imaging is verified in Subsection 9.4.4. The mechanism workspace and required actuator stroke requirements are verified in Subsection 9.4.5, followed by a quantitative analysis of the mechanism accuracy, precision and likely error sources in Subsection 9.4.6. An initial note on the thermal requirements during operations is given below.

Operations Thermal Requirements

Verification Activities: VA-19-[01,02] [TBD]

Requirement M1-MEC-15 states that the PMAO must meet the functional requirements at the operations design temperature of 298 ± 1 K in vacuum. The design thermal uncertainty margin of ± 15 K is added to this range to account for the preliminary design status. Data from ongoing thermo-mechanical efforts by others in the DST team was needed to rigorously verify this requirement. Where possible, first order estimates of the PMAO performance at the design temperatures are provided throughout this section. A plan to complete the remaining verification activities is given in Section 10.3 *Future Work*.

9.4.1. Top Down Systems Budgets

Since the top down budget requirements M1-MEC-01, M1-MEC-04 and M1-MEC-07 were defined for the entire M1 sub-assembly, their verification was integrally dependent on the maturity of the deployment and PMAO mechanism designs. It was acknowledged in Chapter 3 *Requirements Generation* that dependence on other components and availability of a FEA license with an analysis domain capable of capturing the entire sub-assembly would expose the PMAO verification to the risk that some requirements would be unverifiable.

As of the conclusion of the PMAO verification phase, neither the M1 deployment mechanism design had been completed nor was an extended FEA license available. Nevertheless, a qualitative assessment of the PMAO mechanisms' performance was possible for the deployment and in-orbit drift budgets, documented in the following subsections.

It is strongly recommended that the top down budgets be decomposed to the subsystem level so that verification is possible with the resources available to MSc students. The addition of the PMAO *SPACAR* package to the ETEP model is a sound step in this direction. A plan to continue the verification work is given in Section 10.3 *Future Work*.

Deployment Tolerance Budget

Verification Activities: VA-12 [TBD]

The deployment tolerance budget will be dominated by the repeatability of the deployment mechanism kinematic interface. Smaller contributions will come from "settling" of the bolted interfaces throughout the PMAO and deployment mechanism from mechanical loads during launch and deployment, as well as from

thermal creep [106]. Rigorous verification of the deployment tolerance budget therefore requires definition of each of the interfaces and settling forces. As a minimum, a first pass model of the contact stresses in the deployment mechanism interface is needed. Defining the interfaces is a subject for more detailed, future work[1].

In Orbit Drift Tolerance Budget

Verification Activities: VA-13 [TBD], VA-17 [partial]

In-Plane Drift

Requirement PMAO-MEC-35 was verified via verification activity VA-17, which requires a check of the location of the thermal centre. Conceptually, inspection of the kinematics of the PMAO suggest that, due to symmetry in the $X_M Y_M$ plane, the use of exact constraint design principles, monolithic fabrication of the in-plane constraints and use of a single material throughout the structure, a thermal centre at the mirror centroid will be maintained. This conclusion also assumes that the entirety of the structure can be maintained at the same bulk temperature.

In reality, imperfections in the dimensions of assembly and fabrication, inhomogeneities in the material and temperature gradients will all cause small but non-zero drifts. Sensitivity analyses can be used to establish budgets for the allowable operational gradients however this is well beyond the scope of this thesis. At the conclusion of the current tranche of MSc projects, the overall design will be in a very good position to begin this level of verification. It was concluded that the design was partially compliant with PMAO-MEC-35 though it is recommended that a coupled thermo-mechanical FEA study of the whole PMAO mechanism be conducted.

Out of Plane Drift

Verification activity VA-13 refers to the in-orbit drift budget. An initial estimate of the thermal drift in the piston direction is possible without detailed analysis tools. The results from the following drift, athermalisation and assembly tolerance analyses are summarised in Table 9.6 at the end of this analysis. The vertical dimension of each of the components connected in series from the DST housing to the underside of the mirror, shown schematically in Figure 9.6, contribute to the piston drift. Assuming that all components are maintained at the same temperature, then the piston drift Δz is equal to

$$\Delta z = \left(h_{FF}\alpha_{FF} - h_{stack}\alpha_{stack} + (h-q)\alpha_{strut}\right)\Delta T \tag{9.3}$$

Taking α_{Ti} from Appendix K *Material Properties* and dimensions from Table 8.16 with the assumption that the outer frames of the PPA actuators are made from Ti-6Al-4V, the piston drift for a non-athermalised design over the nominal operations temperature swing of ± 1 K is approximately 1.2 μm. With the design thermal uncertainty margin of ± 15 K applied, the drift increases to 19.1 μm. The maximum allowable in orbit drift in the Z_M direction per Table 3.3 is 20 nm so clearly athermalisation is required.

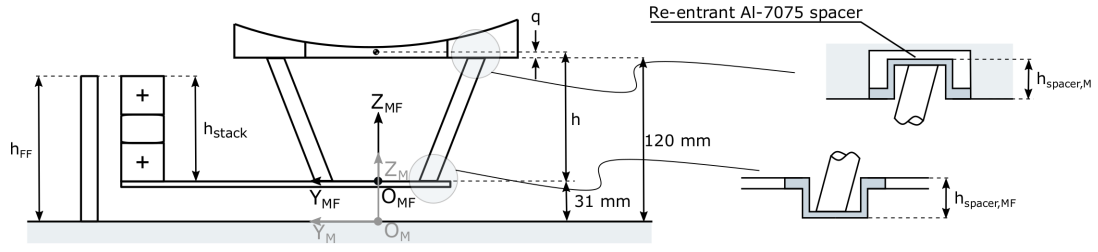

Figure 9.6: Component contributions to piston drift and conceptualisation of an athermalisation method.

Passive Athermalisation

The thermal expansion can be nulled by introducing a spacer that will expand or contract in opposition to the net growth of the assembly. This is called passively compensated athermalisation. Figure 9.6 illustrates a simple embodiment of this concept where the Titanium strut is mated to the mirror with a re-entrant spacer made of a material with much higher CTE. The detailed design of the spacer, its interactions with the stress

[1] Smith & Chetwynd give a simple but useful introduction to the position errors that arise from Hertzian stresses in kinematic joints [106, p. 131].

distribution within the mirror and launch survival analysis were not investigated, though each task is not expected to expose the PMAO feasibility to high technical risk.

With the addition of a spacer, equation 9.3 becomes

$$\Delta z = \left(h_{FF}\alpha_{FF} - h_{stack}\alpha_{stack} + (h-q)\alpha_{strut} - h_{spacer}\alpha_{spacer}\right)\Delta T \tag{9.4}$$

For an Al-7075 spacer, this yields a required height of 50.9 mm to null the drift. As suggested in Figure 9.6, the spacer could be divided into two lengths of 25.45 mm that could be accommodated within both the mirror substrate and below the moving frame. The resulting Δz drift is 0.8 nm for the ± 1 K swing case and 12.8 nm for the ± 16 K swing case, both compliant with requirement M1-MEC-04 and the top-down budget in Table 3.3.

Effect of Assembly Tolerances

It is interesting to look at the sensitivity of the athermalisation to fabrication tolerances. Standard (non-precision) machining methods can provide 0.2 mm dimensional accuracy. The worst-case stacking of this error from each of the components results in a thermal drift of 48 nm for the ± 1 K case and 760 nm for the ± 16 K case. Clearly, fabrication tolerances must be tighter than 0.2 mm, though some of this could be actively compensated by the actuators.

Table 9.6: Contributions from PAMO components to piston thermal drift. Unless noted otherwise, all mechanism components are made of Ti-6Al-4V and the spacer, when used, is Al-7075. All components assumed at the same bulk temperature in each case. Predicted thermal drifts Δz that exceed the 20 nm requirement for M1 are underlined. I-36 refers to Invar-36. "fab. tol." refers to the worst-case (greatest drift) inclusion of 0.2 mm fabrication tolerances on each of the height dimensions in equation 9.4.

Description	**ΔT** [K]	**Δh_{FF}** [μm]	**Δh_{stack}** [μm]	**Δh_{strut}** [μm]	**Δh_{spacer}** [μm]	**Δz** [μm]
No spacer	1	1.040	0.740	0.892	-	1.192
No spacer	16	16.64	11.84	14.27	-	19.07
50.9 mm spacer	1	1.040	0.740	0.892	1.191	0.001
50.9 mm spacer	16	16.64	11.84	14.27	19.06	0.013
50.9 mm spacer, fab. tol.	1	1.042	0.702	0.894	1.186	0.048
50.9 mm spacer, fab. tol.	16	16.67	11.23	14.30	18.98	0.760
I-36 struts, no spacer	1	1.040	0.740	0.112	-	0.412
I-36 struts, no spacer	16	16.64	11.84	1.798	-	6.598
I-36 struts, 17.6 mm spacer	1	1.040	0.740	0.112	0.412	0.001
I-36 struts, 17.6 mm spacer	16	16.64	11.84	1.798	6.589	0.009

Alternatively, the extent of the thermal expansion and contraction of the mechanism could be reduced by changing the material of the fixed frame and/ or the bipods. A common candidate in these applications is Invar-36, which has a CTE almost eight times less than Ti-6Al-4V at room temperature. Recall from Section 8.3 *Material Selection*, that Invar-36 has a density almost twice that of Ti-6Al-4V, a higher modulus of elasticity and a yield strength nearly a quarter that of Ti-6Al-4V, so the structure would be heavier and/ or weaker than the existing design. Nevertheless, simply changing the struts to Invar-36 would reduce the necessary Al-7075 spacer length to a more manageable 17.6 mm.

Thermal Drift Conclusion

The 20 nm piston drift budget is challenging and the relatively large piston thermal drift of the PMAO mechanism is certainly one of its major weaknesses. The analysis shows that it *is* possible to meet the piston drift budget, even with temperature swings of up to ± 16 K. For simplicity, the recommended design retains the 50.9 mm Al-7075 spacer with the knowledge that there is some flexibility offered by changing the strut material or using the PMAO for active correction.

It is acknowledged that tilt drifts have not been analysed here, nor have the effects of gradients or contributions from the deployment mechanism. It is recommended that the current PMAO design be retained until the thermal modelling, thermal control system design and assembly tolerance modelling mature, enabling more informed decisions regarding both what is necessary and what is possible.

Structural Stability Tolerance Budget

Verification Activities: VA-14 [TBD]

There is little that can be concluded regarding the structural stability tolerance budget without modelling of the harmonic response of the combined PMAO and deployment mechanism assemblies. It is recommended that student access to a commercial FEA license be secured to verify this requirement. A consistent verification strategy, including standardisation of indicative excitation sources should also be considered to improve the consistency and efficiency of verification work across the team.

9.4.2. End To End Performance Simulation Setup

The PMAO *SPACAR* model was integrated into the ETEP model to simulate the performance of the PMAO at the telescope level. The results summarised in Subsections 9.4.3 to 9.4.6 are based on two Monte Carlo analysis datasets, each comprised of 500 unique deployment cases simulated with the telescope ETEP model. The aim of this analysis was to establish the following:

1. Verify the predicted segment workspace, and thus the required actuator stroke.
2. Quantify the average position and orientation error of the mechanism.
3. Demonstrate that the PMAO is able to facilitate retrieval of a diffraction limited image, indicated by a calibrated Strehl Ratio >0.80, and understand the degradation in performance compared to the ideal model used in previous ETEP modelling.

In each run of the Monte Carlo simulation, the position, orientation and shape of each of the optical elements were perturbed by pseudo-randomly generated values extracted from a *continuous* normal distribution based on the deployment tolerance budgets in Table 3.3.

Note that the PMAO was designed to the top down budget requirements which are based on the 2σ values from normal distributions of position and orientation errors. Since the Monte Carlo method selects the perturbation from a continuous distribution, approximately 5% of the deployed segment positions will be beyond the as-designed range of the PMAO. This was an acknowledged trade-off between relaxing the design requirements and ensuring that the primary mirror can be calibrated post-deployment. Thus the PMAO, as a minimum, can only be expected to correct 95.4% of the deployment errors in each degree of freedom of each segment, though it is possible that more deployment cases can be corrected depending on the nature of the deployment errors.

Each Monte Carlo run was executed in three phases:

1. **Phase 1: Post-deployment**
   Position, orientation and shape of all optical elements were randomly perturbed from their nominal state according to the tolerance budgets listed in Table 3.3. Optional coarse calibration can follow, though this is not currently implemented.
2. **Phase 2: M1 co-alignment and co-phasing**
   Execution of the primary mirror calibration procedure per Figure 3.8. The PMAO was manipulated to remove discontinuous wavefront errors. Typically two to ten iterations of the calibration procedure were needed to complete this phase.
3. **Phase 3: Aberration Correction System**
   Continuous wavefront errors were removed using the deformable mirror.

In the early stages of Phase 2, each segment is normally scanned through the full piston range in 100 nm steps to simulate how the control system would determine the wavefront error after deployment in orbit. To eliminate unnecessary computation time, the Phase 2 simulation was started at step four "Piston Phasing" in Figure 3.8, by assuming that the wavefront error was known, removing the need to simulate the piston scan. The results presented herein are no less valid for having made this simplification since the scan does not remove any of the deployment errors.

Both Monte Carlo datasets used the same initial set of 500 unique deployment cases. The first was generated using the original serial piston scan calibration procedure previously described in Subsection 3.2.5 *Primary Mirror Calibration Procedure*. The second dataset was generated using a modified calibration procedure that made more efficient use of the available actuator stroke[2]. The results from the original calibration algorithm are discussed in the next subsection.

[2]The strategy and execution of the calibration procedure modifications, as well as integration of the *SPACAR* & ETEP models, were contributed by Dennis Dolkens as part of his ongoing PhD research.

9.4.3. Modification of Serial Piston Scan Calibration Algorithm

The histograms in Figure 9.7 show the commanded displacement in each of the three controlled degrees of freedom for the first telescope simulation dataset, using the original serial piston scan algorithm. Figure 9.8 shows the histograms for commanded stroke for each of the four actuators. Aggregated statistics for the displacements in each degree of freedom, along with the actuator strokes necessary to achieve them, are given in Table 9.7.

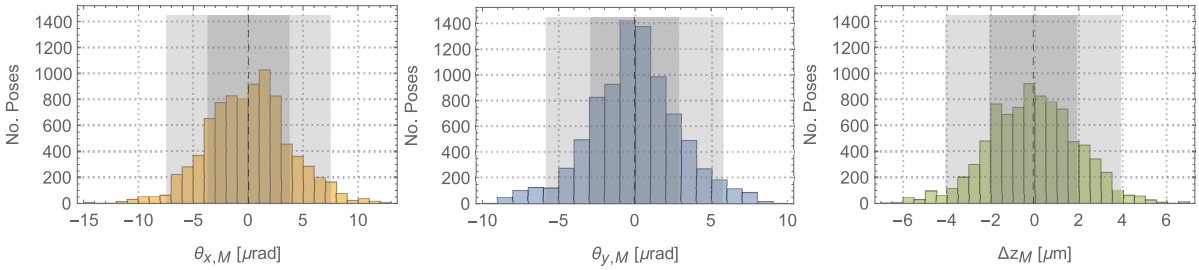

Figure 9.7: Histograms of commanded pose from M1 calibration ETEP simulations. The 1σ and 2σ standard deviation bounds are shaded in dark and light grey respectively. The arithmetic mean is indicated by the dashed line.

The required workspace was much bigger than the design ranges originally predicted in Chapter 7 *Mechanism Architecture Selection.* Almost 12% of the Monte Carlo simulations required actuator strokes exceeding the $\pm 5\ \mu m$ PPA10XL stroke limit at some point in the M1 calibration procedure, rendering the PMAO unable to remove the discontinuous wavefront errors. The largest commanded stroke was a little beyond 7.6 μm, requiring a total actuator stroke of almost 16 μm.

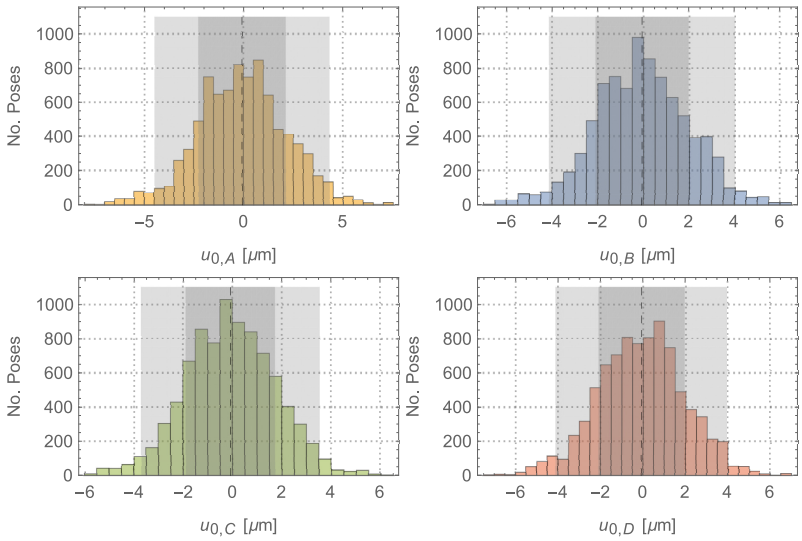

Figure 9.8: Histograms of commanded stroke u_0 for actuators A through D from M1 calibration ETEP simulations. The PPA10XL has an available stroke of $\pm 5\ \mu m$. The 1σ and 2σ standard deviation bounds are shaded in dark and light grey respectively. The arithmetic mean is indicated by the dashed line.

Table 9.7: Statistics for the commanded pose and actuator strokes u_0 from ETEP simulations with original calibration procedure.

	$\theta_{X,M}$ [μrad]	$\theta_{Y,M}$ [μrad]	$\Delta_{Z,M}$ [μm]	$\mathbf{u_{0,A}}$ [μm]	$\mathbf{u_{0,B}}$ [μm]	$\mathbf{u_{0,C}}$ [μm]	$\mathbf{u_{0,D}}$ [μm]	$\mathbf{u_{0,all}}$ [μm]
Minimum	-14.36	-9.10	-6.71	-7.63	-6.61	-5.79	-7.28	-7.63
Maximum	12.28	9.18	6.69	7.35	6.46	6.02	6.91	7.35
Mean	0.03	-0.05	-0.08	-0.07	-0.07	-0.08	-0.08	-0.08
σ (68.2%)	±3.73	±2.90	±1.99	±2.20	±2.03	±1.81	±2.02	±2.02
2σ (95.4%)	±7.47	±5.79	±3.98	±4.40	±4.07	±3.62	±4.04	±4.04

Such a high percentage of failed calibrations suggested that the cause was not merely the presence of deployment cases beyond the 2σ design bounds. In the original calibration procedure, the first mirror segment was kept stationary, to be used as the reference datum off of which the remaining segments were co-phased. In cases where this segment was deployed near the edges of the deployment tolerance budget, such as the case shown for segment one in Figure 3.9 on page 33, the remaining segments must undergo very large piston displacements for the co-phasing (piston alignment) *plus* any extra stroke needed for co-alignment (tip/tilt alignment). The resulting total stroke requirement was likely to exceed the capability of the PPA10XL actuators.

This effect was exacerbated by the omission of remote centre error corrections in the actuator stroke flow down requirement calculation. These errors are quantified in Subsection 9.4.6. The statistics in Table 9.7 demonstrate that this could be more than $\pm 14\ \mu rad$ in $\theta_{x,M}$, compared to the anticipated $\pm 4\mu rad$ range requirement in Figure 3.8.

Recognising this, it was decided to modifying the optimisation algorithm. The inverse kinematic equations 7.30 to 7.33 show that actuator stroke is directly proportional to the commanded piston displacement whereas the tip and tilt rotations are mediated by the actuator mounting radius. The piston displacements thus have a much stronger influence on the required actuator stroke than the tip or tilt rotations.

To illustrate this effect, consider the statistics given in Table 9.8 for the commanded workspace and requisite actuator stroke requirements for all simulations that did *not* the exceed the $\pm 5\ \mu m$ actuator stroke capability.

Table 9.8: Statistics for the commanded pose and actuator strokes from ETEP simulations with original calibration procedure that did not exceed $\pm 5\ \mu m$ actuator stroke capability.

	$\theta_{\mathbf{X,M}}$ $[\mu rad]$	$\theta_{\mathbf{Y,M}}$ $[\mu rad]$	$\Delta_{\mathbf{Z,M}}$ $[\mu m]$	$\mathbf{u_{0,A}}$ $[\mu m]$	$\mathbf{u_{0,B}}$ $[\mu m]$	$\mathbf{u_{0,C}}$ $[\mu m]$	$\mathbf{u_{0,D}}$ $[\mu m]$	$\mathbf{u_{0,all}}$ $[\mu m]$
Minimum	-11.10	-8.60	-4.31	-4.70	-4.67	-4.40	-4.62	-4.70
Maximum	11.71	8.13	4.40	4.93	4.86	4.03	4.31	4.93
Mean	-0.01	-0.06	-0.01	0.00	-0.01	-0.02	-0.01	-0.01
σ (68.2%)	3.58	2.56	1.75	1.92	1.79	1.60	1.78	1.78
2σ (95.4%)	7.16	5.13	3.50	3.84	3.57	3.20	3.57	3.55

The largest commanded segment piston displacement was reduced by 2.3 μm from 6.7 μm to 4.4 μm, reducing the maximum required actuator stroke from 7.6 μm to 4.9 μm: a difference of 2.7 μm. The reduction in piston displacement at the segment level reduced the required actuator stroke by 85%. Thus the most efficient improvement to the calibration algorithm was expected to be a reduction in the piston displacement requirement. This was achieved by[3]:

1. Including a penalty against large piston displacements in the optimisation error function.
2. Moving *all* mirror segments to a position that minimises the largest piston stroke necessary to achieve that position, rather than leaving one segment stationary.

This was a much simpler solution than the comparatively complex task of modifying the PMAO design and was one of the key outcomes from the inclusion of the PMAO mechanical model in the ETEP modelling.

Incidentally, the results using the original calibration algorithm were still useful as they give an indication of the telescope performance should one segment fail. In this case, the failed segment would be used as a stationary reference, off of which the remaining segments would be co-aligned and co-phased [49]. It would be harder to retrieve a diffraction limited image, but still possible for almost 88% of deployment cases.

A second 500 run Monte Carlo data set was generated to evaluate the performance of the PMAO mechanism with the modified calibration procedure. The remaining verification activities are based on this second dataset.

[3]It is reiterated that this strategy was developed by D. Dolkens as part of his ongoing PhD research.

9.4.4. Retrieved Image Quality

Verification Activities: VA-20 [Pass]

The left plot in Figure 9.9 illustrates the improvement in image quality through each phase of the calibration procedure. The right hand plot contrasts the predicted image quality using the ideal PMAO model previously used in the DST ETEP model, with results using the *SPACAR* finite element model and modified calibration algorithm. Accompanying statistics are given in Table 9.9. The same set of 500 unique deployment cases was used to seed both Monte Carlo datasets.

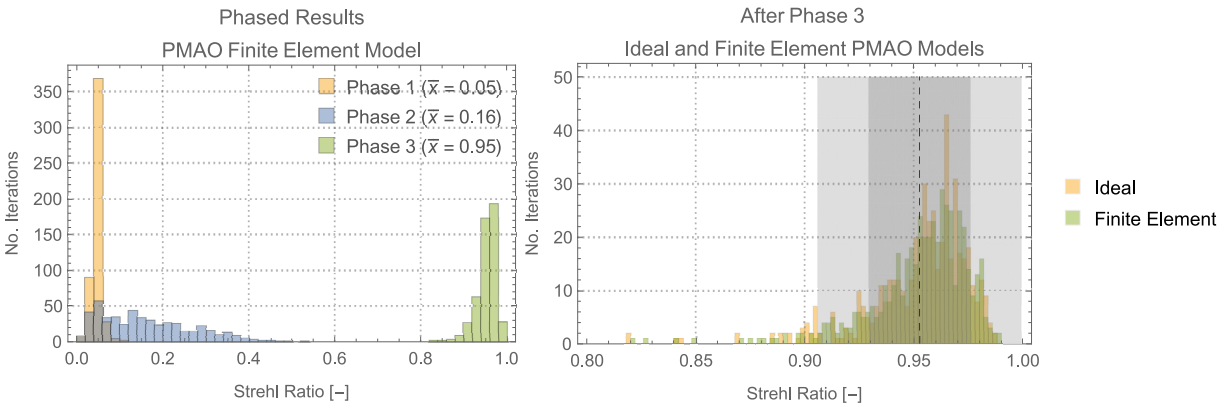

Figure 9.9: Left: Results of the Monte Carlo analysis after each phase of the calibration simulation with the new PMAO finite element *SPACAR* model. The mean values are the mean Strehl ratio after each phase. Right: Comparison of the final calibrated image quality with the ideal PMAO model and the finite element PMAO model. The 1σ and 2σ regions are shaded dark and light grey respectively. All results in both figures are for the central field (0°).

The PMAO mechanism is used in the second phase: M1 co-alignment and co-phasing. The image quality is still very poor after this phase because the Aberration Correction System (ACS) must still remove the continuous wavefront errors: the image quality requirement need only be met *after* the ACS has done its job.

Table 9.9: Monte Carlo analysis statistics for the Strehl ratio at the end of the calibration procedure for the ideal PMAO model with the original calibration algorithm, and for the *SPACAR* finite element PMAO model with the modified calibration algorithm, now including a penalty against large piston displacements.

	Ideal Model	***SPACAR* Model**
Calibration Algorithm	Original	Modified
Minimum	0.819	0.820
Maximum	0.987	0.989
Mean	0.953	0.953
σ (68.2%)	0.024	0.023
2σ (95.4%)	0.047	0.047
$> 2\sigma_L$ (97.7%)	0.906	0.906
Average No. iterations	5.53	5.81

The average Strehl ratio for the central field after Phase 3 was 0.95 with a minimum of 0.82, indicating that the modified calibration algorithm with the combined PMAO and ACS systems were able to correct the deployment errors in *all* considered deployment scenarios. The PMAO design thus meets mission requirement MIS-REQ-07. In approximately 97.7% of the cases, the Strehl ratio was 0.91 or greater, indicated by the lower 2σ bound. This was achieved with an average of 5.81 calibration iterations compared to 5.53 iterations using the ideal model. This small increase was attributed to the position errors and range of motion limitations that are now included in the ETEP modelling, which takes the calibration optimisation algorithm a little longer to correct.

Note that the data in Figure 9.9 is for the central field only. The optical performance for images formed by light entering at the edge of the field of view has been shown to be much lower than for the central field due to field dependent aberrations [51]. Decentration caused by the remote centre errors are expected to exacerbate this degradation. The in orbit drift and structural stability errors have also not been applied to the Phase 3 calibration results, which will cause even greater loss of performance.

A possible solution would be to increase the number of DOFs controlled by the PMAO to more efficiently correct the decentre errors, however the PMAO mechanism is already physically congested. Adding another actuator would be difficult. A further solution would be to recover the lost image details using post-processing techniques [48]. A phase diversity system is currently being investigated by MSc student Dirk Risselada.

9.4.5. Workspace Definition Verification and Actuator Performance

This subsection verifies the segment level ranges of motion in each of the controlled degrees of freedom. The actuator range of motion and step size requirements are then verified.

Workspace Definition Verification

Verification Activities: VA-23 [pass], VA-24 [pass], VA-25 [pass], VA-26 [pass]

Histograms for the commanded displacement in each of the three controlled degrees of freedom are shown in Figure 9.10.

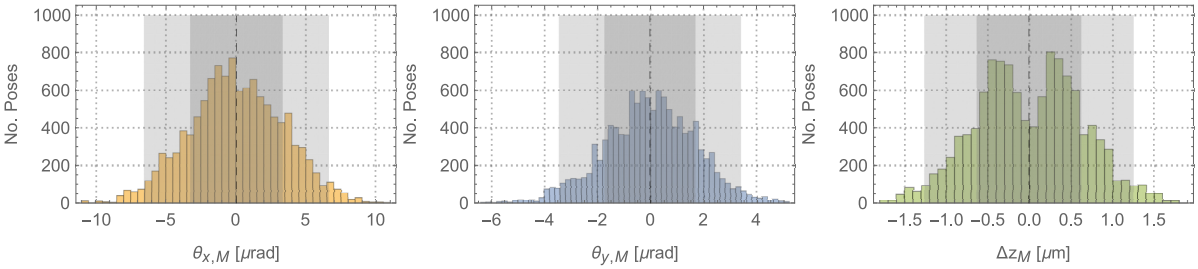

Figure 9.10: Histograms of commanded pose from M1 calibration ETEP simulations with modified calibration algorithm. The 1σ and 2σ standard deviation bounds are shaded in dark and light grey respectively. The arithmetic mean is indicated by the dashed line.

The accompanying statistics for both the workspace and actuator displacements are given in Table 9.10. The modified calibration algorithm made a significant difference to the required workspace with a 73% reduction in the piston range of motion and more modest reductions of 18% and 37% in the $\theta_{X,M}$ and $\theta_{Y,M}$ ranges respectively. This translated to a 69% reduction in the actuator stroke needed to calibrate the primary mirror across all simulated deployment cases, even those that deployed beyond the 2σ tolerances.

Table 9.10: Statistics for the commanded pose from M1 calibration ETEP simulations with modified calibration algorithm. The mechanism is able to meet any combination of poses across all three DOFs within the design or capability ranges of motion.

	$\theta_{\mathbf{X,M}}$ $[\mu rad]$	$\theta_{\mathbf{Y,M}}$ $[\mu rad]$	$\Delta_{\mathbf{Z,M}}$ $[\mu m]$	$\mathbf{u_{0,A}}$ $[\mu m]$	$\mathbf{u_{0,B}}$ $[\mu m]$	$\mathbf{u_{0,C}}$ $[\mu m]$	$\mathbf{u_{0,D}}$ $[\mu m]$	$\mathbf{u_{0,all}}$ $[\mu m]$	$\mathbf{R_M}$ $[mm]$
Minimum	-10.98	-6.24	-1.77	-2.05	-2.27	-2.08	-2.37	-2.37	-
Maximum	10.72	5.18	1.80	2.11	2.30	1.99	2.20	2.30	-
Mean	0.04	-0.03	-0.01	0.00	0.00	-0.01	-0.01	-0.01	-
σ (68.2%)	3.31	1.71	0.63	0.66	0.72	0.65	0.7	0.68	-
2σ (95.4%)	6.61	3.42	1.26	1.31	1.44	1.29	1.40	1.36	-
Design range	±4.00	±2.00	±4.00	±5.00	±5.00	±5.00	±5.00	-	239.8
Capability range	±9.00	±9.00	±4.00	±5.00	±5.00	±5.00	±5.00	-	100.0

There is a prominent double peak in the piston data of Figure 9.10, which is also visible in the actuator C data in Figure 9.11. This is an artefact of the modified calibration approach. Since the algorithm now attempts to minimise the *peak* segment displacement in piston rather than the *mean* displacement of all segments with respect to the nominal deployment position, the mean of the *absolute* piston pose will be non-zero. When the direction above or below the datum is included in addition to the magnitude of the displacement, a double peak symmetric about the datum results [49].

The peaks are not as visible for actuators B and D. They must correct for twice the deployment tolerance about the X_M axis than actuators A and C do about the Y_M axis, so the contribution of those corrections to the total actuator stroke masks the piston double peak [49]. A smaller masking effect is visible for actuator A. It might be expected that the histograms for the actuators in each pair should be identical due to the symmetry of the mechanism. This is not necessarily the case, as illustrated by the scenario in Figure 9.12. Consider a case where the segment is, on average, equally often in pose I or pose II. It is possible for the actuator stroke

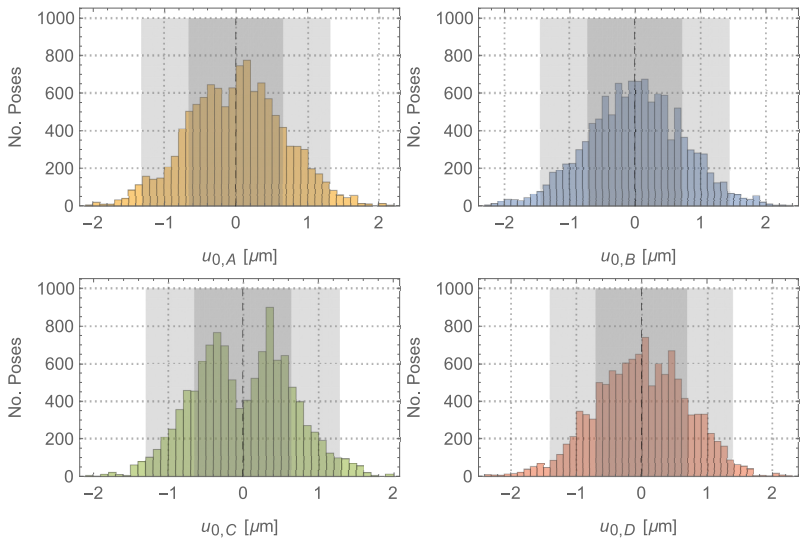

Figure 9.11: Histograms of commanded stroke for actuators A through D from M1 calibration ETEP simulations with modified calibration algorithm. The 1σ and 2σ standard deviation bounds are shaded in dark and light grey respectively. The arithmetic mean is indicated by the dashed line.

contributions from the piston and tip or tilt requirement to balance one another such that the mean net stroke from actuator A is close to zero for most deployments. In contrast, the same piston and tip/ tilt contributions to the actuator C stroke can additively stack giving large, non-zero mean net strokes.

This is not a definitive answer. There are other scenarios that could generate similar results and it is difficult to interpret the behaviour of the optimisation algorithm by analysing the pose and stroke data alone. Further analysis is a topic for future work.

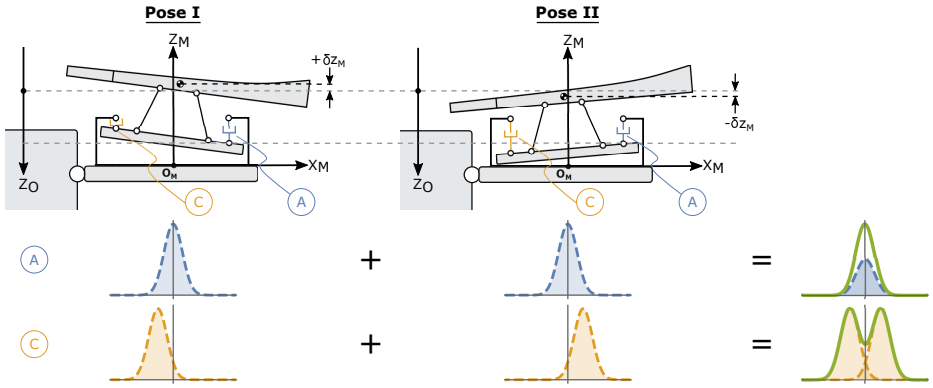

Figure 9.12: Example of a scenario where the net stroke from the two actuators in a pair need not be similar.

The results also show that the mechanism was able to achieve poses well beyond the design workspace. This is partly because the actuators were originally sized on a mounting radius R_M of 239.8 mm compared to the design radius of 100 mm. Thus a smaller actuator displacement is now required to achieve the same tip or tilt rotation at the segment level. This also means that the minimum step size in tip and tilt has increased, however the fact that all deployment cases were successfully calibrated imply that this is not a cause for concern. The resulting range of motion capability for a simultaneous piston/ tip/ tilt pose is given in the bottom row of Table 9.10.

Furthermore, the mechanism was able to correct for certain poses beyond its design range if large displacements were not needed in all three DOFs at once. For example, a pure $\theta_{x,M}$ or $\theta_{y,M}$ rotation of up to 50 μrad is possible if no other simultaneous displacements are needed. The probability that the mechanism must correct large deployment errors occurring simultaneously in multiple DOFs is small compared to the likelihood of having to correct for large single DOF errors. Many deployment cases with a deployment error beyond the 2σ bound should be correctable. Indeed approximately 43% of the deployment cases exceeded

the 2σ bound in at least one of piston, tip or tilt [49] yet a Strehl ratio greater than 0.8 was achieved in all cases.

The ETEP modelling verified the predicted workspace requirements PMAO-MEC-29 to -31 and confirmed the designs' compliance despite omission of the remote centre tip and tilt correction range. In fact, the aggregate statistics for the actuator stroke data suggest that the workspace prediction was too big. Actuators with half the stroke of the PPA10XL would have sufficed. Regardless, the results in Subsection 9.4.3 demonstrated that the workspace and actuator stroke requirements were very sensitive to the calibration approach so it is recommended that 10 μm range actuators be retained to provide some design margin as the DST evolves. The extra range also allows calibration of the mirror for up to 88% of deployment cases with a failed segment, adding to the reliability of the telescope.

Actuator Performance

The actuator stroke and force required to drive the mechanism throughout the nominal workspace are summarised in Table 9.11. Note that 1g of Earth gravity was applied in the negative Z_M direction to simulate the worst-case inertial loads during AIT on Earth.

Table 9.11: Summary of actuator performance at limits of verified workspace. See Figure 8.30 for a depiction of the actuator locations. The force is the total force required at the actuator to support the mechanism at each pose.

Pose			**Required Stroke**				**Actuator Force**			
$\theta_{\mathbf{x}}$ $[\mu rad]$	$\theta_{\mathbf{y}}$ $[\mu rad]$	Δ_z $[\mu m]$	$\mathbf{u_{0,A}}$ $[\mu m]$	$\mathbf{u_{0,B}}$ $[\mu m]$	$\mathbf{u_{0,C}}$ $[\mu m]$	$\mathbf{u_{0,D}}$ $[\mu m]$	$\mathbf{F_A}$ $[N]$	$\mathbf{F_B}$ $[N]$	$\mathbf{F_C}$ $[N]$	$\mathbf{F_D}$ $[N]$
0.000	0.000	0.000	0.000	0.000	0.000	0.000	19.913	19.955	19.989	19.947
-9.000	-9.000	-4.000	-3.100	-4.900	-4.900	-3.100	19.898	19.912	19.946	19.932
-9.000	-9.000	4.000	4.900	3.100	3.100	4.900	19.956	19.970	20.004	19.990
-9.000	9.000	-4.000	-4.900	-4.900	-3.100	-3.100	19.871	19.912	19.974	19.932
-9.000	9.000	4.000	3.100	3.100	4.900	4.900	19.929	19.970	20.032	19.990
9.000	-9.000	-4.000	-3.100	-3.100	-4.900	-4.900	19.898	19.940	19.946	19.904
9.000	-9.000	4.000	4.900	4.900	3.100	3.100	19.956	19.998	20.004	19.963
9.000	9.000	-4.000	-4.900	-3.100	-3.100	-4.900	19.871	19.940	19.974	19.904
9.000	9.000	4.000	3.100	4.900	4.900	3.100	19.929	19.998	20.032	19.963
				Maximum without gravity load			±0.043	±0.043	±0.043	±0.043

The small actuation forces are masked by the force needed at each actuator to hold the ≈8 kg mechanism and mirror mass in the 1g environment. The final line in Table 9.11 is the maximum force needed at each actuator to displace the mechanism with the gravity load subtracted. As a sanity check of the results, application of equation 9.1 finds that a force of approximately 39 mN is needed for a 4 μm piston displacement of a wire flexure, which is same order of magnitude in the force needed to achieve the full displacement in one direction in the table. The maximum drive capability of the PPA10XL actuator is expected to be on the order of 6550 N [29, 31], which far exceeds the required actuator forces in Table 9.11.

9.4.6. Accuracy, Precision and Sources of Error

Verification Activities: VA-21 [pass], VA-22 [pass]

Verification of the accuracy of the mechanism was broken down into two groups of analysis. First, the performance for pure piston, tip and tilt motions were examined individually to quantify the parasitic and remote centre errors. Secondly, the data from the Monte Carlo simulations was used to quantify the overall accuracy and precision of the mechanism in operation.

This subsection begins with an introduction to the concepts of accuracy and precision, followed by a summary of how the pose error was calculated. Results for the simple single DOF scans are then presented. The subsection concludes with the pose error results from the Monte Carlo analysis.

Accuracy and Precision

Accuracy is defined here as the arithmetic mean of the difference between the desired and (simulated) achieved pose. Precision is quantified by the two standard deviation bound, indicating an expectation that 95.4% of the pose manipulations should have an error equal to the stated mean plus/ minus the 2σ value assuming a normal distribution of results. All results are given in the fixed mechanism coordinate frame $\mathbf{O_M}$.

Error Calculation Method

The attitude of the mirror segment was extracted from the simulation results using the TRIAD[4] method which calculates the Direction Cosine Matrix (DCM) from two vectors rigidly attached to the mirror centre of mass. The rotation angles θ_{X_M},θ_{Y_M} and θ_{Z_M} were then extracted from the direction cosines. The procedure is set out in Appendix J *Pose Error Calculations*.

The total error e_T in each degree of freedom of the mirror pose was broken down into *remote centre* errors e_{RC} and *parasitic* errors e_P. Since the mechanism rotates about $\mathbf{O_{MF}}$ below the mirror, a desired pure rotation of the mirror about its centre of mass $\mathbf{O_{COM}}$, called the *ideal* pose τ^*_{COM}, manifests as a rotation in combination with a small translation to give the *actual* pose τ_{COM}.

These small, unwanted, position errors can be predicted from the kinematics of the mechanism. It is known that all rotations occur about $\mathbf{O_{MF}}$ and the position of $\mathbf{O_{COM}}$ with respect to $\mathbf{O_{MF}}$ is also known, thus giving the *expected* pose $\overline{\tau}_{COM}$ inclusive of remote centre errors.

The remaining pose error was attributed to parasitic errors. Causes include, but are not limited to, fabrication errors, assembly errors, misalignment of the constraints, poor constraint design (ie. insufficient decoupling) and stress stiffening. The results below do not include any fabrication or dimensional error effects, and all parts were far from their elastic limit, so the parasitic errors are attributed mostly to poor decoupling of the constraint DOFs and stress stiffening. A more rigorous analysis with assembly tolerances included is a topic for future work.

The full procedure to calculate the errors is also set out in Appendix J. To summarise that procedure, the total error e_T was found be subtracting the ideal pose τ^*_{COM} from the (simulated) actual pose τ_{COM}; the parasitic error e_P by subtracting the ideal pose from the expected pose and the remote centre error by finding the difference between the two:

$$e_T = \tau_{COM} - \tau^*_{COM} \tag{9.5}$$

$$e_P = \tau_{COM} - \overline{\tau}_{COM} \tag{9.6}$$

$$e_{RC} = e_T - e_P \tag{9.7}$$

Single Degree of Freedom Scans

Verification Activities: VA-27 [pass]

The single DOF scans were executed over the full capability ranges of motion as listed in Table 9.10. The results are given in Figures 9.13 to 9.15. A summary of the average step sizes and maximum error contributions is given in Table 9.12.

Table 9.12: Summary of average step size and maximum parasitic and remote centre errors for scans through the full capability range of motion in each controllable degree of freedom. The maximum parasitic and remote centre errors occur at the maximum extents of the range of motion in each DOF.

DOF Scan	No. Tests	Range	Mean Step Size	$\mathbf{e_{P,max}}$	$\mathbf{e_{RC,max}}$
$\theta_{x,M}$	74	$\pm 9\ \mu rad$	$0.1\ \mu rad$	$1.89\ nrad\ (\mp\theta_{X,M})$	$1.074\ \mu m\ (\mp Y_M)$
$\theta_{y,M}$	74	$\pm 9\ \mu rad$	$0.1\ \mu rad$	$1.89\ nrad\ (\mp\theta_{Y,M})$	$1.074\ \mu m\ (\pm X_M)$
$\Delta_{z,M}$	102	$\pm 4\ \mu m$	$10\ nm$	$0.39\ nm\ (\mp\Delta_{Z,M})$	$0.000\ \mu m$

Small parasitic errors were present in each of the DOF scans, acting to shorten the achieved range of motion slightly relative to the desired pose. The parasitic errors in each DOF were below the structural stability budgets and thus did not exceed the threshold necessary to achieve diffraction limited imaging.

No remote centre errors were present in the piston scan as there were no rotations. As expected, remote centre errors were found in the tip and tilt scans, manifesting as small translations in the $X_M Y_M$ plane. The very small remote centre translations in the Z_M direction were below the machine precision threshold and thus negligible. Despite these errors far exceeding the stability tolerance budget, the results from the Monte Carlo analysis in the next subsection demonstrate that the total errors in each DOF were tolerable in terms of optical performance.

The parasitic and remote centre errors are static effects so they can be corrected by the PMAO itself and the Aberration Correction System. Both errors were well behaved so could forseeably be calibrated out of the system. It was concluded that the PMAO was able to deliver controllable 3DOF motion of the mirror

[4] TRIaxial Attitude Determination.

segment. The 10 nm step size requirement at the actuator level was confirmed as sufficient and was verified by inspection with the PPA datasheet.

It is emphasised that this analysis assumed *no* assembly errors and perfectly controllable actuators. It is expected that inclusion of assembly tolerances and a more realistic actuator model in the simulation would cause less well behaved errors. The *SPACAR* model was built to facilitate these studies, though they are topics for future work.

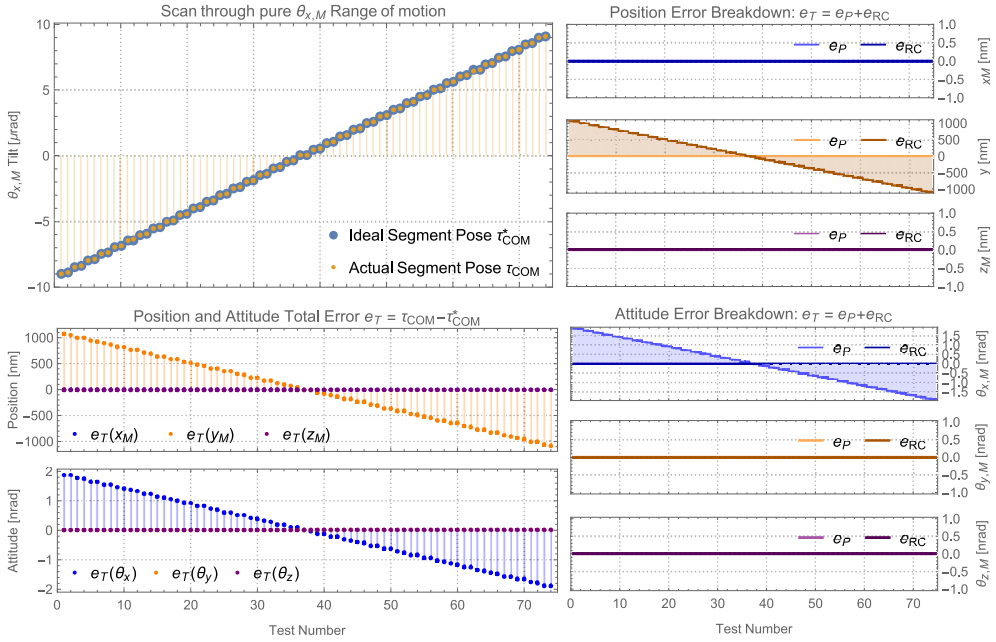

Figure 9.13: Pose error breakdown for a scan through $\theta_{x,M}$ range of motion.

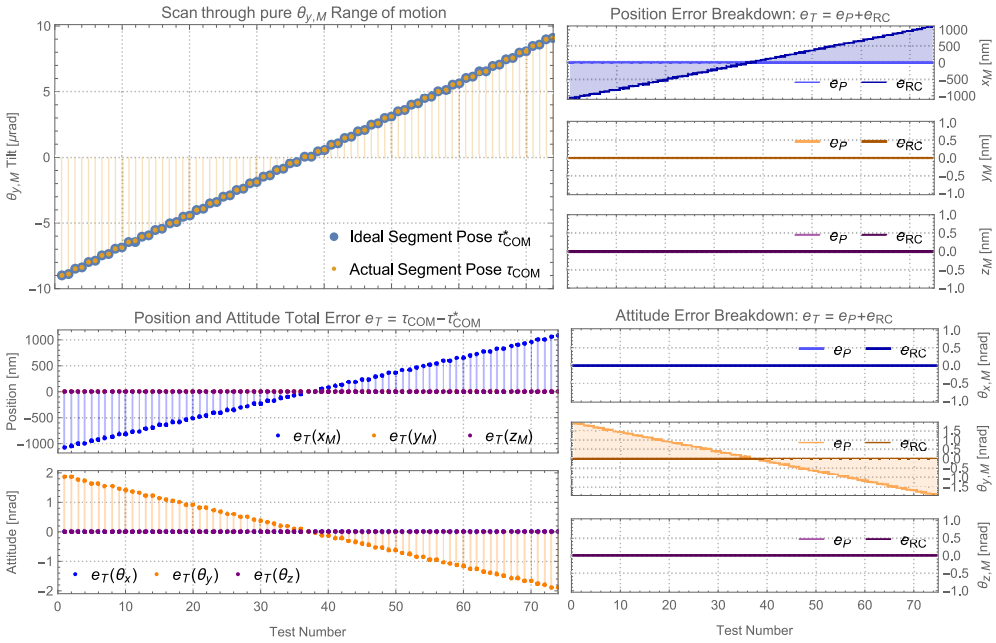

Figure 9.14: Pose error breakdown for a scan through $\theta_{y,M}$ range of motion.

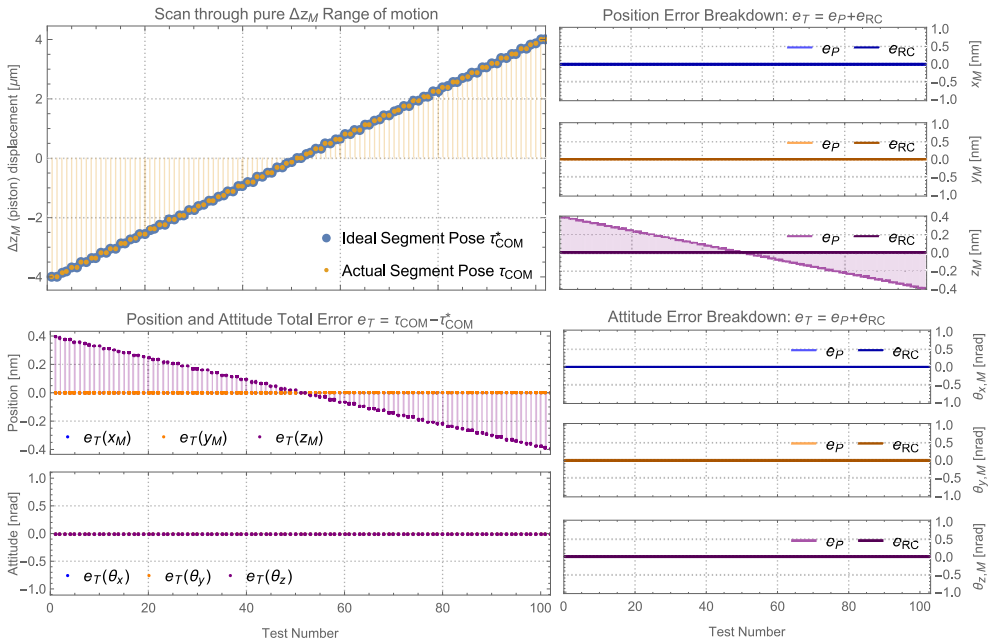

Figure 9.15: Pose error breakdown for a scan through piston $\Delta_{z,M}$ range of motion.

Monte Carlo Results: Overall Mechanism Accuracy and Precision

The position and orientation errors from the Monte Carlo results are shown in Figure 9.16. The statistics are given in Table 9.13. The results suggest that the mechanism has good accuracy with the mean errors close to zero for all DOFs, however precision in X_M and Y_M position suffers due to the parasitic and remote centre errors.

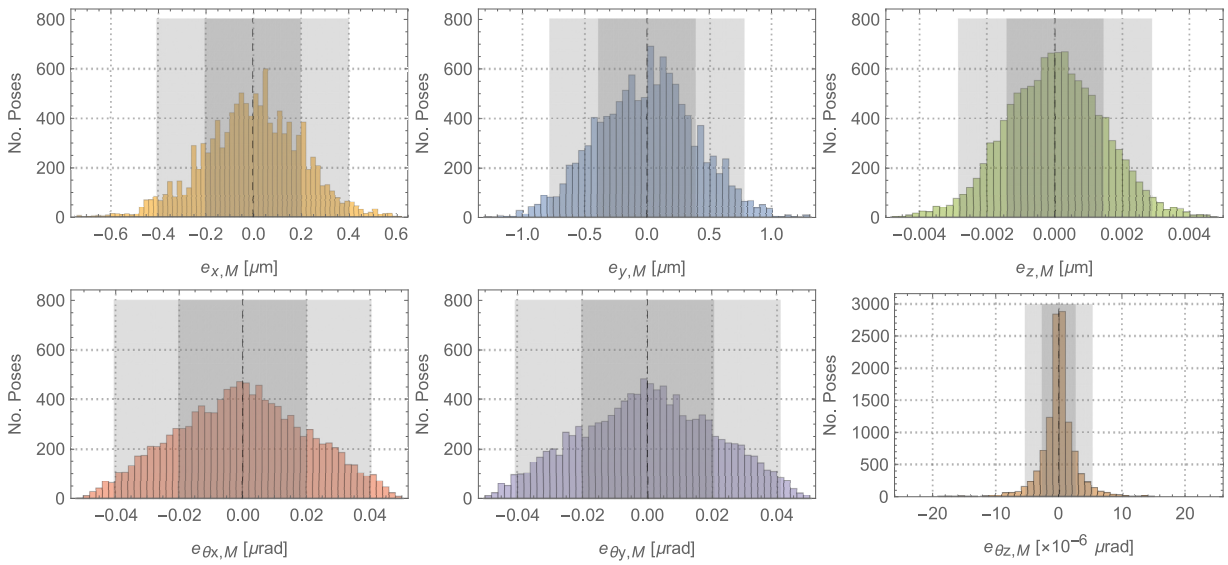

Figure 9.16: Histograms of the total error in the segment centre of mass pose. One and two σ regions shaded in dark and light grey respectively. Mean indicated by dashed line.

These results can only be considered preliminary at best. They represent the best case accuracy and precision that can be expected. It will be very useful to analyse the effect of realistic assembly tolerances on the regularity of these errors. In particular, whether it is reasonable to expect that they are systematic and can be calibrated out.

Table 9.13: Statistics for the error in the segment centre of mass position and orientation over all calibration iterations and Monte Carlo simulations.

	$\mathbf{e_x}$ $[\mu m]$	$\mathbf{e_y}$ $[\mu m]$	$\mathbf{e_z}$ $[\mu m]$	$\mathbf{e_{\theta x}}$ $[\mu rad]$	$\mathbf{e_{\theta y}}$ $[\mu rad]$	$\mathbf{e_{\theta z}}$ $[\times 10^{-6} \mu rad]$
Minimum	-0.737	-1.268	-0.005	-0.051	-0.050	-18.114
Maximum	0.613	1.297	0.005	0.050	0.049	14.059
Mean	-0.003	-0.005	0.000	0.000	0.000	-0.058
σ (68.2%)	0.202	0.390	0.001	0.020	0.021	2.670
2σ (95.4%)	0.403	0.780	0.003	0.040	0.041	5.339

9.5. Summary of Verification Results

This concludes the revised baseline design verification work. The verification results are summarised in Tables 9.15 to 9.18. Verification compliance definitions are given in Table 9.14. Several flow down requirements from the mechanical design and verification phases are formalised in the next section.

Table 9.14: Verification compliance definitions.

Compliance	Definition
PASS	Sufficient information available for preliminary verification and design was compliant with requirement.
FAIL	Sufficient information available for preliminary verification and design was not compliant with requirement.
PARTIAL	Insufficient information available for preliminary verification. Design was compliant with requirement to the extent that information was available.
TBD	Insufficient information available. Design could not be verified, further work needed.

9.6. Flow Down Requirements

The feasibility of the PMAO concept is based not only on the requirements verified so far in this chapter, but also on the flow down requirements to other subsystems. This section formalises several of these. Most relate to the thermal control subsystem and are covered in Subsection 9.6.1. Actuator and mirror flow down requirements are summarised in Subsections 9.6.2 and 9.6.3 respectively.

9.6.1. Thermal Control System

The critical thermal load strength calculations were summarised for the final design in Table 9.5. They are formalised as flow down requirements here in Table 9.19. Additional requirements for the actuators and sensing concept are also included. All of the Thermal Control System (TCS) flow down requirements are survival requirements, with the exception of the temperature gradient for displacement sensing.

The non-operational temperature range was taken by analogy from the Rosetta SPICE instrument, which also used Cedrat PPA actuators. Evidently, since the worst-case LEOP temperatures are predicted to fluctuate from 163 to 409 K, with qualification thermal uncertainty margins, the actuators will need thermal control to survive. Calculation of the maximum allowable temperature gradient across the actuators in a push/pull pair is given in the next subsection.

Maximum Allowable Thermal Gradient for Actuator Displacement Sensing

The concept for sensing the displacement of the PPA actuator pairs was introduced in Section 7.3.1. The advantage of this arrangement was that it rendered the sensors immune to bulk temperature changes. This performance was predicated on the assumption that there was a "negligible" temperature difference between the actuators in a pair. An estimate of the allowable difference is derived below and added to the list of flow down requirements for the thermal control system in Table 9.19.

The strains in equations 7.8 & 7.9 measured by the strain gauges shown in Figure 7.7 on page 86 have mechanical and thermal components. In the earlier discussion, it was assumed that the thermal strain ϵ_{therm} in all of the strain gauges was the same. In reality, they will be slightly different, here given values $\epsilon_{therm,A}$ and

Table 9.15: PMAO system level and programmatic requirements verification summary.

ID	Short Description	Verification Activities	Compliance	Comment
System				
M1-MEC-13	Four deployable segments.	VA-01	PASS	By inspection.
PMAO-SYS-02	Combined mass of four mechanisms ≤ 24.8 kg.	VA-02	PASS	23.416 kg with margins.
PMAO-SYS-03	No ITAR controlled parts.	VA-03	PASS	All European components.
PMAO-SYS-06	AIT require no new technology	VA-04	PASS	Inspection of feature size and methods.

Table 9.16: PMAO launch survival requirements verification summary. QSL = Quasi Static Load.

ID	Short Description	Verification Activities	Compliance	Comment
Structural				
PMAO-MEC-03	Support the mirror segment during launch, stowed.	VA-05	PARTIAL	Strut k_{axial}/k_{bend} = 974 ≤ 1000 required.
Mechanical				
PMAO-MEC-40	Survive launch in the stowed configuration.	VA-06	PASS	Static & dynamic requirements met.
PMAO-MEC-40-01	Survive a QSL of 30g x and y loads, stowed.	VA-06-01-[01,02]	PASS	MSy = 0.82, MSbuckle = 0.25, IPC wires.
PMAO-MEC-40-02	Survive a QSL of 30g x and z loads, stowed.	VA-06-02-[01,02]	PASS	MSy = 0.33, actuators.
PMAO-MEC-40-03	Survive a QSL of 30g y and z loads, stowed.	VA-06-03-[01,02]	PASS	MSy = 0.33, actuators.
PMAO-MEC-40-04	First natural frequency ≥ 100 Hz, stowed.	VA-06-04	PASS	ω_1 = 197.6 Hz.
Electrical				
PMAO-ELE-01	No power during launch.	VA-07	PASS	Inspection of design, verification assumptions.

Table 9.17: PMAO operations survival requirements verification summary. TCS = Thermal Control System.

ID	Short Description	Verification Activities	Compliance	Comment
Mechanical				
PMAO-MEC-04	Support the mirror segment during launch, stowed & deployed.	VA-08-[01,02]	PARTIAL	See VA-05 results.
PMAO-MEC-41	Survive operations, stowed and deployed.	VA-09-[01-03]	PARTIAL	Strength OK. See PMAO-MEC-41-01.
PMAO-MEC-41-01	Survive steady state temperatures between 188 and 384 K, stowed.	VA-10	PARTIAL	Need design & verification of TCS for actuators.
PMAO-MEC-42	Survive deployment	VA-11	TBD	Deployment loads not quantified yet.

Table 9.18: PMAO operations functionality requirements verification summary.

ID	Short Description	Verification Activities	Compliance	Comment
Top Down Budgets				
M1-MEC-01	Deployment & PMAO mechanisms meet deployment tolerance budget.	VA-12	TBD	Needs FEA, M1 deployment design maturation.
M1-MEC-04	Deployment & PMAO mechanisms meet in orbit drift tolerance budget.	VA-13	TBD	Needs FEA, M1 deployment, TCS and thermal env. maturation.
M1-MEC-07	Deployment & PMAO mechanisms meet stability tolerance budget.	VA-14	TBD	Needs FEA, M1 deployment design maturation.
DST Compatibility				
M1-MEC-14	1600 mm from primary to secondary mirror.	VA-15	PASS	
M1-MEC-17	120 mm between mirror backplane and DST housing, stowed.	VA-16	PASS	
PMAO-MEC-35	Thermal centre of mechanism at segment centroid.	VA-17	PARTIAL	Rigorous confirmation requires FEA, testing.
PMAO-MEC-50	Do not impede deployment of the primary or secondary mirror.	VA-18-01	PASS	
PMAO-MEC-50-01	Do not protrude laterally beyond the periphery of mirror.	VA-18-02	PASS	
Environment				
M1-MEC-15	Deployment and PMAO mechanisms to operate at 298 K ± 1 K, deployed.	VA-19-[01,02]	TBD	Need design & verification of M1 deployment mechanism & TCS for PMAO actuators.
Optical				
PMAO-OPT-01	Remove discontinuous wavefront errors in operations and AIT.			
PMAO-MEC-01	Provide independent, piston, tip & tilt control of mirror.	VA-21	PASS	Max. 472 nm remote centre error, acceptable.
Mechanical: Mechanism				
PMAO-MEC-23	Segment to have 10 nm step size in piston direction.	VA-22	PASS	10 nm without assembly tolerances.
PMAO-MEC-29	Segment to have range of motion of ±4 μrad about X_M axis.	VA-23	PASS	Sufficient for 100% of simulated deployments.
PMAO-MEC-30	Segment to have range of motion of ±2 μrad about Y_M axis.	VA-24	PASS	Sufficient for 100% of simulated deployments.
PMAO-MEC-31	Segment to have range of motion of ±4 μm along Z_M axis.	VA-25	PASS	Sufficient for 100% of simulated deployments.
Mechanical: Actuators				
PMAO-MEC-32	PMAO actuators to have 10μm range of motion.	VA-26	PASS	Sufficient for 100% of simulated deployments.
PMAO-MEC-33	PMAO actuators to have 10 nm step size.	VA-27	PASS	Sufficient for 100% of simulated deployments.

$\epsilon_{therm,B}$ for the gauges on the first actuator stack and second actuator stack. Repeating the same derivation gives the output voltage V_O

$$V_O = \frac{GF\left(2\epsilon_{mech} + \epsilon_{therm,A} - \epsilon_{therm,B}\right)}{2 + GF\left(\epsilon_{therm,A} + \epsilon_{therm,B}\right)} V_{exc} \tag{9.8}$$

The smallest mechanical displacement to be measured is on the order of 10 nm, a single step, generated by an actuator approximately 20 mm long, gives a strain of 5×10^{-7} m/m. Assuming that the contribution of the thermal strain should be less than 1% of the strain to be measured, the difference between $\epsilon_{therm,A}$ and $\epsilon_{therm,B}$ should be on the order of

$$\frac{\epsilon_{therm,A} - \epsilon_{therm,B}}{2\epsilon_{mech}} < 0.01 \tag{9.9}$$

$$\epsilon_{therm,A} - \epsilon_{therm,B} < 0.01 \times 2 \times 5 \times 10^{-7} \tag{9.10}$$

$$\approx 10^{-8} \tag{9.11}$$

The thermal strain is a function of the CTE of the piezo ceramic and the temperature difference between the calibration temperature and the bulk temperature of the piezo,

$$\epsilon_{therm,A} = \alpha_{piezo}\left(T_{calib} - T_A\right) \tag{9.12}$$

$$\epsilon_{therm,B} = \alpha_{piezo}\left(T_{calib} - T_B\right) \tag{9.13}$$

Assuming the CTE of the ceramic is on the order of 10^{-6} $/K$ [10] and combining the above relations gives

$$\epsilon_{therm,A} - \epsilon_{therm,B} = \alpha_{piezo}\left(T_B - T_A\right) \tag{9.14}$$

$$\therefore T_B - T_A \approx 10^{-8}/10^{-6} \tag{9.15}$$

$$\approx 0.01K \tag{9.16}$$

This is a very difficult condition to maintain, especially over the ≈ 200 mm distance between the actuators in each pair and could well be a killer requirement for this concept. The four PPA option was chosen primarily because these actuators are available as "near COTS" components and have space heritage, whereas the NLA actuators are new, custom products. The expense incurred in the thermal design necessary to maintain such a small gradient across actuators 200 mm apart might justify a change to the more expensive NLA option.

9.6.2. Actuator

Since the mechanism successfully facilitated retrieval of a diffraction limited image in every Monte Carlo simulation, the maximum 10 nm step size of the actuators is sufficient. The driving force is the largest force found in Table 9.11 with a motorisation factor of 1.25 applied per the *DST Requirements and Verification* guidelines document in Appendix D. Both requirements are listed in Table 9.20.

It is worth noting the very large difference between the required driving force in actuator requirement PMAO-MEC-51 and the ≈1700 N load they must withstand during launch. Clearly the dominant sizing requirement is the need to survive launch. Smaller, cheaper actuators could be used if they can be removed from the primary load path.

9.6.3. Mirror

In order to progress the design of the PMAO mechanism in the absence of a mature mirror design, several simplifying assumptions were made that can now be formalised as flow down requirements. These are not hard requirements. There is scope for the PMAO design to be modified should the flow down requirements for the mirror listed in Table 9.21 be too strict.

Table 9.19: Flow down requirements for the thermal control system. Thermal uncertainty margins not included.

ID	Description	Reference/ Comment
Component Bulk Temperature Limits		
PMAO-THE-01	The bulk temperature of the universal joints shall not deviate more than 2285 K from the assembly temperature (nominally 298 K).	Table 9.5, buckling.
PMAO-THE-02	The bulk temperature of the in-plane constraint wire flexures shall not deviate more than 318 K from the assembly temperature (nominally 298 K).	Table 9.5, buckling.
PMAO-THE-03	The bulk temperature of the moving frame plate shall not deviate more than 442 K from the assembly temperature (nominally 298 K).	Table 9.5, universal joint yield.
Component Steady State Heat Flow Limits		
PMAO-THE-04	The steady state heat flow through the universal joint shall not exceed 27.4 W.	§8.5.1, eqn 8.37 & 8.27, buckling.
PMAO-THE-05	The steady state heat flow through each in-plane constraint wire flexure shall not exceed 0.2 W.	Table 9.5, buckling.
Instrumentation Limits		
PMAO-THE-06	The maximum gradient between the actuators in a push/ pull pair (actuators A,C and B,D) shall not exceed 0.01 K. There is no requirement on the gradient between the pairs.	Wheatstone circuit is immune to transients.
PMAO-THE-07	The bulk temperature of the actuators in non-operational phases shall not exceed the range 288 K to 373 K.	Analogy, Rosetta SPICE [60].
PMAO-THE-08	The bulk temperature of the actuators in operational phases shall not exceed the range 288 K to 298 K.	PPA40XL data sheet [29].

Table 9.20: Actuator flow down requirement.

ID	Description	Reference/ Comment
PMAO-MEC-32	Each actuator of the PMAO mechanism shall have a total range of motion of 10 μm.	Per Monte Carlo simulation.
PMAO-MEC-33	Each actuator of the PMAO mechanism shall have a maximum step size of 10 nm.	Per Monte Carlo simulation.
PMAO-MEC-51	The PMAO actuators shall be capable of providing a driving force of no less than 25 N.	Simulation data, Table 9.11 & motorisation factor from App. D.

Table 9.21: Mirror flow down requirement.

ID	Description	Reference/ Comment
M1-MEC-18	The mass of a primary mirror segment shall be no more than 6 kg.	PMAO launch load limit.
M1-MEC-19	The primary mirror segment shall be supported by a three or six point bipod support during all flight phases.	PMAO support concept.
M1-OPT-01	The primary mirror segment shall be supported by an external metrology support for terrestrial AIT activities.	PMAO support is designed for microgravity performance.
M1-OPT-02	The backplane of the M1 mirror segment shall be parallel to the PMAO mechanism plane $X_M Y_M$ in the deployed configuration.	

9.7. Chapter Summary

The Monte Carlo verification analysis showed that the performance of the M1 co-phasing and co-alignment procedure was sensitive to the calibration algorithm. In its original guise, the algorithm demanded large strokes from the PMAO mechanism and 12% of the deployment cases could not be calibrated due to large actuator stroke requirements. A modification to the algorithm introduced a penalty against large piston displacements. The result was a diffraction limited image for all deployment cases with 97.7% above Strehl ratio of 0.91, requiring maximum actuator strokes of no more than $\pm 2.4\ \mu m$.

The mechanism was largely compliant with the survival requirements, the *SPACAR* simulations showing that the launch loads strongly dominate the strength criteria. The PMAO did not fail any verification activities, however compliance with the top down systems budgets and several thermal requirements remain topics for future work as the DST thermal modelling and M1 deployment mechanism designs mature.

The next and final chapter gives a summary of the partially verified design, an assessment of the feasibility of implementing the PMAO in the DST, a summary of general conclusions and recommendations for future work.

10

Conclusions and Recommendations

Chapter 5 *Baseline Functional Verification* established that the original baseline PMAO design needed revision. A bottom up systems engineering approach was adopted to develop and verify a new design that could meet the ultimate aim of enabling the DST to acquire diffraction limited imagery in a compact package. Section 10.1 summarises the resulting mechanism design. Conclusions regarding the feasibility of implementing the PMAO mechanism followed by general comments from an academic and project perspective are presented in Section 10.2. The chapter ends with a summary of recommendations for future work in Section 10.3.

10.1. Final Design

The revised PMAO mechanism design rectified deficiencies identified in the original baseline design, caused by poor constraint of the mirror, and a lack of independence of the transmission output from the thermo-elastic stress state of the mirror. All components are now also independent of any ITAR or US patent controlled hardware. A summary of the major design features is given below, followed by a comparison with the Euclid M2MM mechanism as a sanity check against the current state of the art in space qualified fine pointing mechanisms.

Summary of Design Features

The revised mechanical arrangement was shown in Figure 8.30 on page 146. A fixed frame provides a foundation for the mechanism and interface to the M1 deployment mechanism. The structure is mirror-symmetric and incorporates the fundamental elements of exact constraint design. Flexured compliant elements provide constraint as necessary absent microdynamic and friction effects. Wire flexures arranged in an equilateral triangle pattern constrain the in-plane degrees of freedom of the moving frame, which mates the mirror support to the actuators. They also defined the mechanism thermal centre, in line with the centre of mass of the mirror. Constraint redundancy was used to prevent thermo-elastic rotations of the mirror about the Z_M axis. The mirror is isolated from internal stresses built up from that overconstraint by the intervening moving frame and flexured bipods.

Four linear piezoelectric actuators arranged in two push/ pull pairs drive the mechanism without the need for a transmission. Displacement is monitored using foil strain gauges in a Wheatstone circuit, configured to render the gauge readouts immune to transient bulk temperature fluctuations, provided the spatial thermal gradient can be kept negligibly small by the thermal control system.

The actuators manipulate the moving frame platform, upon which the mirror and support are mounted. Passive athermalisation of the struts will be necessary to meet the thermal drift budget in the piston direction, which can be achieved within the volume requirements with standard alloys, even for temperature fluctuations 15 K beyond the nominal operations range. The remaining structure is made from Ti-6Al-4V to minimise differential strains within the mechanism itself. All compliant elements are intended to be manufactured monolithically using wire electro-discharge machining to minimise assembly errors.

Comparison with the State of the Art

The performance characteristics for the revised PMAO mechanism are summarised in Table 10.1. Similar data from the ESA Euclid visible to near-infrared space telescope M2 mirror mechanism, shown in Figure 10.1, is provided for comparison.

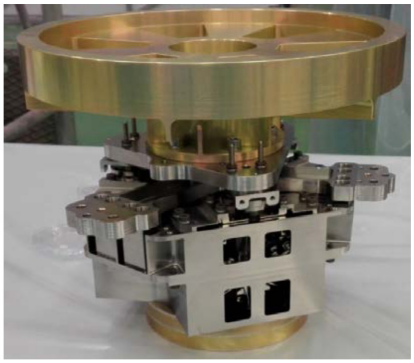

Figure 10.1: Euclid M2 mirror fine positioning mechanism, adapted from [8].

Despite differences in the range and resolution requirements, the PMAO mechanism to mirror mass ratio scales similarly to the M2MM, the form factors are similar, and the first natural frequencies are not too far removed. The DST PMAO has a much smaller range of motion and step size requirement, suggesting that thermal control and structural stability will be critical. Few conclusions can be drawn regarding comparison of the mechanism accuracies as the PMAO simulation assumes perfect actuators and no assembly, thermal or stability errors, whereas the M2MM data are taken from experimental results.

Nonetheless, the comparison confirms that the PMAO design and verification output provides a realistic mass, volume, dynamic and kinematic estimate for the implementation of a fine actuation mechanism for the DST M1 mirror segments.

Table 10.1: Summary of final PMAO performance characteristics and comparison with Euclid M2MM mechanism from [8]. PMAO accuracy values are the 2σ standard deviation. PMAO mechanism values are given per segment. The range of motion is the maximum range for all DOFs extended simultaneously. Effect of assembly and actuator errors not considered in the PMAO accuracy specifications.

Item	**PMAO Mechanism**	**Euclid M2MM**
Mirror mass	<6.0 kg	< 3.1 kg
Mass without/ with electronics	5.85 kg/ 7.41 kg	< 3.0 kg/ -
Quasi static load qualification	30g	28g
First resonant frequency	198 Hz	161 Hz
DOF control	3DOF tip/tilt/piston	3DOF tip/tilt/piston
Mechanism range of motion	±4 μm/ ±9 μrad	±200 μm/ ±1500 μrad
Mechanism step size	10 nm/ 0.1 μrad	< 55 nm/ < 2 μrad
Number of actuators	4× linear piezo	3× DC stepper
Actuator stroke	±10 μm	± 220 μm
Actuator step size	10 nm	-
Position accuracy	0.005±0.780 μm (2σ)	< ± 3μm
Orientation accuracy	0.000±0.041 μrad (2σ)	< 40 μrad
Position sensing	Strain gauge on actuators	Microswitch turn counters
Operational temperature	288 to 298 K	100 to 298 K
Non-operational temperature	288 to 373 K	-
Hold down mechanism?	No	No
Power off hold?	Datum pose only	Yes
Power	-20 to 150 VAC, 1 Hz	-
Volume	Cylinder	Hexagonal
	D290 mm × H104 mm	214 mm × H150 mm
Design year	2018	2017 (launch 2020)

10.2. Conclusions

This section presents the final conclusions from the work conducted in this thesis. The first research question was answered early in the thesis at the culmination of the front-end systems engineering and original baseline functional verification in Chapter 5. With the revised design and verification activities complete, the second research question regarding the technical feasibility of implementing the PMAO mechanism could be answered, now addressed in Subsection 10.2.1. General conclusions from academic and perspectives are presented in Subsection 10.2.2.

10.2.1. Feasibility

The second thesis research question was concerned with the technical and economic feasibility of implementing the preliminary PMAO design in a space telescope. This subsection addresses that query, with a focus on the mechanical, thermal, optical and systems engineering disciplines.

Economic Feasibility

Any statements purporting to establish the feasibility of implementing a subsystem in a commercial application are undeniably stronger if a sound financial justification can be made. Unfortunately, no data regarding the cost of this, or similar, opto-mechatronic mechanisms could be found in the academic or commercial literature. Actuator suppliers were very reluctant to discuss cost without better definition of the project expectations, schedule or resources. The only conclusion that can be drawn is qualitative: the design uses standard materials and manufacturing methods with established COTS actuator technology, however they are at the state of the art in precision actuators so are likely to be expensive. Testing will also be expensive due to the very small motions that must be measured, but this is not beyond the existing capabilities of commercial suppliers.

Mechanical Feasibility

The verification results showed that can meet the kinematic requirements within the allotted usable volume using COTS hardware, and standard materials & precision manufacturing techniques. The high margins of safety in both the launch yield and buckling analyses demonstrated that the PMAO design is conservative, especially considering the large 30g quasi-static loads and generous 6 kg mirror mass. Critically, the load analysis showed that it is feasible to support the mirror through launch without a hold down and release mechanism.

The Monte Carlo ETEP modelling demonstrated that the remote centre and parasitic pose errors were tolerable. Although the ETEP modelling verified the PMAO's ability to correct the segment pose in the presence of the top down tolerance budget errors, the ability of the mechanism to meet those budgets itself could not be verified. This is a significant gap in the PMAO mechanism verification status. Figure 10.2 in Section 10.3 *Future Work* sets out a map of tasks to rectify this.

The Cedrat Technologies PPA10XL piezoelectric actuators were a suitable choice, meeting both the strength and kinematic requirements. There is flexibility to consider using three actuators instead of four to withstand the launch loads. An alternative design is possible, since the actuator load requirement is dominated by the need to survive launch, rather than the force needed to manipulate the mechanism. If the actuators can be removed from the primary load path with a transmission or addition of an HDRM, then smaller, cheaper actuators could be used.

The mirror support was sized for the mirror design at the time of writing. Flexured bipods are standard in the field of opto-mechatronics, offering wide design flexibility in terms of dimensions, material and athermalisation choices. Reasonable changes to the mirror design should not diminish the mechanical feasibility of the PMAO mirror supports.

Thermal Control Feasibility

The thermal flow down requirements carry the greatest technical risk for the revised design. In the absence of any characterisation of the transient thermal environment beneath the M1 segments, it was assumed that it would be difficult to maintain the small allowable transient fluctuations necessary for stable actuation. This assumption led to the use of push/ pull actuator pairs with a split Wheatstone bridge sensing circuit to gain immunity to thermal transients. The trade-off was a very tight 0.01 K gradient requirement between the two actuators in each pair. This is a potential killer requirement.

The temperature of the actuators in both LEOP and imaging operations must be controlled, though it will not be clear whether active or passive thermal control will be necessary until the instrument thermal model

matures. The actuators themselves are not expected to dissipate any more than, conservatively, ≈200 mW of heat each, even during intense calibration, which is expected to be manageable in terms of thermal effects on the mirror segments.

The structural components are very robust to the thermal loads experienced during both imaging and LEOP. The mechanism must be athermalised to to meet the thermal drift budget. Conceptually, passive compensation will be sufficient, even with inclusion of a ±15 K thermal uncertainty margin. Further compensation is possible if Invar-36 is used for the support bipods.

A key outcome of the ongoing thermal modelling will be to find whether meeting a gradient requirement across the actuators, or a transient requirement within the actuator pairs, is more difficult (and thus expensive). There is still some flexibility in the design to change to the 3×NLA option originally presented in Chapter 7 *Mechanism Architecture Selection* if small transient fluctuations are easier to maintain. Using four actuators through launch gave a margin of safety against failure of 33%, so there is some structural margin available to remove an actuator. Additionally, the kinematic calculations in Chapter 7 showed that there was little difference in the stroke requirement between the three and four actuator concepts. If the baffle and TCS are able to provide a very stable transient environment as well as provide even heating over the PMAO, then no push/ pull pairs may be needed at all and the PMAO could be simplified even further.

To summarise, the thermal control feasibility of the PMAO remains an open question, however the concept can still be tailored to the findings of the thermal modelling.

Optical Feasibility

The difficulty of using a 3DOF system with a centre of rotation behind the mirror, is that correcting a decentre with a tilt in one direction induces a decentre in the orthogonal direction. A full 6DOF mechanism, such as the one to be used on the James Webb Space Telescope primary mirror segments, would provide faster convergence of the calibration algorithm since each DOF can be controlled directly. The trade-off is the need for more actuators and thus mass, volume, complexity and cost.

The Monte Carlo ETEP modelling verified that despite these remote centre displacements, it was possible to retrieve a diffraction limited image in all deployment cases based on the top down system budgets. All told, 97.7% of the cases achieved a Strehl ratio of 0.91 or higher after calibration but before application of the in orbit drift and stability tolerances. The simulations also showed that the mechanism could be used to achieve a minimum Strehl ratio of 0.80 in nearly 88% of the deployment cases if one segment fails, demonstrating the robustness of the PMAO, ACS and calibration algorithm interaction.

The thesis has also answered an open question in an earlier thesis by G. van Marrewijk, namely whether a mechanism like the PMAO could be used in conjunction with the ACS to correct for discontinuous wavefront errors [116, p.103]. The results summarised in 9.4.4 demonstrated that the PMAO was indeed able to correct these discontinuous errors. Thus, with the ACS and PMAO combined, it is feasible to overcome the budgeted deployment, in orbit drift and stability errors.

Systems Feasibility

The total mass of the M1 subsystem now stands at approximately 68 kg including 20.916 kg for the deployment mechanism [33], 23.42 kg for the PMAO and 24 kg for the mirrors. With a further 8 kg for the M2 subsystem [72] and an estimated 50 kg for the Aberration Correction System, baffle, tertiary mirror, detectors and instrument housing, the total instrument mass is approximately 126 kg.

Mission requirement MIS-REQ-08 stipulates a goal mass of 50 kg and threshold mass of 100 kg for the entire DST instrument. In its current state, it is not reasonable to expect that the DST will meet the goal mass, and an overall weight saving of ≈30% will be needed to meet the threshold requirement. No mass optimisation has been performed on any components so far, so this may yet be feasible. For its part, the revised PMAO design is conservative: the quasi static launch loads are large and the aerial density of the mirror is much greater than the current state of the art, so the mass could certainly be reduced with a modest amount of effort. The PMAO fixed frame could also be merged with the deployment mechanism support frame to further save mass and volume.

The total power draw for the PMAO actuators is not expected to be any more than 16 W (1 W per actuator) as an upper limit, which is feasible for a LEO small satellite. A more pressing concern is the high voltage requirement. Traditionally, this would have been a problem for standard spacecraft buses but piezoelectric actuators are increasingly well accepted in modern spacecraft [4], and a high voltage AC power source is nonetheless necessary for the ACS. The power requirements are considered feasible.

It is *not* feasible to use the revised PMAO arrangement for coarse alignment (displacements greater than low tens of microns). Longer stroke requirements require longer linear piezo actuators. There is a small

amount of space left behind the mirror to increase the stroke to no more than 20 μm, though this would require a creative arrangement with the M1 deployment winches.

Overall, the design cannot categorically be deemed feasible until its ability to meet the top down systems budgets is verified, though the verification work completed so far does suggest that the PMAO concept is broadly feasible. A complete assessment hinges upon maturation of the M1 deployment mechanism, verification of compliance with the top down budgets and an assessment of the feasibility of the TCS flow down requirements from the thermal modelling.

10.2.2. General Conclusions

The goal of the thesis was to generate a preliminary thermo-mechanical design of the PMAO mechanism to enable diffraction limited imaging from low Earth orbit with the Deployable Space Telescope. Integration of a mechanical model of the mechanism in the ETEP simulation as well as a feasibility assessment were also major objectives. Each of these elements have been delivered, in turn providing the basis for answers to the two research questions. The novelty of the output from this thesis therein lies in three parts:

1. First, it has demonstrated that it is mechanically and optically feasible to co-phase and co-align an off-axis segmented mirror with a 3DOF mechanism using the calibration algorithm implemented by D. Dolkens. The tolerance of the optimisation algorithm to the remote centre errors means that only a minimum of three actuators are necessary to remove discontinuous wavefront errors. The current state of the art for active control of segmented space optics, albeit for a very different mission profile, is the JWST primary mirror assembly which uses a six actuator hexapod. This offers much better control of the mirror pose than the 3DOF mechanism presented here.
2. Secondly, the mechanism is capable of supporting a large 6 kg mirror segment without a hold down mechanism through launch and into the dynamic LEO space environment without protection, all in a volume comparable to existing 3DOF fine pointing space mechanisms. On top of surviving these harsh environments, the mechanism is able to provide the stroke, accuracy and resolution needed to calibrate the primary mirror at levels comparable to or exceeding the state of the art in space rated 3DOF fine control mechanisms, despite needing to support a mirror at twice the mass.
3. The third novelty relates to the systems engineering effort within the DST team. The PMAO *SPACAR* model is the first contribution to the ETEP simulation of the Deployable Space Telescope from the bottom up mechanical engineering efforts. The PMAO can now be simulated with feasible stroke, resolution and accuracy estimates. It marks the start of a process to rigorously demonstrate the feasibility of the DST concept through the marriage of both top down and bottom up systems engineering processes.

As it stands, the revised PMAO mechanism concept is a promising solution to the need for correction of discontinuous wavefront errors in the Deployable Space Telescope optics. The current design is relatively conservative with ample scope for improvement as the thermo-mechanical component and environmental characterisations mature, though a considerable amount of work remains to rigorously prove its feasibility.

10.3. Recommendations & Future Work

Numerous tasks for future work at the component level were noted throughout the execution of this document. This section focusses on high level recommendations for future work.

Progression of the PMAO design is integrally linked to almost all other DST work packages. A flowchart setting out the recommended future work is given in Figure 10.2. The overarching goal of the recommendations is to complete the PMAO preliminary design verification with a focus on the top down systems budgets.

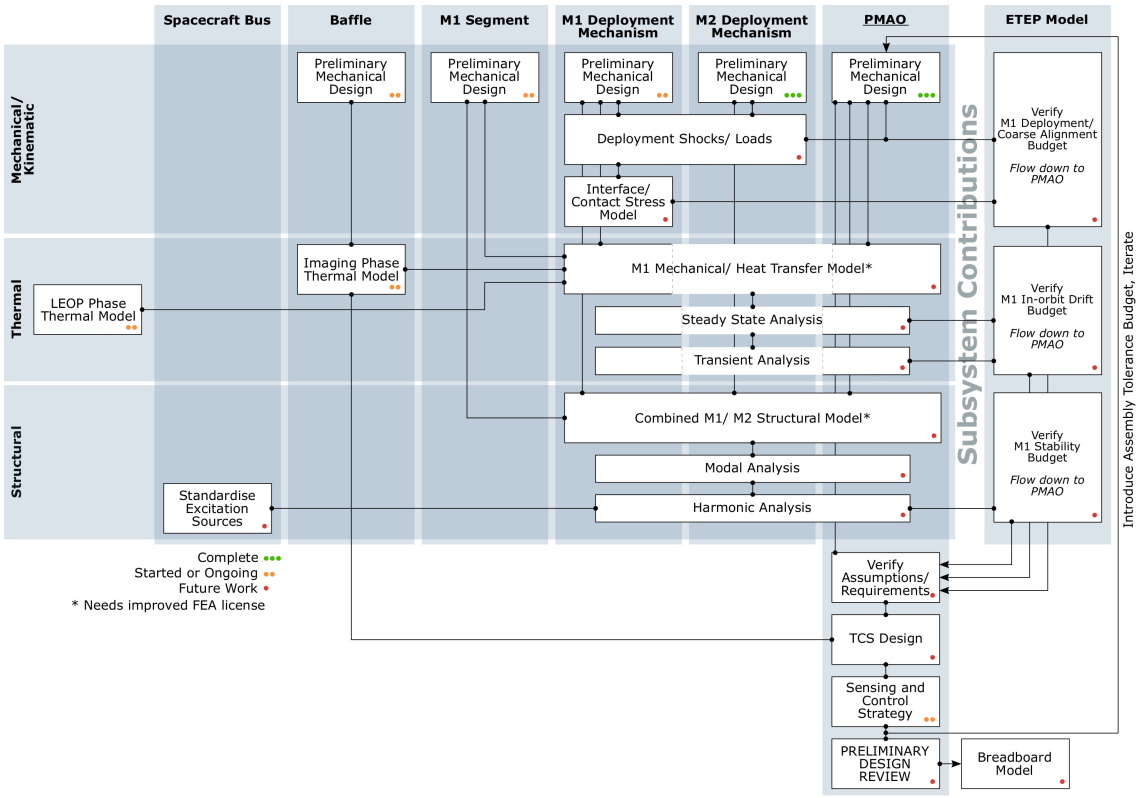

Figure 10.2: Flowchart of remaining work needed to develop the PMAO mechanism. Not all completed design tasks are shown. The broken border of the M1 mechanical/ heat transfer model task over the M2 deployment mechanism column indicates that it does *not* include the M2 assembly. TCS = Thermal Control System.

A broad range of work is needed to progress the PMAO concept, from mechanical design and systems modelling, to thermal, sensing and control design. Recommended MSc thesis work packages are to first complete the *combined* M1 thermo-mechanical modelling to verify the top down budgets. A contact stress model of the M1 kinematic interface should be included in the ETEP model to verify the deployment budget.

The second work package should focus on the PMAO thermal control system and sensing/ control strategies. Although the TCS and control system designs are depicted in series in Figure 10.2, they will be tightly interlinked due to the sensitivity of the sensors to the thermal environment. The thermal flow down requirements may be killer requirements. The design tools developed in this thesis, most notably the parametric implementation of the PMAO mechanism in *SPACAR*, are well suited to these tasks.

Much of this work cannot take place without access to the right tools, particularly an FEA package with a large mesh allowance. Eventually, testing will be necessary to validate the requirements, design and assumptions. Given the limited DST project resources, investing in a breadboard model prior to a formal preliminary design review would be premature.

It is hoped that the output of this thesis has provided a lasting and useful starting point to facilitate this future work.

Bibliography

[1] R.G.K.M. Aarts, S.E. Boer, J.P. Meijaard, D.M. Brouwer, and J. B. Jonker. Analyzing overconstrained design of compliant mechanisms. In *Proceedings of ASME 2011 International Design Engineering Technical Conference & Computers and Information in Engineering Conference*, Washington DC, USA, 2011.

[2] R.G.K.M. Aarts, J.B. Jonker, and J. Van Dijk. Prototype modelling of mechanical systems: An introduction for module 5&8, 2015.

[3] National Aeronautics and Space Administration. Ningaloo National Marine Park, Western Australia, 2008. URL `https://landsat.visibleearth.nasa.gov/view.php?id=9068`.

[4] C. Allegranza, L. Gaillard, R. Le Letty, S. Patti, L. Scolamiero, and M. Toso. Actuators for Space Applications: State of the Art and New Technologies. In *14th International Conference on New Actuators*, 2014.

[5] Arianespace. Soyuz User's Manual Issue 2 Revision 0, 2012. URL `http://www.arianespace.com`.

[6] Arianespace. Vega User's Manual Issue 4 Revision 0, 2014. URL `http://www.arianespace.com`.

[7] Arianespace. Ariane 5 User's Manual Issue 5 Revision 2, 2016. URL `http://www.arianespace.com`.

[8] A. Artiagoitia, C. Compostizo, and L. Rivera. Euclid M2 mirror mechanism. In *Proc. ESMATS 2017*, 2017.

[9] Axelspace. GRUS, 2018. URL `https://www.axelspace.com/en/solution{_}/grus/`.

[10] F. Barillot, R. Le letty, F. Claeyssen, N. Lhermet, and M. Yorck. Design and functional tests of a XY piezoelectric stage for Rosetta/ MIDAS. In *Proc. ESMATS 1999*, 1999.

[11] F. Barillot, H. Fabbro, R. Le Letty, and Ph Guay. Design and tests of normally centred piezo mechanisms and their control electronic. In *Proc. ESMATS 2003*, 2003.

[12] F. Barillot, T. Porchez, and C. Belly. Nanometric Positioning With Piezoelectric Actuator & High Stability Strain-Gages. In *Proc. ESMATS 2015*, 2015.

[13] C. Belly, M. Hihoud, A. Pages, H. Argelaguet, J. Moreno, and C. Mangeot. Cryogenic Piezo Characterisation and Integration in Fine Steering Tip / Tilt Mechanism. In *Actuator 2014*, Messe Bremen, 2014.

[14] P.Y. Bely, editor. *The Design and Construction of Large Optical Telescopes*. Springer-Verlag, New York, first edition, 2002.

[15] N. Bencheikh, A. Guignabert, F. Barillot, C. Benoit, C. Burgui, C. Compostizo, I. Bueno, P. Spanoudakis, L. Kiener, and P. Schwab. Voice Coil Actuators for Two MTG Instruments. In *Proc. ESMATS 2015*, 2015.

[16] H.D. Black. A passive system for determining the attitude of a satellite. *AIAA Journal*, 2(7):1350–1351, 1964.

[17] D.L. Blanding. *Exact Constraint: Machine Design Using Kinematic Principles*. ASME Press, New York, 1999.

[18] S. Boer and T. van der Poel. SpaVisual User Manual, 2011. URL `http://www.spacar.nl/wiki/doku.php?id=manuals`.

[19] S.E. Boer, R.G.K.M. Aarts, D.M. Brouwer, and J.B. Jonker. Multibody Modelling and Optimization of a Curved Hinge Flexure. In *The 1st Joint International Conference on Multibody System Dynamics*, Lappeenranta, Finland, 2010.

[20] D. Bortoluzzi, P. A. Mäusli, R. Antonello, and P.M. Nellen. Modeling and identification of an electromechanical system: The LISA grabbing positioning and release mechanism case. *Advances in Space Research*, 47(3):453–465, 2011.

[21] M. Bougoin and J. Lavenac. From Herschel to Gaia: 3-meter class SiC space optics. In *Proc. SPIE*, volume 8126, 2011.

[22] F. Bourgain, F. Barillot, C. Belly, and F. Claeyssen. ATLID beam steering mechanism and derived new piezoelectric-based devices for optical applications. In *Proc. SPIE*, volume 9626, 2015.

[23] D. M. Brouwer, J. P. Meijaard, and J. B. Jonker. Large deflection stiffness analysis of parallel prismatic leaf-spring flexures. *Precision Engineering*, 37(3):505–521, 2013.

[24] K.H. Brown, C. Morrow, S. Durbin, and A. Baca. Guideline for Bolted Joint Design and Analysis. Technical report, Albuquerque, New Mexico, 2008. URL `https://prod.sandia.gov/techlib-noauth/access-control.cgi/2008/080371.pdf`.

[25] Bryce Space and Technology. State of the Satellite Industry Report: October 2017. Technical report, Satellite Industry Association, 2017. URL `http://www.sia.org/white-papers/`.

[26] R.G. Budynas and J.K. Nisbett. *Shigley's Mechanical Engineering Design*. McGraw-Hill, ninth edition, 2011.

[27] M. Buttery, R. Watters, and E. Roberts. Piezo-Electric Linear Actuators in Vacuum. In *Proc. ESMATS 2011*, 2011.

[28] Cedrat Technologies. Cedrat Technologies Products Catalog Version 4, 2012.

[29] Cedrat Technologies. PPA40XL, 2018. URL `http://www.cedrat-technologies.com/en/products/actuators/parallel-pre-stressed-actuators.html`.

[30] K.B. Choi, J.J. Lee, G.H. Kim, H.J. Lim, and S.G. Kwon. Amplification ratio analysis of a bridge-type mechanical amplification mechanism based on a fully compliant model. *Mechanism and Machine Theory*, 121:355–372, 2018.

[31] F. Claeyssen. Personal communication, 2018.

[32] C. Compostizo, R. Lopez, and L. Rivera. GAIA M2M pointing mechanism qualification. In *Proc. ESMATS 2011*, 2011.

[33] M. Corvers. *Design of a Primary Mirror Deployment Mechanism for a Deployable Space Telescope*. Master thesis, TU Delft, 2018.

[34] A.M. Cruise, J.A. Bowles, T.J. Patrick, and C.V. Goodall. *Principles of Space Instrument Design*. Cambridge University Press, Cambridge, 1998.

[35] F. de Lussy, P. Kubik, D. Greslou, V. Pascal, P. Gigord, and J.P. Cantou. Pleiades-HR image system products and quality Pleiades-HR image system products and geometric accuracy. In *ISPRS*, 2005.

[36] Deimos Imaging. Our Satellites, Deimos-1 and Deimos-2, 2018. URL `http://www.deimos-imaging.com/satellites{#}2`.

[37] G. Denis, A. Claverie, X. Pasco, J.P. Darnis, B. de Maupeou, M. Lafaye, and E. Morel. Towards disruptions in Earth observation? New Earth Observation systems and markets evolution: Possible scenarios and impacts. *Acta Astronautica*, 137(December 2016):415–433, 2017.

[38] N. Devaney, C. Reinlein, N. Lange, M. Goy, A. Goncharov, and P. Hallibert. HYPATIA and STOIC: An active optics system for a large space telescope. In *Proc. SPIE*, volume 9904, 2016.

[39] C. Devilliers, F. Aguilar, J. Ducarne, F. Barillot, and F. Claeyssen. European Patent EP 2887532A1: Roundtrip precision actuator, 2013.

[40] DigitalGlobe. The DigitalGlobe Constellation. URL `https://www.digitalglobe.com/resources/satellite-information`.

[41] DigitalGlobe. WorldView-1 Data Sheet, 2013. URL https://www.digitalglobe.com/resources/satellite-information.

[42] DigitalGlobe. GeoEye-1 Data Sheet, 2014. URL https://www.digitalglobe.com/resources/satellite-information.

[43] DigitalGlobe. WorldView-3: An evolution of the satellites coming before it, 2014. URL http://blog.digitalglobe.com/industry/worldview-3-an-evolution-of-the-satellites-coming-before-it/.

[44] DigitalGlobe. WorldView-2 Data Sheet, 2016. URL https://www.digitalglobe.com/resources/satellite-information.

[45] DigitalGlobe. WorldView-3 Data Sheet, 2017. URL https://www.digitalglobe.com/resources/satellite-information.

[46] DigitalGlobe. WorldView-4 Data Sheet, 2017. URL https://www.digitalglobe.com/resources/satellite-information.

[47] DMC International Imaging. DMC Constellation, 2018. URL http://www.dmcii.com/?page{_}id=9275.

[48] D. Dolkens. *A Deployable Telescope for Sub-Meter Resolutions from MicroSatellite Platforms*. Master thesis, TU Delft, 2015.

[49] D. Dolkens. Personal communication, 2018.

[50] D. Dolkens and J.M. Kuiper. Design and End-To-End Modelling of a Deployable Telescope. In *International Conference on Space Optics*, Biarritz, 2016.

[51] D. Dolkens, J.M. Kuiper, and E.K.A Gill. Design and Optimization of a Deployable Telescope for Earth Observation Applications [Submitted for Publication], 2018.

[52] R.E. Fischer and B. Tadic-Galeb. *Optical System Design*. McGraw-Hill, New York, first edition, 2000.

[53] E. Fishler. IAI is boosting its observation satellites activity, 2015. URL http://www.iai.co.il/2013/32981-46490-en/MediaRoom{_}News.aspx.

[54] P. Fortescue, J. Stark, and G. Swinerd, editors. *Spacecraft Systems Engineering*. John Wiley & Sons, Chichester, England, third edition, 2006.

[55] Geospatial World. MDA-DG combined entity to be rebranded as Maxar Technologies, 2017. URL https://www.geospatialworld.net/news/mda-dg-combined-entity-to-be-rebranded-as-maxar-technologies/.

[56] K. Gunnink, R.G.K.M. Aarts, and D.M. Brouwer. Performance optimization of large stroke flexure hinges for high stiffness and eigenfrequency. In *Proceedings of the 28th Annual Meeting of the American Society for Precision Engineering (ASPE), Saint Paul, MN, USA, ASPE, October, 20-25*, pages 1–6, 2013.

[57] L.C. Hale. *Principles and Techniques for Designing Precision Machines*. Phd thesis, Massachusetts Institute of Technology, 1999.

[58] J. Herder. Personal communication, 2018.

[59] M. Hihoud, A. Pagès, C. Benoit, F. Claeyssen, S. Sanchez, S. Trémolières, and P. Guay. BRUCE – Electromagnetic Actuated Pin Puller. In *Proc. ESMATS 2013*, 2013.

[60] W. Holmes, G. Munro, and O. Poyntz - Wright. Design, Development and Testing of a Scan and Focus Mechanism for the Spice Instrument. In *Proc. ESMATS 2015*, 2015.

[61] J.B. Hopkins and M.L. Culpepper. Synthesis of multi-degree of freedom, parallel flexure system concepts via Freedom and Constraint Topology (FACT) - Part I: Principles. *Precision Engineering*, 34(2): 259–270, 2010.

[62] J.B. Hopkins and M.L. Culpepper. Synthesis of multi-degree of freedom, parallel flexure system concepts via Freedom and Constraint Topology (FACT) - Part II: Practice. *Precision Engineering*, 34(2): 271–278, 2010.

[63] J.M. Howard. Optical integrated modeling activities for the James Webb Space Telescope (JWST). In *Proc. SPIE*, volume 8336, 2011.

[64] ImageSat International N.V. EROS Satellite Overview, 2018. URL `https://www.imagesatintl.com/eros-sat/`.

[65] J. B. Jonker, R. G K M Aarts, and J. Van Dijk. A linearized input-output representation of flexible multibody systems for control synthesis. *Multibody System Dynamics*, 21(2):99–122, 2009.

[66] J.B. Jonker and J.P. Meijaard. SPACAR - Computer Program for Dyanmic Analysis of Flexible Spatial Mechanisms and Manipulators. In *Multibody Systems Handbook*, pages 123–143. Berlin, 1990.

[67] P. Kansakar and F. Hossain. A review of applications of satellite earth observation data for global societal benefit and stewardship of planet earth. *Space Policy*, 36:46–54, 2016.

[68] B.J. Kenton and K.K. Leang. Design and control of a three-axis serial-kinematic high-bandwidth nanopositioner. *IEEE/ASME Transactions on Mechatronics*, 17(2):356–369, 2012.

[69] H. Kim, J. Kim, D. Ahn, and D. Gweon. Development of a nanoprecision 3-DOF vertical positioning system with a flexure hinge. *IEEE Transactions on Nanotechnology*, 12(2):234–245, 2013.

[70] D. Korsch. Anastigmatic three-mirror telescope. *Applied Optics*, 16(8):2074–2077, 1977.

[71] K. Koski. Focus Mechanism for Kepler Mission. In E.A. Boesiger, editor, *39th Aerospace Mechanisms Sympsium*, pages 359–372, Huntsville, Alabama, 2008. National Aeronautics and Space Administration.

[72] A. Krikken. *Design of the Secondary Mirror Support Structure for the Deployable Space Telescope*. Master thesis, TU Delft, 2018.

[73] J.M. Kuiper and D. Dolkens. A Deployable Telescope Concept for Sub-Meter Resolutions. *Acta Futura*, 10:131–144, 2016.

[74] M. S Lake and M.R. Hachkowski. Design of Mechanisms for Deployable , Optical Instruments: Guidelines for Reducing Hysteresis. Technical report, NASA, Hampton, Virginia, 2000.

[75] M. Lampton and M. Sholl. Comparison of on-axis three-mirror-anastigmat telescopes. In *Proc. SPIE*, volume 6687, 2007.

[76] W. Larson, D. Kirkpatrick, J. Sellers, L. Thomas, and D. Verma, editors. *Applied Space Systems Engineering (Space Technology Series)*. McGraw-Hill Higher Education, first edition, 2009.

[77] R. Le Letty, F. Barillot, N. Lhermet, F. Claeyssen, M. Yorck, J. Gavira Izquierdo, and H. Arends. The scanning mechanism for Rosetta/ MIDAS from an engineering model to the flight model. In *Proc. ESMATS 2001*, 2001.

[78] R. Le Letty, F. Barillot, H. Fabbro, F. Claeyssen, and L. Cadiergues. Miniature Piezo mechanisms for optical and space applications. In *9th International Conference on New Actuators*, Bremen, 2004.

[79] P.A. Lightsey, C. Atkinson, M. Clampin, and L.D. Feinberg. James Webb Space Telescope: large deployable cryogenic telescope in space. *Optical Engineering*, 51(1), 2012.

[80] B. Lobitz, L. Beck, A. Huq, B. Wood, G. Fuchs, A.S.G. Faruque, and R. Colwell. Climate and infectious disease: use of remote sensing for detection of Vibrio cholerae by indirect measurement. *Proceedings of the National Academy of Sciences of the United States of America*, 97(4):1438–1443, 2000.

[81] N. Lobontiu. *Compliant Mechanisms: Design of Flexure Hinges*. CRC Press, Boca Raton, 2002.

[82] K.R. Lorell, J. Aubrun, R.R. Clappier, S.W. Miller, and M. Sirota. Design of a prototype primary mirror segment positioning actuator for the Thirty Meter Telescope. In *Proc. SPIE*, volume 62672T, 2006.

[83] H.M.Y.C. Mallikarachchi and S. Pellegrino. Optimized designs of composite booms with integral tape-spring hinges. In *51st AIAA/ASME/ASCE/AHS/ASC Structures, Structural Dynamics, and Materials Conference*. AIAA, 2010.

[84] F.L. Markley. Attitude Determination Using Two Vector Measurements. Technical report, National Aeronautics and Space Administration, Greenbelt, Maryland, 1999. URL https://ntrs.nasa.gov/archive/nasa/casi.ntrs.nasa.gov/19990052720.pdf.

[85] P.A. Mausli, A. Neukom, R. Romano, I. Koker, and S. Durrant. Development of a novel piezo actuated release mechanism. In *Proc. ESMATS 2007*, 2007.

[86] M. Meftah, A. Irbah, R. Le Letty, A. Bataille, E. Ducourt, G. Poiet, and M. Privat. The PICARD / SODISM Pointing Mechanism: From the Design to the Flight Performances. In *Proc. ESMATS 2011*, 2011.

[87] J. P. Meijaard, D. M. Brouwer, and J. B. Jonker. Analytical and experimental investigation of a parallel leaf spring guidance. *Multibody System Dynamics*, 23(1):77–79, 2010.

[88] M. Naves, D. M. Brouwer, and R. G. K. M. Aarts. Building Block-Based Spatial Topology Synthesis Method for Large-Stroke Flexure Hinges. *Journal of Mechanisms and Robotics*, 9(4):041006, 2017.

[89] A.Y.C. Nee, editor. *Handbook of Manufacturing Engineering and Technology*. Springer-Verlag, 2015.

[90] J. Nelson and G.H. Sanders. The status of the Thirty Meter Telescope project. In *Proc. SPIE*, volume 7012, 2008.

[91] A. Neukom, R. Romano, and P.M. Nellen. Testing and Lessons Learnt of LISA GPRM. In *Proc. ESMATS 2009*, 2009.

[92] Newport Corporation. High Precision Hexapods, 2018. URL https://www.newport.com/f/hxp-series-hexapods.

[93] J. Nijenhuis, J. Heijmans, R. den Breeje, R. Hazelebach, J. de Vreugd, W. Crowcombe, D. Naron, E. Fritz, G. Borghi, R. Navarro, L. Sillari, E. Sambenedetto, J. Eder, and F. Kamphues. Designing the primary mirror support for the E-ELT. In *Proc. SPIE*, volume 9906, 2016.

[94] S. Ogden, L. Klintberg, G. Thornell, K. Hjort, and R. Bodén. Review on miniaturized paraffin phase change actuators, valves, and pumps. *Microfluidics and Nanofluidics*, 17(1):53–71, 2014.

[95] Omega Engineering. Practical Strain Gage Measurements, 2018. URL https://www.omega.co.uk/techref/pdf/StrainGage{_}Measurement.pdf.

[96] S. Pepper. *Deployable Space Telescope: Literature Review for the Primary Mirror Active Optics*. Unpublished literature study, Delft, Netherlands, 2018.

[97] Physik Instrumente. PiezoWalk Piezo Motors, 2018. URL https://www.physikinstrumente.com/en/technology/piezoelectric-drives/piezowalk-piezo-motors/.

[98] Phytron. phySPACE Stepper Motor Series, 2017. URL http://www.phytron.com/.

[99] Phytron. MCC-2 Programmable controller for two axes, 2017. URL https://www.phytron.eu/products/driver-controller/mcc-2/.

[100] Planet. Satellite imagery product specifications. Technical report, 2016. URL https://assets.planet.com/docs/1601.RapidEye.Image.Product.Specs{_}Jan16{_}V6.1{_}ENG.pdf.

[101] T. Porchez, F. Barillot, and C. Belly. Nanometric Linear Piezo-Actuator with Integrated Strain Gages for High Stability Positioning. In *15th International Conference on New Actuators*, Bremen, Germany, 2016.

[102] K. Qi, Y. Ding, Y. Xiang, C. Fang, and Y. Zhang. A novel 2-DOF compound compliant parallel guiding mechanism. *Mechanism and Machine Theory*, 117:21–34, 2017.

[103] T.P. Sarafin, editor. *Spacecraft Structures and Mechanisms*. Microcosm, Inc., Torrance, California, 1995.

[104] W.C. Schade. Cryogenic Focus Mechanism for the Spitzer Space Telescope. In E.A. Boesiger, editor, *39th Aerospace Mechanisms Sympsium*, pages 401–414, Huntsville, Alabama, 2008. National Aeronautics and Space Administration.

[105] R.B. Slusher. Motion Reducing Flexure Structure, 1998.

[106] S.T. Smith and D.G. Chetwynd. *Foundations of Ultraprecision Mechanism Design*. Gordon and Breach Science Publishers S.A., Yverdon, second edition, 1994.

[107] W.J. Smith. *Modern Optical Engineering*. McGraw-Hill, New York, third edit edition, 2000.

[108] P. Spanoudakis, L. Zago, O. Chételat, R. Gentsch, and F Mato. Mira. Extremely high-resolution tip-tilt-piston mirror mechanism for the VLT-NAOS field selector. In *Proc. SPIE*, volume 4007, 2000.

[109] H.P. Stahl. JWST primary mirror technology development results. In *Proc. SPIE*, volume 6671, 2007.

[110] D. Stewart. A Platform with Six Degrees of Freedom. *Proceedings of the Institution of Mechanical Engineers*, 180(1):371–386, 1965.

[111] S.A. Streetman and L. Kingsbury. US Patent No. US 6478434B1: Cryo Micropositioner, 2002.

[112] Surrey Satellite Technology Ltd. DMC3/ TripleSat Constellation: Launched 2015, 2018. URL `https://www.sstl.co.uk/space-portfolio/launched-missions/2010-2018/dmc3-triplesat-constellation-launched-2015`.

[113] P.M. Thompson, D.G. MacMynowski, and M.J. Sirota. Control analysis of the TMT primary segment assembly. In *Proc. SPIE*, number 7012, 2008.

[114] TU Delft. AE4S12 Lecture Slides: Space Systems Engineering "From Stakeholder Expectations to Technical System Requirements", 2016.

[115] E. Urgoiti, A. Ramirez, and P. Coste. Gaia M2M Positioning Mechanism. In *Proc. ESMATS 2005*, 2005.

[116] G.P. van Marrewijk. *Aberration Correction System for a Deployable Space Telescope*. Masters thesis, Delft University of Technology, 2018.

[117] B.T. van Putten. *Design of the Deployment Mechanism for the Primary Mirror Elements of a Deployable Space Telescope*. Master thesis, TU Delft, 2017.

[118] D. Vukobratovich and R.M. Richard. Flexure Mounts For High-Resolution Optical Elements. *Proc. SPIE*, (0959):18–36, 1988.

[119] K.J. Waldron and G.L. Kinzel. *Kinematics, Dynamics and Design of Machinery*. John Wiley & Sons, Hoboken, New Jersey, second edition, 2004.

[120] R.M. Warden. Cryogenic Nano-Actuator for JWST. In *38th Aerospace Mechanisms Sympsium*, Williamsburg, Virginia, 2006.

[121] I. Weingrod, C.Y. Chou, B. Holmes, C. Hom, J.W. Irwin, O. Lindstrom, F. Lopez, D.M. Stubbs, and J.P. Wüelser. Design of bipod flexure mounts for the IRIS spectrometer. In *Proc. SPIE*, volume 8830Q, 2013.

[122] J.R. Wertz, D.F. Everett, and J. Puschell, editors. *Space Mission Engineering: The New SMAD*. Microcosm press, Hawthorne, California, 2011.

[123] G. Witvoet and J. Human. Realization and Performance Validation of the In-Field Pointing Mechanism for the Evolved Laser Interferometer Space Antenna. In *Proc. ESMATS 2015*, 2015.

[124] P.R. Yoder. *Mounting Optics in Optical Instruments*. SPIE, second edition, 2008.

[125] P.R. Yoder and D. Vukobratovich. *Opto-mechanical systems design Volume 2: Design and analysis of large mirrors and structures*. CRC Press, Boca Raton, fourth edition, 2015.

[126] P.R. Yoder and D. Vukobratovich. *Opto-mechanical systems design Volume 1: Design and analysis of opto-mechanical assemblies*. CRC Press, Boca Raton, fourth edition, 2015.

[127] M. Yoichi. Applications of Piezoelectric Actuator, 2006.

[128] W.C. Young and R.G. Budynas. *Roark's Formulas for Stress and Strain*. McGraw-Hill, New York, seventh edition, 2002.

A

Market Survey Data

Table A.1: Aggregated market data for Figure 1.1. *Constellation Size* is either current for Incumbents or planned for Future/ New entrants.

Platform	**Year Operational**	**Class**	**Constellation Size**	**GSD** $[m]$	**Spacecraft Mass** $[kg]$	**Reference**
Aquila Space/ Astro Digital	>2018	Future	30	2.5	20	[25, 37]
Axelspace	2022	Future	50	2.5	100	[9]
BlackSky Global	2016	Future	60	1	50	[37]
DigitalGlobe GeoEye-1	2008	Incumbent	1	0.41	1899	[42]
DigitalGlobe WorldView 1	2007	Incumbent	1	0.5	2290	[41]
DigitalGlobe WorldView-2	2009	Incumbent	1	0.46	2615	[44]
DigitalGlobe WorldView-3	2014	Incumbent	1	0.31	2800	[43, 45]
DigitalGlobe WorldView-4	2017	Incumbent	1	0.31	2600	[40, 46]
DMCii: DMC3	2015	New	3	2.5	440	[47, 112]
Hera Systems	>2018	Future	48	1	22	[37]
ImageSat: EROS	2019	New	3	0.45	400	[53, 64]
Jilin (China)	2030	Future	138	0.72	420	[37]
Planet Doves	2017	New	145	3	3	[25, 37]
Planet RapidEye (BlackBridge)	2010	New	5	6.5	150	[37, 100]
Planet SkySats (TerraBella, Skybox)	2013	New	24	0.9	110	[37]
Pleiades 1A/1B	2012	Incumbent	2	0.7	1000	[35]
Satellogic	>2018	Future	300	1	35	[37]
UrtheCast Deimos 2	2015	New	1	0.75	300	[36, 37]
UrtheCast OptiSAR (optical platform)	2020	Future	8	0.5	670	[37]

B

Requirements Discovery Trees

The requirements trees on the following pages were used in the requirements generation process of Chapter 3 *Requirements Generation*.

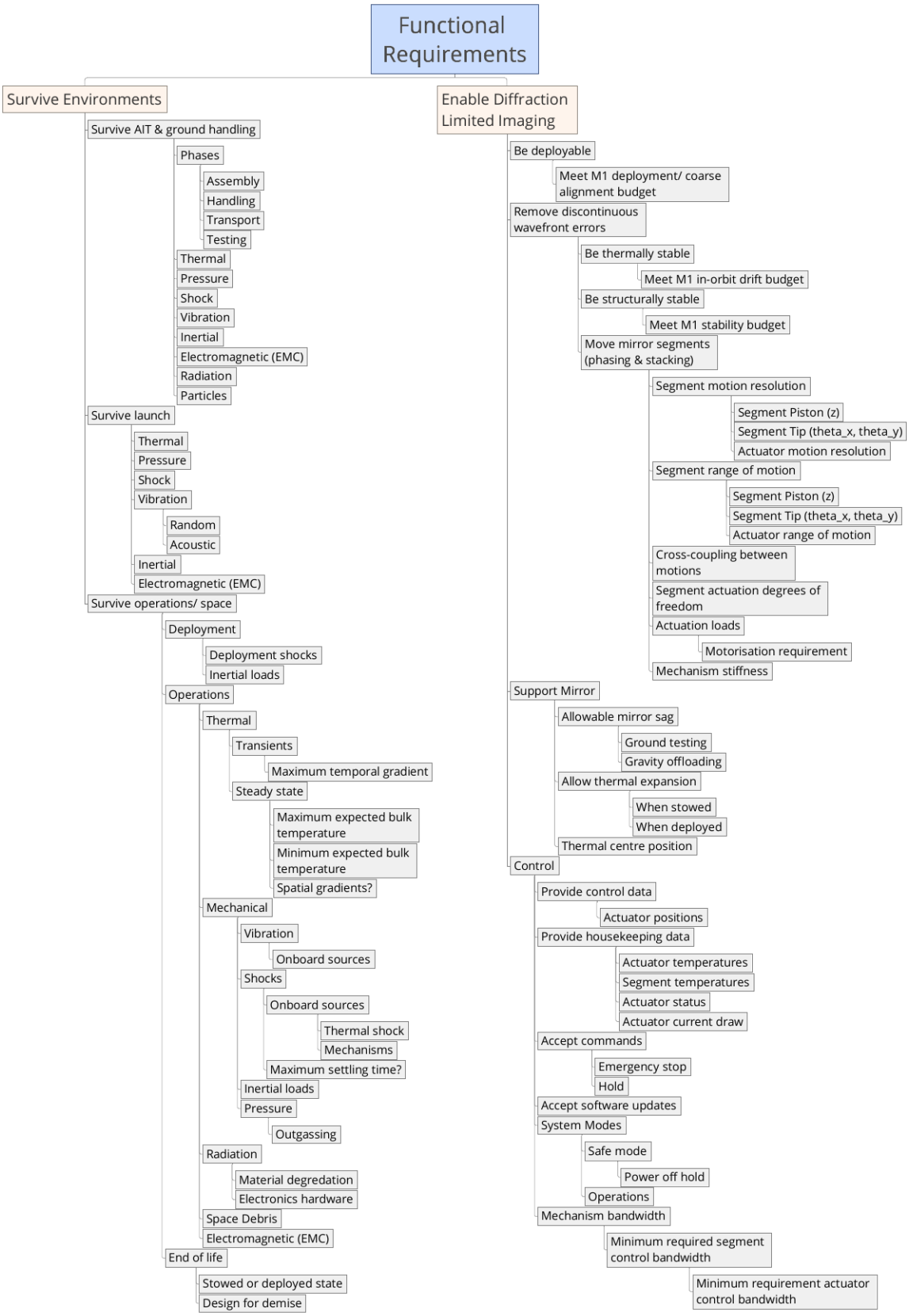

Figure B.1: Functional requirements discovery tree.

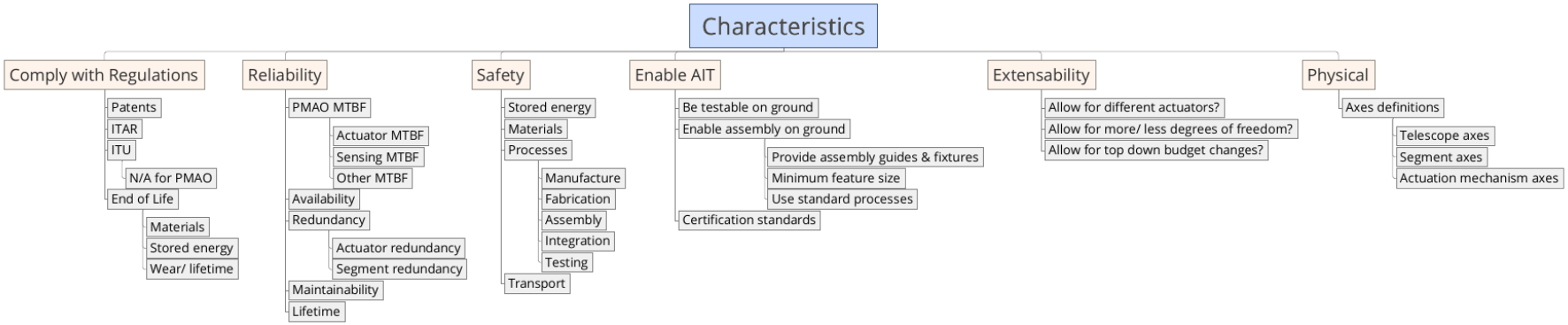

Figure B.2: Characteristic requirements discovery tree.

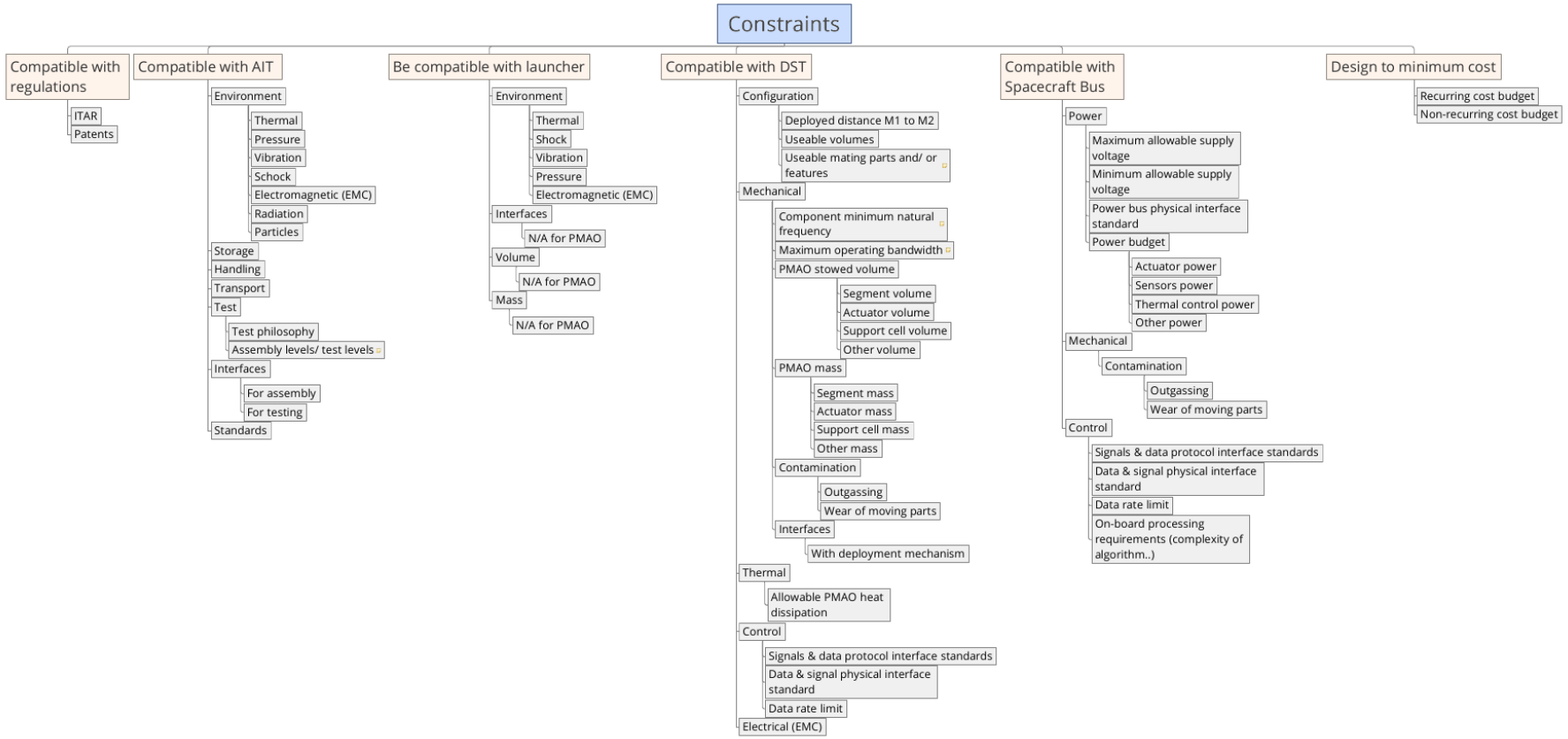

Figure B.3: Constraint requirements discovery tree.

C

Stowed Operations Thermal Model

A simple thermal model was developed to predict worst-case steady state temperatures on the outer components of the DST during LEOP. André Krikken contributed the orbital calculations and collaborated on the methodology and conclusions.

TU Delft	PROJECT	Deployable Space Telescope
	JOB No.	-
SUBJECT **Stowed Operational Thermal Model**	CALC. REF. NO.:	DST-WP1-CALC-001
	SHEET 1 OF 20	REV: B

REF. DRG. NO.:	MADE BY:	CHECKED BY:	APPROVED BY:
N/A	**SP, AK**		
ITEM:	DATE: 6 April 2018	DATE:	DATE:

Revision	Date	Description	By	Review	Approve
A	4/04/2018	Preliminary	SP, AK		
B	6/04/2018	For use. Earth IR potential removed. Minor corrections.	SP, AK		

TUDelft	PROJECT	Deployable Space Telescope
	JOB No.	-
SUBJECT: **Stowed Operational Thermal Model**	CALC. REF. NO.:	DST-WP1-CALC-001
	SHEET 2 OF 20	REV: B

REF. DRG. NO.:	MADE BY:	CHECKED BY:	APPROVED BY:
N/A	**SP, AK**	-	
ITEM:	DATE: 6 April 2018	DATE:	DATE:

Objective

To find the steady state (worst case) hot and cold temperatures of the four M1 and sole M2 mirror segments in the stowed configuration during Launch & Early Operations (LEOP). Results are to be a first estimate for use in thermo-mechanical design sizing calculations.

REFERENCE

Summary of Results

Node	Mass[kg]	Body Material	Inner Coating	Outer Coating
N1: DST	102.3	CFRP M40	N/A	CFRP
N2: PM1	5.9	Sic: RB-30% C	Black paint	Silver, polished
N3: PM2	5.9	Sic: RB-30% C	Black paint	Silver, polished
N4: PM3	5.9	Sic: RB-30% C	Black paint	Silver, polished
N5: PM4	5.9	Sic: RB-30% C	Black paint	Silver, polished
N6: SM1	1.6	Sic: RB-30% C	Silver, polished	CFRP

See p. 10.

Node Definitions - Surface Optical Properties

Node	α (inner)	α (outer)	ε (inner)	ε (outer)
N1: DST	N/A	0.93	N/A	0.85
N2: PM1	0.95	0.04	0.85	0.02
N3: PM2	0.95	0.04	0.85	0.02
N4: PM3	0.95	0.04	0.85	0.02
N5: PM4	0.95	0.04	0.85	0.02
N6: SM	0.04	0.93	0.02	0.85

Q_DST 0 W *Internal heat dissipation in DST housing.*

Overall Temperatures (for Design)

Element	Min	Max	Units
DST Housing	189.1	381.4	K
M1	187.8	384.2	K
M2	181.4	411.1	K

See p. 19.

Conclusion

> With 0 W internal heat dissipation in the instrument housing, the coldest and hottest steady state bulk temperatures experienced by the primary mirror segments are 187 K and 385 K respectively. The hot case is classified as "high temperature" per ECSS-E-30:1 (2000).
> The coldest and hottest steady state bulk temperatures for the secondary mirror with 0 W internal heat dissipation are 181 K and 412 K respectively.
> Increasing internal heat dissipation strongly increases housing & M1 minimum temperatures.
> The largest temperature range is experienced by the secondary mirror, driven by the significantly larger external heat input and outward facing, highly absorptive mirror cell back and spider structure.
> In all cases considered, M2 receives~234 W external heat compared to 0 - 13 W for all other mirrors in all other cases and seasons (see page 13).

TUDelft	PROJECT	Deployable Space Telescope			
	JOB No.	-			
SUBJECT **Stowed Operational Thermal Model**	CALC. REF. NO.:	DST-WP1-CALC-001			
	SHEET 3	OF 20	REV: B		
REF. DRG. NO.:	MADE BY: **SP, AK**	CHECKED BY:	APPROVED BY:		
ITEM:	DATE: 6 April 2018	DATE:	DATE:		

Assumptions

> The DST housing is modelled as a solid, homogeneous rectangular box with controllable internal heat dissipation Q_DST.

> The base of the DST housing, which would normally interface with the spacecraft bus, is assumed to be thermally isolated from the bus and that the bus blocks all radiation incident on the DST housing base.

> The top of the DST housing is covered entirely by M2 and the M2 support cell spider. Assume that the top face of the housing only sees the reflective surface of M2 and that the rear of M2 is Carbon Fibre Reinforced Plastic (CFRP) per current M2 spider design. Assume that the top of the housing, M2 and the M2 spider are all squares of same dimension.

> The rear of M2 sees only space and is at the front of the DST, pointing in the along-track direction.

> The sides of the DST housing are each covered by the four M1 mirror segments. Assume each side sees the rear surface of each segment only and that each segment has the same dimensions as the DST housing.

> Assume DST is detumbled and has no roll rate, thus will receive uneven heating (worst case).

> Assume pitch rate is equal to the mean motion so that one mirror always points in the nadir direction.

> Assume material and optical properties constant with temperature.

> Assume all opposing surfaces are parallel, diffuse surfaces separated by a distance that is small compared to the opposing surface areas. Thus effective emittance can be given by:

$$\varepsilon_{ij} = \frac{\varepsilon_i \varepsilon_j}{\varepsilon_i + \varepsilon_j - \varepsilon_i \varepsilon_j}$$

(p. 368, Fortescue, 2006)

> Only beginning of life (BOL) values for surface optical properties are used since the DST will not be in the stwoed state at EOL.

REFERENCE

TU Delft	PROJECT	Deployable Space Telescope
	JOB No.	-
SUBJECT **Stowed Operational Thermal Model**	CALC. REF. NO.:	DST-WP1-CALC-001
	SHEET 4 OF 20	REV: B

REF. DRG. NO.: N/A	MADE BY: **SP, AK**	CHECKED BY:	APPROVED BY:
ITEM:	DATE: 6 April 2018	DATE:	DATE:

The Spacecraft **REFERENCE**

The spacecraft is in a near-polar orbit with inclination i = 97° and altitude h = 500 km.
Mirrors are modelled as plates, labelled as shown in the diagram below.

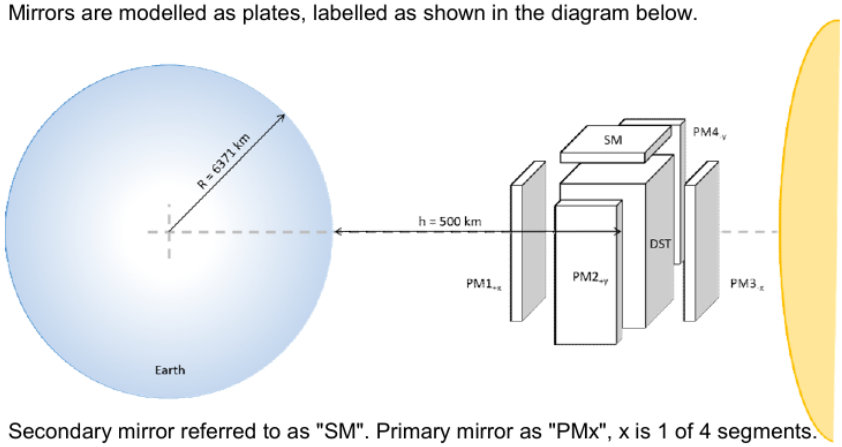

Secondary mirror referred to as "SM". Primary mirror as "PMx", x is 1 of 4 segments.

DST Housing Face Areas (Planar)

Node	Area [m^2]	Comment
Top (SM)	0.168	Fillets ignored
Nadir (PM1)	0.246	Fillets ignored
Zenith (PM3)	0.246	Fillets ignored
C/ Track (PM2	0.246	Fillets ignored
C/ Track (PM4	0.246	Fillets ignored

> Bus is 410 x 410 x 600 mm

CATIA model as of 28 march 2018

View Factors from spacecraft to Earth

Node	View Factor
N1: DST	0
N2: PM1	0.86
N3: PM2	0.3
N4: PM3	0
N5: PM4	0.3
N6: SM1	0.3

> All view factors are calculated using ECSS-E-HB-31-01 Part 1A from December 5th, 2011, section 4.2.2 at page 19.
> Note that these must be changed if orbit changes from h = 500 km

Equivalent Electrical Network

The thermal model is solved using the equivalen thermal network method.
Thermal elements can be modelled as electrical equivalents per the following table:

Thermal		Electrical	
Quantity	*Unit*	*Quantity*	*Unit*
Heat, q	W	Current, I	A
Temperature, T	K	Voltage, V	V
Thermal res., R	K/ W	Resistance, R	Ω
Heat capacity, C	J/ K	Capacitance, C	F
Absolute zero	0 K	Ground	0 V

(Lineykin, 2005)

A detailed description of the network and its solution to find the steady state temperatures is given on the next page.

TU Delft		PROJECT	Deployable Space Telescope		
		JOB No.	-		
SUBJECT	**Stowed Operational Thermal Model**	CALC. REF. NO.:	DST-WP1-CALC-001		
		SHEET 5	OF 20	REV:	B

REF. DRG. NO.:	MADE BY:	CHECKED BY:	APPROVED BY:
N/A	**SP, AK**		
ITEM:	DATE: 6 April 2018	DATE:	DATE:

REFERENCE

The full thermal network is shown in Figure D.1, modelled with potential σT^4 since heat transfer is assumed to be by radiation only. The DST housing is modelled as a single node with thermal inertia $C_{DST} = m_{DST}c_{p,DST}$ and internal power dissipation Q_{DST}. Each of the four side faces as well as the top face are assumed to be entirely covered by the four M1 mirror segments and single M2 mirror respectively.

Each mirror is modelled similarly. A generic mirror nodal sub-network is shown in Figure D.2. It is assumed that the inwards facing surface of each mirror sees only the opposing face of the DST housing with a radiative coupling. Although the mirrors are physically connected to the DST housing it is assumed that the conductive heat transfer through these connections is negligible compared to the radiative heat transfer. This needs to be checked once the mechanical designs are more mature. Each mirror has a thermal inertia $C_i = m_i c_{p,i}$. The outer face of each mirror is modelled with a radiative coupling to space at a ground potential of σT_s^4 with $T_s = 0K$. Each mirror absorbs power from Solar flux Q_S, Earth Albedo Q_A and Earth blackbody radiation Q_{IR}. These parameters can be turned on and off as necessary in the final equations.

The objective of the calculation is to determine the steady state temperature of each of the five mirrors as well as the DST housing. To that end, the thermal network must be reduced through node elimination to the equivalent single node network of the node of choice. Since the calculation is for steady state, the thermal inertias have no effect and are neglected.

The network reduction is completed by reducing the network to an equivalent single node diagram of the DST housing, the central node of the full network. Temperatures for each of the mirrors are then found by adding the mirror node of interest *back* to the network and working backwards to a new single node diagram of the mirror node alone.

Due to their similarity, each of the mirror model sub-networks can be treated the same way. The network is simplified by reducing each mirror sub-network to an equivalent power dissipation and thermal coupling in parallel with the DST housing dissipation. All mirror and DST housing powers and couplings can then be shown in a large parallel network which can be simply summed to find the housing temperature.

The steps for the network reduction are as follows:

1. Simplify mirror sub-networks.
   (a) Consolidate sub-network.
   (b) Eliminate mirror node in network with DST housing node.
2. Re-formulate full network with DST housing as single node with equivalent power dissipations and couplings from mirror sub-networks.
3. Consolidate network to single node diagram. Find DST housing potential.
4. Add back mirror node of choice. Eliminate DST housing node to find single node diagram of mirror node only.
5. Find mirror temperature.

Each of these steps are given in more detail below.

TUDelft	PROJECT	Deployable Space Telescope			
	JOB No.	-			
SUBJECT **Stowed Operational Thermal Model**	CALC. REF. NO.:	DST-WP1-CALC-001			
	SHEET	6	OF 20	REV:	B
REF. DRG. NO.: N/A	MADE BY: **SP, AK**	CHECKED BY:	APPROVED BY:		
ITEM:	DATE: 6 April 2018	DATE:	DATE:		

REFERENCE

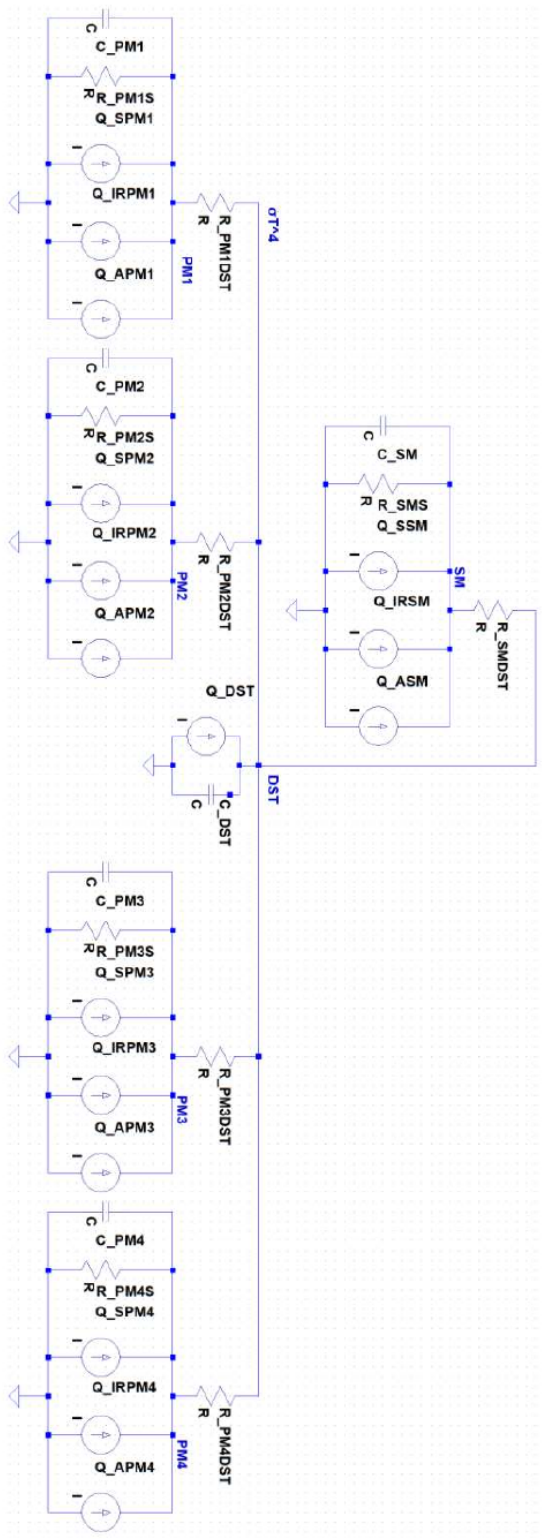

Figure D.1: Full thermal network for stowed operational thermal model.

TUDelft	PROJECT	Deployable Space Telescope		
	JOB No.	-		
SUBJECT **Stowed Operational Thermal Model**	CALC. REF. NO.:	DST-WP1-CALC-001		
	SHEET 7	OF 20	REV:	B

REF. DRG. NO.: N/A	MADE BY: **SP, AK**	CHECKED BY:	APPROVED BY:
ITEM:	DATE: 6 April 2018	DATE:	DATE:

REFERENCE

Step One - Simplify Mirror Sub-networks

An individual mirror sub-network is shown in Figure D.2.

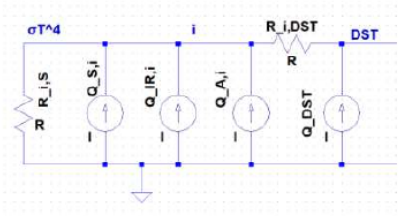

Figure D.2: Generic mirror nodal sub-network connected to DST housing node.

The parallel power dissipations can be combined to give intermediate value Q_i' in Figure D.3:

$$Q_i' = Q_{S,i} + Q_{IR,i} + Q_{A,i} \tag{D.1}$$

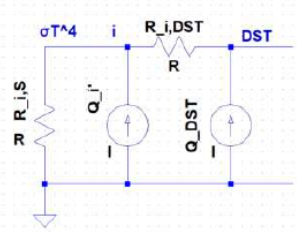

Figure D.3: Intermediate mirror sub-network values.

The mirror node can then be eliminated to give the equivalent dissipation Q_i'' and coupling R_i'' for the generic mirror sub-network in Figure D.4

$$Q_i'' = \frac{R_{i,DST}}{R_{i,DST} + R_{i,S}} Q_i' \tag{D.2}$$

$$R_i'' = \frac{R_{i,DST} R_{i,S}}{R_{i,DST} + R_{i,S}} \tag{D.3}$$

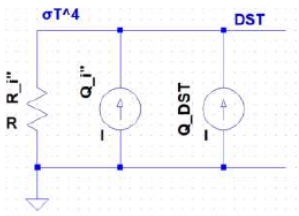

Figure D.4: Elimination of mirror node.

Step Two - Reformulate Network

The full network can then be reformulated with all equivalent mirror sub-network dissipations Q_i'' and couplings R_i'' in parallel with the DST housing dissipation Q_{DST} in an extension of Figure D.4.

REFERENCE

Step Three - DST Housing Single Node Diagram

All parallel dissipations and couplings can be summed to give the effective DST housing dissipation Q'_{DST} and coupling R_{DST}, shown in the single node diagram in Figure D.5.

$$Q'_{DST} = \sum_i Q''_i + Q_{DST} \tag{D.4}$$

$$R_{DST} = \sum_i R''_i \tag{D.5}$$

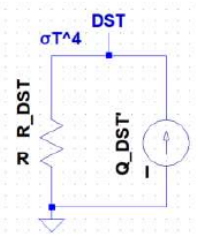

Figure D.5: Single node diagram for DST housing in stowed, operational case.

The DST housing temperature can be found from

$$Q'_{DST} = R_{DST}\sigma T^4_{DST} \tag{D.6}$$

$$\therefore T_{DST} = \sqrt[4]{\frac{Q'_{DST}}{\sigma R_{DST}}} \tag{D.7}$$

Step Four - Add Mirror Node

The steady state temperature of a mirror node is found by adding the node back to the DST housing single node diagram and consolidating to a new single node diagram for the mirror node, shown in Figure D.6. Note that the DST housing dissipation Q''_{DST} and coupling R'_{DST} have an additional prime and are now defined via

$$Q''_{DST} = Q'_{DST} - Q''_i \tag{D.8}$$

$$R'_{DST} = R_{DST} - R''_i \tag{D.9}$$

where i is the mirror of interest.

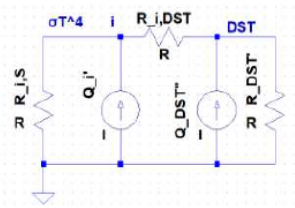

Figure D.6: Adding back a mirror node to the DST housing single node diagram.

The final single node diagram for the mirror, shown in Figure D.7 has dissipation $Q_{i,f}$ and coupling $R_{i,f}$:

$$Q_{i,f} = Q'_i + \frac{R_{i,DST}}{R_{i,DST} + R'_{DST}} Q''_{DST} \tag{D.10}$$

$$R_{i,f} = R_{i,S} + \frac{R_{i,DST} R'_{DST}}{R_{i,DST} + R'_{DST}} \tag{D.11}$$

TUDelft	PROJECT	Deployable Space Telescope		
	JOB No.	-		
SUBJECT **Stowed Operational Thermal Model**	CALC. REF. NO.:	DST-WP1-CALC-001		
	SHEET 9	OF 20	REV:	B

REF. DRG. NO.:	MADE BY:	CHECKED BY:	APPROVED BY:
N/A	**SP, AK**		
ITEM:	DATE: 6 April 2018	DATE:	DATE:

REFERENCE

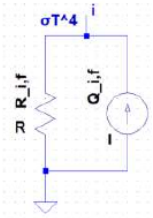

Figure D.7: Single node diagram for a mirror in stowed configuration.

Step Five - Find Mirror Temperature

The mirror temperature can be found from

$$Q_{i,f} = R_{i,f}\sigma T_i^4 \tag{D.12}$$

$$\therefore T_i = \sqrt[4]{\frac{Q_{i,f}}{\sigma R_{i,f}}} \tag{D.13}$$

TU Delft	PROJECT	Deployable Space Telescope
	JOB No.	-
SUBJECT **Stowed Operational Thermal Model**	CALC. REF. NO.:	DST-WP1-CALC-001
	SHEET 10 OF 20	REV: B

REF. DRG. NO.: N/A	MADE BY: **SP, AK**	CHECKED BY:	APPROVED BY:
ITEM:	DATE: 6 April 2018	DATE:	DATE:

Material Properties

Optical

Material	α (BOL)	α (EOL)	ε (BOL)	ε (EOL)	Comment	REFERENCE
CFRP	0.93	0.93	0.85	0.85	Graphite Epoxy	p.801, (Gilmore, 2002)
Silver, polished	0.04	0.04	0.02	0.02	For optical surf.	p.798, (Gilmore, 2002)
Black paint	0.95	0.95	0.85	0.85	Assume no degr.	p. 363, (Fortescue, 2006)
White paint	0.12	0.14	0.9	0.9	silicate	p. 363, (Fortescue, 2006)
MLI			0.01	0.01		(Benthem, 2016)

α - Solar absorptivity, ε - Emissivity

Thermo-Physical

Material	ρ [kg/m^3]	c_p [J/kg K]	k [W/m K]	CTE [10^{-6} / K]	Comment	
CFRP M40	1610	880	55	-	k = 1.3 @ 90deg	(Benthem, 2016)
Sic: RB-30% C	2890	670	155	2.4		(Paquin, 1995)
Al (6061-T6)	2770	961.2	167.9	22.5	not used	p.805, (Gilmore, 2002),

ρ - Density, c_p - Specific heat capacity, k - Thermal conductivity

Node Definitions - Materials

Node	Mass[kg]	Body Material	Inner Coating	Outer Coating	
N1: DST	102.306	CFRP M40	N/A	CFRP	*(van Marrewijk & Kuiper, 2017)*
N2: PM1	5.906	Sic: RB-30% C	Black paint	Silver, polished	
N3: PM2	5.906	Sic: RB-30% C	Black paint	Silver, polished	
N4: PM3	5.906	Sic: RB-30% C	Black paint	Silver, polished	
N5: PM4	5.906	Sic: RB-30% C	Black paint	Silver, polished	
N6: SM	1.6	Sic: RB-30% C	Silver, polished	CFRP	

> All masses from (van Marrewijk & Kuiper, 2017) as of 28 March 2018.
> M1 deployment & support mechanism mass lumped in with DST housing mass.
> M2 support and deployment mechanism mass lumped with DST housing mass.
> DST housing mass is instrument sub-total (inc. 20% margin) less M1 and M2 mirror masses already taken into account in other nodes.

TUDelft	PROJECT	Deployable Space Telescope			
	JOB No.	-			
SUBJECT **Stowed Operational Thermal Model**	CALC. REF. NO.:	DST-WP1-CALC-001			
	SHEET	11	OF	20	REV: B

REF. DRG. NO.: N/A	MADE BY: **SP, AK**	CHECKED BY:	APPROVED BY:
ITEM:	DATE: 6 April 2018	DATE:	DATE:

External Fluxes

External fluxes are calculated as a function of the spacecraft's position in its orbit about the Earth. The beta angle is the smallest angle between the orbit plane and sun vector.

The angle between each surface and the Sun was calculated as function of time during one orbit. The orbit taken was a 500 km Sun synchronous orbit with decending node at 10:30.

Beta angles for all mirrors through whole orbit were plotted, four cases were considered, based on the results. It was observed that the sides in the cross track direction have a constant angle with respect to the sun. Further, the Earth albedo and IR will be constant over the orbit, outside of eclipse. This means that the worst hot cases occur at the locations where the angle between the remaining surfaces (PM1, PM3, SM) and the sun are the lowest. These three locations are chosen for the worst hot cases calculations, and those angles are presented below. For the cold case, a point in eclipse is chosen. This way, the only possible heat flux into the system is the Earth IR, and all the angles between the surfaces and the sun are set to 90 deg, or 1.5708 rad.

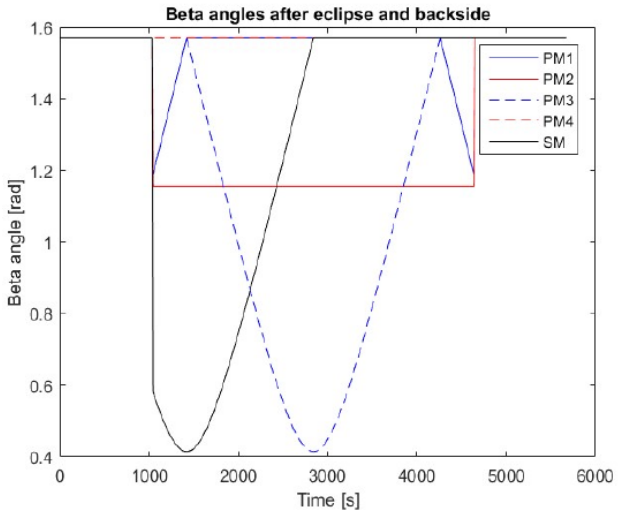

The angles were calculated using the relations presented in SMAD

Angle calculation

The angles are calculated in the spacecraft centered celestial sphere, with the x-axis pointing nadir, the y-axis pointing towards the orbit pole.

For each moment in time, the ange between each surface and the vector towards the sun is calculated. This angle is called β. The β angle is calculated by:

$$\cos(\beta) = \cos(\gamma)*\cos(\beta_s') + \sin(\gamma)*\sin(\beta_s')*\cos(\Delta A_z)$$

(p. 108, Larson, 2005)

In this equation, β_s' is the angle between the sun and the orbit pole, γ is the angle between the surface normal and the orbit pole, and ΔAz is the difference between the azimuth of the sun and the normal of the surface. (see figure below)

REFERENCE

TU Delft	PROJECT	Deployable Space Telescope		
	JOB No.	-		
SUBJECT **Stowed Operational Thermal Model**	CALC. REF. NO.:	DST-WP1-CALC-001		
	SHEET 12	OF 20	REV: B	
REF. DRG. NO.: N/A	MADE BY: **SP, AK**	CHECKED BY:	APPROVED BY:	
ITEM:	DATE: 6 April 2018	DATE:	DATE:	

REFERENCE

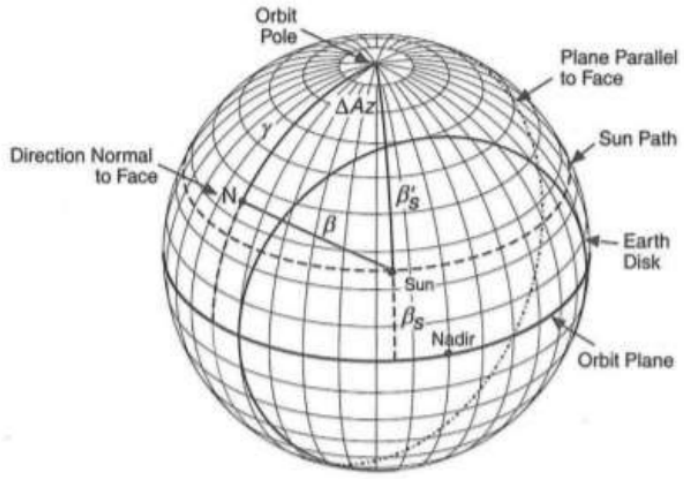

(p. 108, Larson, 2005)

The eclipse of the spacecraft is calculated using the following equation

$$A_{z,\,eclipse} = A_{z,0} \pm \arccos\left(\cos(\rho) / \sin(\beta_s')\right)$$

(p. 107, Larson, 2005)

Where $A_{z,\,eclipse}$ is the azimuth range of the Sun corresponding to eclipse $A_{z,0}$ is the azimuth of the Sun at the midpoint of the eclipse, ρ is the angular radius of the Earth. (see figure below)

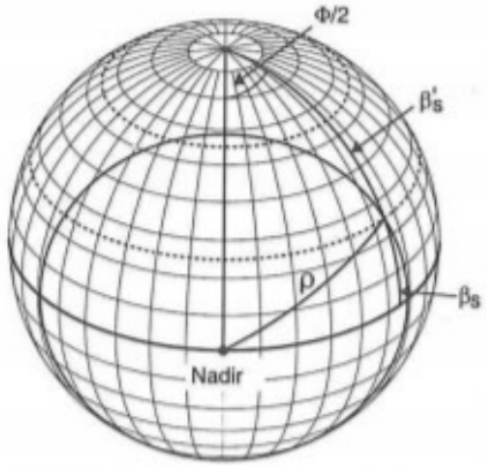

(p. 106, Larson, 2005)

Since the x-axis is pointing nadir, which is the centre of the eclipse, the angle $A_{z,0}$ is 0 as the azimuth is calculated from the x-axis in this definition.

When angle β is larger than 0.5 π rad, sun shines on the back of the panel, and the panel is in shadow. All β angles calculated to be larger than 0.5 π rad were set to 0.5 π rad to ensure the panels do not receive any solar radiation.

TU Delft	PROJECT	Deployable Space Telescope
	JOB No.	-
SUBJECT **Stowed Operational Thermal Model**	CALC. REF. NO.:	DST-WP1-CALC-001
	SHEET 13 OF 20	REV: B

REF. DRG. NO.: N/A	MADE BY: **SP, AK**	CHECKED BY:	APPROVED BY:
ITEM:	DATE: 6 April 2018	DATE:	DATE:

REFERENCE

Beta angles, at times with maximum input for each side

The following tables give the angles between the normal of each respective spacecraft surface and the sun vector for the three hot cases "PM1 max", "PM3 max", "SM max", and single cold case being considered in the steady state analysis.

The angles in each column represent the sun - surface normal angle at the moment in time when the angle between the sun and the surface in the column header is minimal, thus having the max projected area facing the incoming solar flux and receiving its greatest heat input. Variation by season is considered.

Spring/ Autumn

Side	*PM1 max [rad]*	*PM3 max [rad]*	*SM max [rad]*	*Cold case [rad]*
N2: PM1	1.192	1.571	1.570	1.571
N3: PM2	1.182	1.182	1.182	1.571
N4: PM3	1.571	0.389	1.571	1.571
N5: PM4	1.571	1.571	1.571	1.571
N6: SM1	0.558	1.569	0.389	1.571

Northern summer

Side	*PM1 max [rad]*	*PM3 max [rad]*	*SM max [rad]*	*Cold case [rad]*
N2: PM1	1.188	1.571	1.570	1.571
N3: PM2	1.274	1.274	1.274	1.571
N4: PM3	1.571	0.296	1.571	1.571
N5: PM4	1.571	1.571	1.571	1.571
N6: SM1	0.494	1.569	0.296	1.571

Southern summer

Side	*PM1 max [rad]*	*PM3 max [rad]*	*SM max [rad]*	*Cold case [rad]*
N2: PM1	1.188	1.571	1.570	1.571
N3: PM2	1.156	1.156	1.156	1.571
N4: PM3	1.571	0.415	1.571	1.571
N5: PM4	1.571	1.571	1.571	1.571
N6: SM1	0.582	1.569	0.415	1.571

TU Delft	PROJECT	Deployable Space Telescope
	JOB No.	-
SUBJECT: Stowed Operational Thermal Model	CALC. REF. NO.:	DST-WP1-CALC-001
	SHEET 14 OF 20	REV: B

REF. DRG. NO.: N/A	MADE BY: SP, AK	CHECKED BY:	APPROVED BY:
ITEM:	DATE: 6 April 2018	DATE:	DATE:

Power input on the surfaces, due to Sun, Albedo, and Earth IR

External fluxes, user input:

Season	S [W/m2]	Albedo [-]	IR [W/m2]
Spring/ autum	1367	0.35	204
N. summer	1321	0.35	204
S. summer	1412	0.35	204

> Albedo given as a fraction of incident Solar intensity.
> IR 237W/m2 scaled by orbit radius.

REFERENCE

(p. 358, Fortescue, 2006)

(p. 360, Fortescue, 2006)

The following tables calculate the net external power input for each of the mirror nodes, for each of the considered steady state cases in each season.

Spring/ Autumn

Side	PM1 max [W]	PM3 max [W]	SM max [W]	Cold case [W]
N2: PM1	9.88	4.91	4.92	0.86
N3: PM2	6.81	6.81	6.81	0.30
N4: PM3	0.00	12.45	0.00	0.00
N5: PM4	1.71	1.71	1.71	0.30
N6: SM1	212.49	31.49	228.94	8.73

Northern summer

Side	PM1 max [W]	PM3 max [W]	SM max [W]	Cold case [W]
N2: PM1	9.63	4.77	4.79	0.86
N3: PM2	5.46	5.46	5.46	0.30
N4: PM3	0.00	12.43	0.00	0.00
N5: PM4	1.67	1.67	1.67	0.30
N6: SM1	212.28	30.73	227.93	8.73

Southern summer

Side	PM1 max [W]	PM3 max [W]	SM max [W]	Cold case [W]
N2: PM1	10.24	5.04	5.05	0.86
N3: PM2	7.36	7.36	7.36	0.30
N4: PM3	0.00	12.72	0.00	0.00
N5: PM4	1.76	1.76	1.76	0.30
N6: SM1	216.31	32.24	233.93	8.73

TU Delft	PROJECT	Deployable Space Telescope		
	JOB No.	-		
SUBJECT **Stowed Operational Thermal Model**	CALC. REF. NO.:	DST-WP1-CALC-001		
	SHEET 15	OF 20	REV: B	

REF. DRG. NO.: N/A	MADE BY: **SP, AK**	CHECKED BY:	APPROVED BY:
ITEM:	DATE: 6 April 2018	DATE:	DATE:

Radiative Couplings

$$R_{ij} = \varepsilon_{ij} A_i F_{ij}$$

REFERENCE

R_i,j	ε_i	ε_j	ε_ij	A_i = A_j [m^2]	F_i,j	R_ij [m^2]
R_PM1,DST	0.85	0.85	**0.74**	0.246	1.00	**1.82E-01**
R_PM2,DST	0.85	0.85	**0.74**	0.246	1.00	**1.82E-01**
R_PM3,DST	0.85	0.85	**0.74**	0.246	1.00	**1.82E-01**
R_PM4,DST	0.85	0.85	**0.74**	0.246	1.00	**1.82E-01**
R_SM,DST	0.02	0.85	**0.02**	0.168	1.00	**3.35E-03**
R_PM1,S	0.02	N/A	N/A	0.246	1	**4.92E-03**
R_PM2,S	0.02	N/A	N/A	0.246	1	**4.92E-03**
R_PM3,S	0.02	N/A	N/A	0.246	1	**4.92E-03**
R_PM4,S	0.02	N/A	N/A	0.246	1	**4.92E-03**
R_SM,S	0.85	N/A	N/A	0.168	1	**1.43E-01**

Assumes all B_ij = 1.

Miscellaneous Inputs

ID	Value	Unit
Q_DST	0	W
S-B const.	5.67E-08	$Wm^{-2}K^{-4}$

Internal heat dissipation in DST housing.

Calculations

Cases are calculated by season, starting on the next page.

TU Delft	PROJECT	Deployable Space Telescope
	JOB No.	-
SUBJECT **Stowed Operational Thermal Model**	CALC. REF. NO.:	DST-WP1-CALC-001
	SHEET 16 OF 20	REV: B

REF. DRG. NO.:	MADE BY:	CHECKED BY:	APPROVED BY:
N/A	**SP, AK**		
ITEM:	DATE: 6 April 2018	DATE:	DATE:

Spring/ Autumn

ID	PM1 max	PM3 max	SM max	Cold case	Units	REFERENCE
Q_PM1'	9.88	4.91	4.92	0.86	W	(D.1)
Q_PM2'	6.81	6.81	6.81	0.30	W	(D.1)
Q_PM3'	0.00	12.45	0.00	0.00	W	(D.1)
Q_PM4'	1.71	1.71	1.71	0.30	W	(D.1)
Q_SM'	212.49	31.49	228.94	8.73	W	(D.1)
Q_PM1"	9.62E+00	4.78E+00	4.79E+00	8.39E-01	W	(D.2)
Q_PM2"	6.63E+00	6.63E+00	6.63E+00	2.93E-01	W	(D.2)
Q_PM3"	-4.81E-05	1.21E+01	-4.81E-05	-4.81E-05	W	(D.2)
Q_PM4"	1.67E+00	1.67E+00	1.67E+00	2.93E-01	W	(D.2)
Q_SM"	4.87E+00	7.21E-01	5.24E+00	2.00E-01	W	(D.2)
R_PM1"	4.79E-03	4.79E-03	4.79E-03	4.79E-03	m^2	(D.3)
R_PM2"	4.79E-03	4.79E-03	4.79E-03	4.79E-03	m^2	(D.3)
R_PM3"	4.79E-03	4.79E-03	4.79E-03	4.79E-03	m^2	(D.3)
R_PM4"	4.79E-03	4.79E-03	4.79E-03	4.79E-03	m^2	(D.3)
R_SM"	3.27E-03	3.27E-03	3.27E-03	3.27E-03	m^2	(D.3)
Q_DST'	2.28E+01	2.59E+01	1.83E+01	1.62E+00	W	(D.4)
R_DST	2.24E-02	2.24E-02	2.24E-02	2.24E-02	m^2	(D.5)
Q_DST"_PM1	1.32E+01	2.11E+01	1.35E+01	7.86E-01	W	(D.8)
Q_DST"_PM2	1.62E+01	1.93E+01	1.17E+01	1.33E+00	W	(D.8)
Q_DST"_PM3	2.28E+01	1.38E+01	1.83E+01	1.63E+00	W	(D.8)
Q_DST"_PM4	2.11E+01	2.43E+01	1.67E+01	1.33E+00	W	(D.8)
Q_DST"_SM	1.79E+01	2.52E+01	1.31E+01	1.42E+00	W	(D.8)
R_DST'_PM1	1.76E-02	1.76E-02	1.76E-02	1.76E-02	m^2	(D.9)
R_DST'_PM2	1.76E-02	1.76E-02	1.76E-02	1.76E-02	m^2	(D.9)
R_DST'_PM3	1.76E-02	1.76E-02	1.76E-02	1.76E-02	m^2	(D.9)
R_DST'_PM4	1.76E-02	1.76E-02	1.76E-02	1.76E-02	m^2	(D.9)
R_DST'_SM	1.92E-02	1.92E-02	1.92E-02	1.92E-02	m^2	(D.9)
Q_PM1,f	2.19E+01	2.42E+01	1.73E+01	1.58E+00	W	(D.10)
Q_PM2,f	2.15E+01	2.44E+01	1.75E+01	1.52E+00	W	(D.10)
Q_PM3,f	2.08E+01	2.50E+01	1.67E+01	1.48E+00	W	(D.10)
Q_PM4,f	2.10E+01	2.38E+01	1.69E+01	1.52E+00	W	(D.10)
Q_SM,f	2.15E+02	3.52E+01	2.31E+02	8.95E+00	W	(D.10)
R_PM1,f	2.10E-02	2.10E-02	2.10E-02	2.10E-02	m^2	(D.11)
R_PM2,f	2.10E-02	2.10E-02	2.10E-02	2.10E-02	m^2	(D.11)
R_PM3,f	2.10E-02	2.10E-02	2.10E-02	2.10E-02	m^2	(D.11)
R_PM4,f	2.10E-02	2.10E-02	2.10E-02	2.10E-02	m^2	(D.11)
R_SM,f	1.46E-01	1.46E-01	1.46E-01	1.46E-01	m^2	(D.11)
T_DST	366	378	346	189	K	(D.7)
T_PM1	368	377	347	191	K	(D.13)
T_PM2	367	378	348	189	K	(D.13)
T_PM3	363	381	344	188	K	(D.13)
T_PM4	364	376	345	189	K	(D.13)
T_SM	402	256	409	181	K	(D.13)

TUDelft	PROJECT	Deployable Space Telescope		
	JOB No.	-		
SUBJECT **Stowed Operational Thermal Model**	CALC. REF. NO.:	DST-WP1-CALC-001		
	SHEET 17	OF 20	REV: B	
REF. DRG. NO.: N/A	MADE BY: **SP, AK**	CHECKED BY:	APPROVED BY:	
ITEM:	DATE: 6 April 2018	DATE:	DATE:	

Northern Summer

ID	PM1 max	PM3 max	SM max	Cold case	Units	REFERENCE
Q_PM1'	9.63	4.77	4.79	0.86	W	*(D.1)*
Q_PM2'	5.46	5.46	5.46	0.30	W	*(D.1)*
Q_PM3'	0.00	12.43	0.00	0.00	W	*(D.1)*
Q_PM4'	1.67	1.67	1.67	0.30	W	*(D.1)*
Q_SM'	212.28	30.73	227.93	8.73	W	*(D.1)*
Q_PM1"	9.37E+00	4.65E+00	4.66E+00	8.39E-01	W	*(D.2)*
Q_PM2"	5.32E+00	5.32E+00	5.32E+00	2.93E-01	W	*(D.2)*
Q_PM3"	-4.65E-05	1.21E+01	-4.65E-05	-4.65E-05	W	*(D.2)*
Q_PM4"	1.62E+00	1.62E+00	1.62E+00	2.93E-01	W	*(D.2)*
Q_SM"	4.86E+00	7.04E-01	5.22E+00	2.00E-01	W	*(D.2)*
R_PM1"	4.79E-03	4.79E-03	4.79E-03	4.79E-03	m^2	*(D.3)*
R_PM2"	4.79E-03	4.79E-03	4.79E-03	4.79E-03	m^2	*(D.3)*
R_PM3"	4.79E-03	4.79E-03	4.79E-03	4.79E-03	m^2	*(D.3)*
R_PM4"	4.79E-03	4.79E-03	4.79E-03	4.79E-03	m^2	*(D.3)*
R_SM"	3.27E-03	3.27E-03	3.27E-03	3.27E-03	m^2	*(D.3)*
Q_DST'	2.12E+01	2.44E+01	1.68E+01	1.62E+00	W	*(D.4)*
R_DST	2.24E-02	2.24E-02	2.24E-02	2.24E-02	m^2	*(D.5)*
Q_DST"_PM1	1.18E+01	1.97E+01	1.22E+01	7.86E-01	W	*(D.8)*
Q_DST"_PM2	1.59E+01	1.91E+01	1.15E+01	1.33E+00	W	*(D.8)*
Q_DST"_PM3	2.12E+01	1.23E+01	1.68E+01	1.63E+00	W	*(D.8)*
Q_DST"_PM4	1.96E+01	2.28E+01	1.52E+01	1.33E+00	W	*(D.8)*
Q_DST"_SM	1.63E+01	2.37E+01	1.16E+01	1.42E+00	W	*(D.8)*
R_DST'_PM1	1.76E-02	1.76E-02	1.76E-02	1.76E-02	m^2	*(D.9)*
R_DST'_PM2	1.76E-02	1.76E-02	1.76E-02	1.76E-02	m^2	*(D.9)*
R_DST'_PM3	1.76E-02	1.76E-02	1.76E-02	1.76E-02	m^2	*(D.9)*
R_DST'_PM4	1.76E-02	1.76E-02	1.76E-02	1.76E-02	m^2	*(D.9)*
R_DST'_SM	1.92E-02	1.92E-02	1.92E-02	1.92E-02	m^2	*(D.9)*
Q_PM1,f	2.04E+01	2.28E+01	1.59E+01	1.58E+00	W	*(D.10)*
Q_PM2,f	1.99E+01	2.29E+01	1.59E+01	1.52E+00	W	*(D.10)*
Q_PM3,f	1.93E+01	2.36E+01	1.53E+01	1.48E+00	W	*(D.10)*
Q_PM4,f	1.95E+01	2.24E+01	1.55E+01	1.52E+00	W	*(D.10)*
Q_SM,f	2.15E+02	3.43E+01	2.30E+02	8.95E+00	W	*(D.10)*
R_PM1,f	2.10E-02	2.10E-02	2.10E-02	2.10E-02	m^2	*(D.11)*
R_PM2,f	2.10E-02	2.10E-02	2.10E-02	2.10E-02	m^2	*(D.11)*
R_PM3,f	2.10E-02	2.10E-02	2.10E-02	2.10E-02	m^2	*(D.11)*
R_PM4,f	2.10E-02	2.10E-02	2.10E-02	2.10E-02	m^2	*(D.11)*
R_SM,f	1.46E-01	1.46E-01	1.46E-01	1.46E-01	m^2	*(D.11)*
T_DST	359	372	339	189	K	*(D.7)*
T_PM1	362	372	340	191	K	*(D.13)*
T_PM2	360	372	340	189	K	*(D.13)*
T_PM3	357	375	337	188	K	*(D.13)*
T_PM4	358	370	338	189	K	*(D.13)*
T_SM	401	254	408	181	K	*(D.13)*

TUDelft	PROJECT	Deployable Space Telescope
	JOB No.	-
SUBJECT: Stowed Operational Thermal Model	CALC. REF. NO.:	DST-WP1-CALC-001
	SHEET 18 OF 20	REV: B
REF. DRG. NO.: N/A	MADE BY: SP, AK	CHECKED BY:
ITEM:	DATE: 6 April 2018	DATE:
		APPROVED BY:
		DATE:

Southern Summer

ID	PM1 max	PM3 max	SM max	Cold case	Units	REFERENCE
Q_PM1'	10.24	5.04	5.05	0.86	W	(D.1)
Q_PM2'	7.36	7.36	7.36	0.30	W	(D.1)
Q_PM3'	0.00	12.72	0.00	0.00	W	(D.1)
Q_PM4'	1.76	1.76	1.76	0.30	W	(D.1)
Q_SM'	216.31	32.24	233.93	8.73	W	(D.1)
Q_PM1"	9.97E+00	4.91E+00	4.92E+00	8.39E-01	W	(D.2)
Q_PM2"	7.17E+00	7.17E+00	7.17E+00	2.93E-01	W	(D.2)
Q_PM3"	-4.97E-05	1.24E+01	-4.97E-05	-4.97E-05	W	(D.2)
Q_PM4"	1.71E+00	1.71E+00	1.71E+00	2.93E-01	W	(D.2)
Q_SM"	4.96E+00	7.39E-01	5.36E+00	2.00E-01	W	(D.2)
R_PM1"	4.79E-03	4.79E-03	4.79E-03	4.79E-03	m^2	(D.3)
R_PM2"	4.79E-03	4.79E-03	4.79E-03	4.79E-03	m^2	(D.3)
R_PM3"	4.79E-03	4.79E-03	4.79E-03	4.79E-03	m^2	(D.3)
R_PM4"	4.79E-03	4.79E-03	4.79E-03	4.79E-03	m^2	(D.3)
R_SM"	3.27E-03	3.27E-03	3.27E-03	3.27E-03	m^2	(D.3)
Q_DST'	2.38E+01	2.69E+01	1.92E+01	1.62E+00	W	(D.4)
R_DST	2.24E-02	2.24E-02	2.24E-02	2.24E-02	m^2	(D.5)
Q_DST"_PM1	1.38E+01	2.20E+01	1.42E+01	7.86E-01	W	(D.8)
Q_DST"_PM2	1.66E+01	1.97E+01	1.20E+01	1.33E+00	W	(D.8)
Q_DST"_PM3	2.38E+01	1.45E+01	1.92E+01	1.63E+00	W	(D.8)
Q_DST"_PM4	2.21E+01	2.52E+01	1.74E+01	1.33E+00	W	(D.8)
Q_DST"_SM	1.88E+01	2.62E+01	1.38E+01	1.42E+00	W	(D.8)
R_DST'_PM1	1.76E-02	1.76E-02	1.76E-02	1.76E-02	m^2	(D.9)
R_DST'_PM2	1.76E-02	1.76E-02	1.76E-02	1.76E-02	m^2	(D.9)
R_DST'_PM3	1.76E-02	1.76E-02	1.76E-02	1.76E-02	m^2	(D.9)
R_DST'_PM4	1.76E-02	1.76E-02	1.76E-02	1.76E-02	m^2	(D.9)
R_DST'_SM	1.92E-02	1.92E-02	1.92E-02	1.92E-02	m^2	(D.9)
Q_PM1,f	2.28E+01	2.51E+01	1.80E+01	1.58E+00	W	(D.10)
Q_PM2,f	2.25E+01	2.54E+01	1.83E+01	1.52E+00	W	(D.10)
Q_PM3,f	2.17E+01	2.60E+01	1.75E+01	1.48E+00	W	(D.10)
Q_PM4,f	2.19E+01	2.47E+01	1.77E+01	1.52E+00	W	(D.10)
Q_SM,f	2.19E+02	3.61E+01	2.36E+02	8.95E+00	W	(D.10)
R_PM1,f	2.10E-02	2.10E-02	2.10E-02	2.10E-02	m^2	(D.11)
R_PM2,f	2.10E-02	2.10E-02	2.10E-02	2.10E-02	m^2	(D.11)
R_PM3,f	2.10E-02	2.10E-02	2.10E-02	2.10E-02	m^2	(D.11)
R_PM4,f	2.10E-02	2.10E-02	2.10E-02	2.10E-02	m^2	(D.11)
R_SM,f	1.46E-01	1.46E-01	1.46E-01	1.46E-01	m^2	(D.11)
T_DST	370	381	350	189	K	(D.7)
T_PM1	372	381	351	191	K	(D.13)
T_PM2	371	382	352	189	K	(D.13)
T_PM3	367	384	348	188	K	(D.13)
T_PM4	368	380	349	189	K	(D.13)
T_SM	404	257	411	181	K	(D.13)

TUDelft	PROJECT	Deployable Space Telescope
	JOB No.	-
SUBJECT **Stowed Operational Thermal Model**	CALC. REF. NO.:	DST-WP1-CALC-001
	SHEET 19 OF 20	REV: B

REF. DRG. NO.:	MADE BY:	CHECKED BY:	APPROVED BY:
N/A	**SP, AK**		
ITEM:	DATE: 6 April 2018	DATE:	DATE:

Results

REFERENCE

DST Housing Temperature

Season	PM1 max	PM3 max	SM max	Cold case	Units
Spring/ autum	365.8	377.8	346.5	189.1	K
N. Summer	359.2	372.1	339.1	189.1	K
S. Summer	369.8	381.4	350.3	189.1	K

PM1 Temperature

Season	PM1 max	PM3 max	SM max	Cold case	Units
Spring/ autum	368.2	377.5	347.0	190.8	K
N. Summer	361.7	371.9	339.8	190.8	K
S. Summer	372.2	381.0	350.8	190.8	K

PM2 Temperature

Season	PM1 max	PM3 max	SM max	Cold case	Units
Spring/ autum	366.7	378.3	348.1	188.9	K
N. Summer	359.6	372.2	340.2	188.9	K
S. Summer	370.8	382.0	352.0	188.9	K

PM3 Temperature

Season	PM1 max	PM3 max	SM max	Cold case	Units
Spring/ autum	363.4	380.7	344.2	187.8	K
N. Summer	356.8	375.3	336.8	187.8	K
S. Summer	367.4	384.2	348.0	187.8	K

PM4 Temperature

Season	PM1 max	PM3 max	SM max	Cold case	Units
Spring/ autum	364.2	376.1	345.2	188.9	K
N. Summer	357.7	370.4	337.9	188.9	K
S. Summer	368.2	379.6	349.0	188.9	K

SM Temperature

Season	PM1 max	PM3 max	SM max	Cold case	Units
Spring/ autum	401.7	255.5	408.8	181.4	K
N. Summer	401.5	253.7	408.3	181.4	K
S. Summer	403.5	257.2	411.1	181.4	K

Overall Temperatures (for Design)

Element	Min	Max	Units
DST Housing	189.1	381.4	K
M1	187.8	384.2	K
M2	181.4	411.1	K

TU Delft	PROJECT	Deployable Space Telescope			
	JOB No.	-			
SUBJECT **Stowed Operational Thermal Model**	CALC. REF. NO.:	DST-WP1-CALC-001			
	SHEET	20	OF 20	REV:	B
REF. DRG. NO.: N/A	MADE BY: **SP, AK**	CHECKED BY:	APPROVED BY:		
ITEM:	DATE: 6 April 2018	DATE:	DATE:		

References

REFERENCE

> Benthem, B., & Maas, A. (2016). AE4S20: Satellite Thermal Control. Delft, Netherlands: TU Delft.

> Fortescue, P., Stark, J., & Swinerd, G. (Eds.). (2006). Spacecraft Systems Engineering (Third). Chichester, England: John Wiley & Sons.

> Gilmore, D. G. (2002). Spacecraft Thermal Control Handbook, Volume 1 - Fundamental Technologies (Second). El Segundo, California: The Aerospace Press.

> Harnisch, B., Kunkel, B., Deyerler, M., Bauereisen, S., & Papenburg, U. (1998). Ultra-lightweight C/SiC mirrors and structures. ESA Bulletin. Retrieved from http://www.esa.int/esapub/bulletin/bullet95/HARNISCH.pdf

> Larson, W. J., Wertz, J. R. (Eds.) (2005) Space Mission Analysis and Design (third edition, seventh print). Microcosm Press and Kluwer Academic Publishers

> Lineykin, S., & Ben-Yaakov, S. (2005). PSPICE-compatible equivalent circuit of thermoelectric coolers. In IEEE Power Electronics Specialists Conference (pp. 608–612).

> van Marrewijk, G. P., & Kuiper, J. M. (2017). Deployable Space Telescope Design description, Mission, Decisions and Budgets. Delft.

> Paquin, R. A. (1995). Materials for mirror systems: an overview. In Proc. SPIE. SPIE.

> van Putten, B. T. (2017). Design of the Deployment Mechanism for the Primary Mirror Elements of a Deployable Space Telescope. TU Delft.

D

DST Verification Document and Requirements List

D.1. Verification and Requirements Document

Included in this appendix is the Verification and Requirements document for the DST. This document was developed by the author for the team as a direct output of the work conducted in Sections 3 and 4. It is a live document and has since received further additions by other team members.

Appended to the end of the document is the full list of requirements for the DST as of early October 2018. All PMAO requirements and several M1 requirements were derived through the efforts of this thesis. The "Created", "Last Updated" and "Owner" columns have been hidden in this printout to provide more space for the requirement descriptions and comments.

For simplicity, the requirements structure at the system level are kept relatively flat. With multiple students working on the conceptual design, the requirements list can become very fluid. A flat hierarchy reduces the need to manage complex flow down ID relationships. Every requirement has a parent requirement ID explicitly listed to maintain traceability. Since the DST team is structured by discipline, discipline identifiers are added to the requirement ID to help in assigning responsibility.

Deployable Space Telescope

Requirements and Verification

Revision B

Revision	Date	Description	By	Review	Approve
A	02Apr18	Preliminary	S. Pepper		
B	04Apr18	For Review	S. Pepper		

Contents

1. Introduction

The purpose of this document is to document the requirements for the Deployable Space Telescope and to provide guidelines for verification that those requirements have been met. Brief discussions on how to apply margins and factors of safety and how to calculate margin of safety in strength calculations are provided.

2. Requirements

The DST requirements are listed in Appendix A. Each requirement has a parent requirement ID listed to maintain traceability.

1.1 Requirements Hierarchy

Since the DST team is structured by discipline, discipline identifiers are added to the requirement ID to help in assigning responsibility. Table 1 sets out the requirements hierarchy. Table 2 explains the ID breakdown.

Table 1 – Requirements hierarchy.

Level	Format	Example
Mission Objectives	MIS-OBJ-xx	*MIS-OBJ-01*
Mission/ Stakeholder Requirements	MIS-REQ-xx	MIS-REQ-01
System/ Subsystem Requirements	sss-ddd-xx	M1-MEC-01
System/ Subsystem sub-requirement	sss-ddd-xx-yy	M1-MEC-01-01

Table 2 – Requirements ID breakdown.

Element	Description	Example
sss	System/ subsystem	*DST – Telescope level* *M1 – Primary Mirror* *M2 – Secondary Mirror* *BAF – Baffle* *ACS – Aberration Correction System* *PMAO – Primary Mirror Active Optics*
ddd	Discipline	MEC – Mechanical STRU – Structural THE – Thermal OPT – Optical CON – Control ELE - Electrical
xx	Sequential numerical ID	01, 02 …
yy	Sequential sub-ID	01, 02 …

1.2 Launch Survival Requirements

Requirements M1-MEC-09-01 to M1-MEC-09-03 state that to survive launch, the primary mirror must withstand a 30g quasi-static load and have longitudinal and lateral first natural frequencies greater than 100 Hz. These requirements have been taken from the MSc thesis by B. van Putten, in turn adopted after advice given by ADSNL in 2017.

It is understood that the 30g load is an experienced based estimate to cover the worst case combination of static and dynamic loads experienced during launch. The 30g load is to be applied

simultaneously along two orthogonal axes to demonstrate sufficient assembly strength, along the x + y, x + z and y + z axes.

It is assumed that this load also includes thermal loads, and that no further qualification or safety factor needs to be applied to this load to check strength in qualification testing.

3. Verification Plan

A full verification plan has not been developed. Each student will conduct verification per the objectives of his or her thesis, however a number of elements can be defined for common usage across the team.

2.1 Verification Methods

The following verification methods may be used.

Table 3 – Verification methods.

Method	Description
Analysis	Mathematical or computational techniques. Can be deterministic or stochastic.
Inspection/ Review	Inspection of the product itself (inspection) or inspection of design documentation (review of design).
Test	Physically testing a test model of the design in representative conditions.
Similarity	Checking if the item is similar in design, process and quality control to another that has already been verified to the same or more stringent requirements.
Demonstration	Demonstration of the requirement through operation of the item.

2.2 Factors of Safety for Strength Analysis

The application of test factors, factors of safety, limit loads and safety margins follows the philosophy given in *Space Mission Engineering, The New* SMAD [p. 677, Wertz 2011], itself derived from the General Environmental Verification Standard GEVS (GSFC-STD-7000) from NASA Goddard Space Flight Center [NASA 2013]. The standard gives guidance on the minimum strength margin required for structural designs for GSFC. No *model uncertainty factors* are used to account for uncertainty in the derivation of limit loads.

Table 4 gives the factors of safety to be applied to loads (*not* the stress resulting from these loads) in strength analysis and test. The factors of safety have been derived assuming that the DST would undergo protoflight qualification testing.

Factors of Safety (FS) are used to ensure an adequate *margin of safety* (MS) under yield or ultimate conditions. The yield factor of safety is used to decrease the chances of the test article experiencing detrimental permanent plastic deformation during launch or testing. The ultimate factor of safety is greater than the yield factor to separate the yield and ultimate failure modes. It decreases the chances of the test article undergoing rupture or collapse.

The *limit load* is the maximum load that a structure is expected to experience through the course of the nominal mission. The *design load* is the limit load multiplied by the factor of safety, giving either the design yield load or design ultimate load. The test load is the limit load multiplied by the *test factor*. The factors for equipment not critical to personnel safety are used. In Table 4, the test is assumed to be a qualification test of a protoflight model. The test factor does not compound the yield or ultimate factors of safety in design calculations or testing.

Factors of safety should be applied to the limit loads, not the stresses resulting from the limit loads. This is because some failure modes, such as buckling, are non-linear. Applying the factor of safety to the stress would under-represent the uncertainty in the applied load. The converse is also true: applying the factor of safety to the resulting stress can significantly *over* represent the effects of an applied load. An example being the contact stress on a ball bearing, which decreases as contact area increases with load. The net effect would be an overly conservative design.

Table 4 – Summary of safety and test factors used for verification. Factors have been derived assuming DST would undergo protoflight qualification testing. Adapted from [Wertz 2011] unless noted otherwise.
(a) Taken from [p. 374, Sarafin 1995]
(b) One-time stall test at maximum voltage.

Description	FS_y	FS_u	Test	Comment
Static	1.25	1.4	1.25	See stability factor
Sine	1.25	1.4	1.25	2 oct/ min sweep
Random/ Acoustic	1.6	1.8	+3 dB	2 minutes/ axis duration
Thermal[(a)]	1.0	1.0	1.0	See thermal uncertainty margin
Preloads[(a)]	1.0	1.0	As built	
Mechanisms[(a)]				
Nominal operations	1.1	1.25	1.0	
Stall	1.0	1.0	*(b)*	For contingency only

2.2.2 Thermal Margins

The methodology for designating thermal margins is adapted from ECSS-E-30 Part 1 (2000) “System Engineering, Mechanical – Part 1: Thermal Control”. Margins are applied as shown in Figure 1. An abridged interpretation of the standard is given here for use within the DST project. The reader is referred to the standard itself for more detailed guidance if necessary, particularly with regards to cryogenic temperatures (< 120 K), high temperatures (> 400 K), verification and testing. All margins given here are for pre-phase A studies.

Calculated Temperature Range (Clause 3.1.5)

This is the nominal worst case temperature range that the system should experience in the absence of failure cases. It is obtained by analysis or other means. The calculated temperature range plus uncertainties from, for example, inaccuracies in material properties, environmental data or modelling assumptions, is equal to the predicted temperature range and shall be limited to the design temperature range. A typical uncertainty margin for Phase A studies is ±15 K (Clause A.1.1(f)) for a coarse overall spacecraft thermal model with items lumped into the structure.

Design Temperature Range (Clause 3.1.10)

The requirements for the thermal control system design activities. For the DST, equal to the calculated temperature range plus uncertainty margin.

Acceptance Temperature Range (Clause 3.1.1, 3.1.2, A.2(a))

The acceptance margin is a contingency to account for unpredictable thermal control system related events. Addition of the acceptance margin to the design temperature range results in the acceptance temperature range. The acceptance temperature range is the extreme temperature range that the system can reach but never exceed throughout the entire mission based on worst case assumptions. For the DST, an acceptance margin of 5 K shall be used.

Qualification Temperature Range (Clause 3.1.22, 3.1.23, A.2(a))

The qualification margin is a contingency to account for unexpected events. Addition of the qualification margin to the acceptance temperature range results in the qualification temperature range. The qualification temperature range is the range in which the system is guaranteed to function nominally, fulfilling all required performances with the required reliability. For the DST, a qualification margin of 5 K shall be used.

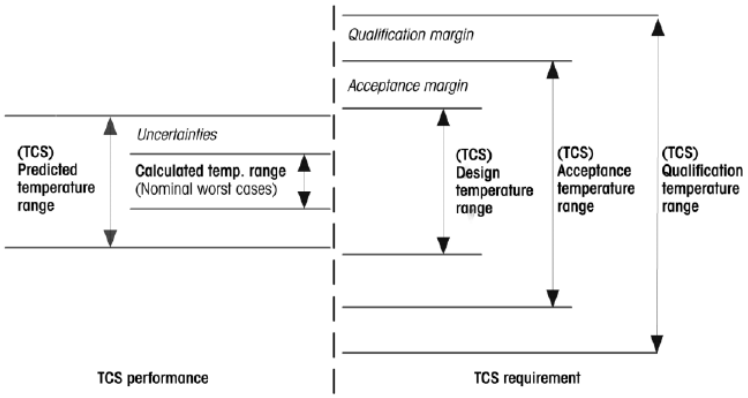

Figure 1 – Temperature definitions for thermal control system. Adapted from ECSS-E-30:1 (2000).

From the standard, the thermal control system shall be able to guarantee that a part is able to fulfil its performance requirements within the qualification temperature range. For the DST project, the application of margins to the nominal worst case temperature range shall be as described in Figure 2 unless otherwise approved by the project manager. A design shall be able to meet all of its prescribed requirements throughout the qualification temperature range.

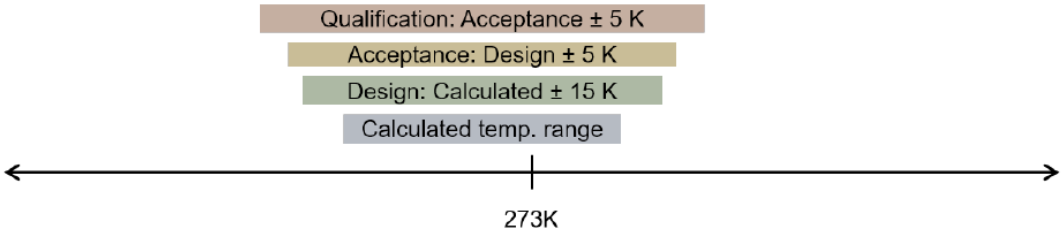

Figure 2 – Application of thermal control system margins for the DST project.

2.3 Design Factors

No factor of safety is used when calculating the nominal limit loads for functional requirement verification. Factors of safety are only used for verification of strength requirements.

2.4 Verification Criteria

2.4.1 Strength

The verification criteria for strength is a *margin of safety* (MS) against yield or ultimate failure greater than or equal to 0. The margins of safety are given in terms of load rather than stress for the same reasons that the factor of safety is applied to the limit load rather than the resulting stress, to

get the design load. Using stress to calculate the margin of safety can erroneously represent a structures remaining strength margin. The yield and ultimate margins of safety are given by:

$$MS_y = \frac{Allowable\ yield\ load}{Design\ yield\ load} - 1$$

$$MS_u = \frac{Allowable\ ultimate\ load}{Design\ ultimate\ load} - 1$$

Loads should be combined as required using suitable interaction equations. See for example Chapter 8.2 of [Sarafin 1995].

2.4.2 Functionality

The verification criteria for functional requirements are the quantities defined in the requirements themselves.

4. References

- NASA. (2013). General Environmental Verification Standards (GEVS) for GSFC Flight Programs and Projects. GSFC-STD-7000A.
- Sarafin, T. P. (Ed.). (1995). Spacecraft Structures and Mechanisms. Torrance, California: Microcosm, Inc.
- Wertz, J. R., Everett, D. F., & Puschell, Jeffery, J. (Eds.). (2011). *Space Mission Engineering: The New SMAD*. Hawthorne, California: Microcosm press.

Appendix A: DST Requirements

See overleaf.

DST Requirement Matrix

Note: In this document you can add, remove or alter requirements. If you do this, make sure that the Compliance Matrix is updated accordingly

Table 1: Subsystem Requirements

	ID	Description	Parent	Comment
Primary Mirror Requirements	M1-MEC-01	The deployment mechanism and primary mirror calibration system shall meet the deployment tolerance budget with a confidence level of >2σ.	MIS-REQ-07	
	M1-MEC-01-01	The deployment mechanism and primary mirror calibration system deployment accuracy shall be less than or equal to 2 µm along the X axis.	M1-MEC-01	van Putten, 2017 MSc thesis
	M1-MEC-01-02	The deployment mechanism and primary mirror calibration system deployment accuracy shall be less than or equal to 2 µm along the Y axis.	M1-MEC-01	van Putten, 2017 MSc thesis
	M1-MEC-01-03	The deployment mechanism and primary mirror calibration system deployment accuracy shall be less than or equal to 2 µm along the Z axis.	M1-MEC-01	van Putten, 2017 MSc thesis
	M1-MEC-01-04	The deployment mechanism and primary mirror calibration system deployment accuracy shall be less than or equal to 2 µrad around the X axis.	M1-MEC-01	van Putten, 2017 MSc thesis
	M1-MEC-01-05	The deployment mechanism and primary mirror calibration system deployment accuracy shall be less than or equal to 4 µrad around the Y axis.	M1-MEC-01	van Putten, 2017 MSc thesis
	M1-MEC-01-06	The deployment mechanism and primary mirror calibration system deployment accuracy shall be less than or equal to 50 µrad around the Z axis.	M1-MEC-01	van Putten, 2017 MSc thesis
	M1-MEC-02	The radius of curvature of the primary mirror segments shall change less than or equal to 0.001 % during deployment and coarse alignment.	MIS-REQ-07	
	M1-MEC-03	The shape error of the primary mirror segments shall be less than or equal to 50 nm during deployment and coarse alignment.	MIS-REQ-07	
	M1-MEC-04	The deployment mechanism and primary mirror calibration system shall meet the in-orbit drift budget with a confidence level of >2σ.	MIS-REQ-07	
	M1-MEC-04-01	The deployment mechanism and primary mirror calibration system in-orbit drift shall be less than or equal to 0.02 µm along the X axis.	M1-MEC-04	
	M1-MEC-04-02	The deployment mechanism and primary mirror calibration system in-orbit drift shall be less than or equal to 0.02 µm along the Y axis.	M1-MEC-04	
	M1-MEC-04-03	The deployment mechanism and primary mirror calibration system in-orbit drift shall be less than or equal to 0.02 µm along the Z axis.	M1-MEC-04	
	M1-MEC-04-04	The deployment mechanism and primary mirror calibration system in-orbit drift shall be less than or equal to 0.01 µrad around the X axis.	M1-MEC-04	
	M1-MEC-04-05	The deployment mechanism and primary mirror calibration system in-orbit drift shall be less than or equal to 0.02 µrad around the Y axis.	M1-MEC-04	
	M1-MEC-04-06	The deployment mechanism and primary mirror calibration system in-orbit drift shall be less than or equal to 5 µrad around the Z axis.	M1-MEC-04	
	M1-MEC-05	The radius of curvature of the primary mirror segments shall change less than or equal to 0.0001 % due to in-orbit drifts.	MIS-REQ-07	
	M1-MEC-06	The shape error of the primary mirror segments shall be less than or equal to 5 nm due to in-orbit drifts.	MIS-REQ-07	
	M1-MEC-07	The deployment mechanism and primary mirror calibration system shall meet the stability budget with a confidence level of >2σ.	MIS-REQ-07	
	M1-MEC-07-01	The deployment mechanism and primary mirror calibration system stability shall be less than or equal to 0.005 µm along the X axis.	M1-MEC-07	
	M1-MEC-07-02	The deployment mechanism and primary mirror calibration system stability shall be less than or equal to 0.005 µm along the Y axis.	M1-MEC-07	
	M1-MEC-07-03	The deployment mechanism and primary mirror calibration system stability shall be less than or equal to 0.005 µm along the Z axis.	M1-MEC-07	
	M1-MEC-07-04	The deployment mechanism and primary mirror calibration system stability shall be less than or equal to 0.0025 µrad around the X axis.	M1-MEC-07	
	M1-MEC-07-05	The deployment mechanism and primary mirror calibration system stability shall be less than or equal to 0.01 µrad around the Y axis.	M1-MEC-07	
	M1-MEC-07-06	The deployment mechanism and primary mirror calibration system stability shall be less than or equal to 0.5 µrad around the Z axis.	M1-MEC-07	
	M1-MEC-09	The stowed mechanism shall be able to survive the launch conditions. Survival is defined as no impairment to the nominal functional capabilities of the system resulting from exposure to a given set of environmental conditions.	MIS-REQ-12	van Putten, 2017 MSc thesis
	M1-MEC-09-01	The stowed mechanism shall be able to survive quasi static accelerations of 30 G. Survival is defined as no impairment to the nominal functional capabilities of the system resulting from exposure to a given set of environmental conditions.	M1-MEC-09	
	M1-MEC-09-02	The stowed mechanism shall have a first longitudinal eigenfrequency higher than 100 Hz in the stowed configuration.	M1-MEC-09	
	M1-MEC-09-03	The stowed mechanism shall have a first lateral eigenfrequency higher than 100 Hz in the stowed configuration.	M1-MEC-09	
	M1-MEC-10	The stowed mechanism shall conform with Guiana Space Centre safety regulations.	MIS-REQ-11	
	M1-MEC-12	The primary mirror assembly shall have a minimum operational lifetime of 5 years.	MIS-OBJ-01	
	M1-MEC-13	The primary mirror shall consist of four deployable segments.	MIS-REQ-07	Optical configuration requirement.
	M1-MEC-14	The distance from the primary mirror plane to the secondary mirror plane along the optical axis shall be 1600 mm +/- TBD µm in the nominal deployed configuration.	MIS-REQ-01	Meet optical configuration
	M1-MEC-15	The deployment mechanism and primary mirror calibration system shall operate at a nominal temperature of 298 K +/- 1 K during operations in the deployed configuration.	MIS-REQ-07	
	M1-MEC-16	The combined mass of the primary mirror deployment and active optics systems shall be no more than 24.8 + (TBD M1 deployment) kg	MIS-REQ-08	Supersedes M1-MEC-11 which was
	M1-MEC-17	The deployment mechanism shall position the mirror segments parallel to the telescope bus with a clearance of less than or equal to 120 mm in the stowed configuration.	MIS-REQ-09	Supersedes M1-MEC-8 which was geometrically impossible
nts	M2-SYS-01	The total mass of the M2 mechanism shall be lower than 14 kg	MIS-REQ-08	Lopes Barreto, 2017 MSC thesis

Secondary Mirror Requiremer			
M2-SYS-02	The mechanism shall provide structural support for M2	MIS-REQ-09	Lopes Barreto, 2017 MSC thesis
M2-SYS-03	The M2 mechanism in stowed configuration shall stay within the boundary box given by the primary mirror segments.	MIS-REQ-09	
M2-SYS-04	The M2 mechanism in stowed configuration height, including the instrument bus, shall be equall or less than 1.27m (goal)/2.55m (threshold)	MIS-OBJ-02	
M2-SYS-05	The development, production, assembly, integration, and test cost of the M2 mechanism shall be equal to or lower than TBD	MIS-REQ-07	Cost budget not available yet
M2-MEC-01	The M2 mechanism shall deploy the M2 along the optical axis (Z axis) to obtain a distance of 1.6 m between M1 and M2, measured between the vertex of both mirrors	MIS-REQ-07	
M2-MEC-02	The M2 mechanism deployment accuracy shall be equal to or less than 15µm measured along the X axis of the telescope coordinate frame	MIS-REQ-07	deployment budget
M2-MEC-03	The M2 mechanism deployment accuracy shall be equal to or less than 15µm measured along the Y axis of the telescope coordinate frame	MIS-REQ-07	deployment budget
M2-MEC-04	The M2 mechanism deployment accuracy shall be equal to or less than 10µm measured along the optical axis (Z axis) of the telescope coordinate frame	MIS-REQ-07	deployment budget
M2-MEC-05	The M2 mechanism deployment accuracy shall be equal to or less than 100µrad measured around the X axis of the telescope coordinate frame	MIS-REQ-07	deployment budget
M2-MEC-06	The M2 mechanism deployment accuracy shall be equal to or less than 100µrad measured around the Y axis of the telescope coordinate frame of the telescope coordinate frame	MIS-REQ-07	deployment budget
M2-MEC-07	The M2 mechanism deployment accuracy shall be equal to or less than 100µrad measured around the optical axis (Z axis of the telescope coordinate frame)	MIS-REQ-07	deployment budget
M2-MEC-08	The radius of curvature of the M2 mirror shall change less than 0.01% due to the deployment of the mechanism	MIS-REQ-07	deployment budget
M2-MEC-09	The shape error of the M2 shall be less than 25 nm due to the deployment of the mechanism	MIS-REQ-07	deployment budget
M2-MEC-10	The M2 mechanism in-orbit drift shall be equal or less than 4 µm measured along the X axis of the telescope coordinate frame	MIS-REQ-07	Drift budget
M2-MEC-11	The M2 mechanism in-orbit drift shall be equal or less than 4 µm measured along the Y axis of the telescope coordinate frame	MIS-REQ-07	Drift budget
M2-MEC-12	The M2 mechanism in-orbit drift shall be equal or less than 2 µm measured along the optical axis (Z axis of the telescope coordinate frame)	MIS-REQ-07	Drift budget
M2-MEC-13	The M2 mechanism in-orbit drift shall be equal or less than 6 µrad measured around the X axis of the telescope coordinate frame	MIS-REQ-07	Drift budget
M2-MEC-14	The M2 mechanism in-orbit drift shall be equal or less than 6 µrad measured around the Y axis of the telescope coordinate frame	MIS-REQ-07	Drift budget
M2-MEC-15	The M2 mechanism in-orbit drift shall be equal or less than 12 µrad measured around the Z axis of the telescope coordinate frame	MIS-REQ-07	Drift budget
M2-MEC-16	The radius of curvature of the M2 mirror shall change less than 0.0001% due to in-orbit drift	MIS-REQ-07	Drift budget
M2-MEC-17	The shape error of the M2 shall be less than 5 nm due to in-orbit drifts	MIS-REQ-07	Drift budget
M2-MEC-18	The M2 mechanism stability shall be equal to or less than 1 µm along the X axis of the telescope reference frame	MIS-REQ-07	Stability budget
M2-MEC-19	The M2 mechanism stability shall be equal to or less than 1 µm along the Y axis of the telescope reference frame	MIS-REQ-07	Stability budget
M2-MEC-20	The M2 mechanism stability shall be equal to or less than 0.5 µm along the Z axis of the telescope reference frame	MIS-REQ-07	Stability budget
M2-MEC-21	The M2 mechanism stability shall be equal to or less than 1.5 µrad around the X axis of the telescope reference frame	MIS-REQ-07	Stability budget
M2-MEC-22	The M2 mechanism stability shall be equal to or less than 1.5 µrad around the Y axis of the telescope reference frame	MIS-REQ-07	Stability budget
M2-MEC-23	The M2 mechanism stability shall be equal to or less than 3 µrad around the Z axis of the telescope reference frame	MIS-REQ-07	Stability budget
M2-MEC-24	The deployed mechanismshall have a minimumnatural frequency of 5 Hz		Lopes Barreto, 2017 MSC thesis
Primary Mirror Active Optics Requirements			
PMAO-SYS-01	The combined mass of all of the primary mirror segments shall be no more than 24 kg.	M1-MEC-11	Systems engineering budgets
PMAO-SYS-02	The combined mass of all four PMAO mechanisms shall be no more than 24.8 kg.	M1-MEC-11	Systems engineering budgets
PMAO-SYS-03	The PMAO shall not use any components, technology or processes controlled by ITAR.	MIS-REQ-10	flowdown. Simplify procurement, reduce cost, increase design transparency and collaboration.
PMAO-SYS-04	The combined cost of the PMAO support and mechanism components shall be no more than TBD over the DST mission lifetime.	MIS-OBJ-02	Meet mission objectives.
PMAO-OPT-01	The PMAO shall remove discontinuous wavefront errors fom the full field of view during imaging operations and AIT.	MIS-REQ-07	Enable diffraction limited imaging.
PMAO-MEC-01	The PMAO mechanism shall enable individual control of each primary mirror segment independently in translation parallel to the z-axis, rotation about the x-axis and rotation about the y-axis of the PMAO mechanism body fixed frame during AIT and operations.	PMAO-OPT-01	Enable removal of discontinuous wavefront errors. Main function of PMAO mechanism.
PMAO-MEC-02	The PMAO support shall support the primary mirror segment during AIT activities without overconstraint in the stowed and deployed configurations.Support is defined as providing a load path to the instrument housing.	PMAO-OPT-01	Withstand loads during AIT, enable AIT activities.
PMAO-MEC-02-01	The primary mirror segments shall have no more than **TBD** nm PV sag in one-g on Earth.	PMAO-MEC-02	To enable testing on Earth.
PMAO-MEC-03	The PMAO support shall support the primary mirror segment during launch without overconstraint in the stowed configuration. Support is defined as providing a load path to the instrument housing.	PMAO-OPT-01	Possibly a driving requirement, may need to have a different mechanism for launch support.
PMAO-MEC-04	The PMAO support shall support the primary mirror segment during operations without overconstraint in the stowed and deployed configurations. Support is defined as providing a load path to the instrument housing.	PMAO-OPT-01	Enable diffraction limited imaging & connect segment to mechanism. Main function of PMAO support.
PMAO-MEC-05	The PMAO deployment accuracy shall be less than or equal to TBD µm along the X axis of the telescope coordinate frame.	M1-MEC-01-01	these should say "during imaging operations".

PMAO-MEC-06	The PMAO deployment accuracy shall be less than or equal to TBD µm along the Y axis of the telescope coordinate frame.	M1-MEC-01-02	Deployment tolerance budget.
PMAO-MEC-07	The PMAO deployment accuracy shall be less than or equal to TBD µm along the Z axis of the telescope coordinate frame.	M1-MEC-01-03	Deployment tolerance budget.
PMAO-MEC-08	The PMAO deployment accuracy shall be less than or equal to TBD µrad around the X axis of the telescope coordinate frame.	M1-MEC-01-04	Deployment tolerance budget.
PMAO-MEC-09	The PMAO deployment accuracy shall be less than or equal to TBD µrad around the Y axis of the telescope coordinate frame.	M1-MEC-01-05	Deployment tolerance budget.
PMAO-MEC-10	The PMAO deployment accuracy shall be less than or equal to TBD µrad around the Z axis of the telescope coordinate frame.	M1-MEC-01-06	Deployment tolerance budget.
PMAO-MEC-11	The PMAO in-orbit drift shall be less than or equal to TBD µm along the X axis of the telescope coordinate frame.	M1-MEC-04-01	In-orbit drift tolerance budget.
PMAO-MEC-12	The PMAO in-orbit drift shall be less than or equal to TBD µm along the Y axis of the telescope coordinate frame.	M1-MEC-04-02	In-orbit drift tolerance budget.
PMAO-MEC-13	The PMAO in-orbit drift shall be less than or equal to TBD µm along the Z axis of the telescope coordinate frame.	M1-MEC-04-03	In-orbit drift tolerance budget.
PMAO-MEC-14	The PMAO in-orbit drift shall be less than or equal to TBD µrad around the X axis of the telescope coordinate frame.	M1-MEC-04-04	In-orbit drift tolerance budget.
PMAO-MEC-15	The PMAO in-orbit drift shall be less than or equal to TBD µrad around the Y axis of the telescope coordinate frame.	M1-MEC-04-05	In-orbit drift tolerance budget.
PMAO-MEC-16	The PMAO in-orbit drift shall be less than or equal to TBD µrad around the Z axis of the telescope coordinate frame.	M1-MEC-04-06	In-orbit drift tolerance budget.
PMAO-MEC-17	The PMAO stability shall be less than or equal to TBD µm along the X axis of the telescope coordinate frame.	M1-MEC-07-01	Stability budget.
PMAO-MEC-18	The PMAO stability shall be less than or equal to TBD µm along the Y axis of the telescope coordinate frame.	M1-MEC-07-02	Stability budget.
PMAO-MEC-19	The PMAO stability shall be less than or equal to TBD µm along the Z axis of the telescope coordinate frame.	M1-MEC-07-03	Stability budget.
PMAO-MEC-20	The PMAO stability shall be less than or equal to TBD µrad around the X axis of the telescope coordinate frame.	M1-MEC-07-04	Stability budget.
PMAO-MEC-21	The PMAO stability shall be less than or equal to TBD µrad around the Y axis of the telescope coordinate frame.	M1-MEC-07-05	Stability budget.
PMAO-MEC-22	The PMAO stability shall be less than or equal to TBD µrad around the Z axis of the telescope coordinate frame.	M1-MEC-07-06	Stability budget.
PMAO-MEC-23	Each primary mirror segment shall have a maximum step size of 10 nm in the z-axis direction of the PMAO mechanism body fixed frame throughout the entire segment workspace.	PMAO-MEC-01	Top-down resolution requirement.
PMAO-MEC-24	Each primary mirror segment shall have a maximum step size of TBD µrad about the x-axis of the PMAO mechanism body fixed frame throughout the entire segment	PMAO-MEC-01	Top-down resolution requirement.
PMAO-MEC-25	Each primary mirror segment shall have a maximum step size of TBD µrad about the y-axis of the PMAO mechanism body fixed frame throughout the entire segment	PMAO-MEC-01	Top-down resolution requirement.
PMAO-MEC-26	Each primary mirror segment shall have a repeatability of no greater than TBD µrad RMS for a single step motion in rotation about the x-axis of the PMAO mechanism body fixed frame throughout the entire segment workspace.	PMAO-MEC-01	Optical control requirements.
PMAO-MEC-27	Each primary mirror segment shall have a repeatability of no greater than TBD µrad RMS for a single step motion in rotation about the y-axis of the PMAO mechanism body fixed frame throughout the entire segment workspace.	PMAO-MEC-01	Optical control requirements.
PMAO-MEC-28	Each primary mirror segment shall have a repeatability of no greater than TBD µm RMS for a single step motion in translation in the z-axis direction of the PMAO mechanism body fixed frame throughout the entire segment workspace.	PMAO-MEC-01	Optical control requirements.
PMAO-MEC-29	Each primary mirror segment shall have a bidirectional rotational range of motion about the x-axis of the PMAO mechanism body fixed frame equal to the primary mirror deployment accuracy budget about the x-axis.	PMAO-MEC-01	Optical control requirements. Added "rotational" for clarity.
PMAO-MEC-30	Each primary mirror segment shall have a bidirectional rotational range of motion about the y-axis of the PMAO mechanism body fixed frame equal to the primary mirror deployment accuracy budget about the y-axis.	PMAO-MEC-01	Optical control requirements. Added "rotational" for clarity.
PMAO-MEC-31	Each primary mirror segment shall have a bidirectional range of motion in the z-axis direction of the PMAO mechanism body fixed frame equal to twice the primary mirror deployment accuracy budget in the z axis.	PMAO-MEC-01	Optical control requirements. Note TWICE the budget.
PMAO-MEC-32	Each actuator of the PMAO mechanism shall have a total range of motion of TBD.	PMAO-MEC-01	Segment level range of motion requirements.
PMAO-MEC-33	Each actuator of the PMAO mechanism shall have a maximum step size of TBD.	PMAO-MEC-01	Segment level range of motion requirements.
PMAO-MEC-34	Each actuator of the PMAO mechanism shall have a repeatability of no more than TBD RMS for a single step motion.	PMAO-MEC-01	Segment level range of motion requirements.
PMAO-CON-01	Each PMAO mechanism shall have a bandwidth of no less than TBD Hz in each degree of freedom.	PMAO-OPT-01	Optical control requirements.
PMAO-CON-01-01	Each actuator of the PMAO mechanism shall have a bandwidth of no less than TBD Hz.	PMAO-CON-01	To meet segment level bandwidth requirements.
PMAO-MEC-35	The thermal centre of each primary mirror segment shall be at the position of the segment centroid in the XY plane of the telescope optical coordinate frame.	PMAO-OPT-01	To reduce bending and shear loads in the mirror substrate. Meet in-orbit drift budget.
PMAO-MEC-36	Each PMAO mechanism shall be able to drive a load of TBD N at the primary mirror segment centre of mass pointing in the negative z-axis direction of the primary mirror segment body-fixed frame.	PMAO-MEC-01	Must be able to move the segment during operations.
PMAO-MEC-37	Each PMAO mechanism shall be able to provide a holding force of TBD N in the z-axis direction of the primary mirror segment body-fixed frame.	PMAO-MEC-01	To hold a calibrated position through thrusting and/ or pointing.
PMAO-MEC-38	The primary mirror segments shall be assembled for optimised performance in zero-g.	PMAO-OPT-01	Minimise optical surface figure error in gravity offloading.

	PMAO-SYS-05	The PMAO shall have a minimum operational lifetime of 5 years.	M1-MEC-12	Flow down from DST requirement.
	PMAO-MEC-39	The PMAO shall be able to survive assembly, integration, testing and ground handling in the deployed and stowed configurations. Survival is defined as no impairment to the nominal functional capabilities of the system resulting from exposure to a given set of environmental conditions.	PMAO-OPT-01	To meet mission objectives
	PMAO-MEC-40	The PMAO shall be able to survive launch in the stowed configuration. Survival is defined as no impairment to the nominal functional capabilities of the system resulting from exposure to a given set of environmental conditions.	PMAO-OPT-01	To meet mission objectives
	PMAO-MEC-40-01	The PMAO shall survive a quasi-static load of 30g applied simultaneously to the x- and y- axes in the launcher coordinate frame in the stowed configuration during launch.	PMAO-MEC-40	Inclusive of qualification and thermal loads? TBC
	PMAO-MEC-40-02	The PMAO shall survive a quasi-static load of 30g applied simultaneously to the x- and z- axes in the launcher coordinate frame in the stowed configuration during launch.	PMAO-MEC-40	Inclusive of qualification and thermal loads? TBC
	PMAO-MEC-40-03	The PMAO shall survive a quasi-static load of 30g applied simultaneously to the y- and z- axes in the launcher coordinate frame in the stowed configuration during launch.	PMAO-MEC-40	Inclusive of qualification and thermal loads? TBC
	PMAO-MEC-40-04	The PMAO first-mode natural frequency shall be greater than 100 Hz in the stowed configuration during launch.	PMAO-MEC-40	Inclusive of qualification and thermal loads? TBC
	PMAO-MEC-41	The PMAO shall be able to survive the operational environment in the stowed and deployed configurations. Survival is defined as no impairment to the nominal functional capabilities of the system resulting from exposure to a given set of environmental conditions.	PMAO-OPT-01	To meet mission objectives
	PMAO-MEC-41-01	The PMAO shall survive steady state temperatures between 188 and 384 K (design temperatures) in the stowed configuration during LEOP.	PMAO-MEC-41	
	PMAO-MEC-42	The PMAO shall be able to survive deployment. Survival is defined as no impairment to the nominal functional capabilities of the system resulting from exposure to a given set of environmental conditions.	PMAO-MEC-41	To meet mission objectives
	PMAO-SYS-06	The PMAO manufacture, fabrication and assembly shall not require development of new technology, equipment or processes.	MIS-OBJ-02	Decrease cost, risk, increase availability of possible suppliers.
	PMAO-SYS-07	The PMAO shall allow safe handling by technicians during AIT activities.	MIS-REQ-12	Occupational health & safety.
	PMAO-MEC-43	The PMAO shall operate at ambient temperature, pressure and humidity.	PMAO-SYS-06	Simplify AIT facility requirements.
	PMAO-MEC-44	The PMAO shall accommodate a total assembly error of no more than TBD µm in the x-axis direction of the telescope body-fixed frame between the nominal and actual locations of each primary mirror segment body-fixed frame origin in the nominal deployed configuration.	PMAO-SYS-06	To make assembly practical at reasonable cost.
	PMAO-MEC-45	The PMAO shall accommodate a total assembly error of no more than TBD µm in the y-axis direction of the telescope body-fixed frame between the nominal and actual locations of each primary mirror segment body-fixed frame origin in the nominal deployed configuration.	PMAO-SYS-06	To make assembly practical at reasonable cost.
	PMAO-MEC-46	The PMAO shall accommodate a total assembly error of no more than TBD µm in the z-axis direction of the telescope body-fixed frame between the nominal and actual locations of each primary mirror segment body-fixed frame origin in the nominal deployed configuration.	PMAO-SYS-06	To make assembly practical at reasonable cost.
	PMAO-MEC-47	The PMAO shall accommodate a total assembly error of no more than TBD µrad about the x-axis of the telescope body-fixed frame between the nominal and actual locations of each primary mirror segment body-fixed frame origin in the nominal deployed configuration.	PMAO-SYS-06	To make assembly practical at reasonable cost.
	PMAO-MEC-48	The PMAO shall accommodate a total assembly error of no more than TBD µrad about the y-axis of the telescope body-fixed frame between the nominal and actual locations of each primary mirror segment body-fixed frame origin in the nominal deployed configuration.	PMAO-SYS-06	To make assembly practical at reasonable cost.
	PMAO-MEC-49	The PMAO shall accommodate a total assembly error of no more than TBD µrad about the z-axis of the telescope body-fixed frame between the nominal and actual locations of each primary mirror segment body-fixed frame origin in the nominal deployed configuration.	PMAO-SYS-06	To make assembly practical at reasonable cost.
	PMAO-ELE-01	The PMAO shall not require power during launch.	MIS-REQ-11	Simplify launch compatibility
	PMAO-SYS-08	The PMAO shall conform with Guiana Space Centre safety regulations.	M1-MEC-10	Compatability with European launch providers.
	PMAO-MEC-50	The PMAO shall not impede deployment of the primary or secondary mirror.	MIS-REQ-01	
	PMAO-MEC-50-01	The PMAO shall not protrude laterally beyond the periphery of the primary mirror segment in the stowed or deployed configurations.	PMAO-MEC-50	Limit of useable volume. Straylight control.
	PMAO-MEC-50-02	The depth of the PMAO from the underside of the primary mirror segment to the top of the deployment mechanism support frame shall be no more than TBD mm when in the stowed configuration.	PMAO-MEC-50	Limit of useable volume.

Table 2: Mission Objectives

ID	Description	Parent	Comment
MIS-OBJ-01	The Ground Sample Distance of the DST shall be no larger than the state of the art in commercial visual spectrum Earth Observation imaging platforms. As of 2017 this is DigitalGlobe's WorldView-4 satellite with a Ground Sample Distance of 0.31 m in the panchromatic band.	N/A	TBD

MIS-OBJ-02	The lifetime cost of the DST shall be less than the state of the art in commercial visual spectrum Earth Observation imaging platforms. As of 2017 this is DigitalGlobe's WorldView-4 satellite with an estimated cost of USD$850 million including ground network upgrades.	N/A	TBD

Table 3: Mission Requirements

ID	Description	Parent	Comment
MIS-REQ-01	The Ground Sampling Distance of the instrument shall be equal to 25 cm in the panchromatic band from an orbital altitude of 500 km	MIS-OBJ-01	Dolkens, 2015 MSc thesis
MIS-REQ-02	The swath width of the instrument shall be wider than 1 km (threshold) / 5 km (goal)	MIS-OBJ-01	Dolkens, 2015 MSc thesis
MIS-REQ-03	The system shall have one panchromatic channel from 450 to 650 nm with a 25 cm GSD at an altitude of 500 km.	MIS-OBJ-01	Dolkens, 2015 MSc thesis.
MIS-REQ-04	The system shall have four multispectral bands with the wavelength ranges and GSD indicated (at 500 km): Blue (450 - 510 nm) - 100 cm Green (518 - 586 nm) - 100 cm Yellow (590 - 630 nm) - 100 cm Red (632 - 692 nm) - 100 cm	MIS-OBJ-01	Dolkens, 2015 MSc thesis.
MIS-REQ-05	The Signal-to-Noise Ratio (SNR) of the instrument shall be higher than 100 for a reflectance of 0.30 and a sun Zenith angle of 60˚	MIS-OBJ-01	Dolkens, 2015 MSc thesis
MIS-REQ-06	The nominal Modulation Transfer Function (MTF) at both the Nyquist frequency and half the Nyquist frequency shall be higher than 5% (threshold) / 15% (goal)	MIS-OBJ-01	Dolkens, 2015 MSc thesis
MIS-REQ-07	After calibration, the residual Strehl ratio of the system shall be higher than 0.80.	MIS-OBJ-01	Dolkens, 2015 MSc thesis
MIS-REQ-08	The mass of the instrument shall be lower than 100 kg (threshold) / 50 kg (goal).	MIS-OBJ-02	Dolkens, 2015 MSc thesis
MIS-REQ-09	In the stowed configuration, the volume of the instrument shall not exceed 1.5 m3 (threshold) / 0.75 m3 (goal)	MIS-OBJ-02	Dolkens, 2015 MSc thesis
MIS-REQ-10	The DST shall not use any ITAR controlled components or technology.	MIS-OBJ-02	TBC
MIS-REQ-11	The DST shall be designed for compatibility with the TBD launcher.	MIS-OBJ-02	TBC
MIS-REQ-12	The DST shall comply with national (NL) and international regulations during AIT activities, launch, operations and end of life.	MIS-OBJ-01	Must not violate laws.

D.2. Additional Information Regarding Extended Requirements List

PMAO-CON-01

Bandwidth is a measure of the mechanisms' performance. It is a measure of how well the mechanism output can track a sinusoidal input of a given amplitude at a given frequency. Here, it is taken as the frequency at which the mechanisms' output falls to $1/\sqrt{2}$ of an input amplitude equal to the mechanism range of motion in each degree of freedom (piston, tip and tilt).

PMAO-MEC-38

Requirement PMAO-MEC-38 states that the primary mirror segments shall be assembled for optimised performance in zero-g. This requirement has been created on the assumption that a gravity-offload kit will be needed for assembly as found in prior work on the mirror supports [117]. Moreover, requirement PMAO-MEC-02-01 gives a limit to the allowable sag of the primary mirror segment in the presence of one-g to enable optical testing activities. It is anticipated that this sag requirement in would be less onerous than the sag requirement in zero-g as it only needs to enable adequate testing, rather than operational performance levels. This requirement also removes some of the burden from the design phase at the expense of added complexity in the AIT phase.

PMAO-SYS-07 & PMAO-MEC-43 to -49

The driving requirement for AIT compatibility will likely be the need to make sure the PMAO mechanism assembly can accommodate a certain level of assembly error. This requirement is designed to ease the burden on assembly processes, metrology and workmanship. The total allowable assembly error is still TBD pending advice from Airbus and tolerance modelling in the end to end performance model. A requirement to operate at ambient temperature, pressure and humidity is also designed to ease AIT complexity costs. The literature study found that having to maintain low humidity environments for testing, to enable a certain lubricant choice, greatly increased the complexity of development for the Euclid M2 mirror mechanism [8].

PMAO-MEC-38, PMAO-MEC-02 & 02-01

Van Putten found that the primary mirror should be assembled with a gravity offload kit to minimise sag in orbit [117]. This is formalised in the PMAO functional requirements by stating that the PMAO segments be assembled for optimised performance in zero-g. A flow on effect of this requirement is that the mirror will experience sag during testing on Earth. To make sure that the optics can be tested and calibrated during AIT, there is a requirement that the peak to valley sag not exceed a certain amount in the presence of 1g. This may become a driving requirement for the PMAO support.

Reliability

No reliability requirements were formally generated as part of this thesis though understanding the reliability requirements of the PMAO design would be very useful. A few requirements that could be included in future work are included in Table D.1. A motorisation factor is used to account for possible losses in actuator and power train performance. This goes on top of any load factors as it is related to actuator performance rather than uncertainty in driven loads. A factor 2.0 has been dictated based on the value used in the design for the Euclid secondary mirror mechanism [8].

D.3. Launch Survival Requirements Analysis

A survey of launch load requirements and verification was carried out to verify the design estimates provided by Airbus Defence & Space and now included in the DST Verification and Requirements Document. The results of this survey are included below for use by future students.

Launch survival requirements are mostly dictated by the launch vehicle user manuals. The requirements are defined using the design loads given in the environment description sections. Verification should be achieved using the qualification or acceptance loads as defined in and required by the spacecraft compatibility and verification sections. Not included in this survey is thermo-elastic deformation, pressure gradient and electromagnetic compatibility.

The survey combined the worst cases of the three major European launchers as of writing in early 2018: Ariane 5, Vega and the European Soyuz [5–7]. Ariane 6 is not considered as it is not yet flight proven. Overall, these requirements are conservative however this provides margin for design maturation. Eventual selection of a single launcher and launch configuration will also allow more refined requirement definition.

Table D.1: Example PMAO assembly reliability requirements for future work.

ID	Description
TBD	The PMAO mechanism shall continue to operate in the event of up to two actuator failures. The mechanism need not continue to meet the nominal range of motion, step size and repeatability requirements in this instance. Actuator failure is defined to be a complete inability to provide mechanical displacement in response to a commanded input or loss of power condition.
TBD	The PMAO mechanism assembly shall meet the stability budget in the event of any number of actuator failures in the PMAO mechanism. Actuator failure is defined to be a complete inability to provide mechanical displacement in response to a commanded input or loss of power condition.
TBD	The PMAO mechanism assembly shall meet the in-orbit drift budget in the event of any number of actuator failures in the PMAO mechanism. Actuator failure is defined to be a complete inability to provide mechanical displacement in response to a commanded input or loss of power condition.
TBD	The PMAO mechanism actuators shall have a motorisation factor of 2.0.

Critical loads normally occur during the qualification level random vibration tests which deliberately exceed normal launch conditions [34, p. 67]. Compliance with vibration requirements can be helped by designing to have as many low frequency modes above 200 Hz as possible [34].

Loads

Quasi-Static Loads

Load factors are taken from the launch vehicle user guides as design guidelines for conceptual design. These are sufficient for preliminary design, at least until a coupled loads analysis can be completed [122, p. 848] [103, p. 51]. This can't be done for the DST until the bus and instrument housing reach preliminary design levels. These load factors only apply if the first natural frequencies in the longitudinal and lateral directions are above a limit set by the launch provider [103, p. 49]. This limit is discussed in the next subsection. It is assumed that the QSL's given by the launch providers only cover steady-state accelerations and effects of low-frequency transients.

Quasi-static loads are normally given in terms of load factors, which are a multiple of Earth standard g's, indicating the inertial force imposed upon a structure. The structure's *weight* on Earth, rather than mass, is multiplied by the load factor to retrieve the applied load. They typically include gravity already. The sign of the load factor is opposite to that of the acceleration [103, p. 40].

The load factors apply at the spacecraft centre of mass under the assumption that the spacecraft is a rigid body. A lateral QSL can act in any direction within the plane orthogonal to the longitudinal axis of the launcher and is superimposed upon the longitudinal QSL. The load factors are expected to dominate the strength requirements of the primary load bearing elements of the PMAO [54, p. 248].

The load factors do not necessarily apply to all spacecraft configurations but are a good first start but may be conservative for short, stowed configurations unless other on board structures have low first natural frequencies [122, p. 848].

The *design* (as opposed to acceptance or qualification loads) quasi-static loads for each launch vehicle are given in Table D.2. Note the minimum frequency requirements set out in the next subsection. The manuals give separate load factors for static and dynamic loads in the longitudinal direction for different stages of flight. These have been combined into a single worst-case combined static *plus* dynamic load case. Lateral load factors are natively given as a combined value. The Ariane 5 manual states that there is a 4.5g tension case during SRB (Solid Rocket Booster) jettison for spacecraft under 1,200 kg wet mass and first longitudinal frequency above 40 Hz. This has been included for conservatism, and indeed defines, the worst-case scenario for the Ariane 5. Lateral loads can act in combination with longitudinal loads.

Minimum First Natural Frequency

The first natural frequency of the spacecraft must be greater than a threshold limit set by the launch vehicle provider so that interaction between the spacecraft and launch vehicle do not inhibit the structural and control functionality of the launch vehicle. This frequency must also be met so that the load factors given in the previous section remain applicable.

Table D.2: Worst-case launch vehicle design load factors for quasi-static loads. The loads apply at the payload centre of mass. Negative signs in the longitudinal axis indicate compression. Vega QSL values are for spacecraft masses greater than 300 kg. Compiled from [5–7].

Launcher	Longitudinal	Lateral
Ariane 5	-6.0 / +7.7 g	-2.0 / +2.0 g
Soyuz	-5.0 / +1.8 g	-1.8 / +1.8 g
Vega	-7.0 / +3.0 g	-0.9 / +0.9 g

Adhering to this requirement does *not* guarantee that the coupled interaction will not damage the spacecraft itself. This is a topic for future work as it can't be checked until there is at least a preliminary design of the spacecraft bus and DST payload.

Table D.3 assumes the spacecraft is cantilevered at the launch vehicle interface. It is good practice to have a 15% margin on the first natural frequency requirement at the preliminary design level [122, p. 671].

Table D.3: Minimum first natural frequency requirement for launch vehicles. Assumes spacecraft is less than 4,500 kg at launch and cantilevered at launch vehicle interface. Compiled from [5–7].

Launcher	Longitudinal	Lateral	Notes
Ariane 5	31 Hz	10 Hz	$m_{SC} < 4{,}500kg$, CoG ≤1.9 m
Soyuz	35 Hz	15 Hz	-
Vega	60 Hz	15 Hz	-

Acoustic Noise and Random Vibration

Acoustic loads are caused by sound pressure waves. They are dominant at lift-off while the launch vehicle is close to the pad where sound waves reflect off the pad and ambient air pressure is highest [54]. They can also be significant through the transonic phase of flight. The launch vehicle itself also responds to acoustic vibrations and are manifested as random vibrations at the launch vehicle/ spacecraft interface.

The acoustic *environment* is described by sound pressure levels (SPL) expressed in decibels with respect to some reference level. Sound pressure levels are the root mean square pressure within a frequency band and are typically given at the centre frequencies of one-third octave bands on a log scale from 20 to 10,000Hz [103, p. 44].

If the fundamental frequencies of a part are known, the magnitude of its response can be found by using the SPL at the relevant octave band [54]. The acoustic *response* of a structure is described by a Power Spectral Density (PSD) plot which is the mean square of acceleration of the structure taken in 1 Hz bands over the given acoustic spectrum.

The launch vehicle's response to acoustic noise can be reported as a PSD plot of the random vibrations that result at the vehicle/ spacecraft interface, though it is not always provided. Indeed, it is only reported for the Soyuz vehicle. For Ariane 5 and Vega, Arianespace simply report that the random vibrations are a combination of the sine-equivalent vibrations and/ or the acoustic vibrations.

Structures with low areal density (mass divided by exposed surface area) respond to acoustic loads most severely, compared to denser, heavier structures. However, these heavier structures can still be excited by the response of the more susceptible structures. Vibroacoustic response often drives the electro-mechanical and electrical components in a spacecraft [103, p. 45]. For small payloads, the majority of the acoustic vibration is transmitted through the launch vehicle interface. For larger payloads the vibroacoustic response is driven by excitation of large appendages such as solar arrays and dishes [103, p. 215]. It is necessary to have a good understanding of the spacecraft configuration and structural properties for vibroacoustic verification [103, p. 47].

The translation of these vibrations to loads on the PMAO is strongly dependent on the coupling between the launch vehicle and spacecraft, both of which are not yet defined. A realistic vibroacoustic analysis is therefore not possible for the PMAO mechanism assembly.

Table D.4 summarises the acoustic environment for the three European launchers. Worst-case filling factor values are taken for Soyuz. Lift-off values are taken for Vega, which are worse than the atmospheric phase, though they last only 3 seconds compared to 55 seconds for the atmospheric phase.

Table D.4 shows that in general, Ariane 5 and Soyuz have higher acoustic noise levels at low to mid frequencies and Vega has higher levels at higher frequencies. These are the design limits and do not have the

Table D.4: Acoustic noise spectra under launcher fairings. OASPL = Overall Acoustic Sound Pressure Level. Reference SPL 0 dB = 2 × $10^{-5} Pa$. Compiled from [5–7].

Octave Centre Frequency	**Flight Limit Level**		
	Ariane 5	**Soyuz**	**Vega**
$[Hz]$	$[dB]$	$[dB]$	$[dB]$
31.5	128	126	112
63	131	133	123
125	136	136	126
250	133	138	135
500	129	134	138
1000	123	125	127
2000	116	121	120
OASPL (20 - 2828 Hz)	139.5	141.9	140.3

recommended 3 dB qualification test margin applied as recommended by the user manuals.

The sine-equivalent dynamics are given in Table D.5. These are present during powered flight, predominantly during atmospheric and transonic phases. These levels apply only when the spacecraft meets the minimum natural frequency requirements.

Table D.5: Sine equivalent dynamics. Compiled from [5–7].

Frequency	**Longitudinal Sine Amplitude**		
	Ariane 5	**Soyuz**	**Vega**
$[Hz]$	$[g]$	$[g]$	$[g]$
1 - 2	N/A	0.4	0.4
2 - 5	1.0	0.4	0.4
5 - 10	1.0	0.5	0.8
10 - 20	1.0	0.8	0.8
20 - 30	1.0	0.8	0.8
30 - 40	1.0	0.5	0.8
40 - 50	1.0	0.5	1.0
50 - 60	0.8	0.5	1.0
60 - 100	0.8	0.3	1.0
100 - 110	N/A	N/A	1.0
110 - 125	N/A	N/A	0.2

Frequency	**Lateral Sine Amplitude**		
	Ariane 5	**Soyuz**	**Vega**
$[Hz]$	$[g]$	$[g]$	$[g]$
1 - 2	N/A	0.4	0.4
2 - 5	0.8	0.4	0.4
5 - 10	0.8	0.6	0.5
10 - 20	0.8	0.6	0.5
20 - 30	0.8	0.4	0.5
30 - 40	0.6	0.4	0.5
40 - 50	0.6	0.3	0.5
50 - 60	0.6	0.3	0.5
60 - 100	0.6	0.3	0.5
100 - 110	N/A	N/A	0.5
110 - 125	N/A	N/A	0.2

Shocks

Shocks are high impulsive loads imparted to a structure by pyrotechnic mechanisms, release mechanisms or instantaneous release of strain energy (ie. thermal shock). Exposure of sensitive equipment can be reduced by using Non-Explosive Actuators (NEA). Shock response is very difficult to verify by analysis even with full vehicle definition. No specific survival requirement relating to shock is given as it cannot be verified at such an early stage of design. It will be assumed that no pyrotechnic shock devices will be used near the DST during payload separation. This is a feasible assumption for now since low shock separation systems or mechanical isolation can be used to reduce or damp shock transmission to the payload [122, p. 841]. Moreover, shocks are dissipated relatively quickly through a structure and the PMAO will be at the end of the load path from the launch vehicle interface to the mirror. For a load path with three or more mechanically fastened joints, the peak shock reduces to approximately 0.22 times the peak at the source [103, p. 407].

E

PMAO Requirements Verification Plan

PMAO Requirements Verification Matrix

** See end of table for description of verification method and factors of safety as well as notes on load cases.*

Activity ID	Requirement		Verification Method*	Assembly Level	Phase/ Configuration	Load Case(s)	Factor of Safety*	Pass Criteria	Comment
	ID	Short Description							
System Level									
VA-01-01	M1-MEC-13	Four segments	IR	Telescope (sum of all items)	All phases & configurations	N/A	N/A	Four segments present	Inspection of design
VA-01-02	M1-MEC-13	Four segments	IR	Telescope (sum of all items)	All phases & configurations	N/A	N/A	Segments can be deployed	Inspection of design
VA-02	PMAO-SYS-02	Combined mass	AN	PMAO Assembly (sum of all items)	All phases & configurations	N/A	N/A	24.8 kg	Estimate from calculation or CAD
VA-03	PMAO-SYS-03	Non-ITAR	IR	PMAO Assembly (sum of all items)	All phases and configurations	N/A	N/A	No ITAR controlled components	Inspect datasheets
VA-04-01	PMAO-SYS-06	No low TRL AIT	SI	PMAO Assembly (sum of all items)	All phases and configurations	N/A	N/A	Minimum feature size 0.5 mm	Inspection of design
VA-04-02	PMAO-SYS-06	No low TRL AIT	SI	PMAO Assembly (sum of all items)	All phases and configurations	N/A	N/A	Standard aerospace materials	Inspection of design
Launch Survival									
VA-05-01	PMAO-MEC-03	Support mirror in launch	IR	PMAO (representative)	Launch/ stowed	N/A	N/A	PMAO-MEC-40-01 to -03 verified	Inspect verification results
VA-05-02	PMAO-MEC-03	Support mirror in launch	IR	PMAO (representative)	Launch/ stowed	N/A	N/A	Support does not over constrain mirror	Inspect support kinematics
VA-05-03	PMAO-MEC-03	Support mirror in launch	AN	PMAO (representative)	Launch/ stowed	N/A	N/A	Support lateral stiffness ≤ 1000x mirror lateral (radial) stiffness	Assumption until mirror design matures. To make sure mirror isolated from mechanism/ support strains.

VA-06	PMAO-MEC-40	Survive launch	IR	PMAO (representative)	Launch/ stowed	N/A	N/A	PMAO-MEC-40-01 to -04 verified	Inspect verification results
VA-06-01-01	PMAO-MEC-40-01	30g XY load	AN	PMAO (representative)	Launch/ stowed	(a)	D (1.0)	MS yield ≥ 0 in members	Finite element analysis
VA-06-01-02	PMAO-MEC-40-01	30g XY load	AN	PMAO (representative)	Launch/ stowed	(a)	D (1.0)	MS buckling ≥ 0 in members	Finite element analysis
VA-06-02-01	PMAO-MEC-40-02	30g XZ load	AN	PMAO (representative)	Launch/ stowed	(a)	D (1.0)	MS yield ≥ 0 in members	Finite element analysis
VA-06-02-02	PMAO-MEC-40-02	30g XZ load	AN	PMAO (representative)	Launch/ stowed	(a)	D (1.0)	MS buckling ≥ 0 in members	Finite element analysis
VA-06-03-01	PMAO-MEC-40-03	30g YZ load	AN	PMAO (representative)	Launch/ stowed	(a)	D (1.0)	MS yield ≥ 0 in members	Finite element analysis
VA-06-03-02	PMAO-MEC-40-03	30g YZ load	AN	PMAO (representative)	Launch/ stowed	(a)	D (1.0)	MS buckling ≥ 0 in members	Finite element analysis
VA-06-04	PMAO-MEC-40-04	Natural frequency > 100 Hz	AN	PMAO (representative)	Launch/ stowed	N/A	N/A	$\omega_1 \geq 100$ Hz	Finite element analysis.
VA-07	PMAO-ELE-01	No power in launch	IR	PMAO (representative)	Launch/ stowed	N/A	N/A	PMAO-MEC-03 and -40 met without power	Inspect design drawings, concept, verification results
Operations Survival									
VA-08-01	PMAO-MEC-04	Support mirror in operations	IR	PMAO (representative)	AIT/ LEOP/ imaging. Stowed & deployed	N/A	N/A	PMAO-MEC-03 and PMAO-MEC-40 verified.	Assume if can support mirror in launch, can do so in operations.
VA-08-02	PMAO-MEC-04	Support mirror in operations	AN	M1 + PMAO (representative)	AIT/ LEOP/ imaging. Stowed & deployed	(b)	Q (±25 K)	MS yield ≥ 0 in mirror support	Hand calculations for mirror support
VA-09-01	PMAO-MEC-41	Survive operations stowed & deployed	IR	PMAO (representative)	AIT/ LEOP/ imaging. Stowed & deployed	N/A	N/A	PMAO-MEC-40 verified.	Assumptions per VA-08-01
VA-09-02	PMAO-MEC-41	Survive operations	IR	PMAO (representative)	AIT/ LEOP/ imaging.	N/A	N/A	PMAO-MEC-41-01 verified.	

		stowed & deployed			Stowed & deployed				
VA-09-03	PMAO-MEC-41	Survive operations stowed & deployed	AN	PMAO (representative)	Imaging, deployed.	(c)	D(1.25)	MS yield ≥ 0 in all members	Actuation loads
VA-10	PMAO-MEC-41-01	Survive steady state LEOP temperatures	AN	PMAO (representative)	AIT/ LEOP/ imaging. Stowed & deployed	(d)	Q (±25 K)	MS yield ≥ 0 in all relevant PMAO components	Thermal loads. Hand calculations for all relevant PMAO components
VA-11	PMAO-MEC-42	Survive deployment	IR	PMAO (representative)	LEOP stowed/ deployed	N/A	N/A	Expected deployment loads less than launch	Compare expected deployment loads (derived by others) to launch loads
Operations Functionality									
VA-12	M1-MEC-01	Deployment tolerance budget	AN	M1 segment assembly (representative)	LEOP, stowed & deployed	N/A	N/A	Top down system tolerance budget	Stochastic analysis (FORTA/ ETEP model) or estimate by hand calculation
VA-13	M1-MEC-04	In orbit drift budget	AN	M1 segment assembly (representative)	Imaging, deployed	Operations temperature per M1-MEC-15	D (±15 K)	Top down system tolerance budget	Finite element analysis or estimate by hand calculation
VA-14	M1-MEC-07	Stability budget	AN	M1 segment assembly (representative)	Imaging, deployed	On board excitations	N/A	Top down system tolerance budget	Finite element analysis or estimate by hand calculation
VA-15	M1-MEC-14	M1 location	IR	Telescope	Imaging, deployed	N/A	N/A	1600 mm	Inspect mechanical drawings
VA-16	M1-MEC-17	Deployment, PMAO usable volume	IR	M1 segment assembly (representative)	Launch/ LEOP stowed	N/A	N/A	120 mm clearance	Inspect mechanical drawings

VA-17	PMAO-MEC-35	Thermal centre location	AN or IR	M1 segment assembly (representative)	Imaging, deployed	Operations temperature per M1-MEC-15	D (±15 K)	x, y in orbit drift top down system budget	Finite element analysis or estimate by hand calculation
VA-18-01	PMAO-MEC-50	PMAO usable volume	IR	M1 segment assembly (representative)	LEOP (stowed), imaging (deployed)	N/A	N/A	PMAO does not conflict with deployment mechanism action	Inspection of mechanical design (CAD/ drawings)
VA-18-02	PMAO-MEC-50-01	PMAO usable volume	IR	M1 segment assembly (representative)	LEOP (stowed), imaging (deployed)	N/A	N/A	PMAO does not conflict with deployment mechanism action	Inspection of mechanical design (CAD/ drawings)
VA-19-01	M1-MEC-15	Operations temperature requirement	SI	M1 segment assembly (representative)	Imaging (deployed)	298 ± 1K	D (±15 K)	Component allowable temperature range meets design temps in vacuum	Compare components to others that have already been space qualified at these temps
VA-19-02	M1-MEC-15	Operations temperature requirement	IR	M1 segment assembly (representative)	Imaging (deployed)	298 ± 1K	D (±15 K)	Operations functionality requirements met at design temps	Inspection of operations functionality verification results and inputs
VA-20	PMAO-OPT-01	Remove discontinuous wavefront errors	AN	Telescope	Imaging (deployed)	N/A	N/A	Strehl Ratio > 0.80	ETEP modelling in FORTA
VA-21	PMAO-MEC-01	3DOF control	AN	M1 segment assembly (representative)	Imaging (deployed)	N/A	N/A	Mathematical proof that actuators can controllably manipulate mechanism in 3DOFs	Hand calculations, physical modelling or finite element analysis

VA-22	PMAO-MEC-23	Segment level step size	AN	M1 segment assembly (representative)	Imaging (deployed)	N/A	N/A	10 nm step size in piston	Finite element analysis
VA-23	PMAO-MEC-29	Segment level tilt range of motion	AN	M1 segment assembly (representative)	Imaging (deployed)	N/A	N/A	± 2 µrad	Finite element analysis
VA-24	PMAO-MEC-30	Segment level tip range of motion	AN	M1 segment assembly (representative)	Imaging (deployed)	N/A	N/A	± 4 µrad	Finite element analysis
VA-25	PMAO-MEC-31	Segment level piston range of motion	AN	M1 segment assembly (representative)	Imaging (deployed)	N/A	N/A	± 4 µm	Finite element analysis
VA-26	PMAO-MEC-32	PMAO actuator range of motion	IR	Actuator (representative)	Imaging (deployed)	N/A	N/A	± 9.918 µm	Inspection of datasheet
VA-27	PMAO-MEC-33	PMAO actuator step size	IR	Actuator (representative)	Imaging (deployed)	N/A	N/A	10 nm	Inspection of datasheet

Load Cases

(a) Launch Loads: two separate 30g quasi static launch loads applied in indicated directions. Launch loads are applied in the worst case combination of positive/ negative directions in axes of interest for each verification activity. Assume 30g load is inclusive of thermal loads and all necessary safety factors.
(b) Maximum differential thermo-elastic strain between mirror and support in worst case (steady state) min/ max LEOP temps. See DST-WP1-CALC-001.
(c) Maximum actuation loads: the mechanism is actuated to the edge of the workspace, simultaneous displacement to the greatest tip, tilt and piston ranges of motion.
(d) Maximum thermo-elastic strain for over constrained components in worst case (steady state) min/ max LEOP temps. See DST-WP1-CALC-001.

Factors of Safety	**Method**
D – design	AN – Analysis
A - acceptance	IR – Inspection/ Review
Q – qualification	TE – Test
	SI – Similarity
	DE - Demonstration

F

PMAO Baseline Transmission Flexure FEA Results

	Δy_{top} = 0 µm Δz_{mid} = 100 µm	Δy_{top} = 0.209 µm Δz_{mid} = 100 µm
Equivalent Stress (von Mises) σ_y= 880MPa	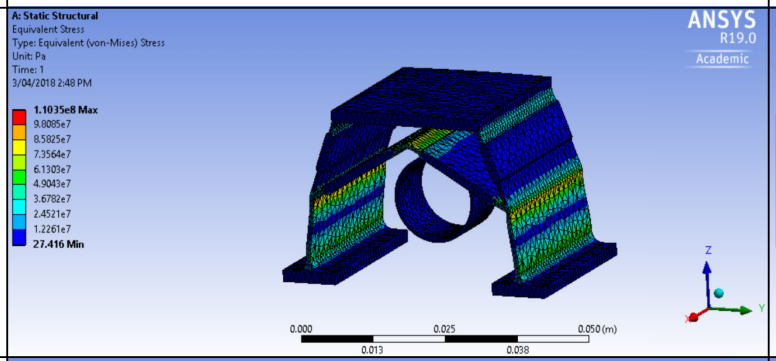	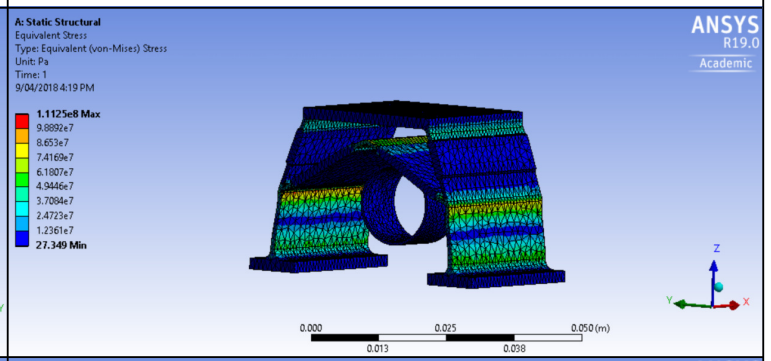
Directional Deformation ±z *top face*	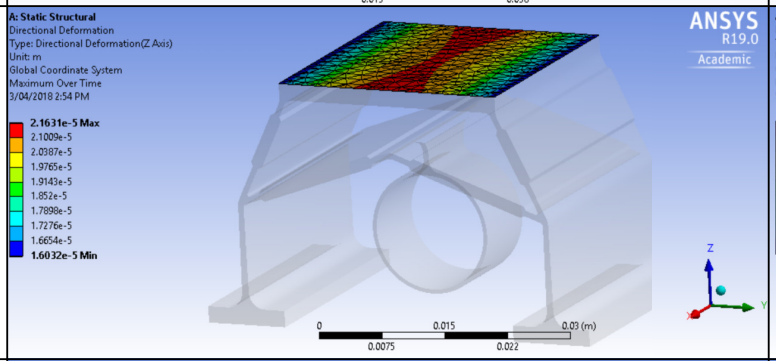	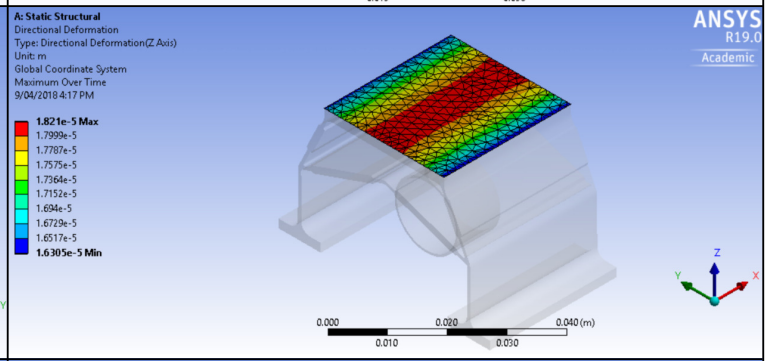
Total Deformation	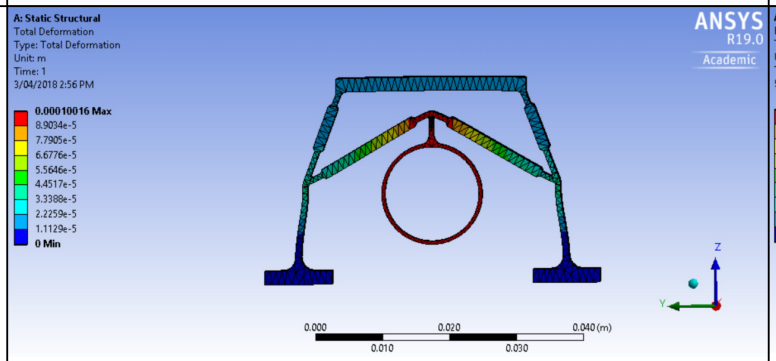	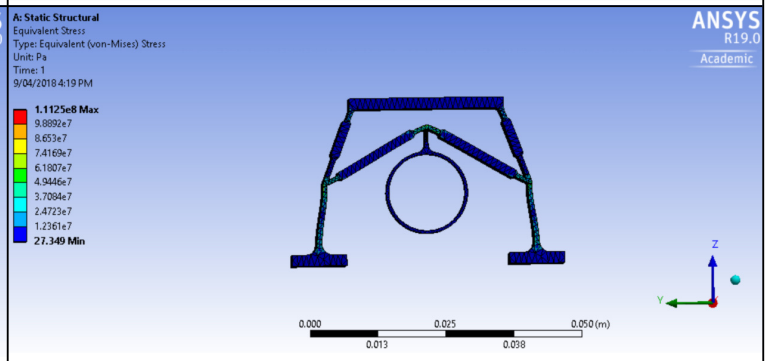

Figure F.1: Extract of results from finite element analysis of baseline transmission flexure.

G

Actuator Strength and Stroke Requirement Calculations

Included in this appendix are the calculations used to flow down the strength and stroke requirements for the NLA and PPA actuators in concepts A and B for the overall mechanism architecture, discussed in Chapter 7 *Mechanism Architecture Selection*.

G.1. Concept A: 3x NLA Actuator Assemblies

G.1.1. Launch Load Calculations

These calculations continue from the assumptions set out for concept A in Subsection 7.3.2.

In-Plane Loads

First consider an in-plane load in the $+X_{MF}$ direction, illustrated in Figure 7.8. In this instance the reaction loads R_I, R_{II}, R_{III} are calculated via

$$\sum F_{Z_{MF}} = 0 \tag{G.1}$$

$$R_I + R_{II} + R_{III} = 0 \tag{G.2}$$

$$\sum M_{Y_{MF}} = 0 \tag{G.3}$$

$$M_L - R_I(s_1 + s_2) = 0 \tag{G.4}$$

$$\therefore R_I = \frac{M_L}{s_1 + s_2} \tag{G.5}$$

$$\sum M_{X_{MF}} = 0 \tag{G.6}$$

$$+R_I s_3 + R_{III}(s_3 + s_4) = 0 \tag{G.7}$$

$$\therefore R_{III} = -\frac{s_3}{s_3 + s_4} R_I \tag{G.8}$$

$$-R_{III}\frac{s_3 + s_4}{s_3} + R_{II} + R_{III} = 0 \tag{G.9}$$

$$\therefore R_{II} = \frac{s_4}{s_3} R_{III} \tag{G.10}$$

With the geometry as shown in Figure 7.8,

$$s_1 = \frac{R_M}{2} \tag{G.11}$$

$$s_2 = R_M \tag{G.12}$$

$$s_3 = s_4 = \frac{3}{2\sqrt{3}} R_M \tag{G.13}$$

Such that for a load F_L in the $+X_{MF}$ direction,

$$R_I = \frac{2}{3}\frac{M_L}{R_M} \tag{G.14}$$

$$R_{II} = R_{III} = -\frac{1}{3}\frac{M_L}{R_M} \tag{G.15}$$

A similar process for a load F_L in the $+Y_{MF}$ direction gives

$$R_{II} = -R_{III} = \frac{M_L}{s_3 + s_4} = \frac{\sqrt{3}}{3}\frac{M_L}{R_M} \tag{G.16}$$

$$R_I = 0 \tag{G.17}$$

Reactions for the $-X_{MF}$ and $-Y_{MF}$ load cases are found by reversing the sign in the above results. Combining the results above, Table G.1 summarises the net reaction forces on the moving frame, imposed by the actuators for each of the four possible in-plane load cases.

Table G.1: Summary of in-plane reaction loads on moving frame for initial piezoelectric actuator selection. The first two columns indicate the direction of the launch loads F_L along each of the X_{MF} & Y_{MF} axes.

$F_{L,X_{MF}}$	$F_{L,Y_{MF}}$	R_I	R_{II}	R_{III}
-	+	$\frac{-2M_L}{3R_M}$	$\frac{1+\sqrt{3}}{3}\frac{M_L}{R_M}$	$\frac{1-\sqrt{3}}{3}\frac{M_L}{R_M}$
-	-	$\frac{-2M_L}{3R_M}$	$\frac{1-\sqrt{3}}{3}\frac{M_L}{R_M}$	$\frac{1+\sqrt{3}}{3}\frac{M_L}{R_M}$
+	+	$\frac{2M_L}{3R_M}$	$\frac{-1+\sqrt{3}}{3}\frac{M_L}{R_M}$	$\frac{-1-\sqrt{3}}{3}\frac{M_L}{R_M}$
+	-	$\frac{2M_L}{3R_M}$	$\frac{-1-\sqrt{3}}{3}\frac{M_L}{R_M}$	$\frac{-1+\sqrt{3}}{3}\frac{M_L}{R_M}$

The reaction loads indicated in Table G.1 are equal in magnitude but opposite in direction to the loads experienced by the actuators. The largest loads experienced by the actuators due to an external in-plane load are therefore

$$F_{max,in-plane} = \pm\left(\frac{1+\sqrt{3}}{3}\frac{M_L}{R_M}\right) \tag{G.18}$$

Where a positive load indicates compression in the actuator. These loads occur in actuator II for the $-X_{MF}, +Y_{MF}$ and $+X_{MF}, -Y_{MF}$ load cases and in actuator III in the $-X_{MF}, -Y_{MF}$ and $+X_{MF}, +Y_{MF}$ load cases.

Out of Plane Loads

By inspection of equations G.14 to G.17, it can be seen that the largest reaction force due to a *single* external in-plane load occurs in actuator I in response to either of the $\pm X_{MF}$ load cases, since $s_1 + s_2 < s_3 + s_4$.

Either of the $\pm Z_{MF}$ out of plane loads are distributed evenly between each of the actuators. Therefore the largest loads experienced by an actuator in the eight out of plane load cases is given by

$$F_{max,out-plane} = \pm\left(\frac{1}{3}F_L + \frac{2}{3}\frac{M_L}{R_M}\right) \tag{G.19}$$

Recall that the launch survival requirements stipulate $30g$ accelerations with g the acceleration due to gravity such that $F_L = 30g m_M$ with m_M the estimated mass of a single M1 mirror segment, moment $M_L = F_L h$ and h as shown in Figure 7.8. Tension in the actuator is indicated by a negative sign.

Overall Maximum Launch Load

Equating equations G.18 and G.19 shows that these two loads will be equal when $h/R_M = 1.366$, with the greatest load case on an actuator given by

$$For\ \frac{h}{R_M} < 1.366, |F_{max,in-plane}| < |F_{max,out-plane}| \tag{G.20}$$

$$For\ \frac{h}{R_M} > 1.366, |F_{max,in-plane}| > |F_{max,out-plane}| \tag{G.21}$$

The worst-case launch load is when h is large. The centre of mass of the mirror segment is approximately 28 mm from the backplane of the mirror in the Z_M direction and the maximum available distance from the mirror backplane to the moving frame is 120 mm, limited by the current design of the M1 deployment mechanism and the location of the instrument housing wall in the stowed configuration. Therefore the largest value for h is roughly 150 mm and likely to be smaller.

For the actuator loads, it is desirable for R_M to be as large as possible. Since the mirror segment is 450 mm wide the largest possible value for R_M such that all three actuators fit within the periphery of the segment is $\frac{\sqrt{3}}{3} * 450 \approx 260\ mm$. An initial estimate of the *minimum* allowable mounting radius is 100 mm, limited by the spacing needed to physically fit the actuators, in-plane constraints and support bipods next to each other. The actuator mounting radius drives the size of the moving frame and thereby the whole mechanism. It is a strong driver of overall mechanism mass and should be as small as practical.

With the estimates for the maximal h and R_M, the ratio h/R_M is therefore likely to be in the range 0.77 $\leq h/R_M \leq$ 1.50 and the out of plane launch loads should dominate in most design scenarios.

The width of the current deployment support frame is 250 mm, dictated by the width of the instrument housing and volume reserved for the stowed M2 booms. To fit the mechanism on the existing support frame, an initial estimate of R_M = 125 mm was taken, giving h/R_M = 1.2. Assuming a mirror mass of 6 kg per the original baseline design, equation G.19 gives a maximum load of 2,000 N to be withstood by an actuator during launch. This mounting radius is also compatible with the configuration in Concept B to ensure a like-for-like comparison of performance.

G.1.2. Inverse Position Kinematic Calculations

The derivation of the linearised inverse position kinematics concept A continues here from the definition of coordinate frames in Subsection 7.3.3.

Homogeneous Transform Matrix

The position ${}^{\mathbf{M}}\mathbf{p}$ of a point p in the fixed mechanism coordinate frame $\mathbf{O_M}$ is given by

$$ {}^{\mathbf{M}}\mathbf{p} = {}^{\mathbf{M}}\mathbf{r_{MF}} + \mathbf{R_{M/MF}}.{}^{\mathbf{MF}}\mathbf{p} \tag{G.22} $$

where ${}^{\mathbf{M}}\mathbf{r_{MF}}$ is the position of the origin of segment frame $\mathbf{O_{MF}}$ with respect to mechanism frame $\mathbf{O_M}$, $\mathbf{R_{M/MF}}$ is a rotation matrix describing the rotation of $\mathbf{O_{MF}}$ with respect to $\mathbf{O_M}$ and ${}^{\mathbf{MF}}\mathbf{p}$ is the position of point p in the mobile body fixed coordinate frame $\mathbf{O_{MF}}$. The preceding superscripts M, MF indicate the coordinate frame in which the vector is given.

The rotation matrix $\mathbf{R_{M/MF}}$ is given by two consecutive rotations $\theta_{x,M}$ then $\theta_{y,M}$ about the X_M and Y_M axes respectively:

$$ \begin{aligned} \mathbf{R_{M/MF}} &= \begin{bmatrix} cos(\theta_{y,M}) & 0 & sin(\theta_{y,M}) \\ 0 & 1 & 0 \\ -sin(\theta_{y,M}) & 0 & cos(\theta_{y,M}) \end{bmatrix} . \begin{bmatrix} 1 & 0 & 0 \\ 0 & cos(\theta_{x,M}) & -sin(\theta_{x,M}) \\ 0 & sin(\theta_{x,M}) & cos(\theta_{x,M}) \end{bmatrix} \\ &= \begin{bmatrix} cos(\theta_{y,M}) & sin(\theta_{x,M})sin(\theta_{y,M}) & cos(\theta_{x,M})sin(\theta_{y,M}) \\ 0 & cos(\theta_{x,M}) & -sin(\theta_{x,M}) \\ -sin(\theta_{y,M}) & sin(\theta_{x,M})cos(\theta_{y,M}) & cos(\theta_{x,M})cos(\theta_{y,M}) \end{bmatrix} \end{aligned} \tag{G.23} $$

The position ${}^{\mathbf{M}}\mathbf{r_{MF}}$ of frame $\mathbf{O_{MF}}$ with respect to frame $\mathbf{O_M}$ is simply a piston translation $\Delta_{z,M}$

$$ {}^{\mathbf{M}}\mathbf{r_{MF}} = \{0, 0, \Delta_{z,M}\}^T \tag{G.24} $$

Then

$$\left[\begin{array}{c} {}^{\mathbf{M}}\mathbf{p} \\ \hline 1 \end{array}\right] = \left[\begin{array}{ccc|c} 1 & 0 & 0 & \\ 0 & 1 & 0 & {}^{\mathbf{M}}\mathbf{r}_{\mathbf{MF}} \\ 0 & 0 & 1 & \\ \hline 0 & 0 & 0 & 1 \end{array}\right] \cdot \left[\begin{array}{ccc|c} & \mathbf{R}_{\mathbf{M/MF}} & & \begin{matrix}0\\0\\0\end{matrix} \\ \hline 0 & 0 & 0 & 1 \end{array}\right] \cdot \left[\begin{array}{c} {}^{\mathbf{MF}}\mathbf{p} \\ \hline 1 \end{array}\right]$$

$$= \mathbf{T}_{\mathbf{M/MF}} \cdot \left[\begin{array}{c} {}^{\mathbf{MF}}\mathbf{p} \\ \hline 1 \end{array}\right] \tag{G.25}$$

where $\mathbf{T_{M/MF}}$ is the homogeneous transformation matrix (HTM) for piston motion $\Delta_{z,M}$, tilt $\theta_{x,M}$ and tip $\theta_{y,M}$, given by

$$\mathbf{T}_{\mathbf{M/S}} = \left[\begin{array}{c|c} \mathbf{R}_{\mathbf{M/S}} & {}^{\mathbf{M}}\mathbf{r}_{\mathbf{S}} \\ \hline \mathbf{0} & \mathbf{1} \end{array}\right] \tag{G.26}$$

$$= \left[\begin{array}{ccc|c} cos(\theta_{y,M}) & sin(\theta_{x,M})sin(\theta_{y,M}) & cos(\theta_x)sin(\theta_{y,M}) & 0 \\ 0 & cos(\theta_{x,M}) & -sin(\theta_{x,M}) & 0 \\ -sin(\theta_{y,M}) & sin(\theta_{x,M})cos(\theta_{y,M}) & cos(\theta_x)cos(\theta_{y,M}) & \Delta_{z,M} \\ \hline 0 & 0 & 0 & 1 \end{array}\right] \tag{G.27}$$

$$= \left[\begin{array}{cccc} 1 & 0 & \theta_{y,M} & 0 \\ 0 & 1 & -\theta_{x,M} & 0 \\ -\theta_{y,M} & \theta_{x,M} & 1 & \Delta_{z,M} \\ \hline 0 & 0 & 0 & 1 \end{array}\right] \tag{G.28}$$

The approximations $sin(\theta) \approx \theta$, $cos(\theta) \approx 1$ have been applied since all motions are very small.

The transformation $\mathbf{T_{M/MF}}$ is used to describe the translation and rotation of coordinate system $\mathbf{O_{MF}}$ relative to frame $\mathbf{O_M}$. The HTM is applicable to position vectors only.

Joint Positions

Since the FACT synthesis requires that the actuator links all be parallel to provide the requisite motions, $\alpha = \beta$ and $R_{MF} = R_M$. The positions of joints D, E and F with respect to coordinate system $\mathbf{O_{MF}}$ are defined by

$${}^{\mathbf{MF}}\mathbf{r}_{\mathbf{D}} = \left\{\begin{array}{c} R_M cos(\alpha) \\ R_M sin(\alpha) \\ 0 \end{array}\right\} \tag{G.29}$$

$${}^{\mathbf{MF}}\mathbf{r}_{\mathbf{E}} = \left\{\begin{array}{c} -\frac{R_M}{2}cos(\alpha) - \frac{\sqrt{3}}{2}R_M sin(\alpha) \\ -\frac{R_M}{2}sin(\alpha) + \frac{\sqrt{3}}{2}R_M cos(\alpha) \\ 0 \end{array}\right\} \tag{G.30}$$

$${}^{\mathbf{MF}}\mathbf{r}_{\mathbf{F}} = \left\{\begin{array}{c} -\frac{R_M}{2}cos(\alpha) + \frac{\sqrt{3}}{2}R_M sin(\alpha) \\ -\frac{R_M}{2}sin(\alpha) - \frac{\sqrt{3}}{2}R_M cos(\alpha) \\ 0 \end{array}\right\} \tag{G.31}$$

The positions can then be given in the mechanism world coordinate system $\mathbf{O_M}$ with

$$\left[\begin{array}{c} {}^{\mathbf{M}}\mathbf{r}_{\mathbf{D\to F}} \\ \hline 1 \end{array}\right] = \mathbf{T}_{\mathbf{M/MF}} \cdot \left[\begin{array}{c} {}^{\mathbf{MF}}\mathbf{r}_{\mathbf{D\to F}} \\ \hline 1 \end{array}\right] \tag{G.32}$$

The positions of joints A, B and C in $\mathbf{O_M}$ are similarly:

$$ {}^{\mathbf{M}}\mathbf{r_A} = \begin{Bmatrix} R_M cos(\alpha) \\ R_M sin(\alpha) \\ 0 \end{Bmatrix} \tag{G.33} $$

$$ {}^{\mathbf{M}}\mathbf{r_B} = \begin{Bmatrix} -\frac{R_M}{2} cos(\alpha) - \frac{\sqrt{3}}{2} R_M sin(\alpha) \\ -\frac{R_M}{2} sin(\alpha) + \frac{\sqrt{3}}{2} R_M cos(\alpha) \\ 0 \end{Bmatrix} \tag{G.34} $$

$$ {}^{\mathbf{M}}\mathbf{r_C} = \begin{Bmatrix} -\frac{R_M}{2} cos(\alpha) + \frac{\sqrt{3}}{2} R_M sin(\alpha) \\ -\frac{R_M}{2} sin(\alpha) - \frac{\sqrt{3}}{2} R_M cos(\alpha) \\ 0 \end{Bmatrix} \tag{G.35} $$

Actuator Link Lengths

The length L_i of each actuated leg for a desired pose is given by the distance between the two joints of each actuated leg:

$$ \begin{aligned} L_I &= \left| {}^{\mathbf{M}}\mathbf{r_D} - {}^{\mathbf{M}}\mathbf{r_A} \right| \\ &= \left(\left(R_M \theta_{x,M} \theta_{y,M} sin(\alpha) \right)^2 + \left(\Delta_{z,M} + R_M \theta_{x,M} sin(\alpha) - R_M \theta_{y,M} cos(\alpha) \right)^2 \right)^{1/2} \end{aligned} \tag{G.36} $$

$$ \begin{aligned} L_{II} &= \left| {}^{\mathbf{M}}\mathbf{r_E} - {}^{\mathbf{M}}\mathbf{r_B} \right| \\ &= \left(\left(\theta_{x,M} \theta_y \frac{R_M}{2} \left(\sqrt{3} cos(\alpha) - sin(\alpha) \right) \right)^2 + \left(\Delta_{z,M} + \theta_{x,M} \frac{R_M}{2} \left(\sqrt{3} cos(\alpha) - sin(\alpha) \right) + \theta_{y,M} \frac{R_M}{2} \left(cos(\alpha) + \sqrt{3} sin(\alpha) \right) \right)^2 \right)^{1/2} \end{aligned} \tag{G.37} $$

$$ \begin{aligned} L_{III} &= \left| {}^{\mathbf{M}}\mathbf{r_F} - {}^{\mathbf{M}}\mathbf{r_C} \right| \\ &= \left(\left(\theta_{x,M} \theta_{y,M} \frac{R_M}{2} \left(-\sqrt{3} cos(\alpha) - sin(\alpha) \right) \right)^2 + \left(\Delta_{z,M} + \theta_{x,M} \frac{R_M}{2} \left(-\sqrt{3} cos(\alpha) - sin(\alpha) \right) + \theta_{y,M} \frac{R_M}{2} \left(cos(\alpha) - \sqrt{3} sin(\alpha) \right) \right)^2 \right)^{1/2} \end{aligned} \tag{G.38} $$

These are the analytical expressions for the inverse kinematic relations, giving the actuator lengths required to achieve a desired segment pose. They are non-linear and cannot be easily inverted to get exact analytical equations for the forward kinematics.

Linearised Inverse Position Kinematic Equations

Equations G.36-G.38 can be linearised for small motions of the segment $\Delta\mathbf{P}$ about the initial position of the segment ${}^{\mathbf{M}}\mathbf{r_{MF,0}}$.

Linearisation is achieved by finding the derivative of the function $\Delta\mathbf{L}$ at the initial pose ${}^{\mathbf{M}}\mathbf{r_{MF,0}}$ by using the Jacobian matrix $\mathbf{J}$ of $\Delta\mathbf{L}$

$$ \mathbf{J} = \begin{bmatrix} \frac{\partial L_I}{\partial \Delta_{z,M}} & \frac{\partial L_I}{\partial \theta_{x,M}} & \frac{\partial L_I}{\partial \theta_{y,M}} \\ \frac{\partial L_{II}}{\partial \Delta_{z,M}} & \frac{\partial L_{II}}{\partial \theta_{x,M}} & \frac{\partial L_{II}}{\partial \theta_{y,M}} \\ \frac{\partial L_{III}}{\partial \Delta_{z,M}} & \frac{\partial L_{III}}{\partial \theta_{x,M}} & \frac{\partial L_{III}}{\partial \theta_{y,M}} \end{bmatrix} \tag{G.39} $$

The Jacobian matrix of the function $\Delta\mathbf{L}$ gives a linear approximation of $\Delta\mathbf{L}$ at the point ${}^{\mathbf{M}}\mathbf{r_{MF,0}}$.

Assuming no assembly errors or offsets caused by launch, thermo-elastic expansion, creep and other non-ideal effects, the initial pose ${}^{\mathbf{M}}\mathbf{r_{MF,0}} = \{\Delta_{z,M0}, \theta_{x,M0}, \theta_{y,M0}\}$ of $\mathbf{O_{MF}}$ with respect to $\mathbf{O_M}$ is given by

$$ {}^{\mathbf{M}}\mathbf{r_{MF,0}} = \{l_0, 0, 0\}^T \tag{G.40} $$

for $l_0 > 0$. Then the required actuator length increment $\Delta\mathbf{L} = \{\Delta L_I, \Delta L_{II}, \Delta L_{III}\}$ for a desired small perturbing pose change $\Delta\mathbf{P}$ can be found with

$$\Delta \mathbf{L} = \mathbf{J}|_{\{l_0,0,0\}} \Delta \mathbf{P} \tag{G.41}$$

where

$$\mathbf{J}|_{\{l_0,0,0\}} = \begin{bmatrix} 1 & R_M sin(\alpha) & -R_M cos(\alpha) \\ 1 & \frac{R_M}{2}\left(\sqrt{3}cos(\alpha) - sin(\alpha)\right) & \frac{R_M}{2}\left(cos(\alpha) + \sqrt{3}sin(\alpha)\right) \\ 1 & -\frac{R_M}{2}\left(\sqrt{3}cos(\alpha) + sin(\alpha)\right) & \frac{R_M}{2}\left(cos(\alpha) - \sqrt{3}sin(\alpha)\right) \end{bmatrix} \tag{G.42}$$

Giving

$$\Delta L_I = R_M\left(sin(\alpha)\theta_{x,M} - cos(\alpha)\theta_{y,M}\right) + \Delta_{z,M} \tag{G.43}$$

$$\Delta L_{II} = \frac{R_M}{2}\left(\left(\sqrt{3}cos(\alpha) - sin(\alpha)\right)\theta_{x,M} + \left(cos(\alpha) + \sqrt{3}sin(\alpha)\right)\theta_{y,M}\right) + \Delta_{z,M} \tag{G.44}$$

$$\Delta L_{III} = \frac{R_M}{2}\left(\left(-\sqrt{3}cos(\alpha) - sin(\alpha)\right)\theta_{x,M} + \left(cos(\alpha) - \sqrt{3}sin(\alpha)\right)\theta_{y,M}\right) + \Delta_{z,M} \tag{G.45}$$

Equations G.43 to G.45 give the linearised inverse kinematic relations, valid for small motions.

G.2. Concept B: 4x PPA Actuators

G.2.1. Launch Load Calculations

The load calculation continues from the introduction in Subsection 7.4.2.

In-Plane Loads

Consider an in-plane load in the $+X_{MF}$ direction as illustrated in figure 7.13. Assuming quasi-static equilibrium conditions, the following relations hold:

$$\sum F_{Z_{MF}} = 0 \tag{G.46}$$

$$= R_I + R_{II} + R_{III} + R_{IV} \tag{G.47}$$

$$\sum M_{Y_{MF}} = 0 \tag{G.48}$$

$$= M_L + R_{III}s_1 - R_I s_2 \tag{G.49}$$

From inspection of the geometry, the moment arm of R_{II} and R_{IV} with respect to the line of action of load F_L is zero such that the moment M_L can be reacted by loads R_I and R_{III} only. Thus, noting that $s_1 = s_2 = R_M$,

$$R_{III} = -\frac{M_L}{2R_M} \tag{G.50}$$

$$R_I = -R_{III} \tag{G.51}$$

$$R_{II} = R_{IV} = 0 \tag{G.52}$$

From symmetry, similar relationships hold for the reaction forces for launch loads F_L applied in the $+Y_{MF}$ direction. That is,

$$R_{II} = -\frac{1}{2}\frac{M_L}{R_M} \tag{G.53}$$

$$R_{IV} = -R_{II} \tag{G.54}$$

$$R_I = R_{III} = 0 \tag{G.55}$$

For launch loads F_L applied in the $-X_{MF}$ and $-Y_{MF}$ directions, the signs of each of the above results need only be reversed.

The worst-case loads experienced by an actuator due to in-plane launch loads are therefore

$$F_{max,in-plane} = \pm\frac{1}{2}\frac{M_L}{R_M} = \pm\frac{30gm_M h}{2R_M} \tag{G.56}$$

Out of Plane Loads

From symmetry, an out of plane launch load in the $\pm Z_{MF}$ direction will be reacted equally by the four actuators such that

$$R_I = R_{II} = R_{III} = R_{IV} = \pm\frac{F_L}{4} \tag{G.57}$$

For a combination of launch loads in the $\pm Z_{MF}$ direction and either of the $\pm X_{MF}$ or $\pm Y_{MF}$ directions, the worst-case out of plane loading on an actuator, recalling the results found above, is

$$F_{max,out-plane} = \pm\left(\frac{F_L}{4} + \frac{1}{2}\frac{M_L}{R_M}\right) \tag{G.58}$$

Overall Maximum Launch Load

Comparison of equations G.56 and 7.29 show that the largest load on an actuator will be for the out of plane load cases.

G.2.2. Inverse Position Kinematic Calculations

This section derives the linearised position kinematics. As for the kinematics of concept A, the joint positions are first found in the mechanism coordinate frame $\mathbf{O_M}$ using the linearised homogeneous transformation matrix. The transformation matrix is modified to account for the new position ${}^{\mathbf{M}}\mathbf{r_{MF}}$ of frame $\mathbf{O_{MF}}$ with respect to frame $\mathbf{O_M}$. There is a sign change in the $\Delta_{z,M}$ coordinate to give

$${}^{\mathbf{M}}\mathbf{r_{MF}} = \{0, 0, -\Delta_{z,M}\}^T \tag{G.59}$$

Next, the required actuator length for a given pose is found using the Euclidean norm between the two connected joints. The analytic inverse kinematic equations are linearised about the initial position ${}^{\mathbf{M}}\mathbf{r_{MF,0}} = \{l_0, 0, 0\}^T$, which can then be used to calculate the flow down requirements for the actuators.

Coordinate Systems

The origin $\mathbf{O_M}$ of the mechanism coordinate frame is fixed to the fixed frame and resides in the plane of the joints mating the actuators to the fixed frame. The origin $\mathbf{O_{MF}}$ of the moving frame coordinate frame is fixed to the moving frame in the plane of the joints attaching the actuators to the moving frame. The orientation and notation of the coordinate systems remain unchanged from concept A as illustrated in Figure G.1.

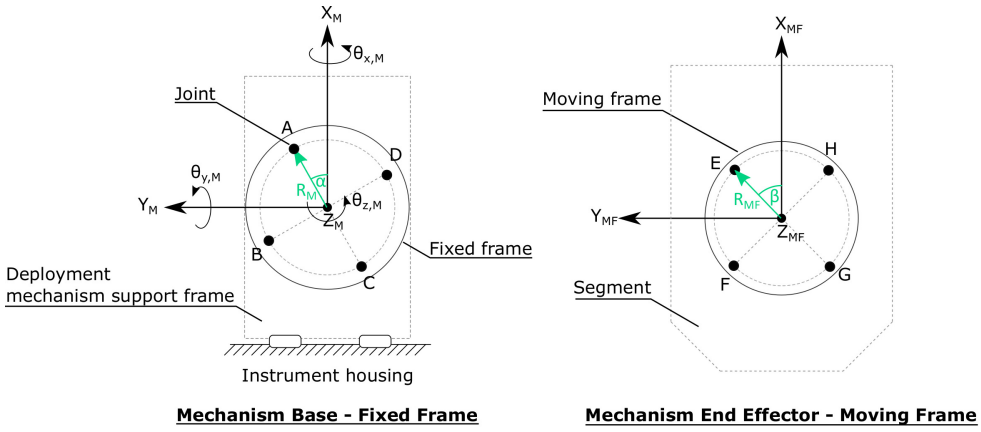

Figure G.1: Projected geometry of the 3DOF mechanism for concept B. The centre of the mounting circle for the joints coincides with the projection of the centroid of the M1 segment to the fixed and moving frame interface planes. The orientation can be adjusted through angles α and β on the mechanism fixed and moving frame respectively. Joint attachments are on circles of radius R_M and R_{MF} respectively. Segment and base (deployment support frame) outline shown to illustrate orientation of coordinate frames.

Joint Positions

The geometry for concept B is shown schematically in G.1. The four actuators mate with the mechanism base at joints A, B, C and D and the segment at joints E, F, G and H. Radii R_M, R_{MF}, angles α, β and coordinate frames $\mathbf{O_M}, \mathbf{O_{MF}}$ are defined as for the concept A geometry. Similarly, since the FACT synthesis requires that

the actuator links all be parallel, $\alpha = \beta$ and $R_{MF} = R_M$. The joints are equally spaced about the mounting radii. The positions of joints E, F, G and H with respect to coordinate system $\mathbf{O_{MF}}$ are defined by

$$^{\mathbf{MF}}\mathbf{r_E} = \begin{Bmatrix} R_M cos(\alpha) \\ R_M sin(\alpha) \\ 0 \end{Bmatrix} \tag{G.60}$$

$$^{\mathbf{MF}}\mathbf{r_F} = \begin{Bmatrix} -R_M sin(\alpha) \\ R_M cos(\alpha) \\ 0 \end{Bmatrix} \tag{G.61}$$

$$^{\mathbf{MF}}\mathbf{r_G} = \begin{Bmatrix} -R_M cos(\alpha) \\ -R_M sin(\alpha) \\ 0 \end{Bmatrix} \tag{G.62}$$

$$^{\mathbf{MF}}\mathbf{r_H} = \begin{Bmatrix} R_M sin(\alpha) \\ -R_M cos(\alpha) \\ 0 \end{Bmatrix} \tag{G.63}$$

The positions can then be given in the mechanism world coordinate system $\mathbf{O_M}$ with

$$\begin{bmatrix} ^{\mathbf{M}}\mathbf{r_{D\to F}} \\ \hline 1 \end{bmatrix} = \mathbf{T_{M/MF}} \cdot \begin{bmatrix} ^{\mathbf{MF}}\mathbf{r_{D\to F}} \\ \hline 1 \end{bmatrix} \tag{G.64}$$

where $\mathbf{T_{M/MF}}$ is defined in equation G.26. The positions of joints A, B, C and D in $\mathbf{O_M}$ are similarly:

$$^{\mathbf{M}}\mathbf{r_A} = \begin{Bmatrix} R_M cos(\alpha) \\ R_M sin(\alpha) \\ 0 \end{Bmatrix} \tag{G.65}$$

$$^{\mathbf{M}}\mathbf{r_B} = \begin{Bmatrix} -R_M sin(\alpha) \\ R_M cos(\alpha) \\ 0 \end{Bmatrix} \tag{G.66}$$

$$^{\mathbf{M}}\mathbf{r_C} = \begin{Bmatrix} -R_M cos(\alpha) \\ -R_M sin(\alpha) \\ 0 \end{Bmatrix} \tag{G.67}$$

$$^{\mathbf{M}}\mathbf{r_D} = \begin{Bmatrix} R_M sin(\alpha) \\ -R_M cos(\alpha) \\ 0 \end{Bmatrix} \tag{G.68}$$

Actuator Link Lengths

The length of each actuated leg for a desired pose is given by the Euclidean distance between the two joints of that leg. The analytical inverse kinematic relations are then

$$\begin{aligned} L_I(z,\theta_x,\theta_y) &= \left|{}^{\mathbf{M}}\mathbf{r_E} - {}^{\mathbf{M}}\mathbf{r_A}\right| \\ &= \left(\left(R_M\theta_x\theta_y sin(\alpha)\right)^2 + \left(R_M\theta_x sin(\alpha) - R_M\theta_y cos(\alpha) + z\right)^2\right)^{1/2} \end{aligned} \tag{G.69}$$

$$\begin{aligned} L_{II}(z,\theta_x,\theta_y) &= \left|{}^{\mathbf{M}}\mathbf{r_F} - {}^{\mathbf{M}}\mathbf{r_B}\right| \\ &= \left(\left(R_M\theta_x\theta_y cos(\alpha)\right)^2 + \left(R_M\theta_x cos(\alpha) + R_M\theta_y sin(\alpha) + z\right)^2\right)^{1/2} \end{aligned} \tag{G.70}$$

$$\begin{aligned} L_{III}(z,\theta_x,\theta_y) &= \left|{}^{\mathbf{M}}\mathbf{r_G} - {}^{\mathbf{M}}\mathbf{r_C}\right| \\ &= \left(\left(R_M\theta_x\theta_y sin(\alpha)\right)^2 + \left(-R_M\theta_x sin(\alpha) + R_M\theta_y cos(\alpha) + z\right)^2\right)^{1/2} \end{aligned} \tag{G.71}$$

$$\begin{aligned} L_{IV}(z,\theta_x,\theta_y) &= \left|{}^{\mathbf{M}}\mathbf{r_H} - {}^{\mathbf{M}}\mathbf{r_D}\right| \\ &= \left(\left(R_M\theta_x\theta_y cos(\alpha)\right)^2 + \left(-R_M\theta_x cos(\alpha) - R_M\theta_y sin(\alpha) + z\right)^2\right)^{1/2} \end{aligned} \tag{G.72}$$

Linearised Inverse Position Kinematic Equations

The equations can be linearised for small motions $\Delta\mathbf{P}$ about the initial position of the segment ${}^{\mathbf{M}}\mathbf{r_{MF,0}}$ by using the Jacobian matrix $\mathbf{J}$ of $\Delta\mathbf{L}$ previously defined in equation G.42. The resulting linearised inverse kinematic equations for concept B, assuming small motions are then

$$\Delta L_I = R_M\left(sin(\alpha)\theta_{x,M} - cos(\alpha)\theta_{y,M}\right) + \Delta_{z,M} \tag{G.73}$$

$$\Delta L_{II} = R_M\left(cos(\alpha)\theta_{x,M} + sin(\alpha)\theta_{y,M}\right) + \Delta_{z,M} \tag{G.74}$$

$$\Delta L_{III} = R_M\left(-sin(\alpha)\theta_{x,M} + cos(\alpha)\theta_{y,M}\right) + \Delta_{z,M} \tag{G.75}$$

$$\Delta L_{IV} = R_M\left(-cos(\alpha)\theta_{x,M} - sin(\alpha)\theta_{y,M}\right) + \Delta_{z,M} \tag{G.76}$$

H

Mechanical Design - Supplementary Material

This appendix includes additional studies and derivations used to support the results in Chapter 8 *Mechanical Design*.

H.1. Sheet Flexure Constraint Warping & Discretisation Study

Results from the *SPACAR* simulation were verified against the theoretical predictions from Euler-Bernoulli beam theory presented in Section 8.4.1 and a higher order simulation in ANSYS. The first three eigenfrequencies, eigenmodes, critical buckling loads and buckling modes were compared.

Models with one to ten elements were considered. The number of elements for which torsion should be rigid was found by dividing the length of each sub-element into the rigid length and rounding down to nearest integer (ie. the `floor` of the result). Thus in the case of the single element, the torsion deformation mode was not constrained.

The results for the first three eigenfrequencies are given in Table H.1. No external loads, including gravity, were applied. The three, four and five element models were simulated with and without constraint warping.

Table H.1: Comparison of results for modal analysis of sheet flexure models. Theoretical results from Section 8.4.1. *SPACAR* results are identified with the format SP (x,y) where x is the number of beam elements and y the number of torsionally rigid elements at the clamped end.

	Eigenfrequencies [Hz]			**Difference to ANSYS [%]**		
Test/ Mode	**n = 1**	**n = 2**	**n = 3**	**n = 1**	**n = 2**	**n = 3**
ANSYS	11992	19858	41629	-	-	-
Theory	11470	-	-	4.35	-	-
SP (1,0)	11510	11560	106700	4.02	41.8	156
SP (2,0)	11460	12510	30200	4.44	37.0	27.5
SP (3,0)	11460	12690	34670	4.44	36.1	16.7
SP (3,1)	11460	18760	45300	4.44	5.53	8.82
SP (4,0)	11460	12730	36320	4.44	35.8	12.8
SP (4,1)	11460	16920	46230	4.44	14.8	11.1
SP (5,0)	11450	12780	37100	4.52	35.6	10.9
SP (5,2)	11450	21150	57790	4.52	6.51	38.8
SP (6,2)	11450	19130	54480	4.52	3.67	30.9
SP (7,2)	11450	17900	51940	4.52	9.86	24.8
SP (8,3)	11450	20460	59360	4.52	3.03	42.6
SP (9,3)	11450	19200	56290	4.52	3.31	35.2
SP (10,4)	11450	21330	62550	4.52	7.41	50.3

It was found that only one element was needed to correctly predict the first two eigenmodes since constraint warping was not automatically included, however the eigenfrequencies for the second and third modes

were very inaccurate. Additionally, none of the models correctly predicted the shape of the third eigenmode (not shown), so those results are not considered in this comparison. The fluctuation in the error of the second eigenfrequency for four or more elements is due to poor discretisation of the rigid length of the flexure caused by constraint warping.

While there was no strong dependence on the number of elements or consideration of constraint warping in the prediction of the first eigenfrequency & mode, a much more accurate prediction of the second eigenfrequency was found for three or more elements compared to the lower order models. The lowest order model to give good predictions of the first and second eigenmodes & frequencies was the (3,1) model.

The results of the linear buckling analysis are given in Table H.2.

Table H.2: Comparison of results for linear buckling analysis of sheet flexure models. Theoretical results from Section 8.4.1. *SPACAR* results are identified with the format SP (x,y) where x is the number of beam elements and y the number of torsionally rigid elements at the clamped end.

	Critical Buckling Load [N]			**Difference to ANSYS [%]**		
Test/ Mode	**n = 1**	**n = 2**	**n = 3**	**n = 1**	**n = 2**	**n = 3**
ANSYS	892	2683	7737	-	-	-
Theory	821	7389	20530	7.92	175	165
SP (1,0)	827	10710	330900	7.23	299	4177
SP (2,0)	822	7635	25640	7.87	185	231
SP (3,0)	821	7445	21500	7.91	178	178
SP (3,1)	821	7445	21500	7.91	178	178
SP (4,0)	821	7408	20880	7.91	176	170
SP (4,1)	821	7408	20880	7.91	176	170
SP (5,0)	821	7397	20680	7.91	176	167
SP (5,2)	821	7397	20680	7.91	176	167
SP (6,2)	821	7393	20600	7.92	176	166
SP (7,2)	821	7391	20570	7.92	176	166
SP (8,3)	821	7391	20550	7.92	176	166
SP (9,3)	821	7390	20540	7.92	176	166
SP (10,4)	821	7390	20540	7.92	176	166

Like the theoretical buckling calculation in the previous section, *SPACAR* only predicts one dimensional buckling modes (not shown) whereas ANSYS predicts multi-dimensional buckling modes. Therefore direct comparison of buckling modes beyond the first is not valid. *SPACAR* requires only a single beam element to make a good estimate for the Eulerian critical buckling load as it also uses the linear theory presented in Section 8.4.1.

To keep the dimension of the model low, particularly as it grows into the full integrated model of the mechanism, three elements are used to model the flexure and the effects of constraint warping were included.

While the first mode for both the modal & buckling analysis was predicted with less than 10% error, the assumptions used to idealise the behaviour of the flexure led to poor results beyond the second eigenmode and beyond the first buckling mode. The *SPACAR* results for the (3,1) case were conservative compared to the ANSYS results, predicting eigenfrequencies and critical buckling loads lower than those reported by ANSYS. The results also justify inclusion of only the torsion and out of plane deformation modes.

It is only the fundamental frequency that is critical for the preliminary design of the PMAO so the lower accuracy at higher modes is deemed acceptable for preliminary design. Similarly, as soon as there is any buckling of a flexure, the PMAO will be unable to fulfil its operational requirements so only the first buckling mode is most important.

Note that the flexure was modelled in the fixed/ free configuration whereas all of the flexures in the PMAO are in a fixed/ fixed configuration. These latter implementations are modelled as the mirror of the sheet flexure presented here, with a total of six elements and constraint warping included at both fixed ends.

It is acknowledged that the assumptions and model of a flexure presented here are for one aspect ratio only and may not be relevant as a generic model of all flexure geometries. A more detailed model can be considered in future work.

H.2. Universal Joint ANSYS Mesh Convergence

Generating a valid mesh within the ANSYS license limits was non-trivial. The thin sheet flexures required a very small element size, which led to large node counts throughout the remaining bulk of the joint.

The size of the analysis domain could be reduced by exploiting the symmetry of the part. By defining two symmetry planes, only a quarter model needed to be meshed. Since the compliance of the flexures is so much larger than that of the effectively rigid end bodies and central frustum, the majority of the mesh detail could be concentrated on the two half flexures and still retrieve meaningful results. Spheres of influence are a meshing tool that allows the user to instruct the meshing function to increase the density of elements around regions of critical stresses are more complex responses. One sphere was used on each of the two flexure halves in the quarter model, shown in Figure H.1.

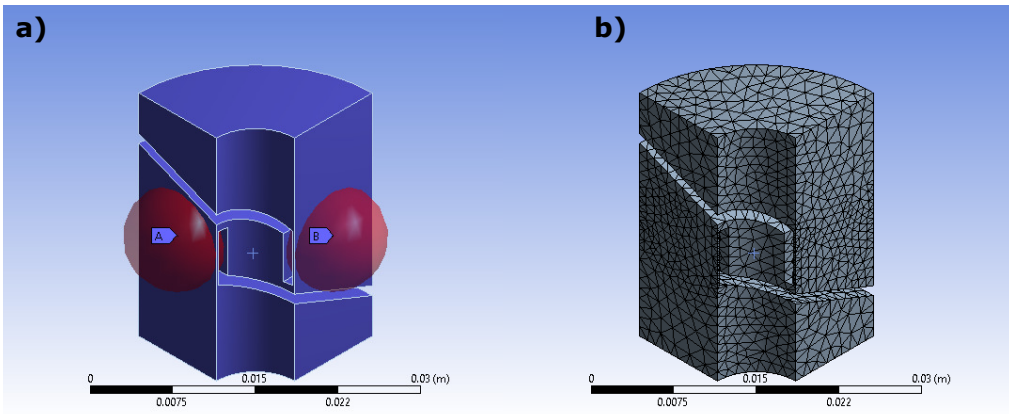

Figure H.1: Mesh for finite element analysis of universal joint quarter model in ANSYS. a) location and size of spheres of influence; b) The mesh with slightly higher density of elements at flexure locations.

While the use of symmetry did improve the mesh, four separate analyses had to be executed for each combination of symmetric/ anti-symmetric boundary conditions at the two symmetry planes in order to retrieve a complete setting of eigenmodes and buckling modes. The lowest positive load factor was taken as the critical buckling load.

Four meshes were generated with different minimum element sizes in the spheres of influence. The first three eigenfrequencies were extracted from a modal analysis at each of the four settings to compare the accuracy of the results, presented in Table H.3. The 0.3 mm setting was taken as the benchmark since the resulting ≈224k nodes was close to the license limit.

A fifth analysis with a full solid model of the universal joint was also conducted to confirm that the symmetry model was set up correctly. The minimum element size was set to 1 mm with spheres of influence placed at the centre of each of the flexures. The modal results are also given in Table H.3.

Table H.3: Modal analysis results of convergence study for universal joint ANSYS modelling. Two spheres of influence encapsulating the flexures were set to the element sizes indicated. ANSYS Academic Teaching Mechanical license is limited to 256k nodes.

Element Size $[mm]$	**No. Nodes**	**1st Mode** $[Hz]$	**2nd Mode** $[Hz]$	**3rd Mode** $[Hz]$
Quarter Model				
0.3	224101	139	180	693
0.5	82990	139	181	700
1	42856	141	184	721
2	38350	148	188	850
Full Model				
1	142536	141	182	722

The study revealed that increasing the element size to 1 mm in the quarter model gave a five fold decrease in the number of mesh nodes yet only a 1.4% error in prediction of the first eigenmode. The error in eigenfrequency prediction increased for higher eigenmodes as the element size was increased, however still only a 4.1% error was present for the third eigenfrequency in the 1 mm case. The 2 mm case gave comparatively

poor results with an error of 6.7% in the first mode alone and 22.6% in the third mode. The 0.3 mm setting gave marginally better results than the 0.5 mm case.

Table H.4: Buckling analysis results of convergence study for universal joint ANSYS modelling.

Element Size [mm]	**No. Nodes**	$\mathbf{P_{cr,1}}$ [N]	$\mathbf{P_{cr,2}}$ [N]	$\mathbf{P_{cr,3}}$ [N]
Quarter Model				
0.3	224101	32.4	34.4	301
Full Model				
1	142536	337	339	7478

The full solid model analysis demonstrated that the quarter model was providing sensible modal results with marginally better predictions of all eigenfrequencies compared to the full model with 1 mm element size. However, the quarter model was far more efficient, using approximately a third of the total number of nodes. Comparison of the buckling results between the 0.3 mm quarter and 1 mm full models, listed in Table H.4, demonstrated that the quarter model buckling loads were grossly inaccurate. The cause for this error could not be found. The symmetry conditions were assumed to be correct given the sensible modal results.

The convergence studied showed that there was less than a 4 % error in the first three eigenfrequency predictions between the 1 mm full and 0.3 mm quarter models which was much less than the expected error between the *SPACAR* and ANSYS models. Therefore it was assumed that the 1 mm full model buckling results would be sufficiently accurate for the *SPACAR* verification. The same model was used for the launch load equivalent stress analysis. A quarter of the launch load listed in Table 8.5 was applied since only a quarter of the part is present in the model.

H.3. Mirror Support Bipod Launch Load Solution

The first section below derives the quasi-static loads experienced by the mirror support struts during launch. The following section provides a program to derive the full analytical solutions in *Mathematica*. The final section provides the code for an interactive program that can be used to quickly size the support assembly geometry, again written for *Mathematica*.

H.3.1. Derivation of Bipod Strut Loads

See Figure 8.23 for a description of the geometry and coordinate frames used throughout this section. Vectors defined with respect to one of the local bipod coordinate frames $\mathbf{O_{Bi}}$ are prefixed with the raised notation ${}^{\mathbf{OBi}}\mathbf{r_{BA1U}}$. The preceding indice is removed for vectors defined in moving frame coordinates $\mathbf{O_{MF}}$ for clarity.

The position vectors $\mathbf{r_{OBi}}$ of each of the bipod origins $\mathbf{O_{Bi}}$ in the moving frame coordinate system are given by

$$\mathbf{r_{OBi}} = \left\{R_B \cos(\psi_{ii}), R_B \sin(\psi_{ii}), 0\right\}^T \tag{H.1}$$

with $\psi = \{\psi_{AA}, \psi_{BB}, \psi_{CC}\} = \{0, 2\pi/3, 4\pi/3\}$. Position vectors ${}^{\mathbf{OBi}}\mathbf{r}$ defined in the bipod local frames can be transformed into the moving frame coordinate frame via

$${}^{\mathbf{MF}}\mathbf{r} = \mathbf{r} = \mathbf{r_{OBi}} + \boldsymbol{\mathcal{R}}_\mathbf{i}.{}^{\mathbf{OBi}}\mathbf{r} \tag{H.2}$$

where $\boldsymbol{\mathcal{R}}_\mathbf{i}$ is the rotation matrix for coordinate frame origin $\mathbf{O_{Bi}}$ given by

$$\boldsymbol{\mathcal{R}}_\mathbf{i} = \begin{bmatrix} \cos(\psi_{ii} - \pi/2) & -\sin(\psi_{ii} - \pi/2) & 0 \\ \sin(\psi_{ii} - \pi/2) & \cos(\psi_{ii} - \pi/2) & 0 \\ 0 & 0 & 1 \end{bmatrix} \tag{H.3}$$

Thus the position vectors $\mathbf{r_{BijL}}$ of the lower coordinates of each strut are given by

$$\mathbf{r_{BijL}} = \mathbf{r_{OBi}} + \boldsymbol{\mathcal{R}}_\mathbf{i}.\{d_B/2, 0, 0\}^T \tag{H.4}$$

The position vectors ${}^{\mathbf{OBi}}\mathbf{r_{BijU}}$ of the upper coordinates of each strut in their local coordinate frames are

$${}^{\mathbf{OBi}}\mathbf{r_{Bi1U}} = \left\{\delta x, p - \delta y, h - q\right\}^T \tag{H.5}$$

$${}^{\mathbf{OBi}}\mathbf{r_{Bi2U}} = \left\{-\delta x, p - \delta y, h - q\right\}^T \tag{H.6}$$

where the parameters δx and δy are shown in Figure 8.23, and with p, are given by

$$\delta x = q d_B/2h \tag{H.7}$$

$$\delta y = pq/h \tag{H.8}$$

$$p = R_S - R_B \tag{H.9}$$

These parameters can also be used to find the length of the strut s_B between the attachment points

$$s_B = \sqrt{\left(\frac{d_B}{2} - \delta x\right)^2 + (p - \delta y)^2 + (h - q)^2} \tag{H.10}$$

Again making use of equation H.2, the position vectors of the upper strut coordinates in the $\mathbf{O_{MF}}$ frame are

$$\mathbf{r_{BijU}} = \mathbf{r_{OBi}} + \boldsymbol{\mathcal{R}}_\mathbf{i}.{}^{\mathbf{OBi}}\mathbf{r_{BijU}} \tag{H.11}$$

The unit vectors $\hat{\mathbf{r}}_\mathbf{Bij}$ in the direction of each of the struts are

$$\hat{\mathbf{r}}_\mathbf{Bij} = \frac{\mathbf{r_{BijU}} - \mathbf{r_{BijL}}}{|\mathbf{r_{BijU}} - \mathbf{r_{BijL}}|} \tag{H.12}$$

The reaction load exerted by each strut against the mirror as shown in Figure 8.23 are then

$$\mathbf{R_{Bij}} = R_{Bij}\hat{\mathbf{r}}_{\mathbf{Bij}} \tag{H.13}$$

where R_{Bij} is the scalar magnitude of the reaction force. The launch load $\mathbf{F_L}$ can be decomposed into coordinates

$$\mathbf{F_L} = \left\{F_{L,X}, F_{L,Y}, F_{L,Z}\right\}^T \tag{H.14}$$

and is imposed upon the system at position $\mathbf{r_F} = \{0,0,h\}$. As in all other component sizing exercises, the launch load was set to a $30g$ acceleration of the 6 kg mirror mass in the orthogonal directions. The reaction loads were then found by solving the set of simultaneous equations arising from

$$\sum \mathbf{F} = \mathbf{0} \tag{H.15}$$

$$= \mathbf{F_L} + \mathbf{R_{BA1}} + \mathbf{R_{BA2}} + \mathbf{R_{BB1}} + \mathbf{R_{BB2}} + \mathbf{R_{BC1}} + \mathbf{R_{BC2}} \tag{H.16}$$

$$\sum \mathbf{M} = \mathbf{0} \tag{H.17}$$

$$= \mathbf{r_F} \times \mathbf{F_L} + \mathbf{r_{BA1U}} \times \mathbf{R_{BA1}} + \mathbf{r_{BA2U}} \times \mathbf{R_{BA2}} + \mathbf{r_{BB1U}} \times \mathbf{R_{BB1}} + \mathbf{r_{BB2U}} \times \mathbf{R_{BB2}} + \mathbf{r_{BC1U}} \times \mathbf{R_{BC1}} + \mathbf{r_{BC2U}} \times \mathbf{R_{BC2}} \tag{H.18}$$

The solutions for the $\mathbf{R_{BAi}}$ in fully parametric form are very large, running to several pages so are not included for brevity. A short program that can be used to derive the full analytical solutions in *Mathematica* is given in the next section.

H.3.2. Analytical Solution for Bipod Strut Loads

The *Mathematica* code below produces the (very) long analytical solutions that supply the reaction loads in the mirror support bipod struts during launch, derived in Section 8.8.1. To execute the program, directly copy and paste the below code into a *Mathematica* notebook, select all and execute.

```
(*Azimuths of Bipod base coordinates Subscript[O, Bi] from \
Subscript[O, MF]*)
\[Psi] = {0, 2 \[Pi]/3, 4 \[Pi]/3};

(*Rotation about Z_MF axis by angle Subscript[\[Psi], i]*)
(*Note that the bipod A local frame x axis is -\[Pi]/2 from XMF axis \
etc*)
\[ScriptCapitalR]i[\[Psi]_] := {
   {Cos[\[Psi] - \[Pi]/2], -Sin[\[Psi] - \[Pi]/2], 0},
   {Sin[\[Psi] - \[Pi]/2], Cos[\[Psi] - \[Pi]/2], 0},
   {0, 0, 1}};

(*Position vectors of bipod base coordinates Subscript[O, Bi] in \
Subscript[O, MF] frame*)
rOBA = {RB Cos[\[Psi][[1]]], RB Sin[\[Psi][[1]]], 0};
rOBB = {RB Cos[\[Psi][[2]]], RB Sin[\[Psi][[2]]], 0};
rOBC = {RB Cos[\[Psi][[3]]], RB Sin[\[Psi][[3]]], 0};

(*Geometry for position vectors*)
p = RS - RB;
\[Delta]x = (q dB)/(2 h);
\[Delta]y = (p q)/h;

(*Length of strut from assembly geometry*)
sB = Sqrt[(dB/2 - \[Delta]x)^2 + (p - \[Delta]y)^2 + (h - q)^2];
(*Position vectors of strut attachment to moving frame in base frames \
Subscript[O, Bi]*)
rBA1L = rOBA + \[ScriptCapitalR]i[\[Psi][[1]]].{dB/2, 0, 0};
```

```
rBA2L = rOBA + \[ScriptCapitalR]i[\[Psi][[1]]].{-dB/2, 0, 0};
rBB1L = rOBB + \[ScriptCapitalR]i[\[Psi][[2]]].{dB/2, 0, 0};
rBB2L = rOBB + \[ScriptCapitalR]i[\[Psi][[2]]].{-dB/2, 0, 0};
rBC1L = rOBC + \[ScriptCapitalR]i[\[Psi][[3]]].{dB/2, 0, 0};
rBC2L = rOBC + \[ScriptCapitalR]i[\[Psi][[3]]].{-dB/2, 0, 0};

(*Position vectors of strut attachment to underside of mirror in \
bipod base frames Subscript[O, Bi]*)
OBArBA1U = {\[Delta]x, p - \[Delta]y, h - q};
OBArBA2U = {-\[Delta]x, p - \[Delta]y, h - q};
OBBrBB1U = OBArBA1U;
OBBrBB2U = OBArBA2U;
OBCrBC1U = OBArBA1U;
OBCrBC2U = OBArBA2U;

(*Position vectors of strut attachment to underside of mirror in \
Subscript[O, MF] frame*)
rBA1U = rOBA + \[ScriptCapitalR]i[\[Psi][[1]]].OBArBA1U;
rBA2U = rOBA + \[ScriptCapitalR]i[\[Psi][[1]]].OBArBA2U;
rBB1U = rOBB + \[ScriptCapitalR]i[\[Psi][[2]]].OBBrBB1U;
rBB2U = rOBB + \[ScriptCapitalR]i[\[Psi][[2]]].OBBrBB2U;
rBC1U = rOBC + \[ScriptCapitalR]i[\[Psi][[3]]].OBCrBC1U;
rBC2U = rOBC + \[ScriptCapitalR]i[\[Psi][[3]]].OBCrBC2U;

(*Position vector of mirror CoM in Subscript[O, MF] frame*)
rF = {0, 0, h};

(*External launch load vector*)
FL = {FLX, FLY, FLZ};

(*Unit vectors in direction of struts in Subscript[O, MF] frame*)
rhatBA1 = Normalize[rBA1U - rBA1L];
rhatBA2 = Normalize[rBA2U - rBA2L];
rhatBB1 = Normalize[rBB1U - rBB1L];
rhatBB2 = Normalize[rBB2U - rBB2L];
rhatBC1 = Normalize[rBC1U - rBC1L];
rhatBC2 = Normalize[rBC2U - rBC2L];

(*Reaction loads along line of strut applied to underside of mirror*)


RBA1 = RRBA1*rhatBA1;
RBA2 = RRBA2*rhatBA2;
RBB1 = RRBB1*rhatBB1;
RBB2 = RRBB2*rhatBB2;
RBC1 = RRBC1*rhatBC1;
RBC2 = RRBC2*rhatBC2;

(*Solve reaction forces*)
soln = Solve[{RBA1 + RBA2 + RBB1 + RBB2 + RBC1 + RBC2 + FL == {0, 0,
       0},
     Cross[rBA1U, RBA1] + Cross[rBA2U, RBA2] + Cross[rBB1U, RBB1] +
       Cross[rBB2U, RBB2] + Cross[rBC1U, RBC1] + Cross[rBC2U, RBC2] +
       Cross[rF, FL] == {0, 0, 0}}, {RRBA1, RRBA2, RRBB1, RRBB2,
     RRBC1, RRBC2}][[1]]
```

SPACAR Model Maps

I.1. Element and Nodal Maps

The following figures map out the element and nodal ID's used in each of the PMAO component *SPACAR* models. The ID's refer to the element and nodal numbers used in the `datBuilder` files for each model, stored on the TU Delft project repository. They do *not* refer to the nodal coordinates in the raw *.dat setup files, which are written by `spascripting` via `datBuilder`.

Universal Joint

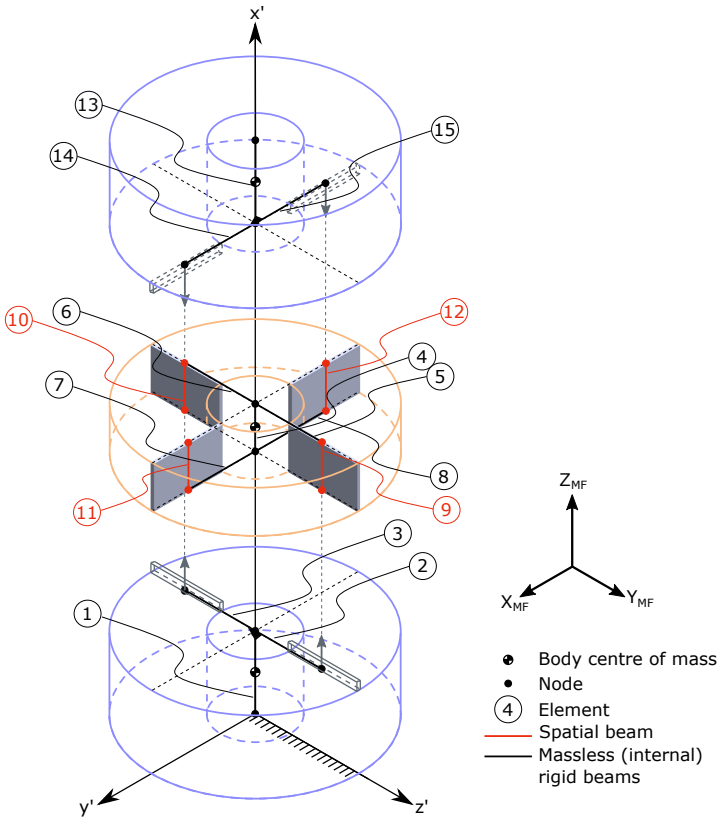

Figure I.1: Exploded view of *SPACAR* universal joint model showing beam elements and node positions in local $x'y'z'$ coordinate frame. Moving frame coordinate system shown for orientation to global frame. Cylinders shown for illustration purposes only, they are not modelled as circular hollow beams in *SPACAR*.

Moving Frame & In-Plane Constraints

The layout and geometry of the moving frame and in-plane constraint model is shown in Figure I.2. Massless "dummy" rigid beams were added in the top plane of the plate element to provide nodes for the wire flexures. The default settings for the Shampine-Gordon numerical integrator were modified from a maximum of 10 iterations to calculate the stationary solution to 20 and the number of load steps were increased from 4 to 90 in order for the solution to converge.

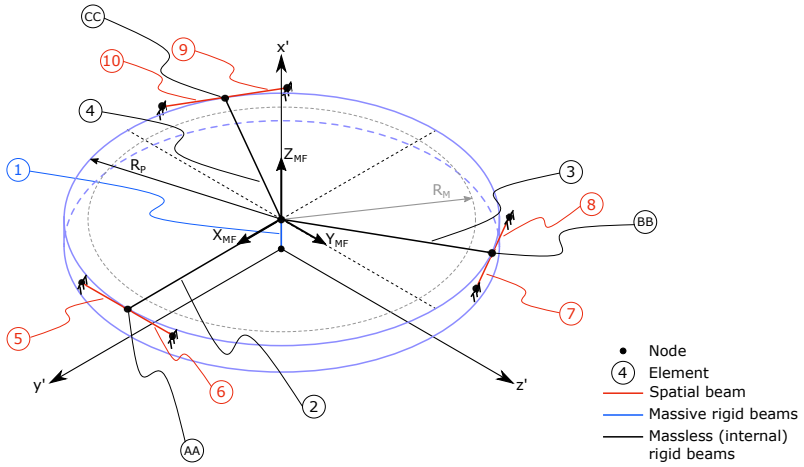

Figure I.2: *SPACAR* model of moving frame and in-plane constraints.

Support Bipod Strut

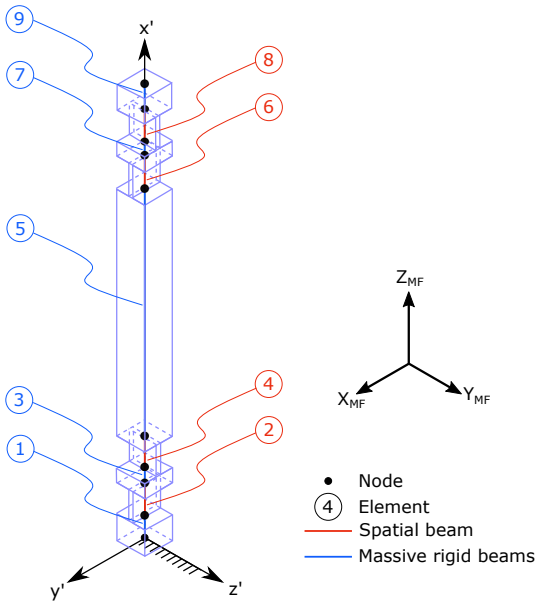

Figure I.3: *SPACAR* model of bipod strut. The local frame of the strut $x'y'z'$ is shown with the x' axis along the longitudinal axis of the strut. The *SPACAR* global coordinate frame, equivalent to the moving frame X_{MF}, Y_{MF}, Z_{MF} is also shown.

I.2. Example *SPACAR* Setup File

Example *SPACAR* *.dat setup file for the sheet flexure model. Remaining model files are very large, with up to 2,500 lines for the integrated model. They are stored on the TU Delft project repository.

```
beam    1   1  2  3  4    0 0 1
beam    2   3  4  5  6    0 0 1
beam    3   5  6  7  8    0 0 1

x       1          0.0000000000    0.0000000000  0.0000000000
x       3          0.0020000000    0.0000000000  0.0000000000
x       5          0.0040000000    0.0000000000  0.0000000000
x       7          0.0060000000    0.0000000000  0.0000000000

fix     1
fix     2

end
halt

em      1   0.022   0.00000018      0.00000018    0.000000000458 0
em      2   0.022   0.00000018      0.00000018    0.000000000458 0
em      3   0.022   0.00000018      0.00000018    0.000000000458 0
estiff  1   575000  0.0174461424996 4.79166666667 0.0119791666667
estiff  2   575000  0.0174461424996 4.79166666667 0.0119791666667
estiff  3   575000  0.0174461424996 4.79166666667 0.0119791666667
end halt

% INV DYN and LINEARISATION

% Other options

end
end

visualization
BEAMPROPS 1  2  3
CROSSDIM 0.0005 0.01
VIBRATIONMODE 1
ENLARGEFACTOR 1
TRANSPARENCY 0.6
```

J

Pose Error Calculations

This Appendix describes the method used to calculate the pose error. The main quantities of interest in the analysis of the mechanisms' performance are the three position and three orientation coordinates $\{x, y, z, \theta_x, \theta_y, \theta_z\}$ of the mirrors pose in the fixed mechanism frame $\mathbf{O_M}$. The errors are also desirable.

J.1. Definitions

A variety of notation is used in the following derivations in an effort to clearly communicate the various coordinate transform operations. Note that as elsewhere in this document, vectors are bold and scalars are regularly typefaced. Prescripts explicitly define the coordinate system in which a vector is defined. Post subscripts describe the object to which the quantity refers to. A summary of the notation is provided below.

$^{\mathbf{M}}\mathbf{r}^{*}_{\mathbf{COM}}$ Star: The ideal value of a quantity. This would be the value of the quantity in the absence of all error sources.

$^{\mathbf{M}}\bar{\mathbf{r}}_{\mathbf{COM}}$ Overbar: The expected value of a quantity. The value that is expected due to known, quantifiable error sources (here, only the remote centre errors are considered known and quantifiable.)

$^{\mathbf{M}}\mathbf{r}_{\mathbf{COM}}$ No star or overbar: The actual (simulated) value of a quantity, inclusive of all error sources that are capable of being modelled in the simulation.

$^{\mathbf{M}}\mathbf{r}_{\mathbf{COM,0}}$ Subscript 0: Quantity given at time t=0, before any motion. The nominal resting state of the mechanism.

$\mathbf{T_{A/B}}$ Homogeneous Transform Matrix (HTM). Transformation matrix that applies a translation and rotation from coordinate frame B to coordinate frame A. Applies to position vectors *only*, cannot be applied to vectors describing a relative quantity without a position in space.

$\mathcal{R}_{\mathbf{ZYX}}$ Rotation matrix that when post-multiplied by a vector in the world coordinate frame, gives that same vector in the body-fixed coordinate frame. Applies to vectors *only*, not to points in space. Use the HTM to transform points.

τ Pose row vector $\{x, y, z, \theta_X, \theta_Y, \theta_Z\}$.

$\mathbf{e}$ Error, the difference between an ideal and simulated quantity. A RC subscript denotes a remote centre error, P a parasitic error and T the total error (remote centre and parasitic combined).

Three coordinate frames are of interest:

$\mathbf{O_M}$ The mechanism coordinate frame, treated here as the fixed world frame. Located on the DST instrument housing wall in the stowed state, otherwise 120 mm below the mirror centre of mass in the nominal deployed state.

$\mathbf{O_{MF}}$ The moving frame coordinate frame, located on the top surface of the moving frame, in the centre. Commanded tip and tilt rotations occur about the axes of this frame. The axes are aligned with the mechanism coordinate frame in the resting state.

$\mathbf{O_{COM}}$ The mirror segment centre of mass coordinate frame, located at the centre of mass of the mirror segment. The axes are aligned with the mechanism coordinate frame in the resting state. This frame is assumed to be rigidly connected to the moving frame coordinate frame so will rotate and translate due to pose changes.

The following position vectors are reported by *SPACAR* at the end of a simulation:

$^{\mathbf{M}}\mathbf{r_{COM}}$ Position of the mirror segment centre of mass (and origin of the $\mathbf{O_{COM}}$ coordinate frame) in the $\mathbf{O_M}$ frame.

$^{\mathbf{M}}\mathbf{r_{COMx}}$ Position of a point 0.1 m along the X axis of the $\mathbf{O_{COM}}$ frame. Used to determine the segment attitude with the TRIAD algorithm.

$^{\mathbf{M}}\mathbf{r_{COMy}}$ Position of a point 0.1 m along the Y axis of the $\mathbf{O_{COM}}$ frame. Used to determine the segment attitude with the TRIAD algorithm.

$^{\mathbf{M}}\mathbf{r_{COMz}}$ Position of a point 0.1 m along the Z axis of the $\mathbf{O_{COM}}$ frame. Used to determine the segment attitude with the TRIAD algorithm.

$^{\mathbf{M}}\mathbf{r_{MF}}$ Position of the moving frame coordinate frame origin in the $\mathbf{O_M}$ frame.

$^{\mathbf{M}}\mathbf{r_{MFx}}$ Position of a point 0.1 m along the X axis of the $\mathbf{O_{MF}}$ frame. Used to determine the moving frame attitude with the TRIAD algorithm.

$^{\mathbf{M}}\mathbf{r_{MFy}}$ Position of a point 0.1 m along the Y axis of the $\mathbf{O_{MF}}$ frame. Used to determine the moving frame attitude with the TRIAD algorithm.

$^{\mathbf{M}}\mathbf{r_{MFz}}$ Position of a point 0.1 m along the Z axis of the $\mathbf{O_{MF}}$ frame. Used to determine the moving frame attitude with the TRIAD algorithm.

J.2. Ideal and Expected Mirror Pose

The *initial* expected (nominal) positions of the centre of $\mathbf{O_{COM}}$ with respect to $\mathbf{O_{MF}}$ and $\mathbf{O_{MF}}$ with respect to $\mathbf{O_M}$ are given in metres by the ideal assembly geometry chosen in Chapter 8 *Mechanical Design*:

$$^{\mathbf{MF}}\mathbf{r}^*_{\mathbf{COM,0}} = {}^{\mathbf{MF}}\bar{\mathbf{r}}_{\mathbf{COM,0}} = {}^{\mathbf{MF}}\mathbf{r}_{\mathbf{COM,0}} = \{0,0,h\}^T \tag{J.1}$$

$$^{\mathbf{M}}\mathbf{r}^*_{\mathbf{MF,0}} = {}^{\mathbf{M}}\bar{\mathbf{r}}_{\mathbf{MF,0}} = {}^{\mathbf{M}}\mathbf{r}_{\mathbf{MF,0}} = \{0,0,0.12+q-h\}^T \tag{J.2}$$

$$^{\mathbf{M}}\mathbf{r}^*_{\mathbf{COM,0}} = {}^{\mathbf{M}}\mathbf{r}^*_{\mathbf{MF,0}} + {}^{\mathbf{MF}}\mathbf{r}^*_{\mathbf{COM,0}} \tag{J.3}$$

In the current *SPACAR* simulation, no assembly errors are included so the ideal (starred), expected (overbarred) and actual initial positions of the mirror and moving frame coordinate frames are equal. If there were assembly errors included (thus errors would be present even time t=0), then the expected values would be the same as the actual values, but differ from the ideal values.

The calibration algorithm expects that the mirror will be rotated and translated the *ideal* commanded tilt, tip and piston amounts θ_x^*, θ_y^* and Δ_z^*. These are defined in the mechanism coordinate frame $\mathbf{O_M}$. The ideal mirror pose after a commanded motion as assumed in the derivation of the top down system budgets, is thus given by

$$^{\mathbf{M}}\tau^*_{\mathbf{COM}} = \left\{ {}^{\mathbf{M}}\mathbf{r}^*_{\mathbf{COM}}{}^T, \theta_x^*, \theta_y^*, 0 \right\} \tag{J.4}$$

with

$$^{\mathbf{M}}\mathbf{r}^*_{\mathbf{COM}} = {}^{\mathbf{M}}\mathbf{r}^*_{\mathbf{COM,0}} + \{0,0,\Delta_z^*\}^T \tag{J.5}$$

However, due to the kinematics of the PMAO design the actual centre of rotation is about the position of $\mathbf{O_{MF}}$. Assuming no parasitic errors, the mirror segment will have a slightly different expected position and thus pose (note that the expected attitude description remains the same as the commanded tip and tilt rotations since the mirror is expected to be rigidly attached to the moving frame),

$$^{\mathbf{M}}\bar{\tau}_{\mathbf{COM}} = \left\{ {}^{\mathbf{M}}\bar{\mathbf{r}}_{\mathbf{COM}}{}^T, \theta_x^*, \theta_y^*, 0 \right\} \tag{J.6}$$

The expected position ${}^{\mathbf{M}}\bar{\mathbf{r}}_{\mathbf{COM}}$ can be found by applying a homogeneous transform matrix $\mathbf{T}_{\mathbf{M/MF}}$ describing the attitude of the $\mathbf{O}_{\mathbf{MF}}$ frame, which moves with the moving frame, with respect to the fixed world frame to the position vector ${}^{\mathbf{MF}}\mathbf{r}^*_{\mathbf{COM}}$,

$$
{}^{\mathbf{M}}\bar{\mathbf{r}}_{\mathbf{COM}} = \left[\begin{array}{ccc|c} 1 & \theta_x^*\theta_y^* & \theta_y^* & \\ 0 & 1 & -\theta_x^* & {}^{\mathbf{M}}\bar{\mathbf{r}}_{\mathbf{MF}} \\ -\theta_y^* & \theta_x^* & 1 & \\ \hline 0 & 0 & 0 & 1 \end{array}\right] \cdot \left[\begin{array}{c} {}^{\mathbf{MF}}\bar{\mathbf{r}}_{\mathbf{COM}} \\ \hline 1 \end{array}\right] \tag{J.7}
$$

$$
= \mathbf{T}_{\mathbf{M/MF}} \cdot \left[\begin{array}{c} {}^{\mathbf{MF}}\bar{\mathbf{r}}_{\mathbf{COM}} \\ \\ \hline 1 \end{array}\right] \tag{J.8}
$$

Once again, since assembly errors are not being considered, the expected position ${}^{\mathbf{MF}}\bar{\mathbf{r}}_{\mathbf{COM}}$ of the mirror with respect to the moving frame is equal to the ideal position ${}^{\mathbf{MF}}\mathbf{r}^*_{\mathbf{COM}}$. Additionally, the expected position of $\mathbf{O}_{\mathbf{MF}}$ is similarly only a function of the initial expected position of the moving frame and the commanded piston displacement. These results are summarised via

$$
{}^{\mathbf{MF}}\bar{\mathbf{r}}_{\mathbf{COM}} = {}^{\mathbf{MF}}\bar{\mathbf{r}}_{\mathbf{COM,0}} \tag{J.9}
$$

$$
{}^{\mathbf{M}}\bar{\mathbf{r}}_{\mathbf{MF}} = {}^{\mathbf{M}}\bar{\mathbf{r}}_{\mathbf{MF,0}} + \left\{0, 0, \Delta_z^*\right\}^T \tag{J.10}
$$

J.3. Actual Mirror Pose

J.3.1. Determining the Actual Mirror Attitude

A method to extract the attitude of the mirror segment from the position information of the mirror COM is needed. This is achieved using the TRIAD algorithm [16], first developed in 1964 to determine the attitude of a satellite from two vector measurements.

The TRIAD Algorithm

The TRIAD algorithm determines the 3×3 orthogonal attitude matrix A describing the orientation of an object with respect to a given reference frame. The implementation follows the symmetrical method presented by Markley [84].

Two *measured* unit vectors $\mathbf{b_1}$ and $\mathbf{b_2}$ in the body fixed frame are required. These can be to two points or a measured vector in a vector field, such as Earth's magnetic field. For the implementation here, they are the positions of two points trivially aligned with the $\mathbf{O}_{\mathbf{COM}}$ x and y axes,

$$
\mathbf{b_1} = \{1, 0, 0\}^T \tag{J.11}
$$

$$
\mathbf{b_2} = \{0, 1, 0\}^T \tag{J.12}
$$

Two *reference* vectors $\mathbf{r_1}$ and $\mathbf{r_2}$ describing the positions of these same two points in the reference frame $\mathbf{O}_{\mathbf{M}}$ are also needed. These are retrieved from the *SPACAR* simulation output and converted to unit vectors via

$$
\mathbf{r_1} = \frac{{}^{\mathbf{M}}\mathbf{r}_{\mathbf{COMx}} - {}^{\mathbf{M}}\mathbf{r}_{\mathbf{COM}}}{|{}^{\mathbf{M}}\mathbf{r}_{\mathbf{COMx}} - {}^{\mathbf{M}}\mathbf{r}_{\mathbf{COM}}|} \tag{J.13}
$$

$$
\mathbf{r_2} = \frac{{}^{\mathbf{M}}\mathbf{r}_{\mathbf{COMy}} - {}^{\mathbf{M}}\mathbf{r}_{\mathbf{COM}}}{|{}^{\mathbf{M}}\mathbf{r}_{\mathbf{COMy}} - {}^{\mathbf{M}}\mathbf{r}_{\mathbf{COM}}|} \tag{J.14}
$$

Note that the *direction* vectors (from $\mathbf{O}_{\mathbf{COM}}$ to $\mathbf{O}_{\mathbf{COMx}}$) are used, not the position vectors. Additionally, only unit vectors are needed because the length of the vectors holds no information about the orientation of the body. Furthermore, the only condition on the measured and reference vectors is that they not be parallel or

antiparallel, else the cosine of the angle between them will be null and the attitude can no longer be uniquely retrieved. The attitude matrix A_{COM} is then such that

$$A_{COM}\mathbf{r_1} = \mathbf{b_1} \tag{J.15}$$
$$A_{COM}\mathbf{r_2} = \mathbf{b_2} \tag{J.16}$$

Three forms of the TRIAD algorithm are available. The third form, which treats the two measured and reference vectors symmetrically is used, forming the orthogonal triads $\{\mathbf{b}_+, \mathbf{b}_-, \mathbf{b_3}\}$ in the body fixed segment frame and $\{\mathbf{r}_+, \mathbf{r}_-, \mathbf{r_3}\}$ in the fixed world frame respectively. The unit vectors are found via

$$\mathbf{r}_+ = \frac{\mathbf{r_2} + \mathbf{r_1}}{|\mathbf{r_2} + \mathbf{r_1}|} = \frac{\mathbf{r_2} + \mathbf{r_1}}{\sqrt{2(1 + \mathbf{r_1} \cdot \mathbf{r_2})}} \tag{J.17}$$
$$\mathbf{r}_- = \frac{\mathbf{r_2} - \mathbf{r_1}}{|\mathbf{r_2} - \mathbf{r_1}|} = \frac{\mathbf{r_2} - \mathbf{r_1}}{\sqrt{2(1 - \mathbf{r_1} \cdot \mathbf{r_2})}} \tag{J.18}$$

and

$$\mathbf{b}_+ = \frac{\mathbf{b_2} + \mathbf{b_1}}{|\mathbf{b_2} + \mathbf{b_1}|} = \frac{\mathbf{b_2} + \mathbf{b_1}}{\sqrt{2(1 + \mathbf{b_1} \cdot \mathbf{b_2})}} \tag{J.19}$$
$$\mathbf{b}_- = \frac{\mathbf{b_2} - \mathbf{b_1}}{|\mathbf{b_2} - \mathbf{b_1}|} = \frac{\mathbf{b_2} - \mathbf{b_1}}{\sqrt{2(1 - \mathbf{b_1} \cdot \mathbf{b_2})}} \tag{J.20}$$

Vectors $\mathbf{b_3}$ and $\mathbf{r_3}$ can also be found with the equations below, though they aren't necessary to find A using the symmetric method.

$$\mathbf{r_3} = \frac{\mathbf{r_1} \times \mathbf{r_2}}{|\mathbf{r_1} \times \mathbf{r_2}|} \tag{J.21}$$
$$\mathbf{b_3} = \frac{\mathbf{b_1} \times \mathbf{b_2}}{|\mathbf{b_1} \times \mathbf{b_2}|} \tag{J.22}$$

The attitude matrix A_{COM} is finally given by

$$A_{COM} = \mathbf{b}_+ {\mathbf{r}_+}^T + \mathbf{b}_- {\mathbf{r}_-}^T + (\mathbf{b}_+ \times \mathbf{b}_-)(\mathbf{r}_+ \times \mathbf{r}_-)^T \tag{J.23}$$

Euler Angles

With the attitude matrix found, the Euler angles, equivalent to the actual tilt $\theta_{X,M}$, $\theta_{Y,M}$ and tilt about z $\theta_{Z,M}$, describing the orientation of the mirror in the $\mathbf{O_M}$ frame can be extracted. The orientation depends on the order of rotations applied to the body from the reference frame to the final body fixed frame. The ETEP model uses the convention $\theta_z \leftarrow \theta_y \leftarrow \theta_x$ for three extrinsic rotations about the fixed world frame axes [49]. This operation is encapsulated in the rotation matrix

$$\boldsymbol{\mathcal{R}}_{\mathbf{ZYX}} = \begin{bmatrix} c\theta_y c\theta_z & c\theta_x s\theta_z + c\theta_z s\theta_x s\theta_y & s\theta_x s\theta_z - c\theta_x c\theta_z s\theta_y \\ -c\theta_y s\theta_z & c\theta_x c\theta_z - s\theta_x s\theta_y s\theta_z & c\theta_z s\theta_x + c\theta_x s\theta_y s\theta_z \\ s\theta_y & -c\theta_y s\theta_x & c\theta_x c\theta_y \end{bmatrix} \tag{J.24}$$

The abbreviations c = cos and s = sin have been used for brevity. Since the angles are very small the rotation matrix can be simplified by linearising,

$$\boldsymbol{\mathcal{R}}_{\mathbf{ZYX}} = \begin{bmatrix} 1 & \theta_z & -\theta_y \\ -\theta_z & 1 & \theta_x \\ \theta_y & -\theta_x & 1 \end{bmatrix} \tag{J.25}$$

Note that the error from linearising is approximately 1% for the sine of 14° or cosine of 8°. The angles used in the PMAO are on the order of 0.0002° at most, so this simplification is acceptable.

The actual segment attitude angles can then be taken directly from the elements of the attitude matrix A

$$A_{COM} = \begin{bmatrix} a_{11} & a_{12} & a_{13} \\ a_{21} & a_{22} & a_{23} \\ a_{31} & a_{32} & a_{33} \end{bmatrix} \tag{J.26}$$

with

$$\theta_{x,COM} = a_{23} \tag{J.27}$$
$$\theta_{y,COM} = a_{31} \tag{J.28}$$
$$\theta_{z,COM} = a_{12} \tag{J.29}$$

J.3.2. Actual Mirror Pose

SPACAR directly reports the actual position of the mirror segment after the motion with ${}^{\mathbf{M}}\mathbf{r}_{\mathbf{COM}}$. Thus the actual pose of the mirror is

$${}^{\mathbf{M}}\tau_{\mathbf{COM}} = \left\{ {}^{\mathbf{M}}\mathbf{r}_{\mathbf{COM}}{}^{T}, \theta_{x,COM}, \theta_{y,COM}, \theta_{z,COM} \right\} \tag{J.30}$$

J.4. Moving Frame Pose

The ideal, expected and actual moving frame poses are found with the same method described for the mirror segment above. Here, the only difference between the ideal and expected poses of the moving frame are the presence (or not) of fabrication and assembly errors. In the current *SPACAR* simulations, they are equal,

$${}^{\mathbf{M}}\tau^{*}_{\mathbf{MF}} = \left\{ {}^{\mathbf{M}}\mathbf{r}^{*}_{\mathbf{MF}}{}^{T}, \theta^{*}_{x}, \theta^{*}_{y}, 0 \right\} \tag{J.31}$$
$${}^{\mathbf{M}}\overline{\tau}_{\mathbf{MF}} = {}^{\mathbf{M}}\tau^{*}_{\mathbf{MF}} \tag{J.32}$$
$${}^{\mathbf{M}}\tau_{\mathbf{MF}} = \left\{ {}^{\mathbf{M}}\mathbf{r}_{\mathbf{MF}}{}^{T}, \theta_{x,MF}, \theta_{y,MF}, \theta_{z,MF} \right\} \tag{J.33}$$

where ${}^{\mathbf{M}}\mathbf{r}_{\mathbf{MF}}$ is reported explicitly by *SPACAR* at the end of the run and the actual moving frame attitude angles are calculated using the TRIAD method from the position vectors ${}^{\mathbf{M}}\mathbf{r}_{\mathbf{MF,x}}$ and ${}^{\mathbf{M}}\mathbf{r}_{\mathbf{MF,y}}$, also reported by *SPACAR*.

J.5. Pose Errors

Finally, the errors in the moving frame and segment poses can be calculated trivially via

$$\mathbf{e}_{\mathbf{COM,T}} = {}^{\mathbf{M}}\tau_{\mathbf{COM}} - {}^{\mathbf{M}}\tau^{*}_{\mathbf{COM}} \tag{J.34}$$
$$\mathbf{e}_{\mathbf{COM,RC}} = {}^{\mathbf{M}}\overline{\tau}_{\mathbf{COM}} - {}^{\mathbf{M}}\tau^{*}_{\mathbf{COM}} \tag{J.35}$$
$$\therefore \mathbf{e}_{\mathbf{COM,P}} = {}^{\mathbf{M}}\tau_{\mathbf{COM}} - {}^{\mathbf{M}}\overline{\tau}_{\mathbf{COM}} \tag{J.36}$$

Since the ideal and expected poses of the moving frame are identical in the current *SPACAR* model, the total error is assumed to be composed of only parasitic errors,

$$\mathbf{e}_{\mathbf{MF,P}} = {}^{\mathbf{M}}\tau_{\mathbf{MF}} - {}^{\mathbf{M}}\overline{\tau}_{\mathbf{MF}} \tag{J.37}$$

K

Material Properties

Table K.1: Thermo-physical material properties. Values have generally been taken from [126] first. Where a range was found, values closest to those stated in either [103] or [57] have been used. Specific heat capacity for Al6061 was used for Al7075. value for yield strength of 304SS in [126] is extremely high. Value from [26] taken. ρ - Density; E - Young's Modulus; ν - Poisson's Ratio; S_Y - Yield Strength; α - Coefficient of Thermal Expansion; k - Thermal Conductivity; c_p - Specific Heat Capacity; κ - Electrical Conductivity.

	ρ $[kg/m^3]$	**E** $[GPa]$	ν $[nd]$	$\mathbf{S_Y}$ $[MPa]$	α $[\times 10^{-6}/K]$	**k** $[W/m.K]$	$\mathbf{c_p}$ $[J/kgK]$	κ $[\Omega.m]$	**Reference**
BOOSTEC SiC	3150	420	0.17	400	2.2	180.0	-	10^5	[21]
Aluminium 6061	2680	68	0.33	276	23.6	167.0	896	-	[126, p.146], [57]
Aluminium 7075	2790	72	0.33	503	23.4	142.0	896	-	[126, p.146], [103]
Beryllium I-70	1850	303	0.08	350	11.3	194.0	1900	-	[126, p.146], [57]
Beryllium-Copper	8250	127	0.35	1340	17.8	100.0	380	-	[126, p.146], [57]
Invar-36	8050	141	0.26	276	1.26	10.4	460	-	[126, p.146], [57]
Magnesium AZ31B	1770	45	0.35	255	25.2	97.0	1000	-	[126, p.146], [57]
304 Stainless Steel	8000	193	0.27	276	14.7	16.2	500	-	[126, p.146], [57], [26]
Titanium-6Al-4V	4400	115	0.33	1060	10.0	7.2	565	-	[126, p.146], [57]